Advanced
Polymeric Materials

Structure Property Relationships

Advanced Polymeric Materials

Structure Property Relationships

Edited by
Gabriel O. Shonaike
Suresh G. Advani

CRC PRESS

Boca Raton   London   New York   Washington, D.C.

Visit the CRC Press Web site at www.crcpress.com

Preface

A book on advanced polymeric materials could not possibly be written by the two editors alone. The areas that we have covered here are currently undergoing explosive growth, and it is imperative that these topics be addressed by scientists at the vanguard of their specialties. Therefore, *Advanced Polymeric Materials: Structure Property Relationships* is presented as a contributed volume and has been segmented into four major sections: fiber-reinforced composites, nanocomposites, polymer blends, and bioengineering. It contains fourteen chapters written by polymer researchers and scientists from various laboratories worldwide.

The bioengineering section covers a wide range focusing on the application of both synthetic polymers such as poly(α-hydroxyesters) poly(anhydrides) in tissue engineering and drug delivery. Polymerization, structure, and properties and applicability of the polymers are discussed in detail. The book also addresses the recent advances in nano materials which have led to the development of nano-structured biomaterials for tissue engineering. The increasing demand for absorbable biodegradable polymeric materials for biomedicine where the material absorbs *in vivo* but degrades *in vitro* is well explained via mechanisms which may be enzymatic and/or hydrolytic.

One of the major problems associated with thermoset composites, and particularly vinyl ester resin composites, is their brittle behavior. The book explains how to overcome this problem through the use of pre-formed core-shell rubber particles produced through emulsion polymerization. The dependency of mechanical, thermal, physical, and chemical properties on copolymer composition and degree of cross-linking of IPN-like systems made of LDPE and vinyl polymers are fully analyzed.

Advanced Polymeric Materials: Structure Property Relationships also discusses the recent advances in barrier polymers, which are increasingly in demand and are replacing the traditional materials in the packaging, medical, and automotive industries. The success of these materials based on their properties and processing techniques, including multi-layered structures, are well documented.

Fiber-reinforced composites, which are still in great demand, especially in aerospace application, are examined. Various processing techniques — particularly close mold and manufacturing of Z-pinned composites — along with the design optimization are discussed to accentuate their versatility. A review of nanotechnology is presented, with chapters on carbon nanotubes and their properties, and also on nanocomposites based on clay.

Advanced Polymeric Materials: Structure Property Relationships addresses the issues, characterization, durability, processing, and properties of advanced polymeric materials in various applications.

Editors

Gabriel O. Shonaike is a consultant associated with Borden Chemical Inc., Oilfield Products Research Laboratory, Houston, Texas. He earned his master's degree at the University of Strathclyde, Glasgow, Scotland. A three-year research led to the award of a Ph.D. in materials science at the University of London in 1986.

Dr. Shonaike has worked in both academia and private industry, lecturing at institutions in three countries. He has been an advisor at Nippon Gohsei, Japan, and has worked as a senior scientist at Noltex LLC, Houston, and Borden Chemical. He also worked at Omron Corporation, Kyoto. He has taught at Kyoto Institute of Technology, Kyoto, University Sains, Malaysia, and Himeji Institute of Technology, Japan. Dr. Shonaike is the author or coauthor of over 100 research papers and book chapters in the areas of polymer blends and composites. He also co-edited the book *Polymer Blends and Alloys* (Mercel Dekker, N.Y., 1999).

Dr. Shonaike is a chartered engineer (Engineering Council, UK) and member of various professional institutions, including the Institute of Materials (UK), the Textile Institute (UK), and the Society of Plastics Engineers (USA). His research activities include studies on deformation of polymeric materials, structure–property relationship, fabrication and characterization of mechanical properties of thermoplastic composites, polymer blends, and coatings.

Suresh G. Advani is a professor in the Mechanical Engineering Department and associate director of the Center for Composite Materials at the University of Delaware. He received his B. Tech. Degree in mechanical engineering from the Idian Institute of Technology, Bombay in 1982 and his Ph.D. in mechanical engineering from University of Illinois at Urbana–Champaign in 1987. His research interests are in rheology; fluid mechanics and heat transfer as applied to manufacturing processes especially for polymers, nano composites, and polymer composite processing. He has co-authored over 200 journal and conference proceedings articles and has contributed chapters to and co-edited over 20 books. He has also co-authored a recent text, *Process Modeling in Composites Manufacturing (Manufacturing Engineering and Materials Processing, 59)* (Marcel Dekker, 2002). Advani is a Fellow of the American Society of Mechanical Engineers and was recently appointed as the North American editor for the journal *Composites A: Applied Science and Manufacturing*. Professor Advani also serves on the Scientific Advisory Committee of the *Journal of Forming Processes* and the International Conference on Flow Processes in Composites Manufacturing. He is a member of Amer-

ican Society of Mechanical Engineers, Society of Plastic Engineers, Society of Rheology, and Society for Advancement of Materials and Processes.

Contributors

Sarp Adali   School of Mechanical Engineering, University of Natal, Durban, South Africa

Suresh G. Advani   Department of Mechanical Engineering, University of Delaware, Newark, Delaware

Abdellatif Ait-Kadi   Department of Chemical Engineering, École Polytechnique of Montreal, Montreal, Canada

Vincenza Antonucci   Department of Materials and Production Engineering, University of Naples, Naples, Italy

Andre Benard   Department of Mechanical Engineering, Michigan State University, East Lansing, Michigan

Tony Bonnington   Aztex Inc., Waltham, Massachusetts

Peter J. Burchill   DSTO, AMRL, Melbourne, Australia

Karen J.L. Burg   Clemson University, Clemson, South Carolina

Kathleen A. Carrado   Chemistry Division, Argonne National Laboratory, Argonne, Illinois

Denis D.R. Cartié   Advanced Materials Department, Cranfield University, Cranfield, Befordshire, England

Wayne D. Cook   School of Physics and Materials Engineering, Monash University, Clayton, Australia

Roberto Greco   Institute of Chemistry and Technology of Polymers, Comprensorio Olivetti, Pozzuoli, Italy

Miroslav Grmela   Department of Chemical Engineering, École Polytechnique of Montreal, Montreal, Quebec, Canada

Rakesh K. Gupta   Department of Chemical Engineering, West Virginia University, Morgantown, West Virginia

Kuang-Ting Hsiao   Department of Materials and Production Engineering, University of Naples, Naples, Italy

Dhirendra S. Katti   Center for Advanced Biomaterials and Tissue Engineering, Department of Chemical Engineering, Drexel University, Philadelphia, Pennsylvania

Cato T. Laurencin   Center for Advanced Biomaterials and Tissue Engineering, Department of Chemical Engineering, Drexel University, Philadelphia, Pennsylvania

Yiu-Wing Mai   School of Aerospace, Mechanical and Mechatronic Engineering, University of Sydney, Sydney, Australia

Ivana K. Partridge   School of Industrial and Manufacturing Science, Cranfield University, Cranfield, Befordshire, England

Karen N. Roberts   School of Physics and Materials Engineering, Monash University, Clayton, Australia

Gabriel O. Shonaike   Borden Chemical, Inc., Houston, Texas

George P. Simon   School of Physics and Materials Engineering, Monash University, Clayton, Australia

John Summerscales   Department of Mechanical and Marine Engineering, University of Plymouth, Plymouth, United Kingdom

Haipeng Wang   School of Physics and Materials Engineering, Monash University, Clayton, Australia

Shing-Chung Wong   Department of Mechanical Engineering and Applied Mechanics, North Dakota State University, Fargo, North Dakota

Vladimir Zmievski   Department of Chemical Engineering, École Polytechnique of Montreal, Montreal, Quebec, Canada

Acknowledgments

We would like to thank all the authors for the timely delivery of their chapters and all the reviewers who were able to make critical suggestions to revise the chapters. Finally, many thanks to Amy Rodriguez and Jamie Sigal, who have done an excellent job of helping us with the technical editing of this volume, and Susan Farmer for keeping us on track.

<div align="right">

Gabriel O. Shonaike
Suresh G. Advani

</div>

Contents

Dedication

To my parents, Kamla and Gopaldas Advani, my brother, Dr. Devidas Advani,

and my family, Yolanda, Machu, and Diana.

S. Advani

To my parents, Edward and Comfort Shonaike and my family, Garrett,

Kennett, Amy, and Victoria.

G.O. Shonaike

1

Design Optimization of Composite Laminates under Deterministic and Uncertain Conditions

Sarp Adali

CONTENTS

Abstract

The issues, problems, and techniques concerning the optimization of composite structures are discussed, and specific cases of design optimization are presented. Section 1.1 serves as a general introduction to issues involving the optimization of composites with particular emphasis on objectives, methods of optimization, design guidelines, design variables, and problem complexities. Section 1.2 presents results involving the stiffness and strength optimization of composites and the relevant techniques. Section 1.3 is devoted to the discussion of complicating effects such as thermal loads, stiffeners, and multiple objectives in the buckling and postbuckling optimization of composites. The results for Section 1.2 and Section 1.3 involve optimization under deterministic design conditions with the main ideas illustrated using specific examples. The design uncertainties are the subject of the last section, where design techniques such as convex modeling and anti-optimization are illustrated again by means of specific examples and applied to the optimization of composites subject to uncertain material, load, and geometric data. In the references, emphasis is given to the recent results, and more than 150 references are provided on the above subjects.

1.1 Introduction

1.1.1 Design Optimization

Optimization of a design to achieve superior performance is a natural extension of the basic design process that aims at determining the geometry, material properties, and proportions of a structure to satisfy a set of requirements, usually referred to as design specifications. In general, these require-

ments can be met using a variety of design options with regard to shape, dimension, and materials; i.e., the solution is far from being unique, hence the phase of concept generation in the design process. The next steps of this process involve evaluation and selection to reduce the possible choices to a few before a final decision can be made, usually based on several other considerations such as manufacturability, cost, aesthetics, resources, etc. Optimizing the design adds another dimension to the design process and could be viewed as an inverse problem, compared to *analysis*, which provides the solution for a given design as opposed to providing the best solution to an initially unknown design, as is the case with optimization. It is an essential step in a design methodology that can take the design to a higher level of performance by introducing the idea of "best" into the process, with "the best" defined according to the dictates of the design goal.

As *product competitiveness* became a catchword in today's global markets and survival of a company very much depended on its ability to introduce timely, cost-effective, and superior products into the market place, design optimization became an integral and necessary part of the product design cycle in an effort to achieve an advantage over the competitive products. The need to produce superior products is becoming more and more vital, partly due to market pressures and partly due to the requirements of high-tech applications arising in diverse fields such as aerospace, electronics, biomechanics, and materials. This trend can only be expected to strengthen and spread as technology, globalization, and competitiveness take hold in every facet of life from product design to consumer satisfaction.

Interestingly enough, design optimization with its vital importance in today's technological world is by no means a modern problem. As far back as 1638, Galilei studied the optimal cantilever problem and found that a parabolic height function produces the minimum weight design for a tip-loaded, constant-width cantilever (Maute et al., 1999). As this result was obtained before the theories of beams and elasticity were developed, it is all the more remarkable. Although some optimization problems such as the cantilever one can be solved analytically, this, in fact, is possible only in the case of fairly simple problems; more complicated ones require the use of numerical techniques at both the analysis and optimization stages.

1.1.2   Optimization of Composites

Nowadays optimization is used in every field of technology in order to achieve superior results, and composites are naturally no exception. However, it should be noted that in the case of composites, optimization is a necessary tool not only to realize their full potential and improve the structural performance, but also to avoid designs that could produce a worst-case scenario due to the directional nature of the material, i.e., *anisotropy*, which is what makes the field of composites not only a challenging one in terms of design complications, but also a rewarding one in terms of improvements

that can be achieved by the judicious use of available design variables. This property contrasts sharply with that of the conventional materials, the defining characteristic of which is *isotropy*. This property alone, i.e., anisotropy, leads to a situation in which the full potential of composites can be realized only by optimization, which in turn brings out the natural superiority of fiber composites against isotropic materials.

Another distinguishing characteristic of the composites is their constitution, which is obtained by combining one or more strong materials (fibers) with a weaker material (matrix). These and other properties such as layered structure, stacking sequence, and residual stresses create a design space that cannot be matched in versatility by any other material. However, for optimization purposes the most effective and widely used design property is anisotropy, which can be employed very effectively and efficiently to produce designs having properties that are beyond the reach of ordinary materials. Anisotropy in practice translates into fiber orientation and stacking sequence design, the optimization of which yields the so-called *tailor-made* materials. These tailoring capabilities in turn lead to structures that are a few of the intrinsic properties of composites. Design optimization is an essential tool to take full advantage of and bring out the natural potential of fiber composites. Alternatively, not optimizing a composites design is likely to lead to a severe underperformance compared to what could be achieved by optimization using so many design variables. Books that deal specifically with the optimization of composites include those by Gürdal et al. (1991, 1999) and Vasiliev and Gürdal (1999). Books by Tsai (1988, 1992), Barbero (1999), Berthelot (1999), and Jones (1999) have sections devoted to the design and optimization of composites. Practical applications of composites design optimization are given for automotive roofs (Botkin, 2000), torque wrenches (Chang, 2001), rings for energy storage (Ha et al., 1998), magnet rotors (Ha et al., 1999), leaf springs (Yu and Kim, 1998; Rajendran and Vijayarangan, 2001), and level gears (Vijayarangan and Ganesan, 1994).

A partial list of optimization objectives, design constraints, and recommendations on materials and construction is given in Table 1.1.

1.1.3   Methods of Composite Optimization

The optimization process seeks to find the values of design variables that give the extremum (minimum or maximum) value of an objective function without violating any of the constraints. This can be achieved by any number of mathematical techniques, which can be classified as:

- Mathematical programming techniques
- Optimality criteria methods
- Evolutionary algorithms

TABLE 1.1

Design Optimization Objectives, Constraints, and Recommendations

Optimize	Objectives	Constraints	Recommended Materials and Construction
Stiffness	Minimum deflection Maximum stiffness coefficients	Thickness Weight Strength	Fiber: high stiffness Construction: sandwich or hybrid
Weight	Minimum weight Minimum thickness	Stiffness Strength Buckling load Vibration frequency Dimensional stability	Fiber: high specific stiffness high specific strength Construction: sandwich or hybrid
Strength	Maximum load-carrying capacity Minimum failure index	Weight Thickness Stiffness Buckling load	Fiber: high-strength woven fabric high interlaminar strength Construction: fibers oriented in the load directions
Buckling/ postbuckling load	Maximum buckling load Maximum postbuckling load	Weight Thickness Strength	Fiber: high stiffness high strength Construction: sandwich or hybrid
Vibration frequency	Maximum fundamental frequency Maximum higher-order frequencies Maximum frequency separations	Weight Thickness	Fiber: high specific stiffness Construction: Sandwich or hybrid
Dimensional stability	Minimum thermal expansion coefficient Minimum moisture expansion coefficient	Weight Strength	Fiber: low coefficient of thermal/moisture expansion, anisotropic fibers Construction: hygrothermo elastic isotropy
Vibration damping	Maximum structural damping	Weight Thickness Vibration frequency	Matrix: ductile Construction: viscoelastic layers
Damage tolerance	Maximum impact resistance Maximum resistance to crack growth Maximum compressive strength after impact	Weight Thickness Strength Stiffness	Matrix: tough resins thermoplastic polymers Construction: interleaving

There exist other optimization techniques that have various degrees of rigor and efficiency, but nevertheless produce optimum or near-optimum solutions. In all cases, the optimization process synthesizes the input data given in terms of materials, geometry, and loading with the free parameters (design variables) to produce an optimum solution via a mathematical

technique. However, it should be stated from the outset that optimization results should be tempered with sound engineering judgment and intuition to produce a viable solution that can be implemented taking cost, safety, and manufacturing issues into account (Cohn, 1994). A short discussion of various optimization techniques follows.

1.1.3.1 Mathematical Programming Techniques

Mathematical programming (MP) is a direct method of optimization and has been used extensively since the 1960s in structural optimization (Schmit, 1981), as well as for composites optimization. These techniques and their engineering applications have been covered in numerous books, including those by Kirsch (1981, 1993), Vanderplaats (1984), Arora (1989), Borkowskii and Jendo (1990), and Haftka et al. (1990), which also includes a section on the optimization of laminated composites. Although quite powerful, MP runs into convergence and computational efficiency problems when the number of design variables becomes large.

1.1.3.2 Optimality Criteria Methods

Optimality criteria methods (OCM) are indirect methods of optimization and formulate an inverse problem, the solution of which yields the optimum and can be computed without the use of MP techniques. Optimality criteria take advantage of the specific characteristics of the physical problem and are more computationally efficient than MP, but these methods are of a more limited nature, as they take generality. This approach has also been studied in several books, including those by Save and Prager (1985), Rozvany (1989), Arora (1989), Haftka et al. (1990), and Haftka and Gürdal (1993). The combination of MP and OCM and the exploitation of duality between them led to the development of techniques that combined the advantages of both methods (Schmit and Fleury, 1980; Fleury and Braibart, 1985).

1.1.3.3 Evolutionary Algorithms

Evolutionary algorithms (EAs) are based on the biological principles of evolution and, in particular, the Darwinian theory of survival of the fittest; for this reason, they are usually referred to as genetic algorithms (GAs). GAs became a widely used composites optimization technique in the last decade due to a mainly exponential increase in computational power and their advantages over other methods, such as robustness and simplicity. They search from a population of design points, use only function values without derivative information, and any design variable, material selection, stacking sequence, etc., can be coded in terms of binary or decimal integer numbers.

Presently GAs are applied to a vast number of optimal design problems involving laminated composites. The early examples of composites optimization using GAs include those by Callahan and Weeks (1992), LeRiche and

Haftka (1993), Hajela and Erisman (1993), Nagendra et al. (1993), Ball et al. (1993), Gürdal et al. (1994), and Kogisa et al. (1994a, 1994b). More recent applications of GAs to composites optimization include the works by McMahon et al. (1998), Sivakumar et al. (1998), Todoroki and Haftka (1998), Liu et al. (1998, 2000), Todoroki and Sasai (1999), Autio (2000, 2001), and Soremekun et al. (2001). The details of the technique can be found in books such as those by Goldberg (1989), Bäck (1996), and Blachut and Eschenauer (2001); and its applications to composites can be found in Gürdal et al. (1999).

There exist other techniques that cannot be included in any of the above categories of optimization. Some of these techniques are discussed below.

1.1.3.4   Knowledge-Based Expert Systems

Expert systems (ESs) enable the designer to use the accumulated knowledge in composites design in an effective manner by incorporating this knowledge in an ES shell. Such a system can come up with alternative designs when the analysis indicates a shortcoming and provide assessment of competing designs, leading to a more informed design decision. The key to the development of an expert system is a set of design rules that it can use to make decisions. These rules are usually termed design heuristics and are often based on rules of thumb obtained through experience and trial and error, which leads to human expertise. An expert system can harness this body of knowledge and use it in an effective manner. One of the first applications of an ES to composites design was made by Pecora et al. (1985) and Zumsteg et al. (1985). Subsequently, Allen and Bose (1987) developed a knowledge-based software for preliminary composites design. In a series of papers, Webber and Morton (1990), Wu et al. (1991), and Morton and Webber (1990, 1991, 1993, 1994) developed a composites design expert system and applied it to the design of laminated plates and columns. Other studies using ESs in composites design include those by Miki and Sugiyama (1990), Wu (1992), Kim and Hong (1992), and Todoroki et al. (1996). More recently, Kim et al. (1998a, 1998b, 1999a, 1999b, 2000) developed a knowledge-based ES for the strength optimization of laminated composites using GAs as the optimization tool. Several rules of design heuristics were incorporated into the ES shell as constraints, and the designs were confined to a population of symmetric, balanced laminates with $0°$, $\pm45°$, and $90°$ ply angles, with $\pm45°$ plies grouped together to reduce bending–twisting coupling. In essence, the design rules are used to optimize the structure in the sense that the satisfaction of these rules leads to a better design, not in the sense of minimizing or maximizing an objective function, but improving the design mostly in a practical sense, which is what really counts most at the end of a design cycle. As such rules should ideally be part of any design optimization process, an example of these rules as used for improvement of the strength is given here as they are stated in Kim et al. (1999a):

1. Homogeneous lay-ups are recommended for strength-controlled design. Heterogeneous laminate should be evaded for strength-

critical designs. In the case where heterogeneous laminates cannot be evaded, it is generally best to stack primary load-carrying plies toward the laminate core (*Military Handbook 17*, 1996).

2. Minimize groupings of plies with same orientations to create a more homogeneous laminate and to minimize interlaminar stress and matrix cracking during the service period. If plies must be grouped, prevent grouping more than four plies of the same orientation (*Military Handbook 17*, 1996).

3. Avoid grouping of 90° plies and separate 90° plies by a 0° or 45° ply to minimize interlaminar shear and normal stress (*Military Handbook 17*, 1996; *Composite Design Manual*; *Northrop Composite Design Manual*).

4. Separate ±° plies to reduce interlaminar shear stress (*Military Handbook 17*, 1996; *Composite Design Manual*; *Northrop Composite Design Manual*).

5. Shield primary load-carrying plies by positioning inside of laminate to increase tensile strength and buckling resistance (*Military Handbook 17*, 1996; *Composite Design Manual*; *Northrop Composite Design Manual*).

6. To avoid large-scale matrix cracking and delamination, the ply angle difference between the adjacent plies must not exceed 45° (Todoroki et al., 1996).

7. Avoid positioning tape plies with fibers oriented perpendicular to a free edge at the laminate midplane to lessen high interlaminar stress at free edges (*Military Handbook 17*, 1996; *Composite Design Manual*; *Northrop Composite Design Manual*; Kim and Hong, 1992).

8. If tape plies with fibers oriented perpendicular to a free edge should be stacked at midplane, stack no more than approximately three plies (*Military Handbook 17*, 1996).

9. When there exists a hole, avoid locating tape plies with fibers oriented perpendicular to loading direction at the laminate midplane to lessen high interlaminar stress around a hole (Rybicki and Schmueser, 1978).

These rules in combination with GAs were applied to the strength optimization of laminated composites under uniform transverse loading by minimizing the Tsai–Hill failure criterion. Comparison of results with a quasi-isotropic lay-up of $(0_2/45_2/90_2/{-}45_2)_s$ indicates that the objective function is reduced by as much as 50% (simply supported) and 66% (clamped) for square laminates, with the corresponding figures being 80 and 88% for laminates with an aspect ratio of 2 (Kim et al., 1999a). Application of the procedure to a square laminate with a circular hole produced similar reductions in the objective function. However, the existence of curved free edges necessitated different rules of design heuristics compared to the previous cases. The same authors applied the expert system–GA approach to the

weight minimization of tapered laminates subject to a strength constraint by using the location of ply-drops as design variables in addition to ply angles (Kim et al., 1999b).

1.1.3.5 Artificial Neural Networks

The main advantage of the artificial neural network (ANN) approach to optimization is that a neural network can train itself to work toward an optimal solution as opposed to implementing a well-defined procedure to obtain the solution using conventional optimization algorithms. The ANN approach is based on imitating the functions of a human brain explained by means of the brain theory. In essence, an ANN is a very large parallel network system arranged such that it can closely imitate the mechanics of a brain. One of the important functions of the brain that ANN imitates is the learning process, which enables the ANN to use example problems and their solutions to learn the basic solution procedure and apply it to solve similar problems. As a result of ANN's effective capabilities in solving complex problems, it is being used in several branches of science and engineering, and composite optimization is another area of application that has been explored in recent studies (Berke et al., 1993; Jayatheertha et al., 1996; Kodiyalam and Guru- moorthy, 1996; Chen et al., 1999).

Different methods can be adopted to train the neurons to solve an optimi- zation problem. Jayatheertha et al. (1996) used a statistical training method that is called simulated annealing because it resembles the annealing of metals and is based on reducing the weights between the neurons as the process converges toward an optimum. This technique was applied to the minimum weight design of a laminated plate subject to strength and stiffness constraints using the layer thicknesses as the design variables (Jayatheertha et al., 1996).

The first example involved a $(0/90/\pm45)_s$ laminate subject to a shear load with constraints on A_{11}, A_{22}, and strains; the second and third, a normal load with a lower bound on A_{66} with $(0/90/\pm45)_s$ laminations. Comparison of numerical results with the analytical solutions showed a good agreement, indicating the potential application of the technique to more complex opti- mization problems. An overview of the subject as applied to structural optimization was given by Hajela and Berke (1992).

1.1.3.6 Carpet Plots

Graphical representations of the stiffness and strength properties of a lami- nate provide invaluable visual tools to design and optimize the lay-up con- figurations of composites. In many applications it is common practice to restrict the ply orientations to 0°, ±45°, and 90° angles. Then plots can be generated for a given laminate property such as apparent moduli or failure load in terms of the percentages of various ply angles. These plots can then be used to determine the ply combinations that will produce the desired

property, and several of these plots can be employed simultaneously to ensure that the design constraints are also satisfied. A typical example would involve symmetric laminates of $(0_m/90_n/\pm45_p)_s$ configuration, which can be normalized with respect to the total number of plies by defining

$$\alpha = 2m/K, \quad \beta = 2n/K, \quad \gamma = 4p/K$$

where $K = 2(m + n + 2p)$ with $\alpha + \beta + \gamma = 1$, resulting in $(0/90/\pm45_\gamma)_s$ configurations. Examples of carpet plots for various elastic moduli can be found in Tsai (1988), Ashbee (1989), Gibson (1994), Daniel and Ishai (1994), and Barbero (1999). The last two references also provide carpet plots for strength. A preliminary design process using carpet plots for a laminate with thickness H and stiffnesses A_{ij} would first determine the value of the required property, say, in-plane E_x, given by

$$E_x = A_{11}A_{22} - A_{12}^2 /A_{22}H$$

by choosing the suitable α, β, and γ values; several combinations of ply angles give the same value of E_x, providing several design options. The constraints on other material properties can be checked using similar plots, and the procedure of using the plots iteratively may be employed to select a satisfying ply combination that would necessarily be a compromise solution. Once the lay-up design is selected, the total laminate thickness can be determined on the basis of strength, buckling load, or any other requirement. Examples of the design procedure using carpet plots can be found in Barbero (1999).

1.1.4 Fiber Composite Decision and Design Variables

A designer can tailor composite materials in order to optimize the structure with respect to given design objectives by utilizing a number of decision and design variables. Decision variables refer to the specific choices involving the type of material, laminate construction, joints, etc., and quite often are specified as part of the design process, rather than as part of the optimization process, based on considerations of cost, manufacturing techniques, end use, fiber–matrix interface, damage tolerance, etc. Design variables refer to the specific values involving the amount and orientation of fibers, layer thicknesses, locations of supports, etc. These variables can be classified in terms of material, configuration, and geometry and are discussed next.

1.1.4.1   Material-Related Variables

Material-related variables can be discrete decision or continuous design variables. The decision ones refer to the actual material and can be classified as follows:

- Fiber material
- Fiber pattern
  - Continuous fibers
    - Unidirectional
    - Biaxial
    - Woven fabric
  - Discontinuous fibers
    - Randomly oriented
    - Preferred orientation
- Matrix material
  - Polymer
    - Thermosets
    - Thermoplastics
  - Metal
  - Carbon
  - Ceramic

Continuous design variables include the following:

- Fiber volume content
- Concentration of fibers with respect to location

1.1.4.2 Configuration-Related Variables

Configuration-related decision variables involve selection of the type of lamination, viz.:

- Nonhybrid laminate
- Hybrid laminate
- Sandwich structure

Configuration-related design variables are the ones most used in the optimization process and include:

- Fiber orientation
- Stacking sequence
- Layer thicknesses

1.1.4.3 Geometric Design Variables

Geometric decision variables include:

- Locations and type of joints
- Form of the centerline or the midsurface (e.g., cylindrical, spherical, or parabolical shells, etc.)
- Cross-sectional shape (e.g., I beam, L beam, etc.)

Geometric design variables refer to the overall structure and include:

- Cross-sectional dimensions
- Locations of supports

1.1.5   Design and Optimization Issues

In designing composites or, more accurately, in optimization of composites, one also encounters several issues that have to be dealt with and overcome in order to produce a practical structure that can be manufactured and maintained in a cost-effective manner. For this purpose, the industry adopted Integrated Product and Process Development methods (Kedward, 1997), which are, in fact, applicable to any design problem. These methods were developed basically to deal with considerable design complications that can arise with fiber composite materials, with optimization adding another dimension to these complications by virtue of extensive computational time and the need for design practicality.

One complication in composite design is the very large number of possible combinations of fiber orientations and stacking sequences, making the optimization process a particularly difficult one (computational time). The final design should be easy and inexpensive to manufacture, avoiding fiber and ply discontinuities (design practicality). However, if the design space is restricted too much in an effort to simplify the problem and achieve manufacturability, the potential offered by fiber composites ends up being diluted and the advantages not fully utilized (Manne and Tsai, 1998a). There are several ways of dealing with design complexity in an optimization process that may become unduly elaborate in the absence of any simplifying restrictions. A careful look at the complexity indicates that it can be classified as:

- Modeling complexity
- Analysis complexity
- Optimization complexity

as suggested by Venkataraman and Haftka (1999). Each type of complexity needs to be dealt with using conceptual and engineering tools, which are discussed next.

1.1.5.1   Modeling Complexity

Modeling complexity (MD) refers to the level of complexity employed in modeling a structure that could be a certain type of laminate, a stiffened panel, a segmented plate, or a grid shell, to give a few examples. A stiffened panel may be, for example, modeled using smeared properties to reduce the level of MC. As the laminates are the primary focus in the present study, a brief outline of modeling issues with a view toward reducing MD in a laminate design is given next.

1.1.5.1.1 Lamination Types and Restrictions

Three of the most common restrictions on laminate design are symmetry, balance, and the use of a limited number of discrete ply angles, such as 0°, ±45°, and 90°, which can be distributed symmetrically with respect to mid-plane with the same numbers of +45° and –45° plies used in the design (balance).

Symmetric laminates offer the following advantages:

- No bending–twisting coupling
- No warpage due to hygrothermal effects
- Simplified analysis due to uncoupling of forces and curvatures, and moments and strains

as noted by Manne and Tsai (1998a). Various ways of restricting the laminate configurations include:

- Balanced laminate: contains equal numbers of same positive and negative ply angles.
- Fully populated laminate: does not contain less than 10% of any one orientation by thickness.
- Fully populated and balanced laminate: satisfy both of the above restrictions.
- Three-angle laminate: contain at least three different ply orientations.
- Quasi-isotropic laminate: have identical in-plane stiffnesses in all directions with zero shear coupling coefficients.

Although restricting the design to one of the above types simplifies the optimization problem, there is a downside to this practice; namely, the trade-off results in an increase in the weight of the structure. The weight penalty relative to an unrestricted optimization may range from 15–20% for balanced laminates, to 300% for three-angle laminates, up to more than 400% for fully populated and balanced laminates, and even to higher weight penalties depending on the applied load configurations (Manne and Tsai, 1998a).

Instead of specifying the laminate types as above at the outset, the design can also be based on the type of coupling that needs to be avoided as the specific application requires. In this case, the unwanted coupling determines the laminate class, and optimization can be performed within that class. Next, various types of couplings and the laminate types eliminating these couplings are discussed (Kedward, 2001):

- Extension–shear coupling: Using an equal number of positive and negative fiber orientations in the stacking sequence, resulting in a balanced laminate, eliminates this coupling. Using a cross-ply lay-up also eliminates this coupling.
- Extension–torsion coupling: Use of a symmetric lay-up eliminates this coupling.
- Extension–bending coupling due to B_{11}, B_{12}, and B_{22}: Use of a four-layer or a three-layer symmetric cross-ply laminate, i.e., $(0°/90°)_s$ or $(0°/90°/0°)$, eliminates this coupling.
- Bending–twisting coupling due to D_{16} and D_{26}: The use of an anti-symmetric or cross-ply lay-up eliminates this coupling. In the case of symmetric laminates that exhibit this coupling, D_{16} and D_{26} can be reduced substantially by using a $[(\theta/-\theta)_n]_s$ configuration with n as large as possible since D_{16} and D_{26} go to zero as n goes to infinity.

Further discussions of coupling can be found in Kedward (2001) and Hyer (1998).

1.1.5.2 Analysis Complexity

Analysis complexity (AC) refers to the constitutive and geometric properties used in the structural analysis, with linear elastic analysis being the simplest case. The level of complexity will increase as plastic, nonlinear, and probabilistic effects are taken into account. The type of analysis also has increasing levels of complexity ranging from stress–strain to eigenvalue (buckling–vibration) analysis with postbuckling, hygrothermal effects and nonlinear deformations adding further levels of complexity. Under deterministic conditions, the analysis can be completed in one cycle. However, the presence of material, loading, and geometric uncertainties, such as data scatter, unknown magnitude of loads, and imperfections necessitates the use of probabilistic methods (reliability analysis, Monte Carlo simulations, etc.), which in general require several cycles of analysis for convergence, making the solution process computationally quite expensive. As the optimization itself is an iterative procedure, the level of complexity introduced at the analysis phase is multiplied several times to obtain an optimal solution.

1.1.5.3 Optimization Complexity

Optimization complexity (OC) refers to the type of optimization problem that may require complicated or relatively simple techniques for its solution. On one end of the scale are the optimization problems with few continuous design variables requiring a local solution. These problems can be solved using mathematical programming techniques (Vanderplaats, 1984). Problems with a large number of discrete design variables requiring global solutions constitute the other end of the scale and require integer programming techniques for their solution (Venkataraman and Haftka, 1999). Global solutions can be obtained using random search and stochastic methods, which increase the computational time substantially due to the large number of iterations needed for convergence. A promising approach was developed by Foldager et al. (1998) to impose convexity onto the design space by use of lamination parameters, thereby reducing the number of design variables.

Recent optimization techniques applied successfully to composite optimization problems include evolutionary algorithms such as the genetic algorithms and response surface (RS) methods. The advantages of GAs include the elimination of function differentiations, which reduce OC, as well as the generations of the several near-optimum solutions, which provide the designer with alternative configurations. RS methods are also instrumental in reducing OC by cutting down the number of function evaluations (Venkataraman and Haftka, 1999).

1.2 Stiffness and Strength Optimization of Laminates

1.2.1 Design of Laminates with Required Stiffness

There have been several approaches to this problem with the objective of achieving the required mechanical properties by stacking sequence design. The method proposed by Grediac (1999, 2000, 2001) in a series of papers produced such designs with the minimum number of plies. This procedure is outlined below. Let the normalized stiffness matrices be defined as

$$A^* = A/h, \quad B^* = 2B/h^2, \quad D^* = 12D/h^3 \tag{1.1}$$

where h is the total plate thickness. Using the invariants U_i, $i = 1, \ldots, 5$, and the lamination parameters $V_{j\alpha}, j = 1, \ldots, 4$, $\alpha = A, B, D, A^*, B^*$, and D^* can be expressed as

$$[A^*] = [U] + U_2 [V_{1A}] + U_3 [V_{2A}] \tag{1.2}$$

$$[B^*] = U_2[V_{1B}] + U_3[V_{2B}] \tag{1.3}$$

$$[D^*] = [U] + U_2[V_{1D}] + U_3[V_{2D}] \tag{1.4}$$

where

$$[U] = \begin{bmatrix} U_1 & U_4 & 0 \\ U_4 & U_1 & 0 \\ 0 & 0 & U_5 \end{bmatrix} \quad [V_{1\alpha}] = \begin{bmatrix} V_{1\alpha} & 0 & V_{3\alpha}/2 \\ 0 & -V_{1\alpha} & V_{3\alpha}/2 \\ V_{3\alpha}/2 & V_{3\alpha}/2 & 0 \end{bmatrix} \tag{1.5}$$

$$[V_{2\alpha}] = \begin{bmatrix} V_{2\alpha} & -V_{2\alpha} & V_{4\alpha} \\ -V_{2\alpha} & V_{2\alpha} & -V_{4\alpha} \\ V_{4\alpha} & -V_{4\alpha} & -V_{2\alpha} \end{bmatrix}$$

$$\left(V_{1\alpha}, V_{2\alpha}, V_{3\alpha}, V_{4\alpha}\right) = \sum_{i=1}^{n} w_{\alpha}(i)\left(\cos 2\theta_i, \cos 4\theta_i, \sin 2\theta_i, \sin 4\theta_i\right) \tag{1.6}$$

with $w_{\alpha}(i)$ defined as

$$w_A(i) = n_{-1}, \quad w_B(i) = n^{-2}\left[(i-n/2)^2 - (i-1-n/2)^2\right] \tag{1.7}$$

$$w_D(i) = 4n^{-3}\left[(i-n/2)^3 - (i-1-n/2)^3\right]$$

Let $[\theta_i]$ denote the laminate with the stacking sequence $(\theta_1/\theta_2/ \ldots /\theta_n)$. The problem of finding a design with the required stiffness can be stated as a minimization problem, viz.,

$$\min_{\substack{\theta_i}} \; F[\theta_i] \tag{1.8}$$

with $F[_i]$ defined as

$$F[\theta_i] = k_A \sum_{i=1}^{4}\left(V_{iA} - v_{iA}\right)^2 + k_B \sum_{i=1}^{4}\left(V_{iB} - v_{iB}\right)^2 + k_D \sum_{i=1}^{4}\left(V_{iD} - v_{iD}\right)^2 \tag{1.9}$$

where $k_{\alpha} > 0$ are weighting factors that can be used to emphasize in-plane, coupling, or bending properties, and $v_i\alpha$ are the required values of $V_i\alpha$. For $F[\theta_i] = 0$, the laminate possesses the assigned lamination parameters. In

general, $F[\theta_i] > 0$ and becomes smaller as the number of plies increases. Equation (1.8) can be solved by any optimization routine with $\theta_i \in [0, \pi]$. Results for $v_{i\alpha} = 0$, $\alpha = A, B, D$, are given in Grediac (1999) with $k_\alpha = 1$, and for $n = 7$, …, 18, taking AS4/3S01 graphite/epoxy as the fiber composite material.

For $n = 12$, the optimal stacking sequence is given by (0/59/107/129/50/130/178/78/179/21/69/128), which produces a laminate with A_{16}^*, A_{26}^*, B_{ij}^*, D_{16}^*, and D_{26}^* less than 0.12. Thus fairly small values of B_{ij}^* are achieved with a nonsymmetric configuration. Results obtained in Grediac (1999) are compared with those given in Jones (1975), Wu and Avery (1992), Fukunaga (1990), Kandil and Verchery (1988), and Paradies (1996), who determined the stacking sequences for various cases of isotropy that required 16 or more plies if both in-plane and bending isotropies were required.

The above procedure was applied to some special cases of lamination by Grediac (2000), using the design area defined by

$$-1 \leq V_{i\beta} \leq 1, \, i = 1, 2 \quad V_{2\beta} \geq 2V_{1\beta}^2 - 1, \, \beta = A, D \qquad (1.10)$$

The first special case is the homogeneous orthotropic uncoupled plates defined as having the properties $A^* = D^*$, $B^* = 0$, for which the assigned lamination parameters are given by

$$v_{iB} = 0, \, i = 1, \ldots, 4 \quad v_{jA} = v_{jD} = 0, \, j = 3, 4 \quad v_{kA} = v_{kD}, \, k = 1, 2 \qquad (1.11)$$

For design points on the parabola $v_{2A} = 2v_{1A}^2 - 1$ as the starting point, two optimum stacking sequences with $n = 12$ are found as (72/113/112/61/119/65/66/102/77/115/114/64) and (54/126/54/126/126/126/53/54/53/127/54/126). The exact solution for this problem is given by (θ/−θ/θ/−θ_4/θ/−θ/θ_3), where $\theta = 1/2\cos^{-1}(V_{1A})$, and for the two cases above, $\theta = 67.2$ and 53.7°, respectively. A horizontal line across the design area defined by Equation (1.10) represents laminates with the same $A_{66}^* = D_{66}^*$ and $A_{12}^* = D_{12}^*$. By taking a starting point on this thin line with $v_{2A} = 0$, the optimum laminations (147/7/92/37/43/17/165/102/176/39) and (168/38/125/171/14/47/187/166/158/127/42/2) are obtained, which exhibit invariant shear stiffness properties.

The second special case is the nonhomogeneous orthotropic uncoupled plate for which $A^* \neq D^*$, and the relations (1.11) hold with the exceptions of

$$v_{1A} \neq v_{1D}, \quad v_{2A} \neq v_{2D} \qquad (1.12)$$

Vanucci and Verchery (2001) used the polar method to obtain laminates with required stiffnesses. The studies aimed at increasing the stiffness of composite laminates by design optimization include Fukunaga and Vanderplaats (1991), Kam and Chang (1992), Avalle and Belingardi (1995), and Todoroki et al. (1996).

1.2.2 Optimization for Maximum Strength

Design of laminates to maximize their load-carrying capacity is achieved by using a suitable strength (failure) theory to characterize the failure. Several failure criteria were developed over the years to describe the failure state that could be stress- or strain-based. A criterion itself could be in the form of a single inequality based on energy considerations such as Tsai–Hill or Tsai–Wu criteria, which reduce to von Mises' criterion in the case of isotropic materials. Alternatively, it could be in the form of several inequalities based on maximum stress or strain in the material directions. For further study of failure criteria, refer to one of the books on the mechanics of composite materials (Gibson, 1994; Daniel and Ishai, 1994; Hyer, 1998; Berthelot, 1999; Jones, 1999). In the present section, maximum strength designs of composite laminates are discussed based on a given failure theory.

First, the optimization under in-plane loads is considered. Let the in-plane stresses acting on the k-th layer be denoted by σ_{xk}, σ_{yk}, and σ_{xyk}, corresponding to normal stresses in the x and y directions and the shear stress in the xy plane. Let the applied stresses be denoted as N_x, N_y, and N_{xy}. Then the strength ratio R_k for the k-th layer can be defined as

$$R_k = \min\left(\max_k \sigma_{xk} / N_x, \ \max_k \sigma_{yk} / N_y, \ \max_k \tau_{xyk} / N_{xy}\right) \tag{1.13}$$

where the maximum stresses satisfy the chosen failure criterion. The strength ratio provides quantitative information on the relation between the applied stresses and the maximum stresses that can be applied before failure.

The lowest value of R_k, viz.,

$$R_k = \min_k R_k \tag{1.14}$$

gives the strength ratio for the laminate. The optimal design problem can be stated as

$$\max_{\theta_i} R \tag{1.15}$$

subject to σ_{xk}, σ_{yk}, and τ_{xyk} satisfying the failure criterion for all $k = 1, 2, \ldots, K$, where K is the total number of layers. Susuki (1991) determined the optimal ply angles under various loading conditions using the discrete set of angles (0°, ±45°, 90°) for graphite/epoxy (T300-N5208) laminates subject to Tsai–Wu failure criterion. For $N_x = 1$ MPa and $N_{xy} = 0.1$ MPa, it was found that (0°($p\%$)/45°($r\%$)) gives the optimum ply angles for –0.069 MPa ð N_y ð 0.147 MPa, where p changes from 100 to 81.7% and r from 0 to 18.3%. Similarly, (0°($p\%$)/45°($r\%$)/–45($s\%$)) gives the optimum design for 0.147 MPa ð N_y ð 0.8 MPa, where p decreases from 67.2 to 10.6%, r increases from 30.1 to 51.2%, and s increases from 2.7 to 38.2% as N_y increases. For the range –0.506 MPa ð N_y ð

TABLE 1.2

Optimal Ply Angles and Percentages for $N_x = 1$ MPa, -1 MPa $\eth$ N_y $\eth$ 1 MPa, and $N_{xy} = 0.1$ MPa

N_y (MPa)	0° (%)	90° (%)	45° (%)	−45° (%)
−1.0 to −0.506	64–74.5	30–16.7	0	6–8.8
−0.506 to −0.069	100	0	0	0
−0.069 to −0.147	100–81.7	0	0–18.3	0
0.147–0.80	67.2–10.6	0	30.1–51.2	2.7–38.2
0.80–1.0	51.3–42.5	38.3–48.3	10.4–9.2	0

−0.069 MPa, (0°) laminate is the optimum, and for −1.0 MPa $\eth$ N_y $\eth$ −0.506 MPa, (0°(p%)/45°(q%)/−45(s%)) gives the optimal design, with p increasing from 64 to 74%, q decreasing from 30 to 16.7%, and s increasing from 6 to 8.8% as N_y increases. Full results are given in Table 1.2.

The highest $R = 954.6$ is obtained at $(N_x, N_y, N_{xy}) = (1.0, 0.05, 0.1)$ MPa for (0/45) configuration. These results were obtained by considering a tetrahedron of ply angle percentages corresponding to 0°(p%), 90°(q%), 45(r%) with −45($s = 1 - p - q - r$%). The vertices, edges, and surfaces of the tetrahedron make up a 14-ply angle. Combinations and the optimal percentages of each ply angle can be determined by considering these combinations individually. Applying this procedure, the optimum percentages p, q, r, and s can be computed for any stress combination. Strength optimization of laminates under transverse loading was studied by Song et al. (1995), who used the finite element method for analysis and the BFGS method (named after Broyden, Fletcher, Goldfarb, and Shanno) for numerical optimization. The objective function was chosen as the Tsai–Hill failure criterion so that the optimal design problem was expressed as

$$\min_{\theta_k} F(\theta_k) \tag{1.16}$$

where $F(\theta_k) = (\sigma_1/X)^2 - \sigma_1\sigma_2/X^2 + (\sigma_2/Y)^2 + (\tau_{12}/S)^2$, with σ_1, σ_2, and τ_{12} denoting the stresses in the material direction and X, Y, and S the strength values. The results were given for 4-, 6-, and 8-layered symmetric laminates made of T300/NS208 graphite/epoxy subject to simply supported or clamped boundary conditions. For laminates with an aspect ratio of 2 and under a uniform loading, the optimum stacking sequences are given as (87.5/ −52.9/35.7/36.8)$_s$ and (82.3/−41.2/2.4/−86)$_s$ for simply supported and clamped boundary conditions. The corresponding result for the simply supported case under a central point loading is (85.4/−50.6/47.3/18.7)$_s$. Comparisons of worst and best designs show large differences in the objective function, indicating that failure to optimize the design will result in very low carrying capacity.

More recently, optimization techniques were developed taking not only strength, but also stiffness and manufacturing ease into account to produce

more rounded designs. Manne and Tsai (1998b) developed a thickness scaling technique to meet the strength and stiffness requirements of a design in which layer thicknesses are multiplied by a factor λ to be determined using a suitable failure criterion or a displacement modulus. Using the Tsai–Wu criterion and defining λ as $\bar{z} = \lambda z$ so that the original thickness t_k of each ply becomes λt_k, the thickness scaling criterion can be derived as

$$\sum_{i=0}^{4} a_i \lambda^i = 0 \tag{1.17}$$

where the coefficients a_i are computed for symmetric and unsymmetric laminates. Similarly, introducing a thickness scaling factor μ for displacement and a displacement modulus d_0 defined as

$$d_0 = \left(u_0^2 + v_0^2 + w_0^2 \right)^{1/2} \tag{1.18}$$

where u_0, v_0, and w_0 are midplane displacements, one can compute the scaled displacement modulus $\overline{d_0}$ given by

$$\overline{d_0} = \left[\left(u_0 / \mu \right)^2 + \left(v_0^2 / \mu \right)^2 + \left(w_0 / \mu^3 \right)^2 \right]^{1/2} \tag{1.19}$$

The value of $\overline{d_0}$ can be decreased or increased by adjusting μ. Both strength and displacement scaling factors, i.e., λ and μ, can be combined as $\eta = \lambda \max (\mu, 1)$ to design laminates that can meet both the strength and displacement requirements (Manne and Tsai, 1998b). The scaling and manufacturing concepts can be used to design optimum laminates using ply-drop tapering as the design variables (Manne and Tsai, 1998c). Recent studies on the strength optimization of composites include those of Fine and Springer (1997), Wang and Karihaloo (1999), and Park et al. (2001).

1.3 Buckling and Postbuckling Optimization: Complicating Effects

An extensive review of the state of the art in the buckling optimization of laminated plates has been given in Adali (1995). In the present section, emphasis is placed on complicating effects such as thermal loads, stiffened laminates, thickness tailoring, cost, and optimization in the postbuckling range. These considerations arise routinely in advanced applications, and their inclusion in the optimization process leads to efficient optimal

designs. In this section, the optimization of composites including these effects is illustrated by means of specific examples in which these effects can be observed.

1.3.1 Thermal Effects and Uniform Temperature Distribution

Buckling optimization was studied by Spallino and Thierauf (2000) for symmetric laminates subject to a uniform temperature increase ΔT. The lay-ups were limited to 0°, 90°, and +45°/–45° pair of plies stacked to produce a balanced configuration. The optimal designs were obtained for graphite/epoxy laminates using an evolutionary algorithm under strain and ply contiguity constraints for a simply supported plate with fixed dimensions. Results for optimal and near-optimal configurations indicate that several optimum solutions could be found with the corresponding buckling load close to the maximum one.

The effects of thermal residual stresses on the optimal design of laminates stiffened in the load direction were taken into account by Foldager et al. (2001), who considered laminates under a unidirectional compressive force. The results were given for square plates made of graphite/epoxy (1M7/8551) material with boundaries that are restrained from moving in the transverse direction. The optimization procedure makes use of the results of a sensitivity analysis, which include the thermal effects. It was shown that plates stiffened along the edges produced higher buckling loads than plates stiffened along the edges and across the middle for the same volume of stiffeners used in both cases. Moreover, stiffeners with a smaller width and higher thickness were more efficient than ones with a larger width and lower thickness when compared on an equal volume basis. Optimal laminates with stiffeners of 40% of the total volume and 25% of the total width of the plate produce a buckling load that is 4.1 times higher than that of an unstiffened plate with $(45/–45)_s$ lay-up when the thermal stresses are neglected and 5.6 times when thermal stresses based on a uniform $\Delta T = 100°C$ are included. For this case, the optimal lay-up is $(73/–67)_s$ for the plate and $(–3)_s$ for the stiffeners. If the optimization includes the effect of thermal stresses, the optimal plate lay-up is $(78/–72)_s$ and stiffener lay-up is $(–1)_s$, which produces six times higher loads than an unstiffened plate of $(45/–45)_s$. Thus, the presence of thermal stresses leads to higher buckling loads, and consequently, neglecting the residual stresses yields lower buckling loads. Furthermore, the thermal residual stresses can be tailored to increase the buckling load of stiffened plates, as shown by de Almeida and Hansen (1997).

The buckling temperature was maximized for 3-, 4-, and 5-layered simply supported and clamped plates by Singha et al. (2000) using both ply angles and thicknesses as design variables. The optimum solutions were obtained using a genetic algorithm coupled to finite element analysis based on first-order shear deformation theory. The results were given for graphite/epoxy laminates with aspect ratios 1.0, 1.5, and 2.0 and width-to-thickness ratios of

100. In the case of plates with aspect ratios 2, the optimum stacking sequences were determined as (63/–88/–53), (68/–57/58/–63), and (59/–62/–85/56/–69) for simply supported plates and (73/3/–75), (76/–22/29/–65), and (63/–38/–15/46/–66) for clamped plates, with the ply angles rounded to the nearest decimal point. Compared to laminates with stacking sequences $(-1)^{i+1}45°$, where i denotes the i-th ply, the maximum buckling temperature increased by 68, 62, and 77% for 3-, 4-, and 5-layered simply supported plates, respectively, with the corresponding figures being 40, 37, and 47% for clamped plates. Including the layer thicknesses among the design variables increases the maximum buckling temperature further, with this increase being substantial for 3-layered plates and minimal for 4- and 5-layered plates.

1.3.2 Thermal Effects and Variable Temperature Distribution

Optimal design of symmetrically laminated plates under a variable temperature distribution was studied by Walker et al. (1997) using the fiber orientations as the design variables and specifying maximum buckling temperature T_b as the design objective. Let the temperature distribution be given by $T(x, y) = T_b t(x, y)$, where $t(x, y)$ is the temperature distribution corresponding to a unit temperature input. The critical buckling temperature $T_{cr}(\theta)$ is given by

$$T_{cr}(\theta) = \min_{m,n}\left[T_{b,mn}(m, n; \theta)\right] \tag{1.20}$$

where $T_{b,mn}$ is the buckling temperature corresponding to the half-wave numbers m and n in the x and y directions, respectively. The design objective is to maximize $T_{cr}(\theta)$ with respect to θ, viz.,

$$T_{max} \equiv \max_{\theta}\left[T_{cr}(\theta)\right] \quad 0° \leq \theta \leq 90° \tag{1.21}$$

where $T_{cr}(\theta)$ is determined for a given θ from the finite element solution of the thermal buckling problem defined by Equation (1.20). The temperature can be described along the edges of the plate, resulting in a temperature distribution across the plate that is a function of x and y. Solution of the buckling problem (Equation (1.20)) involves the computation of the temperature distribution across the plate, which yields the thermal stress field for the given temperature boundary conditions. This solution is used in the eigenvalue problem (Equation (1.20)) in order to compute the corresponding buckling temperature. The solution method involves the following steps:

1. The solution of the temperature distribution problem for given temperatures along the edges by finite elements

2. The solution of the thermal buckling problem for a given θ by finite elements

3. The solution of the optimization problem to determine θ_{opt} corresponding to the maximum buckling temperature

The results were obtained for three different thermal loadings, i.e., uniform, linear, and nonlinear temperature distributions across the plate. For a square, 4-layered laminate made of T300/5208 graphite epoxy material under uniform temperature, the maximum buckling temperature occurs at $\theta_{opt} = 45°$ for (S, S, S, S) boundary conditions, at $\theta_{opt} = 37.5°$ and 54.3° for (C, C, C, C) boundary conditions, and at $\theta_{opt} = 53.4°$ for (C, S, C, S) boundary conditions, where S represents the simply supported and C the clamped boundary. Optimal ply angle decreases with increasing aspect ratio for simply supported plates and stays fairly uniform for (C, S, C, S) plates. In the case of clamped plates, the optimal angle is less than 40° for aspect ratios less than 1 and above 50° for higher aspect ratios. In the case of a linear variation of the temperature across the plate, the trends for θ_{opt} remain similar to those for the uniform temperature case, with minor changes in θ_{opt}.

The third loading case was obtained by setting the temperature of two adjacent edges differently and keeping the other two edges thermally insulated. For square plates, $T_{cr}(\theta)$ is no longer symmetrical with respect to 45°, and θ_{opt} is 46.1° for (S, S, S, S), 52.1° for (C, C, C, C), and 54.4° for (C, S, C, S). Further recent results on the optimization of composites subject to thermal effects can be found in Fukunaga et al. (1997), Lee et al. (1999), Aiello and Ombres (1999), and Autio (2001).

1.3.3 Optimization with Stiffeners

Optimization of composite panels with various types of stiffeners was studied by Kassapoglou and Dobyns (2001), who considered the problem of minimum weight and cost using stiffener spacings and thicknesses of the stiffeners, frame, and panel as the design variables, as shown in Figure 1.1. The designs were subject to maximum strain, buckling, and postbuckling failure constraints. The results were given for panels with an aspect ratio of 1.2 having 17% 0° plies, 66% 45° plies, and 17% 90° plies and subject to an in-plane shear load as well as an in-plane load in the stiffener direction. The material of the panel was specified as fabric with equal moduli in the x and y directions. The stiffeners were also made of the same material with the exception of the top sections, which were made from a fiber composite tape. In the case of hat stiffeners, the optimum stiffener spacing was found to be 84 mm for the minimum weight problem and 257 mm for the minimum cost problem. The Pareto sets for all stiffeners were given in the form of cost vs. weight curves, which enable the designer to choose a compromise solution for each stiffener shape. For example, in the case of L stiffeners, which provide the best stiffness, the compromise solution is 51-mm spacing when
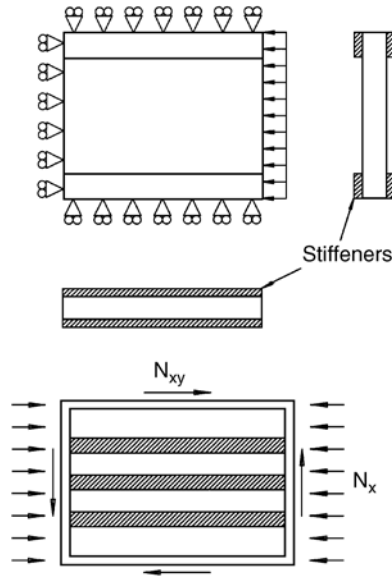
FIGURE 1.1
Stiffened plate configuration and the loading.

cost and weight are considered equally important and 76 mm when cost is considered twice as important as the weight, with the panel thickness 33% higher in the second case.

1.3.4 Multiple Prebuckling, Buckling, and Postbuckling Objectives

In cases when structures are subjected to loads that may be below or beyond their buckling limit, they are required to be strong before and after buckling occurs in order to reduce the possibility of catastrophic failure. In particular, this necessitates a design procedure that takes the prebuckling and post-buckling stiffnesses into account. Design optimization involving more than one objective can be handled by a multiobjective approach leading to designs that are balanced and satisfactory from an overall strength viewpoint. Multi-objective solutions for laminated composites were studied by Adali (1983), Kumar and Tauchert (1992), Saravanos and Chamis (1992), and Adali et al. (1995a), where it was observed that compromise designs can perform in a satisfactory manner under different loading conditions. In the present study, the multiobjective optimization is illustrated by optimizing a symmetric laminate with respect to prebuckling, buckling, and postbuckling loading (Adali et al., 1996).

For a symmetrically laminated and balanced rectangular plate of length a, width b, and thickness H, the stacking sequence is specified as $(\pm\theta_1/\pm\theta_2/ \ldots)_s$. It is subjected to biaxial compression $N_x = \lambda N$ in the x direction and $N_y = N$ in the y direction. In the case of uniaxial compression, the unloaded

edges $y = 0$, a are elastically restrained from translating in the y direction, giving rise to Poisson's effect.

Next the prebuckling stiffness is computed for the uniaxial case. In this case, $N < N_{cr}$, where N_{cr} is the buckling load and the force resultants are given by $N_x = N$, $N_{xy} = 0$, $N_y = kv_{xy}N$, where N_y is due to Poisson's effect, k is the elastic constant of the in-plane restraints with $k = 0$ corresponding to no elastic restraint and $k = 1$ to rigid boundaries, and v_{xy} is Poisson's ratio given by $v_{xy} = A_{12}/A_{11}$ for balanced laminates. Thus $N_y = kA_{12}N/A_{11}$. For balanced laminates under in-plane loads, the strain–force relations are given by $\varepsilon_x = a_{11}N_x + a_{12}N_y$, where a_{ij} values are the in-plane flexibility coefficients given by $a_{ij} = A_{ij}^{-1}$. Thus $\varepsilon_x = N(a_{11} + \lambda a_{12})$, where $\lambda = kA_{12}/A_{11}$. The prebuckling stiffness K_x in the x direction is defined as the stress per unit strain in the load direction, viz.,

$$K_x = \frac{\sigma}{\varepsilon} = \frac{N}{H\varepsilon_x} = \frac{1}{\left(a_{11} + \lambda a_{12}\right)H} \tag{1.22}$$

For the biaxial case, $N_x = N$ and $N_y = \lambda N$, with > 0, and the prebuckling stiffness in the x direction is again given by Equation (1.22), with $\lambda = N_y/N$ denoting the load ratio. The corresponding expression in the y direction is given by

$$K_y = \frac{\lambda}{\left(a_{12} + \lambda a_{22}\right)H} \tag{1.23}$$

The second objective is the buckling load that is given by

$$N_{cr} = \min_{m,n} \frac{D_{11}\alpha_m^4 + 2\left(D_{12} + 2D_{66}\right)\alpha_m^2\beta_n^2 + D_{22}\beta_n^4}{\alpha_m^2 + \beta_n^2\lambda} \tag{1.24}$$

for the simply supported plates where $\alpha_m = m\pi/a$ and $\beta_n = n\pi/b$. Equation (1.24) applies to both uniaxial and biaxial loading cases, with λ given by $\lambda = kv_{xy}$ and $\lambda = N_y/N$, respectively.

The third objective is the initial postbuckling stiffness with the applied force N exceeding the buckling load, i.e., $N > N_{cr}$ and the strain $\varepsilon > \varepsilon_c$, where ε_c is the elastic limit. The initial postbuckling stiffness is defined as the slope of the load–strain curve at $\varepsilon = \varepsilon_c$, i.e., $dN(\varepsilon_c)/d\varepsilon$. An expression for the initial postbuckling stiffness in the x direction can be obtained as

$$\frac{dN_x}{d\varepsilon} = P_x = \frac{a_{22} + \mu_{mn}^4 a_{11}}{2a_{11}a_{22}\left(1 + \lambda\mu_{mn}^2\right) + \left(a_{22} + \mu_{mn}^4 a_{11}\right)\left(a_{11} + \lambda a_{12}\right)} \tag{1.25}$$

where $\mu_{mn} = \beta_n \alpha_m = na/mb$ and $\lambda = kA_{12}/A_{11}$ (in the uniaxial case) or $\lambda = N_y/N$ (in the biaxial case). The corresponding expression in the y direction is given by

$$\frac{dN_y}{d\varepsilon} = P_y = \frac{a_{11} + \mu_{mn}^4 a_{22}}{2a_{11}a_{22}\left(1 + \lambda\mu_{mn}^2\right) + \left(a_{11} + \mu_{mn}^4 a_{22}\right)\left(a_{22} + \lambda a_{12}\right)} \tag{1.26}$$

The stiffnesses derived above are normalized by introducing the following nondimensionalized quantities:

$$K_x^* = \frac{K_x}{K_0}, \quad K_y^* = \frac{K_y}{K_0}, \quad N^* = \frac{N_{cr}}{N_0}, \quad P_x^* = \frac{P_x}{P_0}, \quad P_y^* = \frac{P_y}{P_0} \tag{1.27}$$

for prebuckling, buckling, and postbuckling strengths. In Equation (1.27) the subscript 0 denotes the values of K_x, N_{cr}, and P_x for a $(0°/0°/ \dots /0°)_s$ laminate, i.e., $K_0 = K_x(\theta = 0°)$, $N_0 = N_{cr}(\theta = 0°)$, $P_0 = P_x(\theta = 0°)$.

1.3.4.1   Optimization Problem

The objective is to maximize a weighted sum of the prebuckling stiffness K^*, the critical buckling load N^*, and the initial postbuckling stiffness P^*, and the design index is given by

$$DI = \mu_1 K_* + \mu_2 N_* + \mu_3 P_* \tag{1.28}$$

with $\mu_1, \mu_2, \mu_3 \; \check{S} \; 0$, $\mu_1 + \mu_2 + \mu_3 = 1$. As the weighting factors μ_i are varied, the emphasis of the optimization shifts to different objectives, resulting in compromise solutions. In the uniaxial case, with loading only in the x direction, $K^* = K_x^*$, and $P^* = P_x^*$ with $\lambda = kA_{12}/A_{11}$. In the biaxial case, the prebuckling stiffness K^* is chosen as $K^* = \min(K_x^*, K_y^*)$ subject to the condition that $K_x^*, K_y^* \; \check{S} \; 0$. Similarly, the initial postbuckling stiffness P^* under biaxial loading is defined as $P^* = \min(P_x^*, P_y^*)$.

Due to the specific nature of the problem involving conflicting design objectives, several laminate configurations with ply angles of θ, 0°, and 90° are considered as candidate designs. More specifically, the configurations of the candidate designs are taken in the form of $(\theta/-\theta/ \dots /0°/ \dots /90°/ \dots /0°/ \dots)_s$. The best design gives the highest design index, DI, leading to the optimal laminate configuration. Let DI_i designate the maximum design index for laminate i. The best design is given by the laminate configuration corresponding to the highest DI, which is obtained from

$$DI^* = \max_i DI_i \tag{1.29}$$

with $i = 1, 2, \dots, I$, where I denotes the number of candidate laminates. Thus the complete design optimization involves the solution of the problem

$$\max_i \left(\max_\theta DI_i \right), \quad i = 1, 2, \ldots, I \tag{1.30}$$

In the case of discrete design variables, the fiber orientations are chosen from a given set of angles, the most practical ones being 0°, 45°, –45°, and 90°.

1.3.5 Numerical Results

The results are given for a T300/5208 graphite/epoxy material with the plate thickness ratio specified as $H/b = 0.01$. The elastic constants are given by E_1 = 181 GPa, E_2 = 10.3 GPa, G_{12} = 7.17 GPa, and ν_{12} = 0.28. Five laminate configurations with eight layers referred to as laminate types 1, 2, 3, 4, and 5 are specified as candidate designs with stacking sequences $\{\theta, -\theta, \theta, -\theta\}_s$, $\{\theta, -\theta, 90, 0\}_s$, $\{\theta, -\theta, 0, 0\}_s$, $\{\theta, -\theta, 0, 90\}_s$, and $\{\theta, -\theta, 90, 90\}_s$. The weighting factors are taken as $\mu_1 = 0.25$, $\mu_2 = 0.5$, and $\mu_3 = 0.25$.

Figure 1.2 shows the dependence of K^*, N^*, P^*, and DI on θ for a type 1 laminate. Both P^* and K^* have $\theta_{opt} = 0°$, while θ_{opt} for maximum N^* is around 30°, with a second maximum at $\theta = 76°$. The DI curve has the maximum point at $\theta = 17°$. Figure 1.2 shows that a multiobjective approach is needed to obtain compromise solutions. The dependence of DI on θ for all five laminate types is shown in Figure 1.3 for an aspect ratio of 1.5 and $k = 1$. Laminate 2 is optimal for 0° ð θ ð 24°, then laminate 3 becomes the best,
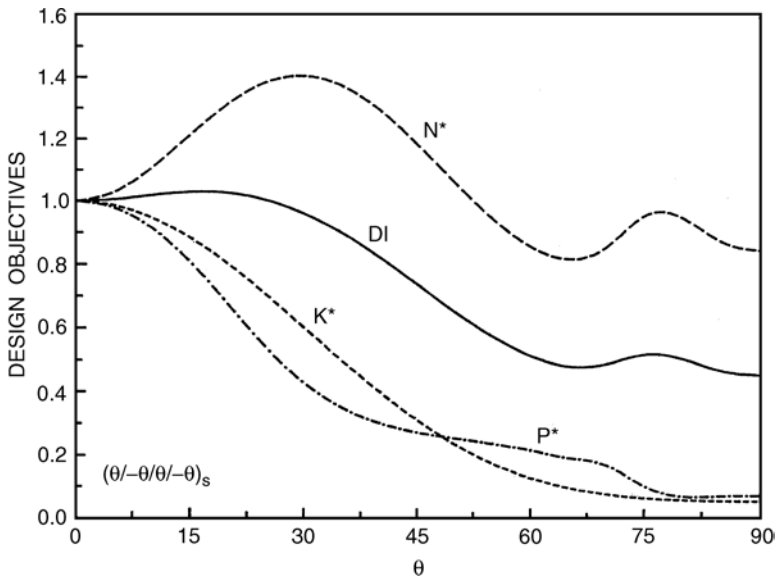

FIGURE 1.2
Design objectives vs. for $(\theta/-\theta/\theta/-\theta)_s$ lamination with $k = 1$ and $a/b = 1.5$. (Reprinted from S. Adali et al., 1996, *Composite Struct.*, 35:117–130. Copyright 1996, with permission from Elsevier Science.)

FIGURE 1.3
Design index vs. θ for different laminations with $k = 1$ and $a/b = 1.5$. (Reprinted from S. Adali et al., 1996, *Composite Struct.*, 35:117–130. Copyright 1996, with permission from Elsevier Science.)
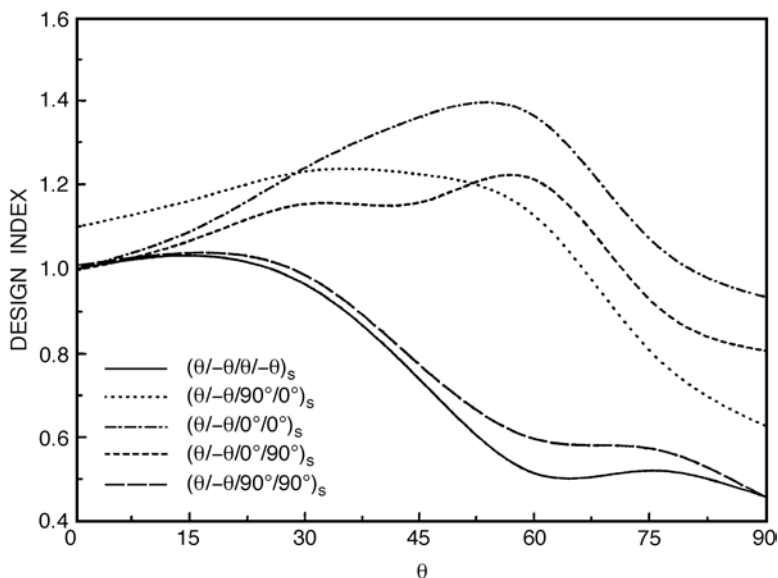
with the highest design index *DI* given at $\theta_{opt} = 58.1°$. Table 1.3 compares the objective functions for different aspect ratios with $DI = 0.25K^* + 0.5N^* + 0.25P^*$. When the plate is narrow (a/b ð 0.8), θ_{opt} is $0°$, and the optimal laminate is both types 1 and 3. When $a/b > 0.8$, θ_{opt} becomes nonzero, with the value first increasing, then decreasing with increasing a/b. The values of K^*/K_{max}, N^*/N_{max}, and P^*/P_{max} are shown in columns 4, 5, and 6 with K_{max}, N_{max}, and P_{max} being the maximum value of the corresponding quantity based on single objective designs. As a/b increases, K^*/K_{max} and P^*/P_{max} decrease, while N^*/N_{max} remains close to 1. The last two columns of the table show the pre- and postbuckling stiffnesses evaluated at $\theta = \theta_{opt}^N$, which is the optimal θ value for maximum N^*. We observe that the designs based on

TABLE 1.3

Results for Different Aspect Ratios with $k = 1$ and $\mu_1 = 0.25$, $\mu_2 = 0.5$, and $\mu_3 = 0.25$

a/b	Laminate	θ_{opt}	K^*/K_{max}	N^*/N_{max}	P^*/P_{max}	$K(\theta_{opt}^N)/K_{max}$	$P(\theta_{opt}^N)/P_{max}$
0.2	1 and 3	0	1	1	1	1	1
0.6	1 and 3	0	1	1	1	1	1
1.0	3	28.2	0.82	0.94	0.74	0.68	0.62
1.5	3	58.1	0.57	1	0.83	0.57	0.83
2.0	3	52.8	0.61	1	0.84	0.61	0.45
3.0	3	47.2	0.64	0.94	0.73	0.59	0.30

Source: S. Adali et al., *Composite Struct.*, 35: 117–130, 1996, with permission from Elsevier Science.
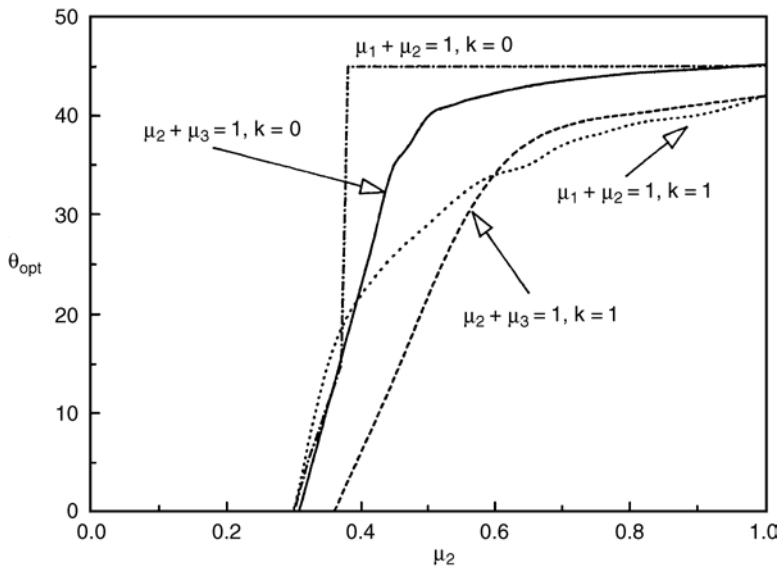
FIGURE 1.4
Optimal ply angle vs. the weighting factor μ_2 with $a/b = 1$. (Reprinted from S. Adali et al., 1996, *Composite Struct.*, 35:117–130. Copyright 1996, with permission from Elsevier Science.)

N_{max} only would produce laminates that are markedly lower in pre- and postbuckling stiffness.

The effect of the weighting factors on θ_{opt} is shown in Figure 1.4 for two-objective problems. Figure 1.4 shows the importance of shifting weighting factors on θ_{opt}.

Next, the case of discrete ply angles is studied by choosing θ from a given set of orientations. In the present problem, $0°$, $\pm45°$, and $90°$ are specified as the given set. The numerical results are given in Table 1.4, which shows the optimal stacking sequences for various aspect ratios with $k = 1$.

In the biaxial case, all edges are loaded and the elastic restraints on the boundaries do not exist. The biaxial results are given for the case $\lambda = 1$, i.e.,

TABLE 1.4

Optimal for Various Aspect Ratios with Discrete Ply Angles and $k = 1$ and $\mu_1 = \mu_2 = \mu_3 = 1/3$

a/b	Lay-up	K^*/K_{max}	N^*/N_{max}	P^*/P_{max}
0.2	$(0°/0°/0°/0°)_s$	1	1	1
0.6	$(0°/0°/0°/0°)_s$	1	1	1
1.0	$(0°/0°/0°/0°)_s$	1	0.73	1
1.5	$(90°/0°/0°/0°)_s$	0.76	0.81	1
2.0	$(45°/-45°/0°/0°)_s$	0.66	1	0.65
3.0	$(45°/-45°/0°/0°)_s$	0.66	1	0.73

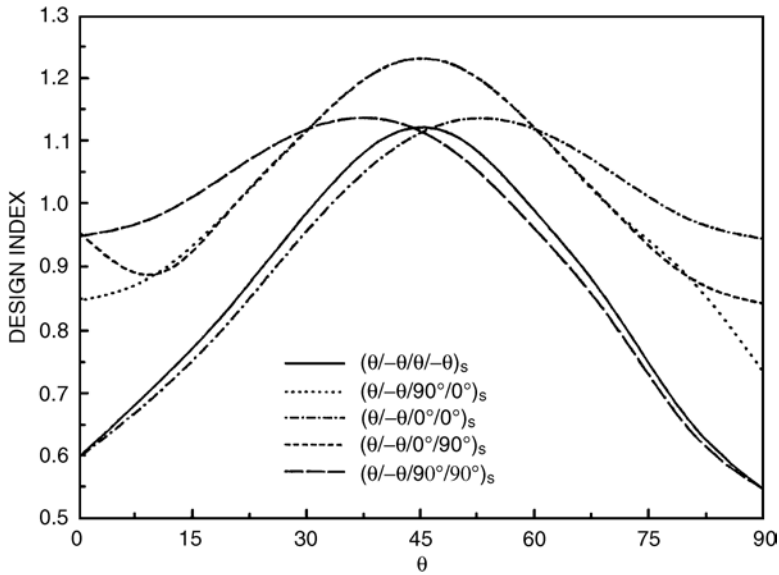*Source:* S. Adali et al., *Composite Struct.*, 35: 117–130, 1996, with permission from Elsevier Science.

FIGURE 1.5
Design index vs. θ for different laminations under biaxial load with λ = 1 and *a*/*b* = 1. (Reprinted from S. Adali et al., 1996, *Composite Struct.*, 35:117–130. Copyright 1996, with permission from Elsevier Science.)

$N_x = N_y$ with $\mu_1 = \mu_3 = 0.25$ and $\mu_2 = 0.5$ in Figure 1.5, which shows the design indices for different laminates with *a*/*b* = 1.5. Figure 1.5 illustrates the necessity of investigating different laminates to identify the optimal configuration and the effect of biaxial loading on the design index. The optimal laminate configurations with discrete ply angles are shown in Table 1.5 for various aspect ratios. It is observed that 90° layers are placed in the outer layers as *a*/*b* increases. The buckling load remains close to its maximum value while *P** increases with increasing *a*/*b*.

Recent studies on the buckling optimization of composite laminates include those by Joshi and Biggers (1996), Walker et al. (1996), Moh and Hwu (1997), Walker (1998, 1999), Hu and Chen (1999), and Khong (1999).

TABLE 1.5

Optimal for Various Aspect Ratios with Discrete Ply Angles and = 1, $\mu_1 = 0.25$, $\mu_2 = 0.5$, and $\mu_3 = 0.25$

a/*b*	Lay-up	K^*/K_{max}	N^*/N_{max}	P^*/P_{max}
0.2	$(0°/45°/0°/-45°)_s$	1	1	0.36
0.6	$(0°/45°/0°/-45°)_s$	1	1	0.26
1.0	$(45°/-45°/0°/0°)_s$	1	0.95	0.40
1.5	$(90°/45°/-45°/0°)_s$	0.17	0.99	0.84
2.0	$(90°/45°/-45°/0°)_s$	0.17	0.99	0.88
3.0	$(90°/45°/-45°/0°)_s$	0.17	0.99	0.93

Source: S. Adali et al., *Composite Struct.*, 35: 117–130, 1996, with permission from Elsevier Science.

1.4 Optimization under Material, Load, and Geometric Uncertainties

Optimal design in structures, and in particular composite structures, under deterministic conditions has the drawback that the design becomes unreliable if these conditions change even slightly under service conditions.

The optimization of composites using deterministic material and load data leads to designs that are optimal under those specific conditions. Such designs do not take structural variabilities and load uncertainties into account and as such may be sensitive to changes in the material properties, load directions, etc. For example, process-induced variabilities arise due to the difficulties for achieving a required level of quality control in the manufacturing process and may include fiber volume content, fiber size and orientation, ply thickness, strength parameters, fiber/matrix bond, and geometric imperfections. Randomness in load directions may arise under service conditions due to unexpected loading conditions, accidents, etc. Such variabilities naturally affect the performance of a design and the level of structural reliability unless taken into account at the design and optimization phase.

There have been various approaches and techniques to deal with the uncertainties in the optimization of composites. Miki et al. (1989, 1990a, 1990b, 1993, 1997), Yang and Ma (1989), Shao et al. (1991, 1992, 1993), Murotsu et al. (1994), Boyer et al. (1997), and Nozomu et al. (1998) applied reliability methods for the optimum design of laminated composites subject to load and material uncertainties.

Nonprobabilistic techniques were also employed to study the behavior of structures subject to uncertain load conditions when there is no information available on statistical distributions and probability functions of relevant quantities. Convex modeling of uncertain structures was developed by Ben-Haim and Elishakoff (1990) to compute the least favorable response of a structure when the information on some of the input data is incomplete.

Convex modeling was applied to a number of structural analysis problems with different uncertainties. Geometrical imperfections of shells were investigated by Ben-Haim and Elishakoff (1989) and Elishakoff and Ben-Haim (1990); initial imperfection of a column by Elishakoff et al. (1994a); vibrations of beams and composite plates under uncertain excitations by Elishakoff and Colombi (1993) and Sadek et al. (1993); scatter in material properties by Elishakoff et al. (1994b); and the failure of a beam with uncertain initial deflection by Ben-Haim (1993).

Application of the convex modeling approach to the optimal design of composite structures with load uncertainty was developed by Adali (1993). The optimal designs for sandwich plates and angle-ply laminates subject to uncertain loads and uncertain initial deflections were given by Adali et al. (1994b, 1995b, 1995c).

In the next three sections, various optimal design procedures are discussed for composite laminates subject to material, load, and geometric uncertainties, and the techniques are illustrated using specific examples.

1.4.1 Material Uncertainty

Fiber composites are characterized by superior material properties as well as scatter in the mechanical properties as a result of manufacturing imperfections that are augmented due to the directional nature of the material. For example, fiber misalignment, imperfect bonding (matrix/fiber or between laminate), and variations in the fiber/matrix content can easily occur and affect the values of elastic constants and the strength parameters. A suboptimum design may result if the scatter in the material data is not taken into account in the optimization process. One method of including this data in the design optimization is by convex modeling, which requires information only on the bounds of the uncertain properties (Ben-Haim and Elishakoff, 1990). Convex modeling provides a convenient method for taking the material uncertainties into account and producing a design that can function under least favorable conditions. Adali et al. (1994a) used this technique in the optimal design of laminates to maximize the buckling load in the presence of material uncertainty (MU). The method is illustrated in the context of this buckling maximization problem.

The composite structure to be optimized is specified as a simply supported angle-ply symmetric laminate with the vector of uncertain elastic moduli given as $[E] = (E_1, E_2, E_3, E_4)$, where $E_1 = E_{11}$, $E_2 = E_{22}$, $E_3 = v_{12}$, and $E_4 = G_{12}$, which can be expressed as a sum of deterministic and uncertain parts such that

$$[E] = [E^0] + [\tilde{E}] \tag{1.31}$$

where $E_1 = E_1^0 + \tilde{E}_1$, $E_2 = E_2^0 + \tilde{E}_2$, $v_{12} = v_{12}^0 + \tilde{v}_{12}$, and $G_{12} = G_{12}^0 + \tilde{G}_{12}$, where the superscripts 0 and ~ refer to the deterministic and uncertain components, respectively. It is assumed that the elastic moduli vary slightly around their average values inside an ellipsoidal set with semi axes e_i, viz.,

$$S = \left\{ [\tilde{E}] \Big| \sum_{i=1}^{4} \left(\frac{\tilde{E}_i}{e_i} \right) \leq \alpha^2 \right\} \tag{1.32}$$

The buckling load $N_{cr}(E)$ can be linearized with respect to uncertain quantities $[\tilde{E}]$ as follows:

$$N_{cr}(E) = N_{cr}(E^0) + (\nabla N_{cr}(E^0), [\tilde{E}]) \tag{1.33}$$

The uncertainty problem can be stated as follows: given an ellipsoid of the uncertain parts of elastic moduli (Equation (1.32)), find the minimum of the buckling load (Equation (1.33)), viz.,

$$N_{cr}^*(E^0, e) = \min N_{cr}(E) \tag{1.34}$$

where the minimization is over $[\tilde{E}] \in S$. The minimum of $N_{cr}(E)$ is on the boundary ∂S of the set S, and

$$\sum_1^4 (\tilde{E}_i / e_i)^2 = \alpha^2$$

so that the minimization is actually over $[\tilde{E}] \in \partial S$. The method of Lagrange multipliers can be employed to minimize the Lagrangian given by

$$L(\tilde{E}) = \left(\nabla N_{cr}(E^0), [\tilde{E}]\right) + \mu \left(\sum_1^4 \left(\tilde{E}_i / e_i\right)^2 - \alpha^2 \right) \tag{1.35}$$

where μ is the Lagrangian multiplier. Let ε be a 4×4 diagonal matrix whose i-th diagonal element is $1/e_i^2$. The extremum condition for the Lagrangian (Equation (1.35)) is given by

$$\frac{\partial L}{\partial [\tilde{E}]} = 0 = \nabla N_{cr}(E^0) + 2\mu[\tilde{E}] \tag{1.36}$$

The least favorable uncertain components of the elastic moduli $[\tilde{E}]$ are calculated from Equation (1.36) as follows:

$$[\tilde{E}] = -(1/2\mu)^{-1} \nabla N_{cr}(\tilde{E}) \tag{1.37}$$

The value of the Lagrange multiplier μ is determined from

$$\mu = -\frac{1}{4\alpha^2} \nabla^T N_{cr}(E^0) \, \varepsilon^{-1} \nabla N_{cr}(E^0) \tag{1.38}$$

Substitution of Equation (1.38) into Equation (1.37) gives the scatter in elastic moduli producing the critical buckling load under least favorable conditions, which is computed by using Equation (1.33) as

$$N_{cr}^* = N_{cr}(E^0) - \alpha \sqrt{ \sum_{i=1}^4 \left(e_i \frac{\partial N_{cr}(E^0)}{\partial E_i} \right)^2 } \tag{1.39}$$

The semi-axes of the uncertainty ellipsoid e_i are linked with the scatter in the i-th elastic modulus. The values of the semi-axes e_i are determined by the value of the error in the corresponding material property E_i. If the error in the material constant E_i equals δ_i, such that $E_i = E_{i0} \pm \delta_i$, then $e_i = 2\delta_i$.

The objective of the optimal design is to maximize critical buckling load of the laminate with respect to the ply angle θ. The optimal design problem can be stated as follows:

Determine N_{max} and the optimal ply angle θ_{opt} so as to maximize N^*, i.e.,

$$N_{max} = \max_{\theta} \min_{e_i} N^* \tag{1.40}$$

where N^* is the minimum critical buckling load of the plate. The optimization procedure gives the values of the optimal ply angle and the corresponding maximum buckling load N_{max} under the worst case of material properties. Numerical results indicate that N_{max} decreases as the level of uncertainty increases, and the optimal ply angle also differs from its deterministic counterpart, but no trend can be detected.

More recently, the convex modeling was applied to the stiffness optimization of composites by Kim and Sin (2001) with the technique applied to the calculation of failure criterion. It was shown that the minimum laminate thickness increases with increasing level of uncertainty. In a number of optimization studies, reliability methods were used to deal with MU and the elastic constants were treated as random variables (Murotsu et al., 1994; Miki et al., 1997; Richard and Perreux, 2000).

1.4.2 Load Uncertainty

Composites designed under deterministic load conditions are more sensitive than their conventional counterparts (i.e., isotropic structures) to changes in the loading conditions due to material anisotropy. A typical example is a composite with all the fiber aligned in the direction of a uniaxial load, which is likely to fail easily if the load direction changes. Most structures are likely to be subjected to a variety of loads under service conditions, and trying to predict all possible load combinations a priori may prove to be a futile exercise. However, load uncertainty (LU), i.e., unpredictability of the load conditions, can be built into the optimization process by a variety of methods, producing optimal designs that can operate under a large class of load combinations. One method of dealing with load uncertainties in the design optimization is convex modeling, which is illustrated next for the minimum weight design of a symmetric laminate subject to multiple uncertain transverse loads (Adali et al., 1995c).

The minimum weight design is given subject to the maximum deflection and buckling constraints using the ply angles as the design variables. The

laminate is simply supported and symmetrical with length a, width b, and thickness $\bar{h}$. The loads are in-plane loads N_x and N_y, and multiple transverse loads $\bar{q}_i$, $i = 1, \ldots, \zeta$, with ζ denoting the number of loads. The transverse loads are given as

$$q^{(i)}(x,y) = q_0^{(i)}(x,y) + \tilde{q}^{(i)}(x,y), \quad i = 1, 2, \ldots, \zeta \tag{1.41}$$

where $x = \bar{x}/a$, $y = \bar{y}/b$, the subscript 0 and the symbol $\sim$ denote the deterministic and uncertain parts with $q^{(i)} = \bar{q}_i/E_{22}$. The uncertain components $\tilde{q}^{(i)}$ satisfy the conditions

$$\left\| \tilde{q}^{(i)} \right\|_2^2 \le \varepsilon_i^2, \ i = 1, 2, \ldots, \theta \tag{1.42}$$

where ε_i is the prescribed level of uncertainty for the i-th loading, and the L_2 norm is defined as

$$\|f\|_2^2 = \int_0^1 \int_0^1 |f(x,y)|^2 \, dx \, dy$$

Let $w_i = w_i\left[x, y; q^{(i)}\right]$ ($w = \bar{w}/b$) denote the deflection of the plate under the i-th loading $q^{(i)}$. The maximum possible deflection $w_i\left[x, y; q^{(i)}\right]$ at a given point (x_0, y_0) and the corresponding expression for $\tilde{q}^{(i)}$ are computed by determining the least favorable deflection:

$$w_i\left(x_0, y_0; \varepsilon_i\right) = \max_{\tilde{q}^{(i)}} w_i\left[x_0, y_0; q^{(i)}\right], \ i = 1, 2, \ldots, \zeta \tag{1.43}$$

The optimal design problem involves the minimization of the laminate weight by determining the minimum thickness such that the maximum deflection does not exceed a given upper bound δ. The laminate is also optimized with respect to the ply angle θ subject to a buckling constraint. Using nondimensional quantities, the weight is given as $W = \bar{W}/(ab^2) = \bar{h}/b = h$. Thus the design problem involves the computation of the minimum thickness h_{min} and the optimal angle θ_{opt} such that

$$\max_{i=1,2,\ldots,\zeta} \ \max_{x_0, y_0} w_i\left(x_0, y_0; \varepsilon_i\right) \le \delta \tag{1.44}$$

subject to $P_i < P_{cr}$, $i = 1, 2, \ldots, \zeta$, where P_i is the in-plane load for the i-th loading condition and P_{cr} is the nondimensional buckling load $P = P_x = N_x/(E_{22}b)$, $\lambda = N_y/N_x$, $P_y = \lambda P$. The function $w_i(x_0, y_0; \varepsilon_i)$ is maximized over the uncertainty coefficients subject to

$$\sum_{m=1}^{M}\sum_{n=1}^{N}\left[\tilde{A}_{mn}^{(i)}\right]^{2} = 4\varepsilon_{i}^{2}, \quad i = 1, 2, \ldots, \zeta \tag{1.45}$$

where $\tilde{A}_{mn}^{(i)}$ values are the Fourier coefficients used to expand the uncertain component $\tilde{q}^{(i)}$ of the i-th load. The method of Lagrange multipliers gives

$$\frac{\partial L_{i}}{\partial \tilde{A}_{mn}^{(i)}} = 0, \quad m = 1, \ldots, M, \quad n = 1, \ldots, N \tag{1.46}$$

where

$$L\left[\tilde{A}_{mn}^{(i)}\right] = w_{i}\left(x_{0}, y_{0}; \varepsilon_{i}\right) + \mu_{i}\left(\sum_{m=1}^{M}\sum_{n=1}^{N}\left[\tilde{A}_{mn}^{(i)}\right]^{2} - 4\varepsilon_{i}^{2}\right) \tag{1.47}$$

with μ_{i} denoting the Lagrangian multiplier. The optimal values of $\tilde{A}_{mn}^{(i)}$ are given by

$$\tilde{A}_{mn}^{(i)} = -\frac{2}{\mu_{i}} \cdot U_{mn}^{(i)}\left(x_{0}, y_{0}\right) \tag{1.48}$$

where

$$U_{mn}^{(i)}\left(x_{0}, y_{0}\right) = \frac{\sin(m\pi x_{0})\sin(n\pi y_{0})}{F_{i}(m, n)} \tag{1.49}$$

$$F_{i}(m, n) = {}^{4}[D_{11}(m/r)^{4} + 2(D_{12} + 2D_{66})(mn/r)^{2} + D_{22}n^{4}] - P_{i}\pi^{2}(m^{2}/r^{2} + \lambda_{i}n^{2})$$

with D_{ij} denoting the nondimensional flexural stiffnesses, $r = a/b$, and $\lambda_{i} = N_{y}/N_{x}$ for the i-th loading. The values of the Lagrange multipliers are determined from the constraints (Equation (1.45)) as

$$\mu_{i} = \mathrm{m}\frac{1}{\varepsilon_{i}}\left\{\sum_{m=1}^{M}\sum_{n=1}^{N}\left[U_{mn}^{(i)}\left(x_{0}, y_{0}\right)\right]^{2}\right\}^{\frac{1}{2}} \tag{1.50}$$

The minimum thickness $h_{\min}$ and the optimal ply angle θ_{opt} are determined using an iterative solution procedure. Starting from the estimates of h and θ, a minimum thickness satisfying the deflection and buckling constraints is calculated. Next, the least favorable deflection is minimized by computing an optimal ply angle for the value of h computed in the previous step. The iterations continue until they converge to the minimum thickness $h_{\min}^{(i)}$ and

the optimal ply angle θ_{opt}. The minimum thickness h_{min} satisfying the deflection and buckling constraints for every loading condition is obtained from

$$h_{min} = \max_{i=1,2,\dots,\zeta} h_{min}^{(i)} \tag{1.51}$$

The numerical results indicate that the minimum thickness increases as the level of uncertainty increases, as expected. Also, the different loading conditions determine the minimum thickness at different uncertainty levels. The optimum ply angles also depend on the level of uncertainty. The minimum thicknesses under multiple loadings are higher than or equal to the thicknesses produced under single-load cases. Moreover, the relative magnitudes of loadings affect the thickness considerably (Adali et al., 1995c).

Next, the optimal design of laminates under load uncertainty is illustrated using the anti-optimization approach to deal with uncertainty. Anti-optimization can be applied in cases when the magnitudes and locations of loads are not known a priori (Elishakoff et al., 1994c). However, these values are required to be defined in an uncertainty domain. In all cases, a two-stage optimization problem needs to be solved. One involves the design variables to obtain the optimum configuration, and the other the optimization of the uncertainty, i.e., anti-optimization. In general, these two problems lead to a nested optimization problem and can be solved iteratively (Lombardi and Haftka, 1998; Venter and Haftka, 2000; Zingales and Elishakoff, 2001). A study of the buckling problem under design uncertainties is given in Elishakoff (2000).

In the present example a symmetric laminate of thickness H under in-plane loads N_x and N_y is optimized for maximum strength, taking the fiber orientations as design variables (optimization problem) subject to uncertain in-plane loads that can produce the least favorable loading conditions for any given lay-up (anti-optimization problem) (Adali and Verijenko, 2000). The resulting solution is an optimal robust design capable of carrying all possible load combinations without failure.

The loads satisfy the constraints $N_{x,min} < N_x < N_{x,max}$, $N_{y,min} < N_y < N_{y,max}$, where the minimum quantities are specified to be less than the buckling load. The applied loads are uncertain in the sense that they lie in an uncertainty domain given by:

Case 1: $\qquad U_1 = \{(N_x, N_y, N_{xy}); N_x/N_{x,m} + N_y/N_{y,m} \leq 1\}$ (1.52)

where m refers to the minimum and maximum values of the respective quantities. Thus the inequalities in Equation (1.52) represent four inequalities that generate a closed region in the load space (N_x, N_y) with vertices at $(N_{x,min}, 0)$, $(N_{x,max}, 0)$, $(0, N_{y,min})$, and $(0, N_{y,max})$.

Case 2: $\qquad U_2 = \{(N_x, N_y); N_{\xi,min} \leq N_\xi \leq N_{\xi,max}, \xi = x \text{ or } y\}$ (1.53)

The load $\{N\} = (N_x, N_y)$ can take any value within the uncertainty domain U_i, and consequently the values of N_x and N_y are unknown a priori.

Let $R_f(\theta_k; N)$ denote the load reserve factor of the problem with respect to a specified failure criterion. Here θ_k denotes the fiber orientation of the k-th layer, with K being the total number of layers. The reserve factor is defined as $\{R_f N\} = \{R_f N_x, R_f N_y\}$, which can be applied on the laminate without causing failure, i.e., $FI(\theta_k; N) \leq 1$, where FI is a suitable failure index. The anti-optimization problem consists of determining the load $\{N\} \in U_i$, $i = 1$ or 2, for a given set of design variables θ_k such that

$$R_f(\theta_k; N^*) = \min_{\{N\} \in U_i} R_f(\theta_k; N) \qquad (1.54)$$

subject to the failure constraint. The solution of the anti-optimization problem yields the values of N_x and N_y corresponding to the worst case of loading, which minimizes the reserve factor. Computing the optimal θ_k requires the solution of the coupled anti-optimization/optimization problem. The coupling of anti-optimization and optimization problems occurs because of the interdependence of uncertainty and design variables. In the optimization problem, the design variables θ_k are computed so as to maximize the reserve factor $R_f(\theta_k; N)$, viz.,

$$R_f(\theta_k^*; N) = \max_{\theta_k} \min_{\{N\} \in U_i} R_f(\theta_k; N) \qquad (1.55)$$

The optimal values of θ_k depend on the anti-optimal values of (N_x, N_y) and vice versa. The solution of this problem produces the best values of the ply angles for the maximum reserve factor under the least favorable loading condition.

Choosing the Tsai–Wu failure criterion, the failure index for the k-th layer is given by

$$FI_k(\theta_k; N) = F_{11}\sigma_{1k}^2 + F_{22}\sigma_{2k}^2 + F_{66}\tau_{12k}^2 + 2F_{12}\sigma_{1k}\sigma_{2k} + F_1\sigma_{1k} + F_2\sigma_{2k} \qquad (1.56)$$

where $F_{11} = (X_t X_c)^{-1}$, $F_{22} = (Y_t Y_c)^{-1}$, $F_{66} = S^{-2}$, $F_{12} = (1/2)(F_{11}F_{22})^{-1/2}$, $F_1 = X_t^{-1} - X_c^{-1}$, $F2 = Y_t^{-1} - Y_c^{-1}$, with (X_t, X_c) and (Y_t, Y_c) denoting the tensile and compressive strengths in the fiber and transverse directions, respectively, and S the shear strength. The nonfailure condition is $FI_k(\theta_k; N) \leq 1$, $k = 1, 2, \ldots, K/2$, for any value of $\{N\} \in U_i$, $i = 1$ or 2. The reserve factor for the k-th layer is defined as the ratio of the maximum load $\{N\}_{max}$ that can be applied without failure to the applied load $\{N\}_{app}$, viz.,

$$R_{fk}(\theta_k; N) = \{N\}_{max}/\{N\}_{app} \qquad (1.57)$$

where $\{N\}_{max}$ is computed from $FI_k = 1$, with $\{N\} = \{N\}_{max}$. From Equation (1.56) it follows that

$$G_{1k}R_{fk^2} + G_{2k}R_{fk} \le 1 \tag{1.58}$$

where $G_{1k} = F_{11}\sigma_{1k^2} + F_{22}\sigma_{2k^2} + F_{66}\tau_{12k^2} + 2F_{12}\sigma_{1k}\sigma_{2k}$ and $G_{2k} = F_1\sigma_{1k} + F_2\sigma_{2k}$. In Equation (1.58), the stresses are evaluated at $\{N\}_{app} \in U_i$, $i = 1$ or 2. Thus $R_{fk} = R_{fk}(\theta_k; N_{app})$. Taking the limiting case of $FI_k = 1$ to compute the maximum load, R_{fk} for $\{N\}_{max}$ is obtained from Equation (1.57). The reserve factor for the laminate is given by

$$R_f = \min_k\ R_{fk}\left(\theta_k; N_{max}\right), \quad k = 1, 2, \ldots, K/2 \tag{1.59}$$

In the case of a deterministic design problem, the applied loads $\{N\}_{app}$ are given as input parameters, and the deterministic optimization problem is stated as

$$\max_{\theta_k}\ R_f = \max_{\theta_k}\ \min_k\ R_{fk}\left(\theta_k; N_{app}\right) \tag{1.60}$$

In the present problem, $\{N\}_{app} \in U_i$ is not known a priori and needs to be determined as part of the solution. The applied load vector $\{N\}_{app}$ is obtained from the solution of the anti-optimization problem (Equation (1.54)), which yields the least favorable loading denoted by $\{N^*\}$. The optimization problem to maximize the reserve factor can be expressed as

$$R_f(\theta_k^*; N^*) = \max_{\theta_k}\ \min_{\{N\}\in U_i}\ \min_k\ R_{fk}(\theta_k; N) \tag{1.61}$$

where θ_k^* denotes the optimal set of ply angles.

Numerical results are given for a graphite/epoxy laminate for which E_{11} = 138 GPa, E_{22} = 10.3 GPa, G_{12} = 7.17 GPa, ν_{12} = 0.28, $X_t = X_c$ = 1500 MPa, Y_t = 40 MPa, Y_c = 246 MPa, and S = 68 MPa. Maximum values of N_x and N_y are specified as 1 MN/m. The notations $R_f(U_1)$ and $R_f(U_2)$ indicate that R_f applies to loading $(N_x, N_y) \in U_i$, $i = 1$ or 2. Table 1.6 gives the values of the reserve factor R_f with $\{N\} \in U_1$ and the optimal lay-ups. The first column is the multiplier of N_x. The last column of Table 1.6 shows the values of R_f under the uncertain loads. A comparison of R_f values under uncertain and deterministic loadings (columns 2 and 6) shows that R_f values of a deterministically designed laminate under uncertain loading are much lower than the corresponding values of a laminate designed for load uncertainty. The corresponding results for $\{N\} \in U_2$ are given in Table 1.7.

Application of the anti-optimization technique to buckling problems can be found in de Faria and Hansen (2001a, 2001b). Optimization of composite

TABLE 1.6

R_f and Lay-Ups for Optimal 12-Layered Laminates (Uncertainty Domain U_1, with $|N_x| \eth \eta_x N_{x,max}$, $|N_y| \eth N_{y,max}$), Deterministic Loading: $N_x = 0$ and $N_y = N_{y,max}$

Design under Uncertain Loads			Design under Deterministic Loads		
η_x	$R_f(U_1)$	Optimal Lay-Up	R_f	Optimal Lay-Up	$R_f(U_1)$
0.0	1500.0	$(90_{12})_s$	1500.0	$(90_{12})_s$	1500.0
0.1	699.0	$(-45/45_2/90_9)_s$	1500.0	$(90_{12})_s$	400.0
0.2	598.0	$(0_2/90_{10})_s$	1500.0	$(90_{12})_s$	200.0
0.4	516.3	$(0_3/90_9)_s$	1500.0	$(90_{12})_s$	100.0
0.8	397.1	$(0_5/90_7)_s$	1500.0	$(90_{12})_s$	50.0
1.0	373.4	$(0_6/90_6)_s$	1500.0	$(90_{12})_s$	40.0

TABLE 1.7

R_f and Lay-Ups for Optimal 12-Layered Laminates (Uncertainty Domain U_2, with $|N_x| \eth \eta_x N_{x,max}$, $|N_y| \eth N_{y,max}$), Deterministic Loading: $N_x = \eta_x N_{x,min}$, $N_y = N_{y,max}$

Design under Uncertain Loads			Design under Deterministic Loads		
η_x	$R_f(U_2)$	Optimal Lay-Up	R_f	Optimal Lay-Up	$R_f(U_2)$
0.0	1500.0	$(90_{12})_s$	1500.0	$(90_{12})_s$	1500.0
0.1	584.6	$(0/90_{11})_s$	1333.3	$(90_{12})_s$	351.7
0.2	514.4	$(0_2/90_{10})_s$	904.2	$(90_{12})_s$	188.9
0.4	429.3	$(0_3/90_9)_s$	529.2	$(90_{12})_s$	97.4
0.8	329.1	$(0_5/90_7)_s$	420.0	$(0_4/90_8)_s$	291.6
1.0	302.0	$(0_5/-45/45/90_5)_s$	389.6	$(0_4/90_8)_s$	241.0

laminates under multiple loads was studied by Fukunaga et al. (1994), Haridas and Rule (1997), Liu and Hollaway (2000), and Kere and Koski (2001).

1.4.3 Geometric Uncertainty

The main source of geometrical uncertainty is the structural imperfections that may occur as a result of manufacturing processes and longtime environmental effects, such as creep or material aging, leading to an initial deflection the exact shape of which is not known a priori. The lack of information on this geometrical imperfection is quite often handled by adopting a procedure in which an approximate shape is assumed, and thereafter a deterministic approach to design is adopted. Such an approach may produce an acceptable analysis solution, but it becomes unacceptable if the objective is to optimize the design under such uncertainty, especially in the presence of compressive forces that tends to magnify the initial imperfections. This is due to the fact that unless the design is based on a worst-case scenario, the final design is likely to violate a maximum deflection constraint under operating conditions. Analysis studies treating the geometrical imperfections in an undeterministic manner include those by Ben-Haim and Elishakoff (1989),

Elishakoff and Ben-Haim (1990), Ben-Haim (1993), Elishakoff et al. (1994a), and Elishakoff (2000), and optimal design studies that use uncertainty analysis include those by Adali et al. (1994a, 1995b, 1997). Next, the procedure for the optimal design of a composite laminate with unknown initial deflection is presented, where the uncertainty is taken into account in the optimization process using a convex model (Adali et al., 1997).

For a rectangular laminate with initial imperfections, the initial deflection can be expressed as

$$w_i^0(x, y) = w_0^0(x, y) + \tilde{w}_i^0(x, y), \quad i = 1, 2, \ldots, \zeta \tag{1.62}$$

where the subscript 0 denotes the deterministic part and the symbol ~ the uncertain part, with ζ the number of loads. The uncertain part $\tilde{w}_i^0$ is an arbitrary function of x and y but is bounded such that

$$\left\| \tilde{w}_i^0 \right\|_2^2 \le \varepsilon_i^2, \quad i = 1, 2, \ldots, \tag{1.63}$$

where ε_i depends on the level of uncertainty in the initial deflection. The least favorable deflection $w_i^l(x, y; \tilde{w}^0)$ of the laminate at a given point (x_0, y_0) and the uncertain initial deflection $\tilde{w}_i^0$ can be determined via convex analysis by computing

$$w_i^l(x_0, y_0; \varepsilon_i) = \max_{\tilde{w}_i^0} w_i^l(x_0, y_0; \tilde{w}_i^0), \quad i = 1, 2, \ldots, \zeta \tag{1.64}$$

where $w_i^l(x_0, y_0; \varepsilon_i)$ is the deflection at (x_0, y_0) under the i-th loading. The minimization of the laminate weight such that the maximum deflection does not exceed an upper bound δ constitutes the optimal design problem. Moreover, the laminate is optimized with respect to ply angle θ subject to a buckling constraint. In terms of the nondimensional quantities, the weight $W = h$, and consequently the laminate thickness h, is used as the design objective. Let $w_i(x, y, \varepsilon_i)$ denote the least favorable deflection at (x, y) subject to the uncertainty level ε_i. The total deflection $w_i(x, y, \varepsilon_i)$ is given by

$$w_i = w_i^l(x, y; \varepsilon_i) + w_i^0(x, y; \varepsilon_i) \tag{1.65}$$

The design problem consists of determining the minimum thickness h_{min} and the optimal angle θ_{opt} such that

$$\max_{i=1,2,\ldots,\zeta} \max_{x_0, y_0} w(x_0, y_0; \varepsilon_i) \le \delta \tag{1.66}$$

$$P_i < P_{cr}, \quad i = 1, 2, \ldots, \delta \tag{1.67}$$

where P_i is the in-plane load for the i-th loading case and P_{cr} is the buckling load. The initial deflection under i-th loading is expanded in terms of a Fourier series with the coefficients $B\,_{mn}^{(i)} = B_{mn} + \tilde{B}_{mn}^{(i)}$, where B_{mn} refers to the deterministic initial deflection and $\tilde{B}_{mn}^{(i)}$ to the uncertain initial deflection. The coefficients $\tilde{B}_{mn}^{(i)}$ are determined such that they yield the least favorable deflection at (x_0, y_0). For this purpose, it is noted that the coefficients $\tilde{B}_{mn}^{(i)}$ form a convex set defined by

$$\mathfrak{R}_i = \left\{ \left(\tilde{B}_{mn}^{(i)} \right) \middle| \sum_{m=1}^{M} \sum_{n=1}^{N} \left(\tilde{B}_{mn}^{(i)} \right)^2 \leq 4\varepsilon_i^2 \right\}, \quad i = 1, 2, \ldots, \zeta \tag{1.68}$$

in the coordinates $\left(\tilde{B}_{mn}^{(i)} \right)$. The deflection function $w_i^l(x, y; \varepsilon_i)$ takes on its maximum value at an extreme point on the boundary of the convex set $\mathfrak{R}_i$, and consequently equality holds for the constraint in Equation (1.68), viz.,

$$\sum_{m=1}^{M} \sum_{n=1}^{N} \left(\tilde{B}_{mn}^{(i)} \right)^2 = 4\varepsilon_i^2, \quad i = 1, 2, \ldots, \zeta \tag{1.69}$$

for the initial imperfection to give the least favorable deflection. To obtain the least favorable deflection at (x_0, y_0), it is necessary to maximize the function $w_i^l(x_0, y_0; \varepsilon_i)$ over the uncertainty coefficients $\tilde{B}_{mn}^{(i)}$ subject to Equation (1.69). The method of Lagrange multipliers is employed to solve this problem with the Lagrangian for the i-th loading given by

$$\mathfrak{I}_i \left(\tilde{B}_{mn}^{(i)} \right) = w_i^l(x_0, y_0; \varepsilon_i) + \mu_i \left(\sum_{m=1}^{M} \sum_{n=1}^{N} \left(\tilde{B}_{mn}^{(i)} \right)^2 - 4\varepsilon_i^2 \right) \tag{1.70}$$

where μ_i is the Lagrange multiplier. The extremum conditions for the Lagrangian (Equation (1.70)) are given by

$$\frac{\partial \mathfrak{I}_i}{\partial \mu_i} = 0, \quad \frac{\partial \mathfrak{I}_i}{\partial \tilde{B}_{mn}^{(i)}} = 0, \quad m = 1 \ldots M, \quad n = 1 \ldots N \tag{1.71}$$

By substituting the expression for the deflection $w_i^l(x_0, y_0; \varepsilon_i)$ into Equation (1.70), and using the extremum conditions (1.71), the optimal values of $\tilde{B}_{mn}^{(i)}$ are computed as

$$\tilde{B}_{mn}^i = -\frac{2}{\mu_i} \cdot V_{mn}^{(i)}(x_0, y_0) \tag{1.72}$$

where $V_{mn}^{(i)}(x_0, y_0) = P_i \pi^2 (m^2/r^2 + \lambda_i n^2) \, U_{mn}^{(i)}(x_0, y_0)$ with $U_{mn}^{(i)}(x_0, y_0)$ given by Equation (1.49).

An iterative optimization algorithm is developed to determine the minimum thickness h_{min} and the optimal ply angle θ_{opt}. An initial design involving the estimates of h and θ is specified within the feasible region, and the deterministic deflection is calculated. Then a minimum thickness satisfying the deflection and buckling constraints (Equation (1.66)), Equation (1.67), is calculated without changing θ. In the next step, the least favorable deflection is minimized by obtaining an optimal ply angle for the value of h computed in the previous step. Thus, one iteration of the solution procedure consists of the following computations:

$$\min_{h^{(i)}} \left| \max_{x_0,y_0} w_i\left(x_0,y_0;\varepsilon_i\right) - \delta \right| \tag{1.73}$$

$$\min_{\theta} \left(\max_{i} \left| \max_{x_0,y_0} w_i\left(x_0,y_0;\varepsilon_i\right) \right| \right) \tag{1.74}$$

The process converges and produces the optimal laminate with the minimum thickness $h_{min}^{(i)}$ and optimal ply angle θ_{opt}. The minimum thickness h_{min} of the laminate satisfying the constraints in Equations (1.66) and (1.67) for every loading is obtained from

$$h_{min} = \max_{i=1,2...,3} h_{min}^{(i)} \tag{1.75}$$

Optimal ply angles θ_{opt} follow from the optimization step (Equation (1.74)).

Numerical results for a symmetric graphite/epoxy laminate are obtained under a uniformly distributed load $q = 10^{-6}$ and three different in-plane loads, namely, $\lambda_1 = 0.0$ (uniaxial load), $\lambda_2 = 0.5$, and $\lambda_3 = 1.0$ (biaxial loads), with $P = 10^{-6}$, where $\lambda = N_y/N_x$ and $P = N_x/(E_{22}b)$ (Adali et al., 1997). The deterministic part of the initial deflection is specified as zero. In the figures, loadings 1, 2, and 3 refer to $P = 10^{-6}$, with $\lambda_1 = 0.0$, $\lambda_2 = 0.5$, and $\lambda_3 = 1.0$, respectively, plus the uniformly distributed load. The relative magnitudes of the deterministic and uncertain deflections are compared by relating L_2 norm of the uncertain initial deflection to the deterministic deflection using the relation

$$\left\| \tilde{w}_i^0 \right\|_2^2 = \varepsilon_i^2 = S_i^2 \left\| w_i^l \right\|_2^2 \tag{1.76}$$

where $\left\| w_i^l \right\|_2^2$ is the deterministic deflection under i-th loading and S_i specifies the level of uncertainty. $S_i = 0$ corresponds to zero uncertainty, i.e., the deterministic case.

Figure 1.6 shows the curves of h_{min} vs. $S = S_1 = S_2 = S_3$ for loading conditions $i = 1$, 2, and 3. As expected, h_{min} increases with increasing S, but this increase depends on the aspect ratio and the loading case. Figure 1.7 shows θ_{opt} results corresponding to the minimum thickness shown in Figure 1.6. It is observed
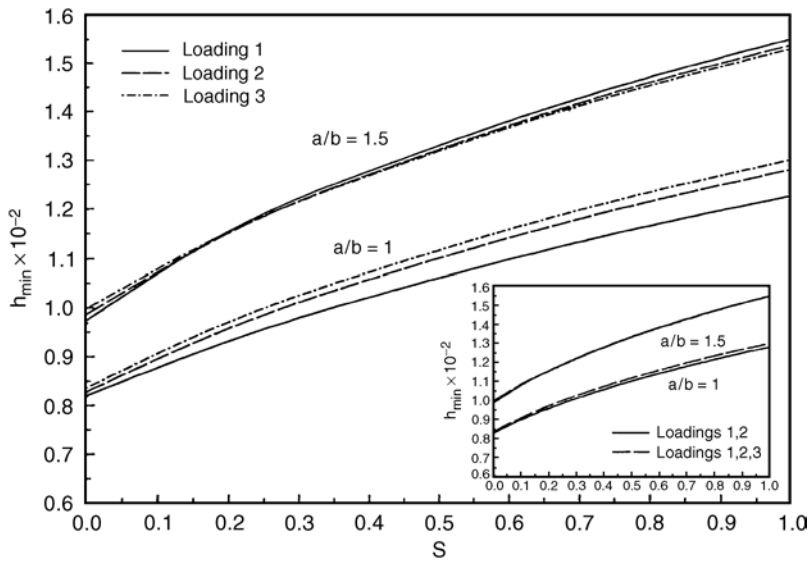
FIGURE 1.6
Minimum thickness vs. the uncertainty parameter for single-load cases, and the insert for multiple-load cases. (Reprinted from S. Adali et al., 1997, *ASME J. Appl. Mech.*, 64:90–96. Copyright 1997, with permission from ASME.)
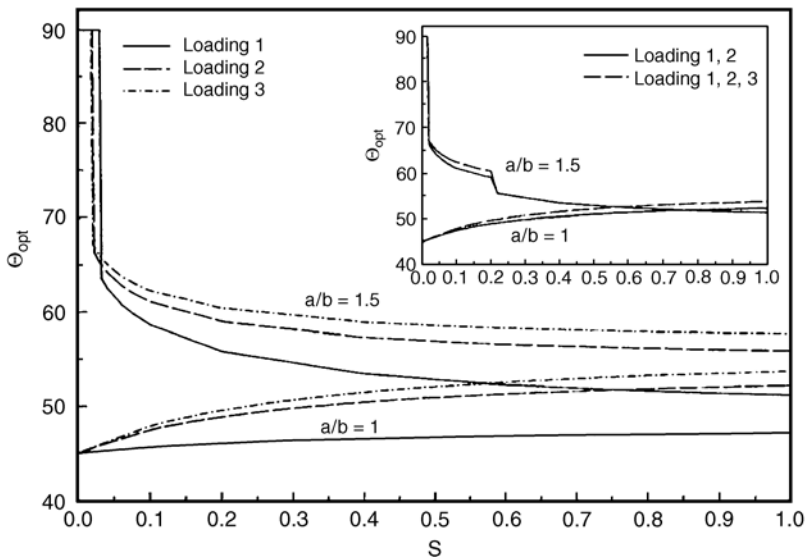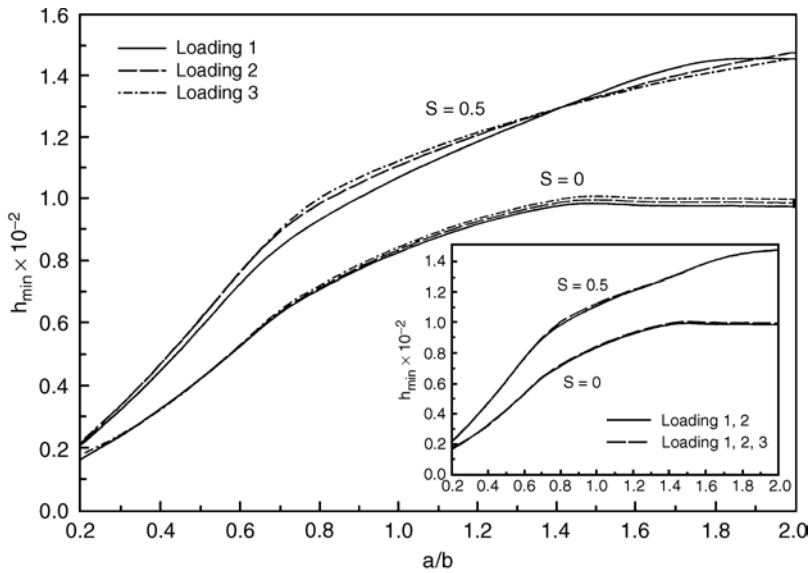

FIGURE 1.7
Optimal ply angle vs. the uncertainty parameter for single-load cases, and the insert for multiple-load cases. (Reprinted from S. Adali et al., 1997, *ASME J. Appl. Mech.*, 64:90–96. Copyright 1997, with permission from ASME.)

FIGURE 1.8
Minimum thickness vs. the aspect ratio for single-load cases, and the insert for multiple-load cases. (Reprinted from S. Adali et al., 1997, *ASME J. Appl. Mech.*, 64:90–96. Copyright 1997, with permission from ASME.)

that values differ considerably for $S = 0$ and $S > 0.5$ when $a/b = 1.5$, indicating that neglecting the effect of uncertainty leads to substantial design errors. The corresponding results for loadings 1, 2 and 1, 2, 3 are shown in the inserts of Figures 1.6 and 1.7. It is observed that loading case 3 is the critical one for all values of S for $a/b = 1$. For $a/b = 1.5$, different loading cases become critical at different values of S. The optimal values of h_{min} and θ_{opt} with respect to the aspect ratio are shown in Figures 1.8 and 1.9, respectively, for different values of S. The inserts of Figures 1.8 and 1.9 indicate that different loadings become effective in determining the optimal values of the thickness and the ply angle at different aspect ratios.

1.5 Concluding Remarks

This chapter focused on the general issues as well as the illustration of specific techniques and problems involving the design and optimization of composite structures operating under deterministic and uncertain conditions. The general issues dealt with the methods of optimization, decision and design variables available to the designer, and complexities arising when modeling, analyzing, and optimizing composites. Various specific examples were given to illustrate the techniques used in the optimization of composites
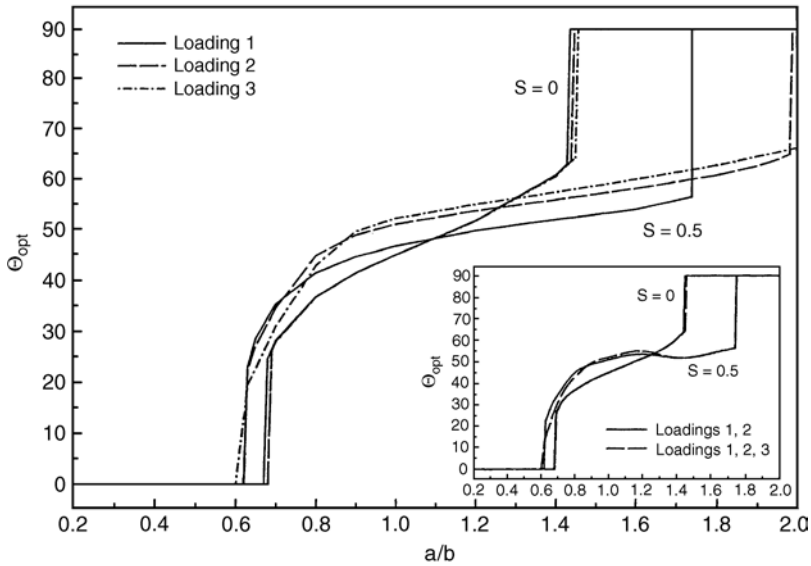
FIGURE 1.9
Optimal ply angle vs. the aspect ratio for single-load cases, and the insert for multiple-load cases. (Reprinted from S. Adali et al., 1997, *ASME J. Appl. Mech.*, 64:90–96. Copyright 1997, with permission from ASME.)

under deterministic conditions. These examples included stiffness and strength optimization, buckling under thermal loads, stiffener optimization, and multiple objectives involving prebuckling, buckling, and postbuckling strengths. Methods for the optimization of composites subject to material, load, and geometric uncertainties were illustrated in the context of specific examples. In particular, convex modeling and anti-optimization techniques were presented for buckling and strength optimization of composites under uncertain conditions.

Presently, one of the trends in the optimization of composites is an integrated approach combining manufacturing concepts and constraints with design optimization (Manne and Tsai, 1998b; Kim et al. 2001). This approach enables the designer to match the processing possibilities to design requirements in an effort to minimize the overall cost. Another trend is the multidisciplinary approach to the optimization of large systems such as aerospace structures, space platforms, and composite vehicles using structural, aerodynamic, and fluid mechanics to produce a complete model of the system (Kim et al., 2002; Guo et al., 2002). This approach enables the designer to take into account various influences of the loading conditions simultaneously. Development of software and algorithms for multidisciplinary design optimization of composites is presently an active area of research (Fischer et al., 2002) due to the need to take a full view of the problems when designing a complex structure.

Main issues in the optimization of composites are the computational time and memory, and the accuracy of design approximations due to the large number of design variables for large systems. The main tools in this respect are approximation techniques such as response surface methods, parallel computation, and the increase in the computational speed and memory as a result of improvements in the integrated circuit technologies. Genetic algorithms are ideally suited for parallel computation, making it a powerful tool for composites optimization. The accuracy obtained by response surface methods and the resulting reduction in the number of computations are important factors in gaining wider usage of this technique for composites optimization (Rikards and Auzins, 2002).

As the refinement of the models and the complexity of the systems increase, and further design and manufacturing requirements and constraints are imposed, composites optimization is will become a more challenging field. One should also add to the above list the future use of nanocomposites in advanced applications, bringing a new dimension to the field of design and optimization of composites (Thostenson et al., 2001; Lau and Hui, 2002). Wider use of nanocomposites in the years to come is likely to bring conceptual changes to the design of composite structures.

References

Adali, S. 1983. Multiobjective design of an antisymmetric angle-ply laminate by nonlinear programming, *ASME J. Mechanisms Transmissions Automation Design*, 105:214–219.

Adali, S. 1993. Convex and fuzzy modelling of uncertainties in the optimal design of composite structures, in *Optimal Design with Advanced Materials*, P. Pedersen, Ed., Elsevier, Amsterdam, pp. 173–189.

Adali, S. 1995. Lay-up optimization of laminated plates under buckling loads, in *Buckling and Post-buckling of Composite Plates*, G.J. Turvey and I.H. Marshall, Eds., Chapman & Hall, London, pp. 334–370.

Adali, S., I. Elishakoff, A. Richter, and V.E. Verijenko. 1994a. Optimal design of symmetric angle-ply laminates for maximum buckling load with scatter in material properties, in *Fifth AIAA/USAF/NASA/ISSMO Symposium on Multidisciplinary Analysis and Optimization*, 7–9 September 1994, Panama City, FL, pp. 1041–1045.

Adali S., A. Richter, and V.E. Verijenko. 1994b. Optimal design of symmetric angle-ply laminates subject to uncertain loads and initial imperfections, in *Proceedings 4th International Conference on Computer Aided Design in Composite Materials Technology* (CADCOMP-94), Southampton, England, pp. 39–48.

Adali, S., A. Ritcher, and V.E. Verijenko. 1995a. Multiobjective design of laminated cylindrical shells for maximum pressure and buckling load, *Microcomput. Civ. Eng.*, 10:269–279.

Adali, S., A. Richter, and V.E. Verijenko. 1995b. Non-probabilistic modelling and design of sandwich plates subject to uncertain loads and initial deflections, *Int. J. Eng. Sci.*, 33:855–866.

Adali, S., A. Richter, and V.E. Verijenko. 1995c. Minimum weight design of symmetric angle-ply laminates under multiple uncertain loads, *Struct. Optimization*, 9:89–95.

Adali, S., A. Richter, and V.E. Verijenko. 1997. Minimum weight design of symmetric angle-ply laminates with incomplete information on initial imperfections, *ASME J. Appl. Mech.*, 64:90–96.

Adali, S. and V.E. Verijenko. 2000. Optimal design of laminated composites subject to load uncertainties via anti-optimization, in *Proceedings of 7th International Conference on Composites Engineering*, 2–8 July 2000, Denver CO, D. Hui, Ed., pp. 3–4.

Adali, S., M. Walker, and V.E. Verijenko. 1996. Multiobjective optimisation of laminated plates for maximum prebuckling, buckling and postbuckling strength using continuous and discrete ply angles, *Composite Struct.*, 35:117–130.

Aiello, M.A. and L. Ombres. 1999. Design of hybrid laminated composite sandwich panels for maximum buckling loads: the influence of thermal actions, in *Proceedings of the 12th International Conference on Composite Materials* (ICCM/12), 5–9 July 1999, Paris, France, 8 pp.

Allen, R.H. and A. Bose. 1987. Acolade: a hybrid knowledge-based system for preliminary composite laminate design, in *Proceedings of ASME Computers in Engineering Conference*, New York, pp. 51–57.

Almeida, S.F.M. and J.S. Hansen. 1997. Enhanced elastic buckling loads of composite plates with tailored thermal residual stresses, *ASME J. Appl. Mech.*, 64:772–780.

Arora, J.S. 1989. *Introduction to Optimum Design*, McGraw-Hill, New York.

Ashbee, K. 1989. *Fundamental Principles of Fiber Reinforced Composites*, Technomic Publishing Co., Lancaster, PA.

Autio, M. 2000. Determining the real lay-up of a laminate corresponding to optimal lamination parameters by genetic search, *Struct. Multidisc. Optimization*, 20:301–310.

Autio, M. 2001. Optimization of coupled thermal-structural problems of laminated plates with lamination parameters, *Struct. Multidisc. Optimization*, 21:40–51.

Avalle, M. and G. Belingardi. 1995. A theoretical approach to the optimization of flexural stiffness of symmetric laminates, *Composite Struct.*, 31:75–86.

Bäck, T. 1996. *Evolutionary Algorithms in Theory and Practice*, Oxford University Press, New York.

Ball, N.R., P.M. Sargent, and D.O. Ige. 1993. Genetic algorithm representations for laminate layups, *Artif. Intelligence Eng.*, 8:99–108.

Barbero, E.J. 1999. *Introduction to Composite Materials Design*, Taylor & Francis, Philadelphia.

Ben-Haim, Y. 1993. Failure of an axially compressed beam with uncertain deflection of bounded strain energy, *Int. J. Eng. Sci.*, 31:989–1001.

Ben-Haim, Y. and I. Elishakoff. 1989. Non-probabilistic models of uncertainty in the non-linear buckling of shells with general imperfections: theoretical estimates of the knockdown factor, *ASME J. Appl. Mech.*, 56:403–410.

Ben-Haim, Y. and I. Elishakoff. 1990. *Convex Models of Uncertainty in Applied Mechanics*, Amsterdam, Elsevier Science.

Berke, L., S.N. Patnaik, and P.L.N. Murthy. 1993. Optimum design of aerospace structural components using neural networks, *Comput. Struct.*, 48:1001–1010.

Berthelot, J.-M. 1999. *Composite Materials*, Springer, New York.

Blachut, J. and H.A. Eschenauer, Eds. 2001. Emerging methods for multidisciplinary optimization, *CISM Courses and Lectures*, No. 425, Springer Wien, New York.

Borkowski, A. and S. Jendo. 1990. *Structural Optimization*, Vol. 2., *Mathematical Programming*, Plenum Press, New York.

Botkin, M.E. 2000. Modelling and optimal design of a carbon fibre reinforced composite automotive roof, *Eng. Comput.*, 16:16–23.

Boyer, C., A. Béakou, and M. Lemaire. 1997. Design of a composite structure to achieve a specified reliability level, *Reliability Eng. Syst. Safety*, 56:273–283.

Callahan, K.J. and G.E. Weeks. 1992. Optimum design of composite laminates using genetic algorithms, *Composites Eng.*, 2:149–160.

Chang, R.R. 2001. Optimal design of laminated composite torque wrench, *Comput. Struct.*, 79:703–713.

Chen, J., S.-S. Jang, D.S.H. Wong, C.-C.M. Ma, and J.-M. Lin. 1999. Optimal design of filament winding using neural network experimental design scheme, *J. Composite Mater.*, 33:2281–2300.

Cohn, M.Z. 1994. Theory and practice of structural optimization, *Struct. Optimization*, 7:20–31.

Composite Design Manual, Bell Helicopter TEXTRON.

Daniel, I.M. and O. Ishai. 1994. *Engineering Mechanics of Composite Materials*, Oxford University Press, New York.

de Faria, A.R. and J.S. Hansen. 2001a. Buckling optimization of composite axisymmetric cylindrical shells under uncertain loading combinations, *ASME J. Appl. Mech.*, 68:632–639.

de Faria, A.R. and J.S. Hansen. 2001b. On buckling optimization under uncertain loading combinations, *Struct. Multidisc. Optimization*, 21:272–282.

Elishakoff, I. 2000. Uncertain buckling: its past, present and future, *Int. J. Solids Struct.*, 37:6869–6889.

Elishakoff, I. and Y. Ben-Haim. 1990. Dynamics of a thin cylindrical shell under impact with limited deterministic information on its initial imperfections, *J. Struct. Safety*, 8:103–112.

Elishakoff, I., G.Q. Cai, and J.H. Starnes. 1994a. Non-linear buckling of a column with initial imperfection via stochastic and non-stochastic convex models, *Int. J. Nonlinear Mech.*, 29:71–82.

Elishakoff, I. and P. Columbi. 1993. Combination of probabilistic and convex models of uncertainty when scarce knowledge is present on acoustic excitation parameters, *Comput. Meth. Appl. Mech. Eng.*, 104:187–209.

Elishakoff, I., R.T. Haftka, and J. Fang. 1994c. Structural design under bounded uncertainty: optimization with anti-optimization, *Comput. Struct.*, 53:1401–1406.

Elishakoff, I., Y.W. Li, and J.H. Starnes. 1994b. A deterministic method to predict the effect of unknown-but-bounded elastic moduli on the buckling of composite structures, *Comput. Methods Appl. Mech. Eng.*, 111:155–167.

Fine, A.S. and G.S. Springer. 1997. Design of composite laminates for strength, weight, and manufacturability, *J. Composite Mater.*, 31:2330–2390.

Fischer, M., D. Kennedy, and C. Featherson. 2002. Multilevel Optimization of a Composite Aircraft Wing using Viconopt MLO, paper presented at 9th AIAA/ISSMO Symposium on Multidisciplinary Analysis and Optimization, 4–6 September 2002, Atlanta, GA.

Fleury, C. and V. Braibant. 1985. Structural optimization: a new dual method using mixed variables, *Int. J. Numerical Methods Eng.*, 23:409–428.

Foldager, J.P., J.S. Hansen, and N. Olhoff. 1998. A general approach forcing convexity of ply angle optimization in composite laminates, *Struct. Optimization*, 16:201–211.

Foldager, J.P., J.S. Hansen, and N. Olhoff. 2001. Optimization of the buckling load for composite structures taking thermal effects into account, *Struct. Multidisc. Optimization*, 21:14–31.

Fukunaga, H. 1990. On isotropic laminate configurations, *J. Composite Mater.*, 24:519–535.

Fukunaga, H., T. Ishikawa, M. Sato, and H. Sekine. 1997. Thermoelastic design of symmetric laminates using lamination parameters, *JSME Int. J.*, 40A:389–397.

Fukunaga, H., H. Sekine, and M. Hiragishi. 1994. Simultaneous optimization of shape and laminate configurations of laminated panels under multiple loadings, *Adv. Composite Mater.*, 3:223–237.

Fukunaga, H. and G.H. Vanderplaats. 1991. Stiffness optimization of orthotropic laminated composites using lamination parameters, *AIAA J.*, 29:641–646.

Gibson, R.F. 1994. *Principles of Composite Material Mechanics*, McGraw-Hill, New York.

Goldberg, D.E. 1989. *Genetic Algorithms in Search, Optimization, and Machine Learning*, Addison-Wesley, Reading, MA.

Grediac, M. 1999. A procedure for designing laminated plates with required stiffness properties: application to thin quasi-isotropic quasi-homogeneous laminates, *J. Composite Mater.*, 33:1939–1956.

Grediac, M. 2000. On the design of some particular orthotropic plates with non-standard ply orientations, *J. Composite Mater.*, 34:1665–1693.

Grediac, M. 2001. On stiffness design of thin woven composites, *Composite Struct.*, 51:245–255.

Guo, J., Z. You, and D. Ren. 2002. A Distributed Multidisciplinary Design Optimization of Architecture for Spacecraft Design, paper presented at 9th AIAA/ISSMO Symposium on Multidisciplinary Analysis and Optimization, 4–6 September 2002, Atlanta, GA.

Gürdal, Z., R.T. Haftka, and P. Hajela. 1991. *Design and Optimization of Laminated Composite Materials*, J. Wiley & Sons, New York.

Gürdal, Z., R.T. Haftka, and P. Hajela. 1999. *Design and Optimization of Laminated Composite Materials*, J. Wiley & Sons, New York.

Gürdal, Z., R.T. Haftka, and S. Nagendra. 1994. Genetic algorithm for the design of laminated composite panels, *SAMPE J.*, 30:29–35.

Ha, S.K., H.M. Jeong, and Y.S. Cho. 1998. Optimum design of thick-walled composite rings for an energy storage system, *J. Composite Mater.*, 32:851–873.

Ha, S.K., H.-I. Yang, and D.-J. Kim. 1999. Optimal design of a hybrid composite flywheel with a permanent magnet rotor, *J. Composite Mater.*, 33:1544–1575.

Haftka, R.T. and Z. Gürdal. 1993. *Elements of Structural Optimization*, 3rd ed., Kluwer Academic Publishers, Dordrecht, Netherlands.

Haftka, R.T., Z. Gürdal, and M.P. Kamat. 1990. *Elements of Structural Optimization*, 2nd ed., Kluwer Academic Publishers, Dordrecht, Netherlands.

Hajela, P. and L. Berke. 1992. Neural networks in structural analysis and design: an overview, *Int. J. Comput. Syst. Eng.*, 3:525–539.

Hajela, P. and Erisman. 1993. Genetic Search Methods in the Design of Thermally Balanced Composite Laminates, paper presented at Proceedings of OPTI '93, 7–9 July 1993, Zaragosa, Spain.

Haridas, B. and W.K. Rule. 1997. A modified interior penalty algorithm for the optimization of structures subjected to multiple independent load cases, *Comput. Struct.*, 65:69–81.

Hu, H.-T. and Z.-Z. Chen. 1999. Buckling optimization of unsymmetrically laminated plates under transverse loads, *Struct. Eng. Mech.*, 7:19–33.

Hyer, M.W. 1998. *Stress Analysis of Fibre Reinforced Composite Materials*, WCB-McGraw-Hill, Boston, MA.

Jayatheertha, C., J.P.H. Webber, and S.K. Morton. 1996. Application of artificial neural networks for the optimum design of a laminated plate, *Comput. Struct.*, 59:831–845.

Jones, R.M. 1975. *Mechanics of Composite Materials*, Taylor & Francis, Philadelphia.

Jones, R.M. 1999. *Mechanics of Composite Materials*, Taylor & Francis, Philadelphia.

Joshi, M.G. and S.B. Biggers, Jr. 1996. Thickness optimization for maximum buckling loads in composite laminated plates, *Composites*, 27B:105–114.

Kam, T.Y. and R.R. Chang. 1992. Optimal lay-up of thick laminated composite plates for maximum stiffness, *J. Eng. Optimization*, 19:233–249.

Kandil, N. and G. Verchery. 1988. Nouvelles methodes de conception des empilementes stratifies, in *Sixth National Conference on Composite Materials*, pp. 891–902.

Kassapoglou, C. and A.L. Dobyns. 2001. Simultaneous cost and weight minimization of postbuckled composite panels under combined compression and shear, *Struct. Multidisc. Optimization*, 21:372–382.

Kedward, K.T. 1997. Design procedures for polymeric composites, in *Proceedings of the 18th Risø International Symposium on Materials Science: Polymeric Composites: Expanding the Limits*, Roskilde, Denmark, S.I. Anderson, P. Brøndsted, H. Lilholt, Aa. Lystrup, J.T. Rheinländer, B.F. Sørensen, and H. Toftegaard, Eds., pp. 43–58.

Kedward, K.T. 2001. Engineering properties of composites, in *Shock and Vibration Handbook*, C.M. Harris, Ed., McGraw-Hill, New York, pp. 35.1–35.31.

Kere, P. and J. Koski. 2001. Multicriterion stacking sequence optimization scheme for composite laminates subjected to multiple loading conditions, *Composite Struct.*, 54:225–229.

Khong, P.W. 1999. Optimal design of laminates for maximum buckling resistance and minimum weight, *J. Composites Technol. Res.*, 21:25–32.

Kim, C.G., J.S. Kim, and C.S. Hong. 1998b. Stacking Sequence Design of Composite Laminate Using Expert System, paper presented at ICCE-5, Las Vegas, Nevada, 5–11 July.

Kim, D.M. and C.S. Hong. 1992. A simple sublimate approach to the design of thick composite laminates for suppression of free-edge delamination, *Composites Sci. Technol.*, 43:147–158.

Kim, J.-S., G.-G. Kim, and C.S. Hong. 1998a. Design of composite laminates using expert system and enumeration method, *J. Kor. Soc. Composite Mater.*, 11:48–49.

Kim, J.S., C.-G. Kim, and C.S. Hong. 1999a. Knowledge-based expert system for optimal stacking sequence design of composite structures, *J. Composite Mater.*, 33:1244–1274.

Kim, J.-S., C.-G. Kim, and C.-S. Hong. 1999b. Optimum design of composite structures with ply-drop using genetic algorithm and expert system shell, *Composite Struct.*, 46:171–187.

Kim, J.-S., C.-G. Kim, and C.-S. Hong. 2001. Practical design of tapered composite structures using the manufacturing cost concept, *Composite Struct.*, 51:285–299.

Kim, J.-S., C.-G. Kim, C.-S. Hong, and H. Thomas Hahn. 2000. Development of concurrent engineering system for design of composite structures, *Composite Struct.*, 50:297–309.

Kim, T. and H. Sin. 2001. Optimal design of composite laminated plates with the discreteness in ply angles and uncertainty in material properties considered, *Comput. Struct.*, 79:2501–2509.

Kim, Y., D. Lee, and Y. Kim. 2002. Multidisciplinary Design Optimization of Super-sonic Fighter Wing Using Response Surface Methodology, paper presented at 9th AIAA/ISSMO Symposium on Multidisciplinary Analysis and Optimization, 4–6 September 2002, Atlanta, GA.

Kirsch, U. 1981. *Optimum Structural Design*, McGraw-Hill, New York.

Kirsch, U. 1993. *Structural Optimization: Fundamentals and Applications*, Springer-Verlag, Berlin.

Kodiyalam, S. and R. Gurumoorthy. 1996. Neural networks with modified back-propagation learning applied to structural optimization, *AIAA J.*, 34:408–412.

Kogisa, N., L. Watson, Z. Gürdal, and R.T. Haftka. 1994a. Genetic algorithms with local improvement for composite laminate design, *Struct. Optimization*, 7:207–218.

Kogisa, N., L. Watson, Z. Gürdal, R.T. Haftka, and S. Nagendra. 1994b. Design of composite laminates by a genetic algorithm with memory, *Mech. Composite Mater. Struct.*, 1:95–117.

Kumar, N. and T.R. Tauchert. 1992. Multiobjective design of symmetrically laminated plates, *Trans. ASME*, 114:620–625.

Lau, K.T. and D. Hui. 2002. The revolutionary creation of new advanced materials: carbon nanotube composites, *Composites Eng.*, 33B:263–277.

Lee, Y.-S., Y.-W. Lee, M.-S. Yang, and B.-S. Park. 1999. Optimal design of thick laminated composite plates for maximum thermal buckling load, *J. Thermal Stresses*, 22:259–273.

LeRiche, R. and R.T. Haftka. 1993. Optimization of laminate stacking sequence for buckling load maximization by genetic algorithm, *AIAA J.*, 31:951–956.

Liu, B., R.T. Haftka, and M.A. Akgun. 1998. Composite wing structural optimization using genetic algorithms and response surfaces, Paper AIAA 98–4854, in *7th AIAA/USAF/NASA/ISSMO Symposium on Multidisciplinary Analysis and Optimization*, 2–4 September 1998, St. Louis, MO, 12 pp.

Liu, B., R.T. Haftka, M.A. Akgun, and A. Todoroki. 2000. Permutation genetic algorithm for stacking sequence design of composite laminates, *Comput. Methods Appl. Mech. Eng.*, 186:357–372.

Liu, J.-S. and L. Hollaway. 2000. Design optimization of composite panel structures with stiffening ribs under multiple loading cases, *Comput. Struct.*, 78:637–647.

Lombardi, M. and R.T. Haftka. 1998. Anti-optimization technique for structural design under load uncertainties, *Comput. Methods Appl. Mech. Eng.*, 157:19–31.

Manne, P.M. and S.W. Tsai. 1998a. Practical considerations for the design of composite structures, *Mech. Composite Mater. Struct.*, 5:227–255.

Manne, P.M. and S.W. Tsai. 1998b. Design optimization of composite plates: Part I: design criteria for strength, stiffness, and manufacturing complexity of composite laminates, *J. Composite Mater.*, 32:544–571.

Manne, P.M. and S.W. Tsai. 1998c. Design optimization of composite plates: Part II: structural optimization by plydrop tapering, *J. Composite Mater.*, 32:572–598.

Maute, K., St. Schwarz, and E. Ramm. 1999. Structural optimization: the interaction between form and mechanics, *ZAMM*, 79:651–673.

McMahon, M.T., L.T. Watson, G. Soremekun, Z. Gurdal, and R.T. Haftka. 1998. A Fortran 90 genetic algorithm module for composite laminate structural design, *Eng. Comput.*, 14:260–273.

Miki, M., Y. Murotsu, and T. Tanaka. 1990a. Optimum Fiber Angle of Unidirectional Composites for Load with Variations, No. AIAA-90-1071, paper presented at 31st AIAA/ASME/ASCE/AHS/ASC Structures, Structural Dynamics and Materials Conference, Long Beach, CA.

Miki, M., Y. Murotsu, T. Tanaka, and S. Shao. 1989. Reliability concept applied to optimum configuration of fibre composites, in *Reliability and Optimization of Structural Systems*, P. Thoft-Christensen, Ed., Lecture Notes in Engineering, No. 48, Springer-Verlag, Berlin, pp. 191–200.

Miki, M., Y. Murotsu, T. Tanaka, and S. Shao. 1990b. Reliability of unidirectional fibrous composites, *AIAA J.*, 28:1980–1986.

Miki, M., Y. Murotsu, N. Murayama, and T. Tanaka. 1993. Application of lamination parameters to reliability-based stiffness design of composites, *AIAAJ*, 31:1938–1945.

Miki, M., Y. Murotsu, T. Tanaka, and S. Shao. 1997. Reliabilility-based optimization of fibrous laminated composites, *Reliability Eng. Syst. Safety*, 56:285–290.

Miki, M. and Y. Sugiyama. 1990. Expert system for composites design with object-oriented language, in *Proceedings of the Fifth Japan–U.S. Conference on Composite Materials*, 24–27 June 1990, Tama-City, Tokyo, Japan, pp. 653–660.

Military Handbook 17, Vol. 3, Department of Defense and Federal Aviation Administration, Washington, D.C., 1996.

Moh, J.-S. and C. Hwu. 1997. Optimization for buckling of composite sandwich plates, *AIAA J.*, 35:863–868.

Morton, S.K. and J.P.H. Webber. 1990. Uncertainty reasoning applied to the assessment of composite materials for structural design, *Eng. Optimization*, 16:43–77.

Morton, S.K. and J.P.H. Webber. 1991. Heuristic methods in the design of composite laminated plates, *Composite Struct.*, 19:207–265.

Morton, S.K. and J.P.H. Webber. 1993. Heuristic optimization of composite structural components, in *Optimal Design with Advanced Materials*, P. Pedersen, Ed., Elsevier Science B.V., pp. 263–279.

Morton, S.K. and J.P.H. Webber. 1994. Heuristic optimization of a laminated composite plate and its comparison with a minimization method, *Commun. Numerical Methods Eng.*, 10:59–65.

Murotsu, Y., M. Miki, and S. Shao. 1994. Reliability design of fiber reinforced composites, *Struct. Safety*, 15:35–49.

Nagendra, S., R.T. Haftka, and Z. Gürdal. 1993. Design of a blade stiffened composite panel by a genetic algorithm, in *Proceedings of the 34th AIAA/ASME/ASCE/ASC Structures, Structural Dynamics and Materials Conference*, 19–22 April 1993, La Jolla, CA, pp. 2418–2436.

Northrop Composite Design Manual, Northrop Corporation.

Nozomu, K., S. Shaowen, and Y. Murotsu. 1998. Reliability-based design of symmetric laminated plate with initial imperfection, No. AIAA-98-4912, in *7th AIAA/ USAF/NASA/ISSMO Symposium on Multidisciplinary Analysis and Optimization*, St. Louis, MO, pp. 1528–1537.

Paradies, R. 1996. Designing quasi-isotropic laminates with respect to bending, *Composites Sci. Technol.*, 56:461–472.

Park, J.H., J.H. Hwang, C.S. Lee, and W. Hwang. 2001. Stacking sequence design of composite laminates for maximum strength using genetic algorithms, *Composite Struct.*, 52:217–231.

Pecora, D., J.R. Zumsteg, and F.W. Crossman. 1985. An application of expert systems to composite structural design and analysis, in *Proceedings of ASME Winter Annual Meeting*, November 1985, Miami Beach, FL, pp. 135–147.

Rajendran, I. and S. Vijayarangan. 2001. Optimal design of a composite leaf spring using genetic algorithms, *Comput. Struct.*, 79:1121–1129.

Richard, F. and D. Perreux. 2000. A reliability method for optimization of $[+,]_n$ fiber reinforced composite pipes, *Reliability Eng. Syst. Safety*, 68:53–59.

Rikards, R. and J. Auzins. 2002. Response Surface Method in Design Optimization of Carbon/Epoxy Stiffened Shells, paper presented at 9th AIAA/ISSMO Symposium on Multidisciplinary Analysis and Optimization, 4–6 September 2002, Atlanta, GA.

Rozvany, G.I.N. 1989. *Structural Design via Optimality Criteria: The Prager Approach to Structural Optimization*, Kluwer Academic Publishers, Dordrecht, Netherlands.

Rybicki, E.F. and D.W. Schmueser. 1978. Effect of stacking sequence and lay-up angle on free edge stresses around a hole in a laminated plate under tension, *J. Composite Mater.*, 12:300–313.

Sadek, I.S., J.M. Sloss, S. Adali, and J.C. Bruch, Jr. 1993. Non-probabilistic modelling of dynamically loaded beams under uncertain excitations, *Math. Comput. Model.*, 18:59–67.

Saravanos, D.A. and C.C. Chamis. 1992. Multiobjective shape and material optimization of composite structures including damping, *AAIA J.*, 30:805–813.

Save, M. and W. Prager. 1985. *Structural Optimization*, Vol. 1., *Optimality Criteria*, Plenum Press, New York.

Schmit, L.A. 1981. Structural synthesis: its genesis and development, *AIAA J.*, 19:1249–1263.

Schmit, L.A. and C. Fleury. 1980. Discrete-continuous variable structural synthesis using dual methods, *AIAA J.*, 18:1515–1524.

Shao, S., M. Miki, and Y. Murotsu. 1991. Optimum Fiber Orientation Angle of Multiaxially Laminated Composites Based on Reliability, No. AIAA-91-1032, AIAA 32nd Structures, Structural Dynamics and Materials Conference, Baltimore.

Shao, S., M. Miki, and Y. Murotsu. 1992. Reliability-based optimum design for multiaxial fiber reinforced laminate systems, in *Reliability and Optimization of Structural Systems*, R. Rackwitz and P. Thoft-Christensen, Eds., Lecture Notes in Engineering, No. 76, Springer-Verlag, Berlin, pp. 339–350.

Shao, S., M. Miki, and Y. Murotsu. 1993. Optimum fiber orientation angle of multiaxial laminated composites based on reliability, *AIAA J.*, 31:919–920.

Singha, M.K., L.S. Ramachandra, and J.N. Bandyopadhyay. 2000. Optimum design of laminated composite plates for maximum thermal buckling loads, *J. Composite Mater.*, 34:1982–1997.

Sivakumar, K., N.G.R. Iyengar, and K. Deb. 1998. Optimum design of laminated composite plates with cutouts using a genetic algorithm, *Composite Struct.*, 42:265–279.

Song, S.R., W. Hwang, H.C. Park, and K.S. Han. 1995. Optimum stacking sequence of composite laminates for maximum strength, *Mech. Composite Mater.*, 31:290–300.

Soremekun, G., Z. Gürdal, R.T. Haftka, and L.T. Watson. 2001. Composite laminate design optimization by genetic algorithm with generalized elitist selection, *Comput. Struct.*, 79:131–143.

Spallino, R. and G. Thierauf. 2000. Thermal buckling optimization of composite laminates by evolution strategies, *Comput. Struct.*, 78:691–697.

Susuki, I. 1991. Strength optimization of multidirectional laminates in an in-plane combined stress state, *Mater. Sci. Eng.*, 143A:175–185.

Thostenson, E.T., R. Zhifeng, and T.-W. Chou. 2001. Advances in the science and technology of carbon nanotubes and their composites: a review, *Composites Sci. Technol.*, 61:1899–1912.

Todoroki, A. and R.T. Haftka. 1998. Stacking sequence optimization by a genetic algorithm with a new recessive gene-like repair strategy, *Composites*, 29B:277–285.

Todoroki, A., N. Sasada, and M. Mitsunori. 1996. Object-orientated approach to optimize composite laminated plate stiffness with discrete ply angles, *J. Composite Mater.*, 30:1020–1041.

Todoroki, A. and M. Sasai. 1999. Improvement of design reliability for buckling load maximization of composite cylinder using genetic algorithm with recessive-gene-like repair, *JSME Int. J.*, 42A:530–536.

Tsai, S.W. 1988. *Composites Design*, 4th ed., Think Composites, Dayton, OH.

Tsai, S.W. 1992. *Theory of Composites Design*, Think Composites, Dayton, OH.

Vanderplaats, G.N. 1984. *Numerical Optimization Techniques for Engineering Design*, McGraw-Hill, New York.

Vannucci, P. and G. Verchery. 2001. Stiffness design of laminates using the polar method, *Int. J. Solids Struct.*, 38:9281–9294.

Vasiliev, V.V. and Z. Gürdal, Eds. 1999. *Optimal Design*, Technomic Publishing Co., Lancester, PA.

Venkataraman, S. and R.T. Haftka. 1999. Optimization of composite panels: a review, in *Proceedings of the 14th Annual Technical Conference of the American Society of Composites*, 27–29 September 1999, Dayton, OH, 10 pp.

Venter, G. and R.T. Haftka. 2000. Two-species genetic algorithm for design under worst case conditions, *Evol. Optimization Int. J. Internet*, 2:1–19.

Vijayarangan, S. and N. Ganesan. 1994. Static stress analysis of a composite level gear using a three-dimensional finite element method, *Comput. Struct.*, 51:771–783.

Walker, M. 1998. Optimization of symmetric laminates with internal line supports for maximum buckling load, *Struct. Eng. Mech.*, 6:633–641.

Walker, M. 1999. Optimal design of symmetric laminates with cut-outs for maximum buckling load, *Comput. Struct.*, 70:337–343.

Walker, M., S. Adali, and V.E. Verijenko. 1996. Optimization of symmetric laminates for maximum buckling load including the effects of bending-twisting coupling, *Comput. Struct.*, 58:313–319.

Walker, M., T. Reiss, S. Adali, and V.E. Verijenko. 1997. Optimal design of symmetrically laminated plates for maximum buckling temperature, *J. Thermal Stresses*, 20:21–33.

Wang, J. and B.L. Karihaloo. 1999. Optimum in-situ strength design of laminates under combined mechanical and thermal loads, *Composite Struct.*, 47:635–641.

Webber, J.P.H. and S.K. Morton. 1990. An expert system for laminated plate design using composite materials, *Comput. Struct.*, 37:1051–1067.

Wu, K.M. and B.L. Avery. 1992. Fully isotropic laminates and quasi-homogeneous anisotropic laminates, *J. Composite Mater.*, 26:2107–2117.

Wu, C.M.L., J.P.H. Webber, and S.K. Morton. 1991. A knowledge based expert system for laminated composite strut design, *Aeronaut. J.*, 95:1–20.

Wu, C.M.L. 1992. Bolted joints in a laminated composite strut design expert system, *Composite Struct.*, 22:63–85.

Yang, L. and Z.K. Ma. 1989. Optimum design based on reliability for composite laminate layup, *Comput. Struct.*, 31:377–383.

Yu, W.J. and H.C. Kim. 1998. Double tapered FRP beam for automobile suspension leaf spring, *Composite Struct.*, 39:279–300.

Zingales, M. and I. Elishakoff. 2001. Hybrid aeroelastic optimization and antioptimization, *AIAA J.*, 39:161–175.

Zumsteg, J.R., D. Pecora, and V.J.A. Pecora. 1985. A prototype expert system for the design and analysis of composite material structures, in *Proceedings of ASME International Computers in Engineering Conference*, pp. 137–143.

2

In-Process Monitoring for Control of Closed-Mold Techniques for the Manufacture of Thermosetting Matrix Composites

John Summerscales

CONTENTS

It is the aim of this chapter to review the technologies available for monitoring the progress of the processes employed for manufacture of continuous-fiber-reinforced thermosetting matrix composites in closed-mold techniques. The manufacturing techniques of special interest are usually referred to by the generic names liquid molding technologies (LMTs)[1] or liquid composite molding (LCM)[2] and, more specifically, resin transfer molding (RTM)[3,4] or resin infusion under flexible tooling (RIFT).[5] A variety of other acronyms have been used for these processes.[6] The techniques may also be applicable to other composite manufacturing processes (e.g., compression molding, vacuum bagging, and autoclave cure).

   The physical changes that take place during composite manufacture include heating and cooling, pressure changes, and fluid flow. Each of these can influence the performance of the finished component in a variety of ways. Insufficient heating may result in a low glass transition temperature and consequent creep under stress. Inadequate pressure or flow may result in high levels of porosity or large voids. On-line sensor systems, which do not compromise the integrity of the finished component, would be a useful step toward improved quality in composites manufacture. The chapter concludes with a brief survey of advanced process control and optimization techniques.

2.1   Temperature

Elevated temperatures are often used in LCM processes to promote more rapid flow of the resin and shorter cure cycles. A balance must be struck between the reduction in resin viscosity (and hence more rapid flow) and a faster cure (and hence a shorter gel time) in order to achieve an optimized mold filling cycle. Thermal management of the process may include either injecting cold resin into hot molds or injecting hot resin into cold molds. The rate of heat transfer between the mold walls (and the preloaded reinforcement) and the resin may be critically important to the success of the process. The resin flow and cure of epoxy resins in RTM and RIFT, and hence heat transfer, are relatively slow processes. However, for unsaturated polyester resins in these processes, and especially for processes such as structural

Calibration	Couple	Temperature Range (°C)	SLOE (%)
B	Pt–30% Rh:Pt–6% Rh	800–1700	±0.5
E	Ni–10% Cr:Cu–Ni	0–900	±0.5 or ±1.7
J	Fe:Cu–Ni	0–750	±0.75 or ±2.2
K	Ni–10% Cr:Ni–5% Al–Si	0–1250	±0.75 or ±2.2
R	Pt–13% Rh:Pt	0–1450	±0.25 or ±1.5
S	Pt–10% Rh:Pt	0–1450	±0.25 or ±1.5
T	Cu:Cu–Ni	0–350	±0.75 or ±1

reaction injection molding (SRIM), there may be a significant generation of heat (exotherm) as the polymerization–cross-linking reaction proceeds.

2.1.1 Thermocouples[7]

A thermocouple is a sensor for measuring temperature. Two different metals or alloys in contact produce a small voltage at a given temperature. This voltage is measured and interpreted by appropriate instrumentation. Thermocouples are available in different combinations of metals (calibrations). The most common calibrations are summarized in Table 2.1 with the standard limits of error (SLOEs) — the percentage of the temperature being measured expressed in degrees Celcius, referenced to 0°C.

Each calibration has a different temperature range and working environment. The maximum temperature varies with the diameter of the wire used in the thermocouple. The following criteria should be used in selecting a thermocouple and sheath: temperature range; chemical, abrasion, and vibration resistance; precision and accuracy; and installation restrictions. The American Society for Testing and Materials (ASTM) has published a manual on the use of thermocouples in temperature measurement.[9]

Thermocouple probes are normally available in one of three junction types:

- In the exposed junction, the junction extends beyond the sheath to give a fast, accurate response. The sheath insulation is sealed where the junction protrudes to prevent penetration of moisture or gas, which could cause errors. Exposed junctions are limited to noncorrosive and nonpressurized applications.

- In a grounded probe, the thermocouple wires are physically attached to the inside of the sheath. This probe gives an intermediate response time in the absence of lag due to the thermal mass of the sheath.

- In an ungrounded probe, the thermocouple junction is detached from the probe wall. Response time is relatively slow, but the thermocouple wire is physically insulated from the thermocouple sheath.

The response time for a thermocouple is defined by the time constant: "the time required by a sensor to reach 63.2% of a step change in temperature under a specified set of conditions. Five time constants are required for the sensor to stabilise at 100% of the change value."[7]

2.1.2 Thermistors[10]

Thermistors are thermally sensitive resistors and have either a negative (NTC) or a positive (PTC) resistance/temperature coefficient. Manufactured from the oxides of the transition metals (manganese, cobalt, copper, and nickel), NTC thermistors are temperature-dependent semiconductor resistors with a range of −200 to + 1000°C. They are supplied in glass bead, disk, chips, and probe formats. NTCs should be chosen when a continuous change of resistance is required over a wide temperature range. They offer mechanical, thermal, and electrical stability, together with a high degree of sensitivity. The excellent combination of price and performance has led to the extensive use of NTCs in applications such as temperature measurement and control, temperature compensation, surge suppression, and fluid flow measurement.

Wen et al.[11] reported that cross-ply continuous-fiber polymer–matrix composites were found to be thermistors due to the decrease in electrical resistivity with increasing temperature. The resistivity was the contact resistivity between cross-ply laminae. The activation energy of electrical conduction was up to 0.12 eV. Each junction between cross-ply fiber groups of adjacent laminae was a thermistor, while the fiber groups serve as electrical leads.

2.1.3 Infrared Thermocouples[7]

Infrared thermocouples receive the heat energy radiated from the target object and use the thermoelectric effect to convert that heat passively to a millivolt electrical potential. The devices are self-powered, using the incoming infrared radiation to produce a signal through thermoelectric effects. The signal is subject to the nonlinearity inherent in the thermal physics of radiation. Infrared thermocouples normally work in a limited part of this nonlinear response. They are usually accurate to within 2 or 5% of the values from a conventional thermocouple over their working range.

Temperatures may also be measured using a variety of other techniques, including resistance probes, optical fibers, or thermochromic coatings (e.g., liquid crystals or paints). However, some of these techniques have limited applicability to on-line monitoring and control.

2.2 Pressure[12]

The international atmosphere is defined as 1.013 bar (101.3 kPa or 14.7 lbf/in^2). Typical process pressures may be from −1 atm (~−1000 mbar) for a

TABLE 2.2

The Principal Pressure Designations

Designation	Imperial	Measurement
Gauge (the most common type)	PSIG	Pressure with respect to the local atmospheric pressure
Sealed	PSIS	Pressure relative to 1 atm at sea level regardless of local atmospheric pressure
Absolute	PSIA	Pressure relative to a perfect vacuum
Differential	PSID	Pressure difference between two input pressures

"rough" vacuum up to 7 atm in an autoclave cure of thermoset matrix composites in an autoclave. A pressure measurement system normally comprises three main components:

- Pressure transducer
- Excitation power supply
- Signal processor

There are four principal designations for pressure, as indicated in Table 2.2.

The three primary considerations in selecting a transducer are the working pressure, working temperature range, and the chemical environment. The recommended range for a pressure transducer is 125% of the normal working pressure, providing that the proof and burst pressure ratings give an adequate safety margin. The transducer diaphragm is usually of silicone (greater accuracy but limited to low pressures and dry gas media) or stainless steel (high pressures, superior corrosion resistance, and wide media compatibility).

Millivolt systems are of relatively low cost as the signal conditioning functions are remote from the actual sensor. This allows the transducer to be comparatively small in size. These transducers are compatible with most strain gauge and load cell instrumentation. Millivolt systems require a regulated power supply. *Amplified voltage* systems contain instrumentation grade amplifiers within the transducer. They are commonly used in laboratory applications and electrically noisy environments. They are generally compatible with process controllers and computer interface systems. *Current loop* systems are particularly well suited to applications where long distances and high noise immunity are required. This is achieved by building a 4 to 20 mA current transmitter into the transducer. Wire runs may be over 300 m (1000 ft) with virtually no signal degradation. These systems are often selected for use in the process industry and interface directly with industrial process controllers, most computers, and data acquisition systems.

There are two types of calibration equipment. A precision dead-weight tester provides an accurately known signal to the system for comparison. Electronic digital gauge standards are also available. Generally, calibration should be traceable to a national standard.

2.3   Viscosity and Flow Rate

It is critically important in the processing of most polymer matrix composites that the resin flows. The resistance to flow is measured as *viscosity*, normally expressed in terms of a relationship between an applied shearing stress and the resulting rate of strain in shear. The optimum viscosity depends on the manufacturing process. The unit for viscosity is Pascal seconds (Pa·s), although older texts use poise (1 Pa·s = 10 poise). It is normal to quote viscosity for fluid resin systems in milliPascal seconds or centipoise (the numerical values in these units are identical).

In liquid composite molding processes, e.g., resin transfer molding and resin infusion under flexible tooling, the resin flows long distances in comparison to most other processing techniques. Rudd et al.[1] suggest that the most significant practical limitation on the suitability of a resin system is imposed by viscosity. Resins with extremely low viscosity may be unsuitable for LCM processes, as they may result in high porosity or gross voidage. Becker[13] quotes an upper limit for viscosity in RTM of 800 mPa·s. The non-injection point (NIP) is defined as a viscosity of 1000 mPa·s.[14] At this viscosity, the flow front is effectively stationary at the low pressures used in LCM processes. High-performance resins for RTM (e.g., PR-500 or RTM-6) may be solid at ambient temperatures and require heating to reduce the viscosity to a level suitable for the process.

For vacuum bagging of wet lay-up carbon fiber/epoxy composites, Stringer[15] suggested that cure should be allowed to progress (dwell) until the viscosity is in the range of 75 to 165 poise (7500 to 16500 mPa·s) before the vacuum is applied. If vacuum is applied at low viscosity (< 75 poise), then high levels of voids result. If vacuum is applied at higher viscosity (> 165 poise), then low void levels and low fiber volume fractions (< 49%) result. In the defined viscosity range, the void content was low (< 2%) and the fiber volume fraction was up to 58%.

In-line viscometers are available commercially. Reference to specific devices below is purely an indication of the equipment currently available and should not be taken as an endorsement of those products or of their suitability for use with resin systems. Indeed, one system is described as "ideal for food and dairy industry applications." Conversely, the exclusion of a product does not imply that it is unsuitable for use with resin systems.

The Nametre Viscoliner®[16] consists of a transducer and an electronic controller. The transducer is "electromagnetically driven into torsional oscillation and is servo-controlled at a constant torsional amplitude of oscillation of 1 μm." A change in viscosity of the material surrounding the probe results in a change in the amount of electrical power required to maintain a constant oscillation amplitude. This change in power is a mathematical function of the fluid viscosity. The Viscoliner systems are able to measure viscosities in the range of 0.1 to 1,000,000 mPa·s, with calibration

(traceable to National Institute of Standards and Technology [NIST] standards) covering up to five continuous decades of viscosity.

Cambridge Applied Systems[17] viscometers use patented technology with one moving part, a piston, driven electromagnetically through the fluid in a small measurement chamber. Proprietary circuitry then analyzes the piston travel time to measure absolute viscosity and monitor temperature. The total two-way travel time is an accurate measure of the fluid absolute viscosity to within a ±1% specification.

The Brookfield SST100 Process Viscometer[18] uses a co-axial cylinder measurement geometry for viscosity at defined shear rates. It has a viscosity range of 350 to 250,000 mPa·s and shear rate range of 7.5 to 225/sec.

A specific apparatus, the Vibrating Needle Curemeter (VNC),[19] monitors the viscosity of the fluid resin system and early stiffness changes after gelation. A steel needle, suspended in the formulation, is vibrated along the vertical axis by an electrodynamic vibrator and resistance to needle movement is recorded. The shape of the trace is dependent on the driver frequency. This technique is normally confined to the laboratory bench rather than used *in situ* during the process.

2.4   Flow Front Position

The arrival of a resin front in any of the liquid composite molding techniques will be indicated by a change in the local temperature (if the mold and the resin are not at the same temperature) or by a change in pressure. Some alternative techniques for monitoring the arrival of the flow front at specific positions are considered below.

The Plastech AGC (Arrival-Gel-Cure) sensor[20] is based on the principle of the galvanic or voltaic cell. The cell uses dissimilar metals for the rod core and tubular sheath, which are insulated from each other by cured resin. When there is no resin on the face of the transducer, no voltage is generated. When resin passes over the face of the transducer, the ionic species in the resin conduct electricity and an increasing voltage indicates the arrival of the flow front. As the resin cures, ion mobility is restricted and the voltage dies away (Figure 2.1).

Walsh[21] proposed and made initial investigations into the use of electrical interrogation of conductive wires placed within nonconductive fiber preforms to monitor the progress of mold filling and changes in the resin rheological behavior. The technique was referred to as the SMART (sensors mounted as roving threads) weave method. Kikuchi et al.[22] substituted a sensing circuit (DC power supply and two resistors in circuit) in place of Walsh's electrometers.

The SMARTweave™ system[23,24] was developed commercially to enable rapid in-process measurements of the extent of mold fill. The presence or
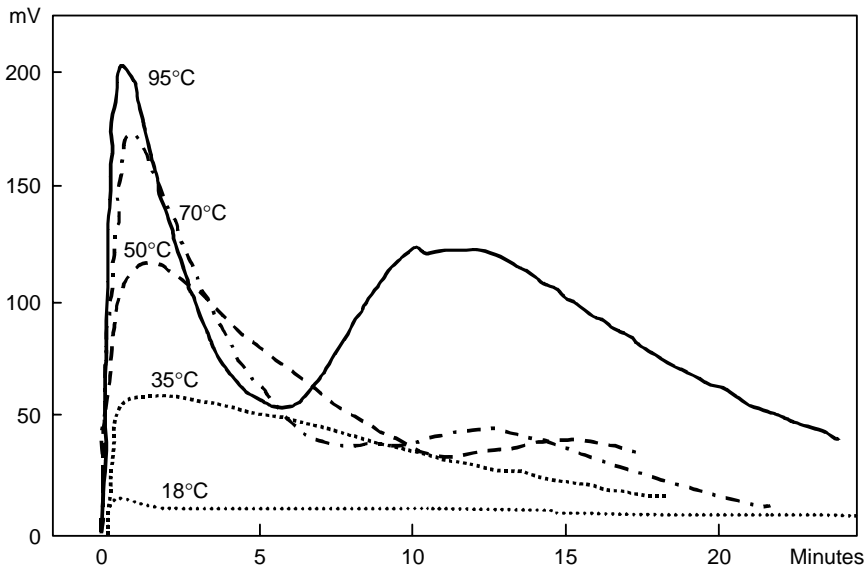
FIGURE 2.1
AGC sensor voltage variation for unsaturated polyester resin cured with 1% methyl ethyl ketone peroxide (MEKP) at different temperatures.

absence of resin at any location is determined by measurement of the electrical resistance between two electrodes at that position. The sensor grid consists of electrically conductive filaments (metal wires, carbon fibers, or metal-coated aramid fibers) that cross on nonintersecting planes to produce a *sensing gap*. Direct current voltage measurements are made across each sensing gap to enable rapid sampling at multiple locations. An indication of the state of cure can be gained from the plot of voltage against time for each location.

Ballata et al.[25] have used a modified version of SMARTweave during the determination of transverse permeability of a fabric preform. Vaidya et al.[26] used the SMARTweave system to compare the flow and "curl" [*sic*] of resin through stitched and nonstitched preforms in resin infusion under flexible tooling. The results indicated that SMARTweave was a viable alternative to interdigitated dielectric (IDEX) sensors (see Section 2.5.2, "Dielectric Sensors") for obtaining resin position and cure state and was superior in terms of obtaining spatial information.

Quinn et al.[27] used SMARTweave to characterize the through-thickness flow front position during a study of the influence of fiber finish on the mechanical properties of a glass fiber composite. A grid of shielded copper wires, with the shielding removed at nodal crossover points, was incorporated within the preform before manufacture by RTM.

Dielectric sensors (see Section 2.5.2) can be used to determine flow front position as the response of the sensor changes when covered by resin.

Bernstein and Wagner[28] used a distributed fiber-optic sensor array and optical time domain reflectometry (OTDR) to monitor the position of the flow front during resin infusion molding (SCRIMP™). The sensor components were of small size and low cost and were incorporated in the part. The optical fibers were 100/140 μm graded index silica fiber (Corning 100/140 CPC3) liquid level sensors. The sensors (6 × 6 × 19 mm) measured the reflectivity at eight ~0.5-mm gaps created by placing the ends of two flat-cleaved fibers in a V-groove cut in a small polycarbonate block and at the fiber end. Arrival of the resin at a sensor position resulted in more onward transmission through the fiber and a lowering of the reflection peak for that position.

Green and Walsh[29] have demonstrated the use of x-ray computed tomography (CT) to generate three-dimensional images of resin flows in laminate composites. The paper does not specify fiber type, resin system, or process used. Resin flow was stopped prematurely before complete "wetting out" of the laminate. Multiple CT scans (slices) were performed and stacked to construct volumetric data that was image-processed to create three-dimensional point cloud models of resin location, and in turn, surfaces were generated.

Stöeven et al.[30] used tool-mounted ultrasonics in the through-transmission mode to monitor the extent of impregnation of the reinforcement during RTM. The time of flight for the ultrasonic wave between source and receiver was influenced by the position of the flow front. An inflection in the time of flight vs. time graph was interpreted as the arrival of first capillary then bulk flow fronts. The flow data acquired in this way were used to estimate a permeability transverse to the plane of the fabric.

2.5   Gel Point and Degree of Cure

A complete characterization of the cure state in real time would be beneficial to the successful manufacturing of composites. As the degree of cross-linking in a resin is increased, the distance between cross-links decreases and a tighter, less-flexible network is formed. In consequence, segmental motion of the polymer becomes more restricted such that the glass transition temperature (T_g) could eventually reach the decomposition temperature. At a high degree of cross-linking, only the amorphous rigid (glass-like state) will exist, as is commonly encountered in the technically important polymers: phenolic, aminoplastic, and epoxide resins.

Maistros and Partridge[31] state that the glass transition temperature is the most sensitive parameter for monitoring the advancement of the cure process and the thermoset network density. The fact that T_g increases nonlinearly with the degree of cure makes it more sensitive in the later stages of the cure when the reaction rates are low and T_g is close to the cure temperature. They suggest that when the cross-linking characteristics of a molecular network depend only on the level of chemical conversion (and not on the thermal

history of the cure process), a unique one-to-one relationship between T_g and conversion can be expected.

Calado and Advani[32] have reviewed the curing reactions of thermosetting resins and discussed the three approaches widely used to characterize and model the reactions:

- Kinetic (phenomenological and mechanistic) models
- Gelation theory
- Rheological models

The equations used to describe the coupled phenomena (resin flow–heat transfer–cure reactions) inherent in any polymer composite manufacturing process are presented and discussed.

Measurement of the degree of cure of a resin or composite is usually undertaken using thermal methods, e.g.:

- Differential thermal analysis (DTA)
- Differential scanning calorimetry (DSC)
- Modulated DSC (MDSC)

or thermomechanical methods (e.g., differential mechanical thermal analysis [DMTA]). A complementary technique for photosensitive or ultraviolet (UV)/light-cured resins is photodynamic mechanical analysis (photo-DMA).[33] These techniques are based on retrospective sampling using laboratory instruments. It would be useful to be able to monitor the state of cure *in situ* during the process with a view to feedback control. A variety of potential techniques could be brought to this problem as indicated below.

2.5.1 Electrochemical

The Plastech AGC sensor, discussed in Section 2.4, "Flow Front Position," gives an indication of the state of cure of the material on the sensor face. The data are normally presented as a graph of AGC voltage response against time (Figure 2.1).

2.5.2 Dielectric Sensors

Dielectric measurements can be made over many decades of frequency, variously from microHertz to megaHertz. Measurements can be taken continuously throughout the entire cure process and converted to the complex permittivity, ε^*, where

$$\varepsilon^* = \varepsilon' - i\varepsilon''$$

with single prime denoting the real part and double prime denoting the imaginary part. The dielectric impedance, Z, of a material is characterized by the equivalent capacitance, C, and conductance, G, where

$$Z^{-1} = G + i\omega C$$

where $\omega = 2\pi f$ and f is the measured frequency. C and G are used to obtain the calculated complex permittivity, ε^*. The real and imaginary parts of ε^* are then given by

$$\varepsilon'(\omega) = \frac{C^{mat}(\omega)}{C_o} , \quad \varepsilon''(\omega) = \frac{G(\omega)}{2\pi f C_o}$$

where $C^{mat}(\omega)$ is the capacitance of the sensor material and C_o is the air replacement capacitance of the sensor. Both the real and the imaginary parts of ε^* can have a dipolar and an ionic component. The change in the value of the dipolar and the ionic mobility can be determined from the frequency dependence of $\varepsilon'(\omega)$ and $\varepsilon''(\omega)$, which can in turn be correlated to laboratory measurement of viscosity and degree of cure.

2.5.2.1 Low (ð MHz) Frequency

The abbreviations for the chemical components of epoxy resin systems referred to in this section are listed in Table 2.3.

The dielectric technique was pioneered primarily by two groups: one at Massachusetts Institute of Technology (MIT)/Holometrix-Micromet[34] and the other at the College of William and Mary (CWM).[35,36] Parallel work was conducted at the Institute of Polymer Mechanics in Russia/Latvia.[37] A comprehensive review of work prior to 1990 has been published by the author.[38]

TABLE 2.3

Abbreviations for the Components of Epoxy Resin Systems

Abbreviation	Molecular Name
AEP	*N*-Aminoethylpiperazine
DADODD	4,9-Dioxa-4,12-dodecane diamine
DDS	Diaminodiphenylsulfone
DEA	Diethylamine
DGEBA	Diglycidylether of bisphenol A (e.g., Dow Chemical DER 332)
DGEBD	1,4-Butanediol diglycidylether
DICY	Dicyandiamide
DMHDA	*N,N'*-Dimethyl-1,6-hexane diamine
PGE	Phenylglycidylether
PHTP	Phenolic hydroxyl-terminated polysulfones
TGDDM	Tetraglycidyl-4,4'-diaminodiphenyl methane
TGDDS	Tetraglycidyl-4,4'-diaminodiphenyl sulfone

During cure, the capacitance and conductance of the material are recorded. The value of ionic conductivity is deduced from this data. Ciriscioli and Springer[39] reviewed dielectric cure monitoring techniques with particular reference to the MIT/Micromet and CWM methods, as these are the most commonly used in conjunction with commercial equipment. Although the two methods differ in detail, they provide nearly identical ionic conductivity values. In order to determine the absolute values of viscosity and degree of cure, it may be necessary to take into account additional parameters (e.g., temperature, dipolar mobility, and rates of change in permittivity, loss factor, and ionic conductivity).

Keller and Dominski[40] demonstrated computer control sequences based on real-time data from thermocouples and 1- to 10-kHz dielectric sensors in autoclave processing. Three materials (APC-2 AS-4 carbon/PEEK, T-300 carbon/phenolic resin precursor for carbon/carbon composites, and T-300 carbon/PMR-15 polyimide) were processed at temperatures up to 270°C. Control was achieved using "the characteristic topography or distinctive shape features of the dielectric loss curves." All critical process events (e.g., release of volatiles, chemical reactions, maximum and minimum viscosities, gelling, solidification, and completion of cure) were detected or anticipated in real time.

Mijović et al.[41] reviewed both the fundamental and pragmatic aspects of the dielectric monitoring of cure. They identified "dielectric measurements [as] the only current commercially developed technique for *in situ* monitoring of cure." The major disadvantages were stated to be the "lack of fundamental models of dielectric behavior during cure and the consequent empiricism and sample specificity." Maffezzoli et al.[42] presented a method for the complete thermal, rheological, and dielectric characterization of an epoxy resin. Ionic resistivity data from the dielectric response were used to develop quantitative correlations. Good agreement was found between the model predictions and experimental data under isothermal and nonisothermal conditions. Bartolomeo et al.[43] used this link between ionic conductivity and conversion to demonstrate the application of the Williams–Landel–Ferry (WLF) equation[44] to the evolution of ionic conductivity vs. temperature and to directly extract conversion from the glass transition temperature calculation.

Jin Soo Kim and Dai Gil Lee[45] developed a 1-kHz dielectric monitoring system. Korean USN 150 carbon fiber/epoxy prepreg (equivalent to Amoco T300/5208) was measured during vacuum bag–autoclave processing with peel ply separating the sensors and the fibers. This was used to compare the derivative of the dissipation factor, dD/dt, with the isothermal degree of cure, β, from a kinetic model using DSC data with various temperature profiles up to 140°C. A modified dissipation factor, D^*, was defined:

$$D^* = (D_{max} - D)/(D_{max} - D_{min})$$

where the dissipation factors D_{max} and D_{min} are the maximum value during cure and the minimum value at the end of cure, respectively. The degree

Area 3 mm × 3 mm
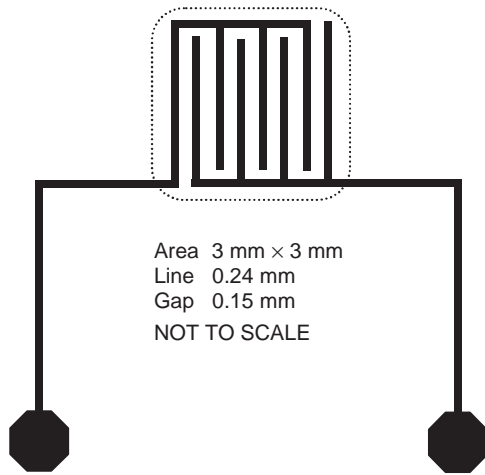Line 0.24 mm
Gap 0.15 mm
NOT TO SCALE

FIGURE 2.2
Schematic of a planar interdigitated capacitor. (After JS Kim and DG Lee, *J. Composite Mater.*, 1996, 30, 1436–1457. With permission.)

of cure calculated from D^* gave a good correlation to the isothermal degree of cure.

Maistros et al.[46] studied a one-part untoughened epoxy resin (Ciba Composites RTM = 6) cured at 160°C using dielectric analysis (DEA) in the frequency range of 100 Hz to 1 MHz using a Solartron 1260A impedance analyzer. Capacitance and conductance data were analyzed to obtain the frequency dependence of the permittivity, ε, and the dielectric loss, ε''. Vitrification times were estimated from the frequencies of maximum dipolar loss. Results were correlated to tests using MDSC and DMTA with the same thermal cycle. Subsequent work has concentrated on:

- Estimation of viscosity as a function of cure prior to gelation and vitrification[31]
- A novel flow and cure sensor for use in resin transfer molding[47]
- Identification of *points of control* for complex cure cycles[48]

Skordos and Partridge[49] have used impedance monitoring (a variation on dielectric methods in which the electric response of the resin system is represented as an equivalent electrical circuit) to follow the curing reaction and the accompanying structural changes during cure. Specific features of the imaginary impedance spectrum were correlated to the progress of the reaction under isothermal and dynamic conditions and used to monitor the position of the flow front during mold filling.

The University of Ulster has used DEA in the parallel plate configuration to monitor fiber-reinforced composites during a simulated RTM curing cycle in a laboratory dielectric instrument. The materials studied were:

- Plain-woven 261 tex (grams/kilometer) glass fibers in Ciba LY564/HY2954 produced by RTM and postcured at 145°C[50,51]
- Fiberite® 934 5-harness satin fabric autoclave cured at up to 120°C[52]
- Glass fiber plain-weave fabric in Ciba LY564/HY2954 epoxy resin produced by RTM and postcured at 145°C[52]
- Four layers of 290 gsm (grams/square meter) plain-weave Toray 3K carbon fiber fabric in Ciba LY564/HY2954 epoxy resin produced by RTM and postcured at up to 145°C[53,54]

The conductive fiber reinforcements were insulated from the electrodes by a 75-μm polyimide film. An operational frequency of 1 kHz was identified as the most sensitive for minimum viscosity, gelation, vitrification, and full cure.

Hranac[55] has described the commercial SmarTrac closed-loop process control system. This derives electrical impedance curves from dielectric sensors. The impedance curve is analyzed and correlated to critical milestones to develop a rule base, which is then programmed into an expert system. When the impedance measurements during cure match key features in the programmed signature, process control decisions are implemented. The system is claimed to reduce cycle times by accurate detection of the end of cure and to improve part quality and consistency.

Wenger[56] has proposed a dielectric monitoring system (DEA) for autoclave cure of advanced composite components for the aerospace industry. For the process to be acceptable, the following criteria were identified:

- The resin viscosity during heat-up must reach a minimum.
- The log ion viscosity (LIV) after gelation must reach a characteristic value for the material.
- The first derivative of LIV must reach a constant low value.
- The above value must be reached within a specified period from the start of the dwell.

The verification of the concept was reported to the Civil Aviation Authority (U.K.), who subsequently gave the go-ahead for the introduction of the proposed cure monitoring system.

2.5.2.2 High (Microwave) Frequency

Microwave dielectric analysis (MDA) measurements are typically made over a narrow bandwidth in the 4- to 6-GHz range.[57] A typical sensor is the size of a coin and may be flush-mounted in the mold. The sensors can operate to up to 250°C and autoclave pressures. The sensors are microwave reflection resonators where the fringing electromagnetic fields over the nonmetallic sensor face are coupled to the test polymer. The dynamic dielectric compo-
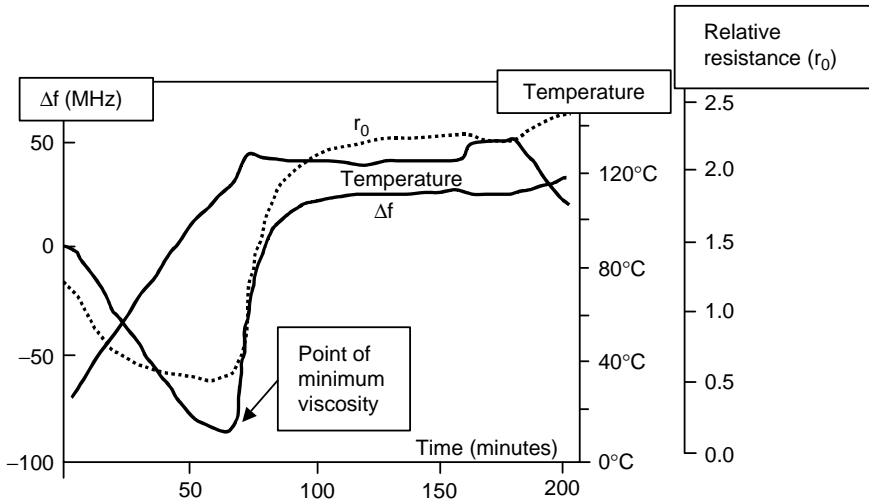
FIGURE 2.3
Microwave dielectric analysis for curing epoxy resin. (After R King et al., *SAMPE J.*, 1992, 28, 35–37. With permission.)

nents (ε', ε'') of the polymer affect the resonant frequency of the sensor (f_r) and normalized input resistance (r_o). For an epoxy resin (DGEBA/TGDDM (1:1)/DICY/diuron) cured at 126°C, f_r and r_o initially decrease, then abruptly reverse signaling the point of minimum viscosity (PMV). Beyond this, the two parameters asymptotically approach their maximum values (Figure 2.3). The resonant frequency of the sensor was correlated with log (viscosity).

Schlegel et al.[58] used X-band (9.35 GHz) and V-band (60 GHz) microwave interferometers in both homodyne and heterodyne configurations to measure the phase differences associated with the volume fraction of glass reinforcement in polyester resin. Homodyne measurements in both bands gave a linear relationship between glass content and phase difference consistent with the rule-of-mixtures prediction. The intention was to develop on-line process monitoring as a substitute for microwave burn-off (ashing) for the determination of fiber volume fraction.

2.5.3 Optical Fibers

2.5.3.1 Traditional Distributed Sensors

The core of an optical fiber may be of similar dimension to the filaments used in composite reinforcement (~7-µm diameter for carbon fibers). Typical diameters are 8–10 µm for single-mode optical fibers or 50–100 µm for multimode optical fibers.[59] Optical fibers are normally clad with a protective polymer coating, which increases the diameter to 125–140 µm. A clad fiber may cause a significant local perturbation in the stress field within the

composite. This disturbed stress field may also initiate early failure of a composite component with such an embedded sensor.

Traditional optical fiber sensors (OFSs)[60] respond to physical perturbations acting along the whole length of the fiber. They are normally interrogated by techniques such as attenuation of illumination intensity, interferometry (Fabry–Perot, Mach–Zender, or Michelson) or time of flight (optical time domain reflectometry). Roberts and Davidson[61] have reviewed the use of fiber-optic sensors (acoustic waveguides, fluorescence spectroscopy, or infrared spectroscopy) for monitoring cure and fabrication of composite materials, including optical monitoring of temperature, pressure, and residual stress.

Liu et al.[62] used embedded optical fiber sensors to monitor changes in the velocity of ultrasound during room temperature cure of an epoxy resin (Hysol EPK 907). Ultrasonic velocity increases as a resin cures. Thus, the relative time delay decreases and is a useful indicator of the state of cure.

Lou et al.[63] showed that a fiber-optic cure monitoring sensor could be integrated with an OTDR strain and temperature sensor. Cure monitoring used a characteristic decay in signal intensity due to the increase in resin refractive index as the cure progressed. Proof of concept was established by monitoring embedded sensors in a Hercules AS4 carbon/3501-6 epoxy composite panel.

Photonetics SA in France[64] markets the Metricor 2000 instrument for fiber-optic sensors in metrology and in process control. An intensity conditioner deals with signals from probes with a limited dynamic range. A dual-wavelength conditioner handles signals from probes requiring referenced operation for opacimetry and chemical concentrations. A third conditioner deals with interferometric sensors operating under white light illumination to return spectrally encoded information without the influence of on-line attenuation. This conditioner can be used with micromachined interferometric temperature, pressure, or refractive index sensors. Amar[65] used this system to study the kinetics of an unspecified resin system and compared the degree of cure with the change in refractive index. Amar states that "the results showed that the refractive index is a good parameter for monitoring the cure although it [is] not sensitive enough," but did not comment further.

2.5.3.2 *Fluorescence*

This technique is based on the fluorescence energy emitted by a probe material mixed with the resin. As the polymer chains cure, mobility of the probe molecules is reduced, leading to a gradual increase in fluorescence intensity.[66,67] The method can detect chemical and rheological events (gelation and vitrification) due to the close link between chain mobility and viscosity.

Levy and Ames[68] reported the use of viscosity dependent fluorescence (VDF) exploiting the microviscosity dependence of a *p-(N,N-dialkylamino)benzylidene malononitrile* probe for monitoring epoxy cure kinetics in a spectrophotometer cell. Neat Ciba-Geigy MY 720 TGDDM epoxy resin was
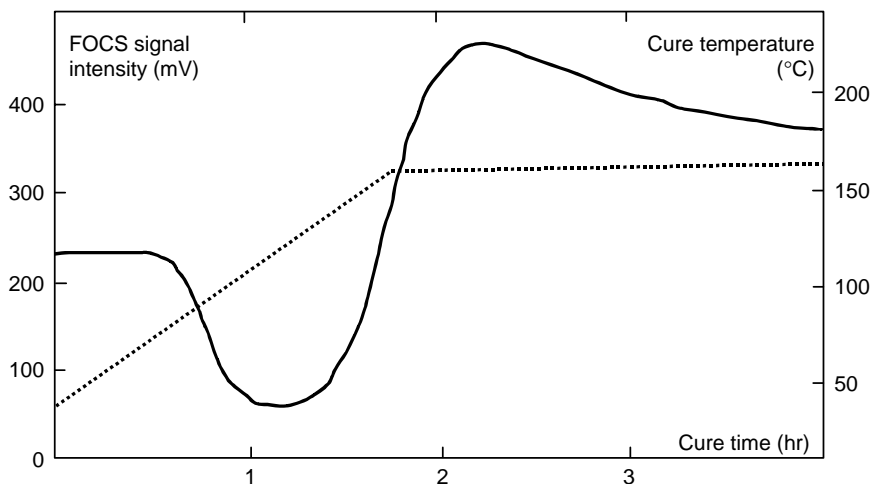
FIGURE 2.4
Signal profile of a tool-mounted fluorescence optrode cure sensor (FOCS). (After RL Levy, *Polym. Mater. Sci. Eng.*, 1986, 54, 321–324. With permission.)

found to exhibit VDF behavior. In a subsequent paper,[69] a plastic-clad all-silica optical fiber (400- or 1000-μm diameter) was used to receive the fluorescence excitation and emission spectra. The above resin cured with DDS and a Hercules 3501-6 carbon fiber composite were monitored. The fluorescence decreased during the initial heating (as the viscosity decreased), then increased with the increase in viscosity as cure progressed, and then (at a point presumed to coincide with the gel point) decreased gradually in proportion to the rate of cure (Figure 2.4). The technique uses the remote end of the optical fiber. The sensor could thus be mounted flush with the mold tool surface.

In fluorescence recovery after photobleaching (FRAP), a photosensitive dye is exposed to an intense laser beam until fluorescence ceases (photobleaching), and then the resin carrier is monitored with a low-intensity probe beam as active probe molecules diffuse into the bleached area, where they fluoresce in the probe beam. Fanconi[70] used optical fibers to measure translational diffusion coefficients of probe dye molecules during the cure of resin. The technique used bare optical fibers of refractive index greater than that of the photosensitive probe–resin system to produce an evanescent field extending into the resin. The data from FRAP measurements consist of a set of fluorescence recovery curves. Fiber-optic FRAP sensors were shown to be capable of measuring diffusion coefficients an order of magnitude smaller than conventional FRAP.

2.5.3.3 Bragg Gratings

Optical fiber Bragg gratings (OFBGs) can be used as sensors to monitor perturbations in their environment. They are immune to electromagnetic interference, provide a high signal-to-noise ratio, and are easily embedded in composite materials. An OFBG consists of a spatially periodic modulation in the refractive index along a short length of optical fiber. This modulation in the fiber permits localized sensing. In 1978, Hill et al.[71] first reported a self-organized Bragg grating induced by the photorefractive effect inside a germanosilicate fiber. In 1989, Meltz et al.[72] reported the use of two-beam UV light holographic exposure to "write" the grating into the fiber. This development stimulated the rapid increase in interest and activity in the field.

The periodicity of the grating determines the wavelength at which light is reflected. The periodicity varies when the fiber is subjected to changes in strain or temperature. By coupling the grating to an appropriate transducer, the grating can be used to monitor a wide variety of parameters. These parameters include strain, temperature, vibration, pressure, and acceleration. An intrinsic disadvantage of both traditional optical fiber and OFBG sensors is their sensitivity to both temperature and strain.

Multiple sensors can be written into a single fiber. This permits the use of a single source and detector, and dramatically reduces the cost per sensor and associated bulk and complexity. It is highly advantageous to multiplex these sensors in linear arrays within a single optical fiber. Several multiplexing schemes have been investigated:

- Special division multiplexing (SDM)
- Time division multiplexing (TDM)
- Wavelength division multiplexing (WDM)

To date, most applications of OFBG sensors in composites have been to monitor structural integrity and to measure strain. The inclusion of these embedded devices in the composite during manufacture should permit their use for monitoring the curing process. Friebele et al.[73] embedded OFBG in glass fiber–vinyl ester composites fabricated by Continuous Resin Transfer Molding™ (CRTM). They reported reflectance spectra of the as-drawn and postprocess gratings and determined that residual tension in the composite was at > 1% strain (Figure 2.5).

2.5.4 Chemical Spectroscopy

Infrared (IR) spectroscopy is the most widely used technique for the identification of specific chemical groups within a material. Each group has characteristic frequencies at which absorption of radiation occurs. To a first approximation, this frequency is independent of the environment of the
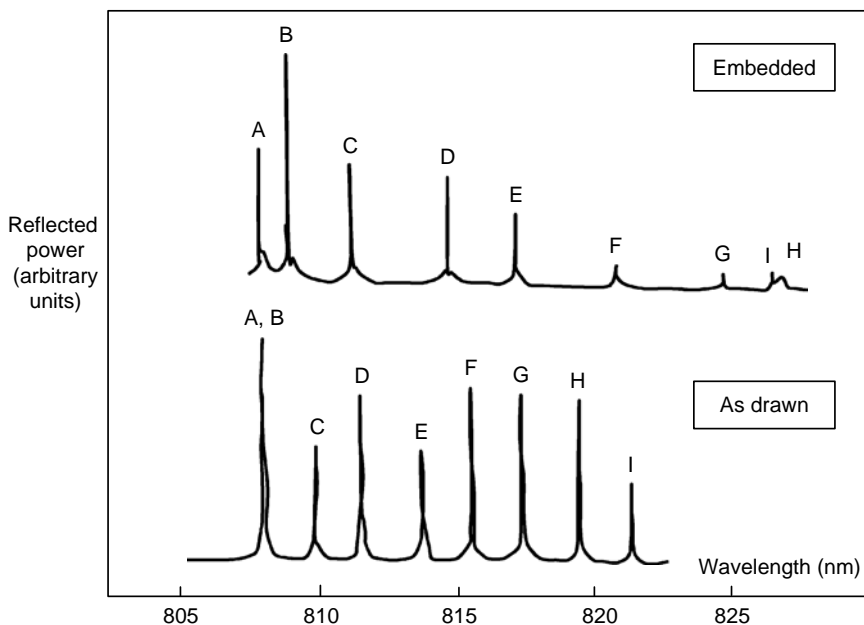
FIGURE 2.5
Reflectance spectra of as-drawn and embedded OFBG sensors. (After EJ Friebele et al., in *SPIE Proceedings*, Vol. 2361, *Second European Conference on Smart Structures and Materials*, Glasgow, 12–14 October 1994, pp. 338–341. With permission.)

chemical group. The spectrum can be obtained by transmission through the bulk or by reflection from the surface of the sample. Traditionally, the spectrum was obtained by scanning through the frequency range (dispersive mode). Modern instruments use a single excitation with Fourier transform (FT) methods to extract the spectrum. The increase in acquisition speed using FT methods permits multiple excitation and result averaging in much reduced times relative to the dispersive instruments. FT can thus produce sharper spectral lines.

When light is scattered by a body, the majority of the light retains the frequency of the incident light and a definite phase relationship to the incident light. This is known as Rayleigh and Tyndall scattering. A very small proportion of the light is scattered with a change in frequency and a random alteration in phase. This is known as the Raman effect. The change in frequency and wavelength is termed Raman shift. This permits chemical characterization of materials provided that strong (laser) light sources are available to produce measurable Raman spectra.

2.5.4.1 Laboratory IR and Raman Spectroscopy

All molecules vibrate with characteristic frequencies. Some modes of vibration may be observed in the IR spectrum. Some modes may be observed

in the Raman spectrum. Some modes are not detected by either technique. For a molecule with a high degree of symmetry, the vibrational modes are absent from both spectra due to the rule of mutual exclusion. As the symmetry is reduced, vibrational modes may be seen in both spectra, albeit with quite different intensities. The observation of a vibrational mode in the IR spectrum requires a change in dipole moment during the vibration. The observation of a vibrational mode in the Raman spectrum requires a change in the electron polarizability, resulting from the movement of the atoms. Two physically distinct experimental approaches have been developed to obtain IR (antisymmetric mode) and Raman (symmetric vibration) spectra. The information from each technique complements that from the other technique due to the different mechanisms (and hence selection rules and intensities).

Urban[74] has reviewed the fundamental principles that govern IR and Raman activity and has discussed the principles and applications of FT detection in vibrational spectroscopy of polymers. Parker[75] reviewed the use of vibrational spectroscopy for PMR-15 polyimide. Edwards et al.,[76] Maddams,[77] and Gi Xue[78] have reviewed Raman spectroscopy of polymeric materials. Allen and Sanderson[79] have reviewed the FT infrared (FTIR) characterization of epoxy adhesives.

Intense laser-induced fluorescence can be a major problem in conventional dispersive Raman spectrometers using visible light lasers, as the signal-to-noise ratio is poor. The use of FT-Raman spectroscopy with near-infrared (NIR) lasers as the excitation source substantially eliminates sample fluorescence, which was a major drawback with earlier dispersive (non-FT) spectrometers. At high temperatures, NIR thermal emission increasingly obscures the Raman signal. Carbon fibers are readily heated by NIR lasers, and the spectrum may be dominated by thermal emission. Williams and Mason[80] have suggested a practical ceiling temperature of 140°C, although cooled cell walls may permit measurement up to 200°C.

Cutler et al.[81] demonstrated that the use of pulsed Nd:YAG NIR lasers and gated detectors can give a significant increase in signal-to-noise ratios when compared to continuous-wave measurements made using the same average laser power. Further, the use of pulsed excitation can greatly reduce long-lived thermal background and, in certain circumstances, can completely eliminate that background.

Agbenyega et al.[82] used FT-Raman spectroscopy to follow the cure reaction in Araldite epoxy resin. The intensity of the decreasing peak at 1257 cm^{-1} (stretching of the aromatic oxygen aliphatic unit) was referenced to the invariant peak at 1608 cm^{-1} (the aromatic ring). The plot of the peak intensity ratio against reaction time (Figure 2.6) indicated completion of the cure after about 10 h.

Walton and Williams[83] used FT-Raman spectroscopy to monitor an epoxy resin (Ciba MY720 TGDDM/DDS) before and after cure at 100°C. After 1 h, the intensities of a number of bands decreased in line with expectations based on the accepted cure mechanisms. The most significant of these bands
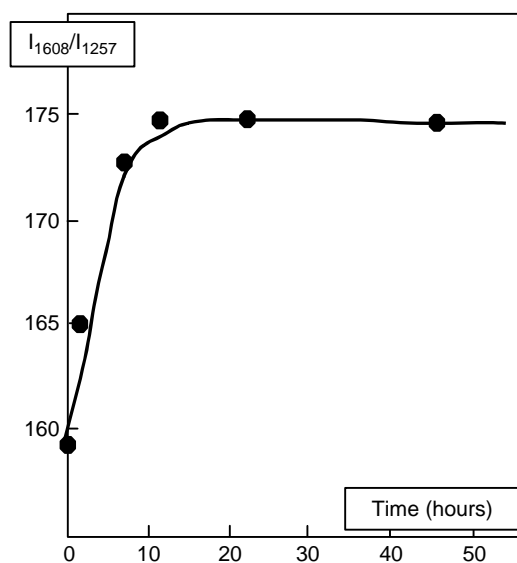
FIGURE 2.6
The intensity ratio I_{1608}/I_{1257} plotted against time for curing Araldite epoxy resin. (After JK Agbenyega et al., *Spectrochim. Acta*, 1990, 46A, 197–216. With permission.)

were assigned to epoxy ring vibrations (1257 and 791 cm^{-1}) and N-H primary amine deformation (1628 and 1495 cm^{-1}). Samples cured for longer periods of time were dark brown, and the combined effects of thermal emission and sample fluorescence swamped the Raman scattering.

De Bakker et al.[84] studied a TGDDS epoxy resin system over the entire cure cycle. Changing peak intensities were again referenced to invariant peaks to monitor the reaction. During the early part of the reaction the FT-Raman was in good agreement with NIR transmission spectroscopy. The techniques diverged in the later autocatalytic stage, probably because the FT-Raman technique interrogated the surface and the IR technique looked at the bulk material.

Min et al.[85–87] used NIR spectroscopy for quantitative analysis of cure reactions in DGEBA/DDS and DGEBA/DDS/PHTP epoxy resin systems. The absorption bands were integrated to quantify their area and then converted to molar concentrations, leading to an understanding of both the reaction mechanism and the cure kinetics.

2.5.4.2   *Fiber-Optic IR and Raman Spectroscopy*

The insertion of samples into laboratory spectrometers is inappropriate for monitoring composite manufacturing processes, especially where automated control is planned. This section will be limited to the use of optical fiber probes for the *in situ* interrogation of the state of the polymer. Compton et al.[88] demonstrated that it was possible to follow the cure of a PMR-15 graph-

ite/polyimide prepreg using mid-infrared fiber optics. FTIR spectra were plotted in differential absorbance units: chemical species consumed in the reaction give rise to negative spectral bands, whereas reaction products give rise to positive bands. Young et al.[89] used the same method for a successful trial during cure of standard LARC-TPI and graphite/PMR-15 polyimide prepreg. They state that the "entire infrared spectrum need not be recorded — a few key absorption bands may be sufficient to follow the cure process."

Williams[90] demonstrated the feasibility of remote sampling in an industrial environment using fiber-optic FT-Raman spectroscopy. The materials studied were indene, polymerizing styrene, and *N*-phenylmaleimide (a model compound used for monitoring the chemistry of the cross-linking reaction in composite materials).

Lyon et al.[91] used a 200-μm diameter quartz fiber-optic sensor to obtain room temperature Raman spectra during cure of an epoxy resin. The resins studied were:

- DGEBA and its reaction products cured with DEA
- PGE cured with AEP

The normalized intensity of the 1240-cm^{-1} Raman peak was linearly related to the molar concentration of epoxide groups, providing a simple relationship for estimating the degree of cure. Chike et al.[92] have demonstrated that both FT-Raman and FTIR spectroscopy have a linear correlation to the epoxide concentration for the DGEBA–DEA system.

Fildes et al.[93] developed a novel optical fiber IR (wavelength = 1.7 to 5 microns) spectroscopic sensor to monitor refractive index changes in epoxy resins during cure. The composites were cross-plied $[(0°/90°)_2, 0°_4]_s$ T300/934 unidirectional prepreg processed at a maximum temperature of 177°C and 100 kPa (vacuum bag) or 690 kPa (autoclave). The spectral data were reduced to between 60 and 130 wavelengths for neural network analysis (see Section 2.7.3) to determine the state of cure during processing.

Maguire and Talley[94] described an FT NIR fiber-optic Raman spectrometer developed with special attention to the efficient implementation of the fiber-optic sensors. They assessed the performance by following the cure kinetics of an epoxy resin (Epon 828/V-40) and a carbon fiber laminate in an autoclave. The use of a thin glass mat or fiberglass sheath on the optical fiber helped to reduce the black body background radiation from the reinforcement. The 1250-cm^{-1} band (attributed to ring stretch of the epoxy group) was amenable to unambiguous interpretation as a signature of the epoxy group. The intensity of the 2870-cm^{-1} band (C-H stretch) was useful as an internal reference as the number of C-H bonds does not change during the curing reaction. The ratio of the two peaks was calculated for each Raman spectrum to estimate the degree of cure. The *in situ* measurement of molecular vibrational spectra was achieved over long (~100 m) distances.
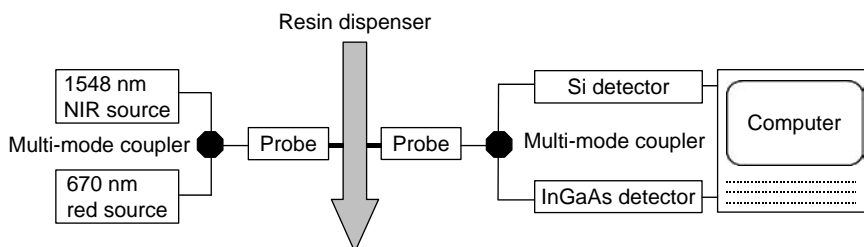
FIGURE 2.7
Schematic of the dual-wavelength optical fiber sensor system for on-line monitoring of amine concentration and mixing. (After T Liu and GF Fernando, *Composites Appl. Sci. Manuf.*, 2001, A32, 1561–1572. With permission.)

Aust et al.[95] have successfully monitored the FT-Raman vibrational spectrum of a high-temperature polymerization reaction using a modulated fiber-optic system. The polymer was 4-phenoxy-4'-phenylethynylbenzophenone (claimed to have potential in aerospace applications) cured at 330°C in a forced-air oven. They claim the first report of real-time FT-Raman spectroscopy above 250°C. The fibers were 200-μm core silica–silica fibers illuminated by a 1064-nm Nd:YAG laser. Probe configuration was 18 collection fibers around a single colinear excitation fiber delivering 350 mW of laser power. Spectra were acquired at 2 sec per scan and averaged over 100 scans. The Raman spectra indicate that the products result from reactions forming a conjugated double-bond system of varying chain lengths and cyclization.

Liu and Fernando[96] have reported the development of an on-line optical fiber sensor for monitoring amine curing agent concentrations and mixing in a flow cell positioned after a static mixer for filament winding. The system employs two laser diodes at NIR (λ = 1548 nm) and red (λ = 670 nm) wavelengths (Figure 2.7). The NIR is sensitive to amine absorption, while the red wavelength is used for correction of the scattering effects. The baseline absorbance of the resin in both wavelength regions and its variation with time were proportional to the extent of scattering in the resin. These parameters have been successfully cross-correlated with the degree of mixing in the resin.

2.5.4.3 Nuclear Magnetic Resonance Imaging

Jackson[97] has established empirical relationships between the observed proton nuclear magnetic resonance (NMR) image intensity and the internal viscosity of the polymer phase in carbon fiber-reinforced epoxy composites during cure at 100°C. The spin–spin relaxation time, T_2, was found to increase from 160 to 2590 μsec on raising the temperature from 20 to 100°C. Calibration curves of viscosity against image signal intensity were developed using an echo time of 5 msec (Figure 2.8). The imaging equipment could then determine any temperature inhomogeneity in the sample during the early

stages of the cure cycle and local viscosity changes after thermal equilibrium had been reached. In a further experiment, the polymer viscosity (derived from the calibration curve) rose from 10 poise after 6 min to 3200 poise (T_2 is then too short for an image to be obtained) after 90 min.
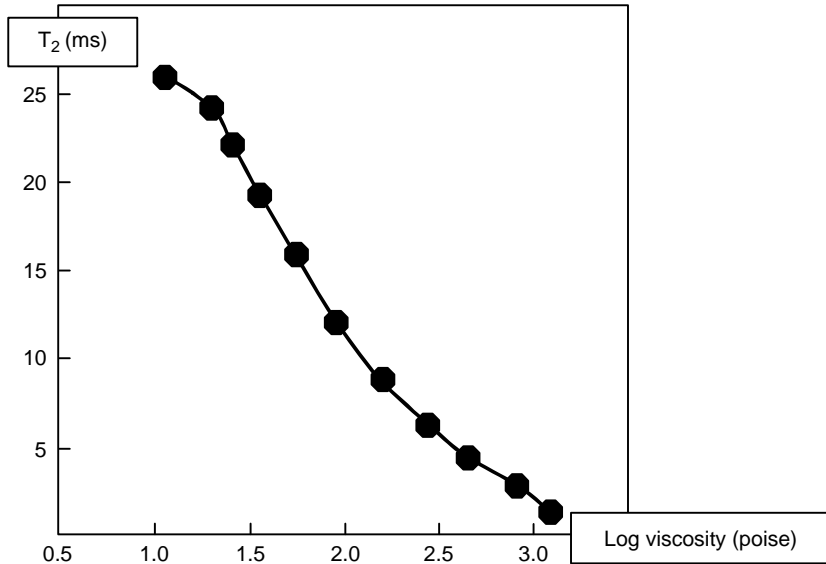

FIGURE 2.8
Master curve of NMR spin–spin relaxation time (T_2) against viscosity of epoxy resin. (After P Jackson, *J. Mater. Sci.*, 1992, 27, 1302–1306. With permission.)

2.5.5 Ultrasonics

A wave is a transient phenomenon that conveys energy through space over time. Electromagnetic waves can propagate in free space (i.e., with no matter present). However, mechanical waves must propagate within matter. Fluid media can only propagate compression (a.k.a. longitudinal) waves, where the particle displacements are parallel to the direction in which the wave is propagating. The propagation of mechanical waves in solids is complex. A shear (a.k.a. transverse or dilational) wave has particle displacements that are perpendicular to the direction in which the wave is propagating. The two waves are classified as P (longitudinal pressure) and S (shear) by earthquake geophysicists. Shear waves can be further subdivided into those parallel (H: horizontal) or perpendicular (V: vertical) to any plane boundary (once again following earthquake notation). Compression waves typically travel at higher speeds than shear waves. Further, the propagation of mechanical waves changes where material boundaries are involved. In addition to bulk waves (infinite media), there exist:

- Surface waves (elliptical particle motion, rapidly attenuated with depth)
- Plate waves (propagation parallel to the midplane between two parallel boundaries)
- Rod waves (in a cylindrical rod or bar)

For wavelengths that are very long compared to the diameter of the bar, wave propagation can be treated as a one-dimensional problem. In this case, longitudinal waves propagate at the bar velocity $\sqrt{(E/\rho)}$ and torsional waves propagate at the wave speed $\sqrt{(G/\rho)}$, where E is Young's modulus, G is the appropriate shear modulus, and ρ is the material density. At megahertz frequencies, small specimens (e.g., 25-mm diameter) can be considered to be infinite when propagation of the center of the wave front is along the center of the bar.[98]

2.5.5.1 Velocity and Attenuation

Speake et al.[99] measured ultrasonic velocity (using an ultrasound critical angle at the solid–liquid interface of immersed material) in order to monitor the cure of amine-cured epoxy resin. The resins were either unfilled or filled with glass beads or unidirectional glass fiber composites. These dynamic mechanical measurements of the elastic moduli were successfully used to yield accurate measurement of the state of cure for all systems. The resin properties had little effect on the longitudinal Young's modulus, but were more important for the transverse Young's modulus and shear modulus.

Lindrose[100] used ultrasonic wave speed and signal attenuation to monitor room temperature cure of an epoxy/amine resin system. Separate 1-MHz transducers were used for each of the longitudinal (compression) and transverse (shear) wave propagation modes. Apparent elastic (bulk, Young's, longitudinal, and shear) moduli were calculated from the wave speeds as a function of cure time. The apparent moduli all increased with time and hence with progress of the cure. Shear moduli were obtained from 25 h to nominal completion of cure at 100 h. A linear approximation for the plot of (longitudinal wave speed squared) against (shear wave speed squared) was extrapolated back to intersect the longitudinal wave speed axis at the point corresponding to the longitudinal wave speed in the initial fluid (Figure 2.9). The apparent Poisson's ratio fell from an initial 0.5 to 0.35 as cure progressed.

Winfree[101] characterized the ambient cure of Epon 815 epoxy resins by measurement of the velocity and attenuation of 5-MHz ultrasonic longitudinal and transverse waves as a function of time. The resin was cast between two parallel glass plates. As cure progressed, the resin changed from a viscoelastic liquid to a cross-linked viscoelastic solid with consequent changes in the bulk and shear moduli of the material and in the ultrasound reflection coefficient for the resin-to-glass interface. A simple mathematical
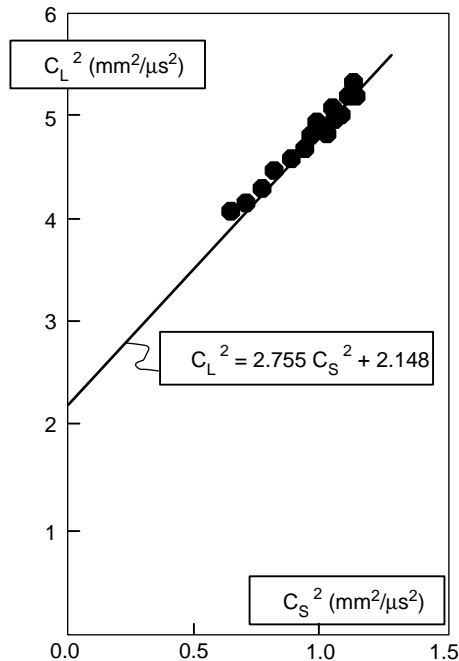
FIGURE 2.9
Plot of (longitudinal wave speed squared) against (shear wave speed squared) for an epoxy/
amine resin system. (After AM Lindrose, *Exp. Mech.*, 1978, 18, 227–232. With permission.)

model, assuming that the resin has a single relaxation time, was found to
explain the changes in elastic properties.

Hahn[102] measured the longitudinal velocity and attenuation in two cast
DGEBA epoxy resins (Epon 828/Z and Epon 815/V140) cured in an oven at
ambient, 50 or 65°C. A 10-MHz transducer operated in pulse-echo mode was
monitored at 10 MHz using an ultrasonic flaw detector. The relative wave
speed (ranging from 1 to ~1.6) and attenuation (ranging from ~24 to 32 dB)
were found to be very sensitive to the degree of cure of the resin.

Prassianakis et al.[103] used the pulse-echo through-transmission technique
to measure the longitudinal velocity and attenuation in curing epoxy resins
(Epicote 828/TET) with 0 to 100% polysulfide plasticizer. Three characteristic
states were clearly determined for neat epoxy resin: liquid, semisolid, and
solid. The addition of plasticizer lowered the ultrasonic velocity and signif-
icantly increased the attenuation.

Gibbs[104] used ultrasonic velocity and attenuation measurements to monitor
the cure of E-glass/chalk/polyester dough molding compound (DMC). Co-
axially aligned standard 2.25-MHz wide-bandwidth lead zirconium titanate
(PZT) probes were mounted in the top (transmit) and bottom (receive) of
the variable 3- to 10-mm cavity mold with a band-pass filter to remove errors
due to preferential absorption of the high-frequency components of the

pulse. Measurements on sections up to 8 mm thick were possible at typical molding temperatures (128 to 155°C).

Shepard and Smith[105] have described a new commercial 5-MHz ultrasonic velocity cure monitoring system for thermoset processing in presses, autoclaves, and liquid composite molding. New sensors maintain good coupling to the composite during thermal cycling to 260°C. For a graphite/epoxy composite, there was a good inverse correlation between ultrasound velocity and log (ionic conductivity) from microdielectrometry (Figure 2.10).
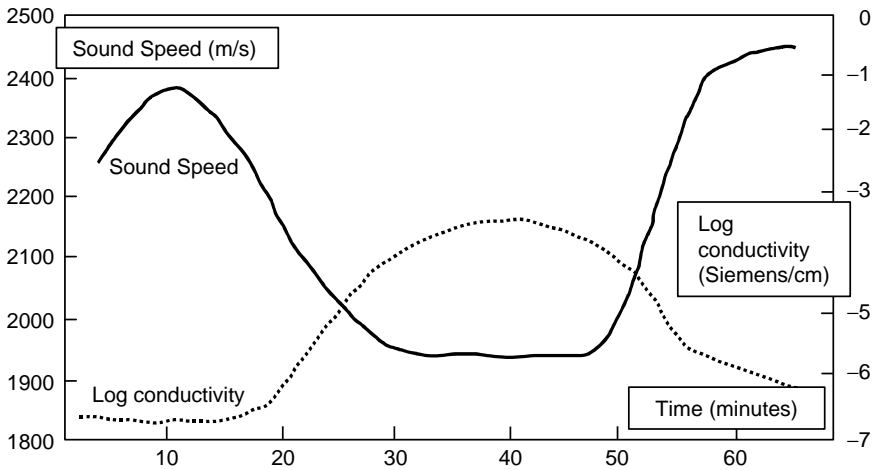
FIGURE 2.10
Ultrasonic velocity and ionic conductivity during the compression molding of graphite/epoxy prepreg. (After DD Shepard and KR Smith, *J. Thermal Anal.*, 1997, 49, 95–100. With permission.)

Brown et al.[106] conducted industrial ultrasonic monitoring trials of injection molding or compression molding with reactive polymer systems (polyesters, amino molding powders, and highly filled materials). The material stiffness (elongational modulus) increases as the reaction proceeds. Time of flight of the ultrasound pulse decreases with increasing degree of cure. The time of flight can be measured with an accuracy of 1 nsec (the range of values quoted in the publication is ~3917 to 4013 nsec). The pulse amplitude is inversely proportional to the material damping (tan δ).

Pulse transmission ultrasound velocity and attenuation have been used for on-line monitoring of the flow and cure behavior of phenolic molding compounds,[107,108] short fiber composites,[107,109] and RTM6 epoxy resin[110] during compression or injection molding. The velocity decreased during softening and then increased with curing time to a level plateau. The relative attenuation reached a maximum value and then decreased.

2.5.5.2 Embedded Waveguides and Optical Fibers

Harrold and Sanjana[111] have demonstrated the versatility of embedded acoustic waveguides for cure monitoring in cross-plied carbon/epoxy (AS4/3501-6) composites. The waveguides were nichrome (Inconel 600), copper, fiberglass/polyester, or carbon/epoxy. Large changes in acoustic attenuation occur at the onset of gelation. The gelation period is identified by changes in the transit time and hence in wave velocity. As the epoxy resin within the composite flows, adheres, and solidifies on the waveguide, most of the acoustic wave then travels in the epoxy layer (slow wave velocity of ~1800 to 2500 m/sec) rather than in the waveguide (fast wave velocity of ~4000 to 7000 m/sec).
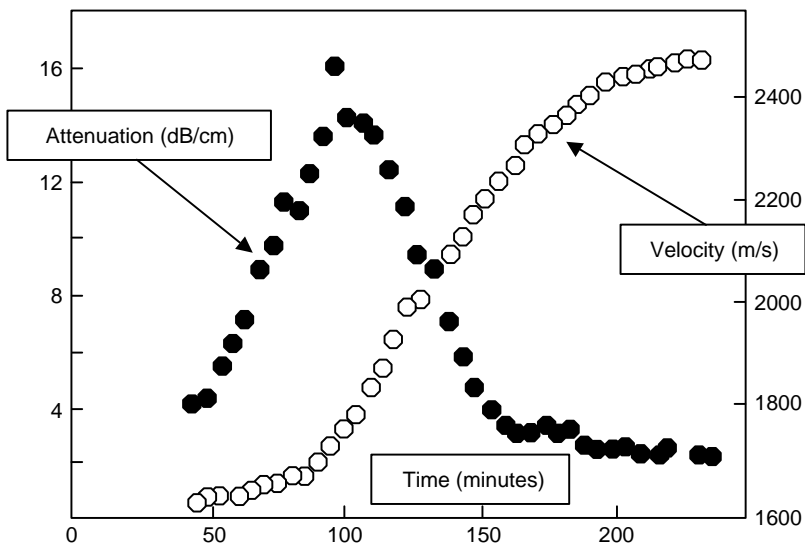
FIGURE 2.11
Ultrasonic signal velocity and ultrasonic attenuation measured during the cure of neat epoxy resin using the embedded Fabry–Perot optical fiber sensor. (After J Dorighi et al., *Res. Nondestructive Eval.*, 1997, 9, 13–24. With permission.)

Ohn et al.[112] used embedded Michelson interferometric fiber-optic sensors to detect ultrasonic pulses propagating in a curing Hysol EPK907 epoxy resin system. Ultrasound pulses were generated by embedded cylindrical piezoelectric transducers. The longitudinal velocity of the resin increased monotonically from ~1500 m/sec at 40 min into cure to ~2000 m/sec at steady state after 320 min.

Dorighi et al.[113] used an embedded Fabry–Perot optical fiber sensor to measure ultrasound velocity and attenuation during the cure of an epoxy resin (Dow DER331/DEH24). The ultrasound pulse was either laser generated and delivered through an external optical fiber or from a surface-mounted piezoelectric transducer. The longitudinal signal velocity increased

from 1650 to 2500 m/sec. The attenuation was initially 4 dB/cm, rose to a peak of 16 dB/cm at 1.5 h, and then fell to 2 dB/cm once cure was complete at ~4 h (Figure 2.11). The peak is attributed to the interrogation frequency being the inverse of the relaxation time of the resin.

2.5.5.3 *Frequency*

Perrissin-Fabert et al.[114,115] embedded thin piezoelectric transducer disks (10-mm diameter, 450 µm thick) in epoxy resins. The disks were excited electrically and caused to vibrate. Changes in the viscoelastic characteristics of the surrounding medium affected the vibration modes and hence the electrical impedance of the piezoelectric sensor. The radial modes of the ceramic were
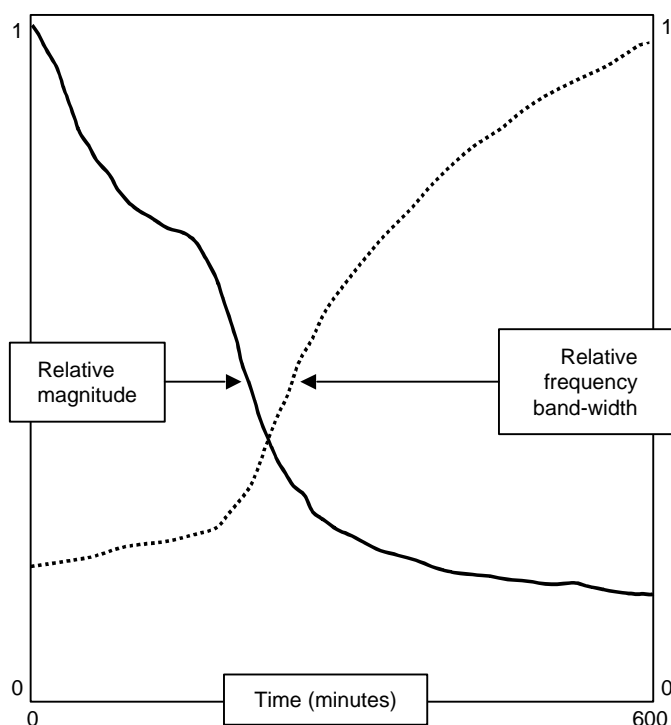
FIGURE 2.12
Variation in the relative magnitude (a) and frequency bandwidth (b) of the piezoelectric transducer first radial mode (235 kHz) during resin gelation. (After I Perrissin-Fabert et al., *Mater. Eval.*, 1994, 52, 1292–1296. With permission.)

very sensitive to the gelation of the resin (Aldrich Chemicals DGEBD/DADODD) as the tangential displacements of the transducer edges produces shear in the resin (Figure 2.12). Vitrification of resin (Dow DER 332 DGEBA/DMHDA) was found to perturb the radial vibrations of the ceramic and then to induce a characteristic asymmetric deformation of a cascade plot of the

electric impedance peaks (magnitude vs. frequency vs. reaction time). The first three transducer radial overtone frequencies were 235, 535, and 835 kHz. The first thickness mode frequency was 5 MHz.

Whitney and Green[116] monitored the resonant spectrum of a steel caul plate every 90 sec during vacuum bagging of a unidirectional AS4/3501-6 carbon epoxy composite. A swept-frequency sine input forced mechanical resonance for analysis by resonant ultrasound (50 to 85 kHz) spectroscopy. As the composite cured, the boundary conditions on the caul plate changed. This affected the amplitude, frequency, and damping spectrum. The curing composite caused significant shifts in this frequency with time.

Chen et al.[117] studied the ultrasonic parameters that are sensitive to cure for both epoxy resin and unidirectional AS4/3501-6 carbon epoxy prepregs fabricated by vacuum bagging and autoclave cure. The cure status of the materials was also characterized using DSC and DMA. Anisotropic elastic moduli were determined from time-of-flight measurements at different angles via the ultrasonic phase velocities. Through-thickness longitudinal dispersion and attenuation were derived from spectroscopic analysis of broadband acoustic pulses.

2.5.6   Mechanical Impedance Analysis

The principle of mechanical impedance analysis (MIA) measurement was proposed by Ferry.[118] Use of the technique for monitoring resin cure was suggested by Jang and Zhu.[119] The sample is continuously excited with a random waveform by an electromagnetic shaker. The output signals are analyzed by fast Fourier transform (FFT) and displayed as a frequency response function (FRF) spectrum. The mechanical dynamic modulus and loss tangent obtained are characteristic of the resin molecular weight.

2.6   Data Fusion

Data fusion is a rapidly evolving technology devoted to the concept of multisensor integration. The aim of data fusion is to combine and manage multisensor data in order to obtain a more complete evaluation of the environment in which the sensors are operating. Books on data fusion in nondestructive testing (NDT), composite inspection, scientific visualization, and performance analysis[120] and specific to NDT case studies[121] are available.

2.7　Process Control

The chapter has reviewed the technologies available for monitoring the progress of the manufacturing processes for thermoset matrix composites in closed molds. The data available from these techniques may be used as a record of the process. In combination with techniques such as statistical process control (SPC), the information can provide a basis for action to improve the process, reduce scrap, and prevent the production of items that do not meet the design intent or customer expectations.[122] Further information can be found in the literature.[123–128]

Modern computers permit the on-line analysis of data that may in turn be used directly for process control.[129] The primary variables are temperatures (resin, reinforcement, molds, etc.), pressures (including vacuum levels), and flow rates (especially for RTM/RIFT). Once the mold cavity is closed, additional information about the dependent variables (flow front position, viscosity, and state of cure) can enhance confidence in the control of the progress of the process.

2.7.1　Proportional-Integral-Derivative Control[130]

The first element of proportional-integral-derivative (PID) control is *proportional* (P) control. This calculates the error (*e*: the difference between the measurement and the set point for the process being controlled). If the error is positive, the controller takes direct action. If the error is negative, the controller takes reverse action. In a direct acting control loop, an increase in the process measurement causes an increase in the control output. The proportional-only equation is *output = (gain × error) + bias*. A proportional-only controller will not bring the process measurement to the set point without a manual adjustment to the bias (or manual reset) term of the equation. In the early days of control the operator, upon observing an offset in the control loop, would correct the offset by manually resetting the controller (adjusting the bias).

Rather than require that the operator *manually reset* the control loop, control functions were developed to *automatically reset* the controller by adjusting the bias term whenever there was an error. This *automatic reset* is also known simply as *reset* or as *integral* (I). The most common way to implement integral mode in analogue controllers is to use a positive feedback into the output. The equation for PI control is *output = gain × (error + integral (error) with respect to time)*.

The third term of PID control is *derivative* (D), also known as rate. The derivative term looks at the rate of change of the input and adjusts the output based on that rate of change. The derivative function can either use the measurement only (excluding changes in the set point) or the time derivative of the error (*de/dt*, including changes in the set point). The equation for the

derivative contribution (assuming derivative on error) is *output = gain ×
derivative × de/dt*.

The PID controller brings the three elements together. Combining these
elements (gain, integral, and derivative), we have the equation *output = G(e
+ R∫edt + D(de/dt))*, where *G* is gain, *e* is error, *R* is reset (repeats), and *D* is
derivative. Note that the gain in the equation is multiplied by all three terms.
This is important for the PID equation to be able to be tuned by any of the
standard tuning methods.

Bickerton et al.[131] investigated active control of RTM focusing on mold
filling. Sensors (measurement of electrical resistance across the tips of two
conducting wires separated by several millimetres) were used to detect the
flow front position. There was a sharp drop in resistance when the test fluid
bridged the gap between the wire tips. A design methodology was presented
for the active control of multiple line injection and automated venting using
decision trees. The system used liquid injection molding simulation (LIMS)
quadrilateral finite elements for the RTM model with a module for the design
of actively controlled injection schemes. Simulations (7800 4-node elements
with 8035 nodes) required up to 15 min on a 400-MHz PC. The algorithm in
this study implemented a model reference feed-forward controller supple-
mented by PID feedback control. The system was successfully used to adjust
flow rates in the presence of race tracking with nonreactive liquids. The
potential to extend the system to control of reactive resin systems was noted.

2.7.2 Fuzzy Logic Control

Zadeh[132] defined the basic operations of fuzzy set theory over 30 years ago.
During the early seventies, fuzzy logic was introduced as a way of formally
describing and manipulating linguistic information. Fuzzy logic is basically
a multivalued logic that allows intermediate values to be defined between
conventional evaluations like *yes/no*, *true/false*, *black/white*, etc. Notions like
rather warm or *pretty cold* can be formulated mathematically and processed
by computers. In this way, an attempt is made to apply a more human way
of thinking in the programming of computers.[133]

It soon became apparent that it could also be used to provide simple
control laws in cases where both the system and the task that needs to be
performed can be described linguistically. There is no requirement for an
explicit model of the system in order for a fuzzy controller to be designed.
Hence, the design process can be extremely simple. This has allowed engi-
neers to produce satisfactory controllers with minimum effort. However, in
spite of the numerous success stories many people in the control community
are still skeptical about fuzzy control. The main argument against it is that
the lack of an explicit model for the plant makes it impossible to formulate
proofs about the performance of the fuzzy controller. This is clearly a major
drawback for a control scheme in cases where precise performance is needed
(for example, for safety).[134] Fuzzy logic control (FLC) incorporates the uncer-

tainty and abstract nature inherent in human decision making into expert-type control systems.[135]

Design methods for conventional automatic control systems involve the construction of mathematical models describing the dynamic system to be controlled and the application of analytical techniques to the model to derive control laws. These models work well provided the system does meet the requirements and assumptions of synthesis techniques. Although application of fuzzy logic to industrial problems has often produced results superior to classical control, the design procedures are limited by the heuristic rules of the system. This implicit assumption limits the application of fuzzy logic controllers. Moreover, the majority of FLCs to date have been static and based upon knowledge derived from imprecise heuristic knowledge of experienced operators. The fuzzy logic-based approach to solving problems in control has been found to excel in systems that are very complex and highly nonlinear and have parameter uncertainty. A fuzzy logic controller may be viewed as a real-time expert system that employs fuzzy logic to analyze input-to-output performance. This provides a means of converting a linguistic control strategy derived from expert knowledge into automatic control strategies and a means of interrogating the control system evolution and system performance.[136]

Fuzzy control, which directly uses fuzzy rules, is the most important application in fuzzy theory. Using a procedure originated by Ebrahim Mamdani in the late seventies, three steps[137] are taken to create a fuzzy-controlled machine:

1. Fuzzification — graphic description of a situation using "membership functions"
2. Rule evaluation — application of fuzzy rules
3. Defuzzification — obtaining the crisp results

Further information can be found in the literature.[138–142]

Sliding mode control is a particular type of variable structure control system (VSCS). A VSCS is characterized by a suite of feedback control laws and a decision rule. The decision rule, termed the switching function, has as its input some measure of the current system behavior. It produces as an output the particular feedback controller to be used at that instant in time. The variable structure system may be regarded as a combination of subsystems. Each subsystem has a fixed control structure and is valid for specified regions of system behavior. One of the advantages of introducing this additional complexity into the system is the ability to combine useful properties of each of the substructures of the system. Furthermore, the system may be designed to possess new properties not present in any of the substructures alone.[143] By combining fuzzy control and sliding mode control, one can reduce the complexity of fuzzy rule bases. This also ensures stability and robustness.[144]

2.7.3 Artificial Neural Networks[145]

The term neural network, or more appropriately, artificial neural network (ANN), has come to mean any computing architecture that consists of many parallel interconnections of simple computing elements. As an area of research, it is of great interest due to the potential to provide insight into the highly parallel computation carried out by the physiological nervous system. Narendra and Parthasarathy[146] suggested that feed-forward neural networks could be used as components in feedback systems. This led to increased interest in neural network-based control, especially for controlling nonlinear systems. Much of the research was heuristic in nature, but it provided empirical evidence that neural networks could outperform traditional methodologies in many applications. Further information on ANNs can be found in the literature.[147–149]

Artificial neural networks have been used for:

- Regression of past operational data for a novel feedback control strategy for autoclave cure of carbon epoxy laminates[150]
- Simulation models to obtain optimal cure cycles[151,152]
- Evaluation and prediction of the degree of cure using a dual-heat-flux sensor[153]

Fildes et al.[93] used unsupervised learning neural network analysis with a novel optical fiber infrared spectroscopic sensor (monitoring the refractive index changes) to follow the state of cure in epoxy resins (see Section 2.5.4.2).

Lichtenwalner[154] developed an artificial neural network-based control system to control laser heating for the fiber placement composite manufacturing process. After learning from experience, the neural network feed-forward control module greatly improved temperature-tracking performance (faster convergence and reduced temperature deviation) when compared to PID controllers.

Nielsen and Pitchumani[155] trained an artificial neural network to provide rapid real-time process simulation for on-line model-predictive control of mold filling in resin transfer molding. A simulated annealing algorithm interacted with the neural network to rapidly derive optimal control decisions. They claim the first *optimal model-based control framework* for this process. The controller was shown to have a general ability to steer fluid through either homogeneous or heterogeneous preform architectures and either symmetric or asymmetric fill patterns using feedback from charge-coupled device (CCD) camera-based imaging with three independent peristaltic pumps serving separate injection ports.

2.7.4 Genetic Algorithms

Holland[156] originated genetic algorithms (GAs). His twin aims were to improve the understanding of the natural adaptation process and to design artificial systems having properties similar to natural systems. The genetic pool of a given population potentially contains the solution, or a better solution, to a given adaptive problem. This solution is not "active" because the genetic combination on which it relies is split between several subjects. Only the association of different genomes can lead to the solution. During reproduction and crossover, new genetic combinations can occur, and eventually a subject can inherit a "good gene" from both parents. The Holland method is especially effective because he not only considered the role of mutation (mutations very seldom improve the algorithms), but also utilized genetic recombination (crossover). The crossover of partial solutions greatly improves the capability of the algorithm to approach and (eventually) find the optimum combination.

Genetic algorithms are stochastic, parallel search algorithms based on the mechanics of natural selection: the process of evolution. GAs were designed to efficiently search large, nonlinear, poorly understood search spaces where expert knowledge is scarce or difficult to encode and where traditional optimization techniques fail. They are flexible and robust with the adaptiveness of biological systems. GAs are generally well suited to searching the large, poorly understood spaces that arise in the design of control strategies. The application of GAs is normally limited to off-line optimization rather than on-line process control. Further information on GAs can be found in the literature.[157–166]

Genetic algorithms have been used for:

- Gate location optimization in liquid composite molding[167]
- Optimal design of process parameters for resin transfer molding[168]
- Integrated product and process design for RTM products using genetic algorithms in combination with a cascade correlation neural network architecture[169]
- Optimization of gate and vent locations in RTM[170]
- Tooling design for resin transfer molding with a neural network–genetic algorithm optimization procedure[171]

2.8 Conclusions

The potential techniques for monitoring the progress of closed-mold composite manufacturing processes have been reviewed. Electrical, and especially dielectric, techniques have achieved the greatest success as commercial

systems. Optical fiber methods show promise for further development, most notably where distinct features in chemical spectra can be obtained.

The monitoring technologies provide the data to permit process control. In composite manufacturing, the vast majority of automated processes are controlled by programmable logic controllers (PLCs) and PID algorithms. Alternative options for process design and process control have been introduced with reference to relevant situations where they have been implemented. Only when the required sensor technology is coupled with appropriate control methodologies will an effective control system be obtained.

Rigorous numerical process simulation is computationally tedious. This constrains the realization of simulation-assisted control for composite manufacturing processes. The simulation timescales need to be comparable to those of the fabrication process. The rapid increases in computing power over recent years, combined with the monitoring techniques considered in this review, should soon permit the implementation of more advanced control systems in composite manufacturing processes. The application of intelligent systems to the control of the composite manufacturing process will be constrained by a number of factors. Primary considerations are the costs of establishing an appropriate database of material–process–property relationships plus the costs of sensor and control systems. Industries that follow this route will be limited to those producing small numbers of high-cost components or to mass production manufacturers. In aerospace, "the smallest of changes demands recertification by the qualifying authorities,"[172] and in consequence, process control will normally be limited to the envelope of previously certified manufacturing parameters if the component is to fly.

References

1. CD Rudd, AC Long, KN Kendall, and CGE Mangin, *Liquid Moulding Technologies*, Woodhead Publishing, Cambridge, U.K., 1997.
2. RS Parnas, *Liquid Composite Moulding*, Hanser Gardner Publications, Munich, Germany, 2000.
3. K Potter, *Resin Transfer Moulding*, Chapman & Hall, London, 1997.
4. TM Kruckenberg and R Paton, Eds., *Resin Transfer Moulding for Aerospace Structures*, Kluwer Academic Publishers, Dordrecht, Netherlands, 1998.

5. CD Williams, SM Grove, and J Summerscales, Resin infusion under flexible tooling (RIFT): a review, *Composites Appl. Sci. Manuf.*, 1996, A27, 517–524.
6. SW Beckwith and CR Hyland, Resin transfer molding: a decade of technology advances, *SAMPE J.*, 1998, 34, 7–19.
7. *Bluecat™ Buyers' Guide Book 1*, Omega Engineering Limited, Manchester, 2000.
8. S Klarsfeld, Guarded hot plate method for thermal conductivity measurements, in *Compendium of Thermophysical Property Measurement Methods 1: Survey of Measurement Techniques*, KD Maglić, A Cezairliyan, and VE Peletsky, Eds., Plenum Press, New York, 1984.
9. Special Technical Publication STP 470B: *Manual on the Use of Thermocouples in Temperature Measurements*, American Society for Testing and Materials, Philadelphia, 1981.
10. http://www.thermometrics.com/htmldocs/whatis.htm, 8 October 2001.
11. SH Wen, SK Wang, and DDL Chung, Carbon fiber structural composites as thermistors, *Sensors Actuators Phys.*, 1999, A78, 180–188.
12. *Bluecat™ Buyers' Guide Book 2*, Omega Engineering Limited, Manchester, U.K., 2000.
13. DW Becker, *Tooling for Resin Transfer Moulding*, Wichita State University, Wichita, Kansas, no date.
14. NRL Pearce, FJ Guild, and J Summerscales, An investigation into the effects of fabric architecture on the processing and properties of fibre reinforced composites produced by resin transfer moulding, *Composites Appl. Sci. Manuf.*, 1998, A29, 19–27.
15. LG Stringer, Optimization of the wet lay-up/vacuum bag process for the fabrication of carbon fibre epoxy composites with high fibre fraction and low void content, *Composites*, 1989, 20, 441–452.
16. http://www.nametre.com/nametre/products.asp#principles, 11 April 2001.
17. http://www.cambridge-applied.com/tech/viscometers.html, 11 April 2001.
18. http://www.brookfieldengineering.com/products/process/sTT100.cfm, 11 April 2001.
19. KW Scott, *The Vibrating Needle Curemeter: A Unique Instrument for Monitoring Liquid Polymer Cures*, RAPRA Technology Limited, Shawbury, U.K., circa 1988.
20. AR Harper, Automating RTM: closing the loop, in *45th Annual Technical Conference*, SPI Reinforced Plastics/Composites Institute, Washington, D.C., 12–15 February 1990, Technomic Publishing, Lancaster, PA, 1990, Session 14B, pp. 1–5.
21. SM Walsh, Artificial intelligence: its application to composite processing, in *Proceedings of the 35th International Symposium*, SAMPE, Anaheim, CA, 2–5 April 1990, pp. 1280–1291.
22. A Kikuchi, E Higuerey, and J Coulter, An experimental investigation of resin flow sensing during molding processes, *Trans. ASME J. Eng. Mater. Technol.*, 1995, 117, 86–93.
23. DD Shepard, Resin flow front monitoring saves money and improves quality, *SAMPE J.*, 1998, 34, 31–35.
24. http://www.micromet.com/holometrix/m_products.asp#smartweave, Website live on 1/16/03.
25. WO Ballata, SM Walsh, and S Advani, Determination of the transverse permeability of a fibrous preform, *J. Reinforced Plast. Composites*, 1999, 18, 1450–1464.
26. UK Vaidya, NC Jadhav, MV Hosur, JW Gillespie, and BK Fink, Assessment of flow and cure monitoring using direct current and alternating current sensing in vacuum-assisted resin transfer moulding, *Smart Mater. Struct.*, 2000, 9, 727–736.

27. J Quinn, AT McIlhagger, R McIlhagger, and PPJ Rogers, Effect of sizing on the flow of resin within a glass fibre composite, in *International Conference on Manufacturing of Advanced Composites*, Institute of Materials, Belfast, 27–28 September 2001, pp. 151–158.

28. JR Bernstein and JW Wagner, Fiber optic sensors for use in monitoring flow front in vacuum resin transfer molding processes, *Rev. Sci. Instrum.*, 1997, 68, 2156–2157.

29. WH Green and SM Walsh, Mapping resin flows three-dimensionally using x-ray computed tomography (CT) imaging, in *Spring Conference and 9th Annual Research Symposium*, American Society of Nondestructive Testing, March 2000, pp. 25–27.

30. T Stöeven, F Weyrauch, P Mitschang, and M Neitzel, Continuous monitoring of three-dimensional resin flow through a fibre preform, in *International Conference on Manufacturing of Advanced Composites*, Institute of Materials, Belfast, 27–28 September 2001, pp. 4–13.

31. GM Maistros and IK Partridge, Monitoring autoclave cure in commercial carbon fibre epoxy composites, *Composites Eng.*, 1998, B29, 245–250.

32. VMA Calado and SG Advani, Thermoset resin cure kinetics and rheology, in *Processing of Composites*, RS Davé and AC Loos, Eds., Carl Hanser Verlag, Munich, 2000, Chap. 2, pp. 32–107.

33. T Renault and AA Ogale, Photo dynamic mechanical analysis for cure monitoring of fiber reinforced photoresin composites, *J. Adv. Mater.*, 1996, 28, 42–47.

34. SD Senturia and NF Sheppard, Dielectric analysis of thermoset cure, *Adv. Polym. Sci.*, 1986, 80, 1–47.

35. DE Kranbuehl and A Loos, Data acquisition: monitoring resin position, reaction advancement and processing properties, in *Resin Transfer Moulding for Aerospace Structures*, TM Kruckenberg and R Paton, Eds., Kluwer Academic Publishers, Dordrecht, Netherlands, 1998, Chap. 12, pp. 412–433.

36. DE Kranbuehl, In-situ frequency dependent dielectric sensing of cure, in *Processing of Composites*, RS Davé and AC Loos, Eds., Carl Hanser Verlag, Munich, 2000, Chap. 4, pp. 137–157.

37. I Matiss, NDT of composite materials: problems and solutions. 1: NDT as source information. 2: Relaxation spectrometry for the structural study of polymers and polymer composites. 3: Modelling of dielectric relaxation phenomena, *Polym. Polym. Composites*, 1996, 4, 181–201.

38. J Summerscales, Dielectrometry, in *Non-Destructive Testing of Fibre-Reinforced Plastics Composites*, Vol. 2, J Summerscales, Ed., Elsevier Applied Science, London, 1990, Chap. 7, pp. 327–360.

39. PR Ciriscioli and GS Springer, Dielectric cure monitoring: a critical review, *SAMPE J.*, 1989, 25, 35–42.

40. LB Keller and M Dominski, Computer controlled processing of composites utilizing dielectric signature curves, *SAMPE J.*, 1992, 28, 25–33.

41. J Mijović, JM Kenny, A Maffezzoli, A Trivisano, F Belluci, and L Nicolais, The principles of dielectric measurements for in situ monitoring of composite processing, *Composites Sci. Technol.*, 1993, 49, 277–290.

42. A Maffezzoli, A Trivisano, M Opalicki, J Mijović, and JM Kenny, Correlation between dielectric and chemorheological properties during cure of epoxy-based composites, *J. Mater. Sci.*, 1994, 29, 800–808.

43. P Bartolomeo, JF Chailan, and JL Vernet, On the use of WLF equation to study resin curing by dielectric spectroscopy, *Polymer*, 2001, 42, 4385–4392.

44. JD Ferry, *Viscoelastic Properties of Polymers*, 3rd ed., Wiley, Chichester, 1980.
45. JS Kim and DG Lee, Measurement of the degree of cure of carbon fiber epoxy composite materials, *J. Composite Mater.*, 1996, 30, 1436–1457.
46. G Maistros, QPV Fontana, D Attwood, and JS Hudd, Use of modulated differential scanning calorimetry to observe vitrification during epoxy resin cure, *J. Mater. Sci. Lett.*, 1997, 16, 273–275.
47. AA Skordos, PI Karkanas, and IK Partridge, A dielectric sensor for measuring flow in resin transfer moulding, *Meas. Sci. Technol.*, 2000, 11, 25–31.
48. MC Kazilas, GM Maistros, and IK Partridge, Controlling complex cure cycles via real time dielectric measurements, in *International Conference on Manufacturing of Advanced Composites*, Institute of Materials, Belfast, 27–28 September 2001, pp. 113–120.
49. AA Skordos and IK Partridge, Impedance cure and flow monitoring in the processing of advanced composites, in *International Conference on Manufacturing of Advanced Composites*, Institute of Materials, Belfast, 27–28 September 2001, pp. 103–112.
50. D Abraham and R McIlhagger, A comparison of dielectric monitoring with thermal and mechanical testing techniques for glass fibre epoxy composite cure, in *Preprints of the Fifth International Conference on Automated Composites*, Institute of Materials, Glasgow, 4–5 September 1997, pp. 149–157.
51. D Abraham and R McIlhagger, Glass fibre epoxy composite cure monitoring using parallel plate dielectric analysis in comparison with thermal and mechanical testing techniques, *Composites Appl. Sci. Manuf.*, 1998, A29, 811–819.
52. AT McIlhagger, ST Matthews, D Brown, and B Hill, Identification of key cure stages in liquid moulding processes by parallel plate dielectric analysis, in *Preprints of the Sixth International Conference on Automated Composites*, Institute of Materials, Bristol, 23–24 September 1999, pp. 133–143.
53. A McIlhagger, D Brown, and B Hill, The development of a dielectric system for the on-line cure monitoring of the resin transfer moulding process, in *Fifth International Conference: Flow Process in Composite Materials (FPCM-5)*, Advanced Composites Manufacturing Centre, Plymouth, U.K., 12–14 July 1999, pp. 161–169.
54. A McIlhagger, D Brown, and B Hill, The development of a dielectric system for the on-line cure monitoring of the resin transfer moulding process, *Composites Appl. Sci. Manuf.*, 2000, A31, 1373–1381.
55. KC Hranac, Process control cures composites' ills, *High-Perform. Composites*, 2001, 9, 41–45.
56. W Wenger, Implementation of a dielectric on-line process monitoring system, in *International Conference on Manufacturing of Advanced Composites*, Institute of Materials, Belfast, 27–28 September 2001, pp. 121–127.
57. R King, M Werner, and G Mayorga, Microwave dynamic dielectric analysis of polymers, *SAMPE J.*, 1992, 28, 35–37.
58. JL Schlegel, JW Wagner, and RE Green, Microwave dielectrometry measurements of glass reinforced polyester resins, *Mater. Eval.*, 1999, 57, 1091–1094.
59. RJ Hoss and EA Lacy, *Fibre Optics*, 2nd ed., Prentice-Hall International, 1993.
60. J Summerscales, Embedded optical sensors in fibre reinforced plastics, *Int. J. Opt. Sensors*, 1986, 1, 287–296.
61. SSJ Roberts and R Davidson, Cure and fabrication monitoring of composite materials with fibre-optic sensors, *Composites Sci. Technol.*, 1993, 49, 265–276.

62. K Liu, A Davis, MM Ohn, B Park, and RM Measures, Embedded optical fiber sensors for damage detection and cure monitoring, in *Conference on Active Materials and Adaptive Structures*, ADPA/AIAA/ASME/SPIE, Alexandria, VA, November 1991, pp. 395–308.

63. K-A Lou, B Zimmermann, and G Yaniv, Combined sensor for process and in-service health monitoring of composite structures, in *SPIE Proceedings*, Vol. 2191, *Conference on Smart Sensing*, *Processing and Instrumentation*, Orlando, FL, 14–16 February 1994, pp. 32–45.

64. P Graindorge, B Laloux, M Girault, P Martin, HC Lefevre, and FX Desforges, Metricor 2000: a multiparameter fiber optic sensor instrument, in *SPIE Proceedings*, Vol. 2839, 1996, pp. 101–110. Fiber Optic and Laser Sensors XIV, Paper 2839-11, Denver CO, 4–9 August 1996.

65. Y Amar (Israel Aircraft Industries Limited), private communication, 27 July 2000.

66. PR Ciriscioli, GS Springer, and WI Lee, An expert system for autoclave curing of composites, *J. Composite Mater.*, 1991, 25, 1542–1587.

67. MW Holl and LW Rehfield, *Composite Materials: Testing and Design 10*, ASTM, West Conshohocken, PA, 1992, pp. 308–319.

68. RL Levy and DP Ames, Monitoring epoxy cure kinetics with a viscosity-dependent fluorescent probe, *Polym. Sci. Technol.*, 1984, 29, 245–256.

69. RL Levy, A new fiber-optic sensor for monitoring the composite-curing process, *Polym. Mater. Sci. Eng.*, 1986, 54, 321–324.

70. BM Fanconi, Monitoring polymer cure by fluorescence recovery after photobleaching, *Rev. Prog. Quant. Nondestructive Eval.*, 1991, 10A, 1127–1134.

71. KO Hill, Y Fujii, DC Johnson, and BS Kawasaki, Photosensitivity in optical fibre waveguides: application to reflection filter fabrication, *Appl. Phys. Lett.*, 1978, 32, 647–649.

72. G Meltz, WW Morey, and WH Glenn, Formation of Bragg gratings in optical fibers by a transverse holographic method, *Opt. Lett.*, 1989, 14, 823–825.

73. EJ Friebele, CG Askins, MA Putnam, J Florio, AA Fosha, RP Donti, and CD Mosley, Distributed strain sensing with fiber Bragg gratings embedded in CRTM™ composites, in *SPIE Proceedings*, Vol. 2361, *Second European Conference on Smart Structures and Materials*, Glasgow, 12–14 October 1994, pp. 338–341.

74. MW Urban, Fourier transform infrared and Fourier transform Raman spectroscopy of polymers: principles and applications, *Adv. Chem. Ser.*, 1993, 236, 3–40.

75. SF Parker, The application of vibrational spectroscopy to the study of polyimides and their composites, *Vib. Spectrosc.*, 1992, 3, 87–104.

76. HGM Edwards, AF Johnson, and IR Lewis, Applications of Raman spectroscopy to the study of polymers and polymerization processes, *J. Raman Spectrosc.*, 1993, 24, 475–483.

77. WF Maddams, A review of Fourier-transform spectroscopic studies on polymers, *Spectrochim. Acta*, 1994, 50A, 1967–1986.

78. G Xue, Fourier transform Raman spectroscopy and its application for the analysis of polymeric materials, *Prog. Polym. Sci.*, 1997, 22, 313–406.

79. RO Allen and P Sanderson, Characterization of epoxy glues with FTIR, *Appl. Spectrosc. Rev.*, 1998, 24, 175–187.

80. KPJ Williams and SM Mason, Future-directions for Fourier-transform Raman-spectroscopy in industrial analysis, *Spectrochim. Acta*, 1990, 46A, 187–196.

81. DJ Cutler, HM Mould, B Bennett, and AJ Turner, Use of Q-switched lasers in near infrared Fourier-transform Raman spectroscopy 1, *J. Raman Spectrosc.*, 1991, 22, 367–374.

82. JK Agbenyega, GE Ellis, PJ Hendra, WF Maddams, C Passingham, HA Willis, and J Chalmers, Applications of Fourier-transform Raman-spectroscopy in the synthetic-polymer field, *Spectrochim. Acta*, 1990, 46A, 197–216 (both Maddams and Gi Xue give no title and the page numbers as 295–).

83. JR Walton and KPJ Williams, In-situ Fourier-transform Raman studies of thermally and photochemically induced curing reactions, *Vib. Spectrosc.*, 1991, 1, 339–345.

84. CJ de Bakker, GA George, NA St John, and PM Fredericks, The kinetics of the cure of an advanced epoxy resin by Fourier-transform Raman and near-IR spectroscopy, *Spectrochim. Acta*, 1993, 49A, 739–752.

85. B-G Min, ZH Stachurski, JH Hodgkin, and GR Heath, Quantitative-analysis of the cure reaction of DGEBA/DDS epoxy resins without and with thermoplastic polysulfone modifier using near-infrared spectroscopy, *Polymer*, 1993, 34, 3620–3627.

86. B-G Min, ZH Stachurski, and JH Hodgkin, Cure kinetics of elementary reactions of a DGEBA/DDS epoxy-resin: 1. Glass-transition temperature versus conversion, *Polymer*, 1993, 34, 4908–4912.

87. B-G Min, ZH Stachurski, and JH Hodgkin, Cure kinetics of elementary reactions of a diglycidyl ether of bisphenol-A diaminodiphenylsulfone epoxy-resin: 2. Conversion versus time, *Polymer*, 1993, 34, 4488–4495.

88. DAC Compton, SL Hill, NA Wright, MA Druy, J Piche, WA Stevenson, and DW Vidrene, In situ FT-IR analysis of a composite curing reaction using a mid-infrared transmitting optical fiber, *Appl. Spectrosc.*, 1988, 42, 972–979.

89. PR Young, MA Druy, WA Stevenson, and DAC Compton, In-situ composite cure monitoring using infrared-transmitting optical fibers, *SAMPE J.*, 1989, 25, 11–16.

90. KPJ Williams, Remote sampling using a fibre-optic probe in Fourier Transform Raman spectroscopy, *J. Raman Spectrosc.*, 1990, 21, 147–151.

91. RE Lyon, SM Angel, and KE Chike, Fiber-optic cure monitoring of composite resins, in *Proceedings of the 6th European Conference on Composite Materials (EC-CM-6)*, Bordeaux, France, 20–24 September 1993, pp. 567–572.

92. KE Chike, ML Myrick, RE Lyon, and SM Angel, Raman and near-infrared studies of an epoxy resin, *Appl. Spectrosc.*, 1993, 47, 1631–1635.

93. JM Fildes, SM Milkovich, R Altkorn, R Haidle, and J Neatrour, In situ infrared spectroscopy and neural network analysis for composite cure monitoring, in *25th International Technical Conference*, SAMPE, Philadelphia, 26–28 October 1993, pp. 887–900.

94. JF Maguire and PL Talley, Remote Raman spectroscopy as a sensor technology in composite materials processing, *J. Adv. Mater.*, 1995, 26, 27–40.

95. JF Aust, JB Cooper, KL Wise, and BJ Jensen, In-situ analysis of a high-temperature cure reaction in real time using modulated fiber-optic FT-Raman spectroscopy, *Appl. Spectrosc.*, 1999, 35, 682–686.

96. T Liu and GF Fernando, Processing of polymer composites: an optical fibre-based sensor system for on-line amine monitoring, *Composites Appl. Sci. Manuf.*, 2001, A32, 1561–1572.

97. P Jackson, Curing of carbon-fibre reinforced epoxy resin: non-invasive viscosity measurement by NMR imaging, *J. Mater. Sci.*, 1992, 27, 1302–1306.

98. EG Henneke II, Ultrasonic nondestructive evaluation of advanced composites, in *Non-Destructive Testing of Fibre-Reinforced Plastics Composites*, Vol. 2, J Summerscales, Ed., Elsevier Applied Science, London, 1990, Chap. 2, pp. 55–159.

99. JH Speake, RGC Arridge, and GJ Curtis, Measurement of cure of resins by ultrasonic techniques, *J. Phys. Appl. Phys.*, 1974, D7, 412–424.

100. AM Lindrose, Ultrasonic wave and moduli changes in a curing epoxy resin, *Exp. Mech.*, 1978, 18, 227–232.

101. WP Winfree, Ultrasonic characterization of changes in viscoelastic properties of epoxy during cure, in *Proceedings of the Ultrasonics Symposium*, Atlanta IEEE, New York, 1983, pp. 866–869.

102. HT Hahn, Application of ultrasonic technique to cure characterization of epoxies, in *Nondestructive Methods of Material Property Determination*, CA Ruud and RE Green, Eds., Plenum Press, New York, pp. 315–326 (Proceedings of the First Symposium, Hershey, PA, 6–8 April 1983).

103. JN Prassianakis, N Kompoti, and J Varakis, Curing effects on the acoustical properties of epoxy polymers, *Exp. Mech.*, 1993, 33, 77–80.

104. PAJ Gibbs, Ultrasonic cure measurements during processing of unsaturated polyester dough moulding compound, in *Preprints of the 19th Reinforced Plastics Congress*, BPF, Birmingham, 22–23 November 1994, Paper 8.

105. DD Shepard and KR Smith, A new ultrasonic measurement system for the cure monitoring of thermosetting resins and composites, *J. Thermal Anal.*, 1997, 49, 95–100.

106. CS Brown, CB Hobbs, and PHJ Spitteler, Ultrasonic Monitoring of Reactive Polymer Processing, National Physical Laboratory Measurement Note CM-MT(MN)059, March 2000.

107. M Rath, J Döring, W Stark, and G Hinrichsen, Process monitoring of moulding compounds by ultrasonic measurements in a compression mould, *NDT&E Int.*, 2000, 33, 123–130.

108. W Stark, J Döring, J McHugh, and C Kürten, On-line monitoring of thermosets moulding process applying ultrasound, in *Abstracts of the 15th World Conference on Non-Destructive Testing*, Rome, 15–21 October 2000, p. 388.

109. J Döring, J Bartusch, J McHugh, and W Stark, Contribution to ultrasound cure control for composite manufacturing, in *Abstracts of the 15th World Conference on Non-Destructive Testing*, Rome, 15–21 October 2000, p. 436.

110. J McHugh, J Döring, W Stark, and IK Partridge, Ultrasonic cure monitoring of RTM6 epoxy resin, in *International Conference on Manufacturing of Advanced Composites*, Institute of Materials, Belfast, 27–28 September 2001, p. 299.

111. RT Harrold and ZN Sanjana, Acoustic characterization of curing processes using waveguides embedded within polymers, in *Review of Progress in Quantitative Nondestructive Evaluation*, Vol. 7B, Plenum, New York, 1988, pp. 1549–1553 (proceedings of the conference at Williamsburg, VA, June 1987).

112. MM Ohn, A Davis, K Liu, and RM Measures, Embedded fiber optic detection of ultrasound and application to cure monitoring, in *Workshop: Fiber Optic Sensor-Based Smart Materials and Structures*, Blacksburg, VA, 15–16 April 1992, pp. 175–184.

113. J Dorighi, S Krishnaswamy, and J Achenbach, A fiber optic ultrasonic system to monitor the cure of epoxy, *Res. Nondestructive Eval.*, 1997, 9, 13–24.

114. I Perrissin-Fabert, Y Jayet, and G Merle, Contrôle de la cuisson de thermodurcissables par implant piézoélectrique: études pratique et théorique, *J. Phys. IV Colloq. C1*, 1992, 2, 887–890 (supplément au J. Phys. III).

115. I Perrissin-Fabert, Y Jayet, and G Merle, An embedded piezoelectric sensor for monitoring thermoset hardening: electric impedance measurements and correlation with ultrasonic method, *Mater. Eval.*, 1994, 52, 1292–1296.

116. TM Whitney and RE Green, Cure monitoring of carbon epoxy composites: an application of resonant ultrasound spectroscopy, *Ultrasonics*, 1996, 34, 347–353.

117. J-Y Chen, SV Hoa, C-K Jen, M Viens, and J-P Monchalin, Ultrasonic evaluation of graphite/epoxy composites with different curing conditions, *Polym. Composites*, 1998, 19, 225–232.

118. JD Ferry, *Viscoelastic Properties of Polymers*, John Wiley & Sons, New York, 1970.

119. BZ Jang and GH Zhu, Monitoring the dynamic mechanical behaviour of polymers and composites using mechanical impedance analysis (MIA), *J. Appl. Polym. Sci.*, 1986, 31, 2627–2646.

120. XE Gros, *NDT Data Fusion*, Arnold, London, 1997.

121. XE Gros, *Applications of NDT Data Fusion*, Kluwer Academic Publishers, Dordrecht, Netherlands, 2001.

122. *Guidelines to Statistical Process Control*, Society of Motor Manufacturers and Traders (SMMT), London, 1986.

123. *Statistical Process Control: A Guide to Quality Improvement through Statistical Methods*, Department of Trade & Industry, London, U.K., 1990.

124. JB Keats and DC Montgomery, *Statistical Process Control in Manufacturing*, Dekker, 1991.

125. D Bissell, *Statistical Methods for SPC and TQM*, Chapman & Hall, London, 1994.

126. JS Oakland, *Statistical Process Control*, 3rd ed., Butterworth-Heinemann, Oxford, U.K., 1996.

127. LA Doty, *Statistical Process Control*, 2nd ed., Industrial Press, New York, 1996.

128. G Box and A Luceno, *Statistical Control by Monitoring and Feedback Adjustment*, Wiley, New York, 1997.

129. RS Burns, *Advanced Control Engineering*, Newnes/Butterworth-Heinemann, Oxford, 2001.

130. J Shaw (Process Control Solutions), The PID Control Algorithm, http://www.jashaw.com/pid/description.htm, 1 February 1996.

131. S Bickerton, HC Stadtfeld, KV Steiner, and SG Advani, Design and application of actively controlled injection schemes for resin transfer moulding, *Composites Sci. Technol.*, 2001, 61, 1625–1637.

132. L Zadeh, Fuzzy sets, *Inf. Control*, 1965, 8, 338–353.

133. P Bauer, S Nouak, and R Winkler, A Brief Course in Fuzzy Logic and Fuzzy Control,
http://www.flll.uni-linz.ac.at/pdw/fuzzy/fuzzy.html, 4 December 1996.

134. CP Coleman and J Lygeros, Model Based Fuzzy Logic Control, http://robotics.eecs.berkeley.edu/~godbole/fuzzy.html, accessed 3 August 2001.

135. Y Li, K Ng, DJ Murray-Smith, and KC Sharman, Fuzzy Logic Control System Design Using Genetic Algorithms, http://www.mech.gla.ac.uk/Research/Control/activity/subsection2_3_6_6.html, accessed 3 August 2001.

136. R Stonier and M Mohammadian, Evolutionary Learning in Fuzzy Logic Control Systems, http://www.csu.edu.au/ci/vol03/stonier/stonier.html, accessed 3 August 2001.

137. SA Aziz, Everything You've Always Wanted to Know about Designing Fuzzy Logic Machines but Were Afraid to Ask, http://www.doc.ic.ac.uk/~nd/surprise_96/journal/vol2/sbaa/article2.html, 1996.

138. W Pedrycz, *Fuzzy Control and Fuzzy Systems*, 2nd extended ed., Research Studies Press, Taunton, Somerset, 1993.

139. J Yen, R Langari, and LA Zadeh, *Industrial Applications of Fuzzy Control and Intelligent Systems*, IEEE Press, New York, 1995.

140. D Driankov, H Hellendoorn, M Reinfrank, R Palm, B Graham, and A Ollero, *An Introduction to Fuzzy Control*, 2nd revised ed., Springer, Berlin, 1996.

141. R Palm, D Driankov, and H Hellendoorn, *Model-Based Fuzzy Control: Fuzzy Gain Schedulers and Sliding Mode Fuzzy Controllers*, Springer Verlag, 1997.

142. KM Passino and S Yurkovich, *Fuzzy Control*, Addison-Wesley, Menlo Park, CA, 1998.

143. C Edwards and SK Spurgeon, *Sliding Mode Control: Theory and Applications*, Taylor & Francis, Basingstoke, 1998.

144. W-L Chiang, K Yeh, and M-Y Liu, Adaptive fuzzy sliding mode control for base-isolated buildings,
Int. J. Artif. Intelligence Tools, 2000, 9, 493–508 (http://ejournals.wspc.com.sg/ijait/09/0904/S0218213000000318.html).

145. KS Narendra and FL Lewis, Editorial, *Automatica*, 2001, 37 (http://www.math.utwente.nl/eic/editorials/ed37_8.html).

146. KS Narendra and K Parthasarathy, Identification and control of dynamical systems using neural networks, *IEEE Trans. Neural Networks*, 1990, 1, 4–27.

147. DA Pomerleau, *Neural Network Perception for Mobile Robot Guidance*, Kluwer Academic Publishers, Dordrecht, Netherlands, 1993.

148. GW Irwin, K Warwick, and KJ Hunt, *Neural Network Applications in Control*, Institution of Electrical Engineers, London, 1995.

149. FL Lewis, S Jagannathan, and A Yesildirek, *Neural Network Control of Robot Manipulators and Nonlinear Systems*, Taylor & Francis, London, U.K., 1999.

150. B Joseph, FW Hanratty, and JL Kardos, Model-based control of voids and product thickness during autoclave curing of carbon/epoxy composite laminates, *J. Composite Mater.*, 1995, 29, 1000–1024.

151. N Rai and R Pitchumani, Neural network-based optimal curing of composite materials, *J. Mater. Process. Manuf. Sci.*, 1997, 6, 39–62.

152. N Rai and R Pitchumani, Rapid cure simulation using artificial neural networks, *Composites Appl. Sci. Manuf.*, A28, 1997, 847–859.

153. HB Su, LT Fan, and JR Schlup, Monitoring the process of curing of epoxy/graphite fiber composites with a recurrent neural network as a soft sensor, *Eng. Appl. Artif. Intelligence*, 1998, 11, 293–306.

154. PF Lichtenwalner, Neural-network-based control for the fiber placement composite manufacturing process, *J. Mater. Eng. Perform.*, 1993, 2, 687–692.

155. D Nielsen and R Pitchumani, Intelligent model-based control of preform permeation in liquid composite molding processes, with on-line optimisation, *Composites Appl. Sci. Manuf.*, 2001, A32, 1789–1803.

156. JH Holland, *Adaptation in Natural and Artificial System*, University of Michigan Press, Ann Arbor, 1975.

157. SR Ladd, Genetic Algorithms in C++, M&T Books, 1996, out of print. Second ed. scheduled for publication by Coyote Gulch Prod., Clearwater, FL, 2/03, (downloadable code: http://www.coyotegulch.com/bookart/GACPP_Disk.zip, 23 August 2001).

158. SJ Louis, A Genetic Algorithm, http://www.cs.unr.edu/~sushil/work/papers/ep/ep97/paper/node2.html, 25 June 1997.

159. D Goldberg, *Genetic Algorithms*, Addison-Wesley, Reading, MA, 1988.

160. J-P Rennard, Introduction to Genetic Algorithms, http://www.rennard.org/alife/english/gavintrgb.html#rTit01, 23 August 2001.

161. M Mitchell, *An Introduction to Genetic Algorithms* (*Complex Adaptive Systems*), MIT Press, Cambridge, MA, 1996.

162. Z Michalewicz, *Genetic Algorithms + Data Structures = Evolution Programs*, 3rd revised extended ed., Springer, Berlin, 1996.

163. M Gen and Runwei Cheng, *Genetic Algorithms and Engineering Design*, Wiley Series in Engineering Design and Automation, Wiley, New York, 1997.

164. AMS Zalzala and PJ Fleming, *Genetic Algorithms in Engineering Systems*, IEE Control Engineering Series 55, Institution of Electrical Engineers, London, 1997.

165. DA Coley, *An Introduction to Genetic Algorithms for Scientists and Engineers*, World Scientific, Singapore, 1999.

166. KF Man, KS Tang, and S Kwong, *Genetic Algorithms: Concepts and Designs*, Springer, London, 1999.

167. WB Young, Gate location optimization in liquid composite molding using genetic algorithms, *J. Composite Mater.*, 1994, 28, 1098–1113.

168. HW Yu and WB Young, Optimal design of process parameters for resin transfer molding, *J. Composite Mater.*, 1997, 31, 1113–1140.

169. J Spoerre, C Zhang, B Wang, and R Parnas, Integrated product and process design for resin transfer molded parts, *J. Composite Mater.*, 1998, 32, 1244–1272.

170. R Mathur, BK Fink, and SG Advani, Use of genetic algorithms to optimize gate and vent locations for the resin transfer molding process, *Polym. Composites*, 1999, 20, 167–178.

171. J Luo, Z Liang, C Zhang, and B Wang, Optimum tooling design for resin transfer molding with virtual manufacturing and artificial intelligence, *Composites Appl. Sci. Manuf.*, 2001, A32, 877–888.

172. G Cather, Keynote Speech: Aerospace Composites Commercial Potential: A Real Option, paper presented at International Conference on Manufacturing of Advanced Composites, Institute of Materials, Belfast, 27–28 September 2001.

3

Manufacture and Performance of Z-Pinned Composites

Ivana K. Partridge, Denis D.R. Cartié, and Tony Bonnington

CONTENTS

Abstract

The chapter provides the first review of the state of the art in the novel technology of Z-Fiber® reinforcement of polymer matrix composites. It describes the manufacture of the reinforcing fiber rodstock and the various means by which the Z-Fibers, so-called Z-pins, are inserted either into uncured lay-up or into polymeric foam (X-Cor™ and K-Cor™), to give rise to three-dimensionally reinforced composite structures. The available experimental data and analytical as well as finite element (FE) modeling tools relating to the mechanical properties of Z-pinned laminates are presented. It is shown that Z-pinning is capable of enhancing the delamination resistance of aerospace-grade continuous carbon fiber–thermoset composites by about an order of magnitude, accompanied by a loss of in-plane stiffness of some 10%. The influence of the presence of the Z-pins upon in-plane strength is dependent on the lay-up and on the mode of loading, but the knock down in these properties correlates well with existing models accounting for increased fiber waviness in the plies. It is shown that the main benefit of Z-pinning is to be expected from the high crack-stopping potential of selective placement of blocks of Z-pins in a composite structure.

 Models for delamination resistance, relevant to z-directional reinforcement, are summarized for the cases of mode I, mode II, and mixed mode I/II loadings. Most of these had been developed previously for stitched composites, but they are being adapted quite successfully to deal with the new form of through-the-thickness reinforcement.

 The chapter concludes with an overview of the current industrial applications of Z-pinning technology, showing its potential as a new tailored engineering solution to overcome the traditional out-of-plane weakness of composite structures.

3.1   Introduction to the Z-Fiber® Pinning Process

The primary weakness of laminated composites is their low strength in the through-thickness direction, making interlaminar delamination a major concern in the application of polymer matrix continuous-fiber-reinforced composites. A new technology of through-the-thickness reinforcement by Z-Fiber
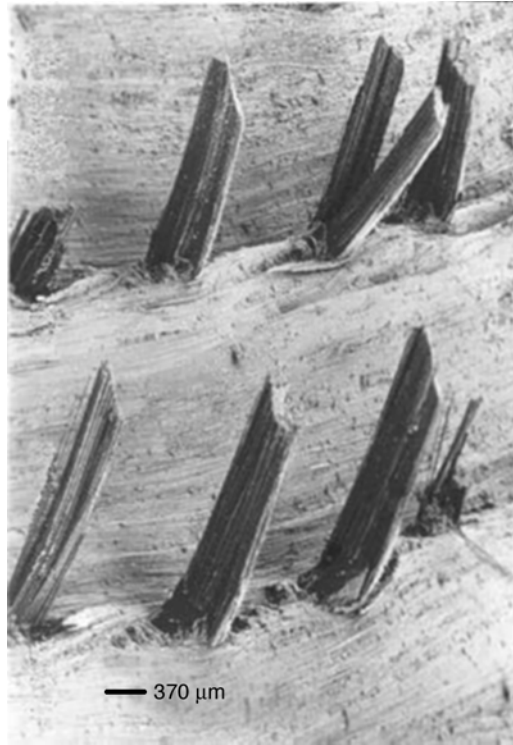
FIGURE 3.1
Scanning electron micrograph of a mode I fracture surface of a Z-Fiber reinforced unidirectional composite.

pinning has been attracting considerable attention and industrial interest in recent years.[1–5] The technique is a newly available alternative to the stitching of laminates in the z-direction, which had in the past produced some promising improvement in the damage tolerance of polymer matrix composites.[6–8]

The Z-Fibers, hereafter referred to as Z-pins, are inserted orthogonally to the plane of the composite plies during the manufacturing process, before the resin matrix is cured, effectively pinning the individual layers together.

Figure 3.1 shows the reinforcing pins pulled out of a unidirectional (UD) laminate beam that had been broken open in the crack-opening mode (mode I delamination fracture).

3.2 Manufacturing Routes

The range of relevant products, all made by Aztex Inc., includes Z-Fiber, X-Cor™, and K-Cor™. These are all designed to reinforce and improve the

damage tolerance of composite structures. The Z-Fiber reinforcement concept has been developed to replace metallic fasteners while also offering improved damage tolerance. X-Cor and K-Cor are reinforced foam products, designed to replace honeycomb in various applications, while at the same time offering improvements in durability of the parts. The manufacturing processes used to make all of these materials are very similar, and in fact, in their simplest forms the same machinery can be used with very little modification. The individual steps involved are described in Sections 3.2.1 to 3.2.4.

3.2.1   Manufacture of Pin Rodstock by Pultrusion

A continuous-fiber tow is pulled through a bath of liquid resin and exits the bath through a die. The diameter of the pin (rodstock) is governed by the diameter of the die. The general aim is to make a rodstock that contains about 70% by weight of fiber. Almost any type of continuous-fiber type can be used. Materials such as polyacrylonitrile (PAN)- or pitch-based carbon fiber, HiNicalon, quartz, glass, and Nextel fibers are the most common types, but other, more exotic, materials have been handled.

The principal requirement is that the fiber has to be either free of size or coated in a size that is compatible with the resin matrix in the pultrusion bath. The removal or addition of size can be carried out on-line before pultrusion. Generally the resin matrix is solvent-free, and low-viscosity systems are preferred. To reduce the viscosity, the bath can be heated and controlled at elevated temperature. The curing oven is also temperature controlled in several zones. It is not critical that the pultruded fiber (rodstock) be fully cured in the ovens. The material has to be sufficiently cured and dry enough to allow the rodstock to be spooled. The final curing or postcuring step can then be carried out off-line.

Pultrusion line speeds vary considerably, depending on the resin matrix, but are generally in the 1 to 10 m/min range. The diameter of the finished rodstock is governed by the filament count of the fiber used. Generally, Aztex Inc. manufactures rodstock with diameters in the range of 0.2 to 1.0 mm. It is possible to pultrude different fiber types through the same die to make a hybrid material.

Figure 3.2 shows a production pultrusion line, together with detail of the spooling of the semifinished rodstock.

3.2.2   Manufacture and Use of Preforms

Preform is the term used for a foam material into which pins (rodstock) have been inserted. A Z-Fiber preform is a foam sandwich, into which the pins are inserted, usually vertically. The foam sandwich for Z-Fiber is only used as a carrier and is discarded after the Z-pins are inserted into the finished part. The sandwich consists of two types of foam: a dense foam, such as
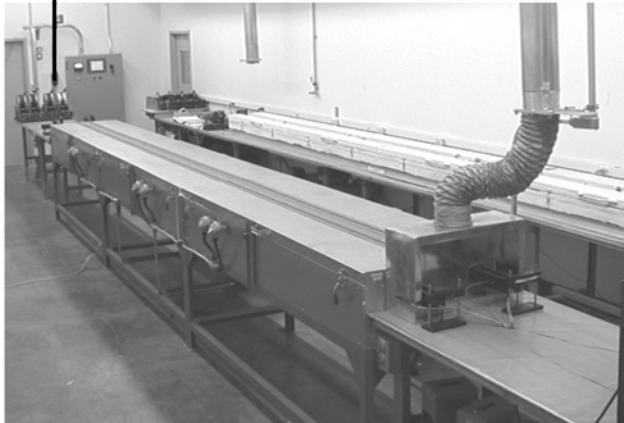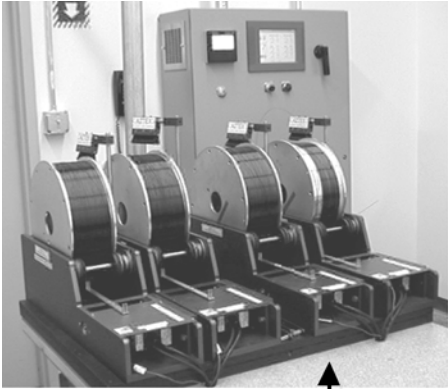
FIGURE 3.2
Typical pultrusion line.

51IG Rohacell, used to locate the pins accurately, and a low-density polysty-
rene foam, which collapses down to almost zero thickness when the pins
are inserted into the part to be reinforced. Normally the polystyrene foam
is made slightly thicker than the thickness of the part to be reinforced.

The rodstock fiber is inserted into the foam using driven rubber nip rollers.
The pin length is measured very accurately using an optical system. The
cutter type used to cut the pin to length varies depending on the nature of
the rodstock. For standard carbon fiber, a shear cutter is used; for harder
materials such us ceramic fibers, the cutter is normally a diamond-tipped
rotary tool. In every case, the pin is cut through at an angle to give it a
sharpened tip. This assists with pin penetration and also reduces the damage
to the base material into which the pin is to be inserted subsequently.

Pin insertion rates are governed by the type of cutter to be used, the length
of the pin, and the spacing between pins. In practice, the insertion rate
currently varies between 1 and 14 pins/sec.

A Z-Fiber preform production machine is shown in Figures 3.3 and 3.4.
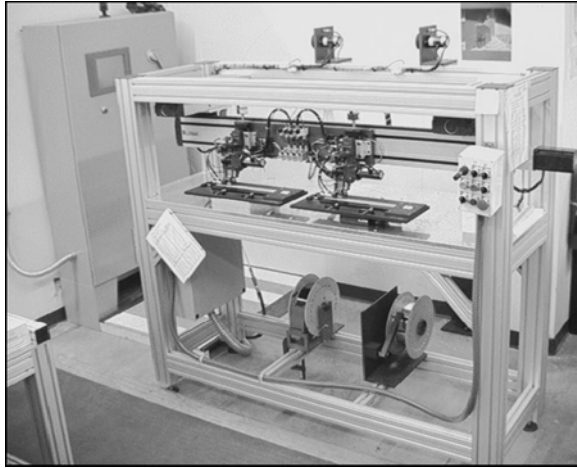
FIGURE 3.3
Z-Fiber preform machine.
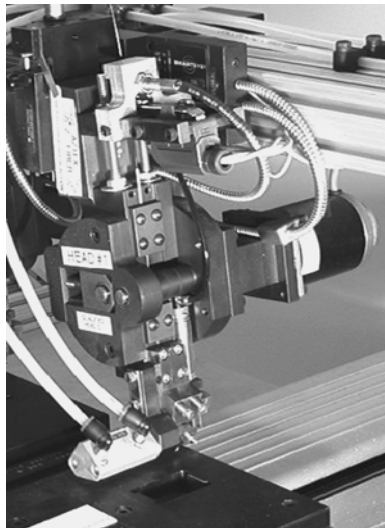
FIGURE 3.4
Close-up on the Z-Fiber insertion head.

Completed Z-Fiber preforms are placed upon the part to be reinforced, which is normally an uncured prepreg lay-up or a stack of dry fabric held together with a binder. The pins are then inserted into the part using an ultrasonics head (Figure 3.5 shows a schematic of the insertion process). The high-frequency sonic action excites the pins, and they are driven out of the foam carrier into the part with very little downward force. The insertion process is facilitated by accompanying localized heating, lowering the viscosity of the matrix resin in the lay-up and making it possible for the Z-pins to

nestle in between the fiber tows, with very little fiber breakage (Figure 3.6). After the pins have been inserted, the compacted foam and any excess length of Z-pins are removed by shear cutting and discarded. It is desirable to control the depth in the laminate to which the Z-pins are inserted. A semiautomated insertion gantry machine used at Cranfield University is shown in Figure 3.7.
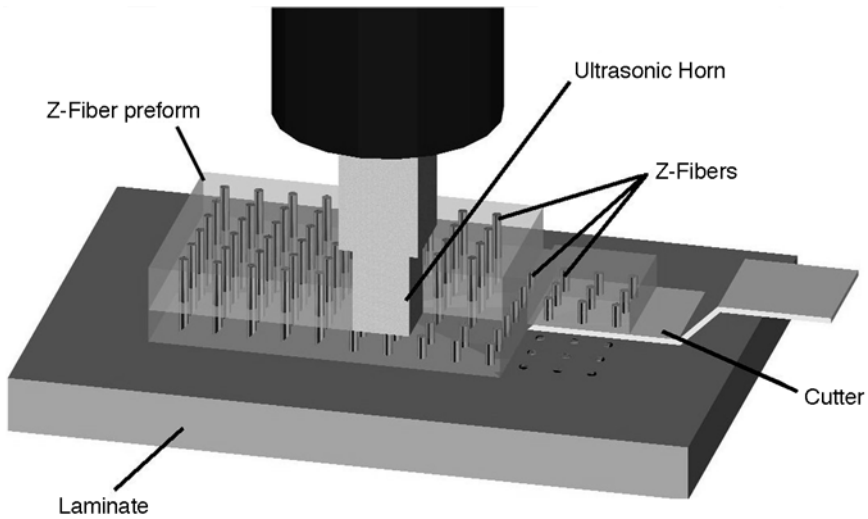
FIGURE 3.5
Schematic of the Z-pinning process: The Z-Fiber preform is located on top of the uncured laminate, directly above the area to be reinforced. The Z-Fibers are inserted into the laminates by the actions of the ultrasonic horn. During insertion, the low-density foam holding the pins is crushed. The pins are shear cut at the surface of the laminate, and the excess pin length and the remaining foam are discarded.
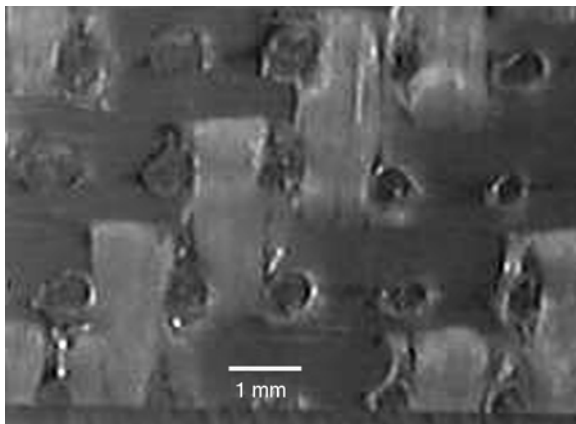
FIGURE 3.6
Surface of a cured Z-pinned sample showing the distortion of the carbon fiber woven-fabric reinforcement caused by the presence of the Z-pins. (Courtesy of M. Troulis.)
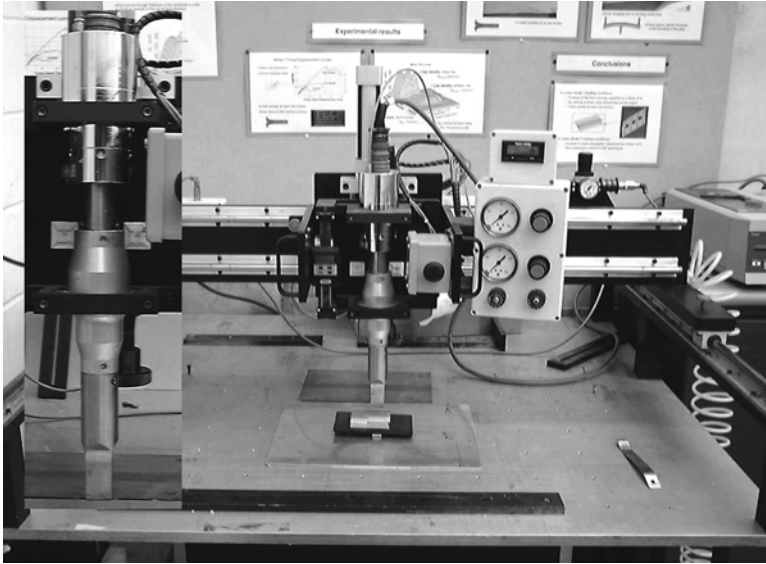
FIGURE 3.7
Semiautomated gantry in use at Cranfield University, plus detail of the insertion horn.

3.2.3 Manufacture of X-Cor and K-Cor

For X-Cor or K-Cor, the pins are inserted into the support foam at an angle to form a truss, and the foam is a part of the eventual structure. For X-Cor, the pins in the truss extend beyond each surface of the foam, for a so-called reveal length, and enter into the surface material plies. When the combined product is cured, the skin-to-core bonding is enhanced by the local multiple insertions of the pultruded rodstock into the skin layer. For K-Cor the pins again extend considerably beyond the foam surface, but the pins are then folded back, flush with the foam surface, prior to the application of the surface plies. Two principal skin-to-core bond mechanisms exist for K-Cor: a foam-to-skin bond and separate multiple bonds between the flattened pin surface and the skin. Precured composite or metallic skins can be used with K-Cor.

As stated above, the foam used for both X-Cor and K-Cor remains in the final structure. Its principal role for X-Cor and K-Cor is to act as the spacer in the sandwich structure. The mechanical properties of the foam contribute very little to the overall structural properties, but the foam has to withstand the processing temperatures during the final part manufacture. The foam also prevents the pins from buckling under load. It is better to work with low-density closed-cell types in order to maximize the effect of the pins, which carry almost all of the shear and compression loads. Foams used so far range from low-density, relatively low-temperature foams such as Divinycell or Airex types to medium-temperature foams such as Rohacell, up to very high-temperature foams such as Aluminium Oxide. The choice
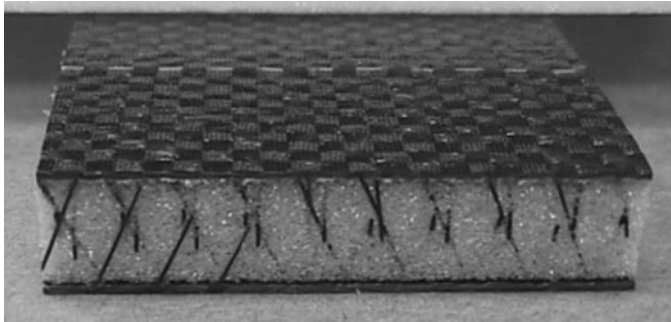
FIGURE 3.8
Section of an X-core panel, with carbon fabric skins.

of foam is highly dependent on the customer's requirements. In some cases, foams with special acoustic, thermal, and electrical properties are used. It is important to understand that these reinforced foams are highly adaptable structures and that by varying the material used to make the pins and with careful foam selection, a fully integrated structure capable of fulfilling multiple functions can be made. Figure 3.8 shows a cross section of an X-Cor panel with carbon fabric skins.

As indicated above, the structural properties of the X-Cor and K-Cor products are almost entirely influenced by the pin densities used. Changing the angle of the pins in the truss alters the balance between the shear and compression properties. For example, for a part where compression loading dominates, the pins should be inserted close to the vertical axis. For improved shear loading resistance, the angle of the pinning needs to be increased. To match typical honeycomb properties, it is found that a pin angle of 20 to 30° represents a good compromise. With X-Cor the reveal length of the (usually small-diameter) pin is chosen such that the pin is long enough to bond to at least the first three plies of the skin. If the part has only one or two plies, other modifications are made to maximize the shear properties of the structure. K-Cor with fewer and larger diameter pins exhibits generally lower mechanical performance, but it has a significantly lower cost.

Both X-Cor and K-Cor can be used in the same way as honeycomb materials. Users have been able to employ the same tooling, bagging materials, and they process the part using the same autoclave cure cycles, both temperature and pressure, as in normal manufacture with honeycombs. Sandwich structures can be made by traditional composite fabrication processes of fabric and tape hand lay-up as well as by the newer low-cost processes such as fiber placement. Initial development work indicates that processing via resin transfer molding (RTM) and vacuum-assisted RTM (VARTM) routes will become viable options. Close interaction with company design engineers at an early stage helps to ensure that acceptable mechanical properties are achieved at the lowest cost.

FIGURE 3.9
Fully automated Z-Fiber insertion robot.

X-Cor sandwich structures are proving to be very durable and not easily damaged. However, if minor damage occurs, current users repair the structure by removing the damaged section and using either epoxy paste or a honeycomb in-fill prior to a wet lay-up patch repair to the skin.

3.2.4   Curved Laminates and Automation

A range of Ultrasonic insertion equipment (UAZ™) is available, from simple handheld machines to sophisticated multiaxis semirobotic machines (see Figure 3.9). Insertion times are generally 3 to 4 sec, typically producing a square inch of pinned area in that time. With fully automated equipment, point-to-point moves can be made in around 10 sec. The robot is preloaded with square-inch charges of preform, and these can be varied in a predetermined manner. This gives high flexibility and hence the possibility of tailoring selected local reinforcement to almost any composites structure.

3.3   Mechanical Properties of Z-Pinned Laminates

In terms of development of through-the-thickness reinforced composites, Z-pinned composites follow in the footsteps of stitched composites. There are

significant differences in the manufacturing approaches in that stitching requires a two-side access to the part to be reinforced, at least until the very latest developments of one-sided stitching become more established. Another important distinction lies in the fact that stitching may be considered as providing continuous reinforcement, while Z-pinning is seen as particularly suitable for localized reinforcement. Whether such reinforcement is global or local, the presence of the Z-pins is expected to increase the delamination resistance of the composites, and this is indeed the case (see Section 3.3.2). Thus the most frequently asked questions at present revolve around the effects of the Z-pins on the in-plane properties of the composites. The manufacturer's claim is that the drop-off in the in-plane properties of Z-pinned composites is lower than that encountered in stitched laminates, and details of the manufacturer's data to support this claim can be found on its website.[9] No valid direct comparison of the mechanical performance of stitched vs. Z-pinned composites has ever been carried out. For practical reasons, it is actually very difficult to achieve such a comparison experimentally, and perhaps the best hope of a valid comparison lies in the rapidly developing modeling techniques (see Section 3.4.2).

The aim of this part of the review is to present new relevant models and representative experimental data on Z-pinned composites that are currently in the public domain. These data are additional to those available from the manufacturer and have been obtained independently.

3.3.1 In-Plane Properties

3.3.1.1 Stiffness

Early work on three-dimensional micromechanical finite element (FE) models of Z-pinned laminates indicates that this approach is suitable to predict the effect of the Z-pins on the individual elastic constants of the laminate. Such models confirm the expected increase in through-the-thickness modulus, an increase of 22 to 30% being achievable from 2% volume fraction addition of Z-pins (see Figure 3.10a). The out-of-plane improvement would be accompanied by a reduction of 7 to 10% in the E_x and E_y moduli (Figure 3.10b). This drop in stiffness is attributed to the combined effects of fiber volume fraction dilution, in-plane fiber deviation, and the existence of resin-rich pockets around the Z-pins. The effect on in-plane shear stiffness of UD and cross-ply Z-pinned laminates is expected to be small, as deviated reinforcing fibers are capable of carrying shear loads and hence compensating for the added compliance of the resin-rich pockets. In angle-ply and quasi-isotropic Z-pinned laminates, the predicted reductions in G_{xy} are 9 and 6%, respectively, for a reinforcement density of 2%. There is currently very little independent experimental data available on the elastic constants of Z-pinned laminates, and these early modeling results require further validation. Nevertheless, they can serve as a useful indicator of what might be expected.[10]
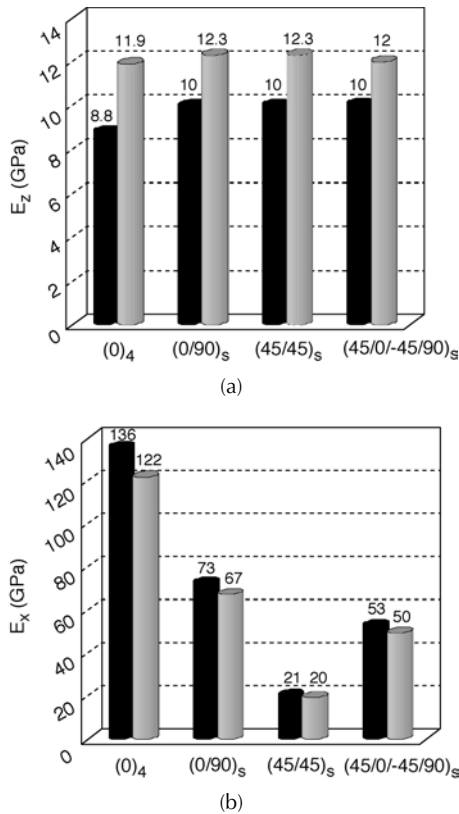
FIGURE 3.10
Stiffness variation for (a) E_z and (b) E_x moduli for different kinds of laminates, without Z-Fibers (▮) and with 0.28-mm-diameter Z-Fiber reinforcement at an areal density of 2% (▯). (Courtesy of M. Grassi et al., submitted to *Composites A*.)

3.3.1.2 Uniaxial Compression Strength of UD Specimens

The in-plane property that has the greatest potential to be degraded by the insertion of Z-pins orthogonal to the test plane is the compression strength. It is to be expected that the extent of the degradation will depend on the closeness of the Z-pins in the array and on the angle (θ) that the Z-pin array makes with the axis of the specimen (Figure 3.11). Steeves and Fleck[11] report data on UD laminates pinned with a square array of Z-pins, 3.5 mm apart and oriented at θ = 0. Premature failure is associated with the phenomenon of microbuckling of fibers in the vicinity of the Z-pins, seen as a direct consequence of the increased fiber waviness caused by the spatial disturbance of the prepreg plies (Figure 3.12). A knockdown in strength of some 30% has been measured and corresponds well with a numerical prediction for composites with a similar initial fiber waviness.

Experiments with single rows of Z-pins oriented at angles θ of 23 and 45° showed that such inclination resulted in slightly reduced local fiber
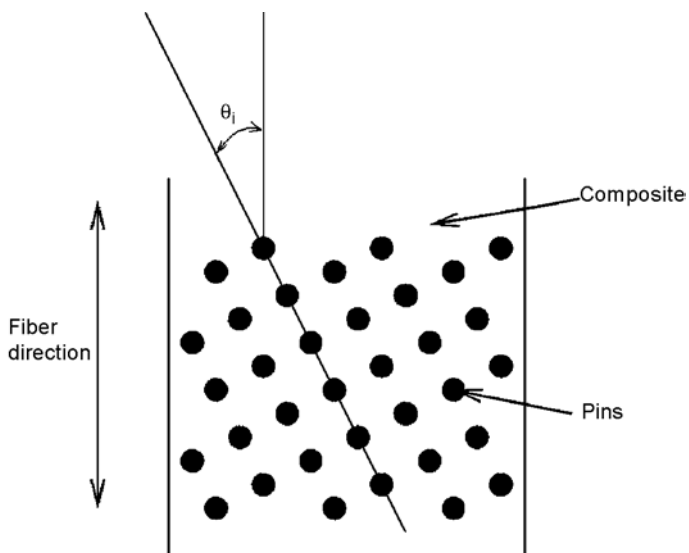
FIGURE 3.11
Orientation of Z-pin pattern with respect to the specimen axis. (Courtesy of C. Steeves.)
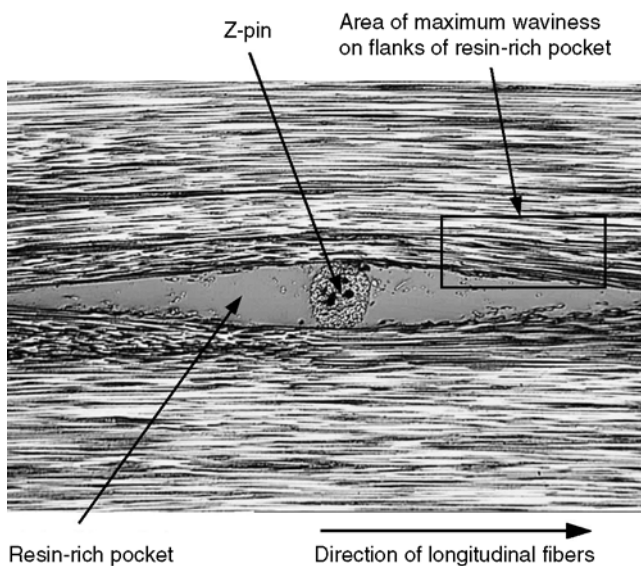

FIGURE 3.12
Resin-rich pocket and fiber disturbance around a Z-pin in a UD composite.

waviness, the effects of which could then be modeled using existing microbuckling models. The overall conclusion was that the critical feature in determining the compressive strength of Z-pinned laminates is the cumulative effect of a field of pins on a group of reinforcing fibers, some of which may weave between the pins (see Figures 3.13 and 3.14). It is likely that the pattern of Z-pin insertion into the composite can be optimized with respect to the fiber waviness distribution and hence the compressive strength of the laminate.[12]

Fibers deflecting around successive z-pins

Fibers "weaving" around z-pins
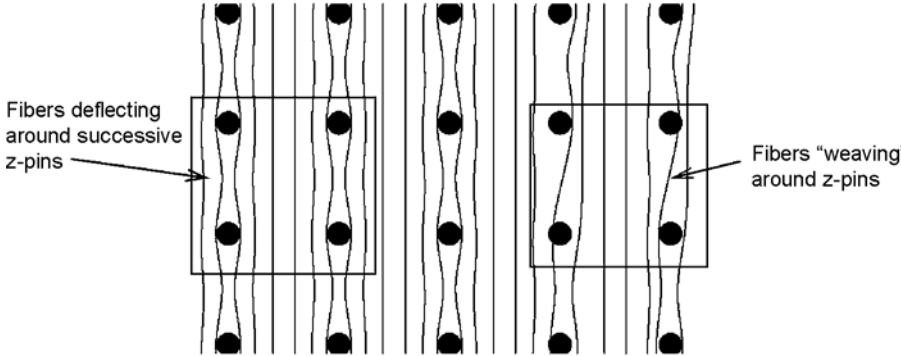
FIGURE 3.13
Sketch of fibers deflecting around Z-pins and weaving through a field of Z-pins. (Courtesy of C. Steeves.)

Z-pin

Region of fiber weaving

Z-pin

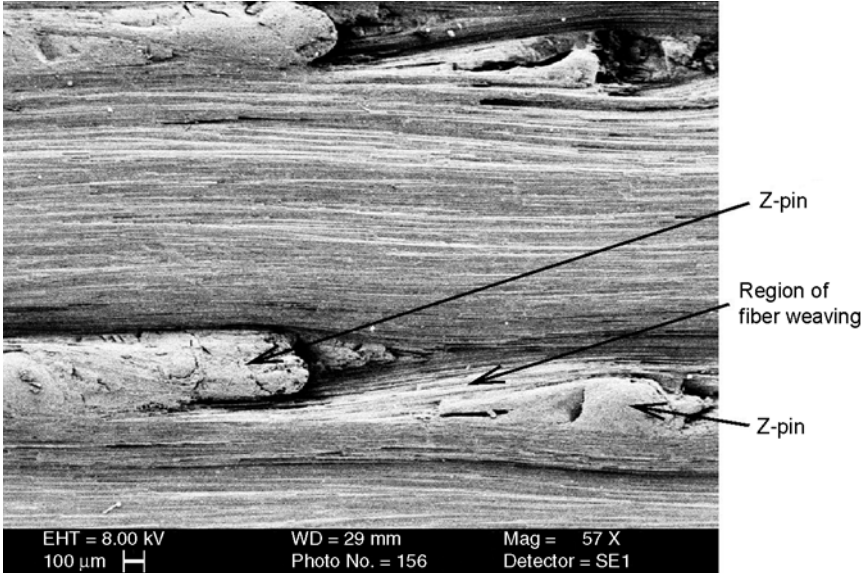| EHT = 8.00 kV | WD = 29 mm | Mag = 57 X |
| 100 µm | Photo No. = 156 | Detector = SE1 |

FIGURE 3.14
Scanning electron microscope image of fibers weaving between two Z-Fibers. (Courtesy of C. Steeves.)

3.3.1.3   Uniaxial Compression Strength of Quasi-Isotropic Specimens

A series of compression-only experiments carried out on Boeing lay-up compression-after-impact (CAI) quasi-isotropic IM7/8552 specimens provided some evidence to suggest that far from having a knockdown effect, partially Z-pinned undamaged laminates can display higher compressive strengths than the control undamaged samples.[13] The Z-pinned coupons had a 25 × 25 mm square of Z-pins in the center of the square sample and consistently failed at higher stresses, 4 to 10% higher depending on the pinning density, than did the control coupons. All these coupons failed near the compressive fixture grip areas, well away from the central Z-pinned regions. This should not be seen as contradictory to the above-quoted results by Steeves and Fleck,[11] but rather to illustrate that the sensitivity of a quasi-isotropic composite to geometrical disturbance produced by Z-pinning is likely to be lower than that in the case of a UD laminate. It also serves to point out that local pinning is liable to alter the stress distribution in any given sample and to shift the failure location to a new position.

3.3.1.4   Uniaxial Tension and Open-Hole Tension

When UD laminates are subjected to uniaxial tension, the dominant failure mode is intralaminar splitting. It is easy to imagine that Z-pins may provide sites for such splitting to initiate. Steeves[12] tested the effect of Z-pins on the ultimate tensile strength of UD T300/914 laminates, pinned in the gauge-length region with a square array of Z-pins at 2% areal density. The initial modulus was not changed by the presence of the pins, but the splitting started early in the Z-pinned specimen in comparison to the control. The final knockdown in strength, caused by the Z-pinning, was approximately 27%. As with the accompanying study of the effects of Z-pinning on compressive strength (see Section 3.3.1.2), the square array of Z-pins in a UD laminate may represent the worst-case scenario.

The effects of 0.28- and 0.51-mm-diameter Z-pins on the tensile strength of carbon fiber/toughened epoxy cross-ply and fabric specimens were tested by the standard open-hole tension test (ASTM D5766/D5766M-95) in order to ensure failure in the gauge section of the specimen.[14] The Z-pinned area was across the entire width of the specimen with the hole drilled in the center. The knockdowns in the ultimate tensile strength of these samples were between 11 and 14%, considerably lower than the 27% reduction in the tensile strength of a Z-pinned UD laminate.

3.3.2   Delamination Resistance

The bulk of the freely available database on the delamination resistance of Z-pinned composite beams originates from the authors' own laboratory,[15–17] although some data and micromechanical models have also been reported from centers in the United States.[18,19] Most of the work has been carried out
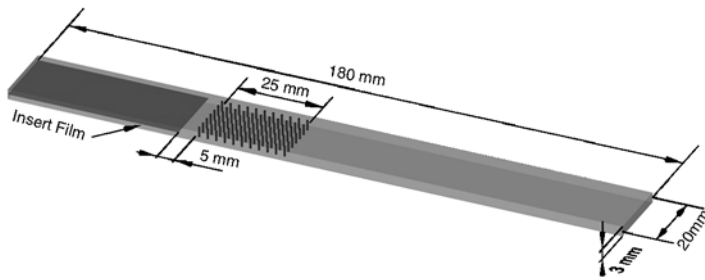
FIGURE 3.15
Configuration of the Z-pinned delamination specimens for studies of crack propagation resistance.

on standard UD composite beams, and delamination loading cases used are mode I (crack opening), mode II (forward shear), and mixed mode I/II. Apart from the issue of how the raw load-displacement data obtained in these tests should be analyzed (see Section 3.4.2), it is very important to be aware of whether any particular test was designed to look at the *initiation* or the *propagation* of a delamination crack in the beam. The tests carried out at Cranfield are designed specifically to consider the situation of a *running delamination crack*. The rationale behind the choice is the recognition that in a complex composite structure, the most likely benefit of Z-pinning is likely to be the crack-stopping potential of this reinforcement. With this in mind, the Z-pinning configuration selected in our samples was as shown in Figure 3.15, with the start of the pinned region some 5 mm behind the standard crack starter film. The expected significant increase in the resistance to delamination cracking is realized under all the loading conditions used (Figures 3.16, 3.17, and 3.18). It must be emphasized that the absolute numbers indicated in these graphs have been obtained using the form of analysis in the current ISO standard,[20] which was not designed to cope with three-dimensional reinforcement. They are also related strictly to the sample configuration in terms of the beam thickness and width, and to the extent and location of the pinned region. Thus the G_c values quoted cannot be regarded in any way as a material property, but must be considered a structure–material property. With this proviso, it is possible to make valid comparisons and to investigate experimentally the effects of some of the more obvious parametric changes, such as the Z-pin diameter and the Z-pinning density. As might be expected, increasing areal density of reinforcement is a determinant factor in increasing the resistance to crack propagation (Figures 3.19, 3.20, and 3.21).

3.3.3 Compression after Impact and Fatigue

The Boeing compression-after-impact test is commonly used as a material selector for composite applications demanding high damage tolerance. The
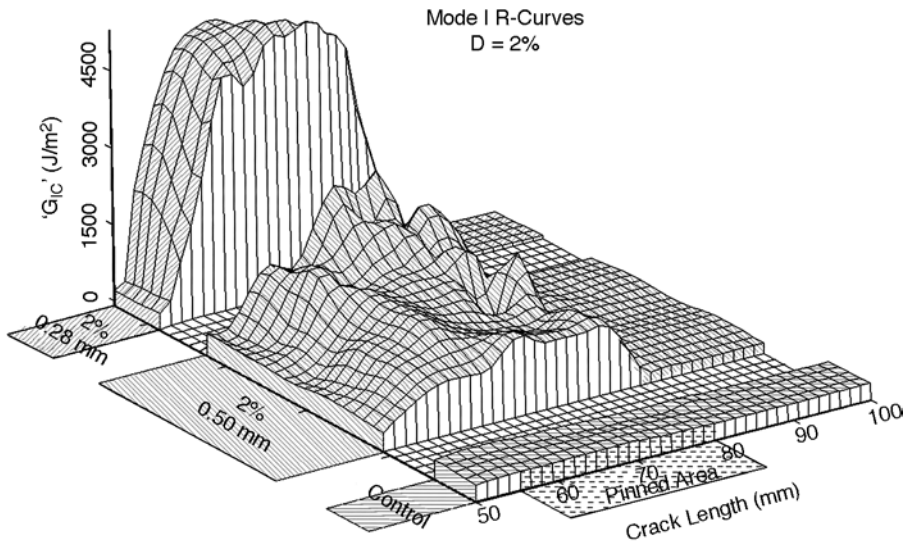
FIGURE 3.16
Mode I loading case R-curves showing the effect of Z-pin diameter at a fixed areal density (2%) in UD laminates of IMS/924.
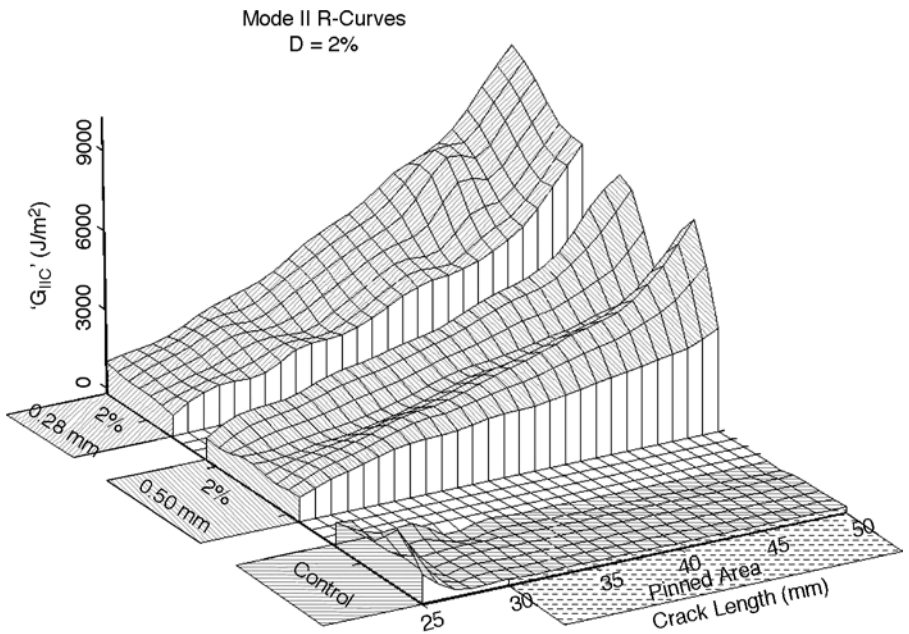

FIGURE 3.17
Mode II loading case R-curves showing the effect of Z-pin diameter at a fixed areal density (2%) in UD laminates of IMS/924.
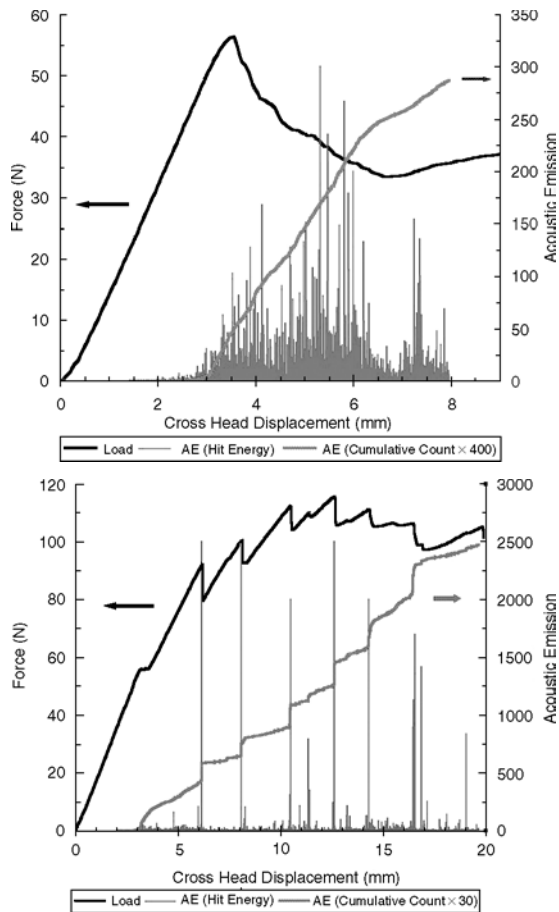
FIGURE 3.18
Load-displacement and acoustic emission traces for control (top) and Z-pinned (bottom) laminates tested in mixed mode I/II = 4/1 loading conditions. Note the coincidence of stick-slip cracking and step increases in acoustic emission.

limited experimental data available relating to the performance of Z-pinned samples in this respect are summarized in this section, together with a preliminary look at the behavior of Z-pinned composites under fatigue loading. There is a need for systematic data generation on both these aspects of composite performance and, in the case of fatigue crack growth measurements, an urgent need for the establishment of appropriate data analysis methods pertinent to the case of through-thickness reinforced composites.

3.3.3.1 Impact and Compression after Impact

Several carbon fiber/epoxy combinations have been used in studies of how the presence of Z-pinning at 0.5, 1, 2, and 4% areal densities of reinforcement
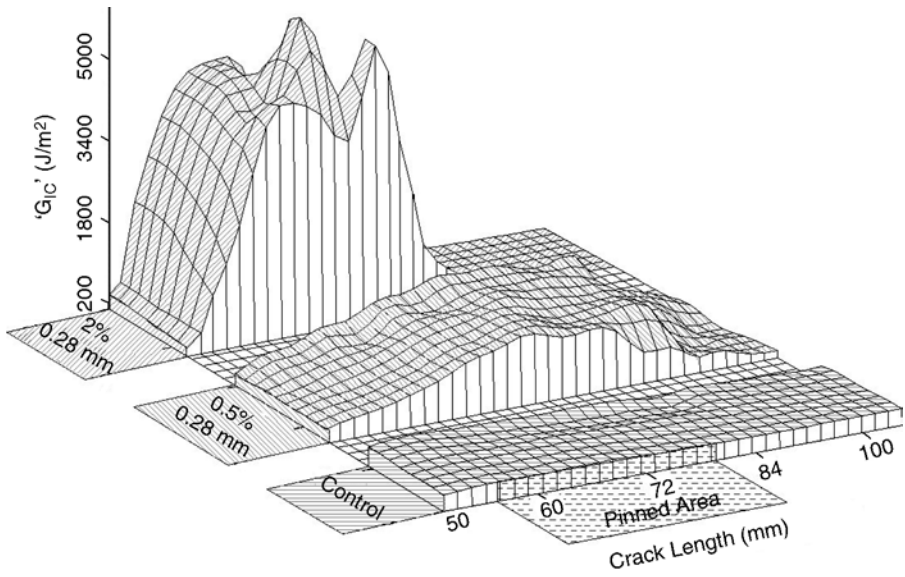
FIGURE 3.19
Mode I loading case R-curves showing the effect of Z-pin areal density at a fixed Z-pin diameter (0.28 mm) in UD laminates of IMS/924.
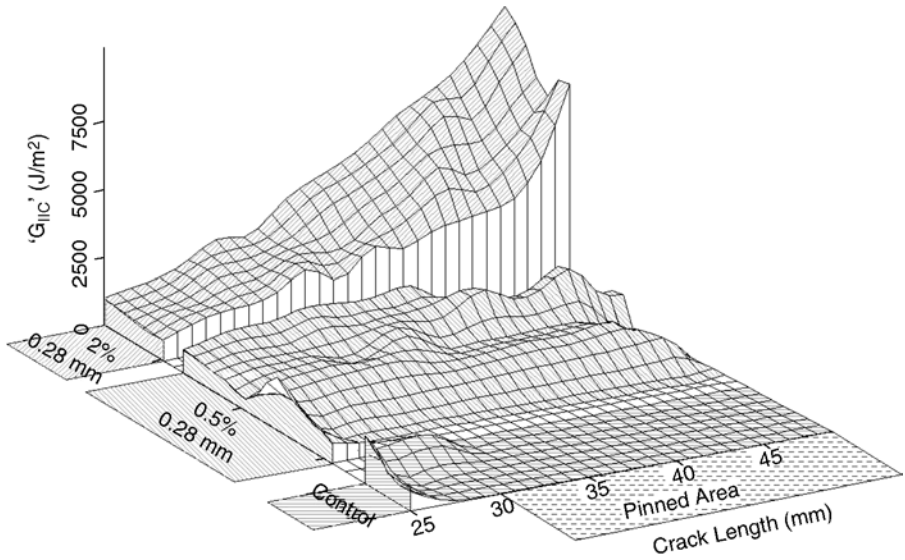

FIGURE 3.20
Mode II loading case R-curves showing the effect of Z-pin areal density at a fixed Z-pin diameter (0.28 mm) in UD laminates of IMS/924.
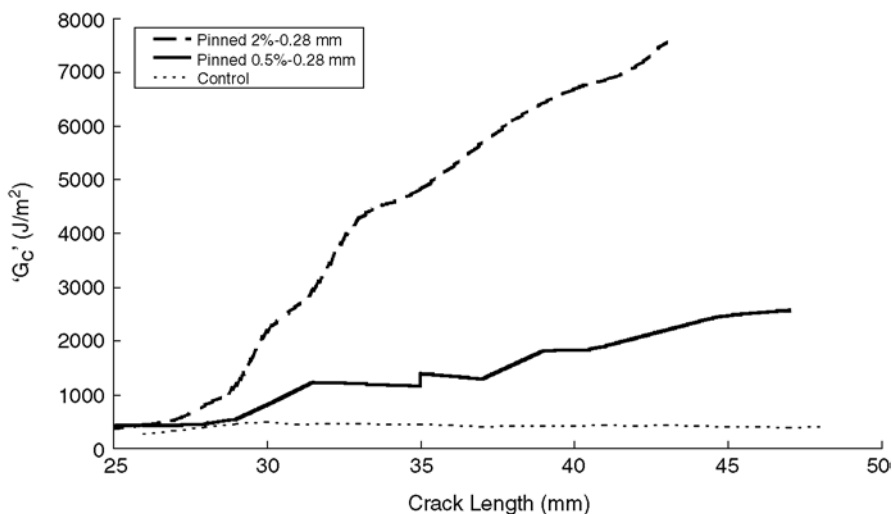
FIGURE 3.21

R-curves for control and two types of Z-pinned specimens tested under mixed mode I/II = 1/ 1 loading conditions. (The specimen geometry, Z-pin diameter, and Z-pinned block geometry are kept constant; the difference is in the pinning density within the Z-pinned block only.)

affects the low-velocity impact and postimpact compressive strength of the laminates. The standard lay-up quasi-isotropic laminates of $(+45_2, -45_2, 0_2, 90_2)_{2S}$ orientation were used for the impact resistance and CAI tests. The coupons were locally reinforced, either over a 25-mm-square area in the center or by a picture frame-type reinforcement pattern surrounding the central area where the impactor strikes (Figure 3.22).

Concerning impact alone, the load-time curves indicate that the Z-pinned regions show no increase in the threshold load for damage initiation. However, the growth of the delamination damage from the point of impact appears limited in its extent by the presence and location of the reinforcement. An example of this is illustrated in Figure 3.23, a penetrant-enhanced x-ray radiograph of one of the full central square quasi-isotropic samples used in the above study. The radiograph indicates a distinct change in the pattern of impact damage formation between the unpinned or only 0.5% Z-pinned sample (Figure 3.23a) and the 4% Z-pinned sample (Figure 3.23b). Four silver-painted corner markers have been used to show the position of the pinned areas. There is the expected evidence of 45° back-face splitting and associated delamination in the samples with no or low-density reinforcement, accompanied by delamination at multiple levels throughout the laminate. In contrast, the damage resulting from the same level of impact on the 4% Z-pinned sample is seen to be rather patchy and shows no evidence of continuous delamination domains.

There are significant improvements in the CAI performance for these Z-pinned laminates compared with the control laminates (Figure 3.24).[13] This kind of an increase in the CAI performance would, in purely material
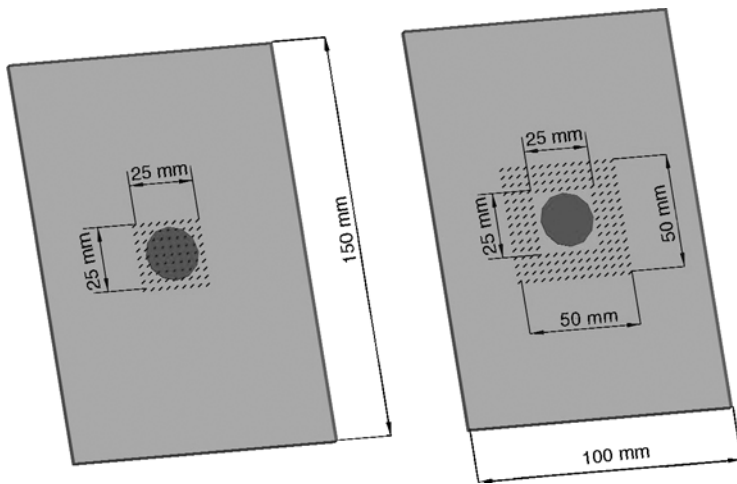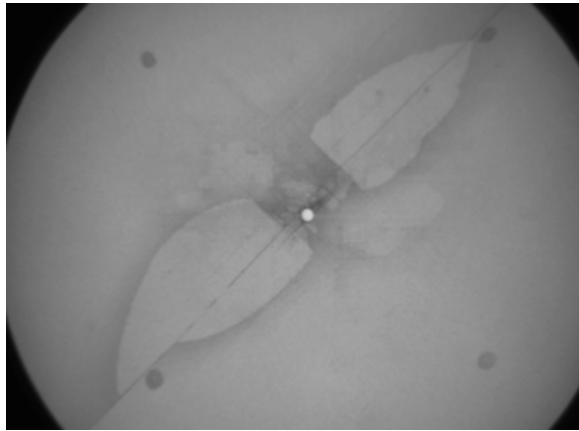
FIGURE 3.22
Full square (left) and picture frame (right) configurations of Z-pinning patterns used in the impact and CAI tests. The shaded circle indicates the location of the impact strike.

selection terms, equate to the replacement of an ordinary first-generation composite by the best of the currently available high-performance fiber–toughened resin combinations.

In the "picture frame" Z-pinned specimens, the CAI performance is still improved over that of the control samples, but to a lesser extent than that noted with the samples impacted onto the central pinned area. A tentative explanation may be that impact onto a Z-pinned area simply results in a smaller total damage area and hence greater resistance to the subsequent compression loading. While these preliminary results from the authors' laboratory cannot be regarded as definitive in any way, recent unpublished work from the University of Rostock (G. Scharr et al.) corroborates the findings.

3.3.3.2 Fatigue

A preliminary investigation of delamination fatigue crack growth in Z-pinned composites was carried out on Z-pinned unidirectional AS4/8552 laminates. The double cantilever beam (DCB) and end-loaded split (ELS) configurations were used for the mode I and mode II tests, respectively. There were some quite specific difficulties encountered in this testing, caused by the characteristics of the Z-pinned samples. In the DCB crack-opening test, these relate to the predictable hysteresis, caused by debonding Z-pins, which do not return to their original positions upon crack closure. In the ELS test, the Z-pins affect the rate of change of compliance with crack extension, causing difficulties in obtaining the experimental compliance calibration required by the standard data analysis. The authors discuss possible options for suitable modifications of the data treatment, and the data must be regarded as very provisional. Nevertheless, the investigation does

(a)
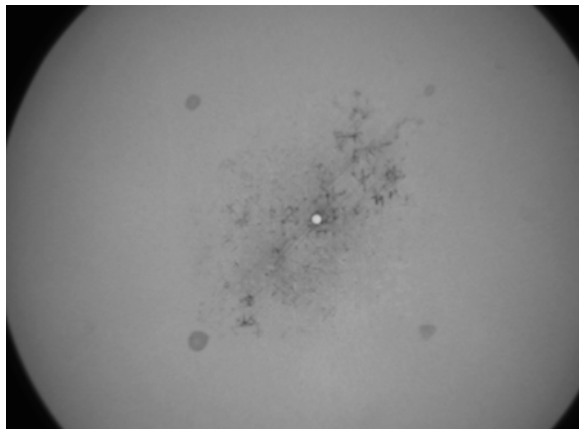
(b)

FIGURE 3.23
Penetrant-enhanced radiographs showing different modes of damage in low areal density pinned (a) and in 4% pinned laminate (b) after a 15 J impact. The four dark spots indicate the limits of the pinned area. (Courtesy of A. Rezai.)

indicate that the delamination crack growth under cyclic loading would be expected to be slowed down by the presence of the Z-pinning (Figure 3.25).[21]

3.4   Models for Delamination, Relevant to Z-Directional Reinforcement Case

This brief overview of currently available relevant models is divided into models depicting the bridging laws operative in z-directionally reinforced
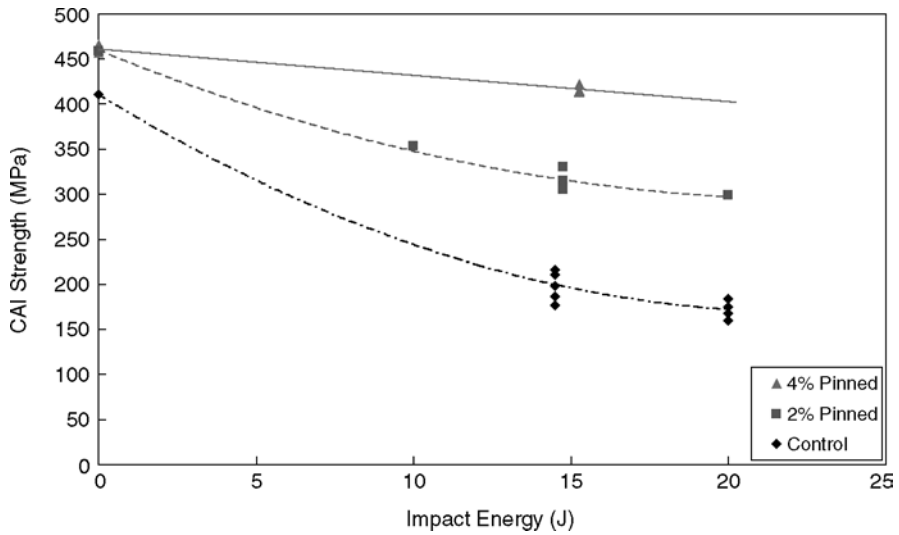
FIGURE 3.24
CAI strength of AS4/8225 laminates pinned in the full square pattern, with 0.28-mm-diameter Z-pins at 2 and 4% areal densities, compared to control samples. (After A. Rezai et al., Interlaminar Damage Resistance of Z-Fiber® Reinforced Structural CFRP, Proceedings of ICCM13, Beijing, China, June 2001.)
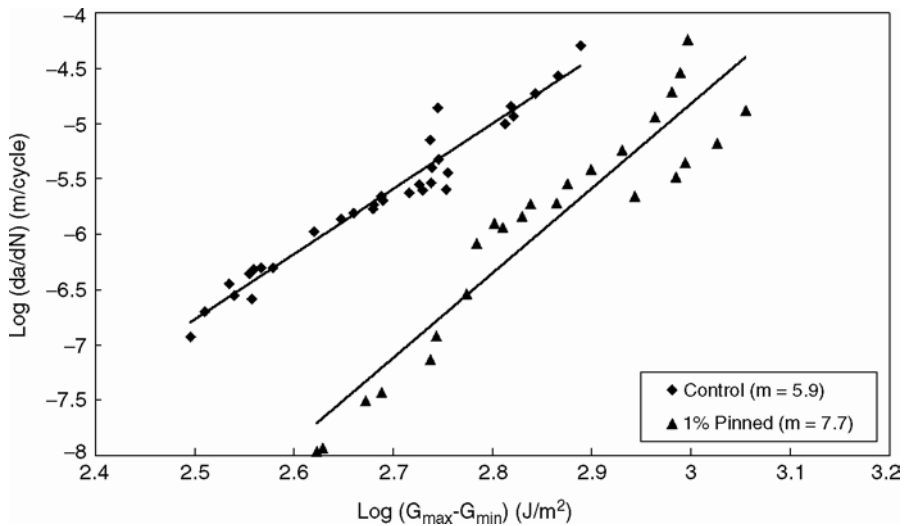

FIGURE 3.25
Fatigue crack growth in control and 1% Z-pinned UD AS48552 coupons, tested in the ELS mode II configuration. (After B. Graftieaux et al., Effects of Z-Pin Reinforcements on the Delamination Toughness and Fatigue Performance of Unidirectional AS4/8552 Composite, Proceedings of ECCM9 Conference, Brighton, U.K., June 4–7, 2000.)

composites and into more structural models utilizing those bridging laws to describe the behavior of a given specimen or structure.

3.4.1 Crack Bridging Laws

The shape of the load-displacement traces of mode I pullout tests of Z-pins from a UD laminate suggests that the pins are weakly bonded in the laminate.[15] Therefore, the energy absorption mechanism in this case can be described as a friction-based problem only. The friction stress, τ, opposing the pullout, can be deduced via classical shear lag theory from the maximum load, F_{MAX}, and the embedded length, l, of the pin that is being pulled out:

$$\tau = \frac{F_{MAX}}{2l\pi R}$$

Here, R is the radius of the Z-pin.

The case of a steady-state fiber pullout has been analyzed in a sequence of three terms or steps at the University of Sydney.[22] First, the elastic deformation of the fiber with a fully bonded interface is considered. Second, a phase of partial debonding of the fiber is analyzed in terms of elastic deformation in the bonded region and frictional slip in the debonded area. Finally, the subsequent frictional sliding of the fully debonded fiber is analyzed. A computer model using this analysis has been constructed. Load/displacement responses expected from each particular step have been obtained numerically, allowing for changes in parameters such as pin modulus and interfacial bonding.[23] A modified version of this model has been applied to the particular case of a Z-Fiber pulling out of a UD composite laminate. The results of this model have been used successfully in a numerical analysis of a DCB beam and calibrated against experimental data from Cranfield.[24] Further computations showed that the improvement in delamination resistance due to Z-pinning is insensitive to the pin Young's modulus, but can be improved greatly by ensuring stable debonding of the pin–laminate interface.

Another set of models dealing with the mode II loading case has been developed by Cox[25]; having identified the behavior of a bridging tow from experimental observation, the state of a tow–Z-Fiber–rod is described by two displacement variables. The problem is solved to obtain the force/displacement results from the actions of the bridging tows.[26] Further developments of this model allowing for mixed-mode loading conditions, and canted tows are shown in a subsequent paper.[27]

The particular case of the (shear) bridging force, $T(u)$, exerted by a rigid, perfectly plastic pin (or any other form of through-the-thickness reinforcement) normal to the plane of the laminate in bridging a crack loaded in pure shear to a shear displacement u is described in a close-form solution by the following equation:[27]

$$T = \left[\frac{s\tau E_t P_n^3}{6A_t^4} \right]^{1/5} [u]^{4/5} + \tau_0 \left\{ 1 - \frac{3}{2} \left[\frac{6P_n^2}{sA_t E_t^2} \right]^{2/5} [u]^{2/5} \right\}$$

Here, E_t is Young's modulus of the z-direction reinforcing element, and s and A_t are its circumference and cross section, respectively. P_n is the force per unit of length of the reinforcing element attributable to the resistance of the substrate to the deformation and lateral "ploughing" of the pin or stitch. Finally, τ_0 is the shear flow stress in the deforming reinforcing element. In contrast to the simplicity of the situation in mode I loading, here the bridging actions are a summation of the actions of a dominant frictional pullout force and of the reaction of the reinforcing element to shear deformation. To date, no direct application of this model in determining the behavior of mode II delamination tests of Z-pinned composites has been reported.

3.4.2 Integrated Models

The models listed in Section 3.4.1 tackle the micromechanical features specific to the z-direction reinforcement (micromodels); this section concentrates on additional models in which a coupon, a subelement, or the whole structure is analyzed.

An early finite element study of Z-pins bridging a delamination crack was carried out by Barrett[19] for the case of fully bonded Z-pins. The analysis carried out in this study showed that Z-pins resist through-the-thickness stresses only when these stresses are applied close to the Z-pins. Therefore, the actions of Z-pins against crack initiation are believed to be small. However, once the crack has propagated through the Z-pinned area, the crack propagation is resisted by the closing action of the Z-pins, which prevents the crack tip from seeing high stresses. The main conclusions of the study appear to be borne out by more recent experiments.

A number of relevant analytical models were developed alongside the research effort in stitched composites, in the mid-1990s. Dransfield et al.[6] and Jain and Mai[28–30] have proposed models based on linear-elastic beam theory in order to calculate the interlaminar fracture toughness G_C as well as the crack growth resistance G_R of stitched laminates under mode I and mode II loading conditions. For mode I loading conditions, the actions of the stitches are described as functions of the distance to the crack tip, which also include geometry and orthotropic correction factors. These functions are integrated in the crack wake for a given crack extension. The mode I crack propagation resistance is then evaluated in terms of stress intensity factors.[28]

The models proposed to solve the problems of stitched laminates subjected to mode II loading conditions are based on shear deformation laminated plate theory and on Griffith's theory for strain energy release rate fracture.[29,30] For the 3-pt end-notched flexure (ENF) configuration, the models assume that the stitch failure process consists of elastic stretching of the threads due

to relative slip of the top and bottom sections of the delaminated region followed by rupture in the crack plane. The actions of the stitches are modeled by introducing a linear shear stress between the crack faces in the delaminated region.[6] Then the strain energy release rate of the beam is expressed as a function of the stitching parameters, shear deformation, and orthotropic correction factors and material properties. The shear stress due to the actions of the stitches is determined numerically, and the mode II delamination resistance strain energy release rate is then deduced.

These models are capable of calculating the mode I and mode II interlaminar fracture resistance values for stitched polymer matrix composites. They have been validated against experiments in a review published by Mouritz and Jain.[31] They require detailed knowledge of physical and interlaminar fracture properties of the unstitched material, the stitching conditions, and the mechanical properties of the stitch material.

Another line of argument has been developed by Massabò et al.[7] and Massabò and Cox.[32–34] Their models use first-order shear deformation theory for anisotropic laminated plates in cylindrical bending and small deformations. It is assumed that the crack growth is controlled by two mechanisms. The first is the intrinsic toughness of the unreinforced laminate, G_C; the second is the shielding effect at the crack tip due to the bridging tractions of the through-the-thickness reinforcement in the delaminated area.

For example, for the case of mode II loading conditions, the analysis considers a thin anisotropic laminate plate loaded by shear tractions acting along the faces of the delamination length. The bridging mechanisms acting along the bridged portion of the delamination by the through-the-thickness reinforcement are represented by a shear traction dependent on the sliding displacement. Two limiting configurations are defined to characterize the crack history of the beam. The first, called the ACK limit in attribution to the work of Aveston, Cooper, and Kelly,[35] corresponds to a crack entirely bridged with intact ligaments. The second, called small-scale bridging limit, describes a situation where the size of the bridged zone is constant, some bridging elements failing as new ones are created. The problem of large-scale bridging, representative of stitching or Z-pinning, is solved assuming a mathematical form of the bridging traction laws. The strain energy release rate is computed using J-integral methods, and the critical shear stress corresponding to crack propagation is deduced. Then the sliding displacements of the crack faces are calculated.

The inverse problem consists of determining the bridging traction, τ_b, from the sliding displacement measured during an ENF test for a given load. The methods proposed to solve the problem use discretized expressions of the bridging stresses represented by a set of basic functions (e.g., Legendre polynomials). The bridging law can be used to determine the structural response in terms of load vs. displacement.[7,25,26,32]

The case of mixed-mode delamination fracture in the presence of large-scale bridging is studied using the principle of superposition, having solved two idealized problems of DCB and ENF specimens.[18,33,34]

3.4.3   Finite Element (FE) Modeling

Analytical models such as those referred to above can offer tests of physical insight into the fundamental micromechanical behavior of through-thickness reinforced composites. However, their development can be lengthy and require successive reevaluation of the fundamental assumptions and simplifications that are made in order for the model problem to have a numerical solution. As already seen in the case of parametric studies of the effects on Z-pins on in-plane stiffness (Section 3.3.1.1), a less elegant, but practical alternative is offered by FE modeling.

3.4.3.1   *An FE Tool for Parametric Studies of Mode I Delamination*

As indicated in Section 3.3, it has been found difficult to carry out experimental studies of the effects of individual parameters such as Z-pin diameter, pin spacing, pin angle, etc., upon the mechanical properties of reinforced laminates. This is because the effects of the manufacturing quality in terms of the accuracy of Z-pin placement (location, angle, depth) are very significant and can mask the differences caused by the variation in the selected parameter itself. For this reason, it has been found convenient to develop and validate a simple two-dimensional FE model to perform such parametric studies on standard mode I delamination test beams containing Z-pins bridging the delamination crack.

The starting point in the construction of the numerical model is a two-dimensional finite element mesh of a representative DCB specimen. Given the favorable specimen geometry, the treatment has been limited to two dimensions, with plane strain calculations, in order to reduce the required computation time. The crack bridging actions of the Z-pins are represented by forces applied at nodes representative of their location. These have been determined in separate single-pin pullout experiments.[15] Figure 3.26 shows the experimental arrangement used in the single-pin testing, and an example of the load-displacement traces obtained is given in Figure 3.27. To transform an experimental load-displacement result into a form suitable for implementation in the model, the experimental curves were corrected for machine compliance and then fitted by a series of polynomial functions.

The simulation is carried out under displacement-control assumptions, and its aim is to reproduce the delamination R-curve. The flow diagram for the computation is shown in Figure 3.28. At each computational step, the bridging force exerted by the pin is determined from the value of the displacement at the appropriate node, at which the force is being applied. At the same time, the energy release rate at the crack tip, G_c, is calculated using a J-integral method. The global energy release rate of the beam is deduced from the applied load (P), displacement (δ), and the crack length (a), computed by the simulation, using a standard beam theory method. Crack increment is assumed to occur when G_c equals a value determined previously by experiment, using unpinned control specimens.
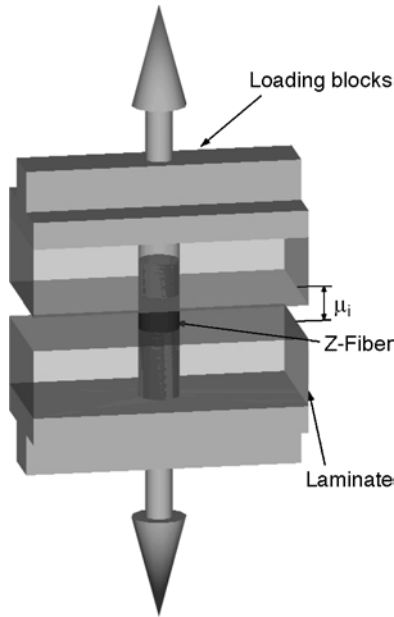
FIGURE 3.26
Single-pin pullout test setup.

FIGURE 3.27
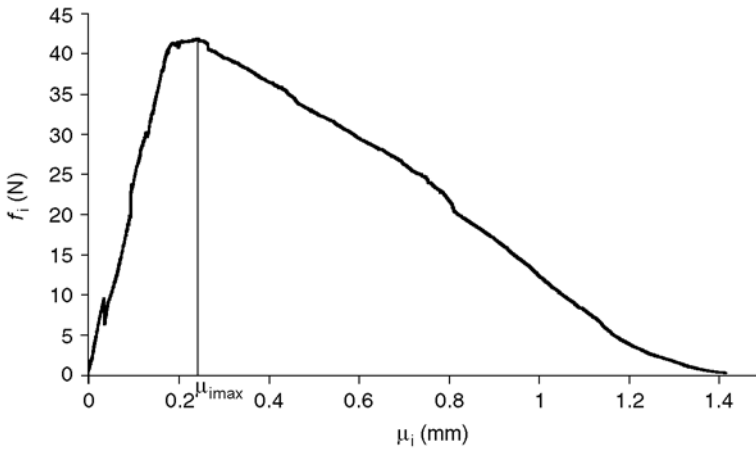Single Z-pin bridging law (no machine compliance correction made).

3.4.3.2   Validation and Example of Use

The mesh and material properties used in the FE model have been validated against experimental data, ensuring that for a given specimen geometry the load-displacement relationship is consistent and that the calculation of the energy release rate at the crack tip is correct. Table 3.1 shows a comparison
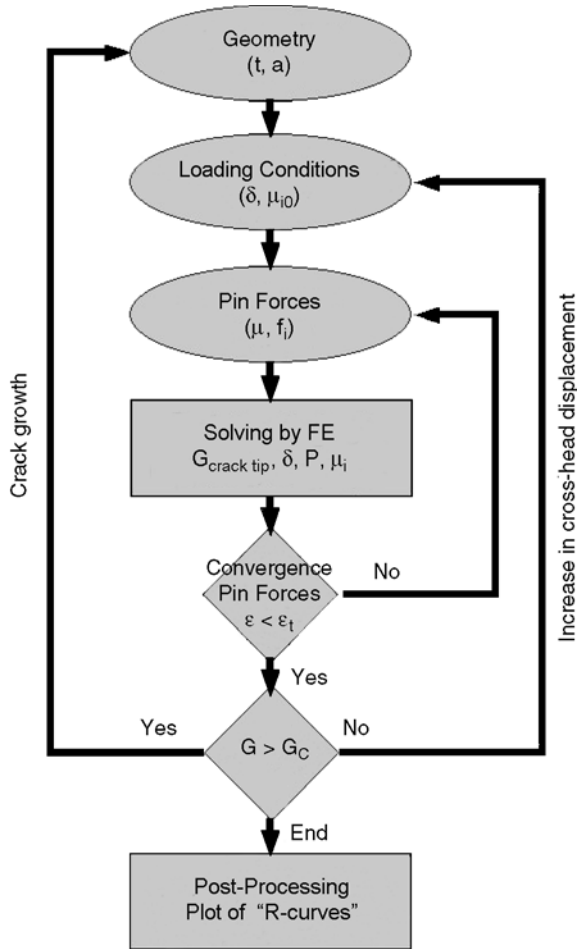
FIGURE 3.28
Algorithm of the computation used during the FE analysis of the DCB specimens.

of the FE model results and results from a DCB test on unidirectional IMS/ 924 composite. The data reduction has been carried out following the procedure described in the ISO 15024 standard for DCB testing. G_{CBT} has been calculated using the corrected beam theory, using the set of *experimental* data for the crack length (a), load (P), and crack-opening displacement (δ). G_{CBT} quoted in the FE column has been calculated inputting a, P, and δ, *results of the FE calculations*, into the same spreadsheet. G_{FE} is the energy release rate calculated locally at the crack tip by a J-integral method.

The case of a DCB specimen reinforced with 0.28-mm-diameter Z-pins at an areal density of 0.5% has been modeled in order to validate the concept. The pinning conditions (i.e., individual pin locations and insertion depths) of the experimental samples have been measured carefully and reproduced in the FE analysis. Figures 3.29 and 3.30 show comparison of the load-

TABLE 3.1

Comparison of Experimental DCB Results and FE Model Output

	IMS/924	
	Experimental	**FE**
Thickness (mm)	3.21	3.2
Crack length a (mm)	49.6	49
Load P (N)	42.8	42.8
δ (mm)	4.3	4.3
G_c (J/m^2)	G_{CBT}: 258 ± 10	G_{CBT}: 261
		G_{FE}: 264

Note: CBT = corrected beam theory; FE = calculated value.

FIGURE 3.29
Comparison of FE output vs. experimental load-displacement trace from a specific test.

displacement traces and resistance curves for the experimental and simulated results. The good agreement between the FE analysis and the experimental results demonstrates that the bridging laws measured experimentally during single-pin pullout testing are representative of the actions of the Z-pins during delamination testing under mode I loading conditions.

More specific test cases have been examined which indicate that within the expected experimental error, this approach is sufficiently accurate to predict effects of manufacturing defects such as missing rows of pins or incomplete pin insertion.[15] It thus seems reasonable at this stage to produce some predictive case studies, such as the one shown in Figure 3.31 which compares the expected mode I R-curves for the case of a fixed areal density of reinforcement but varying Z-pin diameter.
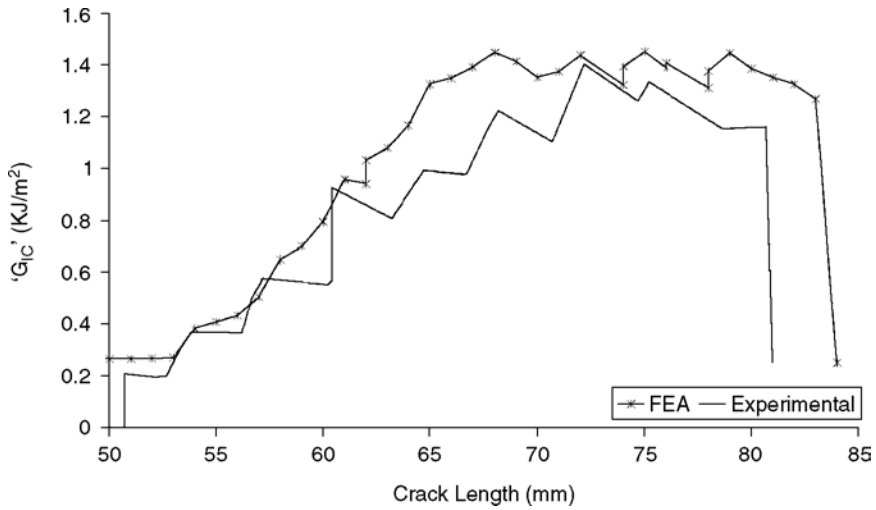
FIGURE 3.30
Experimental mode I R-curve of IMS/924 DCB reinforced with 0.5% 0.28-mm-diameter Z-Fibers and the corresponding FEA calculations.
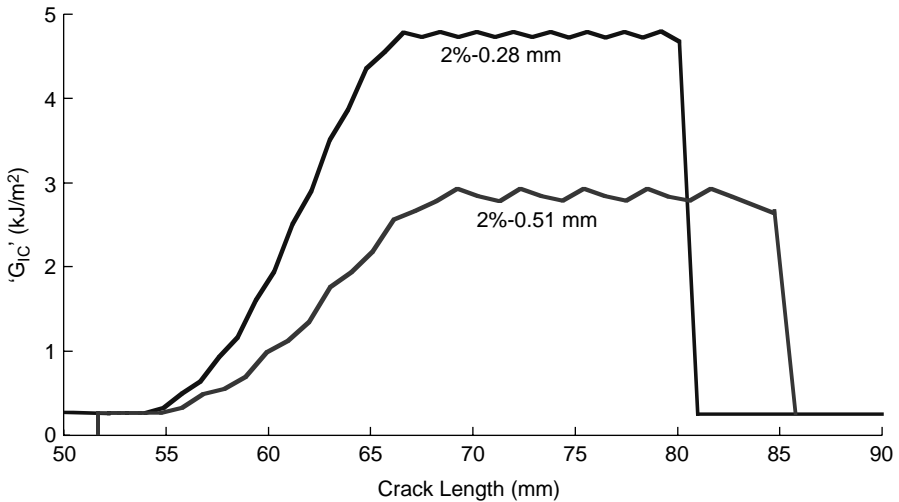
FIGURE 3.31
An FE prediction of the effect of Z-pin diameter on mode I delamination resistance for areal density of pinning of 2%. (The calculation is based on data from control IMS/924 UD beams; the specimen geometry, Z-pinned block geometry, and Z-pinning density are kept constant; the difference is in Z-pin diameter only.)

The above outlined modeling approach relies on separate experimental determination of the bridging law for any specific combination of Z-pin–composite matrix–reinforcement type. If it were possible to use analytical models for the pin bridging laws, then the FE modeling approach would

become much more attractive to industrial users wanting to utilize localized Z-pin reinforcement in complex composite structures.

3.5 Current Industrial Applications Status

It is convenient to split the consideration of industrial applications into two distinct areas: one for the through-the-thickness reinforcement of otherwise standard laminates by the Z-Fiber, and the second for the rapidly emerging markets for honeycomb replacement by the X-Cor and K-Cor product range.

3.5.1 Z-Fiber Applications

The capacity of Z-pins to ensure very significant increases in the delamination crack propagation resistance of laminated composites under a variety of loading conditions is not in dispute. Remaining concerns center on the in-plane properties, where too little work has been done to be able to make generalized statements. Different types of lay-ups and fabrics are likely to show different sensitivities to the spatial disturbance produced by the through-the-thickness reinforcement. Nevertheless, it would seem reasonable to expect the in-plane knockdowns for pinning to be lower than those for stitching in view of the significantly larger-diameter needles used in the stitching process, which are thus more likely to damage the reinforcing fibers. Furthermore, the current primary market for Z-Fiber is for use with prepreg which is very difficult, if not impossible, to stitch.

The Z-pin insertion times compare very favorably with the cycle times needed to install metal fasteners into composite structures. In addition, of course, since the weight of the pins is almost negligible, significant weight savings can be achieved. Figure 3.32 is a typical trade study showing these benefits.

At the time of this writing, most industrial applications of Z-pins are so new that they cannot be described in detail in the open literature. Nevertheless, it can be stated that the use of Z-pins has recently provided urgently needed solutions to increased load-bearing capacity regulations for several Formula 1 racing teams, as well as answered significant structural integrity challenges in the case of military jets. The first truly industrial use of Z-Fiber technology in aerospace has been to replace multiple metal fasteners used on composite duct and aft fuselage structure for the F/A 18 E/F U.S. Navy aircraft. For this application, Z-Fiber technology has been successfully employed since June 2000. The customer has saved 17 kg of weight per aircraft and over $80,000 in costs. This project is being seen as a forerunner to more extensive use on all future military aircraft programs and possibly on similar commercial aircraft structures.
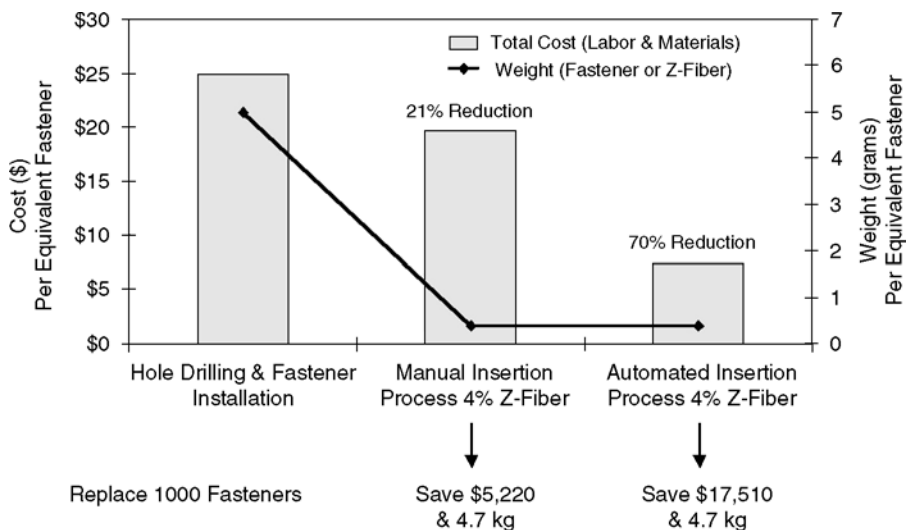
FIGURE 3.32
Trade study of replacement fasteners by Z-Fibers: cost and weight comparisons for equivalent attachment methods.

There are good performance prospects for the use of Z-pins in the classical "hat stiffener" and T-joint structures, as indicated in Figure 3.33.

3.5.2 X-Cor and K-Cor Applications

Although X-Cor and K-Cor can be treated in essentially the same way as honeycomb, it is important to realize that these materials are tailored structures[36] and their behavior under load is quite different and superior to baseline honeycomb products. It has been demonstrated that these reinforced foams in a structure are typically 10 to 20% lighter than the equivalent honeycomb structure. The structure is also highly damage tolerant and, under extreme loading conditions, exhibits a ductile failure, more like a metal part rather than a catastrophic skin-to-core failure seen with a honeycomb stiffened part. An important additional benefit is the fact that the reinforced foam structure absorbs somewhat less moisture than an equivalent honeycomb part.

A recent joint development program between Sikorsky and Aztex Inc. targeted the U.S. Army's RAH-66 Comanche helicopter, developing a materials property database and manufacturing guidelines for the use of the new reinforced foam core material.[37] In a significant new development, the X-Cor "advanced sandwich core material" will be produced in a variety of finished core assemblies and details. Ramped edges, formed contours, and localized high-density reinforcements will become available, enabled by the existence of three-dimensional engineering electronic data generated during the part design by the customer and converted into numerically controlled machine
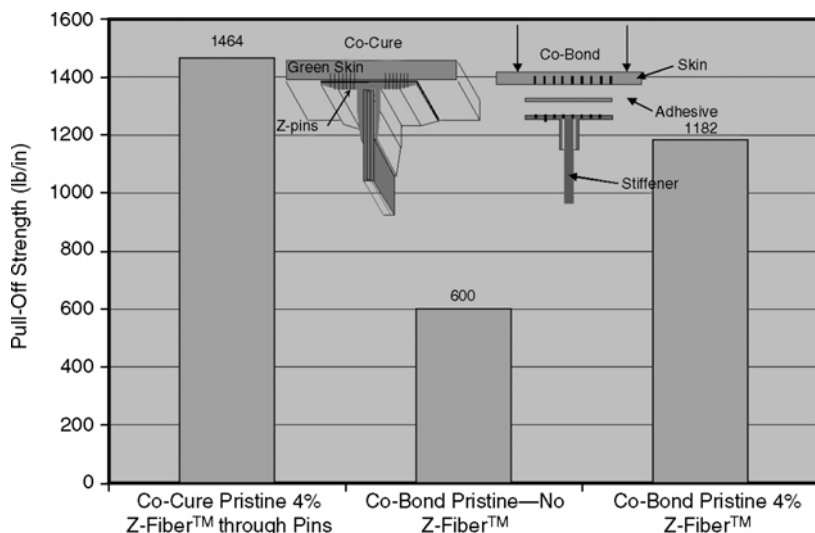
FIGURE 3.33
Comparison of pull-off strengths of unpinned and Z-pinned T-joints, and co-curing vs. co-bonding preparation routes for the Z-pinned joints.

code. Such automation allows for easy tailoring of individual core details to meet specific engineering requirements.

This approach points the way to the future utilization of these exciting new technologies — not as a one-off total material replacement, but as a tailored engineering solution that needs to be considered fully in the design stages of complex composites structures.

References

1. Freitas G., Magee C., Boyce J., and Bott R. Service Tough Composite Structures Using Z-Fiber Process, paper presented at Proceedings of 9th DoD/NASA/ FAA Conference on Fibrous Composites, Lake Tahoe, NV, November 1991.
2. Childress, J.J. and Freitas G.A. Z-Direction Pinning of Composite Laminates for Increased Survivability, AIAA92–1099, paper presented at Proceedings Conference of the American Institute of Aeronautics and Astronautics, Irvine, CA, February 3–6, 1992.
3. Freitas G., Magee C., Dardzinski P., and Fusco T. Fiber insertion process for improved damage tolerance in aircraft laminates, *J. Adv. Mater.*, 24, 36–43, 1994.
4. Freitas G. and Fusco T. Z-Fiber Technology and Products for Enhancing Composite Design, paper presented at 83rd AGARD SMP, Florence, Italy, September 2–3, 1996 (published in *AGARD CP-590*, NATO, 1997).
5. Freitas G., Fusco T., Campbell T., Harris J., and Rosenberg S. Z-Fiber technology and products for enhancing composite design, in *AGARD CP-590*, NATO, 1997, pp. 17.1–17.8.

6. Dransfield K.A., Jain L.K., and Mai Y-W. On the effects of stitching in CFRPs: Parts I and II, *Composites Sci. Technol.*, 58, 815–827, 829–837, 1998.

7. Massabò R., Mumm D.R., and Cox B.N. Characterizing mode II delamination cracks in stitched composites, *Int. J. Fracture*, 92, 1–38, 1998.

8. Mouritz A.P., Leong K.H., and Herszberg I. A review of the effect of stitching on the in-plane mechanical properties of fibre-reinforced polymer composites, *Composites*, 28A, 979–991, 1999.

9. http\\:www.aztex-z-fiber.com and Aztex Inc. Report 6/16/98, Vs. 1.3 Preliminary Lamina, Laminate and Sub-Element Test Results for Z-Fiber™ Reinforced IM7/977–3 Uni-Directional Tape and Fabric.

10. Grassi M., Zhang X., and Meo, M. Prediction of stiffness and stresses in Z-Fiber® reinforced composite laminates, submitted to *Composites A*.

11. Steeves C.A. and Fleck N.A. In-plane properties of CFRP laminates containing through-thickness reinforcing rods (Z-pins), in *Proceedings of ICCM12*, Paris, July 5–9, 1999, Massard T. and Vautrin A., Eds.

12. Steeves C.A. Mechanics of Failure in Composite Structures, Ph.D. thesis, Engineering Department, Cambridge University, U.K., 2001.

13. Rezai A., Cartié D., Partridge I., Irving P., Ashton T., Negre P., and Langer J. Interlaminar Damage Resistance of Z-Fiber® Reinforced Structural CFRP, Proceedings of ICCM13, Beijing, China, June 2001.

14. Troulis E. Unpublished data, Cranfield University.

15. Cartié D.D.R. Effect of Z-Fibres™ on the Delamination Behaviour of Carbon Fibre/Epoxy Laminates, Ph.D. thesis, Cranfield University, U.K., 2001.

16. Cartié D.D.R. and Partridge I.K. Delamination behaviour of Z-pinned laminates, keynote paper in *Proceedings of ICCM12*, Paris, July 5–9, 1999, Massard T. and Vautrin A., Eds.

17. Cartié D.D.R and Partridge I.K. Delamination behaviour of Z-pinned laminates, in *Proceedings of 2nd ESIS TC4 Conference*, Les Diablerets, Switzerland, September 13–15, 1999, ESIS Publication 27, Williams J.G. and Pavan A., Eds. Elsevier, Amsterdam, 2000.

18. Rugg K.L., Cox B.N. and Massabò R. Mixed mode delamination of polymer composite laminates reinforced through the thickness by Z-Fibers, *Composites,* 33A, 77–190, 2002.

19. Barrett D.J. The mechanics of Z-Fiber™ reinforcement, *Composite Struct.*, 36, 23–32, 1996.

20. ISO 15024. Determination of Mode I (Critical Strain Energy Release Rate or Fracture Toughness, G_{IC}) of Unidirectional Fibre-Reinforced Polymer Laminates Using the Double Cantilever Beam (DCB) Specimen, ISO.

21. Graftieaux B., Rezai A., and Partridge I. Effects of Z-Pin Reinforcements on the Delamination Toughness and Fatigue Performance of Unidirectional AS4/8552 Composite, Proceedings of ECCM9 Conference, Brighton, U.K., June 4–7, 2000.

22. Zhang X., Liu H.-Y., Mai Y.-W., and Diao X.-X. On steady state fibre pull-out I: the stress field, *Composites Sci. Technol.*, 59, 2179–2189, 1999.

23. Liu H.-Y., Zhang X., Mai Y.-W., and Diao X.-X. On steady state fibre pull-out II: computer simulation, *Composites Sci. Technol.*, 59, 2191–2199, 1999.

24. Liu H.-Y. and Mai Y.-W. Effects of Z-pin Reinforcement on Interlaminar Mode I Delamination, paper presented at Proceedings of ICCM13, Beijing, China, June 2000.

25. Cox B.N. Constitutive model for a fiber tow bridging a delamination crack, *Mech. Composite Mater. Struct.*, 6, 117–138, 1999.

26. Cox B.N. A constitutive model for through-thickness reinforcement bridging a delamination crack, *Adv. Composites Lett.*, 8, 249–256, 1999.
27. Cox B.N. and Sridhar N. A traction law for inclined fibre tows bridging mixed mode cracks, *Mech. Composite Mater. Struct.*, in press.
28. Jain L.K. and Mai Y.-W. On the effect of stitching on mode I delamination toughness of laminated composites, *Composites Sci. Technol.*, 51, 331–345, 1994.
29. Jain L.K. and Mai Y.-W. Analysis of stitched laminated ENF specimens for interlaminar mode II fracture toughness, *Int. J. Fracture*, 68, 219–244, 1994.
30. Jain L.K. and Mai Y.-W. Determination of mode II delamination toughness of
31. stitched laminated composites, *Composites Sci. Technol.*, 55, 241–253, 1995.
32. Mouritz A.P. and Jain L.K. Further validation of the Jain and Mai models for interlaminar fracture of stitched composites, *Composites Sci. Technol.*, 59, 1653–1662, 1999.
33. Massabò R. and Cox B.N. Concepts for bridged mode II delamination cracks, *J. Mech. Phys. Solids*, 47, 1265–1300, 1999.
34. Massabò R. and Cox B.N. Bridged delamination cracks in curved beams and mixed mode bending specimens, in *Proceedings of ICCM12*, Paris, July 5–9, 1999, Massard T. and Vautrin A., Eds.
35. Massabò R. and Cox B.N. Unusual characteristics of mixed mode delamination in the presence of large scale bridging, *Mech. Composite Mater. Struct.*, 8, 61–80, 2001.
36. Aveston J., Cooper G.A., and Kelly A. Single and multiple fracture, in *The Properties of Fiber Composites*, National Physical Laboratory, IPC Science and Technology Press Ltd., 1971, p. 15.
37. Palazotto A., Gummadi L.N.B, Vaidya U.K., and Herup E. Low velocity impact damage characteristics of Z-Fiber reinforced sandwich panels: an experimental study, *Composite Struct.*, 43, 275–288, 1999.
38. Carstensen C., Cournoyer D., Kunkel E., and Magee C. X-Cor™ Advanced Sandwich Core Material, paper presented at SAMPE, Seattle, WA, November 2001.

4

Modeling Concepts for the Spherulitic Growth in Polymers and Composites

Andre Benard and Suresh G. Advani

CONTENTS

4.1   Introduction

Prediction of microstructure formation in semicrystalline polymers is of technological importance for parts made through processes such as compression molding, injection molding, or extrusion. The microscopic texture of the polymer dictates its physical and chemical properties and thus the quality of the parts. In recent years, there have been several publications dealing with the crystallization of polymers under isothermal and nonisothermal conditions, because crystallization constitutes one of the most important steps in the overall shaping process of semicrystalline polymers. The final microstructure of a part and its temperature during cooling are generally the information sought by such modeling.

   To date, models developed to study the evolution of crystallinity as a function of temperature can be divided into three categories. The most commonly used models are based on concepts developed by various researchers over 50 years ago. These models predict the evolution of the crystallinity as a function of temperature with one single constitutive equation. A recent review of these models was presented by Wasiak.[1] A second approach, based on concepts recently introduced in metallurgy by Rappaz et al.,[2] can also be used for semicrystalline polymers.[3] It consists of describing the growth of spherulites with mass balance, heat balance, and interfacial kinetics. The equations are written for a small control volume and can predict the average microstructure of the small volume considered. It differs from the first approach as more information can be obtained from the models, at the price of increased complexity. A last approach consists of performing direct numerical simulations of the growth process. The boundary of each growing entity is followed throughout the solidification process, and simulations are performed for a small representative volume.[4–11]

   In this chapter, we review the main features of crystallization modeling for semicrystalline polymers and present recent concepts that can be used in predicting the microstructure formation in these materials. Emphasis will be on predictions of the spherulite growth process and the resulting crystallinity. Of the three approaches mentioned above, the first two will be reviewed and their advantages and disadvantages will be discussed. The
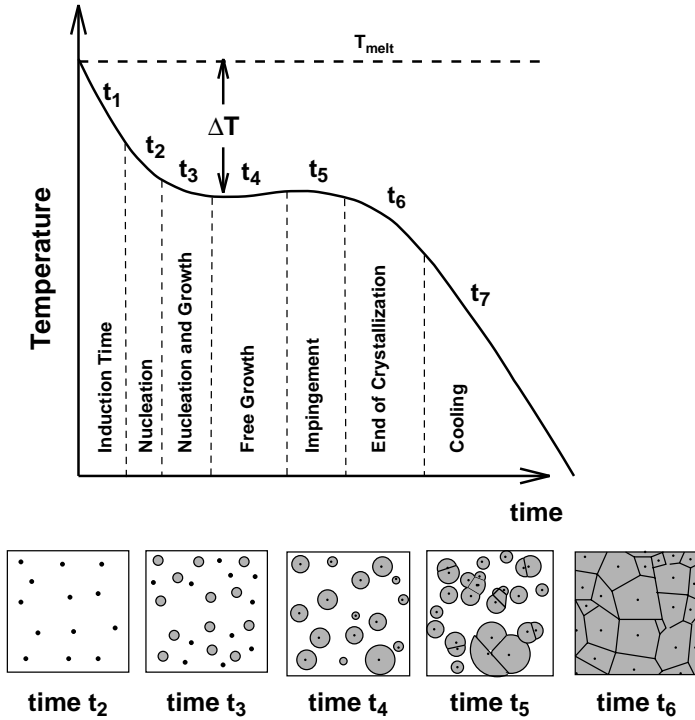
FIGURE 4.1
Various stages of the spherulitic growth process during nonisothermal crystallization.

presentation of the material will initially follow the steps illustrated in Figure 4.1, where the important stages of the microstructure formation in a semicrystalline polymer are illustrated for a nonisothermal process. These stages include an induction time period, where the polymer chains reorganize themselves to form nuclei. A nucleation stage then follows, along with the growth of the initial nuclei. Finally, impingement of the spherulites becomes important near the end of the crystallization process. Models that predict the overall process illustrated in this figure will be presented. Before following the steps in Figure 4.1, the phenomenology behind the spherulitic growth process in polymers will be briefly reviewed, along with a discussion on the interplay between the various mechanisms participating in the formation of spherulites.

4.2   Phenomenology of Spherulitic Growth

Spherulites are the largest microstructural features encountered during the solidification of a quiescent semicrystalline polymer melt. They are

Stacks of Lamellae → **Axialites** → **Nascent Spherulites**
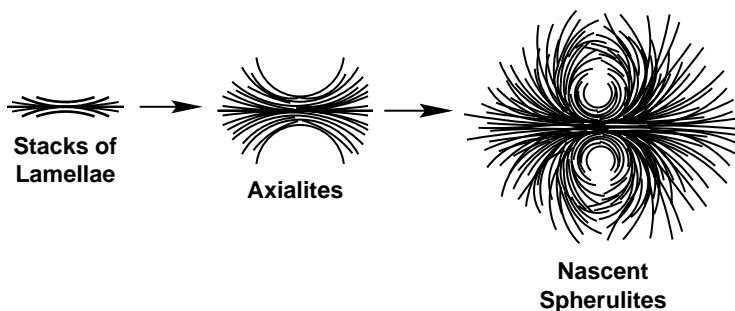
FIGURE 4.2
Schematic of the evolution of the spherulitic morphology, starting from stacks of lamellae.

polycrystalline aggregates formed from a radiating array of crystalline "ribbons" that branch regularly to create a three-dimensional structure of approximate radial symmetry. Spherulitic growth occurs in minerals crystallizing from viscous magna, in polymers crystallizing from the melt, and in organic compounds crystallizing from the melt with added thickeners.[12]

The mechanism of spherulitic crystallization was described as early as 1929 by Bernauer[13,14] and was recast within the framework of modern theories by Khoury and Passaglia.[15] According to this mechanism, after nucleation, which often occurs on small impurities such as catalyst residues or nucleating agent particles, lamellae start growing radially to form axialites, which are precursors of spherulites. The axialites then grow to eventually form spherulites. Spherulites are therefore formed by a process in which they start from stacks of lamellae with a planar geometry, and these stacks are initiated at a nucleating site and evolve into a full spherical entity. This process is illustrated in Figure 4.2, where a side view of this process is shown. A top view of this process would show the shape of the largest lamella until the axialite folds on itself to form a spherical structure.

The mechanisms behind the formation of the spherulitic morphology are still not fully understood today, but great progress has been made in the last decade. A brief account of the evolution of our understanding over time is provided below. Keith and Padden[12,16,17] postulated the first phenomenological theory of spherulitic growth. They studied the growth of spherulites from polypropylene melts and observed that spherulite-forming melts had the character of alloys instead of that of pure substances. They surmised that two conditions were required for the formation of spherulites: high viscosity of the medium and presence of noncrystallizable material. This latter characteristic can arise in polymers from the polydisperse components of the melt, which crystallize less readily than the major component and are rejected from the growing solid[16]; this phenomenon is in effect fractionation of the melt. It can also arise from the atactic chains of an isotactic polymer.[18,19] The rejected component of the system is often called the solute. The solute rejected from the crystal creates an excess concentration of impurity that is pushed ahead of the solid–liquid interface.

Just as in metals, the layer of solute pushed ahead of the interface was assumed to promote the growth of instabilities at the solid–liquid interface. Keith and Padden also suggested that branches of crystalline material would penetrate into the molten polymer and grow preferentially in regions rich in crystallizable material. This was thought to be the basic mechanism behind the formation of spherulites. Keith and Padden postulated that the thickness of the solute layer δ, given by δ = D/G, the ratio of the diffusion coefficient to the growth rate, scales with the size of the branches. If a growing branch would become larger than δ, the growing surface would become unstable and branching or bifurcation would occur at a small, non-crystallographic angle.

The initial theory of Keith and Padden on the formation of the spherulitic texture has been much discussed since their original papers.[20,21] The advent of electron microscopy has shed new light on the mechanisms responsible for the formation of spherulites. It is now apparent that the solute is not the principal reason behind the spherulitic morphology, but that pressure from the interstitial molecules between the lamellae (cilia) causes a strong divergence of adjacent lamellae.[22] Further branching may be associated with the formation of giant screw dislocations.[23,24]

Clearly the solute must also have a bearing on the spherulitic growth of heavily doped polymers, since it can accumulate between the lamellae, between the branches, and between the spherulites. This layer of solute that is pushed ahead of a growing front also has the dual effect of locally depressing the equilibrium crystallization point, thereby reducing the crystallization driving force and reducing the growth rate due to a shortage of crystallizable material. It also appears that spherulitic growth with solute diffusion, with the prevalence of interface kinetics in the formation of the structure, differs somewhat from the instability criterion set forth by Mullins and Sekerka[23,25] for unfaceted crystals, i.e., crystals that present smooth phase change interfaces.

Other effects appear also in branched polymer systems. The presence of branches in the molecules, even at low frequency, increases the strain on the crystals. A certain amount of branches are excluded from the crystals and accumulate between the lamellae. This has the effect of decreasing the lamellae thickness and lowering the melting point of the crystals.[26]

An accurate description of spherulitic growth and the associated crystallinity therefore requires that the effects of nucleation, interfacial kinetics, temperature, and solute all be accounted for in the modeling. Inclusion of the solute is important because it appears in almost every polydisperse polymer. Figure 4.3 gives a schematic representation of the scales at which these various phenomena influence the solidification process. The top diagram in Figure 4.3 represents a small control volume; at this scale it is possible to approximate the crystallizing polymer as a continuous medium. However, the macroscopic properties and phenomena are coupled with microscopic phenomena, and in some cases it is important to keep track of the evolution of the microstructure. For example, the heat transfer is coupled

Physical Scales and Phenomena in Spherulitic Growth

Macroscopic Scale : 1 mm

- Mass
- Momentum   } Transport
- Heat and Species
- Cooling Rate

Spherulite Scale : 10-100 μm
- Local Heat and Species Transport
- Spacings and Texturing

Interface Scale : 1 μm
- Interface Stability
- Capillarity
- Local Equilibrium
- Branch Tip Undercooling

Polymer Chains Scale : 100 nm
- Nucleation
- Interface Structure
- Molecular Attachment Kinetics
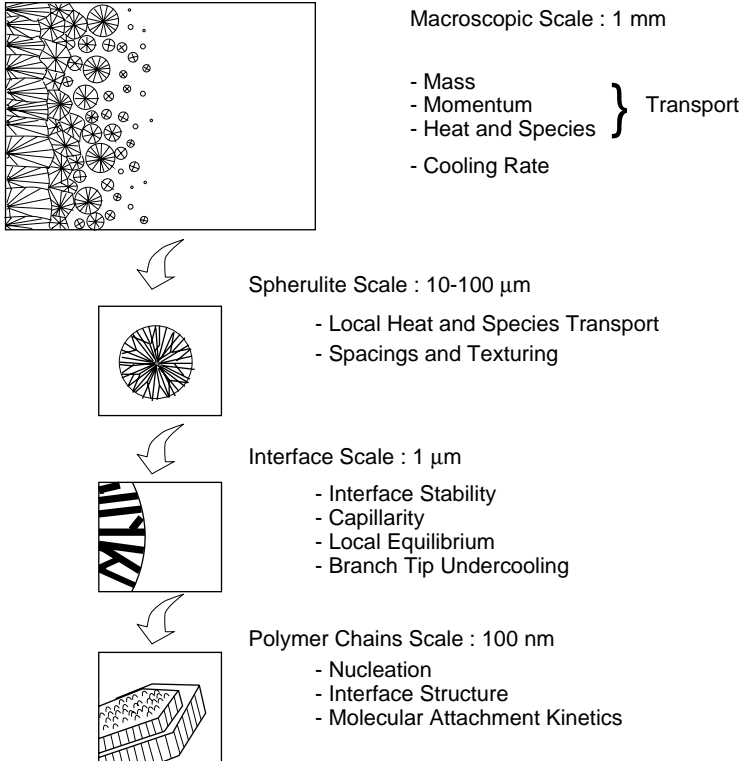
FIGURE 4.3
Various scales of the growth process of spherulites.

with the release of the latent heat of fusion, which is governed by the evolution of the microstructure. All the physical phenomena occurring at various levels are intertwined and affect the development of the microstructure, and ultimately the physical and chemical properties of the entire part.

4.3   Induction Time for Nucleation

The concept of an induction time refers generally to the time required for the first stage of crystallization (nucleation) to become detectable. It can be defined, for example, as 1% of the maximum relative crystallinity.[27] Two causes can be attributed to the induction time period: first, there is a certain time required for the organization of the molecules around a nucleus; the second

cause is simply attributed to the inability of the apparatus to detect the appearance of small nuclei. It is not clear which of these two phenomena is dominant in the induction time period. Furthermore, this finite period of time might vary from one apparatus to another, depending on their sensitivities.

The induction time for the appearance of the spherulites is generally expressed by a function $t_i(T)$, for which the parameters are obtained from isothermal crystallization measurements. It is possible afterwards to compute the induction time of spherulites for a melt undergoing a nonisothermal process with an additivity rule introduced by Cahn.[28]

The additivity of the induction times is expressed as

$$\int_0^t \frac{dx}{t_i(T(x))} = 1 \tag{4.1}$$

where x is a dummy variable, T is the temperature, and t is the time. This expression was applied to polymers initially by Sifleet et al.[29] in their study of nonisothermal crystallization kinetics. Its validity was recently demonstrated by Chew et al.[30] Maffezzoli et al.[31] and Torre et al.[32] recently proposed an expression for the temperature dependence of the induction time:

$$t_i = K_{t0} \exp\left[\frac{E_{t2}}{R(T - T_g)} + \frac{E_{t1}}{T_m^o - T}\right] \tag{4.2}$$

for which the parameters can be obtained from isothermal differential scanning calorimetry (DSC) experiments. The induction time was assumed to be dependent on similar mechanisms as a nucleation phenomenon. Equation (4.2) was therefore chosen for its similarity to expressions describing nucleation processes in polymers. A good agreement was found between their experimental data and the model. The induction times measured were found to be strong functions of temperature, going almost to zero close to $(T_m + T_g)/2$. Measured induction times for polyphenylene sulfide (PPS) are shown in Figure 4.4.[31]

Chan and Isayev[33] also recently incorporated the induction time concept in their study of crystallization kinetics. They used the expression

$$t_i = t_c \exp(T_o/T) \tag{4.3}$$

to represent the induction time during cold crystallization, i.e., crystallization upon heating, which occurs in the amorphous material that can still reorganize itself into a crystalline phase with the addition of heat. The expression

$$t_i = t_m \left(T_m^o - T\right)^{-\alpha} \tag{4.4}$$

was used for melt crystallization. t_m, a, t_c, and T_o are material constants independent of temperature. They also found a good fit with their experimental
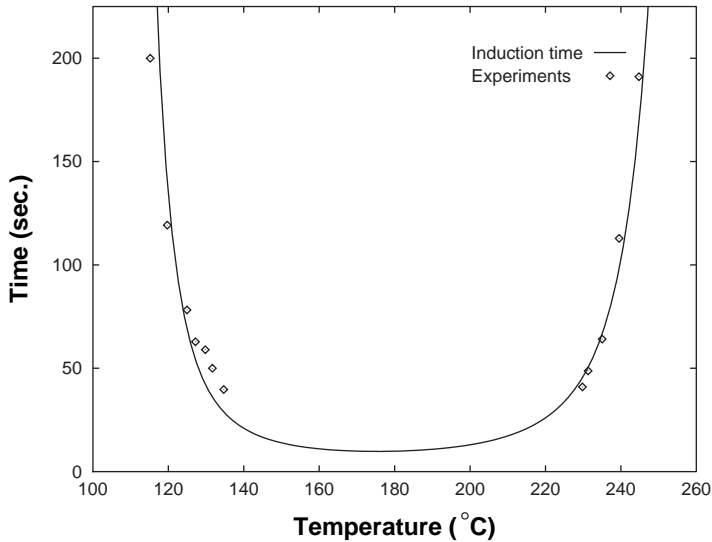
FIGURE 4.4
Induction time measured for PPS (data from Maffezzoli et al.[31] and compared against a best fit
for Equation [4.2]).

data using Equations (4.3) and (4.4). These equations were derived from
empirical considerations.

4.4   Primary Nucleation

Primary nucleation of spherulites in polymers is one of the most important
aspects in modeling the development of the microstructure. The importance
of nucleation stems from its direct impact on the final size of the spherulites.
If the polymer fully crystallizes, the average spherulite size is directly given
by the nuclei density. The spherulite size in turn influences the mechanical
properties of semicrystalline polymers. For example, very fine spherulitic
structures obtained by the addition of nucleating agents enhance ductility,
yield strength, and impact strength.[34]

   Unfortunately, primary nucleation is also one of the most difficult factors
to deal with in modeling real polymer systems, since it can vary from one
batch of a process to another because of its sensitivity to several factors. The
nucleation of polymers is also generally strongly dependent on is thermal
history. Any previous crystallization will affect the nucleation process, as
well as the melting temperature and the time spent in the molten state.
Nucleation often has an activation time and can be a strong function of the
cooling rate.

Nucleation is generally referred to as the formation of stable nuclei that are able to grow for a given set of external conditions. It is called homogeneous when the nuclei are formed spontaneously from aggregates of polymer chains that exceed some critical size. Nucleation is said to be heterogeneous when nuclei are formed on solid particles already existing in the polymer. Heterogeneous nucleation can also occur at the wall of a container or the surfaces of fibers. It is also customary to qualify nucleation as thermal or athermal. Thermal nucleation refers to a nucleation process that occurs throughout the crystallization. Athermal nucleation characterizes a solidification process where all the crystals started growing at the same time. Furthermore, homogeneous nucleation is connected to thermal nucleation, while heterogeneous nucleation can be either thermal or athermal.[27] Heterogeneous and homogeneous are therefore terms used to characterize the origin of the nuclei, while thermal and athermal are terms used to characterize the temperature dependence of the nucleation process.

Cormia et al.[35] have shown that heterogeneous nucleation is the dominant mode of nucleation in polyethylene (PE), and this observation can probably be extended to several systems. Using a fine dispersion of PE particles in an inert liquid medium, they found that some droplets did not contain nucleating centers and crystallized at much lower temperatures than other droplets. Since the degree of undercooling needed for homogeneous nucleation is far greater than for heterogeneous nucleation, it was concluded that homogeneous nucleation plays a minor role in bulk crystallization of polymers.

Experimental evidence shows that primary nucleation in quiescent polymer melts often occurs from a fixed number of predetermined sites per unit volume. The number of these sites depends on the crystallization temperature. This heterogeneous process complicates the modeling of real systems, since we must know in advance the distribution of potential nuclei that will get activated at a given temperature. Furthermore, in describing the nucleation process, a distinction between the apparent nucleation rate, $\dot{n}$, and the true nucleation rate, $\dot{n}'$, is often made. Apparent nucleation is found from direct observation of the specimen considered and cannot effectively measure nuclei that are engulfed by growing spherulites before reaching a detectable size. The true nucleation rate is defined as the nucleation rate per volume of untransformed material. Computation of the true nucleation has been done by some researchers (see Chew et al.,[30] for example). However, the true nucleation rate is often set equal to the apparent nucleation rate, based on the assumption that most sites are activated initially and very few of them are actually "swallowed" by the growing spherulites.

Classical nucleation theory can give us some useful insight into the process of nucleation. For this reason, it is described very briefly below. Approaches used in dealing with heterogeneous nucleation in polymers are reviewed later, starting with the simpler case of isothermal nucleation, and then the nonisothermal process is presented.

4.4.1 Classical Nucleation Theory

Turnbull and Fisher[36] provided the first theory of thermal nucleation along with its temperature dependence. The rate of thermal nucleation according to this theory is given by

$$\dot{N} = \dot{N}_o(T)\exp\left[-\frac{E_D + \Delta F^*}{RT}\right] \tag{4.5}$$

where $\dot{N}_o(T)$ is a material constant and is proportional to temperature T, c is a shape constant, k is the Boltzmann constant, k is the Planck constant, E_D is the free energy of activation of diffusive transport of the molecules in the melt, ΔF^* is the critical free energy of a forming nucleus, and R is the universal gas constant.

The free energy of a nucleus, ΔF, is dependent on the shape of the nucleus and has a critical value. For a spherical nucleus of radius r, the free energy is

$$\Delta F = -\frac{4}{3}\pi r^3 \Delta\phi + 4\pi r^2 \sigma \tag{4.6}$$

The bulk free energy, according to Hoffman,[44] can be expressed as

$$\phi = \Delta h T_c \Delta T / T_m^2 \tag{4.7}$$

where Δh is the heat of transition per unit volume, T_m is the equilibrium melting temperature, T_c is the crystallization temperature, and $\Delta T = (T_m - T_c)$ is the undercooling. ΔF^* shows a maximum at a certain value of r, which gives the critical radius, r^*, for a spherical cluster as

$$r^*(T) = \frac{2\sigma T_m^2}{\Delta h T_c \Delta T} \tag{4.8}$$

The maximum value for the excess free energy is given by

$$\Delta F^* = \frac{16\pi\sigma^3 T_m^4}{3\left(\Delta h T_c \Delta T\right)^2} \tag{4.9}$$

Clusters smaller than r^* are unstable and tend to dissociate, while those larger than r^* grow spontaneously. It can also be seen that the critical radius is a function of crystallization temperature and that it decreases with decreasing T_c.

Polymer nuclei can have a variety of shapes, e.g., spherical or cylindrical, and other expressions for the excess free energy have been derived elsewhere.

4.4.2 Isothermal Nucleation

The most general nucleation case is characterized by a distribution of nucleation mechanisms with different activation times during the solidification process, i.e., activation time spectrum. The introduction of an activation time spectrum by Avrami[37] comes from physical considerations. It was suggested that since the surfaces of alien particles are not identical, nucleation occurs under slightly different conditions from site to site.

In the early model of Avrami,[38] the time dependence of the nucleation rate, under isothermal conditions, was expressed in the form

$$\dot{N}(t) = \dot{N}(0)\exp(-\nu t) \tag{4.10}$$

where $\dot{N}(0) = M\nu$, in which M is the fixed number of potential nuclei and ν is the activation frequency. The nucleation rate is thus an exponentially decreasing function of time. The total number of nuclei, as a function of time, takes the form

$$N(t) = M(1 - \exp(-\nu t)) \tag{4.11}$$

Icenogle[39] found that Equation (4.11) did not match experimental data. He then recommended the use of

$$N(t) = \begin{cases} 0 & \text{for } 0 \leq t \leq t_0 \\ M(t - t_0)/(t_1 - t_0) & \text{for } t_0 \leq t \leq t_1 \\ M & \text{for } t \geq t_1 \end{cases} \tag{4.12}$$

For instantaneous nucleation, the time interval $(t_1 - T_o)$ will be very small. Eder et al.,[40] on the other hand, modified the expression of Avrami so that a spectrum of activation times is introduced, with the objective of better describing the nucleation process. Such an expression is given by

$$N = \overline{N}_1 e^{-t/\tau_1} + \overline{N}_2 e^{-t/\tau_2} + \ldots + \overline{N}_n e^{-t/\tau_n} = \sum_{i=1}^{i=n} \overline{N}_i e^{-t/\tau_i} \tag{4.13}$$

where $\Sigma \overline{N}_i = \overline{N}$. The number of potential nuclei decreases with time as a consequence of activation. The difficulty here comes in evaluating each N_i and the temperature dependency of τ_i.

Icenogle[39] also proposed that $N(t)$ be approximated with

$$N(t) = \frac{M}{\sigma(2\pi)^{1/2}} \int_0^t \exp\left\{-\frac{1}{2}\left(\frac{x-\mu}{\sigma}\right)^2\right\} dx \qquad (4.14)$$

where

$$\sigma = (t_1 - t_0)/(2\pi)^{1/2} \quad \text{and} \quad \mu = (t_1 - t_0)/2$$

which is simply a normal distribution of the potential nuclei.

There are therefore several models available to describe the isothermal nucleation process, and we have mentioned a few of them above. Some are semi-empirical or empirical and based on curve fitting. All of them require a significant amount of experimental data in order to obtain sufficient parameters to adequately describe the entire process. Unfortunately, such data are difficult to find.

4.4.3 Nonisothermal Nucleation

The simple concept of a temperature-dependent number of activated nuclei is often used when dealing with nonisothermal nucleation processes. With cooling, the number of activated nuclei increases strongly with decreasing crystallization temperature, and this phenomenon matches well with experimental observations.[39,40] Eder and Janeschitz-Kriegl[41] suggested that nucleation mechanisms be represented by a temperature-dependent function given by

$$N = N_r \exp \beta(T_r - T) \qquad (4.15)$$

where β and N_r are fitting parameters. This expression gave a satisfactory fit to experimental data on spherulite nucleation in polypropylene. Their results are reproduced in a different format in Figure 4.5 from their published data. The top graph in Figure 4.5 represents the distribution of nuclei with undercooling, computed when crystallinity reaches 0.5. The bottom graph presents the same data in a different manner, to demonstrate the dependence of the overall crystallization process on the cooling rate.

Nonisothermal nucleation was also treated by Icenogle[39] for several polyolefins. He expresses the temperature dependence of the nucleation density by

$$M(T) = \gamma M_o \int_T^\infty \exp\left[-\pi\gamma^2(x - \bar{T})^2\right] dx \qquad (4.16)$$

where M is the actual nuclei density, M_0 is the total nucleation density, $\bar{T}$ is the mean temperature at which sites nucleate, and γ is a measure of the
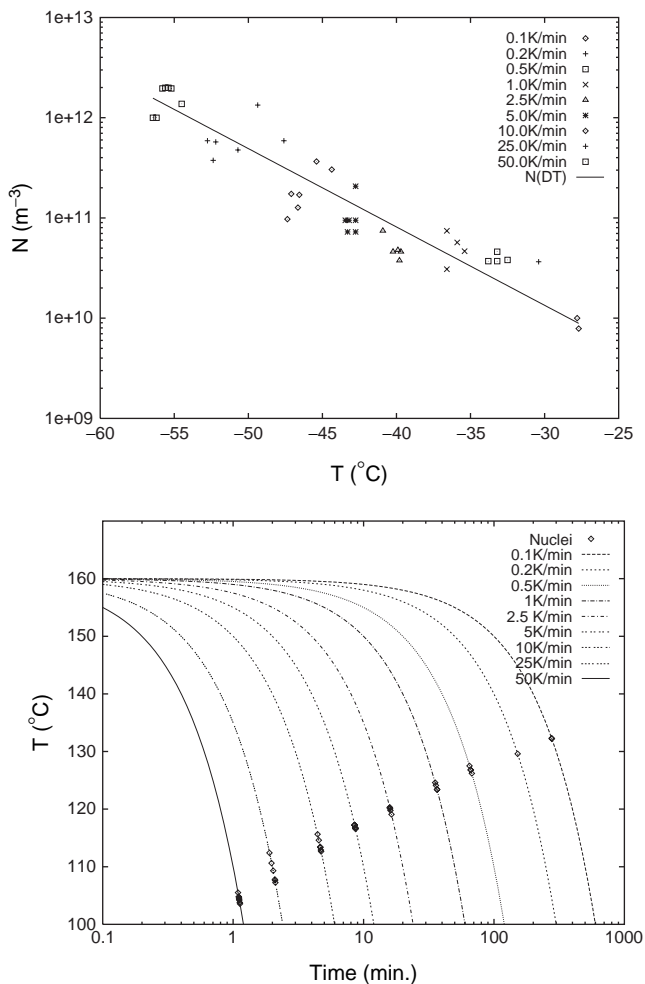
FIGURE 4.5
The spherulite density distribution, at = 0.5, during nonisothermal cooling (data from Eder
and Janeschitz-Kriegl, *1st International Conference of Transport Phenomena in Processing*, S.I. Guceri,
Ed., Technomic Publishing, Lancaster, PA, 1992) is shown on the top diagram, as a function of
the undercooling. The bottom figure presents the same data, in a different format.

breadth of nucleating temperatures. No time dependency of the nuclei is
introduced in this expression. It is again assumed that a particular nucleus
will become activated at a predetermined temperature. The distribution of
nuclei with temperature is also assumed to be normal.

Icenogle also found that a linear approximation represents satisfactorily
the temperature dependence of the nucleation rate for several polyolefins:

$$M(T) = M_o(1 - T/T_o) \tag{4.17}$$

FIGURE 4.6
A model for the distribution of activated nuclei during nonisothermal cooling. (After M. Rappaz, *Int. Mater. Rev.*, 34:93–123, 1989. With permission.)

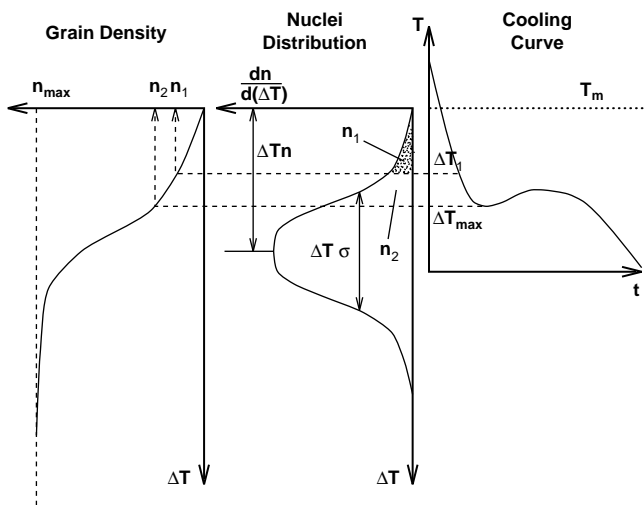In dealing with nonisothermal processes in which the temperature is imposed on the system, the models mentioned above can be used without modification. Such processes are encountered in different scanning calorimetry studies of polymer crystallization. However in real systems, such as in injection molding, an undercooled melt often undergoes recalescence, i.e., a local rise in temperature due to the latent heat release during crystallization. Evidences of this phenomenon have been given recently by Ding and Spruiell.[42] For a nuclei density that is a function of temperature, it is reasonable to assume that nucleation will cease at the onset of the temperature rise associated with recalescence. Such a model was used by Rappaz[43] for nucleation in metals and is represented in Figure 4.6. In this figure, n_1 is the number of nuclei activated for a given undercooling ΔT_1, and n_2 is the maximum number of nuclei associated with the undercooling ΔT_{max}. The onset of recalescence is used to determine n_2.

The nucleation process can therefore be predicted with semi-empirical rules, provided that all the data have been gathered for a specific polymer; i.e., nucleation rate and density and parameters of the nucleation law are computed. This also implies measuring the nucleation rate under isothermal conditions and using the additivity rule to predict nucleation under nonisothermal conditions, provided that the cooling rate is known. However, large variations in the nucleation process can be observed in different samples of the same polymer, which make this process very difficult to predict accurately, and large statistical variations are to be expected. It is also necessary to perform entirely new measurements if a different nucleation agent is used.

4.5 Growth of Spherulites

After the appearance of the nuclei, the growth process is initiated. The growth velocity of spherulites is dominated by interfacial kinetics rather than by a heat diffusion process. The original theory describing the kinetic of growth of polymer crystals was developed by Hoffman and Lauritzen and is summarized in a review presented in 1976.[44] The growth at the tip of each spherulite branch is therefore assumed to follow the kinetics of attachment of polymer chains given by the Lauritzen and Hoffman theory.[44,45] The growth rate of each branch can therefore be represented in a general manner by the equation

$$\frac{\partial R}{\partial t} = G_o \exp\left[\frac{-U^*}{R(T - T_\infty)}\right] \exp\left[\frac{-K_g}{T\Delta Tf}\right] \tag{4.18}$$

The first exponential term represents the temperature dependence of the segmental jump rate in the polymer, while the second term is the contribution of the net rate of attachment of new chains to the crystal. R is the spherulite radius and G_o is a pre-exponential constant that combines terms not strongly dependent on the material.

The growth rate of a polymer crystal therefore results from the rate of deposition of nuclei of a stable size and their subsequent growth, as well as the rate at which untransformed chains are brought to the growing crystal faces. Two extreme situations were initially identified with respect to the crystallization temperature. In a first process, the rate of lateral growth of a nucleus across a crystal face is much faster than the nucleation process itself. In a second process, new growth steps can start before the previous layer has completely filled the substrate. These different growth processes were called regimes I and II. Later, Hoffman incorporated the regime III behavior in his theory. This last regime occurs in highly undercooled melts. Recently, Fatou et al.[46,47] included additional considerations to the theory of polymer crystal growth by studying the effect of molecular weight on the kinetics of crystallization. Two additional regimes were identified, and it appears that the regimes of growth can now be defined as regimes I, Ia, II, III, and IIIa, and they differ in their growth phenomenology. These various regimes are illustrated in Figure 4.7. They manifest themselves with a difference in the slopes of the temperature coefficient of the crystallization process when the crystallization rate is plotted against the temperature function.

4.6 Impingement of Spherulites

As spherulites grow, they are bound to impinge on one another. To account for the impingement of the spherulites with one another and the swallowing
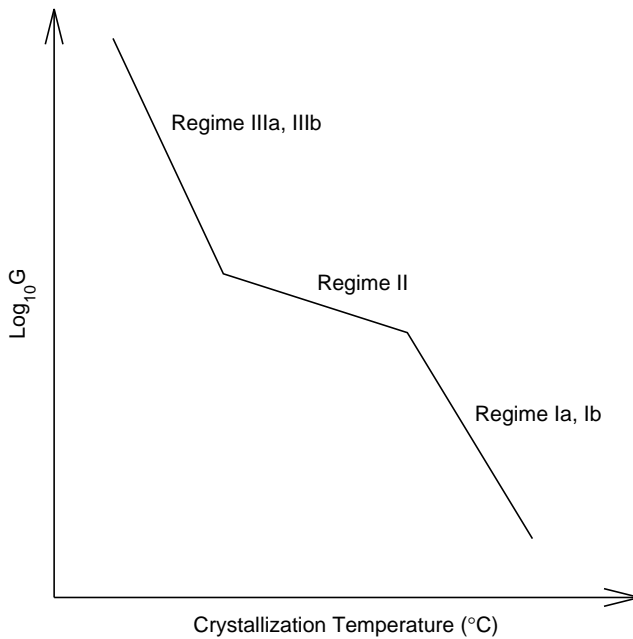
FIGURE 4.7
Schematic of the possible regimes of growth encountered in polymeric crystals as a function of temperature.

of potential nuclei by growing spherulites, Avrami introduced a correction that relates the volume of spherulites growing freely in an infinite medium to the actual volume of impinging spherulites. This correction states that the ratio of change in the actual transformed mass, dM (the spherulites are assumed to have uniform density), to the change of mass in free growing spherulites, dM', is equal to the ratio of untransformed polymer mass, M_{liq}, to the total mass of the system, M_{tot}, i.e.,

$$\frac{dM}{dM'} = \frac{M_{liq}}{M_{tot}} \tag{4.19}$$

Since the crystallinity is defined as $\chi = M_{cryst}/M_{tot}$, we have the well-known Avrami correction

$$\frac{d\chi}{d\chi'} = 1 - \chi \tag{4.20}$$

Tobin,[48,49] however, mentioned that the Avrami correction is often valid at a low degree of phase transformation but fails at a high degree of conversion. Instead, he suggested the use of

$$V = \left(1 - \frac{V}{V_{tot}}\right)V' \qquad (4.21)$$

to account for the impingement of the growing sites, which is a nonlinear equation. V is the actual volume occupied by the spherulites, and V' is the volume occupied by the freely growing spherulites, i.e., growing without impingement.

Attempts at dealing with the impingement process have also been made by several other authors. Price[50] studied numerically the impingement of growing entities of various shapes and spatial packing orders. Rappaz[43] presented correction factors derived analytically for the close-packed and simple cubic models. The Avrami correction, however, is still favored by most researchers, since it often provides a good fit with experimental data.

4.7 Spherulite Size

As mentioned earlier, mechanical properties of semicrystalline polymers are tied to the spherulite size. The maximum size that can be reached by the crystallizing units is directly determined by the spatial density of nuclei. On average, the final volume of the spherulites can be obtained simply with

$$\overline{V}_f = \frac{V_{tot}}{N} \qquad (4.22)$$

if there is instantaneous nucleation of N nuclei for a small control volume of size V_{tot}. It is also assumed that the entire space is occupied by spherulites. For spherical entities, this gives

$$\overline{R}_{max} = \left(\frac{3}{4}\frac{V_{tot}}{N\pi}\right)^{1/3} \qquad (4.23)$$

In the case of nonconstant growth and nucleation rates, an average radius can be defined simply with

$$\overline{R}_s(t) = \left(\frac{1}{n(t)}\int_{t_i}^{t}\dot{n}(\tau)G^3(\tau,t)\{t-\tau\}^3 d\tau\right)^{1/3} \qquad (4.24)$$

for spherical entities. If the undercooling is uniform within the control volume considered, then G, the growth rate, is the same for all nuclei and

$$\overline{R}_s(t) = \left(\frac{G^3(t)}{n(t)} \int_{t_i}^{t} \dot{n}(\tau)\{t - \tau\}^3 \, d\tau \right)^{1/3} \tag{4.25}$$

It then suffices to introduce a volume nucleation rate function in order to carry out the integration. Equation (4.25) gives the average radius at any instant in time. The final radius is obtained at the end of the growth process, $t = t_{final}$. Similar expressions can be derived for nonspherical shapes by modifying the expression for the volume.

4.8   Integration of All Aspects into One Model

Different aspects of the crystallization process were discussed separately in the previous sections. All these aspects, i.e., induction time, nucleation, growth, and impingement, must be accounted for in modeling of the crystallization process. One is also generally interested in the spherulites' density (and their size), the crystallinity, and, in some cases, the distribution of one component with respect to the other, to determine the mechanical properties of a part.

Different paths, mentioned in the introduction, can be taken to accomplish this task. A first method consists of representing the evolution of the crystallinity as a function of time and temperature, with one single constitutive model equation. We refer to the models falling in this category as bulk crystallization models. Expressions have been derived for isothermal and nonisothermal conditions by several investigators, and some of these approaches are reviewed in the next section.

Another approach, referred to here as cell models, can also be used to describe the evolution of the average microstructure within a control volume. Governing equations describing several aspects of the crystallization process are used explicitly and solved simultaneously, instead of using one single constitutive equation. This approach allows a more detailed description, at the price of increased complexity. Those models can then be linked to macroscopic solidification processes.[51]

4.9   Bulk Crystallization Models

Measurements of crystallization often involve the macroscopic determination of crystallinity as a function of time and temperature. Crystallinity measurements are usually conducted with a DSC apparatus or dilatometry and obtained from expressions such as

$$\chi = \frac{(H_l - H_s)}{(H_l - H_c)} \quad \text{or} \quad \chi = \frac{(\overline{V}_l - \overline{V}_s)}{(\overline{V}_l - \overline{V}_c)} \tag{4.26}$$

where H is the enthalpy and $\overline{V}$ is the specific volume. The subscripts s, l, and c refer to the sample, the liquid phase, and the pure crystalline phase, respectively.

The starting point in modeling the overall crystallization process is often the equations developed by Kolmogoroff,[52] Johnson and Mehl,[53] Avrami,[37,38,54] and Evans.[55] We cannot present the various models without reviewing the important expressions derived by these researchers. Below, the method of Avrami is followed in deriving the kinetics equation.

For a spherulite nucleation rate of $\dot{N}$ sec^{-1} and a growth rate of $\dot{v}$ cm^{3}sec^{-1}, the evolution of the crystallinity for spherulites growing in an infinite matrix, without impinging on each other, is given by

$$\chi'(t) = \frac{\rho_c}{M_{tot}} \int_0^t \dot{N}(\tau) v'(t,\tau) d\tau \tag{4.27}$$

where ρ_c is the density of the crystals, M_{tot} is the total mass of the volume considered, and $v'(t, \tau)$ is the unrestricted volume of a spherulite that nucleated at time τ.

Impingement of the spherulites can be accounted for with the expressions presented in the previous section. Equation (4.20) can easily be integrated to give

$$\chi(T(t)) = 1 - \exp(-\chi'(t)) \tag{4.28}$$

With the definition of the unimpeded crystal growth χ' given by Equation (4.27), we have

$$\chi(t) = 1 - \exp\left[\frac{-\rho_c}{M_{tot}} \int_0^t \dot{N}'(\tau) v'(t,\tau) d\tau\right] \tag{4.29}$$

This is the basic crystallization equation, which has been the starting point of numerous models. It still remains to express the functionality of $\dot{N}'$ and $\dot{v}'$ in time and temperature and to solve for $\chi(T(t))$.

Crystallization in polymers must also be interpreted in terms of incomplete crystallinity. This was accomplished by Mandelkern.[56] He expressed the starting point of the Avrami theory in terms of reduced or relative crystallinity, i.e., $\chi_r = \chi/\chi_\times$. The general bulk crystallization kinetics equation can then be put in the following form

$$\chi_r(t) = \frac{\chi(t)}{\chi_\infty} = 1 - \exp\left[\frac{\rho_c}{\rho_l}\int_0^t \dot{n}'(\tau)v'(t,\tau)d\tau\right] \qquad (4.30)$$

where n' is the nucleation rate per unit volume at time τ and $v(t, \tau)$ is the volume at time t of a spherulite formed at time τ.

4.9.1 Isothermal Crystallization Models

Equation (4.30) can be evaluated by specifying nucleation and growth laws. Under isothermal conditions, it is well known that the spherulite growth rate is quasi-steady for most systems; i.e., $v'(t - \tau) = G^3 \cdot (t - \tau)^3$, where G is the linear growth velocity. If nucleation also follows a steady process ($n(\tau) = N_o t$), then $\dot{n}(\tau)$ becomes a constant and the integration of Equation (4.30) gives

$$\chi_r = 1 - \exp\left\{-4\pi\frac{\rho_c}{\rho_l}N_o G^3 t^4\right\} \qquad (4.31)$$

The final expression can be written as

$$\chi_r = 1 - \exp(-Bt^n) \qquad (4.32)$$

where B is a time-dependent scaling parameter related to the half-time of crystallization, $t_{1/2}$, and depends on the temperature. A similar equation is obtained if the growth is not three-dimensional, if nucleation is heterogeneous, or even if the growth velocity is diffusion controlled. In these cases, the definition of B changes and the value of the exponent n changes. n is often considered to be a shape factor of the crystallization process. The values of n for various geometries and nucleation processes are tabulated in Wunderlich.[27] It is noted that different growth and nucleation mechanisms can yield the same Avrami exponent.

The exponent n is found with the help of the Avrami plot. This plot is simply obtained by taking twice the logarithm of Equation (4.32), which yields

$$\ln\ln\frac{1}{1-\chi_r} = \ln B + n\ln t \qquad (4.33)$$

A plot of $\ln\ln(1 - \chi_r)$ vs. $\ln t$ should give a straight line for a fixed value of n on a log-log graph. Two logarithms are required to extract the value of n.

4.9.2   Nonisothermal Crystallization Models

Nonisothermal crystallization modeling has traditionally been approached by starting from the models of Kolmogoroff,[52] Johnson and Mehl,[53] Avrami,[37,38,54] and Evans.[55] Ozawa[57] made the first attempt to obtain an expression describing the nonisothermal crystallization kinetics. Assuming a constant cooling rate, he obtained the expression

$$\log(1 - \chi_r) = \alpha(T) / \dot{T}^n \tag{4.34}$$

where $\dot{T}$ is the cooling rate, α is a temperature-dependent parameter, and n corresponds to the Avrami exponent. This approach was recently modified by Hammami et al.[58] and appears to be very promising for systems with heterogeneous nucleation.

Nakamura et al.[59] later presented a model derived with the isokinetic assumption; i.e., the ratio of the growth and nucleation rates can be represented as a function of temperature. This model gives the expression

$$\chi_r(t) = 1 - \exp\left[-\int_0^t K(T)dt\right]^n \tag{4.35}$$

where $K(T)$ is connected with the crystallization rate constant of the isothermal crystallization, $k(T)$, by $K(T) = k(T)^{1/n}$.[60,61] This expression reduces to the Avrami equation under isothermal conditions, and the Ozawa model is recovered under constant cooling rate.

Kamal and Chu[62] later derived an integral expression similar to the Nakamura model. This expression is given by

$$\chi_r = 1 - \exp\left[-\int_0^t k(T)nt^{n-1}dt\right] \tag{4.36}$$

Several of these models were recently evaluated by Patel and Spruiell,[63] and it appears that a differential form of the Nakamura model, given by

$$\frac{d\chi_r}{dt} = nK(T)(1 - \chi_r)\ln\left\{\frac{1}{1 - \chi_r}\right\}\frac{(n-1)}{n} \tag{4.37}$$

provides a better fit to nonisothermal data. The main distinction between the integral form and its differential counterpart is that time does not appear as an independent variable in the differential model. Both models should be equivalent if the onset of crystallization is properly described. The induction time for nucleation is not included in the Nakamura model or in the previous models. Maffezzoli et al.[31] and Chan and Isayev,[33] as mentioned in a previous

section, recently included the induction time period in modeling crystallization with the Nakamura model. It allowed them to obtain excellent agreement between experimental and predicted values.

We must also mention the work of Schneider et al.,[64] who recast the general equations of Avrami into a set of differential equations. The resulting set of equations is more amenable to computations within the framework of the heat diffusion equation to find the temperature distribution during cooling.[65]

4.9.3 Shortcomings of Bulk Crystallization Models

Shortcomings of bulk crystallization models have been discussed by several researchers.[14,27,66] Deviations of crystallization processes from the model predictions can originate from several sources:

- Simultaneous growth mechanisms
- Accumulation of impurities at the spherulite boundaries
- Time dependence of the density of the growing phase
- Occurrence of secondary crystallization
- Fractionation during crystallization with a large molecular mass distribution
- Lack of validity of the isokinetic assumption over a relatively small temperature range
- The requirement of curve fitting in several models
- Lack of information on the microstructure
- A large number of parameters with little physical meaning

Nonetheless, a good fit between computed crystallization rates and experiments has been found in cases where the spherulites grow as well-formed entities with known nucleation rates, especially when the induction time is accounted for.[31,33,63] When dealing with more complex systems, where prevalent solute diffusion occurs, for example, a more detailed approach must be used to describe the overall crystallization process.

4.10 Cell Model Approach

The spherulite growth process can also be modeled using a cell model approach.[3] This approach is, in some ways, an extension of the bulk crystallization models presented briefly in the previous section. It consists of modeling the crystallization of a small control volume of molten polymer with several equations describing in detail the associated physical phenomena.

These equations are derived from first principles and are generally coupled. The coupling increases the complexity of the model.

In this section, we will discuss models that allow the description of the spherulitic growth occurring in a system where significant diffusion of one of the components occurs. Such a system could correspond to a polymer alloy or to polydisperse polymers as well.

Two extreme cases can be identified, from the solute point of view, in modeling the spherulitic growth in polymers. These cases are illustrated in Figure 4.8(a). A first case, illustrated on top of Figure 4.8(a), corresponds to the growth of well-formed and densely packed spherulites with negligible solute diffusion at the spherulite scale. It is expected that the models mentioned in the previous sections will adequately describe the crystallization process, provided that nucleation and growth can be described accurately. A second case, illustrated on the bottom of Figure 4.8(a), arises when the growth process involves considerable solute diffusion ahead of a growing front. This case is encountered in polymer alloys. Other systems relevant to this latter case are isotactic polymers with substantial atactic content or polydisperse polymers with a significant amount of low-molecular-weight species that can diffuse. The microstructure of the spherulites becomes coarser and more open, with an increase in the amount of solute. The models presented in the previous section are not expected to describe such crystallization processes adequately, since the physics of this problem involves coupled heat and mass diffusion.
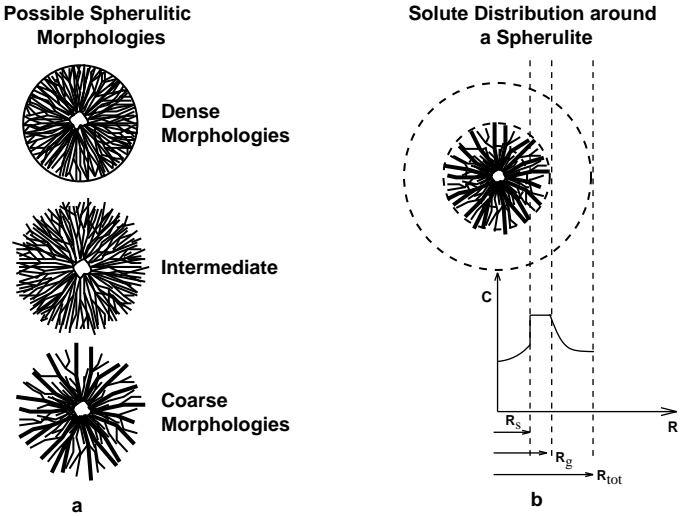

FIGURE 4.8
(a) Spherulitic microstructure commonly encountered in semicrystalline polymers. (b) Cell model that can be used in modeling the spherulitic growth process (Benard, Ph.D. thesis, University of Deleware, Newark, DE, 1995).

4.10.1 Solute Diffusion Models

Several spherulite growth models where solute diffusion is important can be envisaged according to the polymer system considered. A first model can be envisaged where the spherulites grow by forming a dense crystalline core at their center, and thick branches radiate from this core, surrounded by a melt with high solute concentration. To illustrate, we will discuss below the governing equations for this case and present an example. More details on this model can be found in Benard.[67]

The growth of spherulites can be represented by a spherical volume element at uniform temperature. In this volume element three different zones are identified: a solid zone, a "mushy" zone, and a liquid zone. The cell model is represented in Figure 4.8(b).[3] A similar model was originally presented by Rappaz and Thevoz[68,69] to describe the evolution of equiaxed dendritic growth in metal castings. During the growth process a liquid zone, in which solute diffusion occurs, surrounds the grain. Between the solid and liquid zones there is a mushy zone, containing dendrites, and an interdendritic liquid in which complete mixing of the solute is assumed. No solid diffusion is considered in the solid phase. It is also assumed that the solute is well dissolved such that there is no clustering and each grain can grow to a maximum size R_{tot}.

4.10.1.1 Growth Kinetics

The growth of the outside radius of the spherulite is given by the dimensionless form of Equation (4.18):

$$\dot{\hat{R}} = \Lambda_1 \exp\left[\frac{-U^*}{R(T - T_\infty)}\right] \exp\left[\frac{-K_g}{T\Delta Tf}\right] \tag{4.38}$$

where

$$\Lambda_1 = \exp\left[\frac{U^*}{R(T_{max} - T_\infty)}\right] \exp\left[\frac{K_g}{T_{max}\Delta Tf}\right] \tag{4.39}$$

and T_{max} is the temperature that gives the maximum growth rate under regime II and $\dot{\hat{R}} = (\partial R_g / \partial t) / (\partial R_{g\,max} / \partial t)$. This equation could also be rendered dimensionless with D and R_{tot}. It can also be supplemented with other terms to account for the presence of another polymer.[70]

4.10.1.2 Heat Balance

It is possible to write a heat balance for the cell if we assume a uniform cell temperature and the presence of a heat generation term due to the transformation of the solid fraction. The heat balance is then written as

$$\Lambda_3 = -St \frac{\partial f_s}{\partial \tilde{t}} + \Lambda_2 \frac{\partial \hat{c} *}{\partial \tilde{t}} \tag{4.40}$$

where $\tilde{t} = Dt/R_{tot}^2$, $St = H_f/(\rho C_p \Delta T)$, $\Lambda_2 = m/\Delta T$, and $\Lambda_3 = 3Bi/Le$. An equivalent heat transfer coefficient can be introduced as $h_{eq} = q_{ext}/\Delta T$, and the Biot number for the cell, based on the total radius, is then $Bi = h_{eq}R_{tot}/k_{cond}$, where k_{cond} is the thermal conductivity of the polymer. c is the concentration of solute and already dimensionless, being generally expressed in percent; c_o is the initial concentration of noncrystallizing species; q_{ext} is the external cooling rate that can be specified; H_f is the heat of fusion; f_s is the computed solid fraction; and C_p is the heat capacity of the melt. This heat balance will be valid as long as the cell is small (small Biot number). Even though polymers generally have a low thermal conductivity, the cell size is also very small.

4.10.1.3   Diffusion Equation in the Liquid Zone

The diffusion of solute in the liquid region is controlled by the diffusion equation, written in dimensionless spherical coordinates:

$$\frac{1}{\hat{r}} \frac{\partial^2}{\partial \hat{r}^2}(c\hat{r}) = \frac{\partial c}{\partial \tilde{t}} \tag{4.41}$$

where $\hat{r}$ is the dimensionless radial position and the boundary conditions are

$$\left. \frac{\partial c}{\partial \hat{r}} \right|_{\hat{r}=1} = 0 \quad \text{and} \quad c|_{\hat{r}=\hat{R}_g} = c *(\hat{t}) \tag{4.42}$$

The symmetry boundary condition at $\hat{r} = 1$ appears to be fairly realistic, but it cannot take into account phenomena such as triple meeting points of solute layers or regions of unimpeded growth from other spherulites. The boundary condition at $\hat{r} = R_g$ is obtained from the solute balance.

4.10.1.4   Solute Balance

The symmetry boundary condition at $\hat{r} = 1$ implies that solute has to be conserved within the cell. If it is assumed that there is complete mixing within the interdendritic liquid, the solute balance of the cell can be expressed, in dimensionless radial coordinates, as

$$3\int_0^{\hat{R}_s} kc_s^* \hat{r}^2 d\hat{r} + c *(f_g - f_s) + 3\int_{\hat{R}_g}^1 c\hat{r}^2 d\hat{r} = c_o \tag{4.43}$$

where c_o is the initial concentration of solute, c_* is the interface concentration, and k is a partition factor that determines the amount of solute incorporated

in the spherulite (= c_s/c_l, where c_s is the concentration in the solid and c_l is the concentration in the liquid polymer). The factor 3 appearing in the equation above comes from the expression for the volume of a sphere, which does not cancel out with other terms. f_g is the volume fraction of the cell occupied by the spherulite, and f_s is the volume fraction of the cell that is solid. When f_s and f_g are not equal, the spherulite is not entirely solid but possesses dendrites or branches.

4.10.1.5 Solution Technique and Some Results

Various techniques can be used to solve the four equations presented above. The unknowns are f_s, f_g, c, and the solute concentration profile in the liquid zone. All the equations are coupled, making it difficult to solve them simultaneously. However, with an approximate integral technique it is possible to arrive at a simple time-stepping scheme. It does not require any approximation other than the shape of the solute profile with a polynomial.

In solving the governing equations for a small control volume, the processes described in Figure 4.1 must all be described with approximate equations. This means that induction time, nucleation, growth, and impingement must be described with appropriate equations. High-density polyethylene (HDPE) was chosen for the example presented below.

The experimental data of Mandelkern can be used to extract the induction time for various temperatures. Isothermal experiments are used to find the parameters that provide the best fit for Equation (4.44), which was suggested by Isayev and Chan,[33] i.e.,

$$t_i = \frac{t_m}{\left(T_m^o - T\right)^a} \tag{4.44}$$

with $T_m^0 = 417.8$ K, $t_m = 1.098 \times 10^{17}$, and $a = 12.91$. The additivity rule can then be used to compute the induction time, for a constant cooling rate. Substituting Equation (4.44) into Equation (4.1) gives

$$t_i = \left(\frac{(a+1)t_m}{\dot{T}^a}\right)^{1/(a+1)} \tag{4.45}$$

for a constant cooling rate $\dot{T}$.

Nucleation can be described with the expression of Icenogle,[39] although it was obtained for a polyethylene different than the system for which induction time was computed. Nonetheless, it should be sufficient for illustrative purposes. The nucleation process is assumed to be heterogeneous, i.e., quasi-instantaneous, which implies that once the induction time is reached, the nuclei density jumps to a value given by

$$N(T) = M'_o \left(1 - \frac{T}{T_o} \right) \qquad (4.46)$$

with $M'_o = 5.88 \times 10^8$ and $T_o = 401$ K, provided that the polymer nucleates at a temperature below 401 K, as it would give a negative value otherwise. The resulting microstructure has spherulites of about 40 μm, which is consistent with other experimental data.[62,30] The growth was assumed to follow the Hoffman–Lauritzen theory under regime II.

The last and very important phenomenon to be accounted for is the impingement of the spherulites. Three approaches are possible here. A first approach consists of assuming that the final shape of the spherulite is not spherical but given, for example, by a 14-sided object, which corresponds to the average final spherulite geometry. This implies, however, that the diffusion equation must be solved for a complicated domain. Another approach consists in assuming that the final spherulite shape is approximately spherical. This approach, however, gives a very abrupt transition in the crystallinity profile at the end of the growth process.[3] A third possible approach consists in simply using the Avrami correction to modify the value of f_s, which is a link to the crystallinity, while being aware that the diffusion equation is solved for a final spherical shape. The implications of changing f_s and f_g values with the Avrami correction, when the diffusion equation is solved for spherical geometry, are not clear yet. In the results presented below, it was assumed that the final shape of the spherulites is spherical.

For a small sample undergoing a constant cooling rate of 20 K/min, computed values of f_s and f_g and the temperature profile are shown in Figure 4.9. It can be seen that f_s and f_g are identical, which implies that no mushy zone has developed. More details and other results are presented in Benard and Advani.[3]
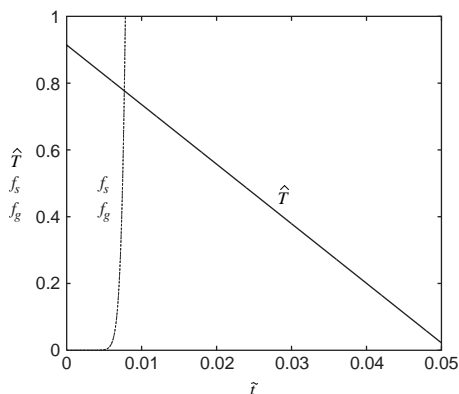

FIGURE 4.9
Dimensionless temperature ($\hat{T}$), grain fraction (f_g), and solid fraction (f_s) vs. dimensionless time ($\hat{t}$) for spherulites growing under a constant cooling rate.
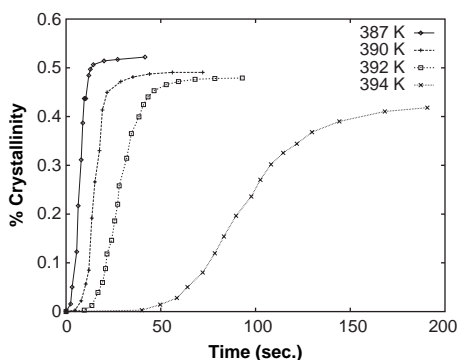
FIGURE 4.10
Percent crystallinity as a function of time for a polyethylene crystallized isothermally at different temperatures (data from Kamal and Chu[62]).

4.10.2 Comparison with Experimental Results

Unavailability of several experimental parameters precludes one from quantitatively comparing the predictions with real systems; the model, however, offers insights for several phenomena observed in crystallization studies of polymers and shows qualitative agreement of trends.

An example of such phenomena is the plateau reached by the crystallinity during isothermal crystallization. In these experiments, the polymer is "forced" to crystallize at a given temperature; the heat flux is adjusted to maintain the set temperature. A striking feature that can be observed in some polymer systems is that at the end of the process, crystallinity reaches a terminal plateau of different values, depending on the crystallization temperature. This is demonstrated in Figure 4.10, where part of the experimental data of Kamal and Chu[62] are reproduced. The polymer used in these experiments did not include nucleating agents,[62] and the spherulites formed were relatively large for a high-density polyethylene, i.e., ca. 45 μm. The same observation can be made with the model presented in this paper. This computed plateau is shown in Figure 4.11. As mentioned above, this is due to the solute pileup at the boundaries of the spherulites. Indeed, the lower the crystallization temperature, the higher the permissible c^* on the phase diagram. This explanation is illustrated in Figure 4.12, where even though T_1 is greater than T_2, the concentration c_2^* is larger than c_1^*, which implies that the maximum solute concentration will be reached much faster at a higher crystallization temperature than at a lower crystallization temperature. Crystallization stops roughly when the maximum concentration allowed by the phase diagram is reached and the spherulites impinge, trapping a layer at c^* at their boundaries.

It is possible to compute the final crystallinity reached by the polymer. A simple mass balance gives
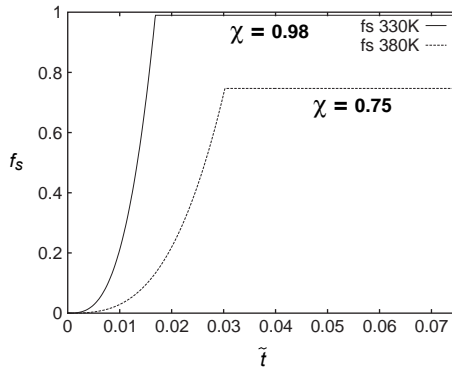
FIGURE 4.11
Solid fraction (or crystallinity) as a function of time calculated for polyethylene ($\hat{t}$ at 380 K was scaled y 1/100).
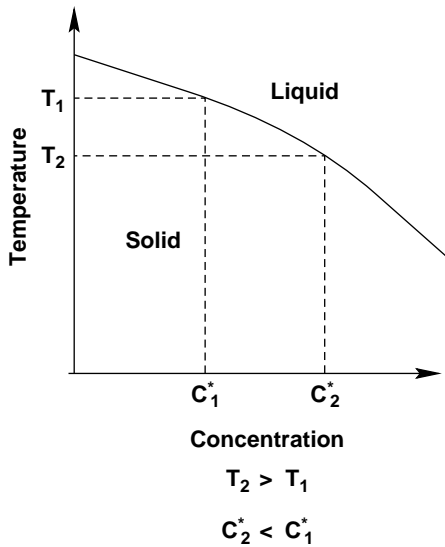

FIGURE 4.12
Relationship between concentration at the liquidus line and crystallization temperature.

$$\left(\frac{4}{3} \pi R_{tot}^3 c * - \frac{4}{3} \pi R_s^3 c * \right) = \frac{4}{3} \pi R_{tot}^3 c_o \tag{4.47}$$

which indicates that the plateau will be reached approximately at

$$\chi \approx \frac{R_s^3}{R_{tot}^3} = \left(\frac{c * - c_o}{c *} \right) \tag{4.48}$$

If the spherulite crystallizes without any mushy zone, then $R_s = R_g$ and additional information can be obtained, such as the time required before the crystallinity plateau is reached, i.e., $t_{plat} = R_g/G_o$, where G_o is the growth rate under isothermal conditions. Other methods such as the lever rule or Scheil's equation can be used for the same computations.[71]

To illustrate the computation of the maximum crystallinity, a simple case is presented here. Consider a polymer with a solidus–liquidus line described with $m = -5$ K/%, a melting point of 420 K, and a uniform concentration of noncrystallizable material of $c_o = 2\%$. If a sample of this polymer is brought quickly to 390 K, its equilibrium concentration is approximately $c_1^* = 8\%$. A second sample, quenched rapidly to 350 K, will have $c_2^* = 14\%$. The first sample will therefore reach a crystallinity of roughly 75%, while the second sample will reach a crystallinity of roughly 85%.

Traditional understanding of polymer crystallization indicates that the higher the crystallization temperature, the higher the final crystallinity. This notion must be refined somewhat, even though it is true that spherulites reach a higher perfection at higher crystallization temperatures due to a higher perfection of the lamellae. However, if the crystallization process occurs with significant solute diffusion, where the solute could be another noncrystallizable polymer or low-molecular-weight species not incorporated in the crystal, DSC measurements should exhibit the plateau discussed above, as they are based on macroscopic quantities; i.e., the measurements are made for a small mass of polymer, typically a few milligrams, and the solidification of the polymer should follow a phase diagram. Small-angle x-ray scattering (SAXS) measurements, on the other hand, will still reflect a higher crystallinity at a higher temperature, as they are based on microscopic quantities such as the lamellae thickness. We must also mention that for systems where very dense nucleation occurs, even when crystallization occurs close to the melting point very little solute diffusion occurs and this plateau is not expected to occur.

Finally, it is also possible to determine the radius at which the effects of the solute become important during the crystallization of the polymer, provided that the phase diagram is known. Solutal effects become important when the amount of solute around the spherulite reaches the concentration of the liquidus, i.e., when $c_{interface} = c_{liq}$. This concentration is controlled by the gap size d between the boundaries of the spherulites, by the total size of the shell R_{tot}, and by the initial concentration of solute c_o. A mass balance for the spherulite enclosed in a spherical shell gives

$$R_{tot}^3 c_o = c * \left(R_{tot}^3 - \left(R_{tot} - d \right)^3 \right) \tag{4.49}$$

which implies that

$$R_{tot} \le \frac{d}{1 - \left(1 - \dfrac{c_o}{c *} \right)^{1/3}} \tag{4.50}$$

for the effect of the solute to be negligible The space between a spherulite and its neighbors has a value of d, where $d = (R_{tot} - R_g)$. For illustrative purposes, assume that a polymer has $c_o = 2\%$ and $c_* = 8\%$. If the spacing between the spherulite and the shell is 1 μm, then R_{tot} must be smaller than 10 μm to prevent the effect of the solute from becoming important in the overall crystallization process. The spacing d can be evaluated from the steady boundary layer thickness.

4.11   TTT and CCT Diagrams

It is important to mention tools that can be useful for the interpretation of the crystallization behavior of various polymers under isothermal and nonisothermal conditions. These tools are called time–temperature–transformation (TTT) and continuous cooling transformation (CCT) diagrams. TTT diagrams are commonly used in metallurgy to study isothermal phase transformations. CCT diagrams are used for processes with a constant cooling rate. Spruiell and White,[72] Motz and Schultz,[73] and Maffezzoli et al.,[31] among others, used this approach for studying the crystallization kinetics of polymers.

TTT plots are valid, strictly speaking, only for isothermal crystallization processes. CCT plots are helpful in describing the crystallization process under constant cooling rate conditions. Other thermal conditions cannot be represented with simple diagrams, and the kinetics model used must be integrated along with the heat diffusion equation in order to obtain quantitative results.

4.12   Modeling the Effects of Reinforcements on the Overall Crystallization

Reinforcements of various shapes are often used to improve the properties of materials, and it is common to be interested in the crystallization of these composites in order to predict, for example, the required cooling time for processing a part. This is especially important for reinforced semicrystalline polymers.

It was demonstrated by previous researchers, using computer simulations and experiments, that fibrous reinforcements can greatly affect the overall crystallization process. The fibers were found to depress the crystallization due to their intersections with growing spherulites. Enhanced crystallization rates are also found in these materials due to increased nucleation at the fiber surfaces (e.g., see Krause et al.[9]). These computer studies were restricted

to fibrous reinforcements, but the same effects can be expected with particulate reinforcements. Other systems in which spherical inclusions are encountered (e.g., foams) are expected to exhibit similar changes in the crystallization kinetics.

The effects of inclusions on the overall crystallization of semicrystalline polymers can be modeled and discussed for isothermal processes, and a conceptually simple approach is outlined below. The inclusions can be of cylindrical or spherical shapes. A schematic of the crystallization process in reinforced polymers, with occasional nucleation at the surfaces of the particles, is shown in Figure 4.13. The inclusions (fibers, particles, bubbles, etc.) are represented with large black circles. The spherulites shown in Figure 4.13 can nucleate preferentially on the reinforcements and can also appear simultaneously (or subsequently) in the molten polymer.

The approach used is based on Avrami's model. Modifications are made to the model to account for the intersection of the spherulites with the reinforcements.[74,75] This approach is similar to models used to account for the geometrical effects encountered in thin films.[76–79]

The presentation of this model begins with a very brief review of Avrami's approach for modeling crystallization processes, followed by a theoretical treatment that incorporates the effects of the inclusions on the overall crystallization rate. A simple example is finally discussed along with the influence of various parameters on the overall crystallization process and the limitations of the model.

4.12.1 Avrami's Phase Change Model Revisited

During crystallization, at time t, the volume fraction of spherulites growing from a uniform distribution of potential nuclei is given by

$$\alpha(t) = 1 - \exp[-\alpha'(t)] \tag{4.51}$$

where $\alpha'(t)$ is the "extended" volume fraction. The concept of extended volume was introduced by Avrami,[37,38,54] and it corresponds to the volume occupied by spherulites as if they grew unconstrained by each other, i.e., without impingement. It also implies that nuclei can be activated in already transformed regions (the so-called phantom nuclei). The model of Avrami, given by Equation (4.51), relates crystallization in a real system where impingement occurs to the growth of hypothetical spherulites growing freely without impingement.

The extended volume fraction can be expressed with

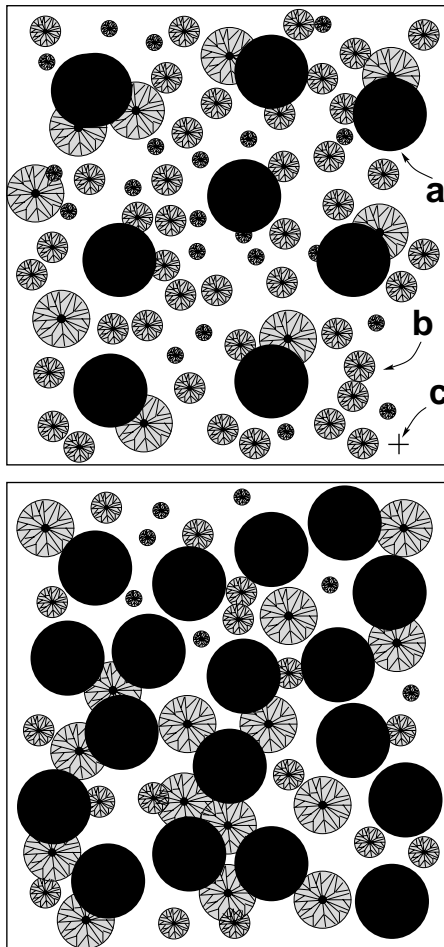$$\alpha'(t) = \int_0^t \dot{n}(\tau) v'(t, \tau) d\tau \tag{4.52}$$

FIGURE 4.13
Illustration of the crystallization process in the presence of inclusions. In the top figure, the spherulites (b) are not significantly impeded by the presence of the inclusions (a) in the molten polymer (c). The bottom figure illustrates a crystallization process where the presence of inclusions would affect the overall process by modifying significantly the shape of the spherulites that intersect with the inclusions during growth.

which is simply the integral of the rate $\dot{n}(\tau)$ at which potential nuclei are activated at time τ multiplied by their unimpinged volume $v'(t, \tau)$ at time t. In order to compute the actual crystallization rate, nucleation and growth characteristics of the spherulites must be specified.

Under isothermal conditions, the growth rate of the spherulites has been found to be constant for several systems and the radius of a spherulite varies linearly with time,[80] i.e., $R(t) = G_o t$. This growth rate can be obtained fairly easily from experimental data. Finding an appropriate nucleation law is more

problematic, as nucleation can be homogeneous, heterogeneous, thermal, athermal, or a combination of all these.[27]

Avrami[38] also presented an expression that allows a description of the nucleation process in a general manner. This expression, which provides the number of potential nuclei per unit volume at a given time, is given by

$$N(t) = N_o \exp(-qt) \tag{4.53}$$

where N_o is the initial number of potential nuclei per unit volume and q is their activation frequency. It is assumed here that the number of nuclei activated decreases with time.

Equation (4.53) can be used to model an instantaneous nucleation process (often associated with heterogeneous nucleation) if q is large, as well as a homogeneous nucleation process if N_o is large and q is small. With Equation (4.53), the extended volume for an unfilled polymer is given by

$$\alpha'(t) = q N_o \int_0^t v'(t, \tau) \exp[-q\tau] d\tau \tag{4.54}$$

where $v'(t, \tau)$ is the volume (without impingement) at time t for a spherulite that nucleated at time τ.

Under isothermal conditions, the extended volume is simply $v'(t, \tau) = 4\pi/3 G_o^3 (t - \tau)^3$, and substituting this equation into Equation (4.54) gives the well-known expression $\alpha'(t) = 8 N_o \pi G_o^3 / q^3 (\exp(-qt) - 1 + qt - -q^2 t^2/2 + q^3 t^3/6)$. If homogeneous nucleation occurs, it is possible to model the process with the expression $\dot{n}(\tau) = N_o$, where N_o is then the steady nucleation rate. The extended volume is then given by $N_o \pi G_o^3 t^4/3$. If heterogeneous nucleation is the dominant nucleation mode, a delta function can be used to represent the nucleation rate, i.e., $\dot{n}(\tau) = N_o \delta(t)$, where N_o is the total number of nuclei. The extended volume is then given by $\alpha'(t) = 4\pi N_o G_o^3 t^3/3$ for an instantaneous nucleation process.

4.12.2   Crystallization with Spherical and Cylindrical Inclusions

Avrami's model can be modified to account for the effects of reinforcements provided that the inclusions are assumed to be of uniform shape and size. With these assumptions, it is possible to incorporate the impingement (intersection) of the spherulites with the inclusions and to account, if relevant, for the enhanced nucleation of the spherulites on the reinforcements. The very first step in developing this model requires an exact expression for the volume of intersection between the reinforcement and a sphere (the spherulite). Two types of inclusions are considered here: spherical and cylindrical.

If the reinforcement/fillers are spherical, one must know the volume of intersection between two spheres at an arbitrary distance from center to center (one of the spheres is a growing spherulite, while the other is an

inclusion). If fibers are used as reinforcements, then one must know the volume of intersection between a cylinder and a sphere at an arbitrary distance from center to center. Both expressions have been presented in Benard and Advani[74] and Benard.[75]

4.12.3 Unit Cells

In order to study the interaction between fibers or particles and growing spherulites, it suffices to consider a representative volume of the overall structure. Several unit cells are possible, and they correspond to a specific packing order of the fibers or particles, e.g., triangular, square, Voronoi, or hexagonal packing for the fibers. The unit cell chosen must be sufficiently large so as to provide a faithful representation of the average microstructure. The cell chosen previously for computing the evolution of the crystallinity in fiber-reinforced composites possesses only one fiber at its center.[74,75] Such a cell will is valid for one fiber truncation per spherulite. If multiple fiber truncations occur on a given spherulite, a larger unit cell that includes several fibers must be used. The shape of the cell is also important in computing the probability of occurrence of each type of truncation. The probability of occurrence is related to the respective area where each truncation is possible. A unit cell for which the outer boundary is represented by a circular cylinder was used previously. This is a simple cell that may approximate well a hexagonal packing arrangement of the fibers.

4.12.4 Probability of a Spherulite Intersecting an Inclusion

The probability of finding one intersection between a spherulite and a particle must be evaluated to compute the extended volume in Avrami's model. To ensure that P_i cannot reach a value greater than 1, it is possible to use combinations of Heavyside step functions to multiply P_i by zero once it has reached 1, but this adds significant algebraic complexity to the computation of the extended volume. A piecewise integration procedure is preferred in this work.

The probability of finding a sphere in a specific configuration with respect to the cylinder can be computed for the three cases discussed above and for the case of an untruncated spherulite. These probabilities are computed from the ratio of the areas where each type of spherulite can occur to the total space available for crystallization within the cell. For example, the absence of any fiber truncation on a spherulite can occur only between $R_f + R_s$ and R_o, and as long as $R_f + R_s < R_o$. The various probabilities can be found in Benard[75] for $V_f ð 1/9$, $1/9 ð V_f ð 1/3$, and $V_f ð 1/3$, respectively.

4.12.4.1 Computation of the Modified Extended Volume

Now that the average volume and the probability of occurrence of the intersections have been found, it is possible to compute the extended volume. In

computing the extended volume, one must pay attention to the fact that the integration process must be done in a piecewise manner to account for the different expressions for the volume of intersection, e.g., t ð $2R_p/G$, and to account for the fact that P_1 and P_2 cannot be greater than 1. The procedure is dependent on the type of intersection and will be different for spherical or cylindrical inclusions.

The extended volume is then given in a general manner by

$$\alpha'(t) = \int_0^t \dot{n}_b(\tau)(1 - P_i)\frac{4}{3}\pi R_s^3 d\tau + \int_0^t \dot{n}_b(\tau)P_i\langle v'(t,\tau)\rangle d\tau \qquad (4.55)$$

The above equation is computed in a different manner according to the volume fraction of the reinforcements; i.e., a different piecewise integration procedure must be used if V_p ð $1/27$. In addition, various nucleation models can be used in the above integrals. Expressions for the general nucleation model of Avrami were derived in Benard and Advani[74] and Benard,[75] as well as for the more simple heterogeneous and homogeneous nucleation processes.

4.12.5 Example and Discussion

The effects of spherical inclusions on the overall crystallization process are studied below with the help of a simple example. The parameters defining the problem are G, the spherulites radial growth rate; $\dot{n}_b$, the rate of nucleation per unit volume in the bulk polymer; V_p, the volume fraction of particles; and R_p, the radius of the particles.

The effects of the volume fraction, particle radius, nuclei density, and nucleation modes can be studied for three nucleation models: the general model of Avrami, instantaneous nucleation in the melt, and homogeneous nucleation in the melt. Here the simple case of instantaneous nucleation in the melt and on the fibers is computed and shown in Figure 4.14.

Additional computations can be performed using such a model; however, the resulting expressions are quite complicated, especially for the case of spherulites interacting with fibers, which limits its practical use. The case of spherulites interacting with spherical inclusions is simpler, and exact computations can be performed for all nucleation models.

Although the model appears quite general, there are a number of limitations that must be mentioned. First, all the limits of Avrami's model are relevant to this work. These limits have been presented and discussed extensively in the literature. Furthermore, multiple truncations of the spherulites due to the intersection with several inclusions are not well accounted for in the current model; e.g., a spherulite can impinge with two inclusions at most. The model also assumes that the inclusions are organized according to a specific cell; other arrangements are obviously possible. Also, when spherulites grow around an obstacle, a "shadow" is created by the growing front
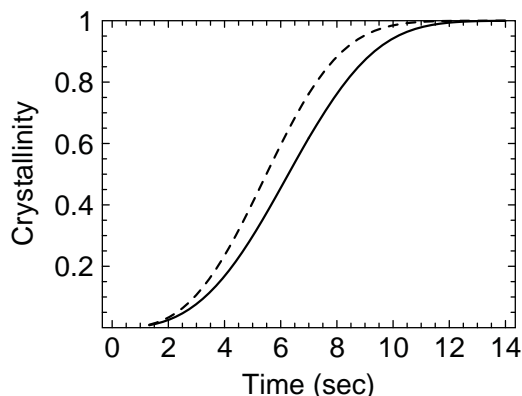
FIGURE 4.14
Computation of the crystallinity vs. time for fibers of 7 microns and a volume fraction of 0.7. A clear decrease in the crystallization rate is observed (from the dashed line to the solid line, which corresponds to unimpeded crystallization and crystallization with fibers, respectively) for a nuclei density of 10^{15} nuclei/m^3.

and spherulites loose their sphericity after the object has been passed. This phenomenon is not accounted for in this model, but its impact on the crystallization curves appears only after a particle has been engulfed by a spherulite and should be minimal. Finally, the author recognizes that no experiments have been performed to validate the current model; this topic will be the subject of future research.

4.13 Outlook

Various approaches for modeling the crystallization (or spherulitic growth) of quiescent semicrystalline polymers were briefly surveyed in this work. Models incorporating induction time for nucleation into their crystallization kinetics equations can provide adequate predictions of the nonisothermal solidification process of well-formed spherulites as long as the isokinetic approximation is valid. For the case of blends or in the presence of diffusion of noncrystallizable material, it is possible to rely on a cell model approach to model the spherulitic growth process. Such an approach provides insight into the interaction between the various parameters affecting the spherulitic growth process and is based on a detailed description of the growth process. It is, however, a rather complex model. The effects of inclusions (reduced or enhanced crystallization rates), such as found when dealing with reinforced polymers, can also be modeled, provided that the cell accounts for the presence of fibers. The shape of the spherulite during the growth process is modified by an intersection with the inclusions, and one can approximate this shape in Avrami's model (and other bulk crystallization models) by

using rather complex expressions. There is a need for simplifying such approaches.

One can also notice that systematic experimental studies of the parameters affecting the crystallization process are required in order to obtain accurate predictions. Namely, the nucleation process, the growth process, the spherulite morphology, the diffusion of noncrystallizable material, and the effect of the molecular weight distribution all need to be accounted for and measured. The effects of other processing conditions, such as pressure, shear, and elongational stresses, on the microstructure also need to be determined in order to obtain a description of a wider range of real-life processing conditions. Approaches such as those presented in Guo et al.[81] can be used for such purposes. Finally, it is possible to obtain further details of the morphology by solving for the orientation of the lamellae as presented recently by Huang and Kamal.[82] The internal lamellar organization can be very important for predicting the properties of a polymer.

References

1. A. Wasiak. Kinetics of polymer crystallization in nonisothermal conditions, *Macromol. Chem.*, 2:211–245, 1991.
2. M. Rappaz. Solidification processes: constitutive equations and microstructures, in *Mathematical Modelling for Materials*, M. Cross, J.F.T. Pittman, and R.D. Wood, Eds., Clarendon Press, Oxford, 1993, pp. 67–91.
3. A. Benard and S.G. Advani. A cell model to describe the spherulitic growth in semi-crystalline polymers, *Polym. Eng. Sci.*, 36:520–534, 1996.
4. A.J. Lovinger and C.C. Gryte. Model for the shape of polymer spherulites formed in a temperature gradient, *J. Appl. Phys.*, 47:1999–2004, 1976.
5. G.E.W. Schulze and T.R. Naujeck. A growing 2d spherulite and calculus of variations: Part I. A 2d spherulite in a linear field of growth rate, *Colloid Polym. Sci.*, 269:689–694, 1991.
6. G.E.W. Schulze and T.R. Naujeck. A growing 2d spherulite and calculus of variations: Part II. A 2d spherulite of polypropylene in a linear field, *Colloid Polym. Sci.*, 269:695–703, 1991.
7. N.A. Mehl and L. Rebenfeld. Computer simulation of crystallization kinetics and morphology in fiber-reinforced thermoplastic composites 1: two-dimensional case, *J. Polym. Sci. Polym. Phys.*, 31B:1677–1686, 1993.
8. N.A. Mehl and L. Rebenfeld. Computer simulation of crystallization kinetics and morphology in fiber-reinforced thermoplastic composites 2: three-dimensional case, *J. Polym. Sci. Polym. Phys.*, 31B:1687–1693, 1993.
9. Th. Krause, G. Kalinka, C. Auer, and G. Hinrichsen. Computer simulation of crystallization kinetics in fiber-reinforced composites, *J. Appl. Polym. Sci.*, 51:388–406, 1994.
10. C. Auer, G. Kalinka, Th. Krause, and G. Hinrichsen. Crystallization kinetics of pure and fiber-reinforced poly(phenylene sulfide), *J. Appl. Polym. Sci.*, 51:407–413, 1994.

11. N.A. Mehl and L. Rebenfeld. Computer simulation of crystallization kinetics and morphology in fiber-reinforced thermoplastic composites iii: thermal nucleation, *J. Polym. Sci. Polym. Phys.*, 33B:1249–1257, 1995.
12. H.D. Keith and F.J. Padden. A phenomenological theory of spherulitic crystallization, *J. Appl. Phys.*, 34:2409, 1963.
13. F. Bernauer. *Gedrillte Kristalle in Forschungen zur Kristalkunde*, Vol. Heft 2, Borntrager, Berlin, 1929.
14. Geza Bodor. *Structural Investigation of Polymers*, Polymer Science and Technology, Ellis Horwood, NY, 1991.
15. F. Khoury and E. Passaglia. The morphology of crystalline synthetic polymers, in *Treatise on Solid State Chemistry*, Vol. 3, N.B. Hannay, Ed., Plenum, New York, 1976, pp. 335–496.
16. H.D. Keith and F.J. Padden. Spherulitic crystallization from the melt: I. Fractionation and impurity segregation and their influence on crystalline morphology, *J. Appl. Phys.*, 35:1270, 1964.
17. H.D. Keith and F.J. Padden. Spherulitic crystallization from the melt: II. Influence of fractionation and impurity segregation on the kinetics of crystallization, *J. Appl. Phys.*, 35:1286, 1964.
18. P.D. Calvert and T.G. Ryan. Redistribution of impurities in crystallizing polymers, *Polymer*, 19:611–616, 1978.
19. N.C. Billingham, P.D. Calvert, and A. Uzuner. Studies of diffusion in polymers by ultraviolet microscopy: 2. Diffusion of atactic fractions in isotactic polypropylene, *Polymer*, 31:258–264, 1990.
20. H.D. Keith and F.J. Padden. A discussion of spherulitic crystallization and spherulitic morphology in high polymers, *Polymer*, 27:1463–1471, 1986.
21. D.C. Bassett and A.S. Vaughan. Reply to a discussion of spherulitic crystallization and morphology, *Polymer*, 27:1472–1476, 1986.
22. D.C. Bassett, R.H. Olley, S.J. Sutton, and A.S. Vaughn. On spherulitic growth in a monodisperse paraffin, *Macromolecules*, 29:1852–1853, 1996.
23. H.D. Keith. Bulk semicrystalline polymers: a status report, in *Crystallization and Related Phenomena in Amorphous Materials*, Vol. 321, M. Kibera, Ed., Materials Research Society, Warrendale, PA, 1994.
24. A. Toda and A. Keller. Growth of polyethylene single crystals from the melt: morphology, *Colloid Polym. Sci.*, 271:328–342, 1993.
25. W.W. Mullins and R.F. Sekerka. Stability of a planar interface during solidification of a dilute binary alloy, *J. Appl. Phys.*, 35:444–451, 1964.
26. J. Minick, A. Moet, and E. Baer. Morphology of hdpe/ldpe blends with different thermal histories, *Polymer*, 36:1923–1932, 1995.
27. B. Wunderlich. *Macromolecular Physics*, Vol. 2, Academic Press, New York, 1976.
28. J.W. Cahn. Transformation kinetics during continuous cooling, *Acta Metall.*, 4:572–575, 1956.
29. W.L. Sifleet, N. Dinos, and J.R. Collier. Unsteady-state heat transfer in crystallizing polymer, *Polym. Eng. Sci.*, 13:10, 1973.
30. S. Chew, J.R. Griffiths, and Z.H. Stachurski. The crystallization kinetics of polyethylene under isothermal and nonisothermal conditions, *Polymer*, 30:874–881, 1989.
31. A. Maffezzoli, J.M. Kenny, and L. Nicolais. A macrokinetic approach to crystallization modeling of semicrystalline thermoplastic matrices for advanced composites, *J. Mater. Sci.*, 28: 4994–5001, 1993.

32. L. Torre, A. Maffezzoli, and J.M. Kenny. A macrokinetic approach to crystallization applied to a new thermoplastic polyimide (new tpi) as a model polymer, *J. Appl. Polym. Sci.*, 56:985–993, 1995.

33. T.W. Chan and A.I. Isayev. Quiescent polymer crystallization: modeling and measurements, *Polym. Eng. Sci.*, 34:461–471, 1994.

34. J.M. Schultz. Microstructural aspects of failure in semicrystalline polymers, *Polym. Eng. Sci.*, 24:770–785, 1984.

35. R.L. Cormia, F.P. Pierce, and D. Turnbull. Empty, *J. Chem. Phys.*, 37:1333, 1992.

36. D. Turnbull and J.C. Fisher. Rate of nucleation in condensed systems, *J. Chem. Phys.*, 17:71–73, 1949.

37. M. Avrami. Kinetics of phase change 1: general theory, *J. Chem. Phys.*, 7:1103–1112, 1939.

38. M. Avrami. Kinetics of phase change 2: transformation-time relations for random distribution of nuclei, *J. Chem. Phys.*, 8:212–224, 1940.

39. R.D. Icenogle. Temperature-dependent melt crystallization kinetics of poly(butene-1): a new approach to the characterization of the new crystallization kinetics of semicrystalline polymers, *J. Polym. Sci. Polym. Phys. Ed.*, 23:1369–1391, 1985.

40. G. Eder, H. Janeschitz-Kriegl, and S. Liedauer. Crystallization processes in quiescent and moving polymer melts under heat transfer conditions, *Prog. Polym. Sci.*, 15:629–714, 1990.

41. G. Eder and H. Janeschitz-Kriegl. Heat transfer and flow: transport phenomena controlling the crystallization processes in polymers, in *1st International Conference of Transport Phenomena in Processing*, S.I. Guceri, Ed., Technomic Publishing, Lancaster, PA, 1992.

42. Z. Ding and J.E. Spruiell. A method of studying nonisothermal crystallization of polymers at very high cooling rates, in *Antec '94: Plastics: Gateway to the Future*, Society of Plastics Engineers, Brookfield, CT, 1994, pp. 1485–1490.

43. M. Rappaz. Modelling of microstructure formation in solidification processes, *Int. Mater. Rev.*, 34:93–123, 1989.

44. J.D. Hoffman, G.T. Davis, and J.I. Lauritzen. The rate of crystallization of linear polymers with chain folding, in *Treatise on Solid State Chemistry*, Vol. 3, N.B. Hannay, Ed., Plenum, New York, 1976, pp. 497–614.

45. J.I. Lauritzen and J.D. Hoffman. Theory of formation of polymer crystals with folded chains in dilute solution, *J. Res. Natl. Bur. Stand. Phys. Chem.*, 64A:73–102, 1960.

46. J.G. Fatou, C. Marco, and L. Mandelkern. The influence of molecular weight on the regime crystallization of linear polyethylene, *Polymer*, 31:1685–1593, 1990.

47. J.G. Fatou, C. Marco, and L. Mandelkern. The crystallization kinetics of low-molecular-weight polyethylene fractions, *Polymer*, 31:890–898, 1990.

48. M.C. Tobin. Theory of phase transition kinetics with growth site impingement 1: homogeneous nucleation, *J. Polym. Sci.*, 12:399–406, 1974.

49. M.C. Tobin. The theory of phase transition kinetics with growth site impingement 2: heterogeneous nucleation, *J. Polym. Sci. Polym. Phys. Ed.*, 14:2253–2257, 1976.

50. C.W. Price. Simulations of grain impingement and recrystallization kinetics, *Acta Metall.*, 35:1377–1390, 1987.

51. A. Benard and S.G. Advani. Linking microscopic and macroscopic effects during solidification of semicrystalline polymers, in *Simulation of Materials Processing: Theory and Applications: Numiform '95*, S.F. Shen and P.R. Dawson, Eds., A.A. Balkema Publishers, Brookfield, VT, 1995, pp. 231–235.

52. A.N. Kolmogoroff. *Izvestiya Akad. Nauk SSSR*, 1:355, 1937.
53. W.A. Johnson and R.T. Rehl. Reaction kinetics in processes of nucleation and growth, *Trans. Am. Inst. Min., Metall. Pet. Eng.*, 135:416, 1939.
54. M. Avrami. Kinetics of phase change 3: granulation, phase change and microstructure, *J. Chem. Phys.*, 9:177–184, 1941.
55. U.R. Evans. The laws of expanding circles and spheres in relation to the lateral growth of surface films and the grain-size of metals, *Trans. Faraday Soc.*, 41:365–374, 1945.
56. L. Mandelkern. *Crystallization of Polymers*, McGraw-Hill, New York, 1964.
57. T. Ozawa. Kinetics of non-isothermal crystallization, *Polymer*, 12:150–158, 1971.
58. A. Hammami, J.E. Spruiell, and A.K. Mehrotra. Quiescent nonisothermal crystallization kinetics of isotactic polypropylenes, *Polym. Eng. Sci.*, 35:797–804, 1995.
59. K. Nakamura, T. Watanabe, K. Katayama, and T. Amano. Some aspects of nonisothermal crystallization of polymers 1: relationship between crystallization temperature, crystallinity and cooling conditions, *J. Appl. Polym. Sci.*, 16:1077–1091, 1972.
60. K. Nakamura, K. Katayama, and T. Amano. Some aspects of nonisothermal crystallization of polymers 2: considerations of the isokinetic condition, *J. Appl. Polym. Sci.*, 17:1031–1041, 1973.
61. K. Nakamura, T. Watanabe, T. Amano, and K. Katayama. Some aspects of nonisothermal crystallization of polymers 3: crystallization during melt spinning, *J. Appl. Polym. Sci.*, 18:615–623, 1974.
62. M.R. Kamal and E. Chu. Isothermal and nonisothermal crystallization of polyethylene, *Polym. Eng. Sci.*, 23:27–31, 1983.
63. R.M. Patel and J.E. Spruiell. Crystallization kinetics during polymer processing: analysis of available approaches for process modeling, *Polym. Eng. Sci.*, 31:730–733, 1991.
64. W. Schneider, A. Koppl, and J. Berger. Non-isothermal crystallization of polymers, *Intern. Polym. Process.*, 2:151–154, 1988.
65. M. Erhun and S.G. Advani. A predictive model for heat flow during crystallization of semi-crystalline polymers, *J. Thermoplast. Composite Mater.*, 3:90–109, 1990.
66. I.H. Hillier. Modified Avrami equation for the bulk crystallization kinetics of spherulitic polymers, *J. Polym. Sci.*, 3A:3067–3078, 1965.
67. A. Benard. Transport Phenomena and Microstructure Development in Semicrystalline Polymers and Composites, Ph.D. thesis, University of Delaware, Newark, DE, 1995.
68. M. Rappaz and Ph. Thevoz. Solute diffusion model for equiaxed dendritic growth, *Acta Metall.*, 35:1487–1497, 1987.
69. M. Rappaz and Ph. Thevoz. Solute diffusion model for equiaxed dendritic growth: analytical solution, *Acta Metall.*, 35:2929–2933, 1987.
70. L. Amelino, E. Martuscelli, C. Sellitti, and C. Silvestre. Isotactic polystyrene/poly(vinyl methyl ether) blends: miscibility, crystallization and phase structure, *Polymer*, 31:1051–1056, 1990.
71. W. Kurz and D.J. Fisher. *Fundamentals of Solidification*, 3rd ed., Trans Tech Publications, Aedermannsdorf, Switzerland, 1992.
72. J.E. Spruiell and J.L. White. Structure development during polymer processing: studies of the melt spinning of polyethylene and polypropylene fibers, *Polym. Eng. Sci.*, 15:660–667, 1975.

73. H. Motz and J.M. Schultz. Solidification of peek: ii. Kinetics, *J. Thermoplast. Composites*, 2:267–280, 1989.
74. A. Benard and S.G. Advani. An analytical model for spherulitic growth in fiber-reinforced polymers, *J. Appl. Polym. Sci.*, 70:1677–1687, 1998.
75. A. Benard. Model for phase-change in polymer composites with significant surface nucleation, *Acta Mater.*, 46:5259–5270, 1998.
76. N. Billon, J.M. Escleine, and J.M. Haudin. Isothermal crystallization kinetics in a limited volume: a geometrical approach based on Evans' theory, *Colloid Polym. Sci.*, 267:668–680, 1989.
77. J.M. Haudin and N. Billon. Solidification of semi-crystalline polymers during melt processing, *Prog. Colloid Polym. Sci.*, 87:132–137, 1992.
78. N. Billon, C. Magnet, J.M. Haudin, and D. Lefebvre. Transcrystallinity effects in thin polymer films: experimental and theoretical approach, *Colloid Polym. Sci.*, 272:633–654, 1994.
79. J.M. Schultz. Effect of specimen thickness on crystallization rate, *Polymer*, 1995.
80. Jerold Schultz. *Polymer Materials Science*, Prentice-Hall, Englewood Cliffs, NJ, 1974.
81. X. Guo, A.I. Isayev, and L. Guo. Crystallinity and microstructure in injection moldings of isostatic polypropylenes: Part I. A new approach to modeling and model parameters, *Polym. Eng. Sci.*, 39:2096–2114, 1999.
82. T. Huang and M.R. Kamal. Morphological modeling of polymer solidification, *Polym. Eng. Sci.*, 40:1796–1808, 2000.

5

Rheological Measurements and Modeling of Noncolloidal Particulate Suspensions*

Abdellatif Ait-Kadi, Miroslav Grmela, Rakesh K. Gupta, and Vladimir Zmievski

CONTENTS

5.1 Introduction

Solid-in-liquid suspensions containing noncolloidal particles are routinely encountered during the processing of both thermoplastic and thermosetting

---

* Dedicated to the memory of Professor Abdellatif Ait-Kadi.

polymers. The tensile strength, stiffness, and dimensional stability of polymers, such as nylons and polyesters, can be increased by compounding them with short glass fibers; the fibers range in length from 3 to 12 mm, and they can make up as much as 50% by weight of the compounded product.[1] Here the glass acts as a reinforcement, and the compounded product is called an engineering polymer because it is used to mold a variety of valves, gears, and mechanical parts. Other particulate fillers that are employed include calcium carbonate, clay, talc, mica, and glass spheres. These materials are either plate-like or are essentially spherical, and they do not provide the same kind of mechanical property improvement as that given by glass fibers. They are called diluents, and they are used either by themselves or in combination with glass fibers primarily in order to reduce cost, but also to improve melt processability.[1] The incorporation of low-aspect-ratio fillers can, however, improve properties such as stiffness, hardness, and the heat distortion temperature of a molding; the effect, though, is isotropic since the fillers cannot be oriented. In the case of thermosets, inert powders, such as sawdust in phenolics and clay in vinyl ester, again lower cost, but they also help to absorb any condensation products and to reduce the maximum temperature attained during curing.

In many instances involving concentrated suspensions, the focus of attention is the suspended solid rather than the suspending medium. During the injection molding of metal or ceramic powders, for example, the polymeric fluid employed merely acts as a binder that has to be removed in a later step. Other examples of solid-in-liquid suspensions of technological interest include paints and building materials, coal-water fuels, drilling and fracturing fluids, thermal grease, and dental adhesives. A study of the rheological properties of particulate suspensions is also mandated by the need to dispose, often by pipeline transport, immense amounts of waste generated by the minerals mining industry. This chapter, therefore, examines the influence of both suspended solid and suspending liquid properties on the flow behavior of noncolloidal suspensions. Note that for such suspensions, one can generally neglect Brownian motion effects as well as effects due to electrostatic, steric, and van der Waals forces. Even so, a variety of interesting phenomena are observed, and these are described and explained in the sections that follow.

5.2 Rheological Measurements

5.2.1 Sample Preparation

Samples of solid-in-liquid suspensions employed for rheological measurements should be spatially homogeneous and should not contain any agglomerates, or else there could be sample-to-sample variations in the results. A

suspension having uniform composition can be prepared by one of several methods. A small amount of solids can be dispersed in a liquid simply by putting the two components in a sealed plastic bag and kneading the mixture by hand. Alternately, one could use a planetary mixer having a mixing bowl fitted with a planetary-designed blade and a scraper to keep material from sticking to the wall of the mixing chamber. If the liquid phase is a polymer melt, the filler particles and the polymer pellets should first be tumble-mixed in dry form by placing them in a baffled container that is rotated about its axis. This mixture can then be fed to an internal mixer that consists of a heated enclosure, typically shaped like a figure eight, and fitted with a pair of intermeshing rotors operating at different speeds.[2] High shear rates lead to homogenization and breakdown of any clumps or agglomerates. For large samples and continuous operation, it is best to use a twin-screw extruder fitted with a strand die; the strand is cooled in a water bath and then pelletized.

5.2.2   Experimental Concerns

In general, rheological measurements can be made on particulate suspensions using standard viscometers, and one uses rotational instruments at low shear rates and a capillary instrument at high shear rates. However, it has to be ensured that true material properties are measured and that these are not affected by the nature of the flow field, the viscometer employed, or the fixture dimensions and geometry chosen. In this regard, it is essential that the largest particulate dimension be small in comparison with the gap size between the measuring elements. This criterion itself often implies the use of a parallel plate viscometer in place of a cone-and-plate viscometer. Another concern with two-phase systems is the possibility of the development of composition nonuniformities during the course of measurement; a mismatch between the densities of the two phases can lead to either sedimentation or creaming. Although the use of a viscous suspending medium can provide stability against sedimentation, standard viscometers can be modified to prevent particle settling,[3] or novel instruments, such as the helical-screw rheometer, can be employed.[4]

   In addition to the above concerns, another complication is the frequent occurrence of either apparent or true slip at the wall. Since the region near the fixture walls is necessarily depleted of solid particles, the presence of a lower-viscosity, liquid-rich layer results in an apparent slip phenomenon. One, therefore, ends up measuring interfacial rather than bulk suspension properties; the procedure for correcting for this error is straightforward, but requires additional experimentation.[5,6] A more serious situation arises when the suspension, especially a heavily loaded one, possesses a yield stress. If the magnitude of the yield stress is larger than the force of adhesion between the suspension and the viscometer wall, the application of a stress that is smaller in value than the yield stress can result in slip of the fluid at a solid

surface rather than the intended deformation in the bulk of the material. If adhesion is restored rapidly, the phenomenon of stick-slip can be witnessed. If adhesion is not restored quickly, there can be complete separation at the solid boundary. Roughening the fixture surface or gluing the sample to the fixture is the recommended cure for this malady.[7,8]

If the suspension remains homogeneous, the chosen viscometer is an appropriate one; there is no wall slip, and the sample remains in the viscometer at all times and does not fracture cohesively. True data should be obtained. If despite addressing all these concerns, the measurements turn out to be time dependent and a steady state is not attained in a reasonable amount of time, it must be concluded that the transients represent real changes in stress levels in the suspension and are the result of structural changes brought about by the imposed deformation.

5.2.3 Limiting Behavior at Low Concentrations

It is possible to theoretically calculate the viscosity of a suspension of spheres in a Newtonian liquid when the solids concentration is low enough that the flow field around one sphere is not disturbed by the presence of other spheres. In this case, the suspension behaves as a Newtonian liquid of viscosity η given by[9]

$$\eta = \eta_s(1 + 2.5\phi) \tag{5.1}$$

where η_s is the viscosity of the suspending liquid, and ϕ is the volume fraction of spheres. This equation was first derived by Einstein from a calculation of energy dissipation in the suspension, and the constant 2.5 is known as the Einstein constant. Equation (5.1) can be rewritten in terms of the intrinsic viscosity $[\eta]$ as

$$[\eta] = (\eta/\eta_s - 1)/\phi = 2.5 \tag{5.2}$$

Although Equations (5.1) and (5.2) have little technological utility, they are often built into similar equations for more concentrated suspensions so that the correct limiting behavior may be obtained at low concentrations. Note that Equation (5.1) implies that the viscosity of a dilute suspension does not depend on the size of spheres or their size distribution, and this has been observed to be true in practice. Calculations have also been done for rigid fillers of other shapes, such as prolate and oblate spheroids, and it is found that the magnitude of the Einstein constant is determined by the degree to which the particles disturb the streamlines in a flowing system. In particular, rods tend to disturb the streamlines more than do spheres and have correspondingly larger Einstein constants. As the solids concentration is increased, particles begin to interact with each other, and the viscosity increases more than linearly with the volume fraction.

5.2.4 Viscosity of a Concentrated Suspension of Spheres

The variables that influence the viscosity of a homogeneous suspension of noncolloidal spheres are shear rate, temperature, solids volume fraction, particle size distribution, and the rheology of the suspending liquid. In general, the suspension viscosity increases as the loading level increases, and it decreases as the temperature increases or the size distribution widens. Also, if the suspending liquid is non-Newtonian, the suspension behavior is non-Newtonian as well. Representative data for the viscosity of suspensions of 15-μm average diameter, narrow-size-distribution glass beads in a Newtonian polybutene oil at 22°C, and taken from the work of Poslinski[10] are shown in Figure 5.1 in a shear rate range of 0.01 to almost 10^4 sec^{-1}.[11] The matrix viscosity is 6.5 Pascal seconds (Pa-s), and the addition of the spheres raises the suspension viscosity uniformly as long as the sphere volume fraction is 0.5 or less. A further increase in the loading level to 60 vol%, however, makes the suspension non-Newtonian, and one observes the appearance of a yield stress; this is not surprising given that one is approaching ϕ_m, the maximum possible value of the solids concentration. When ϕ equals ϕ_m, flow cannot occur, and the suspension viscosity becomes infinitely large.

If one formulates a suspension with a distribution of sphere sizes, there is little effect of size distribution on viscosity as long as $\phi < 0.2$. Beyond this
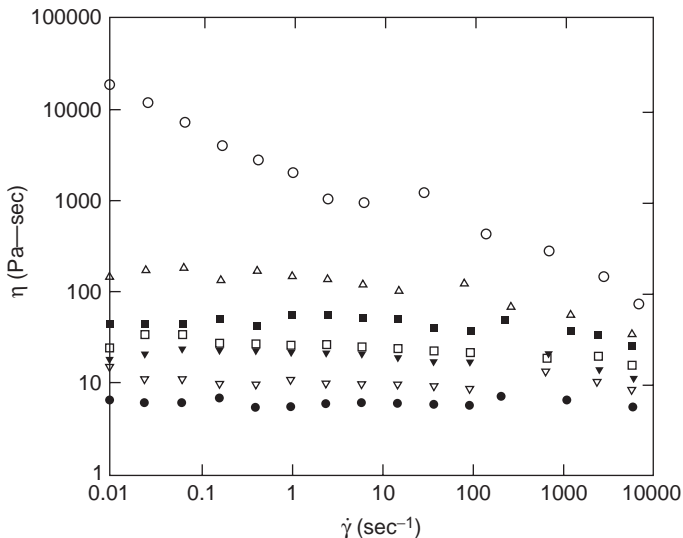

FIGURE 5.1
Shear viscosity at 22°C of 15-μm glass spheres suspended in a polybutene oil of 6.5 Pa-s viscosity. The various symbols are for different solid volume fractions: ● = 0, ▽ = 0.1, ▼ = 0.2, □ = 0.3, ■ = 0.4, △ = 0.5, and ○ = 0.6. (Reprinted with permission from Gupta, R.K., 1994, in *Flow and Rheology in Polymer Composites Manufacturing*, S.G. Advani, Ed., Amsterdam: Elsevier Science, pp. 9–51.)

loading level, however, there can be a dramatic lowering in the viscosity by a proper selection of sphere sizes. This is demonstrated in Figure 5.2 for a bimodal mixture of glass spheres suspended in a polybutene oil of 25 Pa-s shear viscosity[10,11]; glass spheres of 15-μm average diameter were mixed with glass spheres of 78-μm average diameter. All the suspensions were Newtonian, and the data are plotted as relative viscosity η_R vs. the volume fraction of small spheres in the solids mixture; the relative viscosity is defined as the ratio of the suspension viscosity to the suspending liquid viscosity. In Figure 5.2, the different symbols represent the total solid volume fraction, and this quantity ranges from 0.1 to 0.6. Note that the scale on the ordinate is logarithmic, and for a given symbol or solid volume fraction, the suspension viscosity first decreases and then increases as one moves along the abscissa; in each case, the viscosity attains a minimum around a value of the volume fraction of small spheres of about 0.15. It is seen that at the higher loading levels, the suspension viscosity can easily be reduced by 50% through the use of a bimodal mixture of sphere sizes. This reduction arises simply because small spheres can fit into the interstices of large spheres, which can fit into the interstices of still larger spheres, and this facilitates flow. It is for this reason that one cannot obtain a suspension of reasonable viscosity at a loading level of 60 vol% solids through the use of uniformly sized spheres, but can do so with the help of a distribution of sizes.
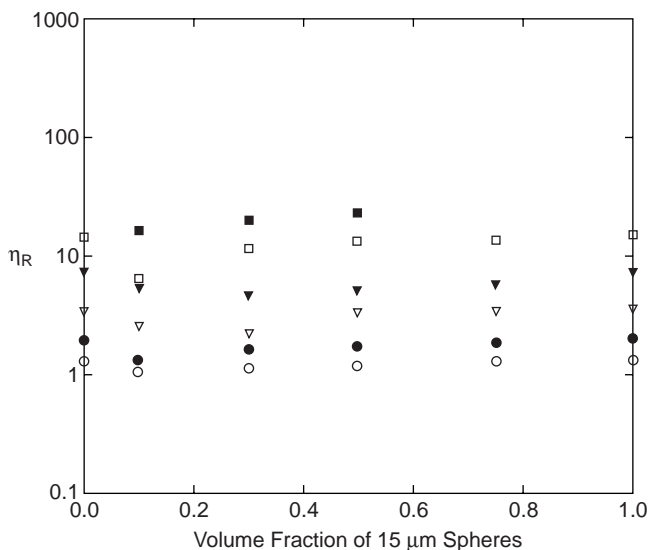

FIGURE 5.2

Relative viscosity as a function of volume fraction of small spheres in a mixture of 15-μm glass spheres and 78-μm glass spheres suspended in a polybutene oil of 25 Pa-s viscosity. The various symbols are for different total solid volume fractions: ○ = 0.1, ● = 0.2, ▽ = 0.3, ▼ = 0.4, □ = 0.5, and ■ = 0.6. (Reprinted with permission from Gupta, R.K., 1994, in *Flow and Rheology in Polymer Composites Manufacturing*, S.G. Advani, Ed., Amsterdam: Elsevier Science, pp. 9–51.)
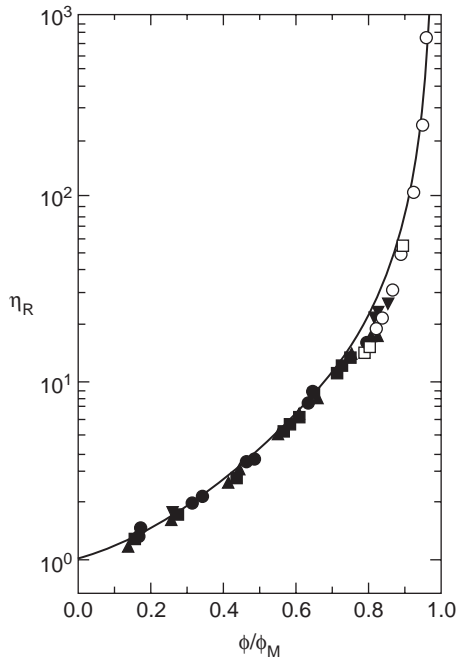
FIGURE 5.3
Data of Figure 5.2 (shown here as filled symbols) replotted in terms of the reduced volume fraction ϕ/ϕ_m. The solid line is Equation (5.3). (Reprinted with permission from Poslinski, A.J. et al., 1988, *J. Rheol.*, 32:751–771.)

In terms of data representation, it is found that all the data of the kinds shown in Figures 5.1 and 5.2 can be combined to give a single master curve if one plots the relative viscosity as a function of ϕ/ϕ_m. This is shown in Figure 5.3, which contains all the data presented earlier in Figure 5.2 and some literature data of other researchers as well.[12] For the spheres of Figure 5.1, ϕ_m is found to be 0.62, while for the mixture of spheres of Figure 5.2, ϕ_m ranges from 0.61 to 0.75. The solid line in Figure 5.3 is the one proposed by Maron and Pierce[13] and evaluated by Kataoka et al.[14] and Kitano et al.:[15]

$$\eta_R = (1 - \phi/\phi_m)^{-2} \tag{5.3}$$

Figure 5.3 shows that all the data fall on a single curve, and the curve itself is well represented by Equation (5.3).

Most polymer melts are non-Newtonian and, in particular, shear thinning. Typical viscosity behavior as a function of shear rate is shown in Figure 5.4 for a thermoplastic polymer at three different temperatures.[10,11] The polymer viscosity is Newtonian below a shear rate of 1 sec^{-1}, and it displays a power-law behavior with a power-law index of 0.5 at shear rates above 10 sec^{-1}. Furthermore, the temperature dependence of the zero-shear viscosity can be
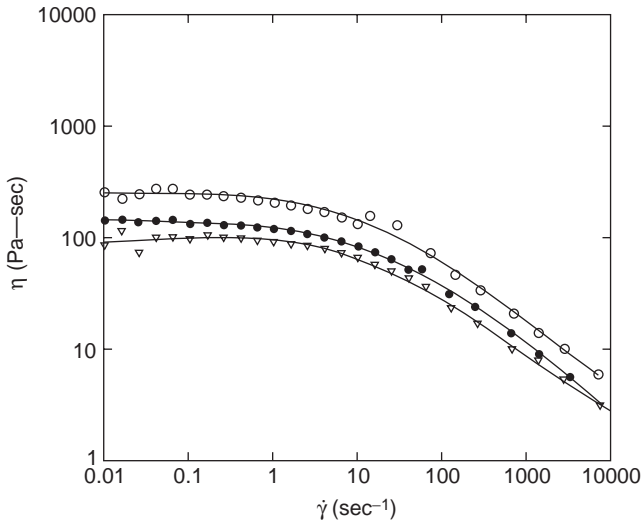
FIGURE 5.4
Shear viscosity of the thermoplastic polymer used by Poslinski[10] as a non-Newtonian suspending medium. The various symbols represent different temperatures: $\bigcirc$ = 130°C, $\bullet$ = 150°C, and $\triangledown$ = 170°C. (Reprinted with permission from Gupta, R.K., 1994, in *Flow and Rheology in Polymer Composites Manufacturing*, S.G. Advani, Ed., Amsterdam: Elsevier Science, pp. 9–51.)

described by the Arrhenius equation.[10] On adding particulates to a shear-thinning liquid, one finds that the addition of the same amount of particulates tends to raise the viscosity proportionately more at low shear rates than at high shear rates. This can be seen in Figures 5.5 and 5.6, where the glass beads of Figure 5.1 have been compounded with the polymer of Figure 5.4; suspension viscosity vs. shear rate data are presented at two different temperatures and over the entire range of filler concentrations.[10] It is observed that while the power-law index of the different suspensions is the same as that of the suspending polymer, the point of onset of shear thinning moves to lower shear rates with increasing particulate concentration. In addition, it is found that the zero-shear viscosity of the suspensions again follows the Arrhenius equation, with a flow activation energy that is identical to that of the matrix polymer.[10]

When the suspending liquid is shear thinning, the suspension relative viscosity can be defined in a number of ways. Kitano et al.[15] found that if the ratio of the suspension viscosity (at a given temperature) to the suspending liquid viscosity (at the same temperature) was calculated at the same value of the shear stress, the relative viscosity $(\eta_R)_\tau$ defined in this manner was a function of the filler volume fraction alone. This is demonstrated in Figure 5.7 using the data of Figures 5.4 and 5.5.[11] Relative viscosities so obtained also superpose well with the data presented in Figure 5.3 and are, therefore, representable by Equation (5.3). Thus, this very simple, empirical equation can be employed to take into account the effect of all the major
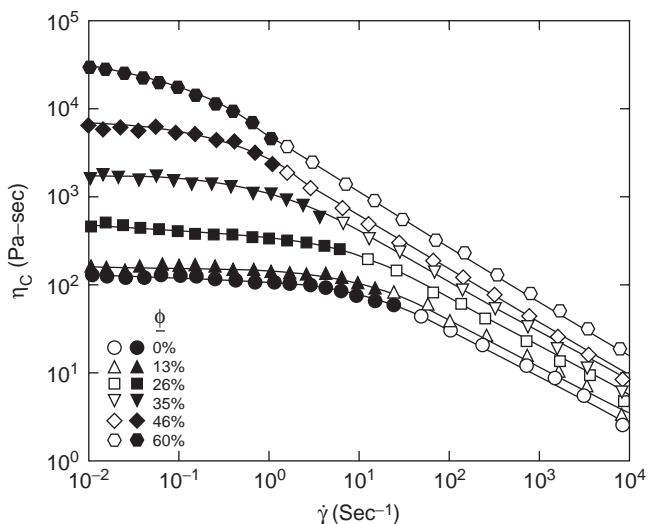
FIGURE 5.5

Shear viscosity at 150°C of 15-μm glass spheres suspended in the thermoplastic polymer of Figure 5.4. Solid symbols are cone-and-plate viscometer data, while open symbols are capillary viscometer data. The solid lines represent the best fit to the experimental data. Data have been taken from the work of Poslinski.[10]
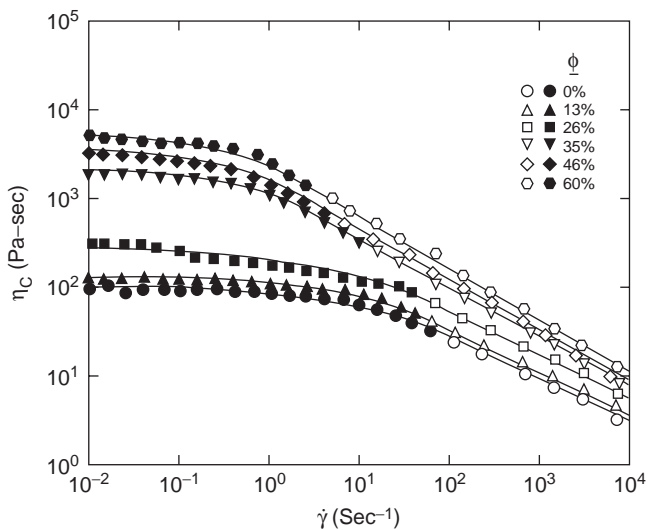

FIGURE 5.6

Same as Figure 5.5 except that the temperature of measurement is 170°C. Data have been taken from the work of Poslinski.[10]
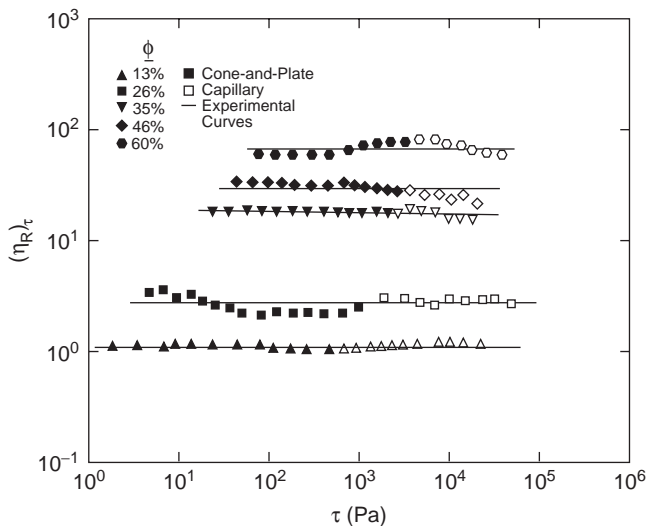
FIGURE 5.7
Data of Figures 5.4 and 5.5 replotted as the relative viscosity at a constant shear stress as a function of the shear stress. (Reprinted with permission from Gupta, R.K., 1994, in *Flow and Rheology in Polymer Composites Manufacturing*, S.G. Advani, Ed., Amsterdam: Elsevier Science, pp. 9–51.)

variables that influence the viscosity of a solid-in-liquid suspension. It cannot, however, provide any explanations for observed behavior; this can only be done with the help of mechanistic models.

In closing this section, we mention that a yield stress is commonly observed in suspensions of colloidal particles but not in a suspension of noncolloidal particles. This is because a yield stress is a manifestation of network formation, whether involving interactions amongst the suspended particles alone, between any polymer molecules in the suspending liquid alone, or between both the suspended solids and the suspending liquid. Such a network forms easily in concentrated suspensions of fine particles due to the presence of colloidal forces, and it leads to flocculation. When large particles are involved, agglomeration can and does occur if a binding mechanism is present. In this case, common binding mechanisms are mechanical interlocking, adsorption of polymer molecules on the surface of more than one particle, and the existence of liquid bridges. Liquid bridging takes place upon the addition of a measured amount of a liquid that preferentially wets the solid surface, but is either immiscible with the suspending liquid or is only sparingly soluble in it.[16] A major consequence of particle agglomeration is an increase in suspension viscosity. However, the effects of this phenomenon can be minimized or even eliminated by modifying the surface of the filler particles so as to interfere with the binding mechanism. A common procedure is to treat the filler with a coupling agent, such as a titanate, that completely covers the solid surface and promotes adhesion between the filler and the suspending liquid.[11]

5.2.5 Particle Migration

Thus far, it has been assumed that a suspension of interest is spatially homogeneous, and it remains so during the process of rheological measurement. This is not always the case[2,11] (see also Section 5.5). It has been found, for example, that during flow through a tube of radius R, the solids in a suspension of neutrally buoyant spheres in a Newtonian liquid tend to collect in a thin annular region located at a radial distance about 0.6R away from the tube axis. This happens due to the influence of fluid inertia. Nonneutrally buoyant spheres that are denser than the suspending liquid migrate toward the wall in downward flow and toward the centerline in upward flow.

When the flow of a dilute suspension of spheres in a non-Newtonian medium is examined, the direction of particle migration appears to depend on the relative influence of elasticity and shear thinning. Under the influence of fluid elasticity, particles move from regions of high shear rate to regions of low shear rate. The effect of shear thinning is just the opposite and leads to migration in a direction of increasing shear rate. When a viscoelastic fluid is also highly shear thinning, particles move toward the wall in Poiseuille flow but do not actually hit the wall.

Whenever there is a velocity gradient, the particle velocity varies with position, and faster-moving particles tend to collide with slower-moving particles whose trajectories are along adjacent streamlines. If, however, the shear rate varies with position in the flow field, the number of collisions experienced by a typical particle per unit time also varies with position. This gradient in the collision frequency across a particle makes the particles move from regions of high shear rate to regions of low shear rate. Thus, in tube flow, migration is toward the centerline, but solid volume fractions in excess of 0.1 are needed to observe concentration differences.

From the viewpoint of making rheological measurements on suspensions, particle migration is clearly undesirable, and process conditions should be chosen to minimize the phenomenon. When working with suspensions in which the matrix material is a molten polymer, the severity of any particle migration can be gauged by sectioning and microscopically examining frozen samples taken during different stages of measurement.

5.3 Rheological Modeling: Semi-Empirical Expressions for the Viscosity of Suspensions of Spheres

A very large number of equations have been proposed for estimating the viscosity of a Newtonian liquid containing spherical particles up to moderate concentrations. One of the more successful equations for monodisperse spheres is due to Frankel and Acrivos,[17] who assumed that the increase in viscosity on adding particulates was due to energy dissipation in the thin

liquid film between neighboring spheres as they moved past each other. These authors further assumed that dissipation due to squeezing was dominant and that due to the sliding motion was negligible. By averaging the energy dissipated by all possible pairs of particles in the suspension, they obtained the following expression for the relative viscosity:

$$\eta_R = \frac{9}{8}\left[\frac{\left(\phi/\phi_m\right)^{1/3}}{1-\left(\phi/\phi_m\right)^{1/3}}\right] \tag{5.4}$$

The above equation depicts data correctly at large values of ϕ, but it does not reduce to Equation (5.1) as ϕ tends to zero.

When the suspending liquid is non-Newtonian, but with viscosity behavior that can be represented by the power-law equation, an analysis similar to that of Frankel and Acrivos suggests that Equation (5.4) should be modified to read:[18]

$$\left(\eta_R\right)_{\dot{\gamma}} = \frac{9}{8}\left[\frac{\left(\phi/\phi_m\right)^{1/3}}{1-\left(\phi/\phi_m\right)^{1/3}}\right]^n \tag{5.5}$$

in which the subscript $\dot{\gamma}$ indicates that both the suspension and suspending medium viscosities are measured at the same shear rate. Note that since the shear rate does not appear explicitly in Equation (5.5), the flow curve for the suspension has the same slope on logarithmic coordinates as the flow curve of the suspending liquid, and one curve is situated directly above the other; the power-law index has to be related to the shear rate in a separate experiment. Also note that Equation (5.5) reduces to Equation (5.4) when n equals unity. This equation was tested by Poslinski and coworkers[10,19] using the data shown in Figures 5.4 to 5.6, and the results are displayed in Figure 5.8. One expects that the relative viscosity will depend on both the power-law index and the loading level, and this is found to be true. Also, Equation (5.5) represents data quite well at each of the three temperatures examined; in calculating the theoretical value of the relative viscosity, ϕ_m has been taken to be 0.62, which is the experimentally measured value of the maximum packing fraction.

The influence of a distribution of sphere sizes can be predicted by taking an "effective medium" approach.[20] Here one begins with the suspending liquid and adds the smallest-size spheres first and assumes that the suspension viscosity is given by Equation (5.1). The next coarser solids are added next, and so on. At each stage, the suspension viscosity is assumed to be given by Equation (5.1), except that η_s is taken to be the same as the viscosity of the suspension at the end of the previous stage. This leads to the result[2]

$$\eta_R = (1 - K\phi)^{-2.5/K} \tag{5.6}$$

where K is a constant that must, on physical grounds, equal the reciprocal of ϕ_m. Also, since the Einstein coefficient equals the intrinsic viscosity, Equation (5.6) becomes

$$\eta_R = (1 - \phi/\phi_m)^{-[\eta]\phi_m} \tag{5.7}$$

which is the same as Equation (5.3), provided that $[\eta]\phi_m$ equals 2. Equation (5.7) is known as the Krieger–Dougherty equation,[21] and it can be expected to fit data better than does Equation (5.3) because it has one additional constant. This equation may also be applied to nonspherical particulates if both the intrinsic viscosity and the maximum packing fraction are determined in an experimental manner.

In order to admit the possibility of a yield stress τ_Y and also to make the suspension viscosity expression explicit in shear rate over the entire range of shear rates, Poslinski and coworkers built on the equations presented earlier and proposed that suspension viscosity be given by[10,19]

$$\eta = (\tau_Y/\dot{\gamma}) + \frac{\eta_0}{(1-\phi/\phi_m)^2}\left[1+(\lambda\dot{\gamma})^2\right]^{(n-1)/2} \tag{5.8}$$

where η_0 is the zero-shear viscosity of the suspending liquid, λ is a constant related to the onset of shear thinning in the suspension, and n is the power-law index describing both the suspension and the suspending liquid. Equation (5.8) is a general expression, and it can be used to represent data that
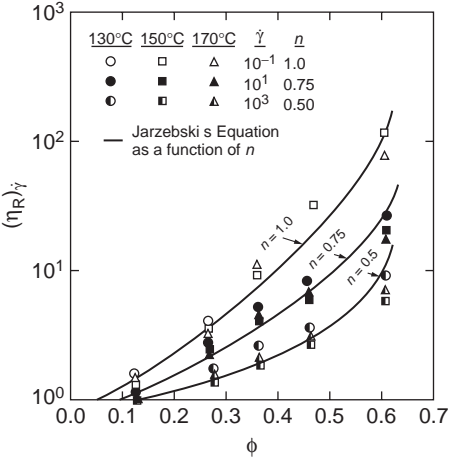

FIGURE 5.8
Data of Figures 5.4 to 5.6 and similar data at 130°C replotted as relative viscosity as a function of filler volume fraction. The solid lines represent the predictions of Equation (5.5). (Reprinted with permission from Gupta, R.K., 1994, in *Flow and Rheology in Polymer Composites Manufacturing*, S.G. Advani, Ed., Amsterdam: Elsevier Science, pp. 9–51.)

exhibit the extremes of rheological behavior. The equation can also account for all the material and processing variables that influence the viscosity of a suspension; Poslinski et al.[19] have also recommended expressions that relate the constants in Equation (5.8) to parameters describing both the matrix and the particulates making up the suspension. These authors demonstrated that Equation (5.8) did an excellent job of describing the data shown earlier in Figure 5.5.[19]

5.4 Rheological Modeling: The Time Evolution of the Internal Structure

Experience shows that some basic features of the flow of suspensions can be estimated in the setting of classical hydrodynamics. This means that the only place where the microscopic nature of the suspension enters this type of modeling is in the viscosity coefficient η (we restrict ourselves to isothermal fluids). In the preceding section we reviewed phenomenological expressions for η that have been proposed in the literature. If we want to proceed now to a more detailed and more realistic modeling, we have to begin by recognizing the fact that suspensions involve an internal (microscopic) structure that in many situations evolves in time on the same scale as the classical hydrodynamic fields and that the time evolutions of the internal structure and the classical hydrodynamic fields are strongly coupled. The internal structure therefore has to be included explicitly into the considerations. Consequently, more realistic modeling consists of two steps: choosing variables describing states of the internal structure and then writing down equations governing the time evolution of all the state variables (i.e., the fields used in classical fluid mechanics and the fields chosen to describe the internal structure). Before embarking on this task, we shall collect some information about the microscopic nature of the suspended particles.

The suspended particles are characterized by their shape and by their deformability when subjected to external forces. In this review of modeling, we are limiting ourselves to spherical and rigid particles. Moreover, we shall assume that all particles are identical. We are thus leaving out completely all the effects that are associated with the orientation and deformation of particles. If we let a denote the radius of any particle, then if $10^{-8}\,\text{m} < a < 10^{-5}\,\text{m}$, we speak about colloidal suspensions. If $a > 10^{-5}\,\text{m}$, on the other hand, the suspensions are called noncolloidal. We also recall that a particle is called a colloidal particle if in the presence of no external forces except the force of gravitation, it remains suspended and does not settle to the bottom. For this to be the case, it is necessary that the potential energy of the particle subjected to the gravitational force be comparable to the energy of thermal fluctuations in the fluid.

An important dimensionless number that is proportional to the particle size is the Reynolds number, $Re = \rho v a / \eta$, where ρ is the mass density and v is a characteristic velocity of the relative fluid–particle motion.

Another important dimensionless number characterizing suspensions is the Péclet number, $Pe = \dot{\gamma} \eta a^3 / k_B T$, where k_B is the Boltzmann constant and T is the temperature. Some authors also include the multiplicative factor 6π in this definition. The Péclet number can be looked upon as the ratio of the characteristic viscous force $\dot{\gamma} \eta a^2$ to the Brownian force kT/a. Hence a large Péclet number corresponds to strong flow fields, to the presence of a large particle size, or to the situation in which thermal fluctuations are negligible.

In general, the interaction forces to which the suspended particles are subjected are of three types: (1) direct particle–particle forces, (2) particle–fluid forces, and (3) indirect (mediated by the fluid) particle–particle forces. The direct particle–particle forces are the forces generated by the particle–particle interaction potential (most importantly the hard-core potential and the Coulomb potential if the particles are electrically charged). The particle–fluid interactions cause the Brownian and thermal motion, and they also determine the Stokes friction force. The indirect particle–particle interaction is called a hydrodynamic interaction. It arises due to the fact that the presence of a particle in the fluid perturbs the flow field, and the resulting perturbation then propagates (with a speed close to the speed of sound) to other particles.

Now, we turn our attention to the internal structure and to its modeling. This is a very large subject to which we cannot do justice in this review. Our goal is therefore limited. In the following sections, we intend to provide to the reader only a glimpse of this vast area. The emphasis is on strategies and methods rather than on results, in the complex network of approaches that have been suggested in the literature. We should also mention that the review presented below is neither complete (since the subject is vast and the space available to us is limited) nor completely objective (since we are obviously influenced by our point of view). We proceed by presenting the main ideas behind the approach followed by Batchelor[22] and Happel and Brenner[23] (Section 5.4.1), molecular simulations (Section 5.4.2), and considerations that take into account explicitly the internal structure (Section 5.4.3). Following this, in Section 5.5, we briefly describe the approach, called GENERIC, that we are following in our own investigations.

5.4.1 Microscopic Derivations

Following statistical mechanics and Batchelor[22] and Happel and Brenner,[23] we begin at a completely microscopic level and formulate the time evolution of all the suspended particles and also of the fluid in which they are suspended. From this formulation, by applying various averaging processes and other approximations, we will arrive at equations governing the time evolution of certain mesoscopic characteristics of the suspended particle.

Then, by following a different sequence of averagings and approximations, we will obtain the extra stress tensor expressed in terms of these mesoscopic characteristics. This approach is very appealing and, in general, very successful. Since it is well described in Batchelor[22] and Happel and Brenner,[23] as well as in many other monographs and research articles, we shall only comment on the main advantages and disadvantages of this approach.

As for the advantages, this approach has a clear point of departure. Since the mesoscopic formulation unfolds from the microscopic formulation, the parameters arising in the mesoscopic formulation have a clear physical meaning. They appear as functions of microscopic characteristics of the suspension.

The main disadvantage of this approach is that the choice of many averaging schemes and approximations (in particular, closure approximations) needed to go from the microscopic point of departure to the resulting mesoscopic theory is guided only by our physical intuition. This then implies that many questions remain unanswered. For example, it is not clear that the sequence of approximations leading to the time evolution equations and another sequence of approximations leading to the expression for the extra stress tensor are compatible with each other. This type of derivation also does not guarantee that solutions to the resulting governing equations will agree with results of certain fundamental experimental observations, for example, the observed compatibility with equilibrium thermodynamics (i.e., the observation that in the absence of external forces, suspensions reach a state, called an equilibrium state, at which their behavior is seen to be well described by equilibrium thermodynamics).

In order to address the disadvantages, some authors have developed complementary methods of investigations. We shall describe some of them in the following sections.

5.4.2 Direct Simulations

Here we take the same point of departure as in the previous section, but we do not proceed to the mesoscopic and macroscopic consequences that can be compared with results of our experimental observations by first reducing the microscopic formulation to mesoscopic governing equations (recall that these reductions involve many unjustified or only partially justified approximations) and then solving them (which again cannot be done without introducing still other approximations). Instead, we shall use the power of present-day computers and calculate directly the trajectories of the suspended particles. From the trajectories, we then extract the macroscopic information of our interest. However, as powerful as the computers are, it is obvious that this task cannot be achieved with the actual number of particles that appear in experiments conducted with actual suspensions. In most simulations, the number of particles whose trajectories are directly followed is about 1000. The governing equations of the direct simulations are Newton's equations (thus they are ordinary differential equations). In

most simulations, Newton's equations are further simplified by neglecting inertia. This then means that the velocity of a particle is determined by the equilibrium of the forces acting on it. It is mainly the way in which the forces are calculated that distinguishes various schools of direct simulations. We shall now describe some of them.

In Brownian simulations,[24,25] the position coordinates $\mathbf{r}_1 \dots \mathbf{r}_N$ and velocities $\mathbf{v}_1 \dots \mathbf{v}_N$ of N particles are upgraded to the status of random variables, whose time evolution is governed by Newton's equations upgraded to the status of stochastic equations by adding to their right-hand side the Gaussian noise $\mathbf{X}$, $(\langle X_i \rangle = 0, \langle X_i(t)X_j(t') \rangle = 2\delta_{ij}\delta(t-t'))$. In the inertialess limit, the time evolution equations become

$$\dot{\mathbf{r}}_i = \mathbf{v} + \nabla \mathbf{v} \cdot \mathbf{r}_i + \sum_{j=1}^{N}\left(\frac{1}{k_B T}\mathbf{G}_{ij}\cdot\mathbf{F}_j^P + \alpha_{ij}\mathbf{X}_j\right) \tag{5.9}$$

where $\mathbf{v}$ is the overall fluid velocity, $\mathbf{F}_j^P$ is any nonhydrodynamic force acting on the j-th particle, and $\mathbf{G}$ is either the Oseen tensor,

$$\mathbf{G}_{ij} = \frac{k_B T}{6\pi\eta a}\left(\mathbf{I} + \frac{(\mathbf{r}_i-\mathbf{r}_j)(\mathbf{r}_i-\mathbf{r}_j)}{(\mathbf{r}_i-\mathbf{r}_j)^2}\right), \quad i \neq j \tag{5.10}$$

or its Rotner–Prager generalization,[26]

$$\mathbf{G}_{ij} = \frac{k_B T}{6\pi\eta a}\left(\mathbf{I} + \frac{(\mathbf{r}_i-\mathbf{r}_j)(\mathbf{r}_i-\mathbf{r}_j)}{|\mathbf{r}_i-\mathbf{r}_j|^2} + \frac{2a^2}{|\mathbf{r}_i-\mathbf{r}_j|^2}\left(\frac{1}{3}\mathbf{I} - \frac{(\mathbf{r}_i-\mathbf{r}_j)(\mathbf{r}_i-\mathbf{r}_j)}{|\mathbf{r}_i-\mathbf{r}_j|^2}\right)\right), \quad i \neq j \tag{5.11}$$

If $i = j$, then in both cases

$$\mathbf{G}_{ii} = \frac{k_B T}{6\pi\eta a}\mathbf{I}$$

The matrix $\mathbf{a}$ is related to the tensor $\mathbf{G}$ by

$$(\mathbf{G}^{-1})_{ij} = \sum_{k=1}^{N} a_{ik}a_{kj} \tag{5.12}$$

In Stokesian simulations,[27–29] the hydrodynamic force is calculated in every time step by solving the corresponding Stokes problem. The partial differential equation representing the Stokes problem is solved analytically in the form of an infinite series or an integral. The analytical, but not close-form, expressions for the solutions are then evaluated numerically. Pressure-driven

flow of suspensions of spherical particles in a channel has been simulated in this way in Nott and Brady[29] and Brady and Morris.[30]

In order to avoid the time-consuming calculations of hydrodynamic forces in Stokesian calculations, it could be advantageous to consider the fluid itself as composed of particles that have to be, of course, much smaller and much more numerous than the suspended particles. Taking this point of view, we arrive at the setting of classical molecular simulations.[31,32] The governing equations in this setting are only Newton's equations (i.e., ordinary differential equations), and the forces involved are only potential-generated forces among particles. The hydrodynamic interactions arise in these simulations as a result of fluid particle–suspended particle and fluid particle–fluid particle interactions. The potentials for both of these interactions could be chosen to be Lennard–Jones-type potentials. The experience from molecular simulations indicates that a suspended particle will feel the fluid particles as a continuous fluid if there are at least 10^2 fluid particles for one suspended particle. Since we need to consider at least 10^2 suspended particles to see the macroscopic behavior, the minimum number of total particles in the simulation is 10^4. Such a number of particles, and even larger numbers, can be simulated with present-day computers. To the best of our knowledge, simulations of this type have not yet been realized.

However, the idea of simulating both the fluid and the particles suspended in it has been realized already in the context of lattice Boltzmann simulations.[33-35] The space of the position vectors and the velocities in these simulations is strictly discrete (it is a lattice). Such a setting is thus particularly computer friendly. In order to make simulations that are pertinent to fluid behavior, the particle dynamics are modified by adopting an appropriate (Boltzmann-type) dissipation. The dissipation drives the particles to states in which they behave collectively as fluids. An attempt to use the lattice Boltzmann simulations for suspensions is reported in Ladd and Behrend.[35] The suspended particles move in these simulations continuously, and the fluid is regarded as in the lattice Boltzmann setting.

5.4.3 Internal Structure

Now, our point of departure will not be the completely microscopic point of view. We begin our investigation at the level of extended fluid mechanics, with the extension consisting of enlarging the set of state variables. In addition to the five hydrodynamic fields of classical fluid mechanics, we include in the set of state variables other fields. In particular, these will be the fields describing the internal structure of the suspension, i.e., fields describing states of the suspended particles. This type of modeling proceeds in the following three steps:

Step 1. A framework for the time evolution equations is proposed. For example, in classical fluid mechanics, the framework consists of local conservation laws. This framework itself, even before filling it with

details, guarantees that solutions to the governing equations agree with the experimentally observed conservation of the total mass, momentum, and energy.

Step 2. The fields or distribution functions describing the internal structure are suggested. The choice is determined by intended applications of our model and by the requirement of dynamical closedness. The latter requirement is that the time evolution of the selected state variables be sufficiently separated from the time evolution of the rest of the microscopic state variables. The dynamical closedness has to be usually verified indirectly by comparing predictions based on the resulting model with results of experimental observations. If the model is found to be inadequate, another internal state variable set has to be chosen. The intended applications influence the choice of internal state variables by creating a need to choose the state variables that are related as closely as possible to the quantities arising in the experimental observations in our disposition.

Step 3. A realization of the framework for the chosen state variables and for the particular suspension under consideration is searched. In the context of classical fluid mechanics, this third step is called a specification of constitutive relations.

In the rest of this section we shall make a few comments about the first step. In the following section, we shall then make two choices of the internal state variable and show the governing equations.

Let ξ be the internal state variable. The general framework introduced in Step 1 is written formally as

$$\frac{d\xi}{dt} = X(\xi, v)$$

$$\sigma = \Sigma(\xi, v)$$

(5.13)

where v is the fluid velocity and σ is the extra stress tensor. The problem now is to restrict the choice of the functions X and Σ by requiring that solutions to the governing equations agree with some type of experimental observations. We shall provide several examples below.

Hinch and Leal[36–38] have based their work that leads to a restricted form of functions X and Σ on the following considerations: (1) Both X and Σ are required to be frame invariant. This implies that X and Σ do not depend on v but only on ∇v, which denotes the gradient of the fluid velocity. (2) Both X and Σ are required to depend on ∇v only linearly. (3) The time evolution equation of the internal state variable ξ (i.e., the first equation in Equation (5.13)) includes a dissipation term that drives the suspension, in the absence of external forces, to thermodynamic equilibrium. The dissipation term is required to include only one relaxation time (denoted by the symbol λ). This

leads to $X(\xi, \nabla\mathbf{v}) = \alpha(\xi)\nabla\mathbf{v} - \beta(\xi)\lambda$, and $\sigma(\xi, \nabla\mathbf{v}) = \mathbf{a}(\xi):\nabla\mathbf{v} + \mathbf{b}(\xi)$, where $\mathbf{a}$ and $\mathbf{b}$ are fourth- and second-order tensors, respectively. Their choice can be further restricted by additional physical considerations. We shall see below an example of such considerations.

Nonequilibrium thermodynamics offers another very useful framework. The fundamental argument in this type of investigation is the requirement that solutions to the governing equations agree with the experimentally observed compatibility with thermodynamics. For example, it has been shown in Grmela[39] that if the time-reversible part $(d\xi/dt)^{rev}$ of the time evolution of the internal state variable S is governed by the equation

$$\left(\frac{d\xi}{dt}\right)^{rev} = X^{rev}(\xi, \nabla\mathbf{v}) \tag{5.14}$$

(note that in the Hinch–Leal formulation $\mathbf{X}^{rev}(\xi, \nabla\mathbf{v}) = \alpha(\xi):\nabla\mathbf{v}$), then the time-reversible part σ^{el} (i.e., the elastic part) of the extra stress tensor is given by

$$\sigma_{ij}^{el} = -\frac{d\Phi}{d\xi}\frac{\partial X^{rev}}{\partial(\nabla_i v_j)} \tag{5.15}$$

where Φ is the free energy. If we apply this formula to Equation (5.13), we obtain

$$\sigma_{ij}^{el} = -\frac{d\Phi}{d\xi}\alpha_{ij}(\xi) \tag{5.16}$$

If we insert the solution of the first equation in Equation (5.13) into Equation (5.16) (if the gradient of the velocity is considered to be a small parameter, then the approximate stationary solution of the first equation in Equation (5.13) is

$$\xi = \xi_{eq} + \frac{\alpha_{ik}(\xi_{eq})}{\lambda\frac{d\beta}{d\xi}(\xi_{eq})}\nabla_i v_k$$

where ξ_{eq} is a solution of $\beta(\xi) = 0$), we then obtain

$$a_{ijkl} = -\frac{1}{\lambda}\frac{\frac{d\Phi}{d\xi}(\xi_{eq})}{\frac{d\beta}{d\xi}(\xi_{eq})}\alpha_{ij}\alpha_{kl}$$

A systematic utilization of the requirement of compatibility with thermodynamics has led in Grmela[40,41] to a particularly powerful and useful framework. Its most complete formulation, developed in the works of Grmela and

Oettinger,[42,43] is known now under the name GENERIC (General Equation for the Non-Equilibrium Reversible–Irreversible Coupling). Governing equations that are shown in the next two sections provide an illustration of the use and power of this framework.

5.5 One Particle Distribution Function or Its Moments

Now we turn to Step 2 and illustrate some choices of the internal state variable ξ. Jackson[44] and Buyevich[45,46] have suggested the use of one particle phase space distribution function $f(\mathbf{r}, \mathbf{w})$ of the suspended particles as a variable characterizing their states; here $\mathbf{r}$ denotes the position vector and $\mathbf{w}$ is the velocity of the suspended particle in the reference frame moving with the velocity $\mathbf{v}$ of the suspension as a whole. In the context of Equation (5.13), we are thus suggesting that $\xi \equiv f(\mathbf{r}, \mathbf{w})$. Next, we want to find the governing equations playing the role of Equation (5.13), i.e., an equation governing the time evolution of the distribution function (called a kinetic equation) and another equation expressing the extra stress tensor as a function of the distribution function. Buyevich[45,46] has investigated this problem in detail. In what follows, we shall write the governing equations as they arise when GENERIC is used in their derivation. Note that the free energy Φ and the dissipative kinetic coefficients, the quantities through which the individual nature of the suspension is expressed in the governing equations, are left unspecified. We shall also leave open the choice of the free energy and the kinetic coefficients. The dissipative kinetic coefficients consist of a 3×3 symmetric and positive definite matrix $\mathbf{K}$ and a scalar positive coefficient κ. It is possible to show that with an appropriate choice of Φ, $\mathbf{K}$, and κ, the governing equations presented below become an extension of the governing equations derived in Buyevich.[45,46] The governing equations arising in GENERIC and playing the role of Equation (5.13) for $\xi \equiv f(\mathbf{r}, \mathbf{w})$ are the following:

$$\frac{\partial f}{\partial t} = -\frac{\partial}{\partial r_\gamma}(f v_\gamma) - \frac{\partial}{\partial r_\gamma}\left(f \frac{\partial f^*}{\partial w_\gamma}\right) + \frac{\partial}{\partial w_\gamma}\left(f \frac{\partial \rho^*}{\partial r_\gamma} + f \frac{\partial f^*}{\partial r_\gamma} + f w_\beta \frac{\partial v_\beta}{\partial r_\gamma}\right)$$

$$+ \frac{\partial}{\partial w_\gamma}\left(f K_{11}\frac{\partial f^*}{\partial w_\gamma} + f K_{12\beta}D_{\beta\gamma} + f K_{13}\frac{\partial}{\partial r_\gamma}\left(w_\alpha w_\beta \frac{\partial v_\beta}{\partial r_\alpha}\right)\right) - \frac{\partial}{\partial r_\gamma}\left(f\kappa \frac{\partial f^*}{\partial r_\gamma}\right)$$

$$\sigma_{\alpha\beta} = \int d\mathbf{w} f\left(w_\beta \frac{\partial f^*}{\partial w_\alpha} - K_{12\beta}\frac{\partial f^*}{\partial w_\alpha} - K_{22}D_{\alpha\beta} - K_{23\beta}\frac{\partial}{\partial r_\alpha}\left(w_\gamma w_\epsilon \frac{\partial w_\epsilon}{\partial r_\gamma}\right)\right)$$

$$+ \frac{\partial}{\partial r_\gamma}\int d\mathbf{w} f w_\alpha w_\beta\left(K_{13}\frac{\partial f^*}{\partial w_\gamma} + K_{23\epsilon}D_{\epsilon\gamma} + K_{33}\frac{\partial}{\partial r_\gamma}\left(w_\epsilon w_\delta \frac{\partial v_\delta}{\partial r_\epsilon}\right)\right)$$

(5.17)

where

$$f^* = \frac{\partial \Phi}{\partial f}, \quad \rho^* = \frac{\partial \Phi}{\partial \rho}, \quad D_{\alpha\beta} = \frac{1}{2}\left(\frac{\partial v_\alpha}{\partial r_\beta} + \frac{\partial v_\beta}{\partial r_\alpha}\right),$$

and Φ is the free energy. We have used in Equation (5.17) the summation convention that the Greek indices assume the values 1, 2, and 3.

Guided by the experience obtained with kinetic theory, we can expect that a simpler but still sufficiently realistic formulation can be obtained by replacing the one particle distribution function f($\mathbf{r}$, $\mathbf{w}$) by some of its moments. We shall naturally suggest the following moments: $\varphi(\mathbf{r})$ = ½d$\mathbf{w}$f expressing the mass density of the suspended particles, $v_\alpha(\mathbf{r})$ = ½d$\mathbf{w}$fw_α expressing the average velocity of the suspended particles in the frame moving with the velocity $\mathbf{v}$ of the suspension as a whole, and $\tau_{\alpha\beta}(\mathbf{r})$ = ½d$\mathbf{w}$f$w_\alpha w_\beta$ expressing the "quasi-turbulent" motion of the particles. The trace of the fluctuation tensor τ is called a particle temperature (also a quasi-turbulent temperature). The governing equations (Equation (5.17)) in which the distribution function f($\mathbf{r}$, $\mathbf{w}$) is replaced by the moments ($\varphi(\mathbf{r})$, $v(\mathbf{r})$, and $\tau(\mathbf{r})$) have been derived, independently of the kinetic theory developed by Buyevich.[47] In Figure 5.9, we show the comparison of calculations done using this technique with experimental data. The physical situation considered is the pressure-driven flow of a concentrated suspension of neutrally buoyant, noncolloidal spheres in a viscous Newtonian liquid through a channel of rectangular cross section[48]; the solids volume fraction ranges from 0.3 to 0.5. It is found that the fully developed concentration profile is nonuniform but symmetric, with a maximum at the channel midsection. Simultaneously, the fully developed velocity profile is nonparabolic and blunted. Additionally, the time-average squared particle velocity fluctuation profile (akin to the temperature profile) is nonuniform. These effects are all accentuated as the suspension concentration increases, but they can be predicted by theory.

5.6   Position and Velocity Pair Correlation Functions

Again, based on the experience collected in statistical mechanics, we can also expect that the suspended particles may develop structures, in both space and velocity coordinates, that can only be characterized in terms of correlation functions. In the space coordinate, such a structure has indeed been observed in Johma and Reynolds[49] and Zarraga et al.[50] Phan-Thien[51] and Brady[52] have derived the governing equations of the type of Equation (5.13) for $\xi \equiv c(\mathbf{r})$, where $c_{\alpha\beta}(\mathbf{r})$ = ½d$\mathbf{R}$f($\mathbf{r}$, $\mathbf{R}$)$R_\alpha R_\beta$, f($\mathbf{r}$, $\mathbf{R}$) is the configuration space pair correlation function, and $\mathbf{R}$ is the vector connecting two particles. The governing equations in which ξ = f($\mathbf{r}$, $\mathbf{R}$) have also been investigated.[53,54]
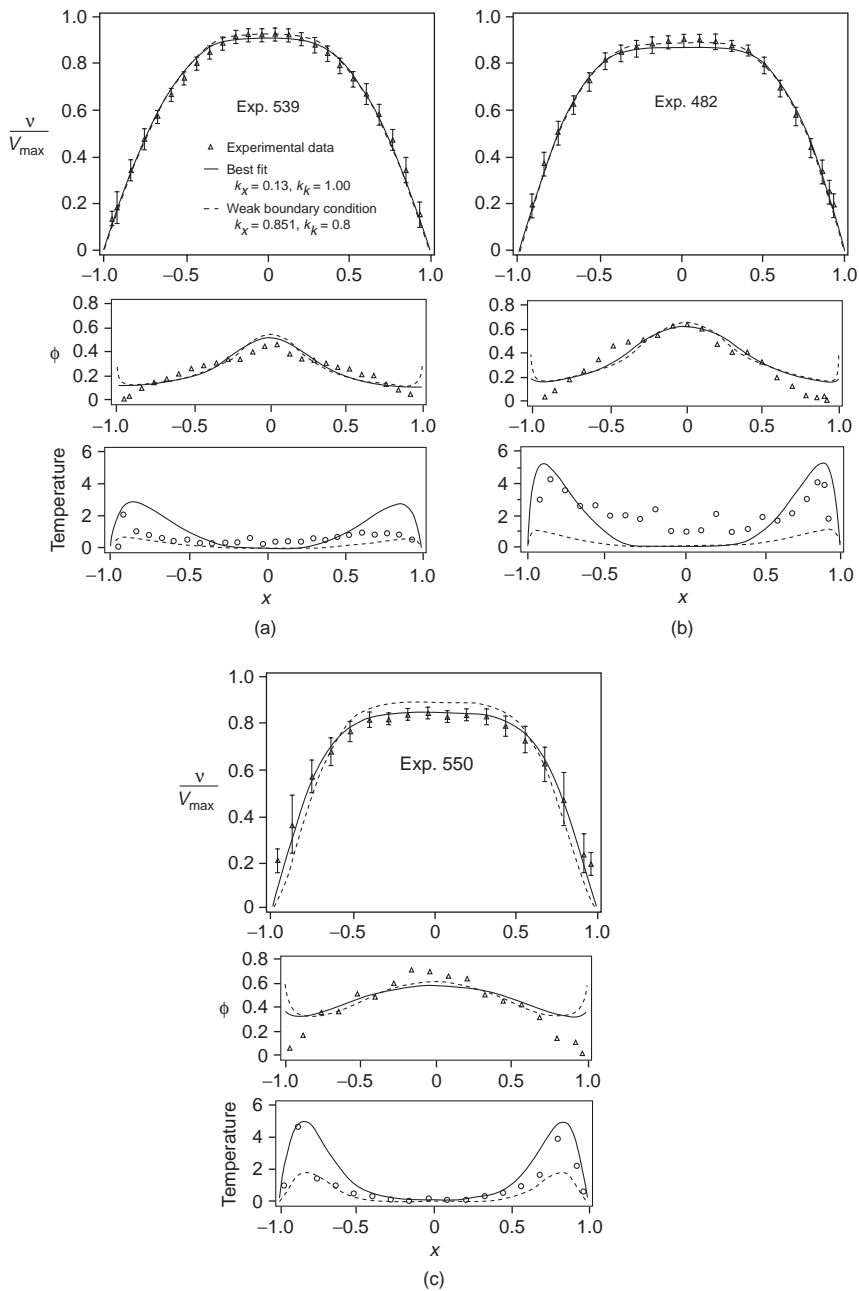
FIGURE 5.9
Comparison of experimental velocity, concentration, and suspension temperature profile data with suspension balance model predictions for (a) $\phi_{bulk} = 0.30$ and $H/a = 14$; (b) $\phi_{bulk} = 0.40$ and $H/a = 24$; and (c) $\phi_{bulk} = 0.50$ and $H/a = 11$. H is half the channel gap, and a is the particle radius. (Reprinted with permission from Lyon, M.K. and L.G. Leal, 1998, *J. Fluid Mech.*, 363:25–77.)

Since the quantities characterizing velocities of the suspended particles have shown to be of great importance in the kinetic-theory-type investigation of suspensions (it is, in particular, the importance of the particle temperature; see Section 5.5), we expect also that velocity pair correlation functions, characterizing the turbulence-type motion of the suspended particles, should be included into the set of state variables. The governing equations (Equation (5.13)) that result are, as they appear in GENERIC analysis, for $\xi \equiv (\mathbf{c}(\mathbf{r}), \mathbf{b}(\mathbf{r}), \mathbf{m}(\mathbf{r}))$, where $c_{\alpha\beta}(\mathbf{r}) = \tfrac{1}{2}d\mathbf{R}d\mathbf{V}R_\alpha R_\beta f(\mathbf{r}, \mathbf{R}, \mathbf{V})$, $b_{\alpha\beta}(\mathbf{r}) = \tfrac{1}{2}d\mathbf{R}d\mathbf{V}V_\alpha R_\beta f(\mathbf{r}, \mathbf{R}, \mathbf{V})$, $m_{\alpha\beta}(\mathbf{r}) = \tfrac{1}{2}d\mathbf{R}d\mathbf{V}V_\alpha V_\beta f(\mathbf{r}, \mathbf{R}, \mathbf{V})$, $f(\mathbf{r}, \mathbf{R}, \mathbf{V})$ is the phase space pair correlation function, and $\mathbf{V}$ is the relative velocity of the two particles connected by the vector $\mathbf{R}$:

$$\frac{\partial c_{ij}}{\partial t} = -\frac{\partial}{\partial r_\alpha}\left(c_{ij}v_\alpha\right) + c_{\gamma i}\frac{\partial v_j}{\partial r_\gamma} + c_{\gamma j}\frac{\partial v_i}{\partial r_\gamma} + 4\left(b_{\gamma i}m^*_{\gamma j} + b_{\gamma j}m^*_{\gamma i}\right) + 2\left(c_{i\gamma}b^*_{j\gamma} + c_{j\gamma}b^*_{i\gamma}\right)$$

$$\frac{\partial b_{ij}}{\partial t} = -\frac{\partial}{\partial r_\alpha}\left(b_{ij}v_\alpha\right) - 4c_{\gamma j}c^*_{\gamma i} + b_{i\gamma}\frac{\partial v_j}{\partial r_\gamma} - b_{\gamma j}\frac{\partial v_\gamma}{\partial r_i} + 4m_{i\gamma}m^*_{\gamma k} + 2b_{i\gamma}b^*_{j\gamma} - 2b_{\gamma j}b^*_{\gamma i}$$

$$- \Lambda_{22}c_{i\gamma}b^*_{\gamma j} - \Lambda_{12}b_{i\gamma}m^*_{\gamma j} - \Lambda_{23}c_{i\gamma}D_{\gamma j}$$

$$\frac{\partial m_{ij}}{\partial t} = -\frac{\partial}{\partial r_\alpha}\left(m_{ij}v_\alpha\right) - m_{\gamma i}\frac{\partial v_\gamma}{\partial r_j} - m_{\gamma j}\frac{\partial v_\gamma}{\partial r_i} - 4\left(b_{i\gamma}c^*_{\gamma j} + b_{j\gamma}c^*_{\gamma i}\right) \qquad (5.18)$$

$$- 2\left(m_{\gamma i}b^*_{\gamma j} + m_{\gamma j}b^*_{\gamma i}\right) - \Lambda_{11}m_{i\gamma}m^*_{\gamma j} - \frac{1}{2}\Lambda_{12}\left(b_{i\gamma}b^*_{\gamma j} + b_{j\gamma}b^*_{\gamma i}\right)$$

$$- \frac{1}{2}\Lambda_{13}\left(b_{i\gamma}D_{\gamma j} + b_{j\gamma}D_{\gamma i}\right)$$

$$\sigma_{\alpha\beta} = -2c_{\beta\gamma}c^*_{\gamma\alpha} + 2m_{\alpha\gamma}m^*_{\gamma\beta} + b_{\alpha\gamma}b^*_{\beta\gamma} - b_{\gamma\beta}b^*_{\gamma\alpha} - \Lambda_{13}b_{\alpha\gamma}m^*_{\gamma\beta}$$

$$- \Lambda_{23}c_{\alpha\gamma}b^*_{\gamma\beta} - \Lambda_{33}D_{\alpha\beta}$$

where

$$c^*_{ij} := \frac{\partial \Phi}{\partial c_{ij}}, \quad b^*_{ij} := \frac{\partial \Phi}{\partial b_{ij}}, \quad m^*_{ij} := \frac{\partial \Phi}{\partial m_{ij}},$$

ϕ is the free energy and

$$\begin{pmatrix} \Lambda_{11}\mathbf{m} & \Lambda_{12}\mathbf{b} & \Lambda_{13}\mathbf{b} \\ \Lambda_{12}\mathbf{b} & \Lambda_{22}\mathbf{c} & \Lambda_{23}\mathbf{c} \\ \Lambda_{13}\mathbf{b} & \Lambda_{23}\mathbf{c} & \Lambda_{33} \end{pmatrix}$$

is the positive definite matrix of dissipative kinetic coefficients.

From Equation (5.18) we can recover the equations derived by Phan-Thien[51] as follows: If we assume that **b** and **m** evolve in time much faster than **c**, we can put in the second and third equations in Equation (5.18),

$$\frac{\partial \boldsymbol{b}}{\partial t} \approx 0, \quad \frac{\partial \boldsymbol{m}}{\partial t} \approx 0$$

and solve these two equations to obtain **b** and **m** expressed in terms of **c**. By inserting these expressions into the first and the fourth equations in Equation (5.18), we obtain an extension of the governing equations derived in Phan-Thien.[51]

5.7 Concluding Remarks

In the first two sections we have provided fundamental information about experimental measurements on noncolloidal suspensions. The rest of the review is a guide to the difficult but very important procedure leading from the microscopic viewpoint of suspensions to the viewpoint described in the first two sections. First, we discuss direct simulations in which trajectories of the suspended particles are calculated. The macroscopic information is then extracted from the trajectories. This approach is often seen as an "experimental" investigation of the micro → macro passage. In view of the rapidly growing availability of computing power, this technique will certainly be used more and more often in the future. However, an understanding of the passage between microscopic and macroscopic properties that has the potential to satisfy fully our curiosity and also our need to predict and control phenomena can be met only in traditional modeling in which the macroscopic properties of the suspension are related to the time evolution of its internal structure. The models of this type are constructed by first choosing a state variable describing the internal structure and then formulating its time evolution and its relation to the macroscopic properties of interest. The more microscopic is the chosen state variable (i.e., the more it is able to describe microscopic details), the more fundamental is the model and our understanding, but also the more complex are the governing equations and, consequently, the more difficult it is to make meaningful predictions. In the construction of the governing equations, it is useful to proceed in two stages. First, a general framework is formulated; second, the framework is filled by using physical insight. The framework arises in an attempt to identify a mathematical structure of the governing equations that guarantees that their solutions agree with results of certain universal experimental observations (as, for example, the conservation laws and the compatibility with thermodynamics).

References

1. Titow, W.V. and B.J. Lanham. 1975. *Reinforced Thermoplastics*, New York: Wiley.
2. Gupta, R.K. 2000. *Polymer and Composite Rheology*, 2nd ed., New York: Marcel Dekker.
3. Overend, I.J., R.R. Horsley, R.L. Jones, and R.K. Vinycomb. 1984. A new method for measurement of rheological properties of settling slurries, in *Proceedings of the IX International Congress on Rheology*, Acapulco, Mexico, 2:583–590.
4. Kraynik, A.M., J.H. Aubert, and R.N. Chapman. 1984. The helical screw rheometer, in *Proceedings of the IX International Congress on Rheology*, Acapulco, Mexico, 4:77–84.
5. Mooney, M. 1931. Explicit formulas for slip and fluidity, *J. Rheol.*, 2:210–222.
6. Yoshimura, A. and R.K. Prud'homme. 1988. Wall slip corrections for Couette and parallel disk viscometers, *J. Rheol.*, 32:53–67.
7. Magnin, A. and J.M. Piau. 1990. Cone-and-plate rheometry of yield stress fluids: study of an aqueous gel, *J. Non-Newtonian Fluid Mech.*, 36:85–108.
8. Navickis, L.L. and E.B. Bagley. 1983. Yield stresses in concentrated dispersions of closely packed, deformable gel particles, *J. Rheol.*, 27:519–536.
9. Hunter, R.J. 1986. *Foundations of Colloid Science*, Vol. 1, Oxford: Clarendon Press, pp. 538–543.
10. Poslinski, A.J. 1987. The Effect of Particulates and Matrix Properties on the Rheological and Extrusion Behavior of Particulate-Filled Polymer Composites, M.S. thesis, Chemical Engineering, State University of New York, Buffalo, NY.
11. Gupta, R.K. 1994. Particulate suspensions, in *Flow and Rheology in Polymer Composites Manufacturing*, S.G. Advani, Ed., Amsterdam: Elsevier Science, pp. 9–51.
12. Poslinski, A.J., M.E. Ryan, R.K. Gupta, S.G. Seshadri, and F.J. Frechette. 1988. Rheological behavior of filled polymeric systems: II. The effect of a bimodal size distribution of particulates, *J. Rheol.*, 32:751–771.
13. Maron, S.H. and P.E. Pierce. 1956. Application of Ree-Eyring generalized flow theory to suspensions of spherical particles, *J. Colloid Sci.*, 11:80–95.
14. Kataoka, T., T. Kitano, M. Sasahara, and K. Nishijima. 1978. Viscosity of particle filled polymer melts, *Rheol. Acta*, 17:149–155.
15. Kitano, T., T. Kataoka, and T. Shirota. 1981. An empirical equation of the relative viscosity of polymer melts filled with various inorganic fillers, *Rheol. Acta*, 20:207–209.
16. Chimmili, S., D. Doraiswamy, and R.K. Gupta. 1998. Shear-induced agglomeration of particulate suspensions, *Ind. Eng. Chem. Res.*, 37:2073–2077.
17. Frankel, N.A. and A. Acrivos. 1967. On the viscosity of a concentrated suspension of solid spheres, *Chem. Eng. Sci.*, 22:847–853.
18. Jarzebski, G.J. 1981. On the effective viscosity of pseudoplastic suspensions, *Rheol. Acta*, 20:280–287.
19. Poslinski, A.J., M.E. Ryan, R.K. Gupta, S.G. Seshadri, and F.J. Frechette. 1988. Rheological behavior of filled polymeric systems I: Yield stress and shear-thinning effects, *J. Rheol.*, 32:703–735.
20. Ball, R.C. and P. Richmond. 1980. Dynamics of colloidal dispersions, *Phys. Chem. Liq.*, 9:99–116.
21. Krieger, I.M. 1972. Rheology of monodisperse lattices, *Adv. Colloid Interface Sci.*, 3:111–136.

22. Batchelor, G.K. 1972. *An Introduction to Fluid Mechanics*, Cambridge, U.K., Cambridge University Press.

23. Happel, J. and H. Brenner. 1965. *Low Reynolds Hydrodynamics*, Englewood Cliffs, NJ: Prentice-Hall.

24. Ermak, D.L. and J.A. McCammon. 1978. Brownian dynamics with hydrodynamic interactions, *J. Chem. Phys.*, 69:1352–1360.

25. Murphy, T.J. and J.L. Aguirre. 1972. Brownian motion of N interacting particles. I. Extension of the Einstein diffusion relation to the N-particle case, *J. Chem. Phys.*, 57:2098–3010.

26. Rotner, J. and S. Prager. 1969. Variational treatment of hydrodynamic interactions, *J. Chem. Phys.*, 50:4831–4840.

27. Durlofsky, L., J.F. Brady, and G. Bossis. 1987. Dynamic simulation of hydrodynamically interacting particles, *J. Fluid Mech.*, 180:21–49.

28. Brady, J.F. and G. Bossis. 1988. Stokesian dynamics, *Ann. Rev. Fluid Mech.*, 20:111–157.

29. Nott, P.R. and J.F. Brady. 1994. Pressure-driven flow of suspension: simulation and theory, *J. Fluid Mech.*, 275:157–199.

30. Brady, J.F. and J.F. Morris. 1997. Microstructure of strongly sheared suspensions and its impact on rheology and diffusion, *J. Fluid Mech.*, 348:103–139.

31. Allen, M.P. and D.J. Tidesley. 1987. *Computer Simulation of Liquids*, Oxford: Clarendon Press.

32. Dlugogorski, B.Z., M. Grmela, P.J. Carreau, and G. Lebon. Viscometric functions for FENE and generalized Lennard-Jones dumbbell liquids in Couette flow: molecular dynamics study, *J. Non-Newtonian Fluid Mech.*, 48:303–335, 1993; Microscopic and mesoscopic results from non-equilibrium molecular dynamics modeling of FENE dumbbell liquids, *J. Non-Newtonian Fluid Mech.*, 49:23–62, 1993; Rheology of several hundred rigid bodies, *J. Non-Newtonian Fluid Mech.*, 53:25–64, 1994; Direct modeling of flow of FENE fluids, *Rheol. Acta*, 34:384–396, 1995.

33. Benzi, R., S. Succi, and M. Vergassola. 1993. The lattice Boltzmann equation: theory and applications, *Phys. Rep.*, 222:145–197.

34. Wolf-Gladrow, D.A. 2000. *Lattice-Gas Cellular Automata and Lattice Boltzmann Models*, Lecture Notes in Mathematics 1725, Springer.

35. Ladd, A.J.C. 1993. Short-time motion of colloidal particles: numerical simulations via fluctuating Lattice-Boltzmann equation, *Phys. Rev. Lett.*, 70:1339–1342; O. Behrend. 1995. Solid-fluid boundaries in particle suspension simulations via the lattice Boltzmann method, *Phys. Rev.*, 52E:1164–1175.

36. Hinch, E.J. 1977. An averaged-equation approach to particle interactions in a fluid suspension, 83:695–720.

37. Hinch, E.J. and L.G. Leal. 1975. Constitutive equations in suspension mechanics: Part 1. General formulation, *J. Fluid Mech.*, 71:481–495.

38. Hinch, E.J. and L.G. Leal. 1976. Constitutive equations in suspension mechanics: Part 2. Approximate forms for a suspension of rigid particles affected by Brownian rotations, *J. Fluid Mech.*, 76:187–208.

39. Grmela, M. 1985. Stress tensor in generalized hydrodynamics, *Phys. Lett.*, 111A:41–44.

40. Grmela, M. 1984. Particle and bracket formulations of kinetic equations, *Contemporary Math*, 28:152–132.

41. Grmela, M. 1988. Hamiltonian dynamics of incompressible elastic fluids, *Phys. Lett.*, 130A:81–86.

42. Grmela, M. and H.C. Oettinger. 1997. Dynamics and thermodynamics of complex fluids: general formulation, *Phys. Rev.*, 56E:6620–6633.
43. Oettinger, H.C. and M. Grmela. 1997. Dynamics and thermodynamics of complex fluids: illustration of the general formalism, *Phys. Rev.*, 56E:6633–6650.
44. Jackson, R. 1963. The mechanics of fluidized beds, *Trans. Instrum. Chem. Eng.*, 41:13–25.
45. Buyevich, Yu.A. 1971. Statistical hydromechanics of disperse systems: Part 1. Physical background and general equations, *J. Fluid Mech.*, 49:489–507; On the fluctuations of concentration in disperse systems: the random number of particles in a fixed volume, *Chem. Eng. Sci.*, 26:1195–1201.
46. Buyevich, Yu.A. 1999. Fluid dynamics of fine suspension flow, in *Advances in the Flow and Rheology of Non-Newtonian Fluids: Part B*, D.A. Siginer et al., Eds., Amsterdam: Elsevier, pp. 1237–1297.
47. Nott, P.R. and J.F. Brady. 1994. Pressure-driven flow of suspensions: simulation and theory, *J. Fluid Mech.*, 275:157–199.
48. Lyon, M.K. and L.G. Leal. 1998. An experimental study of the motion of concentrated suspensions in two-dimensional channel flow: Part 1. Monodisperse systems, Part 2: Bidisperse systems, *J. Fluid Mech.*, 363:25–77.
49. Johma, A.I. and P.A. Reynolds. 1993. An experimental study of the first normal stress difference-shear stress relationship in simple shear flow for concentrated shear thickening suspensions, *Rheol. Acta*, 32:457–464.
50. Zarraga, I.E., D.A. Hill, and D.T. Leighton, Jr. 2000. The characterization of the total stress of concentrated suspensions of noncolloidal spheres in Newtonian fluids, *J. Rheol.*, 44:185–220.
51. Phan-Thien, N. 1995. Constitutive equation for concentrated suspensions in Newtonian liquids, *J. Rheol.*, 39:679–695.
52. Brady, J.F. 2000. Normal stresses in suspensions, in *XIIIth International Congress on Rheology*, Cambridge U.K., 1, pp. 34–37.
53. Lionberger, R.A. and W.B. Russel. 1997. A Smoluchowski theory with simple approximations for hydrodynamic interactions with concentrated dispersions, *J. Rheol.*, 41:399–425.
54. Brady, J.F. 1993. The rheological behavior of concentrated colloidal dispersions, *J. Chem. Phys.*, 99:567–581.

6

Properties and Optical Behavior of PE/Vinyl Copolymer IPN-Like Networks

Roberto Greco

CONTENTS

6.1 Introduction

Multicomponent polymeric systems have acquired in recent times a great scientific and commercial consideration. The chemical nature of the components, their miscibility or immiscibility, their mechanical compatibilization, the type of processing used — all determine the material morphology and hence the final system properties. Therefore, the design of copolymers, blends, and semi- and interpenetrating polymer networks (IPNs) has received much attention in the literature for the possibility of tailoring their properties to specific end uses.[1–8]

For instance, a polymer such as polystyrene (PS), brittle at room temperature (RT), has been toughened by a variety of ways, giving rise to diverse engineering materials like high-impact polystyrene (HIPS), acrylonitrile-butadiene-styrene (ABS), and styrene-butadiene-styrene (SBS). Similarly, several other brittle polymers, like polypropylenes, polyamides, epoxies, polyesters, and polycarbonates, have been toughened by different blending techniques.[9]

A more recent development concerns the last type of multicomponent systems listed above, the IPNs, used in several fields as tough plastics, vibration damping compounds, ion-exchange resins, artificial teeth, burn dressings, and so on.[10] In such materials the polymers are cross-linked, providing a mechanism for controlling domain sizes and shapes and reducing creep and flow as well. There are diverse manners of obtaining IPNs; the most common are listed below:

- *Sequential IPNs*: After making network A, monomer B is swollen in it, together with a suitable cross-linker and an activator, and polymerized *in situ*.
- *Simultaneous IPNs*: Two monomers are mixed together with cross-linkers and activators, and the synthesis is carried out simultaneously by noninterfering reactions.
- *Semi-IPNs*: Materials in which one or more polymers are cross-linked and one or more polymers are non-cross-linked.
- *Gradient IPNs:* Materials in which composition and degree of cross-linking vary throughout on a macroscopic level from site to site.
- *Thermoplastic IPNs:* Systems involving only physical cross-links (such as block copolymer morphologies, ionic linkages, and crystallites) rather than chemical ones. They behave as normal IPNs at customary temperatures of service but will flow at sufficiently elevated ones, like thermoplastic elastomers.

IPN-like systems, made of low-density polyethylene (**PE**) and vinyl polymer networks, obtained by a particular process of synthesis, are the topic of this chapter. Such IPN materials do not strictly fall in one of the categories listed above, as one can note in the discussion that follows. The work

presented here is a review of several papers published in recent years,[11–20] most of them fruit of a joint project between the Polymer Institute of the Slovakian Academy of Sciences (involved mainly in the IPN synthesis) and the Institute of Research and Technology of Plastic Materials of the Italian Research Council (involved mostly in the IPN characterization). During the course of such a work, particular optical behaviors are observed, whose analysis and interpretation is the main object of this chapter. Thermal, mechanical, dynamic mechanical, swelling-in-a-solvent (CCl_4) tests, wide-angle x-ray diffraction, and morphology observations were performed as well, in order to get a more complete material characterization.

6.2   Experimental

6.2.1   Materials

The materials used were the following: (1) low-density **PE**, type Bralen RA 2-19, with a melt flow index (MFI) of 1.7 to 2.3 g/10 min; (2) a series of vinyl monomers combined in different copolymers: styrene (**S**), butyl methacrylate (**B**), methyl methacrylate (**M**), dodecyl methacrylate (**D**), and ethyl hexyl methacrylate (**EH**) monomers; (3) divinyl benzene (DVB) (**d**) (molecular weight (MW) = 130.19 and refractive index (RI) = 1.562) or 1,4-butanediol-dimethacrylate (**b**) (MW = 226.27 and RI = 1.456) as copolymer cross-linkers; and (4) 2.5-dimethyl-2.5-di-(tert-butylperoxy)-hexane (Luperox 101) (**p**), as a radical initiator.

6.2.2   IPN Preparation

PE was dissolved in a monomer or in a mixture of diverse vinyl monomers by stirring at 105°C. 1 mol% of **d** (or alternatively, 1 mol% of **b**) was added to the mixture, together with a fixed amount (3 wt%) of the radical initiator (**p**). The effect on properties of the copolymer/**PE** molar ratio was investigated in the initial papers,[11–13] and then it was kept constantly equal to 1 for all the subsequent papers.[14–21]

   After the **PE** dissolution, the whole mixture was poured in small and flat containers consisting of two glass plates sealed on three sides by a rubber tube of about 2.7-mm diameter (determining grossly the final thickness of IPN sheets) and put in an oven. The synthesis reaction occurred for 6 h at 120°C and a further hour at 160°C.

6.2.3   Thermal Treatment of the Samples

A thermal treatment of the samples was made in order to free the materials from unreacted low-molecular-weight species (such as **S**, **B**, **M**, **D**, and **EH**)

still present after the IPN synthesis and to stabilize the IPN properties. All the samples were heated in a vacuum oven for about 1 h from RT up to 185°C, and kept at this temperature for a further hour. Finally, the heating was turned off and the samples left under vacuum until the oven reached RT.

6.2.4 Specimen Preparation

Specimens of different shapes were obtained from the IPN slabs:

1. Rectangular bars of different dimensions, cut at RT by a saw:
   - $50 \times 3.5 \times 2.7$ mm for swelling measurements in CCl_4
   - $25 \times 12 \times 2.7$ mm for dynamic mechanical tests
2. Other specimens, cut at 170°C by suitable hollow punches:
   - Dumbbells (50-mm length, 8-mm width, 27×4 mm gauge section, and 17-mm gauge length) for tensile tests
   - Discs of 2.7-mm thickness and different diameters: (a) for optical observations in transmitted light (12 mm); (b) for wide-angle x-ray tests (40 mm)

6.2.5 Techniques

6.2.5.1 Wide-Angle X-Ray Scattering

Wide-angle x-ray scattering (WAXS) profiles were obtained at RT in reflection mode by a PW 1050/71 Philips powder diffractometer (CuKα nickel-filtered radiation), scanning continuously the 2θ angle. From the curves, the **PE** crystalline content was calculated according to the Hermans–Weidinger method[21,22] from the ratio between the crystalline diffracted area and the total one (containing also the amorphous halo).

6.2.5.2 Swelling Tests

Swelling measurements in CCl_4 were performed at RT on rectangular bars. This solvent was chosen because of its solubility parameter ($17.7 \ J^{1/2}/cm^{3/2}$), sufficiently close to those of **PB** (17.8 to 18.4), **PS** (17.4 to 19), and **PE** (15.8 to 17.1), as reported in the literature.[23] The increment of the specimens length was measured at equilibrium from time to time as a function of the variables of interest.

6.2.5.3 Dynamic Mechanical Tests

Dynamic mechanical scanning tests in shear were performed on rectangular specimens by a Bohlin VOR analyzer in order to detect the glass transition temperature (T_g) at a frequency of 1 Hertz and a scanning rate of 2°C/min.

6.2.5.4 Mechanical Tensile Tests

Stress–strain curves were performed on dumbbell-shaped specimens at RT and at a crosshead speed of 12 mm/min by a Daventest machine. Young's modulus (E), yield stress (σ_y), elongation at break (σ_r), and stress at break (ε_r) were calculated from the curves on an average of five specimens for each IPN.

6.2.5.5 Impact Properties

Charpy impact tests were performed at RT on razor-notched IPN specimens. The stress as a function of time to deformation was recorded by an automated fracture pendulum manufactured by Ceast Inc.

6.2.5.6 Optical Properties

An automatic exposure meter, mounted on an optical microscope (Axioskop Pol, manufactured by Carl Zeiss Inc.), was used to measure the amount of light crossing the specimens. The time to exposure, needed to impress a film of a given sensitivity in a camera (type MC-100), was monitored by an electronic digital display and recorded as a function of temperature, from RT up to 180°C.

The constant amount of light, Q, crossing the specimens is given by:

$$Q = L \cdot t \tag{6.1}$$

where L is the amount of light per unit time, and t is the exposure time. The exposure meter was calibrated against the time value of a glass sample, t_g, of the same IPN thickness.

From Equation (6.1), one can write

$$Q = t_g \cdot L_g = t_{IPN} \cdot L_{IPN} \tag{6.2}$$

Assuming a 100% transmittance for the glass, the IPN one is given by

$$(T_r)_{IPN} = L_{IPN} = 100 \cdot t_g / t_{IPN} \tag{6.3}$$

6.3 Results and Discussion

6.3.1 Effect of PE/Vinyl Polymer Ratio on IPN Properties

The first investigated system was **PE** with styrene (**S**) as the vinyl polymer,[10] with 0.5 wt% of divinylbenzene (**d**) as the S cross-linking agent, and 3 wt% of di-tert-butyl peroxide (**p**) as radical initiator. The **PE** was dissolved in the

S monomer; the polymerization of the IPNs occurred at 120°C for 5 h, followed by another hour at 160°C. One can assume that polymerization and cross-linking of **S** occur first, incorporating **PE** chains in the **S** network. At the last stages of the synthesis, carried out at a higher temperature, a **PE** network is formed as a result of the presence of the radical initiator. The **PE/S** ratio was varied according to the following values: 0/100, 1/3, 1/1, 3/2, and 100/0 (10–13).

A thermal differential scanning calorimetry (DSC) and a thermo mechanical analysis showed a decrease of the **PE** crystallinity with increasing network density.[11]

Dynamic mechanical tests showed the existence of two distinct **PE** and **S** phases, which were confirmed by transmission electron microscopy (TEM) observations.[12] The **PS** domains at all **PE/PS** ratios result to be encapsulated in a thin **PE** network, as shown in Figure 6.1, where a TEM micrograph of a **PE/PS** IPN (50/50 molar ratio) is shown. As reported in Table 6.1, the higher the **PS/PE** ratio, the larger the **PS** domains and the broader the particle size distribution. This is more clearly illustrated in Figure 6.2, where curves of the **PS** particle distribution frequency, $\Delta N/N$, are plotted as a function of the particle diameter for IPN with diverse **PS/PE** molar ratios, as indicated.

However, both the components are interconnected, forming a **PS/PE** IPN. This is clearly shown in Figure 6.3, where stress–strain curves of several **PS/PE** IPNs are shown, as a function of the **d** copolymer cross-linker content, added to the initial reactant mixture.[13,14] The specimens were tested at a temperature greater than the **PS** T_g (110°C), where the materials exhibit a rubbery behavior. The curve slopes become steeper and steeper with increasing the **d** amount, indicating an increase of the **PS** network degree of cross-
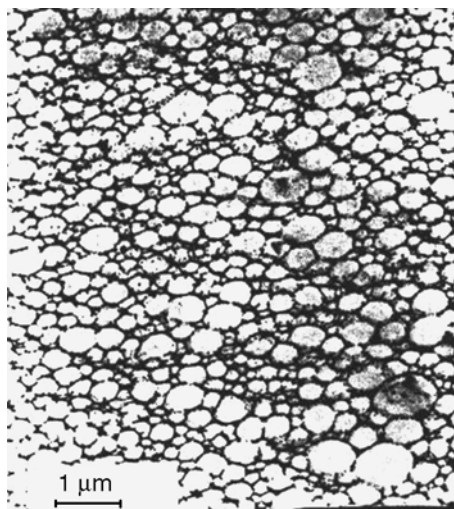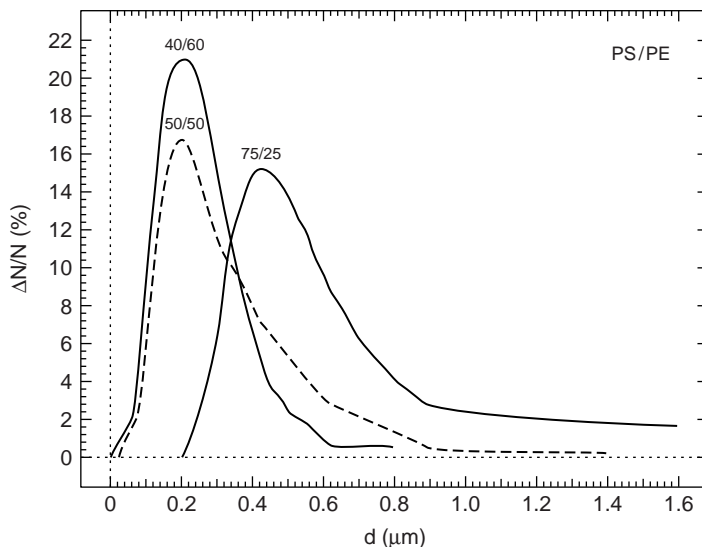

FIGURE 6.1
TEM photograph of a **PS/PE** (50/50 molar ratio) IPN.

TABLE 6.1

Average Diameter and Diameter Range
as a Function of the PS/PE Molar Ratio

PS/PE Molar Range	d_m (μm)	Δd_m (μm)
40/60	0.2–0.3	0.05–0.8
50/50	0.2–0.4	0.05–1.2
75/25	0.4–0.6	0.05–10

FIGURE 6.2
Frequency $\Delta N/N$ of **PS** particle distribution vs. particle diameter profiles at diverse **PS/PE** molar ratios, as indicated.

linking. It is to be underlined that one cannot exclude the presence of some inter-cross-links between **PE** and **PS** networks. Therefore, these materials have been defined as IPN-like systems. However, according to the synthesis procedure and in spite of the assumption of the sequential network formation (first the **PS** network formation and then the **PE** one), the **PE/PS** systems can be considered close to simultaneous IPNs. The mechanical change due to the **d** increment is more clearly shown in Figure 6.4, where the Young's modulus (top figure), calculated from the curves of Figure 6.3, is reported on the left-hand-side axis as a function of the **d** content. It appears to be linearly increasing with the **d** content. In the same figure, the equilibrium storage shear modulus G_e', on the right-hand-side axis, obtained at 200°C by dynamic mechanical measurements, is linearly increasing with **d**. It represents the global cross-link density of both **PE** and **PS** networks. However, since the **d** amount can influence only the **PS** network, such a dependence is further evidence that the **PS** behaves as an interconnected system with
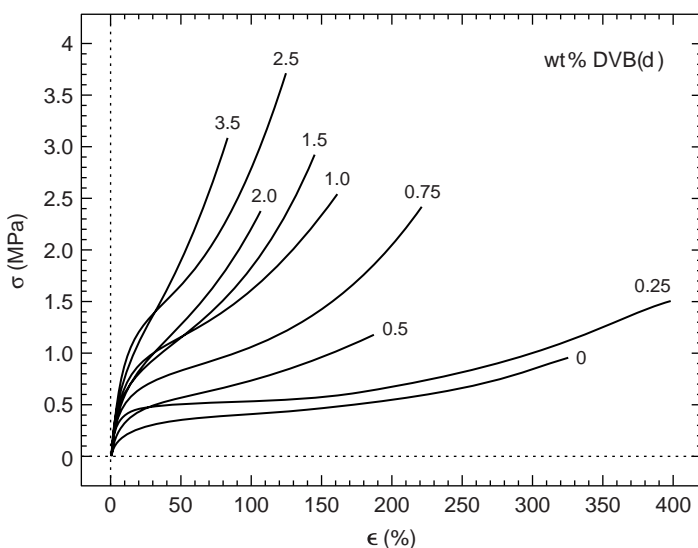
FIGURE 6.3
Stress–strain curves for a **PS/PE** 50/50 IPN for different **d** contents, as indicated.

the **PE** network. The trend is further confirmed by the bottom figure of Figure 6.4, where the increment of the specimen length, due to its swelling in a solvent (CCl_4), is reported as a function of the copolymer cross-linker content. The swelling of the IPNs has a linear decreasing trend with enhancing the **d** content, in complete agreement with the dynamic mechanical storage modulus at equilibrium, shown above (top figure).

6.3.2 IPN Crystallinity Content

For all the investigated IPNs, of constant **PE**/vinyl copolymer ratio equal to 1,[14–21] the **PE** crystallinity after the IPN synthesis was reduced about six times ($4 \div 5\%$) in comparison with the **PE** homopolymer value (about 30%), due to the cross-linking of **PE**.

6.3.3 IPN Optical Behavior and Properties

6.3.3.1 Effect of Copolymer Composition

S was partially or totally substituted by **B** in the vinyl polymer, obtaining a S-co-B random copolymer.[15] The copolymer composition variation, encompassing the whole range from pure **S** up to pure **B**, gave rise to a particular optical effect, which can be observed in Figure 6.5. In this figure a series of disks, having a different IPN copolymer composition (horizontal direction) and degree of cross-linking (vertical direction), are shown: the disks, lying in the horizontal basic line, start from a condition of high opacity on the left-
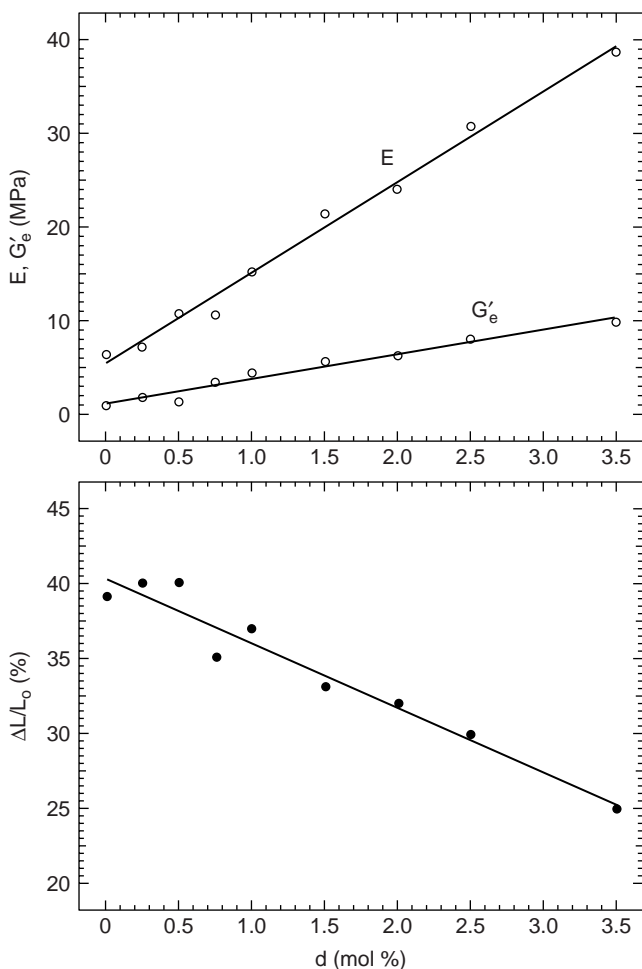
FIGURE 6.4
Young's modulus and equilibrium storage modulus, measured at 200°C (top figure), and swelling length increment at equilibrium in CCl_4 (bottom figure), measured at RT, as a function of the copolymer cross-linker **d** content.

hand side, turning then to a more and more transparent one with increasing the **B** content, up to a complete transparency condition at about 75 mol% of **B** (the four x characters underneath the disks become clearly visible at such a composition). Beyond this value for further **B** increments, the specimens become again more and more opaque.

Now, as it is possible to observe for **PE/PS** IPNs in Figure 6.1 and for **PE**/P(S-co-B) IPNs from the scanning electron microscopy (SEM) image of Figure 6.6, the system is made of two incompatible components, a cellular **PE** structure, made of thin walls, containing inside the cells copolymer round particles. Moreover, the copolymer domains have sizes comparable or higher
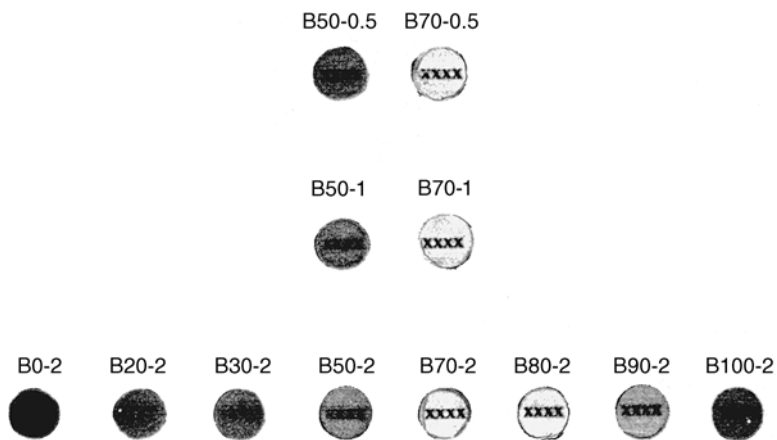
FIGURE 6.5
IPN **PE**/S-co-B copolymer circular samples of different copolymer compositions (the code BXX-YY, where XX stands for the copolymer **B** molar percentage and YY for the copolymer cross-linker content, is specified over each specimen).
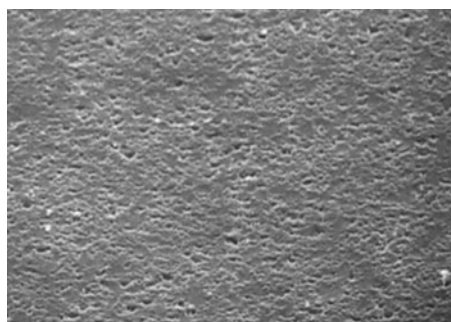

FIGURE 6.6
SEM image of a B80 IPN with 2 mol% of copolymer cross-linker.

than those of the light wavelength; hence all the IPNs should be opaque, due to the dispersion caused by the impingement of light on the **PS** particles inside the material. Since, in spite of this, they become transparent at a given copolymer composition, the only reasonable explanation is the matching of the refractive indexes of **PE** and copolymer networks at that copolymer composition. As a matter of fact, as reported in the literature,[25] at RT the refractive index of **PE** (1.49) is intermediate between those of **PS** (1.59) and **PB** (1.483). Therefore, at a certain copolymer composition, the copolymer RI, lying in between the **PS** and **PB** values, will reach the **PE** value, giving rise to a transparent sample; this phenomenon occurs at about 75% of **B**. This effect is schematically illustrated in Figure 6.7, where the refractive index of **PE** and S-co-B copolymer is reported as function of the copolymer composition. A quadratic curve is constructed from the RIs of pure **PS** and **PB** and
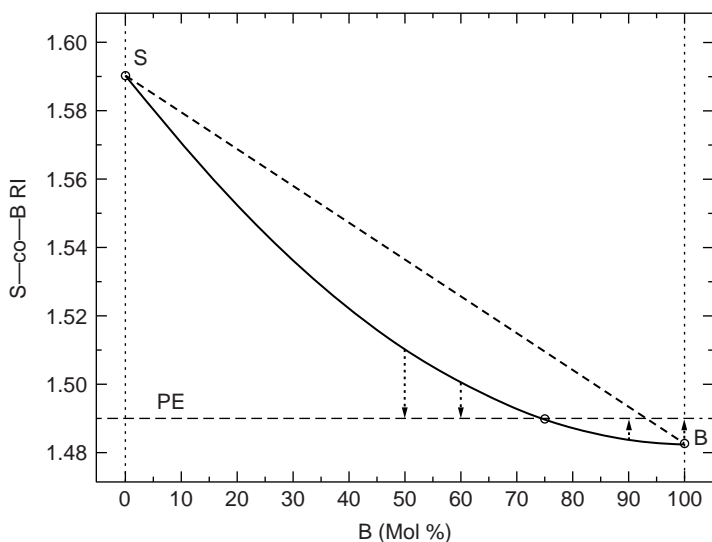
FIGURE 6.7
Copolymer refractive index at RT as a function of **B** copolymer content.

imposing at 75% of **B** an RI value equal to that of **PE** (1.49), since the relative specimen appears to be completely transparent at such a composition.

With respect to the mechanical behavior, all parameters, such as Young's modulus, stress, and elongation at break, measured at a temperature higher than the copolymer T_g (128°C), decrease their values with increasing the **B** content. Furthermore, the impact properties, measured at RT, show an increasing brittleness in the same direction, as shown in Figure 6.8, where the Charpy impact stress, measured at RT, is reported as a function of time to deformation for IPNs of different **B** amounts, at a constant copolymer cross-linker content (**d** = 2 mol%). The systems become more and more brittle with increasing the **B** copolymer content.

6.3.3.2 Effect of Temperature

In Figure 6.7 at compositions lower than 75% of **B** (value for which the RI matching occurs), the copolymer RI is greater than the **PE** one (arrows downward), whereas at higher values the situation is reversed (arrows upward). Now in the first case, if the temperature is increased from RT up, the specimens become more and more opaque; a different behavior is observed in the other case: there is an opaque-to-transparent transition going from RT up to a given temperature (T_m), followed from a reverse transparent-to-opaque transition going from such a temperature to higher temperatures. This different trend as a function of composition and temperature is illustrated in Figure 6.9 for three IPNs containing 50, 70, and 90 mol% of **B**, respectively. B50 (arrow downward) starts opaque and becomes more and

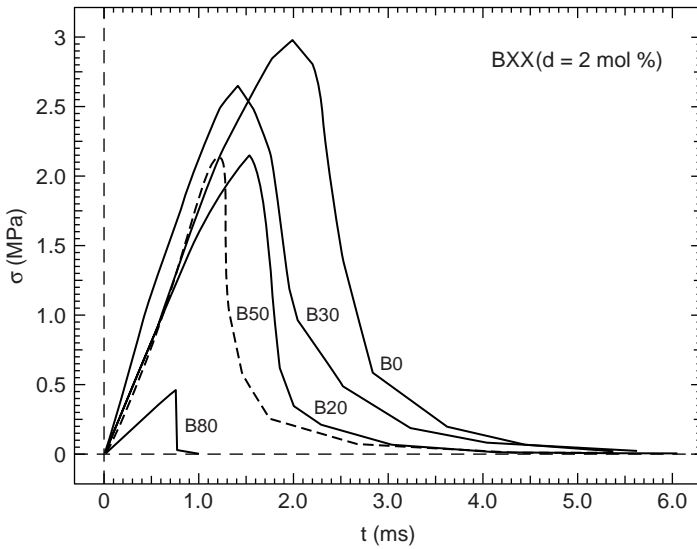**FIGURE 6.8**
Charpy impact stress as a function of time to deformation for B-co-S IPNs at different **B** mol% contents, as indicated.
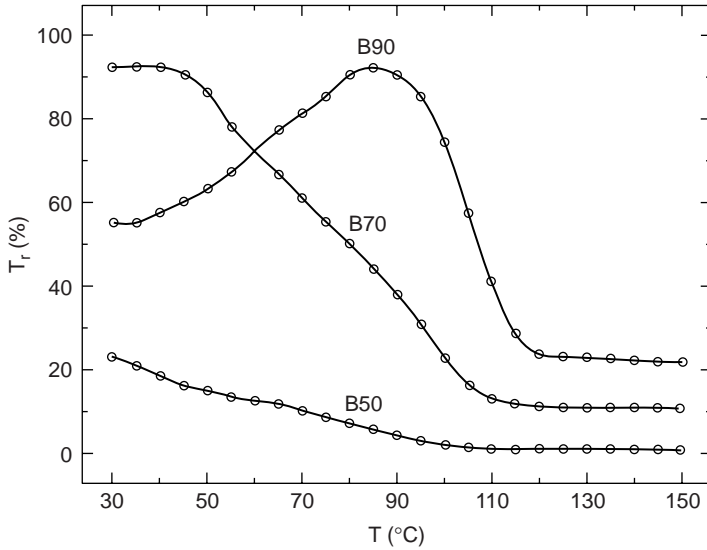

FIGURE 6.9
Transmittance, T_r as a function of testing temperature for three **PE**/B-co-S IPNs with different **B** mol% contents, as indicated.
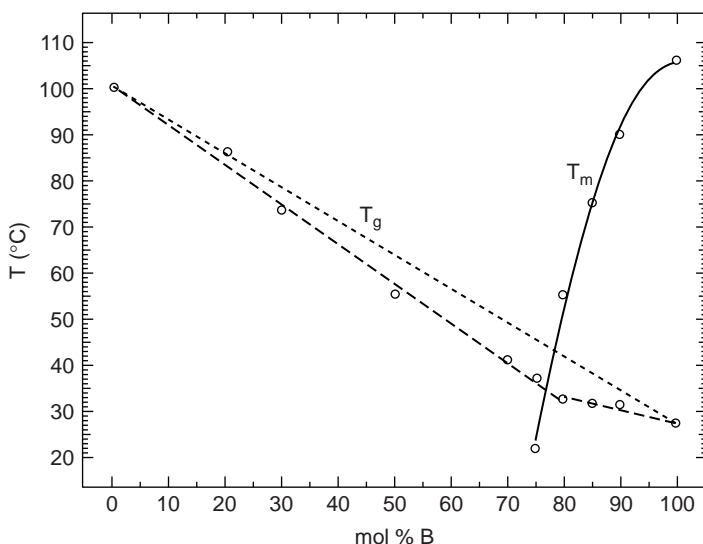
FIGURE 6.10
Glass transition temperature, T_g, and transparency temperature, T_m, vs. **B** copolymer mol% content, as indicated.

more opaque with increasing T; B70 (whose RI is very close to that of **PE** at RT) starts almost transparent and then becomes more and more opaque; B90 (arrow upward) exhibits a maximum value, T_m, at about 85°C.

The T_m as a function of the **B** copolymer content is reported in Figure 6.10, together with the relative T_g. The knowledge of both variables is useful for a graphical treatment of the data in order to obtain the RI temperature trends for IPN **PE** and copolymer networks, as illustrated in Figure 6.11, where the RI is reported as a function of T for **PS**, **PB**, and their copolymers, together with their T_g trend.

In this figure, the RI curves of pure **PS** and **PB**, as a function of T, have been calculated from the corresponding curves of the specific volume against T, available in the literature.[24] As a matter of fact, one can utilize one of the formulas, relating RI to the specific volume, proposed by van Krevelen:[24]

$$RI = [(1 + 2R_{LL}/V)/(1 - R_{LL}/V)]^{1/2}$$

where R_{LL}/V is the ratio between the molar refraction according to Lorentz and Lorenz[24] and the molar volume. R_{LL}/V can be easily calculated by the method of group contributions developed by van Krevelen.[23,24]

The **PS** T_g is given by the break point of the relative curve, and the **PB** T_g value is corresponding to RT; therefore, the relative curve, drawn at T > RT, is that corresponding to its rubbery behavior. Imposing the RI matching between the different compositions of the copolymer (having a parallel trend to that of the rubbery traits of the **PS** and **PB** curves) and the **PE** network,
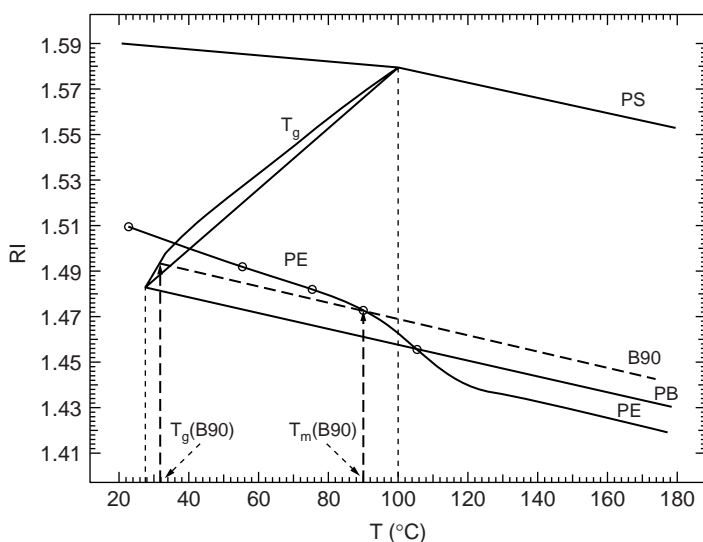
FIGURE 6.11
Refractive index of **PS**, **PB**, B90, and **PE** (calculated imposing the experimental knowledge of T_m and T_g) as a function of the testing temperature, T.

one can draw the RI of **PE** in the IPN at the different investigated temperatures (T_m and T_g of B90 have been indicated by arrows, as an example: the corresponding **PE** value of matching with the copolymer RI is given by the intersection between the B90 RI rubbery straight line, starting from the T_g value, and the vertical line of the relative measured T_m). The empty circles on the **PE** RI curve have been calculated in such a way.

From this semiquantitative analysis of the **PE** and copolymer RI curves vs. T (Figure 6.11), it is possible to understand the trend of the curves of Figure 6.9, taking as an example the B90 IPN.

Starting from the left-hand side at RT, the specimen is opaque due to the RI difference between **PE** and the B90 RI; this difference is reduced more and more with increasing T up to 90°C, where the material becomes transparent; beyond 90°C the RI difference is reversed and increases more and more, making the material again opaque, until it reaches an almost constant value of opacity.

6.3.3.3   *Effect of the Copolymer Cross-Linking Degree*

In the **PE**/B-co-S IPNs of different compositions, different amounts of copolymer cross-linker, DVB (**d**), were added to the initial reactant mixture according to the following values: 0.5, 1.0, 1.5, and 2.0 mol%. The influence on the optical properties is illustrated in Figure 6.12, where the transparency temperature, T_m, is reported as a function of the copolymer cross-linker content and the copolymer composition (in the range of 75 to 100 mol% of **B**). The trends are all linear with respect to the **d** content, with straight lines of
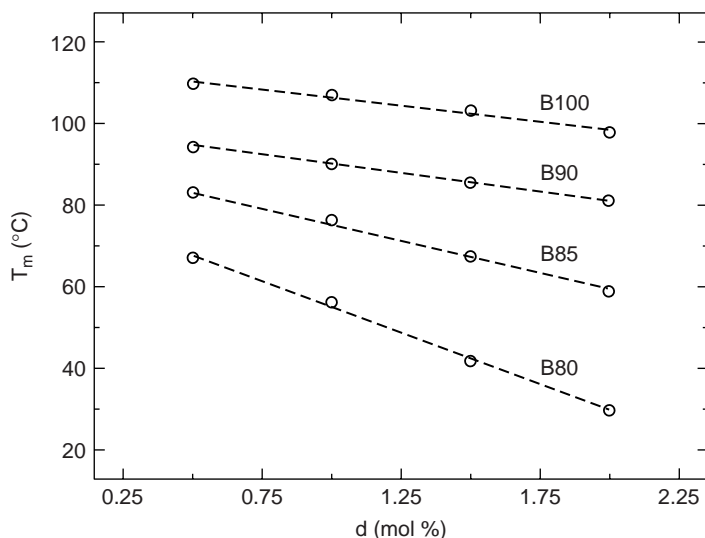
FIGURE 6.12
Transparency temperature, T_m, as a function of the copolymer cross-linker content, **d**, for different copolymer compositions, **B**, as indicated.

decreasing slope with increasing the **B** amount in the copolymer.[16] In fact, at **B** contents (50 and 70 mol%) lower than those relative to Figure 6.12, it is not possible to detect by a visual inspection any difference of opacity among specimens with a diverse degree of cross-linking, as shown in Figure 6.5 above.

From Figure 6.12 the formal dependence of T_m, as a function of **d** and **B**, can be expressed in general as a linear dependence with respect to **d**, with slope and intercept functions of **B**:

$$T_m = f(\mathbf{B}) \cdot \mathbf{d} + g(\mathbf{B})$$

And specifying the values of f(**B**) and g(**B**), both of a quadratic form, from Figure 6.12, one obtains

$$T_m = [-0.073 \; \mathbf{B}^2 + 14.08 \; \mathbf{B} - 682] \; \mathbf{d} + 0.02 \; \mathbf{B}^2 + 5.3 \; \mathbf{B} - 215$$

Utilizing the above equation, it is possible (keeping constant the **PE**/vinyl copolymer molar ratio and equal to 1) to design materials with a desired transparency temperature, T_m, just setting the two synthesis variables of the copolymer: the composition, **B**, and the degree of cross-linking, **d**.

With respect to the impact properties, in Figure 6.13 the Charpy impact stress, measured at RT, is reported as a function of the time to deformation for a B50 IPN having a different degree of copolymer cross-linking: the
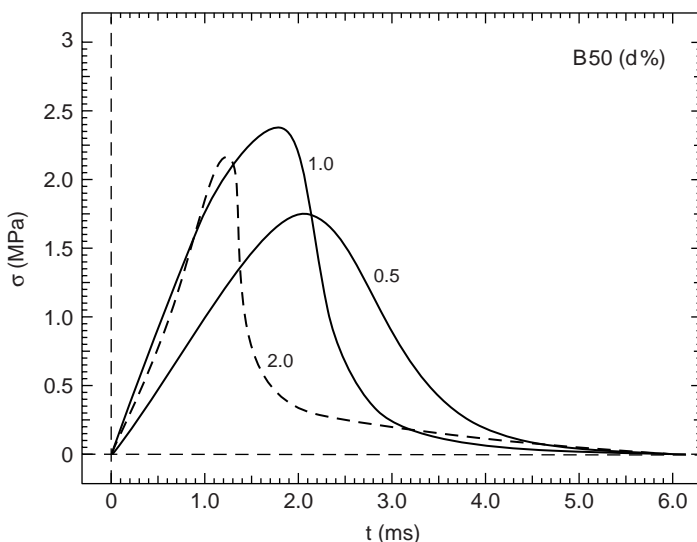
FIGURE 6.13
Charpy impact stress as a function of time to deformation for a B50 IPN at different degrees of copolymer cross-linking, **d**, as indicated.

system becomes less and less ductile with increasing the copolymer degree of cross- linking, **d**.

In other words, the tighter the vinyl network with increasing the **d** value, the less ductile the whole IPN.[16]

6.3.3.4   *Effect of the Cross-Linker Nature*

The effect of the chemical nature of the copolymer cross-linker was also investigated,[19] utilizing two different copolymer cross-linkers: DVB, **d** (RI = 1.562), and 1,4-butanediol-dimethacrylate, **b** (RI = 1.456).

The main results for the optical behavior are shown in Figure 6.14, where for **PE**/B-co-S IPNs the transparency temperature, T_m (top figure); the glass transition temperature, T_g (intermediate figure); and the copolymer refractive index, RI (bottom figure); are reported as a function of the copolymer **B** content, cross-linked with the two different cross-linkers, **d** and **b,** as indicated on the curves.

The **PE**/B-co-S IPNs with the **b** cross-linker exhibit all over the copolymer composition range T_m values higher than those of the **d** one (top figure). This is due to its lower T_g values (intermediate figure) (the relative IPN(**b**)s are slightly softer materials than the IPN(**d**)s ones). In the bottom figure, two different curves relative to IPN(**b**)s and IPN(**d**)s can be drawn, indicating that at RT, where the transparency temperature is slightly different for the two copolymer cross-linkers. This effect, of course, plays its role giving rise to different RI(T) curves in a plot analogous to that of Figure 6.11.
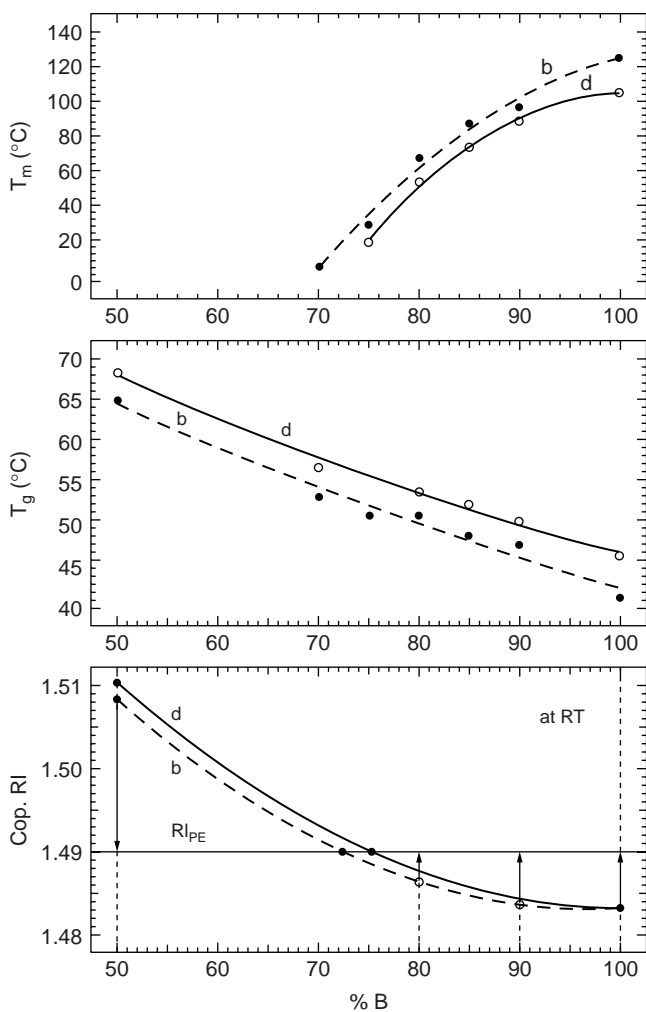
FIGURE 6.14
Transparency temperature, T_m (top figure); glass transition temperature, T_g (intermediate figure); and copolymer refractive index, RI (bottom figure); for **PE**/B-co-S IPNs as a function of the copolymer **B** mol% content, cross-linked with two different cross-linkers, **d** and **b**, as indicated.

Also, the tensile properties are influenced by the type of copolymer, as shown in Figure 6.15, where stress–strain curves are reported for the two different cross-linkers.

The **d** cross-linker yields more rigid IPNs (see curves of top figure) than those obtained with the **b** one, due to the presence of the benzene ring with respect to the softer **B** chain. This is confirmed by the T_g values as well, as shown in the intermediate plot of Figure 6.14.[19]
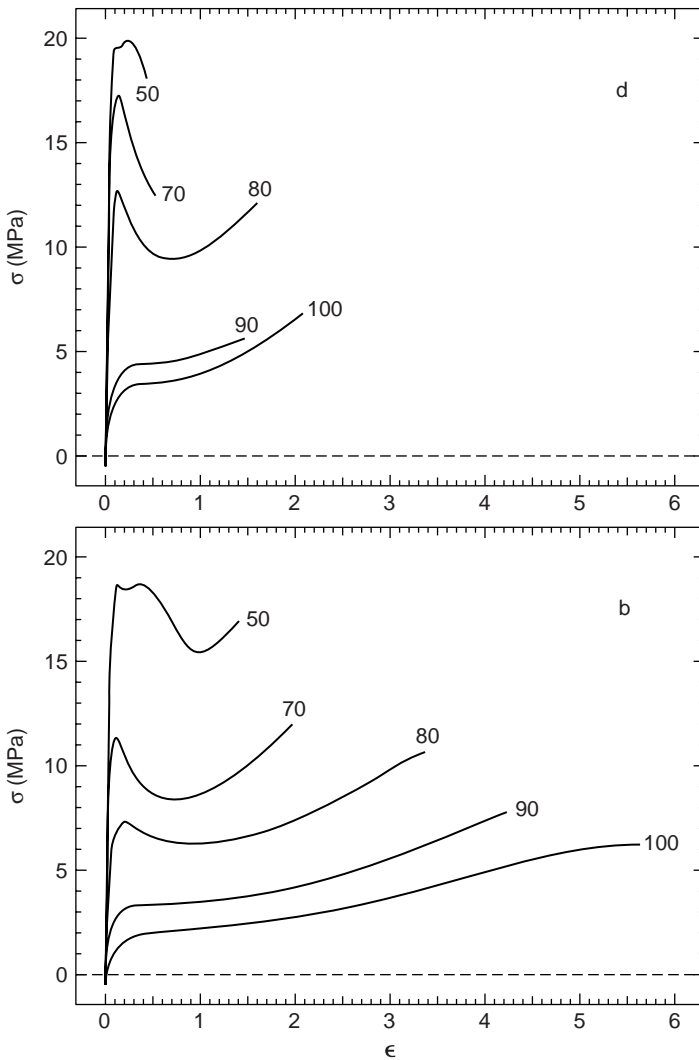
FIGURE 6.15
Stress–strain curves for B-co-S IPNs with different copolymer cross-linkers: **d** (top figure), **b** (bottom figure).

6.3.3.5   Effect of a Different S Comonomer

The effect on the optical IPN behavior of using different **S** comonomers in the vinyl copolymer was investigated as well.[20] In particular, dodecyl methacrylate (**D**) and ethyl hexyl methacrylate (**EH**) monomers were used, and their results were compared with those relative to **PE/B-co-S** IPNs. The optical behavior is illustrated in Figure 6.16, where T_g (top figure) and T_m (bottom figure) as a function of the **S** mol% content are reported for all three IPNs (**PE/B-co-S**, **PE/D-co-S**, and **PE/E-co-S**). The three comonomers, **B**,
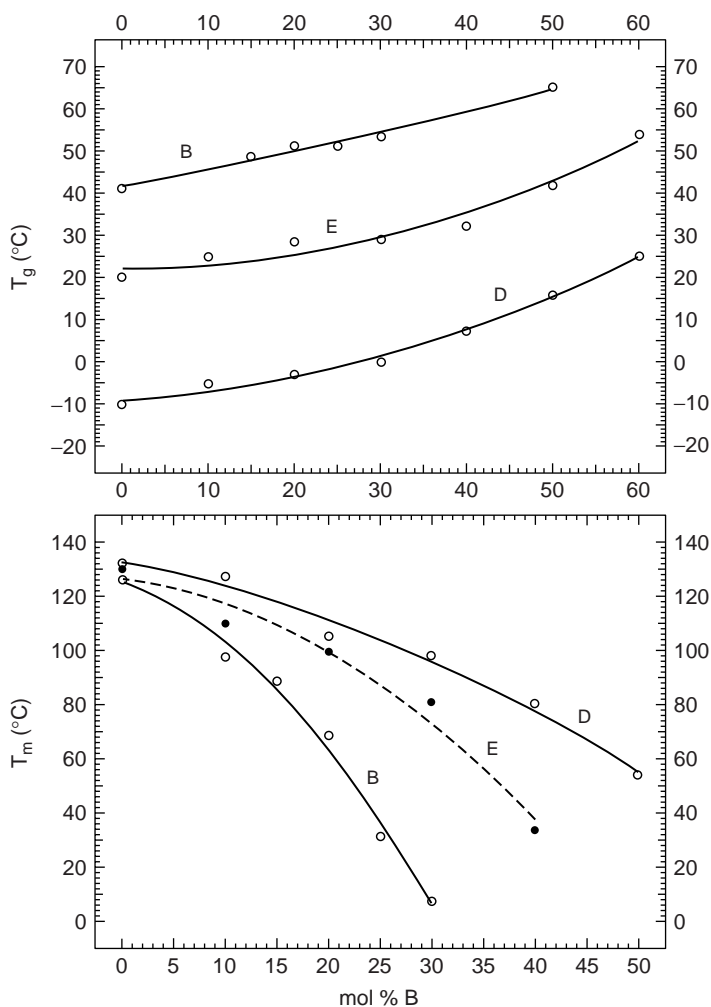
FIGURE 6.16

T_g (top figure) and T_m (bottom figure) as a function of the **S** mol% content for **PE/B-co-S**, **PE/D-co-S**, and **PE/EH-co-S** IPNs.

EH, and **D**, have different levels of T_g, which in turn yield different transparency temperatures, T_m.

Since T_g and T_m curves are of a quadratic form for all three **S** comonomer IPNs, it is possible to get for these IPNs a direct linear correlation between these two variables, as shown in Figure 6.17. In this particular case, the knowledge of the copolymer T_g is sufficient to provide that of T_m.

Of course, the mechanical behavior is also strongly influenced by the chemical nature of the chosen **S** comonomer (**B**, **D**, or **EH**). In Figure 6.18, the Young's moduli of the different IPNs are compared. According to the characteristics of the **S** comonomer, the system results to be more or less
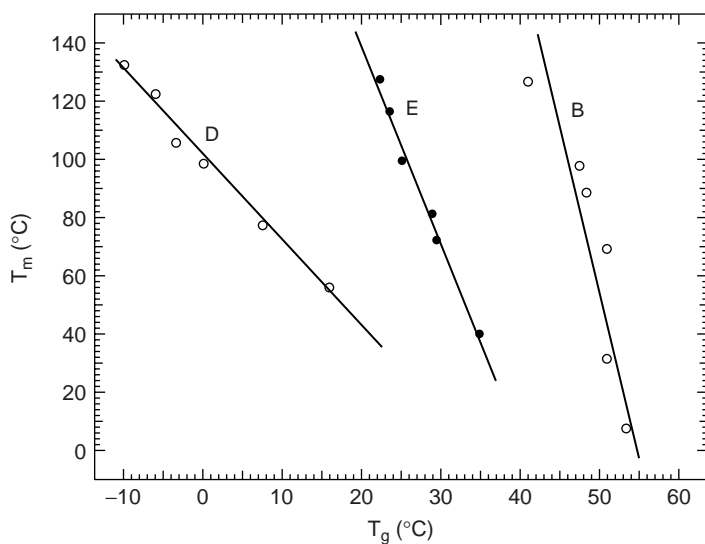
FIGURE 6.17
T_m as a function of T_g for **PE/B-co-S**, **PE/D-co-S**, and **PE/EH-co-S** IPNs.
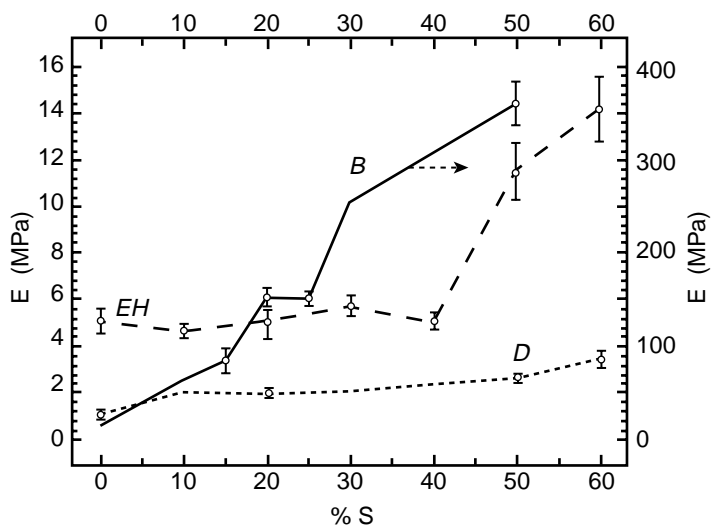

FIGURE 6.18
Young's modulus of **B**, **D**, and **EH** IPNs as a function of the **S** copolymer content.

rigid, due to their diverse chemical structure. At equal compositions, the **D** IPNs exhibit low moduli, which increase only slightly with increasing the **S** copolymer content.

The **EH** ones show values about two times higher than the previous ones, up to 40% of **S**, and then increase much more for further **S** increments. The **B** IPNs exhibit much higher **E** values, due to the shorter lateral chain of butyl methacrylate **S** comonomer with respect to the ethyl hexyl and dodecyl ones.

6.3.3.6   Influence of a Different B Comonomer

The **S** was totally substituted in the vinyl copolymer by methyl methacrylate (**M**). Also in this case, the **PE/B-co-M** IPNs exhibit an optical behavior analogous to that of the **PE/comonomer-co-S** IPNs.[18] In Figure 6.19, a plot analogous to that of Figures 6.7 and 6.12 illustrates this case at RT. The RIs of **PM** and **PB** are 1.49 and 1.483, respectively; therefore, the specimens with a composition in the range of 50 to 100 mol% of **B** are opaque at RT. Their RI difference is represented by the arrows all directed downward (see Figure 6.19). This is similar to the case of **PE/B-co-S** IPNs, discussed above, having a **B** content greater than 75 mol% (cf. Figure 6.7). Also in this case, an increase in temperature determined the appearance of a maximum in the transparency vs. temperature curves. This is illustrated in Figure 6.20, where the T_r is reported against T. The curves show classical peaks, and their maxima define the relative T_m, decreasing with increasing the **M** content in B-co-M copolymer, as indicated by the arrow, pointing to the left-hand side of the plot.

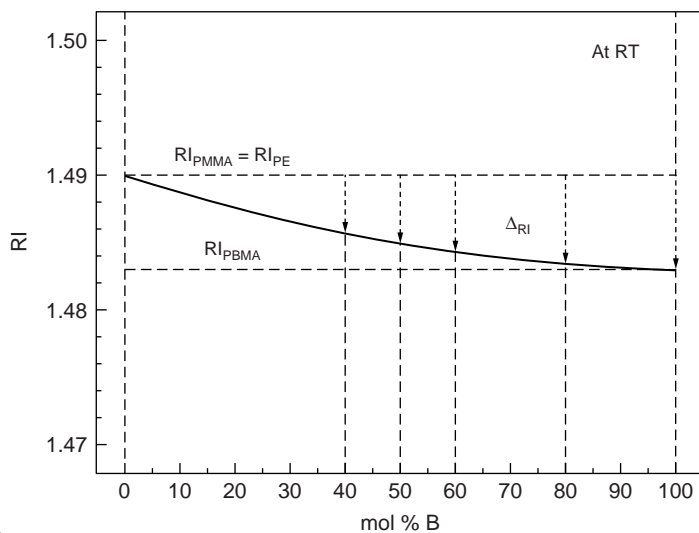**FIGURE 6.19**
Schematic representation of RI as a function of **B** composition for **PE/B-co-M** IPNs.
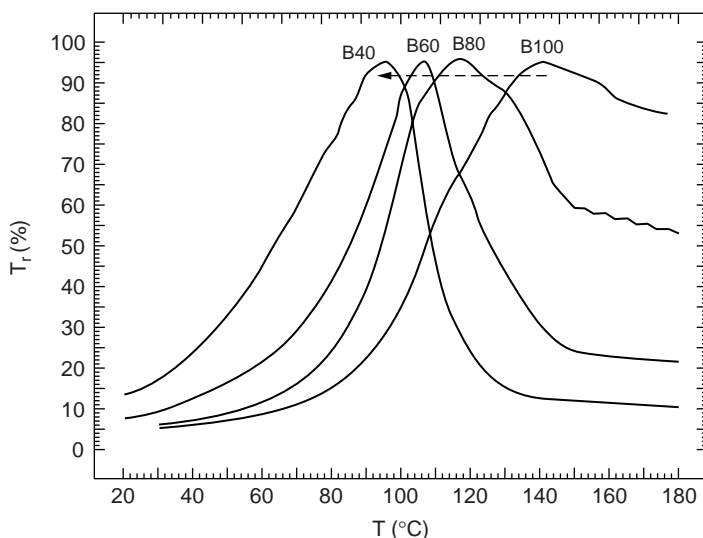
FIGURE 6.20

Transmittance, T_r as a function of the testing temperature, T, for **PE**/B-co-M IPNs of different copolymer **B** mol% contents, as indicated.

The relative T_g and T_m values are reported in Figure 6.21. The T_g exhibits a decreasing linear trend with increasing the **B** content (with absolute values a few degrees lower than the homopolymer ones), whereas T_m shows a more than linear increase in the same direction.

6.4 Conclusion

A series of IPN-like systems, made of a particular low-density **PE** and different vinyl polymers, have been investigated, varying from time to time the **PE/PS** ratio, the copolymer composition, the degree of copolymer cross-linking, the nature of the **S** comonomer, the type of the **B** comonomer, and the kind of copolymer cross-linker.

All the IPNs containing a vinyl copolymer but the **PE/PS** ones exhibited a particular optical behavior, strongly influenced by the copolymer composition and the other investigated variables. Morphological observations indicate a two-phase system in all the cases with copolymer dispersed but interconnected particles, larger in dimensions than the light wavelength. A plausible explanation of such a behavior has been provided on the basis of a matching of the refractive indexes between **PE** and copolymer networks and of particular temperature dependences of the RI of the two networks. The latter are determined by the occurrence in the investigated temperature
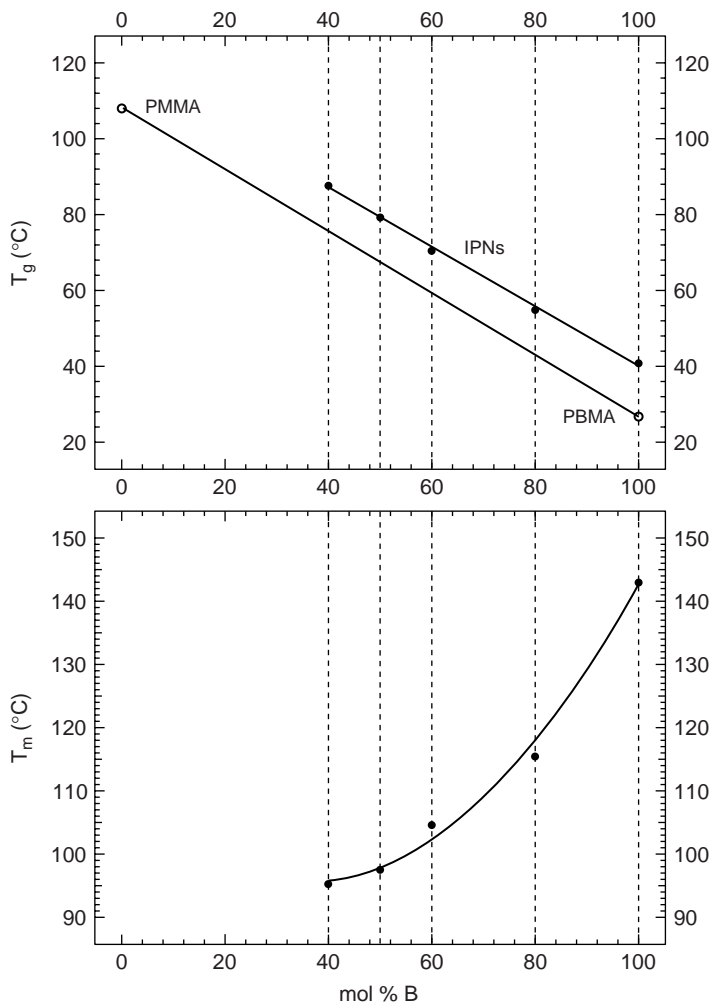
FIGURE 6.21
Glass transition temperature, T_g (top figure), and transparency temperature, T_m (bottom figure), for **PE**/B-co-M IPNs as a function of the copolymer **B** content.

field of the copolymer glass transition and the melting of the small **PE** crystallites, still remaining after the IPN synthesis.

From the data presented above, it is possible to design in the diverse cases materials with desired optical features, just operating on the synthesis variables, particularly copolymer composition and degree of cross-linking.

On the other hand, the other properties, such as thermal, swelling, mechanical, and impact ones, are also depending on the above-mentioned variables, allowing an even more accurate material design with wanted mechanical or impact properties.

The kind of optical mechanisms above illustrated have also been found active in other systems, such as, for instance, blends and IPNs made of **PM** and ethylene vinyl acetate (**EVA**) copolymers.[26–29] The optical behavior of these IPNs may be exploited in the field of optoelectronics.

References

1. L.H. Sperling. *Recent Advances in Polymer Blends, Graft, and Blocks*. New York: Plenum Press, 1974.
2. J.A. Manson and L.H. Sperling. *Polymer Blends and Composites*. New York: Plenum Press, 1976, p. 271.
3. L.H. Sperling. *Interpenetrating Polymer Network and Related Materials*. New York: Plenum Press, 1981, p. 51.
4. R.A. Dickie, S.S. Labana, and R.S. Bauer. *Cross-Linked Polymers, Chemistry Properties and Applications*, ACS Symposium Series. New York: ACS, 1988, p. 376.
5. D. Klempler, L.H. Sperling, and L.A. Utracki. *Interpenetrating Polymer Networks*, Adv. in Chem. Series, Vol. 239, New York: 1994.
6. A.A. Collyer, Ed. *Rubber Toughened Engineering Plastics*. London: Chapman & Hall, 1994.
7. L.H. Sperling, V. Mishra. The current status of interpenetrating polymer networks, in *IPNs Around the World: Science and Engineering*, S.C. Kim and L.H. Sperling, Eds., John Wiley & Sons, New York, 1997, pp. 1–25.
8. S.C. Kim and L.H. Sperling, Eds., *IPNs Around the World: Science and Engineering*, John Wiley & Sons, New York, 1997.
9. L.H. Sperling. Interpenetrating polymer networks: an overview, in *Interpenetrating Polymer Networks*, Adv. in Chem. Series, Vol. 239, D. Klempner, L.H. Sperling, and L.A. Utracki, Eds. New York: 1994, pp. 3–38.
10. E. Borsig, J. Hrouz, A. Fiedlerovà, and M. Ilavsky. The preparation of IPNs of polystyrene–polyethylene and poly(butyl methacrylate)–polyethylene and their dynamic mechanical behavior. *J. Macromol. Sci. Pure Appl. Chem.*, A27:1613–1620, 1990.
11. E. Borsig, A. Fiedlerovà, K.G. Hausler, R.M. Sambatra, and G.H. Michler. Structure and properties of an interpenetrating polymer network-like system consisting of polystyrene–polyethylene: 1. Synthesis, elastomeric and thermo analytical characterization. *Polymer*, 34:4787–4792, 1993.
12. E. Borsig, A. Fiedlerovà, and G.H. Michler. Structure and properties of an interpenetrating polymer network-like system consisting of polystyrene–polyethylene: 2. Electron microscopic investigation. *Polymer*, 37:3959–3963, 1996.
13. R. Greco, M.F. Astarita, A. Fiedlerovà, and E. Borsig. Polystyrene–polyethylene interpenetrating-like networks: influence of the vinyl network cross-linking agent on IPN properties. *Adv. Polym. Technol.*, 13:65–73, 1994.
14. E. Borsig, A. Fiedlerovà, K.G. Hausler, G.H. Michler, and R. Greco. Interpenetrating polymer network (IPN)–like systems. *Macromol. Symp.*, 83:147–156, 1994.
15. R. Greco, A. Fiedlerovà, U. Schulze, and E. Borsig. Polyethylene-poly(butyl methacrylate-co-styrene) copolymers interpenetrating–like networks: I. Influence of the copolymer composition on interpenetrating polymer network properties. *J. Macromol. Sci. Pure Appl. Chem.*, A32:1957–1972, 1995.

16. R. Greco, M. Iavarone, A. Fiedlerovà, and E. Borsig. Optical properties on IPN-like networks: I. Polyethylene/poly(butyl methacrylate-co-styrene) copolymer systems. *J. Macromol. Sci. Pure Appl. Chem.*, A36:305–325, 1999.
17. E. Borsig, A. Fiedlerovà, R. Greco, G.H. Michler, J. Pionteck, and U. Schulze. Morphology of IPN-like systems consisting of polyethyelene and vinyl co-polimers. *J. Macromol. Sci. Phys.*, B38:541–547, 1999.
18. R Greco, M. Iavarone, A. Fiedlerovà, and E. Borsig. Optical properties on IPN-like networks: II. Polyethylene/poly(butyl methacrylate-co-methyl methacrylate) copolymer systems. *J. Macromol. Sci. Pure Appl. Chem.*, A37:433–446, 2000.
19. R. Greco, M. Iavarone, A. Fiedlerovà, and E. Borsig. Optical properties of IPN-like networks polyethylene/poly(butyl methacrylate-co-styrene) copolymer systems: III. Influnce of copolymer cross-linkers. *Polymer*, 42: 5089–5095, 2001.
20. R. Greco, M. Iavarone, A. Fiedlerovà, and E. Borsig. Optical properties of polyethylene/styrene-co-methacrylate copolymers IPN-like networks: effect of different methacrylate comonomers on properties. *J. Mat. Sci.*, 37:3389–3395, 2002.
21. P.H. Hermans and A. Weidinger. On the determination of the crystalline fraction of polyethylene from x-ray diffraction. *Makrom. Chem.*, 44–46: 24, 36, 1960.
22. A. Weidinger and P.H. Hermans. On the determination of the crystalline fraction of polyethylene from x-ray diffraction. *Makrom. Chem.*, 50: 98–115, 1961.
23. D.W. van Krevelen. Cohesive properties and solubility, in *Properties of Polymers*, 3rd ed. Amsterdam: Elsevier, 1990, pp. 198–199.
24. D.W. van Krevelen. Optical properties, in *Properties of Polymers*, 3rd ed. Amsterdam: Elsevier, 1990, pp. 287–297, H.A. Lorentz, *Wied. Am. Phys.*, 9: 641, 1880; L.V. Lorenz, *Wied. Am. Phys.*, 11: 70, 1880.
25. P. Zoller and D. Walsh. *Standard Pressure-Volume-Temperature Data for Polymers*. Lancaster, PA: Technomic Publishing, 1995, pp. 135, 161.
26. P. Laurienzo, M. Malinconico, G. Ragosta, and M.G. Volpe. Synthesis and impact behavior of PMMA/EVA interpenetrated blends. *Die Angew. Makrom. Chem.*, 170:137–143, 1989.
27. G. Carbonara, P. Mormile, U. Bernini, P. Russo, M. Malinconico, and M.G. Volpe. Characterization of PMMA-EVA blends via photo acoustic technique, in *Proceedings of Physical Concepts of Material for Novel Optoelectronic Device Applications: I. Materials Growth and Characterization*. Aachen, Germany, 1990, pp. 1038–1040.
28. G. Carbonara, P. Mormile, G. Abbate, U. Bernini, P. Maddalena, and M. Malinconico. *Proceedings of Physical Concepts of Material for Novel Optoelectronic Device Applications: I. Materials Growth and Characterization*. Aachen, Germany, 1990, pp. 688–691.
29. U. Bernini, G. Carbonara, M. Malinconico, P. Mormile, P. Russo, and M.G. Volpe. Investigation of the optothermal properties of a new polymeric blend poly methyl-methacrylate-polyethylene-co-vinyl acetate. *Appl. Opt.*, 31:5794–5798, 1992.

7

Cure and Rubber Toughening of Vinyl Ester Resins

Karen N. Roberts, George P. Simon, Wayne D. Cook, and Peter J. Burchill

CONTENTS

7.1   Introduction

Vinyl ester resins (VERs) were developed in the early 1960s for use in electrical insulation, corrosion-resistant equipment, matched-metal die moldings, and electrical laminates.[1] Over time, the range of applications for these resins has grown to include construction of parts for automobiles, military ground vehicles, marine applications, and bridges and bridge rehabilitation.[2]

Vinyl ester resins are binary resin systems containing a dimethacrylate monomer, from which the cured material gains most of its properties, and a reactive monomer such as styrene, which acts as a reactive diluent, reducing the viscosity and increasing the ease of room temperature handling of the resin as well as taking part in the cross-linking reaction. One of the most common types of vinyl ester resin utilizes a dimethacrylate monomer based on bisphenol-A and has the excellent thermal and mechanical properties of an epoxy resin, while retaining the handling and curing characteristics of an unsaturated polyester resin.[1,3,4] Although the curing schedule of vinyl ester resins can be tailored to meet the needs of specific fabrication processes, they are generally cured at ambient temperatures.[4]

As with most thermosetting systems, vinyl ester resins are relatively brittle and require toughening. This is commonly achieved through the addition of a rubbery second phase to the brittle thermoset matrix. Most of the research on toughening of thermosetting polymers has involved the use of liquid rubbers in epoxy resins, with a comparatively much smaller focus on vinyl ester resin systems. A newer area of interest involves the use of preformed core-shell rubber particles as the rubbery phase, having many advantages over the traditional liquid rubber systems. When core-shell rubber particles are used in vinyl ester resins, issues of swelling of the particles by low-molecular-weight styrene monomers become important.

This chapter discusses aspects of the chemistry and cure of vinyl ester resins. It also presents a review of the literature and some recent results on the toughening of these materials, in particular, incorporation of core-shell materials. Given only limited work on toughening of these materials, a summary of more general aspects of thermoset toughening is included for completeness.

7.2   Vinyl Ester Resin Constituents

As mentioned above, vinyl ester resins are binary resin systems containing a dimethacrylate monomer and a reactive monomer such as styrene. The dimethacrylate monomer constituent of a vinyl ester resin is produced by reacting an epoxide resin with an ethylenically unsaturated monocarboxylic acid.[1,3] The most common dimethacrylate monomer in vinyl ester resin is formed by reacting methacrylic acid with an oligomerized epoxy based on bisphenol-A,[4] as shown schematically in Figure 7.1. The resulting dimethacrylate monomer has a bisphenol-A epoxy resin backbone with terminal unsaturation. Other types of vinyl ester resins that are available[1] include epoxy novolac vinyl ester resin, which is based on phenol formaldehyde; flame-retardant resins, which have been brominated; urethane-based vinyl ester resin; and rubber-modified vinyl ester resins, which have
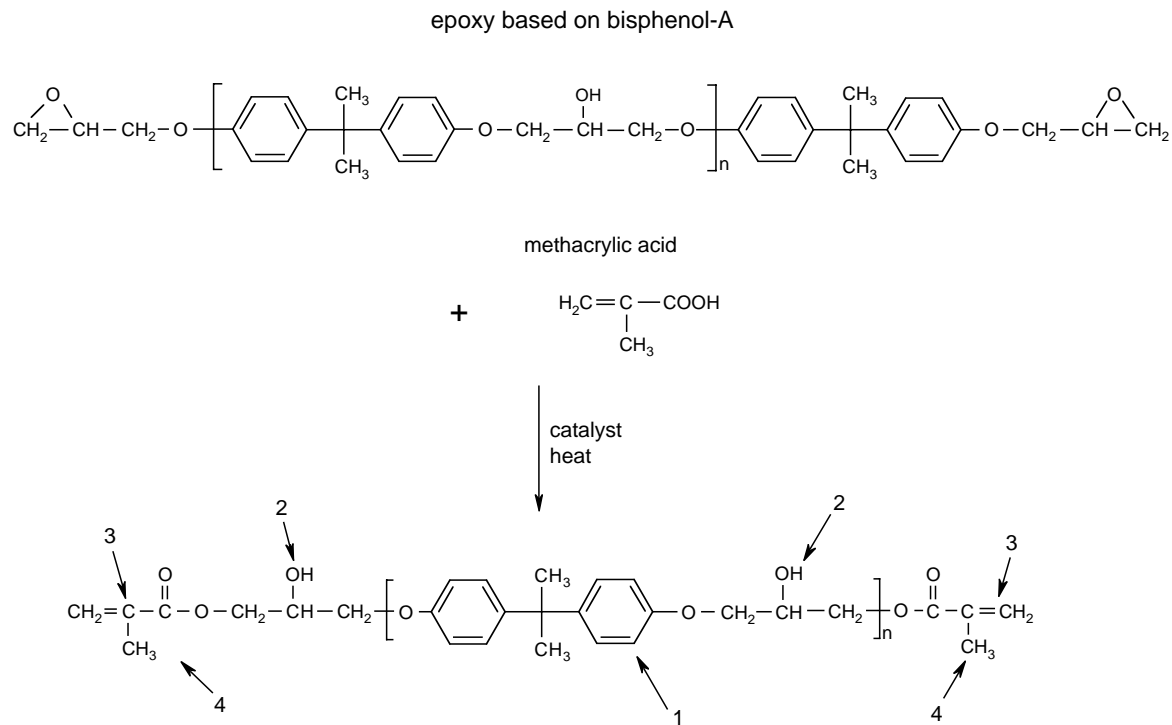
FIGURE 7.1
A schematic showing the synthesis and structure of a dimethacrylate molecule based on bisphenol-A, which forms one part of the binary vinyl ester resin system.[3]

some of the di-epoxide end-capped with carboxyl-terminated butadiene-acrylonitrile (CTBN) rubber.[5]

Some of the features of the structure of the dimethacrylate monomer, in Figure 7.1, that give the material its final properties are:[1,3,4]
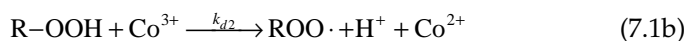
1. Aromatic rings: These are in the backbone and impart superior toughness, mechanical properties, and heat resistance to the resin. The phenyl ether linkages within the backbone give this material good general corrosion resistance and provide superior acid resistance.
2. Pendant hydroxyl groups: These aid adhesion and are a potential reactive site for further modification of the structure. The interaction of the chain secondary hydroxyl groups with the silanol groups on the surface of glass fibers leads to improved wetting and bonding, and thus higher strengths in laminates.
3. Unsaturated acid moiety: This provides the reactive site for cross-linking and gives the product curing characteristics similar to those of polyester resins.
4. Methyl group: This stabilizes the ester group toward hydrolysis, thus increasing resistance to chemical attack.

7.3   Curing Processes in a Vinyl Ester Resin System

In recent years, the use of vinyl ester resins as the matrix material in composite materials and structures has increased. One of the most important aspects of the production of composite materials is the curing characteristics of the matrix material. During the curing process, the physical state of a thermosetting resin changes from a liquid to a gel, and finally to a glassy solid. The rate at which this occurs is governed by the curing kinetics of the vinyl groups, which in turn is dependent on such factors as curing temperature, resin composition, and the initiator/catalyst system. Thus the control of the curing behavior of the matrix material will heavily influence the choice of processing conditions, the methods of composite production, and the suitability of a particular resin to composite production. Since the network structure of the polymer develops during the curing process and determines the final mechanical and chemical properties of the composite material, a detailed understanding of the curing behavior is essential for the successful use of a thermosetting polymer such as a vinyl ester resin in composite materials.

Vinyl ester resins are typically cured via a peroxide-initiated free radical copolymerization process involving both the dimethacrylate and styrene constituent monomers. Commonly used initiators in the cure of VER systems are organic peroxides and hydroperoxides such as methyl ethyl ketone peroxide, benzoyl peroxide, and cumene hydroperoxide.[6] Decomposition of the

peroxide can be achieved either through the application of heat or at low temperatures via a redox reaction with a metal promoter, such as cobalt octoate.[2,6,7] The postulated mechanism for the cobalt/peroxide redox initiation reaction is shown in Equation (7.1):[2,6–8]

$$R-OOH + Co^{2+} \xrightarrow{k_{d1}} RO\cdot + OH^- + CO^{3+} \tag{7.1a}$$

$$R-OOH + Co^{3+} \xrightarrow{k_{d2}} ROO\cdot + H^+ + Co^{2+} \tag{7.1b}$$

where R–OOH and Co represent methyl ethyl ketone peroxide (MEKP) and cobalt species, respectively, and k_{d1} and k_{d2} represent the rate constants for the formation of the alkoxy (RO·) and peroxy (ROO·) radicals, respectively. The free radicals attack the reactive unsaturated sites on the methacrylate and styrene monomer, leading to a chain polymerization process that results in the formation of a three-dimensional polymer network, as shown in Figure 7.2. The methacrylate monomer provides the cross-linking capacity and cross-link junctions in the network, while the styrene monomer provides chain extension.[2] Three main reactions can occur at the sites of unsaturation, as illustrated schematically in Figure 7.2: (1) the dimethacrylate units can homopolymerize, (2) the dimethacrylate units can copolymerize with the styrene units, and (3) the styrene can also homopolymerize.

The isothermal and temperature scanning curing behavior of vinyl ester resins have been extensively studied using differential scanning calorimetry (DSC).[6,7,9–16] Typical characteristics exhibited by vinyl esters under isothermal DSC curing are an autoacceleration in the polymerization rate resulting in a single DSC peak and cessation in polymerization before full conversion is achieved, i.e., vitrification. Increasing the isothermal cure temperature was found to result in an increase in the heat of cure (Q_{iso})[7,9,10,12–14] and, consequently, an increase in conversion at that temperature, and a corresponding decrease in residual heat released during a postcuring DSC scan (Q_{res}). Changing the isothermal curing temperature was found to have a minimal effect on the total heat of cure (i.e., $Q_{iso} + Q_{res}$).[12–14] The heat of cure measured under temperature scanning conditions, which is sometimes referred to as the ultimate heat of cure (Q_{ult}), was found by Mousa and Karger-Kocsis,[12] Lem and Han,[17] and Stone et al.[9] to be greater than $(Q_{iso} + Q_{res})$. Salla and Ramis[18] observed similar behavior in their study of the curing kinetics of an unsaturated polyester. Mousa and Karger-Kocsis[12] and Stone et al.[9] suggest this behavior is due to the temperature of cure being greater than the T_g of the system, and curing under these conditions is not as greatly affected by vitrification. This theory does not explain why $(Q_{iso} + Q_{res})$ is less than (Q_{ult}), when the material has been exposed to the same temperature range in both cases. However, (Q_{ult}) is not universally found to be greater than $(Q_{iso} + Q_{res})$. In a study on the curing behavior of an epoxy resin system, Gonis et al.[19] found (Q_{ult}) to be less than $(Q_{iso} + Q_{res})$ and concluded that it was due to

FIGURE 7.2
A schematic showing the copolymerization reactions occurring during the cure of a vinyl ester resin system.

decomposition of the resin during the temperature scanning curing process. Isothermal DSC studies by several authors[7,12,14] show that vinyl ester resins usually exhibit a single exothermic peak during cure; however, Li et al.[6] observed two overlapping peaks or a shoulder, and suggested this could be the result of two different reactions that are dominant at different stages throughout the curing reaction.

The free radical curing behavior of vinyl ester resins has been analyzed by many workers[2,9–11,17,20] using empirical models based on the autocatalytic model developed by Kamal and Sourour,[21,22] shown in Equation (7.2):

$$\frac{d\alpha}{dt} = \left(k_1 + k_2\alpha^m\right)(1-\alpha)^n \tag{7.2}$$

where k_1 and k_2 are rate constants that have an Arrhenius temperature dependency, m and n are constants that are independent of temperature, and α is the relative degree of cure at time t. This relative degree of cure, α, is often defined by Equation (7.3)[23]:

$$\alpha = \frac{Q}{Q_u} \tag{7.3}$$

where Q is the total amount of heat generated isothermally from the beginning of the reaction up to a given time t, and Q_u is the ultimate heat of cure. Although Kamal and Sourour[21,22] and Lem and Han[17] found that Equation (7.2) adequately describes the isothermal curing behavior of epoxy, unsaturated polyester, and vinyl ester resin systems, it does not model well the vitrification behavior that is commonly observed during the cure of thermosetting polymers. Many researchers[2,9] have modified Equation (7.2), or other models based on it,[2,10,11] to account for the vitrification behavior by replacing the term $(1 - \alpha)$ with the term $(\alpha_{max} - \alpha)$, where α_{max} is the maximum conversion during cure at a specific temperature. Incorporation of the α_{max} term into the kinetic model used by Lam et al.[11] results in a much better fit of the curing behavior of a vinyl ester resin, particularly at high conversions.

DSC is a thermal analysis technique that directly measures the heat evolved during the curing reaction, and although this type of analysis gives information regarding the overall reaction rate, it cannot differentiate simultaneous reactions by differing species and physical changes such as phase formation[6,24] that could occur during a copolymerization process. Fourier transform infrared (FTIR) spectroscopy, however, can be used to monitor the individual reactions that can occur during a copolymerization reaction. The consumption of the dimethacrylate monomer and styrene monomer have been monitored during the cure of vinyl ester resins using FTIR spectroscopy.[2,12,15,16,25] A typical conversion profile for the two monomeric species obtained from such studies is shown in Figure 7.3. Some important features of such a conversion profile are:[2,12,25]

- The initial fractional rate of conversion of dimethacrylate double bonds is greater than that of the styrene double bonds.
- The fractional rate of styrene conversion increases with time.
- The rate of fractional conversion of styrene exceeds the dimethacrylate fractional conversion rate toward the end of the reaction.
- Homopolymerization of styrene continues after the dimethacrylate reaction terminates.
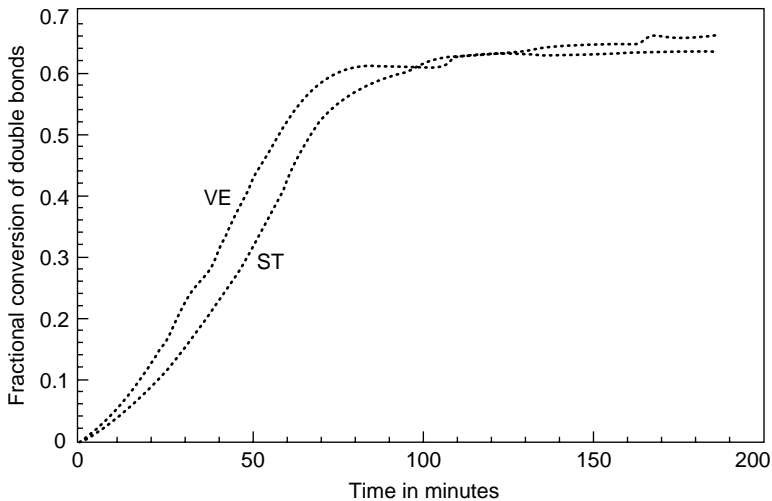
FIGURE 7.3
A typical experimental plot of fractional double-bond conversion of dimethacrylate monomer (VE) and styrene monomer with time. (Based on a figure from Dua et al., 1999, *Polym. Composites*, 20, 379–391.)

- The final conversion of styrene is greater than the dimethacrylate, even after postcuring at elevated temperatures.

Dua et al.[2] and Ganem et al.[26] suggest that the curing process can be divided into three distinct stages. Stage I corresponds to the initial reaction between the dimethacrylate and styrene and the early stages of network formation. The kinetics of copolymerization are thought to be governed by the intrinsic reactivity of the styrene and methacrylate double bonds, not by diffusion.[2,26] Work by Dua et al.[2] suggests that the polymerization in Stage II is dominated by the Trommsdorf effect, while Ganem et al.[26] proposed that the polymerization of the methacrylate decreases and the polymerization of the styrene increases throughout Stage II, due to the smaller size of the styrene molecule, giving it unrestricted mobility throughout the network while the larger dimethacrylate monomer becomes immobilized within it. Ganem et al.[26] suggested this behavior indicates that a two-phase structure forms during Stage II, with one phase consisting of the copolymer network swollen by residual dimethacrylate monomer (and possibly some residual styrene monomer), and the other phase containing unreacted styrene. The reaction in the copolymer phase ceases at the end of Stage II, presumably because of the vitrification of this phase, whereas the styrene phase continues to homopolymerize during Stage III until the residual styrene is consumed or vitrification of this phase stops any further reaction.[26]

Like Ganem et al.,[26] Dua et al.[2] and Ziaee and Palmese[25] propose that the cessation of the dimethacrylate polymerization during the curing process suggests the formation of a multiphase structure. However, Dua et al.[2] and

Ziaee and Palmese[25] also suggest that this behavior indicates the formation of microgels during cure. Similar behavior has been observed[27–30] during the cure of unsaturated polyester systems, which are chemically very similar to vinyl ester resins. Ziaee and Palmese[25] proposed that the thesis results of Stone et al. (since published[9]) indicate that cross-linking is occurring in an isolated second phase, such as a microgel. Stone et al.[9] observed that the evolution of the T_g of a VER with conversion, monitored using torsional braid analysis (TBA), remained constant for conversions of 20 to 40%. Ziaee and Palmese[25] further provide evidence by observing a nodular fracture surface of the cured material using atomic force microscopy (AFM). Cook et al.[7] used DSC analysis to show that T_g increased with increasing fractional conversion over the entire conversion range. The conflicting results of Cook et al.[7] and Ziaee and Palmese[25] could perhaps be due to the different techniques used to determine the variation in T_g with conversion. However, these results raise questions about the true variation of T_g throughout cure, and thus the validity of the conclusions drawn.

Dua et al.,[2] Li et al.,[6] and Ganem et al.[26] studied the effect of styrene content on the curing behavior of VER. Increasing the styrene content was found to decrease the overall isothermal rate of reaction (as determined by DSC[6]), as well as decrease the rate constants for each of the monomeric species (from FTIR analysis[2]). Li et al.[6] also observed the shape of the DSC exotherm to change from one peak to two as the styrene content was raised. Using FTIR, Dua et al.[2] observed that the initial curing behavior was not affected by the styrene content, but that in the latter stages, conversion of styrene to form polystyrene was much greater in systems with higher styrene content. Ganem et al.[26] found similar behavior, with the amount of polystyrene formed increasing suddenly when the styrene content was equal or greater than 40 wt%. Dua et al.[2] found that increasing the styrene content up to 47 wt% led to higher final dimethacrylate conversion, with little effect on the overall styrene conversion. Increasing the styrene content beyond 47 wt% did not further increase the final dimethacrylate conversion.

The isothermal curing kinetics of vinyl ester resins have been found to be influenced by the concentration of the initiator and catalyst used to promote the free radical curing process.[2,6,7] Increasing initiator concentration was found to accelerate the curing reaction under all curing conditions.[2,7] Increasing the catalyst concentration, on the other hand, was found by Dua et al.[2] and Li et al.[6] to increase the reaction rate. In contrast, Cook et al.[7] observed a retardation in the overall curing reaction, particularly at high catalyst levels. Interestingly, both Cook et al.[7] and Martin et al.[31] found that increasing the concentration of both the initiator and the catalyst led to a reduction in the gel time. Cook et al.[7] suggest that the catalyst could accelerate the reaction through the gel point but then act as a retardant. Dua et al.[2] also suggest that different stages of the curing process are affected to a greater or lesser degree by the concentration of catalyst and initiator.

In addition to the thermal characterization techniques, the development of the vinyl ester resin network during cure has been followed through

measurements of the viscoelastic and rheological properties. Torsional braid analysis,[9] dynamic mechanical thermal analysis (DMTA),[31] and rheometry[14,31] have been used to determine the gel point, vitrification point, and glass transition temperature. Stone et al.[9] and Martin et al.[31] used both the TBA and DMTA techniques to monitor the gelation and vitrification of a VER. Han and Lem[14] and Martin et al.[31] monitored the progress of cure of a VER by measuring the changes in viscosity and shear modulus with time, under steady shear and dynamic conditions. The viscosity of a VER under steady shear conditions was found to increase slowly during the early stage of cure, subsequently increasing rapidly.[14] This behavior is as expected since, under steady shear conditions, the gel point is defined as the point at which the viscosity of the system diverges to infinity and also when an equilibrium modulus begins to appear.[32–36] However, determination of the gel point using these two criteria has inherent problems in that it is impossible to physically measure an infinite viscosity or the actual point at which an equilibrium modulus appears.[32,34–36]

Rheological measurements using small amplitude oscillatory shear, however, can be used to measure the continuous evolution of viscoelastic properties through the gel point. The dynamic viscoelastic parameters have been found[32,34,36–41] to exhibit power law behavior with time or frequency at the gel point of thermosetting polymers. In particular, at the gel point of a thermosetting polymer the real (G') and loss (G'') shear moduli vary with frequency (ω) as shown in Equation (7.4):[38,39]

$$G'(\omega) \propto G''(\omega) \propto \omega^n \tag{7.4}$$

It has been proposed by a number of workers[32,36,40] that this behavior is due to the network structure at the gel point being self similar at all length scales. At the gel point, the viscoelastic behavior becomes independent of frequency, and the behavior at the gel point can be defined by Equation (7.5):[34,36–38]

$$G'(\omega) = \frac{G''(\omega)}{\tan\left(\dfrac{n\pi}{2}\right)} \propto \omega^n \tag{7.5}$$

The gel point can also be defined[32,34,37–39,42] as the "crossover" in tan δ, i.e., where tan $\delta = G'/G''$ is independent of frequency. In a recent study on the curing behavior of a VER system,[43] dynamic rheology was used to observe the rheological changes with time during cure. Roberts[43] observed a crossover in the tan δ at the gel point, as shown in Figure 7.4. Han and Lem[14] and Martin et al.[31] used dynamic rheology to monitor the curing behavior of vinyl ester resin systems, but they did not utilize the above theory to determine the gel point of their systems. Although Han and Lem[14] observed variation in G', G'', and tan δ with cure time and angular frequency, they did not draw any conclusions regarding gel or vitrification points from their
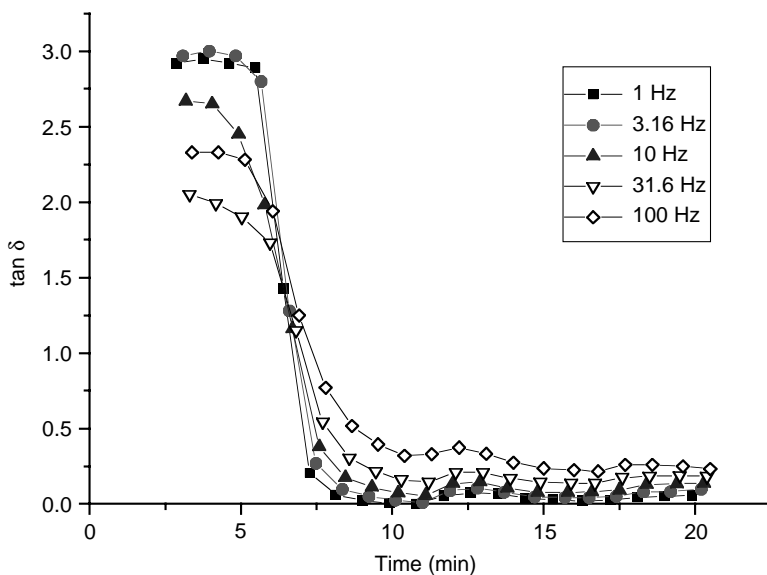
FIGURE 7.4
Crossover in the tan δ during the isothermal cure of a vinyl ester resin. (From Roberts, K.N., Ph.D. dissertation, Monash University, Melbourne, Australia, 2002.)

data. Martin et al.[31] used two different criteria to define the gel point: the time when G' increased above the baseline and the time when the real viscosity, η', attained values of either 100 and 500 Pascal seconds (PaS). They found that the gel time depended on the criterion used, but decreased with increasing curing temperature, allowing determination of an activation energy for the gelation process.

7.4 Toughening of Thermosetting Polymers: Overview

Over the last 30 years a significant amount of research effort has been directed toward improving the toughness of thermosetting resins. Several methods have been identified that are shown to improve the toughness:[44] (1) chemical modification of the polymer backbone to make it more flexible, (2) increasing the monomer molecular weight and modification of the curing process to reduce the cross-link density of the matrix, and (3) incorporation of a second phase into the system. While methods (1) and (2) may increase the toughness of the polymer, they also tend to reduce desirable resin properties such as high modulus and glass transition temperature. Method (3) tends to increase the toughness of the resin without adversely affecting these properties. It has also been found to be the most effective method; a rubbery

second phase, in particular, can provide an order of magnitude improvement in toughness.[44]

It has long been recognized that the toughness of a brittle thermosetting polymer can be improved with the addition of a second phase. Rigid phases, such as micron-size glass beads and other particulate organic fillers, offer smaller improvements in toughness to those achieved through the addition of a discrete, rubbery particulate phase.[45–47] There are two common methods by which a rubbery phase can be added to a thermosetting matrix:[48–55] phase precipitation of rubber and preformed core-shell rubber particles. The most utilized of these two methods is the phase separation method, where liquid rubber is initially dissolved into the uncured resin system. As the system cures, the rubber precipitates out due to a reduction in the entropy of mixing, resulting in discrete, rubbery particles. Although this method is effective in improving the toughness of the matrix material, several problems exist. Firstly, not all of the rubber precipitates out of the matrix, and this can have a deleterious effect in reducing the glass transition temperature and modulus of the system. Secondly, the curing process must be carefully controlled so as to achieve the desired particle size and distribution for optimum toughening. Thus, in the phase separated system, factors that may influence the toughening efficiency of the system, such as particle size, morphology, and composition of both the particles and the matrix, are all interdependent and rely heavily on the curing process.[50–53,55–57]

The second method, which has been used more frequently in recent years, is to blend preformed multiphase core-shell rubber particles into the matrix resin before curing. This method has many advantages over the phase separation method described above. Core-shell rubber particles are preformed, and so the morphology and particle size are independent of the curing process. Known amounts can be added to the matrix, without any rubber plasticization of the matrix material. In studies of core-shell rubber-modified epoxy systems,[48,52,53,55] it has been found that the glass transition temperature of the cured matrix material remains unchanged after rubber additions. Core-shell rubber particles have the added advantage of enabling an independent study of the effect of particle size and composition on the toughening process.

7.5   Liquid Rubbers Used in Thermoset Toughening

As described in Section 7.4, the most utilized method in toughening of polymers via the inclusion of a rubbery phase to a rigid, thermosetting polymer is the phase separation/precipitation method. Initially the liquid rubber is miscible with the uncured resin, but precipitates out during the curing reaction to form discrete particles. The precipitation of the rubber during cure is due to the reduction in compatibility of the resin/rubber system with increasing matrix molecular weight.[57] The morphology

obtained in liquid rubber/resin systems is dependent upon the rates of nucleation and growth of the dispersed phase, compatibility of the rubber, and the rate of the curing reactions.[57] As discussed in Section 7.4, there are many disadvantages with these systems; however, they also offer many advantages, including ease of preparation, choice of chemistries to change level of interaction between the rubber and the matrix, and the molecular weight of the rubber.

Although many different rubber/resin systems have been studied, epoxies, with a range of liquid rubbers, have been the most extensively studied. Elastomers used in combination with epoxy resins can be placed in four main categories:[58] reactive butadiene-acrylonitrile rubbers, polysiloxanes, flouroelastomers, and acrylate elastomers. The most widely studied systems, and consequently the most commercially successful, are the epoxy/butadiene-acrylonitrile rubber systems.[58] The most commonly studied of these systems is the epoxy/carboxyl-terminated butadiene-acrylonitrile rubber system[54]; the structure of CTBN is shown in Figure 7.5, where m is typically equal to 10 and the molar mass is about 3500 g/mol.[59] Butadiene-acrylonitrile rubber systems containing terminal groups other than carboxyl have also been extensively utilized. Other terminal functionalities that have been used include epoxy, hydroxyl, phenol, mercaptan, vinyl, and amine; they are also shown in Figure 7.5.

The compatibility–incompatibility balance between the rubber and the resin, the reactivity of the rubber molecule's end groups, the curing temperature, the volume fraction of the rubber, the molecular weight of the rubber, and the curing agent can greatly affect the morphology and thus the toughness of the rubber/resin system. Initially, for the rubber and resin to be miscible, good compatibility is required, and so the solubility parameters of

$$R-\left[\left(CH_2-CH=CH-CH_2\right)_x\left(CH_2-CH\underset{\underset{CN}{|}}{}\right)_y\right]_m-R$$
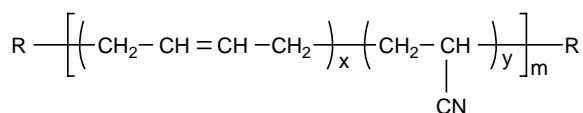
Where:

Carboxyl   R = —— COOH

Phenol   R = —— C_6H_5OH

Epoxy   R = —— $CH\overset{O}{\overset{/\backslash}{-}}CH_2$

Hydroxyl   R = —— COOH

Mercaptan   R = —— CH_2SH

FIGURE 7.5

Chemical structure of butadiene-acrylonitrile rubber, and typical reactive end groups used for modifying thermosetting polymers. (From Kinloch, A.J., in *Structural Adhesives: Developments in Resins and Primers*, Elsevier, London, 1986, pp. 127–162.)

the rubber and resin must be well matched. However, for phase separation to occur, the solubility parameters must be sufficiently different so that during the curing reaction, the change in Gibbs free energy becomes positive and phase separation occurs.[58] The compatibility can be controlled largely by the relative polarities of the resin and the rubber, which for CTBN rubber is determined primarily by the acrylonitrile (AN) content.[59] Increasing the reactivity of the end groups toward the resin can increase the strength of the bond or interface between the rubber and the resin, and thus in many cases the toughness, but it can also decrease the efficiency of the phase separation process.[58] Increasing the elastomer concentration will result in an increase in particle size and volume fraction of precipitated rubbery phase.[59] However, it has been observed that at elastomer concentrations greater than ~20%, phase inversion can occur[57] — clearly undesirable. Increasing the curing temperature can have a variety of effects, due to the kinetic nature of both the curing process and the thermodynamics and kinetics of the phase separation process. However, it is generally observed that increasing the curing temperature will result in an increase in particle size.[57–59]

Like epoxy systems, many different phase-separated vinyl ester resin/liquid rubber systems have been studied.[5,60–66] The types of rubber that have been used include carboxyl-terminated butadiene-acrylonitrile, vinyl-terminated butadiene-acrylonitrile (VTBN, VTBNX), epoxy-terminated butadiene-acrylonitrile (ETBN), hydroxy-terminated polybutadiene (HTBN), hydroxy-terminated polyether (HTE), poly(ethyl hexyl acrylate) (EHA), and poly(butyl acrylate) (PBA). However, unlike epoxy/rubber systems, poor compatibility between the rubber and the matrix is typically observed in VER/liquid rubber systems.[61,66]

7.6 Preparation, Morphology, and Characteristics of Core-Shell Rubber Particles

The most common commercial variety of preformed rubber particles used to toughen polymers are core-shell rubber (CSR) particles.[67] CSR materials are multiphase particles that typically are composed of a soft rubbery core and a rigid shell, as shown in Figure 7.6. These particles are produced via semibatch sequential emulsion polymerization of free radical initiated systems.[50,51,67] Emulsion polymerization has the advantage of allowing the design and production of latexes with a wide range of well-defined morphologies.[68] It relies on the monomer and subsequent polymer, forming stable, emulsified colloids in an aqueous medium with the aid of a surface-active ingredient.[67] The first stage of production of the core is through the formation of seed particles. Monomer and surfactant are added to the seed particles at controlled rates, allowing the reaction to continue until the core phase is of the required size. The core phase is cross-linked during the initial
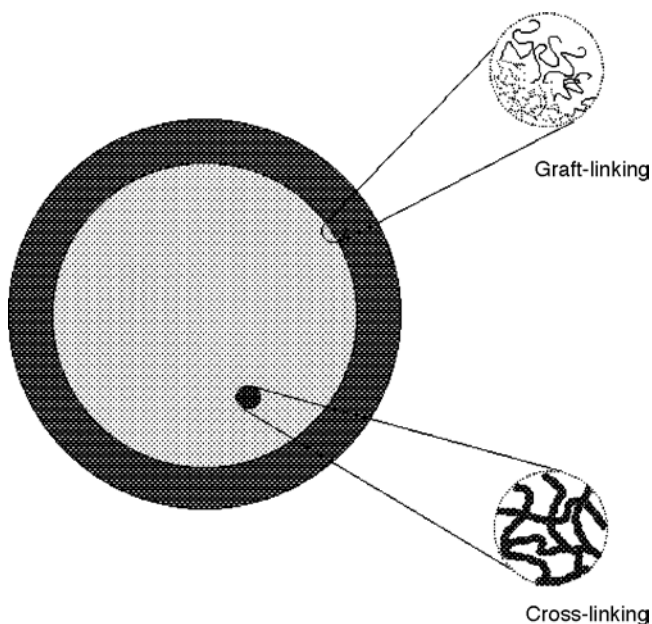
Graft-linking

Cross-linking

FIGURE 7.6
Schematic of a typical two-layered CSR particle. (Published with permission from Cruz-Ramos, *Polymer Blends*, Vol. 2, *Performance*, Paul and Bucknall, Eds., Wiley-Interscience: New York, 2000, pp. 137–175.)

stage of production to ensure that the rubber particles maintain their integrity during subsequent processing.[67] Addition of monomer and surfactant for the next growth stage allows the next layer to graft on to, and around, the core.[51] The process of adding the shell to the core is quite complex, with a balance of thermodynamics and kinetics of the polymerization reaction necessary to achieve the required morphology. Some of the possible morphologies obtainable using emulsion polymerization techniques are shown in Figure 7.7. Not all particles have only a simple two-layer morphology, Lovell[50,51] has performed much work, for example, on three- and four-layered particles. These particles are produced by sequentially polymerizing layers onto the formed particle until the desired number and composition of the layers and particle size has been achieved.

The core-shell structure shown in Figure 7.6 is the most common form of CSR particle. The cross-linked rubbery core materials are typically based on poly(butyl acrylate), or poly(butadiene).[67] The role of the core phase is to provide the soft second phase required to induce the toughening mechanisms in a brittle polymer. The most common shell materials are poly(methyl methacrylate) homopolymer or copolymer, and styrene-acrylonitrile (SAN) copolymers.[67] The shell material is not cross-linked and so is grafted to the core to ensure that it cannot diffuse away.[51,67] The shell phase of a CSR particle serves two main purposes:[51,67] it prevents coalescence of the particles during
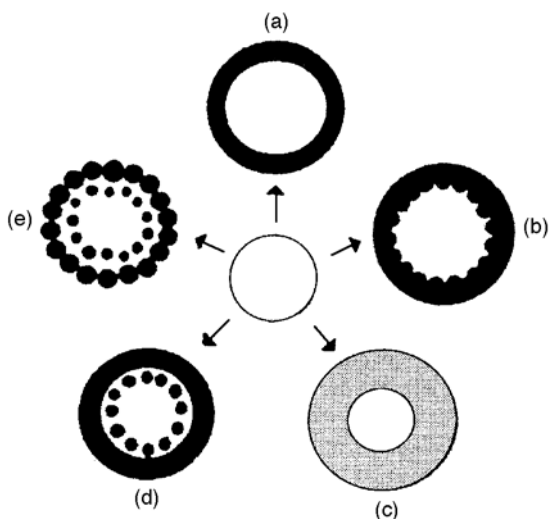
FIGURE 7.7
Possible morphologies of two-layer CSR materials produced via emulsion polymerization: (a) ideal morphology; (b) wavy internal surface; (c) interface with composition gradients; (d) microdomains or occlusions; (e) island shell structures and occlusions. (Published with permission from Cruz-Ramos, *Polymer Blends*, Vol. 2, *Performance*, Paul and Bucknall, Eds., Wiley-Interscience: New York, 2000, pp. 137–175.)

isolation from the emulsion and during drying by providing a hard coating that keeps the rubbery cores from adhering to each other, enabling the particles to be dispersed uniformly upon blending with the matrix; and it mixes with the matrix, ensuring that there is a strong interface between the matrix and the particle, causing efficient transfer of stress from the matrix to the particle. The composition of the shell influences the adhesion of the particle to the matrix and is thus a key factor in the performance of the CSR. CSR materials are typically dispersed in matrices that are dissimilar to the grafted shell. Solubilization of the matrix polymer into the shell must occur for proper interfacial adhesion to develop. One of the advantages of the emulsion polymerization process is that the chemistry of each of the phases can be modified and tailored for the end use. Thus functional groups, such as carboxyl, amine, and hydroxyl, can be incorporated into the shell to enhance the miscibility between the shell and the matrix.

A recent review of CSR materials by Cruz-Ramos[67] highlights many examples of the use of CSR materials for the toughening of both thermoplastic and thermosetting polymers. Effective toughening of thermoplastic polymers, such as poly(methyl methacrylate),[67,69] poly(vinyl chloride),[67] and polycarbonate,[67,70] are also reported. However, in the case of thermosetting polymers, the majority of investigations on toughening with CSR particles have involved epoxy resins.[48,49,52,53,55,56,67,71–77] There have been few studies of modification of VER by core-shell particles, but some very recent data will be presented in this chapter.

7.7 Inclusion of Core-Shell Rubber Particles in Resin

An important aspect of the use of an included phase, such as core-shell rubber particles, in a resin is the effect it has on viscosity. The most commonly observed consequence of addition of a second phase to a polymeric liquid is an increase in viscosity.[78] The particulate phase disturbs the streamlines of flow, which results in additional dissipation of energy.[78]

Most of the reported studies on the rheology of filled polymers focus on polymers containing rigid fillers such as glass beads, calcium carbonate, and clay. There have been only a few reports of the rheological behavior of thermosetting polymers modified with preformed rubber particles.[48,49,53,55,56,79,80] Becu-Longuet et al. and others,[48,49,53,55,56] in their studies on the toughening of epoxy resins using core-shell rubber preformed particles, used steady shear analysis to determine the stability of the dispersion of the CSR particles in the epoxy resin after blending by subjecting the CSR/epoxy mixtures to a cycle of increasing and then decreasing shear rate. No hysteresis in the viscosity was observed, and so it was suggested that the dispersion was stable.[53,55,56] In addition to increasing the viscosity, Becu-Longuet and coworkers found that increasing the concentration of core-shell particles caused the rheology to change from Newtonian to pseudoplastic.[48,49,53,55,56] Similar observations were made by Roberts[43] in a recent study on the rheological behavior of a CSR-modified vinyl ester resin system, as shown in Figure 7.8. The vinyl ester resin showed Newtonian behavior, while increas-
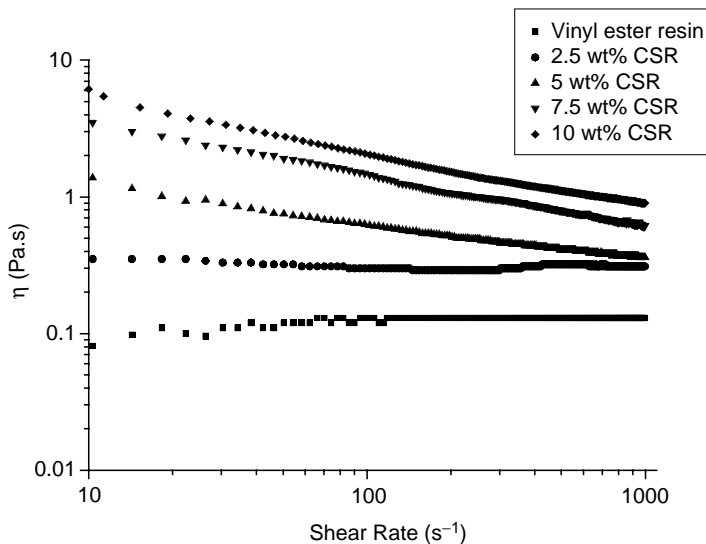

FIGURE 7.8
Variation in shear viscosity with shear rate and CSR content for a CSR/vinyl ester resin blend at 40°C. (From Roberts, K.N., Ph.D. dissertation, Monahs University, Melbourne, Australia, 2002.)
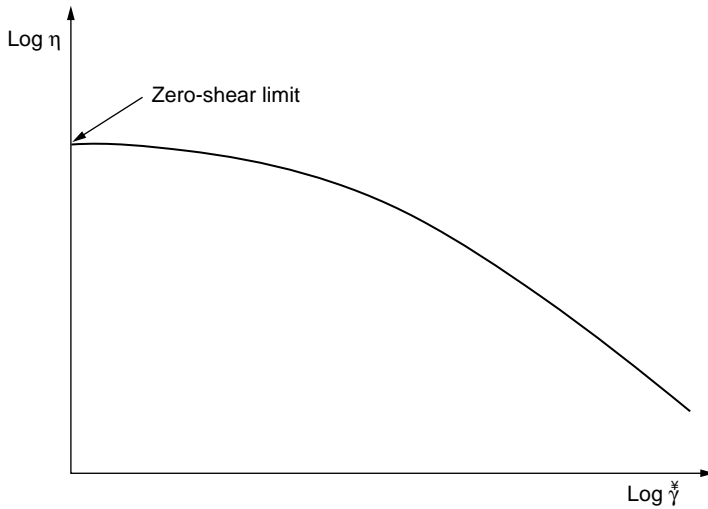
FIGURE 7.9
Typical log η vs. log γ̇ behavior for a non-Newtonian pseudoplastic fluid. (Based on a figure from Shenoy, *Rheology of Filled Polymer Systems*, Kluwer Academic Publishers: London, 1999.)

ing particulate material caused greater fluid "structure" and hence more non-Newtonian behavior, as shown in Figure 7.9. The level of increase in the viscosity observed by Becu-Longuet et al.[49,53,55,56] was found to correlate with the size of the CSR particles and the level of heterogeneity of the dispersion. It was generally found that for the same loading of CSR materials, the viscosity of the CSR/epoxy blends increased with decreasing particle size.[55] In addition, for CSR/epoxy systems where the CSR particles formed agglomerates,[55] smaller agglomerates and a more highly uniform dispersion led to larger increases in viscosity. Nguyen-Thuc and Maazouz[80] found that increasing the interaction between the CSR particles and the epoxy matrix also causes an increase in shear viscosity.

Levita et al.[79] studied the effect of preformed rubber particles and inorganic fillers on the viscosity of an epoxy and a unsaturated polyester resin and suggested that changes in viscosity with the addition of fillers are heavily influenced by the packing efficiency of the filler. They hypothesize that in systems containing fillers with a high specific surface (small particle size), the filler material forms an internal structure within the carrier material, hampering particle motion, which leads to an increase in viscosity. Unlike Becu-Longuet et al. and others,[48,49,53,55,56] Levita et al.[79] found that cyclic shearing of the epoxy/rubber blends resulted in a gradual thinning of the mixture and suggested that this behavior is due to the structured nature of the epoxy/rubber blends.[79] Slightly different behavior was observed in an unsaturated polyester/rubber blend,[79] where the viscosity was found to decrease initially, then increase over a 500-sec test period. It was suggested that this was due to the swelling of the rubber particles by absorption of styrene monomer

from the resin. This has a twofold effect on the viscosity: Firstly, the swelling of the particles leads to an increase in the effective volume of particulate phase, increasing the viscosity. Secondly, the decrease in the styrene content of the resin also leads to an increase in the viscosity, because the monomer with which it is mixed is more viscous.

The swelling of rubber particles in a thermosetting resin containing a low-molecular-weight component such as styrene has also been extensively studied by Roberts[43] in a study of a core-shell rubber/vinyl ester resin system. The ability of the core-shell rubber particles to swell in the styrene of the VER means that they will behave slightly differently than in a higher-molecular-weight epoxy monomer. Recent work has explored the swelling and interaction of core-shell rubber particles with styrene monomer contained in vinyl ester resin systems.[81] The styrene was found to be absorbed into the core-shell rubber particles, leading to a twofold effect on the thermal behavior of core-shell rubber/styrene mixtures. The core-shell rubber material affected the crystallization behavior of the styrene monomer when cooled, as evidenced by the shift in the crystallization peak to lower temperatures with decreasing styrene content, shown in Figure 7.10. This allowed the location of the styrene monomer in the core-shell material to be investigated by thermal means. Analysis of the heat of crystallization for styrene/core-shell rubber mixtures revealed that at temperatures below the glass transition temperature of the CSR/styrene monomer system, the styrene core-shell
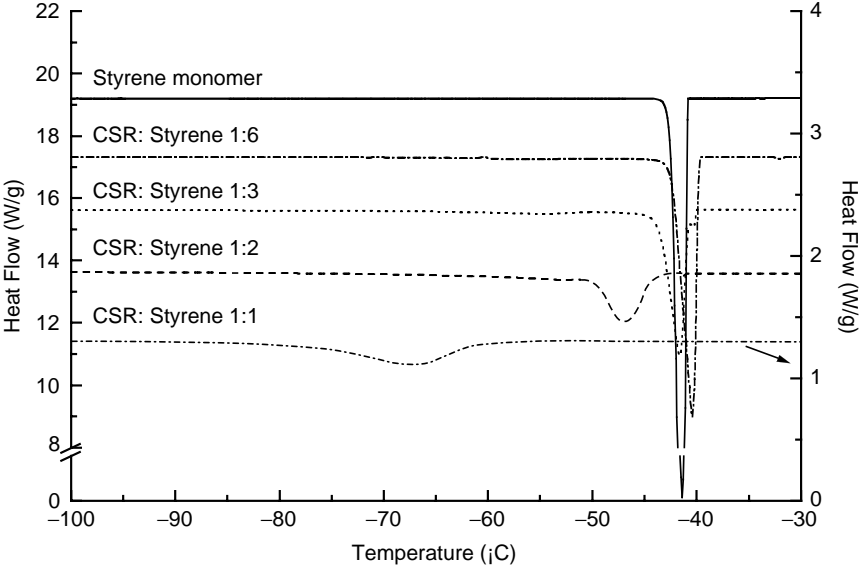

FIGURE 7.10
The shift in crystallization peak with styrene content. (Based on data from Roberts et al., *J. Polym. Sci. Polym. Phys.*, 38B, 3136–3150.)
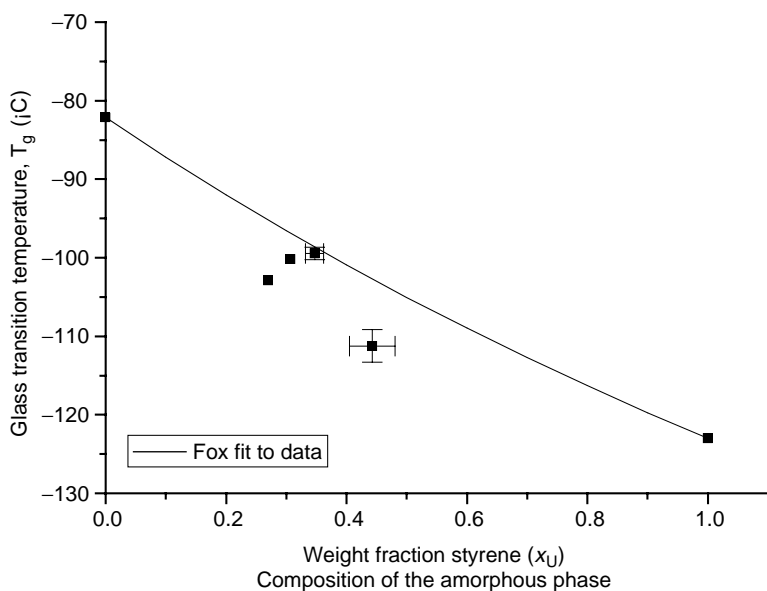
FIGURE 7.11
Variation of the glass transition temperature of the amorphous phase in a CSR/styrene mono-
mer blend, with composition of the amorphous phase. Also shown is a fit of the Fox equation
to the experimental data. (Based on data from Roberts et al., *J. Polym. Sci. Polym. Phys.*, 38B,
3136–3150. With permission.)

rubber mixtures consisted of a glassy, amorphous core-shell rubber/styrene
phase and a pure crystalline styrene phase. This led to the conclusion that
in the CSR/styrene monomer system, the styrene either is associated with
the polymer chains in the CSR and cannot crystallize on cooling, or it does
not interact with the polymer chains and is "free" to crystallize on cooling.
Analysis of the glass transition temperature of the amorphous phase CSR/
styrene phase showed that the styrene monomer plasticizes the core-shell
rubber material, as shown in Figure 7.11. The relationship between styrene
content and glass transition temperature of the amorphous core-shell rub-
ber/styrene phase was estimated using the Fox equation.[82]

7.8   Mechanical Properties of Rubber-Toughened Thermosets

7.8.1   Yielding

Several toughening mechanisms have been proposed for particulate-tough-
ened polymer systems, most of which are shown schematically in Figures
7.12 to 7.14.[44,83] The most effective toughening mechanisms that have been
identified and observed in rubber-toughened thermosetting resins are shear
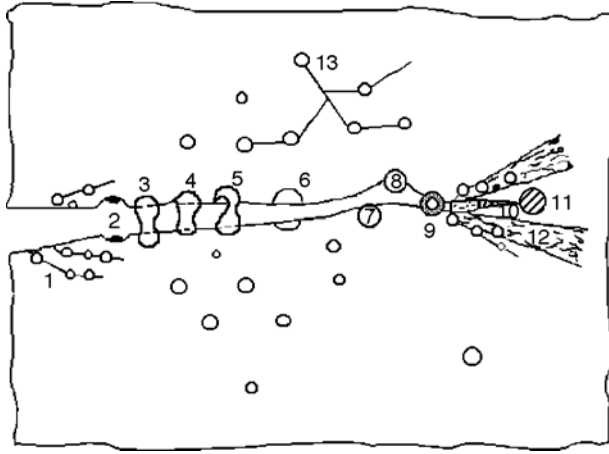
FIGURE 7.12
Toughening mechanisms in particulate-modified polymers: (1) shear band formation near rubber particles; (2) fracture of rubber particles after cavitation; (3) stretching, (4) debonding, and (5) tearing of rubber particles; (6) transparticle fracture; (7) debonding of hard particles; (8) crack deflection by hard particles; (9) voided/cavitated rubber particles; (10) crazing; (11) plastic zone at crack tip; (12) diffuse shear yielding; (13) shear band/craze interaction. (Published with permission from Garg and Mai, 1988, *Composites Sci. Technol.*, 31, 179–223.)

FIGURE 7.13
Crack pinning mechanism. (Published with permission from Sue et al., in *Elastomer Technology Handbook*, Cheremisinoff, Ed., CRC Press: Boca Raton, FL, 1993, pp. 661–700.)

FIGURE 7.14
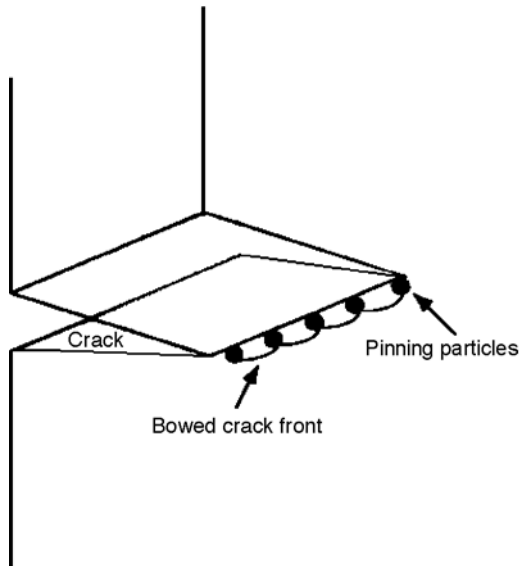(a) Croiding[44] and (b) schematic showing how a dilatational band responds to stress by increasing in thickness and undergoing shear in the plane.[101] (Published with permission from Sue et al., in *Elastomer Technology Handbook*, Cheremisinoff, Ed., CRC Press: Boca Raton, FL, 1993, pp. 661–700; an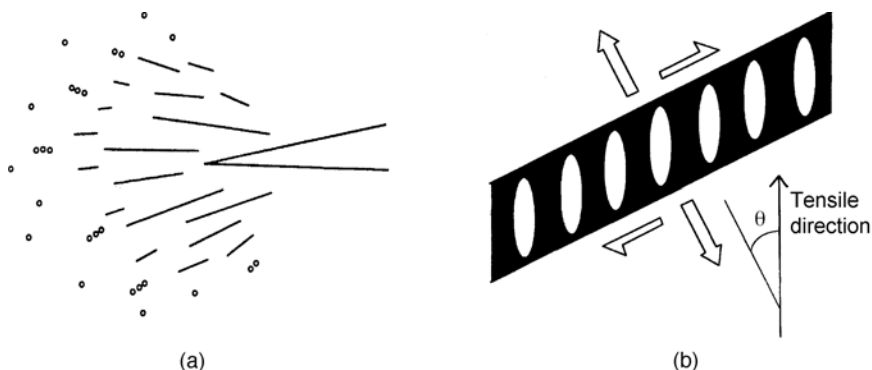d Bucknall, in *Polymer Blends*, Vol. 2, *Performance*, Paul and Bucknall, Eds., Wiley-Interscience: New York, 2000, pp. 83–117.)

yielding or banding of the matrix, cavitation of the rubber particles either by internal cavitation or debonding, and plastic dilation of the matrix or void growth.[44,48,52,74,77,83–97] Shear yielding is the most efficient toughening mechanism as it absorbs the largest amount of energy per unit volume. Other mechanisms such as crack-tip blunting, crack burification, crack deflection, crack pinning, rubber stretching and tearing, crack bridging, and microcracking have also been found to make contributions to toughness,[44] particularly in systems where shear yielding is minimal or does not occur.

The process of matrix shear yielding in a rubber-toughened polymer is identical to that of the matrix itself.[95] Therefore, to gain an understanding of how rubber particles can improve the ability of the matrix to yield, it is important to have an understanding of the process involved and the factors that influence an unmodified material's ability to undergo yielding. Shear yielding is a plastic deformation process that takes place at constant volume and leads to a permanent change in sample shape upon stress release.[98,99] In glassy polymers, it can occur inhomogeneously in the form of highly localized regions, called shear bands, that cover a small area but involve shear strains as high as 250%, or it can occur in diffuse deformation zones that cover a large volume but where the yielded material has undergone only a few percent shear strain more than the surrounding matrix zones.[44,47,100] The localization of shear yielding can be caused by test geometry and the material's intrinsic properties, such as a material's ability to strain soften,[101] and results in the plastic strain in local regions of the material increasing more rapidly than in the bulk.[47,98,99]

Generally, the yield stress will increase with decreasing temperature and increasing strain rate and hydrostatic pressure.[47] The temperature and rate dependence of yielding in many pure polymers and rubber-toughened poly-

mer systems has been described using the Eyring theory of yielding.[101–106] This theory assumes that yielding is a stress-biased, thermally activated rate process where the molecules must overcome an energy barrier for motion. The application of a stress acts to reduce the energy barrier of molecular motion in the forward direction and increase it in the reverse direction. Assuming that the macroscopic strain rate is proportional to the net jump rate of the segments in the forward direction, the relationship[102] between strain rate, $\dot{\varepsilon}$, and yield stress, σ_{yc} is

$$\dot{\varepsilon} = A_E \exp\left(-\frac{\Delta E^* - v^* |\sigma_{yc}|}{RT}\right) \tag{6.6}$$

where A_E is a constant, R is the gas constant, ΔE^* is the activation energy, T is the temperature, and v_* is the activation volume.

At a given temperature, pressure, and strain rate, the intrinsic properties of the polymer, such as molecular structure, cross-link density, and thermal history, will govern the yielding behavior of a polymer. Many studies have shown that the cross-link density, or the molecular weight between the cross-links, influences the yielding behavior.[104–108] As the cross-link density increases, the molecular mobility is reduced, and consequently, the yielding response is suppressed and the yield stress increases. This has consequences when using rubber particles to toughen a brittle polymer matrix, as the toughenability of the resin is governed by the inherent properties of the matrix material. It has been shown[44,71,109,110] that epoxies with high cross-link densities and glass transition temperatures, for example, do not respond as well to rubber toughening as epoxies with lower cross-link densities.

7.8.2 Theories of Toughening

The toughening mechanisms and processes occurring at the crack tip during fracture have been examined primarily through extensive qualitative analysis of the crack-tip process zone around subcritically grown crack tips and the fracture surfaces of failed samples,[44,84,87,88] although some quantitative analysis has been performed using finite element modeling[94,111–113] (FEM) to elucidate and model the processes at a crack tip. While it is generally acknowledged that shear yielding, cavitation of the rubber particles, and plastic dilation of the matrix are the major toughening mechanisms, there is some debate as to the actual significance of each of these mechanisms and the order in which they occur in the fracture process.

At the crack tip, the difference in the shear moduli of the rubber particles and that of the matrix leads to a buildup of stress concentration around each of the particles.[47,95,101] If the particles are close enough together, then the stress fields around each individual particle will interact, leading to an even higher overall stress concentration between the particles,[92,111] as shown in Figure
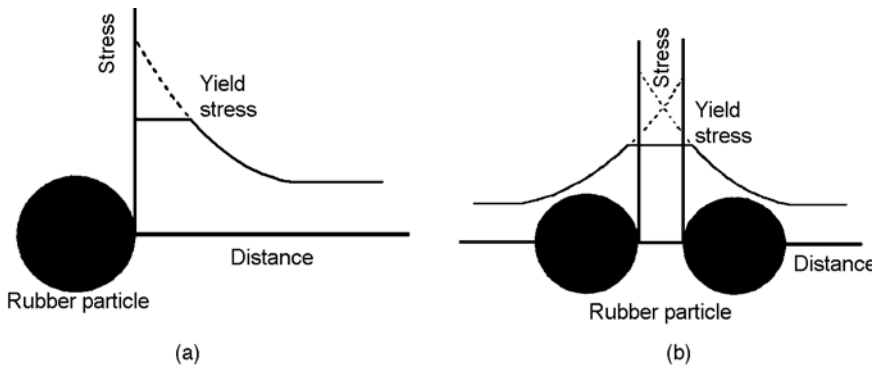
FIGURE 7.15
Schematic of the stress distribution around (a) a single particle, and (b) multiple particles with stress overlap. (Published with permission from Oshima and Sasaki, 1991, *Polym. News*, 16, 198–206.)

7.15. It has been suggested that the points of stress concentration created by the rubber particles provide sites for the initiation of shear bands.[47,95,111,114] From early studies of the impact behavior of rubber/nylon blends, Wu[115] concluded that the critical parameter in promoting toughness was the inter-particle distance — if the interparticle distance is less than a critical value, then sufficient interaction between the stress fields of the particles occurs and tough behavior is predicted. Wu[115] also suggested that the critical value of the interparticle distance is only dependent on matrix material and testing conditions, being independent of particle size and volume fraction of rubber. Although many other workers[77,85,87] have observed the influence of interpar-ticle distance on the extent of plastic deformation at the crack tip (and hence toughness), it was not claimed to have a major influence on toughening. However, recent work by Bagheri and Pearson[116] does suggest that this parameter could have a significant influence on the toughness of the system.

Many studies[44,48,52,72–74,77,85,87,88,90,91,93,101,117–121] on rubber-toughened epoxies, however, have indicated that the role that the rubber particles play in the toughening process is more complicated than simply to act as sites of stress concentration. Two major theories have been proposed to explain how rub-ber particles increase toughness. One is based on yielding induced by particle cavitation, while the other considers the stress enhancement around the rubbery particle.

The first of these two major theories, proposed by Yee and coworkers,[84,87,88] postulated that the toughening process is a combination of particle cavitation and shear yielding. During crack growth, the material at the crack tip is subjected to a triaxial stress field, i.e., a zone of high hydrostatic tension or dilation, which inhibits shear yielding and tends to promote brittle failure of the matrix. However, the applied dilatation stresses on the rubber parti-cles, combined with those stresses within the particle caused by cooling after the curing process, leads to localized cavitation in the rubber particles, or

debonding at the particle/matrix interface.[83,87,112,114] Cavitation relieves the highly triaxial stress state, which then enables shear yielding to occur. While cavitation relieves the triaxial stress, the resultant voids can also act as stress concentrators and their growth further promotes shear yielding.[114] Yee and coworkers[84,87,88] and Sue et al.[44] support this theory through observation of the development of a crack-tip process zone around a subcritically grown crack. The development of the process zone is shown schematically in Figure 7.16 and can be found to initially consist of a circular cavitated zone, within which a shear yielded zone develops. This mechanism is supported by the work of other authors.[52,122] In particular, Li et al.[122] found that if cavitation of the rubber particles is suppressed through the application of an external hydrostatic stress, both the neat and the modified polymer had similar levels of toughness when subjected to the same conditions. Pearson and Yee[90] proposed that rubber with high cavitational resistance would provide better toughening, as it would allow a greater buildup of strain energy prior to cavitation of the particles. Subsequent cavitation of the particles enables the formation of shear bands to proceed at a faster rate, allowing more shear bands to form before the plastic zone cleaves, with the net result being a larger plastic zone, and thus higher toughness.

The role of particle cavitation in the toughening process has been investigated recently by Bagheri and Pearson.[116,123,124] It was found that micron and submicron hollow latex spheres induced similar toughening mechanisms as submicron rubber particles, supporting the view that the role of cavitation is to relieve the plain strain constraint at the crack tip, enabling yielding in the matrix ligaments to occur.[116] However, their data does not support Pearson and Yee's[90] proposal that cavitation resistance is important, and in fact suggests that particle size and interparticle distance dominates mechanical behavior.[116]

An additional toughening mechanism was identified by Sue and coworkers[74,85] and Bucknall and Lazzeri[101,120,121,125] and is described as croiding[74,85] or dilatational yielding,[101,120,121,125] respectively. Croids are highly localized arrays of cavitated particles, which have the appearance and some of the mechanical characteristics of a craze, as shown in Figures 7.14 and 7.17. Sue and coworkers[74,85] found that the damage zone around a crack tip contained a shear-yielded zone that was surrounded by a large craze-like zone. It is thought that the croids initiate at statistically weak particles far away from the crack tip; once these particles have cavitated, the stress concentration in the adjacent particles changes and the neighboring particles cavitate preferentially to the matrix.[74,85] The size of the cavities inside the croids was found to be larger than that inside the circular cavitation zone, indicating that the matrix had plastically deformed to a higher degree around the cavitated particles[74,85] within the croid. Sue[74] proposed that the plastic dilation of the matrix (or dilatational yielding) probably has equal or more significance in increasing toughness than shear yielding.

Bucknall and Lazzeri,[101,120,121,125] in their studies on toughened polymers, have concluded that to understand the toughening process and quantita-
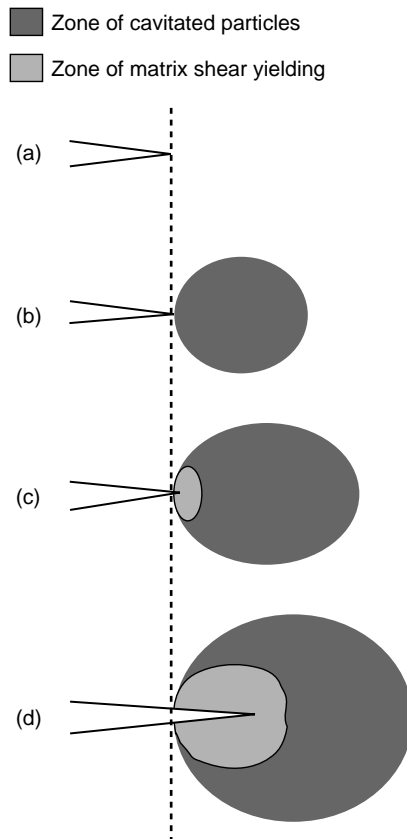
FIGURE 7.16
Schematic of the sequence of toughening mechanisms in a CSR-modified epoxy: (a) the initial starter crack; (b) formation of the cavitation zone; (c) formation of initial shear-yielded plastic zone around the crack tip when the hydrostatic tension is relieved due to cavitation; and (d) once the buildup of strain energy reaches a critical value, the material begins to undergo shear yielding and the crack propagates. (Published with permission from Sue et al., in *Elastomer Technology Handbook*, Cheremisinoff, Ed., CRC Press: Boca Raton, FL, 1993, pp. 661–700.)

tively analyze that process, it is necessary to understand the criteria governing the process of cavitation. They also suggest that the effects of cavitation are only seen under dilatational conditions and are most effective when it occurs in an array of closely spaced particles,[101] particularly when they form a dilatational band. They developed a model that quantitatively describes the particle cavitation process based on a thermodynamic criterion, where the particles cavitate when the available energy exceeds a critical value. It shows that for each particle size there is a critical volume strain required for cavitation, and that the critical volume strain required decreases with increasing particle size. Cavitation allows the matrix surrounding a cavitated particle to yield and stretch to a much greater extent than that prior to cavitation. Bucknall and Lazzeri[101,120,121,125] investigated the relationship
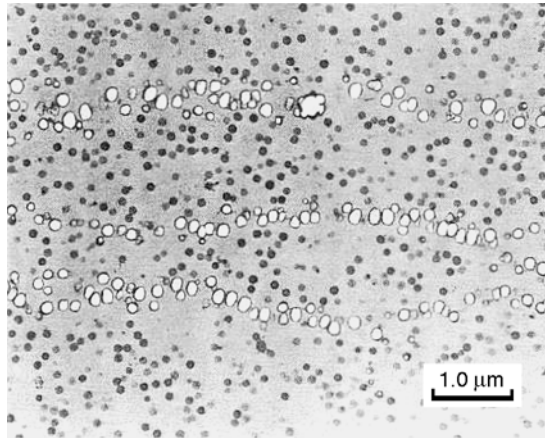
FIGURE 7.17
Transmission electron microscopy image showing mature croids. (From Sue, 1992, *J. Mater. Sci.*, 27, 3098–3107.)

between the process of cavitation and the yielding behavior of rubber-modified systems through the use of cavitation diagrams. The development of these diagrams was based on two principles: (1) cavitation occurs at a critical volume strain; and (2) yielding in polymers is governed by the combination of effective stress and mean stress.[101] These diagrams enable the prediction of the deformation processes occurring with varying contents of cavitated particles and under different loading conditions, and thus tough behavior.

The second major theory of rubber toughening, proposed by Huang and Kinloch,[94,111–113] is based on finite element modeling of the stress fields around a rubbery particle or a void in a glassy matrix. They propose that the role of the rubber particles is to produce stress concentrations in the matrix that initiate microshear bands.[94,111–113] It is thought in this theory that cavitation of the rubber particles is not necessary for shear banding. This is based on Huang and Kinloch's findings that the stress fields around a rubbery particle and a void are identical, indicating that a rubbery particle is equally as likely to promote shear yielding as a cavitated particle. In fact, they have found that cavitation of the rubber particles can occur either before or after shear yielding, and that this is dependent on the modulus and Poisson's ratio of the rubber.[113] Thus cavitation of the particles is a secondary factor, as this process only facilitates the relief of the hydrostatic tension at the crack tip, enabling more extensive void growth.

7.8.3 Effect of Rubber Particle Size

Particle size has been found to greatly influence the toughness of rubber-toughened polymers by controlling the toughening mechanisms that are operative during the fracture process.[55,90,91,123,126] Generally, it is found that

smaller-size rubber particles of ~0.3 to 10 µm lead to greater improvements in fracture toughness than particles smaller than ~0.3 µm or those larger than ~10 µm. Work by Kim et al.[91] and Sultan and McGarry[126] on rubber-toughened epoxies indicate that there is a lower limit to the particle size, below which only modest increases in fracture toughness are observed. Sultan and McGarry[126] showed that 1- to 1.5-µm particles were five times more effective than ~0.1-µm micron particles in increasing the fracture energy. Becu-Longuet et al.[55] found that 0.6-µm CSR particles were more effective in improving toughness than 0.3-µm particles at the same filler levels. Studies of fracture surfaces of an epoxy, modified by 0.16-µm CSR particles, showed particle debonding to be the main toughening mechanism and resulted in limited toughening.[91] This observation led Kim et al.[91] to suggest that the particle size needs to be larger than ~0.2 µm, as extensive cavitation and subsequent shear yielding due to particles smaller than this are limited.

Kim et al.[91] studied rubber-modified epoxy systems containing CSR particles of size 0.12 to 1.2 µm, while Pearson and Yee[90] investigated rubber-modified epoxy systems containing CSR particles of 0.2 µm and CTBN particles of 1 to 200 µm in size. Scanning electron microscopy (SEM) images of fracture surfaces of the rubber-modified epoxies[90,91] revealed cavitation of the rubber particles and plastic deformation of the matrix to be the operative toughening mechanisms for all systems regardless of particle size. In addition to this, Pearson and Yee[90] observed particle debonding in systems containing 10- to 20-µm particles. The similarity of the observed toughening mechanisms in all the systems studied by Kim et al.[91] and Pearson and Yee,[90] however, was not reflected in the values of toughness measured for each system, with the smaller-size particles imparting higher toughness. Pearson and Yee[90] observed a correlation between the size of the process zone (or yielded zone) at the crack tip and the level of improvement in toughness, implying that it is the volume of material undergoing yielding and not necessarily the presence of yielding that governs the ultimate toughness. They also found that both size of the process zone and toughness increased with decreasing particle size.[90] No crack-tip process zone was observed by Pearson and Yee[90] in a system containing 100- to 200-µm particles. Although crack bridging by the rubber particles was observed, it did not have a significant effect on toughness. Similar observations regarding the effect of particle size and toughness have been made by Sue and coworkers[44,93] using three different types and sizes of particles: 0.1-µm CSR particles, 0.4-µm dispersed acrylic rubber particles, and 20-µm Proteus composite particles composed of numerous small (0.2-µm) rubber particles. The CSR particles were found to be the most effective in improving toughness, with cavitation, shear yielding, crack bifurcation, and crack deflection mechanisms being the observed toughening mechanisms. Only crack deflection and crack pinning were observed in systems containing the acrylic rubber and Proteus particles, which resulted in lower toughness.

7.8.4 Effect of Particle Dispersion

Particle dispersion has also been found to affect toughness. Recent studies on the effect of morphology on the toughening of epoxies using preformed CSR particles have suggested that for maximum toughness, the particles need to be locally clustered but globally well dispersed.[44,73,75,117,118] The degree of local dispersion can be changed using shell chemistry,[44,73,75,117,118] cross-link density of the shell,[73,117] thickness of the shell,[75] curing rate,[118] and mixing rate and times,[73,118] both before and after addition of the curing/cross-linking agent.

Qian et al.[73] and Bagheri and Pearson[118] found that longer mixing time influences the dispersion of the particles. Qian et al.[73] reported that increasing the mixing time changed the dispersion from one of macroaggregation (aggregates of the order of > 10 μm) to a state in which the particles were globally well dispersed but were microclustered (aggregates of the order of 1 to 2 μm), and this led to an increase in the fracture toughness. In contrast, Bagheri and Pearson[118] found that a decrease in the CSR aggregate size, from ~2 to ~1 μm, through an increase in the mixing time, led to a decrease in the fracture toughness. A comparison of the results of Qian et al.[73] and Bagheri and Pearson[118] seem to indicate that there is an optimum amount of particle aggregation required for maximum toughness.

In epoxy/CSR systems, the core-shell rubber particle's shell functionality[118] and chemistry[44,75,117] have a profound effect on the type of dispersion. Bagheri and Pearson[118] found that using CSR particles with a functionalized shell led to a uniform dispersion of individual particles and lower toughness than systems containing nonfunctionalized particles, which had a higher toughness and a clustered, interconnected morphology. The shell chemistry controls the level of physical interactions at the interface of the particle and the matrix via the solubility parameter of the shell material. It has been found that decreasing the acrylonitrile content in the shell of the CSR particle with a poly(methyl methacrylate)/AN shell leads to an increasing level of particle aggregation in an epoxy/CSR system.[44,75,117] Reducing the AN content of the CSR's shell from 25 to 12.5 to 0% changed the morphology from a globally random, but locally clustered morphology to a more locally clustered structure, and then to one with large-scale agglomeration, as shown in Figure 7.18.[44,75] Qian et al.[117] observed similar behavior in their CSR/epoxy system, where decreasing the AN content in the shell of the CSR particles from 10 to 0% increased the cluster size from 1 to 5 μm. Both groups observed a decrease in fracture toughness with increasing particle aggregation.

For systems where there is a uniform dispersion or microaggregation of the particles, the toughening mechanisms have been found to be cavitation of the particles followed by shear yielding.[44,73,75,117] In the systems where the particles form large aggregates (~6 μm), crack deflection appears to be the operative toughening mechanism,[44] although in some intermediate systems, both cavitation and shear yielding and crack deflection have also been observed, which have led to a synergistic improvement in fracture
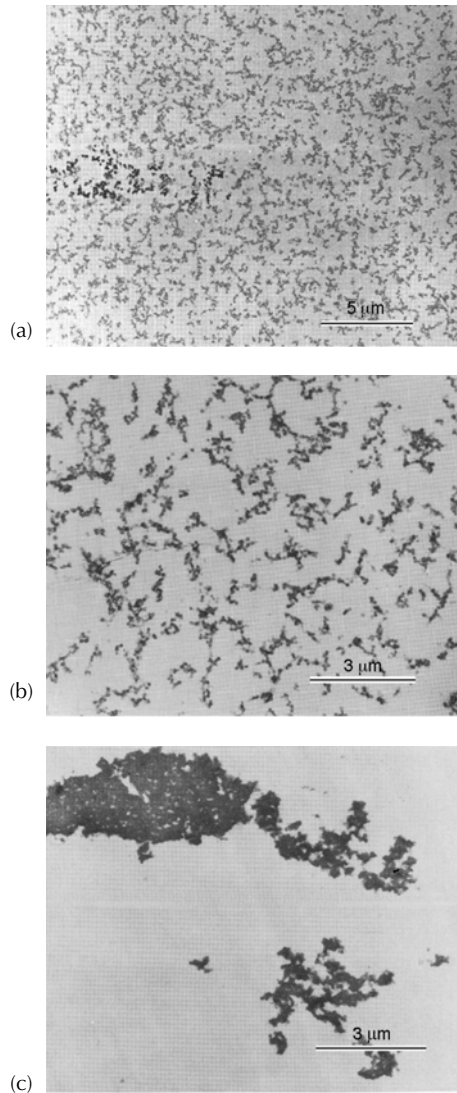
FIGURE 7.18
Transmission electron microscopy image of a crack tip in a CSR-modified epoxy system, showing changes in dispersion of the CSR particles with AN content in the CSR shell. (a) AN content of 25 wt%; (b) AN content of 12.5 wt%; (c) AN content of 0 wt%. (Published with permission from Sue et al., in *Toughened Plastics I: Science and Engineering*, Riew and Kinloch, Eds., American Chemical Society: Washington, D.C., 1993, pp. 259–291.)

toughness.[44,75] Qian et al.[117] have proposed that a microclustered morphology leads to cooperative cavitation in front of the crack tip and results in a much larger plastic zone, as observed previously by Bagheri and Pearson.[118] A more uniform dispersion leads to a random, less-coordinated cavitation of particles, which seems to lead to a lower toughness.

7.8.5 Effect of Interparticle Distance and Stress State

Interparticle distance has been found to be a key variable in understanding fracture toughness in rubber-modified polymers. As noted above, in an initial study of the impact behavior of rubber/nylon blends, Wu[115] found that the distance between the rubber particles was the critical parameter in promoting toughness and proposed that if the interparticle distance was less than a critical value, then there was sufficient interaction between the stress fields of the particles to promote tough behavior. Subsequent to these initial studies, Wu and Margolina[127,128] developed the theory further, and rather than using the interparticle distance as the critical parameter, they used an equivalent parameter — the matrix ligament thickness. These workers proposed that only ligaments that are thinner than the critical thickness can yield, and that the yielding process propagates first through the thin ligaments and then into thicker ones. The propagation of the yielding process was thus formulated as a percolation of thin ligaments. It was suggested that there is a level of connectivity between thin ligaments, which needs to be attained before toughening behavior is observed. It was thought that the onset of tough behavior occurs close to the "first-path" percolation threshold. This theory has implications with respect to particle dispersion. If the particles are clumped, then the ligaments within the clumps are small, but remain large outside, limiting yielding to within the clumps. Wu[128] found that the impact resistance of a nylon/rubber blend decreased dramatically when the particles had flocculated. However, as discussed above, many workers have found that some degree of aggregation results in an improvement of toughness.

Bagheri and Pearson[116] have recently reassessed the influence of interparticle distance on the toughness of a toughened epoxy resin. They observed a brittle-to-ductile transition, similar to that observed by Wu,[115] with decreasing interparticle distance. However, unlike Wu,[115] they did not observe a specific transition point common to all systems, but rather one that varied with type and size of particle. Bagheri and Pearson[116] correlated the fracture toughness to the interparticle distance via a power law, and also found that the variation in fracture toughness with plate thickness could be modeled in the same manner. They conclude, therefore, that the origin of improved fracture toughness in modified epoxies can be explained by means of interparticle distance and a stress-state transition in the ligaments between the particles from a plane strain to a plane stress condition.[116] The observed transition from brittle-to-ductile fracture is influenced by the particle size and originates in the influence that the particle size has on the yielding behavior.

7.9 Rubber-Modified Vinyl Ester Resins

Much less work has been published in the area of rubber-modified vinyl ester resins. Until recently, the two main methods that have been used to

improve the bulk toughness of vinyl ester resins were the creation of rubber particles via phase separation and the incorporation of flexible units into the dimethacrylate backbone of the vinyl ester resin. As discussed previously, in Section 7.5, many different phase-separated vinyl ester resin/liquid rubber systems have been studied.[5,60–66] Incorporation of flexible units into the dimethacrylate backbone is achieved by reacting about 7.5 phr of a carboxyl-terminated butadiene-acrylonitrile liquid rubber into the resin system.[5,64,65,129] The CTBN is chemically bonded through terminal ester groups with 2.2'-bis(4-hydroxypheyl) propane units during manufacture.[61] More recently, preformed core-shell rubber particles have been shown to increase the toughness of vinyl ester resin systems.[43] Additions of core-shell rubber particles have also been found to increase the toughness of vinyl ester resin-based fiber-reinforced composite systems.[130]

A range of morphologies has been observed in rubber-toughened vinyl ester resins, mainly due to the many different rubber additives and curing regimes used. Many workers[61,66] found poor compatibility between the liquid rubber and the resin, which tended to result in large particles that had low adhesion to the matrix.[63,65,66] Particles ranging from ~10 nm with a vinyl-terminated butadiene-acrylonitrile rubber[62] to 40 μm with a hydroxy-terminated polybutadiene (HTBN) rubber[61] have been observed. In a VER/VTBN system, Dreerman et al.[66] found that the particle size and number of particles increased with increasing rubber content. Interestingly, Liao et al.[62] observed very small particles using VTBN, while other workers[61,66] obtained VTBN particles of the size 10 to 20 μm. Liao et al.[62] suggest that the very small particle size obtained was due to the gelation of VER at an early stage in the reaction, which prevented aggregation of the rubber molecules. Of the rubbers used above, Ullett and Chartoff[5] found that addition of EBTN, CTBN, PBA, and HTE to VER formed two-phase particles, while EHA and VTBNX formed single-phase particles. Dreerman et al.[66] also noticed an internal structure in the ETBN particles and suggested that it implies a dual-phase structure in the rubber particles. While the morphology of most systems was more dependent upon type of rubber, Pierce and coworkers[63,65] found that the morphology of epoxy-terminated butadiene-acrylonitrile rubber particles also depended on volume fraction of rubber, because an internal nodular structure develops at lower rubber loadings.[63,65]

As was the case for rubber-modified epoxy resins discussed earlier, the addition of rubber to vinyl ester resins usually leads to an increase in toughness. The extent to which the rubbery phase influences the toughness and fracture behavior was found to depend on one or more of the following factors: the type of rubber, the morphology of the rubber particles,[5] the cure regime,[5] the testing rate,[61,66] and the compatibility or chemistry of the rubber/matrix system.[61] The most commonly used rubber modifiers in vinyl ester resins are VTBN and ETBN,[5,63–66] of which ETBN has been found to be the most effective in increasing toughness. Ullett and Chartoff[5] found that systems containing two-phase particles led to greater increases in toughness than those containing single-phase particles. Examination of the fracture

surfaces of these systems revealed that the toughening mechanisms for the systems with the two-phase particles were cavitation and shear yielding, while only crack bridging and particle deformation were observed for the systems with single-phase particles.[5]

Studies on the effect of rubber particles on the impact behavior of a vinyl ester resin show conflicting results.[62,66] Liao et al.[62] observed impact toughness to increase with additions of VTBN, while Dreerman et al.[66] observed no improvement in toughness using VTBN or ETBN. This difference may be associated with particle size, because Liao et al.[62] found very small particle sizes (~10 nm) and Dreerman et al.[66] observed particle sizes greater than 1 μm. A comparison of the behavior observed by Ullett and Chartoff,[5] Dreerman et al.,[66] and Pham and Burchill[61] highlights the effect of test speed and test type on the fracture behavior of pure VER matrix material and the rubber-modified VER. The pure resin material was found[61,66] to fail catastrophically using the single-edge-notch three-point-bend technique, but when tested using compact tension sample geometry[5] or the much slower double-torsion method,[61] stick/slip or stable crack propagation was observed. Dreerman et al.[66] and Ullett and Chartoff[5] found that additions of rubber changed the fracture mode from catastrophic failure to stick/slip. While Pham and Burchill[61] observed no change in the failure mode with additions of rubber using the single-edge-notch three-point-bend method, all samples failed catastrophically. Toughness values determined in Pham and Burchill's study[61] by the single-edge-notch three-point-bend technique were lower than those determined by the double-torsion technique, highlighting the influence of test conditions on measurements of fracture toughness.

The effect of compatibility between the rubber particulate phase and the matrix was investigated by Pham and Burchill[61] using VTBN and a HTBN, as well as HTBN rubber that had been modified by reaction with a diisocyanate and various alcohols to increase compatibility between the rubbery phase and the matrix resin. The HTBN rubber and modified HTBN rubbers were not miscible with the resin. It was found that as the length of the chain and polarity of the end group of the modified HTBN rubbers increased, so did the toughness.[61] Generally, the size of the end group on the modified HTBN chains did not affect the fracture behavior, except for the modified HTBN with the largest end group, which altered the fracture behavior from stick/slip behavior to one of stable growth. It was suggested that the improvement in toughness with the modified HTBN end-group size was probably the result of an increase in the volume of dispersed phase.[61] The volume fraction of rubber, as determined from polished sections, appeared to be larger than expected from the volume of rubber added to the resin. Results of morphological and spectroscopic analysis showed that it was likely that appreciable amounts of styrene and a lesser amount of the methacrylate component had reacted with the liquid rubber, leading to a two- or threefold increase in the volume of rubber.

Recently, the effect of core-shell rubber particles on the mechanical behavior of vinyl ester resins has been investigated.[43] It was found by Roberts[43]
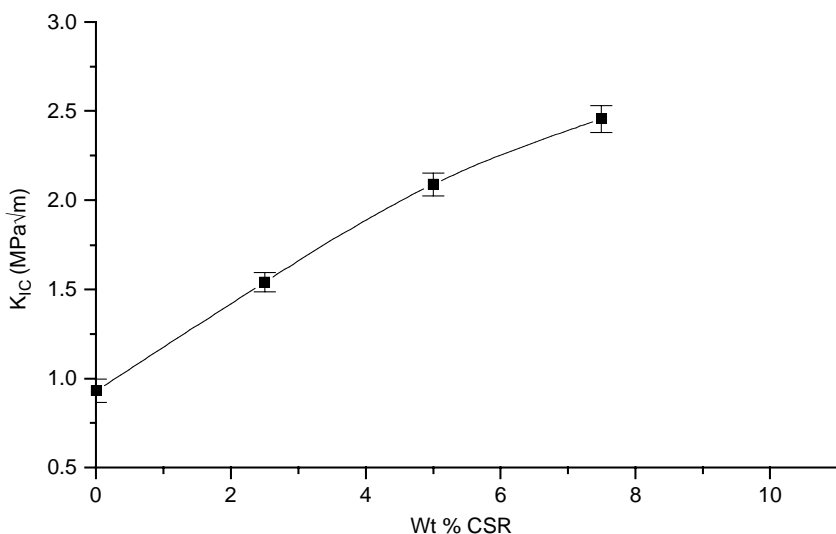
FIGURE 7.19
Variation of the fracture toughness of a CSR/vinyl ester resin system with CSR content. (From Roberts, K.N., Ph.D. dissertation, Monash University, Melbourne, Australia, 2002.)

that additions of CSR particles to a vinyl ester resin matrix reduced the yield stress and increased the fracture toughness. Addition of 5 wt% CSR led to a 124% increase in the value of K_{IC}, as shown in Figure 7.19. Additions of similar levels (i.e., ~5 wt%) of liquid reactive rubbers to vinyl ester resin have been found to have a varying effect on the toughness, ranging in decreases in toughness by up to 16%[61] to increases in toughness of up to 157%.[60] The significant increases in toughness observed by Roberts were unexpected, given that the CSR particles in the CSR/vinyl ester resin system studied formed a clumped morphology, similar to that observed by Bagheri and Pearson[118] in an epoxy/CSR system. The toughening mechanisms in the CSR/VER system appear to be shear yielding and particle cavitation, as observed for the liquid rubber/VER systems discussed previously.

7.10 Concluding Remarks

The increased use of polymeric and composite materials in today's world require the continual improvement and development of materials. Although vinyl ester resins offer many advantages over epoxy resins, expected usage is limited by their poor toughness. The improvement of the brittle nature of thermosetting polymers has been the subject for investigation over the last 30 years. The most effective method is through the addition of a rubbery particulate phase. The most common method used is liquid reactive rubber

systems that are initially miscible in the matrix, but which phase separate during cure, forming discrete rubbery particles. While this method can increase the toughness of the matrix, the final morphology, and thus the toughness, is very dependent upon the system chemistry and curing conditions. These problems have been overcome through the use of preformed core-shell rubber particles, which are produced via emulsion polymerization and whose particle size and shape are predefined and can be simply blended into the matrix material.

The use of a rubbery second phase to increase the toughness of a brittle thermosetting polymer has been extensively studied, particularly in epoxy-based systems. Although the main toughening mechanisms have been identified as shear yielding of the matrix and cavitation of the rubber particles, there is still some debate as to the exact role cavitation plays in the toughening process. Vinyl ester resin/rubber systems have been studied to a much lesser degree than epoxy/rubber systems. Although liquid rubber has been found to increase the toughness of vinyl ester resin systems, the poor compatibility between the rubber and the vinyl ester resin often leads to large particle sizes, and hence minimal increases in toughness. The use of core-shell rubber particles in vinyl ester systems appears to have overcome the problems observed in liquid rubber systems, and can increase the toughness of vinyl ester resins significantly. However, recent studies have shown that the use of core-shell rubber particles in systems such as vinyl ester resin, which contains a low-molecular-weight diluent, may also influence the rheological and processing behavior of such systems. This highlights the need to understand the system as a whole, as an attempt to improve one property may lead to the diminution of another.

References

1. Anderson, T.F. and Messick, V.B., in *Developments in Reinforced Plastics-1: Resin Matrix Aspects*, Prichard, G., Ed., Applied Science Publishers: London, 1980, pp. 29–58.
2. Dua, S., McCullough, R.L., and Palmese, G.R., 1999, *Polym. Composites*, 20, 379–391.
3. Young, R.E., in *Unsaturated Polyester Technology*, Bruins, P.F., Ed., Gordon and Breach Science Publishers: New York, 1976, pp. 315–342.
4. O'Hearn, T.P., in *Engineered Materials Handbook*, Vol. 2, *Engineering Plastics*, ASM International: 1988, pp. 272–275.
5. Ullett, J.S. and Chartoff, R.P., 1995, *Polym. Eng. Sci.*, 35, 1086–1097.
6. Li, L., Sun, X., and Lee, L.J., 1999, *Polym. Eng. Sci.*, 39, 646–661.
7. Cook, W.D., Simon, G.P., Burchill, P.J., Lau, M., and Finch, T.J., 1997, *J. Appl. Polym. Sci.*, 64, 769–781.
8. Kamath, V.R. and Gallagher, R.B., in *Developments in Reinforced Plastics-1: Resin Matrix Aspects*, Pritchard, G., Ed., Applied Science Publishers: New York, 1980, pp. 121–144.

9. Stone, M.A., Fink, B.K., Bogetti, T.A., and Gillespie, J.W., 2000, *Polym. Eng. Sci.*, 40, 2489–2497.
10. Lee, J.H. and Lee, J.W., 1994, *Polym. Eng. Sci.*, 34, 742–749.
11. Lam, P.W.K., Plaumann, H.P., and Tran, T., 1990, *J. Appl. Polym. Sci.*, 41, 3043–3057.
12. Mousa, A. and Karger-Kocsis, J., 2000, *Polym. Polym. Composites*, 8, 455–460.
13. Hong, M.S. and Chung, I.J., 1991, *Polym. J.*, 23, 747–755.
14. Han, C.D. and Lem, K.-W., 1984, *J. Appl. Polym. Sci.*, 29, 1879–1902.
15. Dean, K., Cook, W.D., Burchill, P.J., and Zipper, M., 2001, *Polymer*, 42, 1345–1359.
16. Dean, K., Cook, W.D., Burchill, P.J., and Zipper, M., 2001, *Polymer*, 42, 3589–3601.
17. Lem, K.-W. and Han, C.D., 1984, *Polym. Eng. Sci.*, 24, 175–184.
18. Salla, J.M. and Ramis, X., 1996, *Polym. Eng. Sci.*, 36, 835–851.
19. Gonis, J., Simon, G.P., and Cook, W.D., 1999, *J. Appl. Polym. Sci.*, 72, 1479–1488.
20. Palmese, G.R., Andersen, O.A., and Karbhari, V.M., 1999, *Composites Appl. Sci. Manuf.*, 30A, 11–18.
21. Kamal, M.R. and Sourour, S., 1973, *Polym. Eng. Sci.*, 13, 59–64.
22. Kamal, M.R., 1974, *Polym. Eng. Sci.*, 14, 231–239.
23. Yousefi, A., Lafleur, P.G., and Gauvin, R., 1997, *Polym. Composites*, 18, 157–168.
24. Yang, Y.S. and Lee, L.J., 1988, *J. Appl. Polym. Sci.*, 36, 1325–1342.
25. Ziaee, S. and Palmese, G.R., 1999, *J. Polym. Sci. Polym. Phys.*, 37B, 725–744.
26. Ganem, M., Mortaigne, B., Bellenger, V., and Verdu, J., 1993, *J. Macromol. Sci. Pure Appl. Chem.*, A30, 829–848.
27. Yang, Y.S. and Lee, L.J., 1988, *Polymer*, 29, 1793–1800.
28. Liu, S.B., Lui, J.L., and Yu, T.L., 1994, *J. Appl. Polym. Sci.*, 53, 1165–1177.
29. Hsu, C.P. and Lee, L.J., 1993, *Polymer*, 34, 4496–4505.
30. Hsu, C.P. and Lee, L.J., 1991, *Polymer*, 32, 2263–2271.
31. Martin, J.S., Laza, J.M., Morrás, M.L., Rodríguez, M., and León, L.M., 2000, *Polymer*, 41, 4203–4211.
32. Winter, H.H., in *Encyclopedia of Polymer Science and Engineering*, 2nd ed., Supplement Volume, Wiley-Interscience: New York, 1989, pp. 343–351.
33. Macosko, C.W., 1985, *Br. Polym. J.*, 17, 239–245.
34. Winter, H.H., 1987, *Polym. Eng. Sci.*, 27, 1698–1701.
35. Winter, H.H. and Chambon, F., 1986, *J. Rheol.*, 30, 367–382.
36. Winter, H.H., 1987, *Prog. Colloid Polym. Sci.*, 75, 104–110.
37. Eloundou, J.-P., Gerard, J.-F., Harran, D., and Pascault, J.P., 1996, *Macromolecules*, 29, 6917–6927.
38. Eloundou, J.P., Feve, M., Gerard, J.F., Harran, D., and Pascault, J.P., 1996, *Macromolecules*, 29, 6907–6916.
39. Lairez, D., Adam, M., Emery, J.R., and Durand, D., 1992, *Macromolecules*, 25, 286–289.
40. Vilgis, T.A. and Winter, H.H., 1988, *Colloid Polym. Sci.*, 266, 494–500.
41. Chambon, F. and Winter, H.H., 1987, *J. Rheol.*, 31, 683–697.
42. Winter, H.H., 1999, *Kor. Aust. Rheol. J.*, 11, 275–278.
43. Roberts, K.N., Ph.D. dissertation, School of Physics and Materials Engineering, Monash University, Melbourne, Australia, 2002.
44. Sue, H.J., Garcia-Meitin, E.I., and Pickleman, D.M., in *Elastomer Technology Handbook*, Cheremisinoff, N.P., Ed., CRC Press: Boca Raton, FL, 1993, pp. 661–700.
45. Azimi, H.R., Pearson, R.A., and Hertzberg, R.W., 1996, *Polym. Eng. Sci.*, 36, 2352–2365.

46. Azimi, H.R., Pearson, R.A., and Hertzberg, R.W., 1995, *J. Appl. Polym. Sci.*, 58, 449–463.
47. Kinloch, A.J. and Young, R.E., *Fracture Behaviour of Polymers*, Applied Science Publishers: London, 1983.
48. Maazouz, A., Sautereau, H., and Gerard, J.F., 1994, *Polym. Bull.*, 33, 67–74.
49. Becu-Longuet, L., Gérard, J.-F., Maazouz, A., Pichot, C., and Sautereau, H., *European Symposium on Polymer Blends: Extented Abstracts*, Applied Science Publishers Ltd.: Maastricht, Netherlands, 1996.
50. Lovell, P.A., 1995, *Macromol. Symp.*, 92, 71–81.
51. Lovell, P.A., 1996, *Trends Polym. Sci.*, 4, 264–272.
52. Becu, L., Maazouz, A., Sautereau, H., and Gérard, J.F., 1997, *J. Appl. Polym. Sci.*, 65, 2419–2431.
53. Becu, L., Sautereau, H., Maazouz, A., Gerard, J.F., Pabon, M., and Pichot, C., 1995, *Polym. Adv. Technol.*, 6, 316–325.
54. Day, R.J., Lovell, P.A., and Pierre, D., 1997, *Polym. Int.*, 44, 288–299.
55. Becu-Longuet, L., Bonnet, A., Pichot, C., Sautereau, H., and Maazouz, A., 1999, *J. Appl. Polym. Sci.*, 72, 849–858.
56. Becu, L., Sautereau, H., Maazouz, A., Gerard, J.F., Pabon, M., and Pichot, C., 1994, *Ann. Chim. Sci. Mater.*, 19, 363–367.
57. Gillham, J.K., in *Structural Adhesives: Developments in Resins and Primers*, Kinloch, A.J., Ed., Elsevier Applied Science Publishers: London, 1986, pp. 1–28.
58. Shaw, S.J., in *Chemistry and Technology of Epoxy Resins*, Ellis, B., Ed., Blackie Academic & Professional: Glasgow, 1993, pp. 127–162.
59. Kinloch, A.J., in *Structural Adhesives: Developments in Resins and Primers*, Kinloch, A.J., Ed., Elsevier Applied Science Publishers: London, 1986, pp. 127–162.
60. Auad, M.L., Frontini, P.M., Borrajo, J., and Aranguren, M.I., 2001, *Polymer*, 42, 3723–3730.
61. Pham, S. and Burchill, P.J., 1995, *Polymer*, 36, 3279–3285.
62. Liao, F.-H., Chu, N.-J., and Tong, S.-N., 1988, *J. Appl. Polym. Sci.*, 35, 797–806.
63. Pearce, P.J., Siebert, A.R., Egan, D.R., Guiley, C.D., and Drake, R.S., 1995, *J. Adhesion*, 49, 245–259.
64. Ullett, J.S. and Chartoff, R.P., 1993, *Polym. Mater. Sci. Eng.*, 70, 100–103.
65. Siebert, A.R., Guiley, C.D., and Egan, D.R., in *47th Annual Conference, Composites Institute, The Society of the Plastics Industry*, 1992.
66. Dreerman, E., Narkis, M., Siegmann, A., Joseph, R., Dodiuk, H., and Dibenedetto, A.T., 1999, *J. Appl. Polym. Sci.*, 72, 647–657.
67. Cruz-Ramos, C.A., in *Polymer Blends*, Vol. 2, *Performance*, Paul, D.R. and Bucknall, C.B., Eds., Wiley-Interscience: New York, 2000, pp. 137–175.
68. Landfester, K., Boeffel, C., Lambla, M., and Spiess, H.W., 1995, *Macromol. Symp.*, 92, 109–116.
69. Nelliappan, V., El-Aasser, M.S., Klein, A., Daniels, E.S., Roberts, J.E., and Pearson, R.A., 1997, *J. Appl. Polym. Sci.*, 65, 581–593.
70. Parker, D.S., Sue, H.-J., Huang, J., and Yee, A.F., 1990, *Polymer*, 31, 2267–2277.
71. Lu, F., Kausch, H.H., Cantwell, W.J., and Fischer, M., 1996, *J. Mater. Sci. Lett.*, 15, 1018–1021.
72. Lu, F., Cantwell, W.J., and Kausch, H.H., 1997, *J. Mater. Sci.*, 32, 3055–3059.
73. Qian, J.Y., Pearson, R.A., Dominie, V.L., and El-Aasser, M.S., 1995, *J. Appl. Polym. Sci.*, 58, 439–448.
74. Sue, H.-J., 1992, *J. Mater. Sci.*, 27, 3098–3107.

75. Sue, H.-J., Garcia-Meitin, E.I., Pickelman, D.M., and Yang, P.C., in *Toughened Plastics I: Science and Engineering*, Riew, C.K. and Kinloch, A.J., Eds., American Chemical Society: Washington, D.C., 1993, pp. 259–291.

76. Sue, H.-J., Garcia-Meitin, E.I., Pickelman, D.M., and Bott, C.J., 1996, *Colloid Polym. Sci.*, 274, 342–349.

77. Xiao, K. and Ye, L., 2000, *Polym. Eng. Sci.*, 40, 70–81.

78. Nielsen, L.E., *Polymer Rheology*, Marcel Dekker: New York, 1977.

79. Levita, G., Marchetti, A., Lazzeri, A., and Piatelli, F., 1993, *Mater. Eng. (Modena, Italy)*, 4, 171–183.

80. Nguyen-Thuc, B.H. and Maazouz, A., 2002, *Polym. Eng. Sci.*, 42, 120–133.

81. Roberts, K.N., Simon, G.P., Cook, W.D., and Burchill, P.J., 2000, *J. Polym. Sci. Polym. Phys.*, 38B, 3136–3150.

82. Fox, T.G., 1956, *Bull. Am. Phys. Soc.*, 1, 123.

83. Garg, A.C. and Mai, Y.-W., 1988, *Composites Sci. Technol.*, 31, 179–223.

84. Sue, H.-J. and Yee, A.F., 1993, *J. Mater. Sci.*, 28, 2975–2980.

85. Sue, H.-J., Garcia-Meitin, E.I., and Orchard, N.A., 1993, *J. Polym. Sci. Polym. Phys.*, 31B, 595–608.

86. Sue, H.J., Pearson, R.A., Parker, D.S., Huang, J., and Yee, A.F., 1988, *Polym. Prepr.*, 29, 147–148.

87. Pearson, R.A. and Yee, A.F., 1986, *J. Mater. Sci.*, 21, 2475–2488.

88. Yee, A.F. and Pearson, R.A., 1986, *J. Mater. Sci.*, 21, 2462–2474.

89. Kinloch, A.J., Shaw, S.J., Tod, D.A., and Hunston, D.L., 1983, *Polymer*, 24, 1341–1354.

90. Pearson, R.A. and Yee, A.F., 1991, *J. Mater. Sci.*, 26, 3828–3844.

91. Kim, D.S., Cho, K., Kim, J.K., and Park, C.E., 1996, *Polym. Eng. Sci.*, 36, 755–768.

92. Oshima, J. and Sasaki, I., 1991, *Polym. News*, 16, 198–206.

93. Sue, H.-J., 1991, *Polym. Eng. Sci.*, 31, 275–288.

94. Huang, Y. and Kinloch, A.J., 1992, *J. Mater. Sci.*, 27, 2763–2769.

95. Partridge, I.K., in *Multicomponent Polymer Systems*, Miles, I.S. and Rostami, S., Eds., Longman Scientific and Technical: U.K., 1992, pp. 149–186.

96. Grentzer, T.H., Rust, D.A., Lo, S.K., Spencer, C.J., and Hackworth, G.W., in *46th Annual Conference, Composites Institute, The Society of the Plastics Industry*, 1991.

97. Yee, A.F., Du, J., and Thouless, M.D., in *Polymer Blends*, Vol. 2, *Performance*, Paul, D.R. and Bucknall, C.B., Eds., Wiley-Interscience: New York, 2000, pp. 225–267.

98. Crist, B., in *The Physics of Glassy Polymers*, Haward, R.N. and Young, R.J., Eds., Chapman & Hall: London, 1997, pp. 155–212.

99. Bowden, P.B., in *The Physics of Glassy Polymers*, Haward, R.N., Ed., Applied Science Publishers: London, 1973, pp. 279–339.

100. Wu, J. and Mai, Y.-W., 1995, *Mater. Forum*, 19, 181–199.

101. Bucknall, C.B., in *Polymer Blends*, Vol. 2, *Performance*, Paul, D.R. and Bucknall, C.B., Eds., Wiley-Interscience: New York, 2000, pp. 83–117.

102. Kinloch, A.J., Shaw, S.J., and Hunston, D.L., 1983, *Polymer*, 24, 1355–1363.

103. Vakil, U.M. and Martin, G.C., 1993, *J. Mater. Sci.*, 28, 4442–4450.

104. Cook, W.D., Mayr, A.E., and Edward, G.H., 1998, *Polymer*, 39, 3725–3733.

105. Mayr, A.E., Cook, W.D., and Edward, G.H., 1998, *Polymer*, 39, 3719–3724.

106. Kody, R.S. and Lesser, A.J., 1997, *J. Mater. Sci.*, 32, 5637–5643.

107. Kozey, V.V. and Kumar, S., 1994, *J. Mater. Res.*, 9, 2717–2726.

108. Cook, W.D., Mehrabi, M., and Edward, G.H., 1999, *Polymer*, 40, 1209–1218.

109. van der Sanden, M.C.M. and Meijer, H.E.H., 1993, *Polymer*, 34, 5063–5072.

110. Pearson, R.A. and Yee, A.F., 1989, *J. Mater. Sci.*, 24, 2571–2580.

111. Huang, Y. and Kinloch, A.J., 1992, *J. Mater. Sci.*, 27, 2753–2762.
112. Huang, Y. and Kinloch, A.J., 1992, *J. Mater. Sci. Lett.*, 11, 484–487.
113. Huang, Y. and Kinloch, A.J., 1992, *Polymer*, 33, 5338–5340.
114. Lee, W.H., in *Polymer Blends and Alloys*, Folkes, M.J. and Hope, P.S., Eds., Blackie Academic and Professional: London, 1993, pp. 163–194.
115. Wu, S., 1985, *Polymer*, 26, 1855–1863.
116. Bagheri, R. and Pearson, R.A., 2000, *Polymer*, 41, 269–276.
117. Qian, J.Y., Pearson, R.A., Dominie, V.L., Shaffer, O.L., and El-Asser, M.S., 1997, *Polymer*, 38, 21–30.
118. Bagheri, R. and Pearson, R.A., 1996, *J. Mater. Sci.*, 31, 3945–3954.
119. Yee, A.F., Li, D.M., and Li, X.W., 1993, *J. Mater. Sci.*, 28, 6392–6398.
120. Lazzeri, A. and Bucknall, C.B., 1993, *J. Mater. Sci.*, 28, 6799–6808.
121. Lazzeri, A. and Bucknall, C.B., 1995, *Polymer*, 36, 2895–2902.
122. Li, D., Yee, A.F., Chen, I.-W., Cheng, S.-C., and Takahashi, K., 1994, *J. Mater. Sci.*, 29, 2205–2215.
123. Bagheri, R. and Pearson, R.A., 1996, *Polymer*, 37, 4529–4538.
124. Bagheri, R. and Pearson, R.A., 1995, *Polymer*, 36, 4883–4885.
125. Bucknall, C.B., in *The Physics of Glassy Polymers*, Haward, R.N. and Young, R.J., Eds., Chapman & Hall: London, 1997, pp. 363–412.
126. Sultan, J.N. and McGarry, F.J., 1973, *Polym. Eng. Sci.*, 13, 29–34.
127. Margolina, A. and Wu, S., 1988, *Polymer*, 29, 2170–2173.
128. Wu, S., 1988, *J. Appl. Polym. Sci.*, 35, 549–561.
129. Siebert, A.R., Guiley, C.D., Kinloch, A.J., Fernando, M., and Heijnsbrock, E.P.L., in *Toughened Plastics II: Novel Approaches in Science and Engineering*, Riew, C.K. and Kinloch, A.J., Eds., American Chemical Society: Washington, D.C., 1996, pp. 151–160.
130. Burchill, P.J., Kootsookos, A., and Lau, M., 2001, *J. Mater. Sci.*, 36, 4239–4247.
131. Shenoy, A.V., *Rheology of Filled Polymer Systems*, Kluwer Academic Publishers: London, 1999.

8

Properties of Dendrimers and Hyperbranched Polymers and Their Blends

Haipeng Wang and George P. Simon

CONTENTS

8.1   Introduction

Polymeric materials have made a significant impact on many aspects of our daily lives, and many new types of polymers are being developed. Among them is a very new family of polymers known as dendritic macromolecules (dendrimers and hyperbranched polymers), which are receiving increasing

interest as the search for new, tailor-made polymeric materials with specific properties intensifies.

These polymers are highly branched, with three-dimensional features similar to the structure of trees (they are sometimes known as arborescent polymers). Once a certain size is reached, dendritic molecules usually adopt a globular shape. This proposed globular shape of dendrimers has caused much interest in the recent years because it differs very much from the random coil of conventional linear macromolecules. The high degree of branching for dendritic polymers has a number of consequences, e.g., only small amounts of interchain entanglement and little or no crystallization (usually amorphous, although not always true).[1] The lack of entanglement may often lead to poor mechanical properties (brittleness) but good solubility in solvents and a low melt viscosity[2] for the dendritic macromolecules, as compared to their linear analogues of the same molar mass.

Three broad types of dendritic macromolecules can be identified: hyperbranched polymers, dendrimers, and hybrid dendritic-linear macromolecules.

8.2 Dendrimers and Their Structure

The first dendrimers were introduced in 1978 by Vögtle and coworkers[3] and initially known as "cascade" molecules. In 1985, Tomalia et al.[4,5] published important work with regards to dendrimers. Different names, such as cascade molecules, arborols, and dendrimers, were used to describe the structure now more generally called dendritic. Since then, interest in dendrimers has rapidly grown, and many papers have been published in recent years. Extensive reviews on the above structures have been published, for example, by Tomalia et al. and others.[6-9]

Dendrimers consist of AB_x-molecules combined in several layers around a central core molecule where each layer is known as a generation (Figure 8.1[10]). When AB_x-monomers are reacted under optimal conditions and the reactive mixture is carefully purified, *dendrons* can be obtained where the branching is perfect; i.e., no unreacted B-groups can be found inside the molecule. A dendrimer is obtained when dendrons are coupled to a By-functional ($y \geq 1$) core molecule. When AB_2-monomers are used, both the molar mass and the number of end groups are doubled between successive generations.

8.3 Synthesis of Dendrimers

Dendrimers can be synthesized in many ways, including the divergent dendrimer growth method and the convergent dendrimer growth method. Other
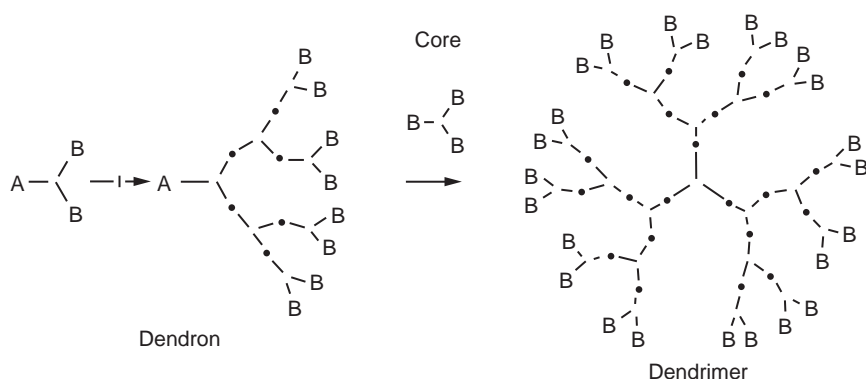
FIGURE 8.1
The formation of a dendron from seven AB$_x$-monomers and, after coupling of three dendrons to a B3-core molecule, a three-generation dendrimer. This is a schematic illustration of the convergent growth. (From Malmström, E., 1997, *JMS Rev. Macromol. Chem. Phys.*, C37, 555–579. With permission.)

methods include double-exponential or mixed-growth and other accelerated growth techniques.[11–15]

The divergent growth approach commences from a polyfuctional core molecule and proceeds radially outward.[16] Tomalia et al.'s Starburst dendrimers[4,17] were first synthesized by the divergent approach in the 1980s. Almost simultaneously, Newkome et al.[5] reported in 1985 the preparation of a cascade molecule termed *arborol*, also using a divergent approach.

Figure 8.2[18] shows a schematic representation of divergent growth. Starting from the reactive core (1), the first-generation analogue (3) is achieved through two steps. The core's functionalities initially react with monomer units, resulting in the first generation. A species (2) with an unreactive group at the periphery is produced at this stage. In the second step, a dendrimer (3) with functionalities similar to those borne by the core can be grown by the reaction of these moieties. The second-generation core analogue (5) is produced through these two steps via the dendrimer with the nonreactive surface (4). The two steps can be repeated until practical or physical considerations prevent further growth.

Terminal group numbers increases for higher generations in a geometrical fashion with divergent growth. Examples inlude polyamidoamine (PAMAM or Starburst) dendrimer synthesis.[4] These systems contain a trifunctional core and difunctional building units. Newkome et al.[5] also used the divergent approach in water-soluble poly(ether amides) terminated by hydroxymethyl groups. Both cases are similar to the divergent approach, with no significant side reactions and high yields during the process of generation growth and activation.

The other method, convergent growth, has been described by Frechet,[1] who primarily developed it. It starts at the chain ends and involves the formation of monodisperse dendrons (or dendritic wedges). Coupling of the dendrons
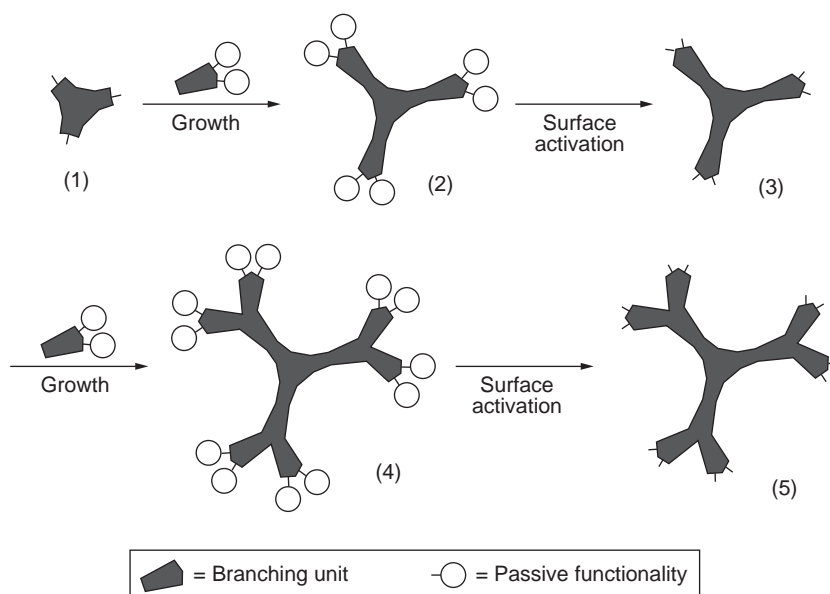
FIGURE 8.2
Concept of divergent dendrimer growth shown schematically. (From Matthews, O.A. et al., 1998, *Prog. Polym. Sci.*, 23, 1–56. With permission.)

to the core is the final step. The schema for the convergent growth route is shown in Figure 8.3. The disconnection approach is used to prepare the highly branched dendritic. Growth starts by coupling of the chain ends or "surface" functional groups, **S**, with the AB_x-monomer (x ≥ 2) (6), where x is the multiplicity of the branch point and leads to the next-generation dendron, which is reactive (**7**). Only one group **P** (protected group) is at the focal point of the reaction dendron while the number of chains has doubled. The reactive functional group **R** is activated by this functionality and hence can again be coupled with the monomer unit. Generation number increase can be achieved by repeating this two-step process, leading to larger and larger reactive dendrons (8 or 9). At the end, several reactive dendrons can be attached to a polyfunctional core **C**, resulting in a dendritic macromolecule (10).

To demonstrate this new methodology, the synthesis of a series of dendritic polyether macromolecules based on 3,5-dihydroxybenzyl alcohol (11) as the monomer unit (Figure 8.4) has been reported.[20,21] Preparation of the first-generation reactive dendron (13) commences from the surface functional group, which is a benzylic ether made by Williamson ether synthesis of a benzyl bromide with the monomer (11). The hydroxymethyl group then becomes the focal point of the growing dendrimer (12), and its activation with carbon tetrabromide and triphenylphosphine reforms the bromomethyl group of reactive dendron (13).

This two-step alkylation/bromination procedure is repeated to produce monodisperse reactive dendrons such as (14) or (15) that have a single
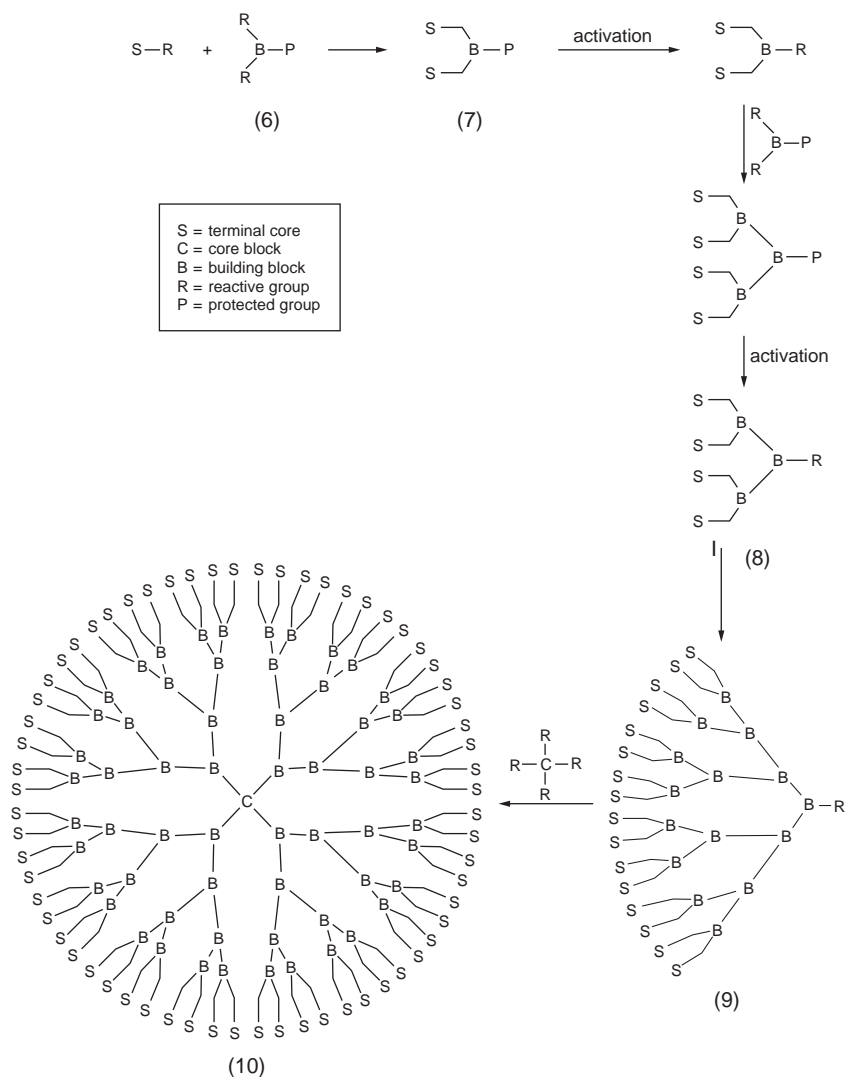
FIGURE 8.3
Concept of convergent dendrimer growth shown schematically. (Modified from Hawker, C.J., 1999, *Adv. Polym. Sci.*, 147, 114–160. With permission.)

functional group at the focal point and may be used in further reactions with monomer (11). This synthesis was used by Hawker and Frechet[20] to create up to a sixth-generation dendron that has 64 terminal groups, 7 layers of aromatic rings, a molecular formula of $C_{889}H_{763}BrO_{126}$, and a molecular weight of 13,851.

   The attachment of the reactive dendrons to a polyfunctional core can also be applied by the same coupling chemistry. Figure 8.4[22] illustrates the attach-
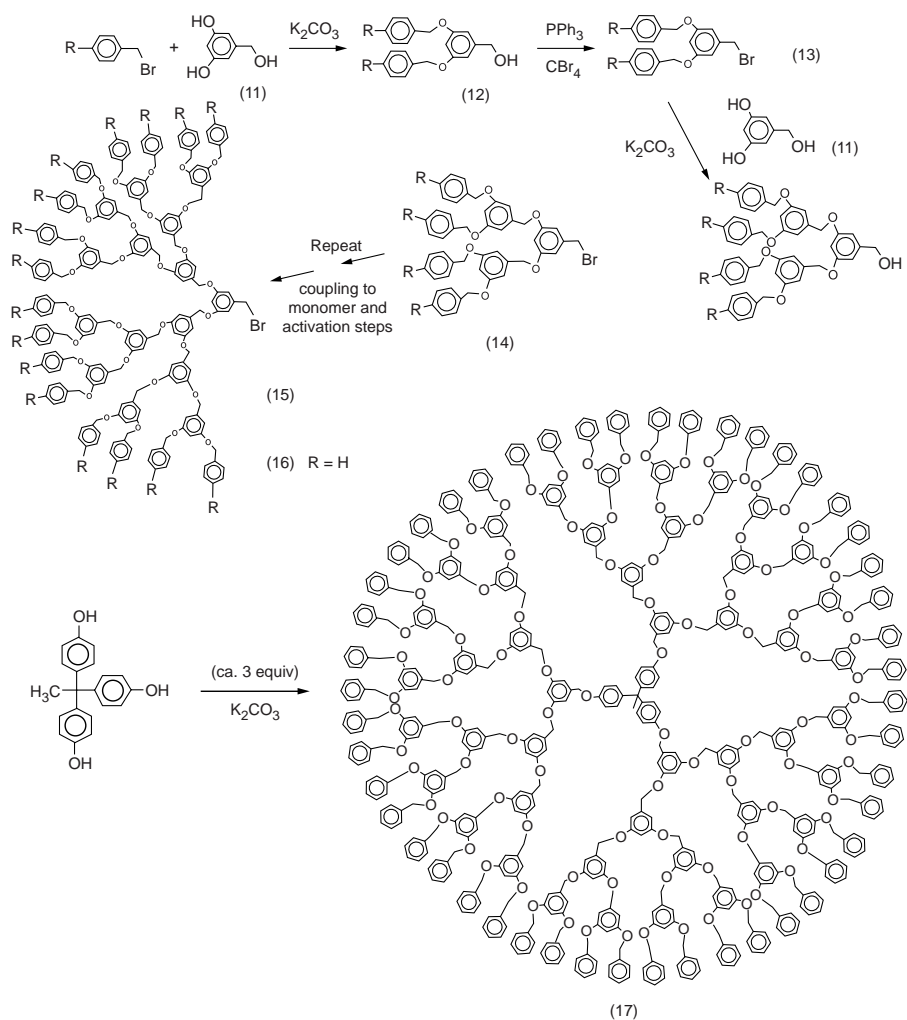
FIGURE 8.4
Convergent growth of polyether dendrimer. (Modified from Hawker, C.J., 1999, *Adv. Polym. Sci.*, 147, 114–160. With permission.)

ment of three molecules of a fourth-generation reactive dendron (16) to the trifunctional core 1,1,1-tris(4'-hydroxy-phenyl)ethane to afford a large dendrimer (17, or G4) with no focal point reactivity.

Overall, for the synthesis of very regular or precisely functionalized dendritic macromolecules, the convergent growth allows a significant greater degree of control than the divergent approach, making easier the synthesis of more "perfect" dendritic macromolecules. There is a greater degree of flexibility in controlling the variety of the terminal groups; interior blocks and the focal point group by convergent growth.[22]

FIGURE 8.5

AB$_2$-monomers are reacted in an uncontrolled manner, yielding a molecule with one A-group. ● represents the bond formed between an A- and a B-group. (From Malmström, E. and Hult, A., 1997, *JMS Rev. Macromol. Chem. Phys.*, C37, 555–579. With permission.)

8.4 Hyperbranched Polymers and Their Structure

Hyperbranched polymers were first introduced in 1952 by Flory,[23] who theoretically outlined them, via the intermolecular condensation of AB$_x$-monomers. Kim and Webster[24] renewed interest with their h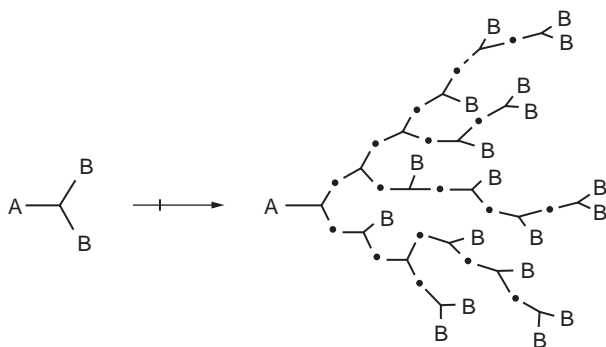ighly branched polyphenylenes with interesting properties and introduced the term *hyperbranched*. These polymers were found to exhibit properties different from those of their linear analogues, such as high solubility in various organic solvents.

Generally, a hyperbranched polymer is formed if AB$_x$-monomers are reacted in an uncontrolled growth process (Figure 8.5).[25] An AB$_x$-monomer has two different types of functional groups (A and B) and x + 1 reactive sites. In a hyperbranched polymer, each molecule will have one unreacted A-group and x + 1 B-groups if x AB$_2$-monomers are reacted together, the resulting product being highly polydisperse. The degree of branching (DB), to be defined later, is generally between 0 to 1 for most hyperbranched materials, indicating they have a branching structure between linear polymers (DB = 0) and perfect dendrimers (DB = 1).

As shown in Figure 8.5, the one-step polymerization of an AB$_2$-monomer is uncontrolled and leads to a complex hyperbranched product containing both linear and dendritic regions. As a result, three different subunits are typically found in hyperbranched structures, and they differ in the number of B functionalities that have undergone reactions to form the polymeric linkages (●). Reaction of both B functionalities leads to the dendritic unit; a linear unit is obtained only if one of the two B functionalities undergoes reaction. Finally, if neither of the B functionalities reacts, a terminal unit is formed that can be considered the chain end or outer layer of a dendritic polymer. Because of

these incomplete reactions, the structures of hyperbranched polymers are intermediate between perfect dendrimers and linear polymers.

8.5   Synthesis of Hyperbranched Polymers

Hyperbranched polymers are almost always based on AB_x-monomers, but lack the core moiety present in dendrimers. In order to obtain high-molecular-weight hyperbranched polymers, a number of conditions must be satisfied. First, the reactive groups A and B should only react with each other in the presence of a catalyst. The reactivity of the functional groups A and B with each other should thus be high to facilitate polymer growth. Side reactions should be minimalized to discourage deactivation or cross-linking of the growing polymer chain.

One hyperbranched material released commercially is from Perstop (Perstop, Sweden) (Figure 8.6), and is of the form AB_2, where the AB_2-monomer is 2,2-bis(hydroxymethyl)propionic acid[26] and known as Boltorn. The hyperbranched polyesters (HBPs) were synthesized according to acid-catalyzed esterification procedures. The esterification reaction was carried out in bulk and proceeded toward high conversion, the water formed being continuously removed. Finally, 2,2-BIS(hydroxymethyl) propionic acid (bis-MPA) (Figure 8.6) was added in successive portions corresponding to the stoichometric amount for each generation,[27] known as pseudogenerations.

A wide variety of monomers have been used for the synthesis of hyperbranched polymers. Kim and Webster reported their preparation of hyperbranched polyphenylenes from AB_2-monomers.[24,28,29] At all molecular weights, hyperbranched polyphenylene was soluble in common solvents such as tetrahydrofuran (THF), in direct contrast to linear polyphenylenes. Frechet et al.[30] and Hawker et al.[31] reported hyperbranched polymers synthesized via a living radical polymerization of 2,2,6,6-tetramethylpiperidin-l-oxyl (TEMPO)-containing vinyl monomers[32] where the degree of polymerization is possible to control.

In the synthesis of hyperbranched polymers, the purification mixture is much less extensive than that for the dendrimers. Workers reporting on the synthesis of hyperbranched polymers in bulk undertake very little purification.[10] The necessity of very little or no purification makes it easier to synthesize hyperbranched polymers on a large scale.

8.6   Hybrid Dendritic-Linear Block Copolymers

Traditional block copolymers are composed of linear blocks, and therefore the one-dimensional nature of these units limits the number of possible

FIGURE 8.6
Two-dimensional theoretical representation of the synthesis of the hydroxy-functional hyper-branched polyester (Perstop). (From Malmström, E., Johansson, M., and Hutt, A., 1995, *Macromolecules*, 28, 1698. With permission.)

arrangements. In contrast, three-dimensional systems (such as dendritic polymers) offer a substantially larger number of possibilities, and a number of interesting and novel structures may be proposed when the concept of block copolymers is considered.

One strategy to produce larger quantities of materials with unusual properties has recently led to the development of novel hybrid dendritic-linear copolymers.[19] For example, dendrimers are reactively coupled with one or more functional groups attached to a linear polymer such as poly(acrylic acid), as illustrated in Figure 8.7.[33]

The three-dimensional nature of dendrimers may be exploited for the design of block copolymers consisting of linear and dendritic components.
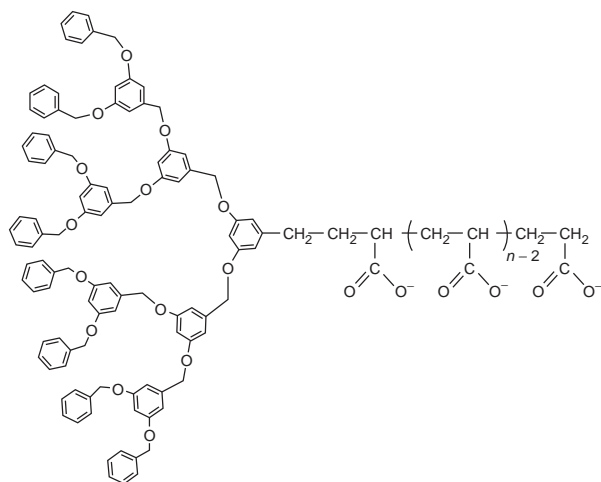
FIGURE 8.7
Novel hybrid dendritic-linear copolymer. (From Zhu, L. et al., 2001, *J. Phys. Chem.*, 105B, 2461–2464. With permission.)

A linear polymer might conceivably be attached to some or all of the terminal groups of a dendrimer to give a multiarm star with a globular core. Numerous other variations are possible, including some in which the linear polymer may have dendritic pendant groups, a combination that affords rather rigid, tubular structures,[34-36] and others in which linear and dendritic components alternate in a "string of pearls" arrangement.[37]

Leduc et al.[38] reported a good approach to the synthesis of a dendritic-linear block copolymer. This is the first use of polyether dendrons as macromolecular initiators for the controlled free radical polymerization of vinyl monomers. Figure 8.8 shows that the third-generation dendrimer was dissolved in a 150 molar equivalence of styrene and heated at 123°C under argon for 48 h to give the hybrid dendritic-linear block copolymer. As with hyperbranched materials, the properties of hybrid dendritic-linear copolymers would be expected to be intermediate between linear and dendritic macromolecules, with the graft-copolymer structure likely to lead to novel types of interfacial materials and compatibilizing materials.

8.7 Branching and Polydispersity

In contrast to the synthesis of these materials, which has reached a rather high level of maturity, the study of the physical properties of these unique globular macromolecules is still in its infancy. Although difficulties are encountered when dendritic polymers are characterized, the number of studies investigating the physical properties of dendritic polymers is increasing
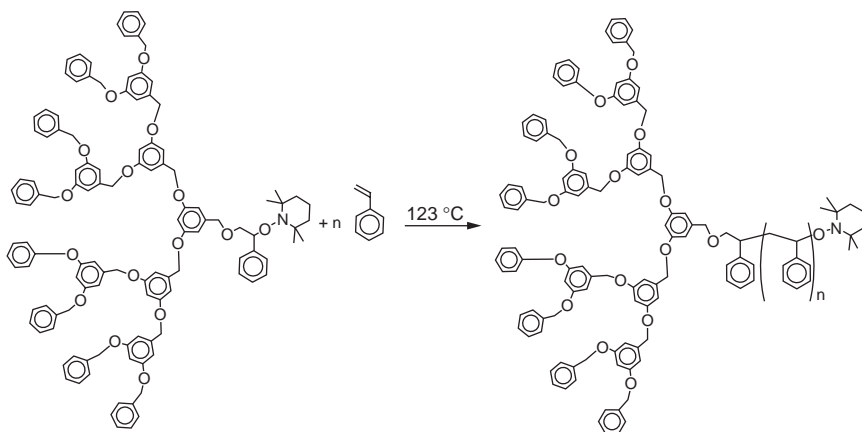
FIGURE 8.8
Schematic polymerization of the hybrid dendritic-linear polymer: polymerization of styrene by the third-generation dendrimer. (From Leduc, M.R. et al., 1996, *J. Am. Chem. Soc.*, 118, 11111–11118. With permission.)
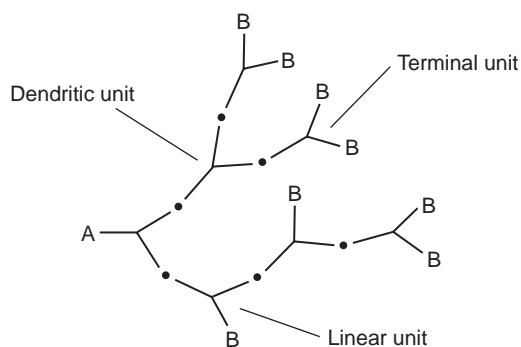

FIGURE 8.9
Three types of repeating units can be found in the hyperbranched polymer: linear, terminal, and dendritic. (From Malmström, E. and Hult, A., 1997, *JMS Rev. Macromol. Chem. Phys.*, C37, 555–579. With permission.)

steadily, and these materials are gaining considerable attention. In part, lack of physical characterization is due to the relatively small amounts of dendrimers synthesized. It is expected that the shape and chain-end functionality of dendritic polymers will result in new properties that have interesting applications. Before discussing the physical properties of dendrimers and hyperbranched polymers, it is necessary to mention an extra degree of structural characterization that is required to describe hyperbranched polymers, compared to the more structurally perfect dendrimers.

A hyperbranched polymer contains three different types of units, as illustrated in Figure 8.9. The constituents are *dendritic units*, fully incorporated AB_x-monomers; *terminal units*, having the two B-groups unreacted; and *linear*

units, having one B group unreacted. Dendrimers contain only two types of units — dendritic and terminal — the hyperbranched backbone additionally containing the linear segments.

The widely used term *degree of branching* has been defined by Hawker:[39]

$$DB = \frac{(\Sigma \text{ dendritic units} + \Sigma \text{ terminal units})}{(\Sigma \text{ linear units } + \Sigma \text{ dendritic units} + \Sigma \text{ terminal units})} \qquad (8.1)$$

By default, a linear polymer would have a degree of branching of 0.0, while a perfectly branched dendritic macromolecule would have a DB of 1.0. When the random structure of hyperbranched polymers is considered, the DB values can range from 0.0 to 1.0, between linear and perfectly dendritic structures. Due to significant property difference between linear and dendritic polymers, large variations in the physical properties of hyperbranched polymers may occur for different degrees of branching. Comparing two hyperbranched polymers with the same chemical composition but different DB results in higher solubility and lower melt viscosity for the sample with the greatest DB.[40] For example, hyperbranched polymers with a low DB (e.g., 0.1) may be expected to have physical properties resembling those of linear polymers, while hyperbranched polymers with a high DB (e.g., 0.9) may be expected to have physical properties resembling those of dendrimers. Therefore, accurate determination of the DB for hyperbranched polymers is required for understanding, prediction, and manipulation of material properties.

Because the degree of branching of hyperbranched polymers has a great effect on both the physical properties and the structure of these macromolecules, it is important to be able to determine it. Two techniques to determine the degree of branching have been presented.[40,41] One method, based on nuclear magnetic resonance (NMR) spectroscopy, relies on the ability to differentiate discrete resonances for the three different subunits present in the macromolecule. Integration of these resonances allows the relative percentage of each subunit to be determined, and hence DB to be calculated.[39] The other method does not rely on spectroscopic methods but is based on the degradation of the hyperbranched backbone, as presented by Kambouris and Hawker.[41] This technique employs a two-step process involving modification of the chain ends, followed by cleavage of the bonds between the repeat units. By two-step modification, the relative percentage of these monomer-like fragments can be determined either by isolation or through a variety of chromatographic techniques, and then used to calculate DB.[41]

Various methods of successful manipulation of the degree of branching for hyperbranched polymers have been reported by Hawker and Chu[42] and Percec et al.[43] For example, Hawker noticed that the deliberate insertion of either a dendritic or linear fragment into a monomer gives an AB_4- or an AB_3-monomer, respectively. The presence of these fragments would be expected to enhance growth and lead to hyperbranched polymers of different degrees

of branching. For example, Hawker and Chu[42] used this method to obtain hyperbranched poly(ether ketone) with a degree of branching of 0.72 and 0.39.

In sharp contrast to conventional synthetic polymers, which have a distribution of molecular weights, dendrimers can be obtained as monodisperse materials. The unprecedented accuracy with which dendrimers can be characterized is the result of their unique features of high symmetry and monodispersity.[7,20,44]

By comparison with narrow polydispersity polystyrene standards prepared by anionic means, it is found that the size exclusion chromatography (SEC) traces for dendritic macromolecules have appreciably narrower peak widths than conventional polymers, as illustrated in Figure 8.10. As expected, the polystyrene equivalent molecular weights calculated for dendrimers from their SEC traces are lower than their nominal molecular weights, and this difference increases as the molecular weight increases. This finding, consistent with the adoption of a globular structure, requires that a technique such as light scattering or, more recently, matrix-assisted laser
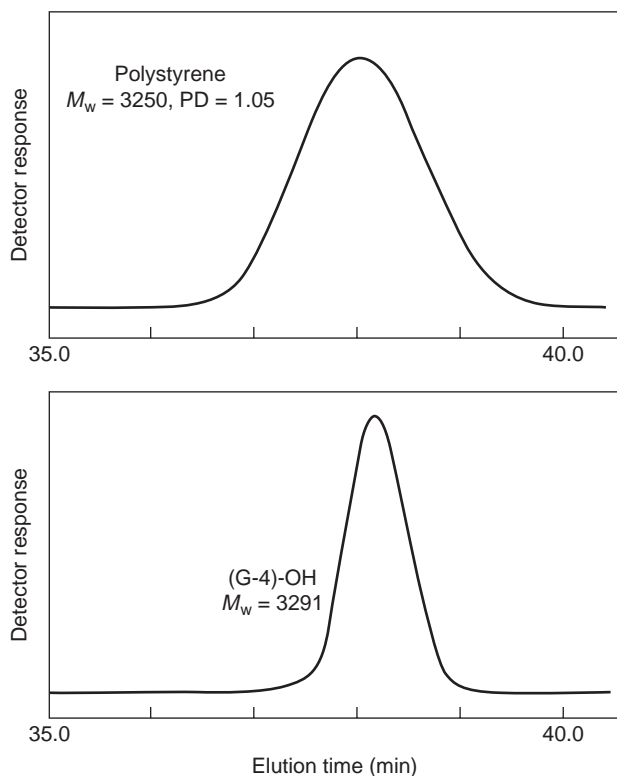

FIGURE 8.10

A comparison of size exclusion chromatography traces for a low polydispersity polystyrene and a convergent dendrimer of analogous molecular weight. (Modified from Hawker, C.J. and Frechet, J.M.J., 1990, *J. Am. Chem. Soc.*, 112, 7638–7647. With permission.)

desorption/ionization time of flight mass spectrometry (MALDI-TOF) be used to confirm the molecular weights of the dendrimers.[20,44]

8.8   Conformation

The shape of a dendrimer, as determined from a wire-frame structure of PAMAM, has been shown to change from an extended structure for low molar mass into a spherical shape for increased molar mass (generation number) (Figure 8.11).[6] The transformation in shape from an extended, open structure to a spherical, densely packed structure is considered to occur between the fourth and the fifth generation, but is dependent on the chemical structure of the repeat unit. Uppuluri et al.'s[45] study of the medium and highly concentrated solutions of polyamidoamine dendrimers in ethylene-diamine (EDA) solvent also supports this assumption. On the basis of their results, it is proposed that the higher-generation dendrimer molecules behave as if consisting of a soft and spongy interior surrounded by a well-defined dense outer shell.

As previously discussed, the branch unit and chain ends play very important roles in the structures of dendritic polymers. It is thus of much importance where the chain ends actually reside. Frechet[1] reported that a comparison of the reactivities of chain-end groups in dendritic, hyper-
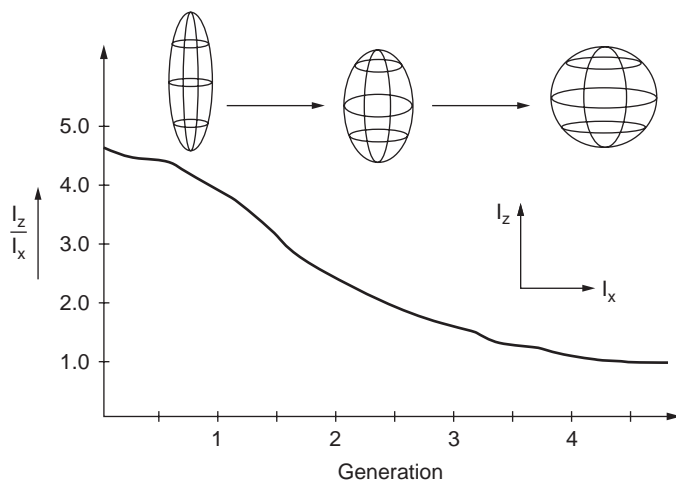

FIGURE 8.11
The shape of PAMAM dendrimers as a fuction of generation (molar mass) as determined from wire-frame strutures. Increasing the number of generations transforms the molecule into a spherical shape. (Modified from Tomalia, D.A., Naylor, A.M., Goddard, W.A., III, 1990, *Angew. Chem. Int. Ed. Engl.*, 29, 138–175. With permission.)

branched, and linear materials with a solid surface confirms that the chain ends of dendritic structures are readily accessible. This suggests that each of the chain ends must be located at or near the surface of the macromolecules, at least for some of the time.

There has been, however, considerable controversy as to the location of the chain ends of dendritic macromolecules. One model[46] predicted an extended structure with the chain ends on the periphery or surface of the structure, while another[47] predicts significant inward folding of chain-end groups to give a density maximum at the center of the structure. Wooley et al.[48] believed that while inward folding does occur, the chain ends are in a dynamic equilibrium that allows them to spend considerable periods of time at or near the outer surface of the macromolecules.

The work by Uppuluri et al.[49] in PAMAM seems to indicate that for generations greater than four, the dendrimers do not move as a single kinetic unit, but that motions of individual dendrons or multiples of them (but not the whole dendrimer) become important. Recent work by Lyulin et al.[50] indicates that at very high generations, segments of the highest generation can be found to be dispersed throughout the whole dendrimer. Likewise, solid-state nuclear magnetic resonance experiments of labeled components indicate, for example, that in a fifth-generation dendrimer, a large fraction of the internal, third-generation units are close to the surface.[51]

Hyperbranched polymers obtained in a single-step polycondensation of an AB_2-monomer are thought to possess an intermediate structure, between dendrimers and linear polymers. The main distinguishing features of hyperbranched polymers, compared to dendrimers, are their one-step preparation and the existence of "linear" units. This has a number of important consequences because the materials obtained are polydisperse in molecular weight and branching, with the molecular weight being much less controllable.

8.9 Glass Transition Temperature

The temperature that marks the transition from the amorphous solid state to the rubbery state is called the glass transition temperature, or T_g. It is the characteristic temperature at which, upon cooling, long-range segmental motions cease and vary widely with polymer structure.[52] In the glassy state, at temperatures below T_g, the only molecular motions that occur are short-range motions, involving small subsections of units along the chain backbone or substituent groups. Molecularly, the glass temperature is lowered by increasing the number of end groups (lower polymer weight), while it usually increases with increasing number of branch points or cross-links.

The glass transition temperature is also strongly influenced by the chemical structure of the repeating unit. Chain flexibility is particularly important in determining T_g. In general, T_g increases with decreasing flexibility of the

polymer chain. Flexibility decreases with increasing aromatic composition of the main chain or by groups in the main chain. For comparable substituent groups, increasing polarity, which may enhance intermolecular interaction, elevates T_g. For example, this is illustrated by T_g data for the vinyl polymers polypropylene ($T_g = -20°C$), poly(vinyl chloride) ($T_g = 89°C$), and polyacrylonitrile ($T_g = 100°C$). In addition, increasing flexibility of the side group can lower T_g, as is evident by comparison of the chemical structures of poly(propyl methacrylate) ($T_g = 105°C$), poly(ethyl methacrylate) ($T_g = 65°C$), and poly(propyl methycrylate) ($T_g = 35°C$).

In the case of dendritic polymers, the glass transition behavior is likely to be very different due to their unique, branched structures. For a high-molecular-weight, linear polymer, the chain ends play only a minor role in the glass transition. Since hyperbranched polymers and dendrimers are not expected to engage in significant chain entanglement, the contribution of the end group becomes significant. It has been suggested that the unusual behavior of these polymers is based on conformational changes and the degree of association of the polymer at different sizes (generations) of the polymer.[53,54] However, the separate roles of the type of chain ends and of the internal structure in the transition temperature are still not completely understood.[55]

There are different explanations about the effect of end groups on the glass transition temperature. Kim and Webster[56] proposed that the glass transition of hyperbranched polymers involve some translational motions of the dendrimer, not just the segmental chain motion usually assumed for linear polymers. This proposal was based on the fact that the T_g values are highly dependent on the end functional groups of the polymers. According to a study by Stutz et al.,[57] the glass transition temperature of dendritic polymers is dependent only on the generation number of dendritic growth, and thus only on the molecular weight of a dendron, not the molecular weight of the whole molecule. It was concluded that T_g is governed primarily by the backbone glass temperature and by the branching functionality.

Usually, a more polar terminal group causes the T_g to be higher, implying that a polar end-group interaction contributes to the activation energy and the glass transition temperature. For example, Kim and Becherbauer[58] found that chain ends have a large effect on the relaxation temperature of hyperbranched polyphenylenes. The glass transition was shifted toward higher temperatures with increasing polarity of the end groups. For instance, the T_g of hyperbranched poly(bromophenylene) (R = H) is 121°C, while the T_g increases to 177°C for end groups changing to CH_3 (R = CH_3), and the T_g is 221°C when R = Br.

A good correlation of the effect of the functional groups between small molecules and polymers implies similarities in the relaxation mechanism. The same features have been observed for dendrimers.[55] It was found that the glass transition temperature (T_g) of a hyperbranched hydroxyfunctional polyester, which is based on 2,2-bis(hydroxymethyl)propionic acid as a AB_2-monomer and a tetrafunctional polyol as a core and end-capped with five

different alkylacyl chlorides, was greatly affected by the nature of the terminal groups.[10]

Recent work has discussed the effect of degree of branching of hyperbranched polymers on their thermal properties. Jayakannan and Ramakrishnan[59] showed that the glass transition temperatures of the branched copolymers first decreased at low extents of branching, passing through a minimum, and then increased to attain the T_g of the pure hyperbranched polymer of ethyl 3,5-bis(2-hydroxyethoxy) benzoate (EBHEB). They argued that the appearance of such a minimum in T_g can be rationalized as being due to two competing factors: the increase in free volume at low branching levels leads to frustrating packing, and the increase in the number of strongly interacting chain ends reduces segment mobility, and hence tends to increase the T_g. The latter factor appears to dominate at high branching contents.

8.10 Solution Viscosity and Solubility

Rheology is the study of the deformation and flow properties of materials in the melt or solution. Understanding the rheological features of molten materials is very important in manufacturing and processing materials such as polymers. In the case of solution rheological measurements, especially dilute solutions, information about the polymer structure can be obtained. The most common method for determining an approximate average molecular weight for a polymer is to measure the viscosity of a dilute solution. The measurement is usually made using a glass capillary viscometer. Several quantities are used to describe the viscosity of a solution as defined below.[60]

The relative viscosity or viscosity ratio is

$$\eta_r = \eta / \eta_s \tag{8.2}$$

where η_s is the solvent viscosity. The specific viscosity is defined as

$$\eta_{sp} = \eta_r - 1 \tag{8.3}$$

The reduced viscosity or the viscosity number is defined as

$$\eta_{red} = \eta_{sp} / C \tag{8.4}$$

where C is the concentration in g/dl (g/100 ml). The inherent viscosity (IV) or the logarithmic viscosity number is

$$\eta_{inh}(IV) = (\ln \eta_r) / C \tag{8.5}$$

The intrinsic viscosity or the limiting viscosity number is

$$[\eta] = \lim_{C \to 0} (\eta_{red}) = \lim_{C \to 0} (\eta_{inh}) \qquad (8.6)$$

Alternatively, the intrinsic viscosity is the approach reduced or inherent viscosity in the limit of zero concentration. It is well known that as the molecular weight of linear polymers increases, their intrinsic viscosity according to the Mark–Houwink–Sakurada equation is

$$[\eta] = KM^{\alpha} \qquad (8.7)$$

where K and α are constants specific to a certain solvent–polymer combination at a certain temperature. The exponent, α, varies between zero and 1 for flexible-chain polymers, but may exceed 1 in rigid-chain systems, where the intrinsic viscosity is strongly molecular weight dependent. In poor solvents, the exponent is less than 0.5 and the polymer chain will adopt a collapsed or globular form. The coefficient, K, varies over many orders of magnitude for different polymer–solvent systems. The coefficient may also depend on the molecular weight, as the motion of the polymer chain departs from ideality as the mass increases.

Figure 8.12 shows the different behavior of intrinsic viscosity as a function of log molar mass among dendrimers, hyperbranched polymers, and their
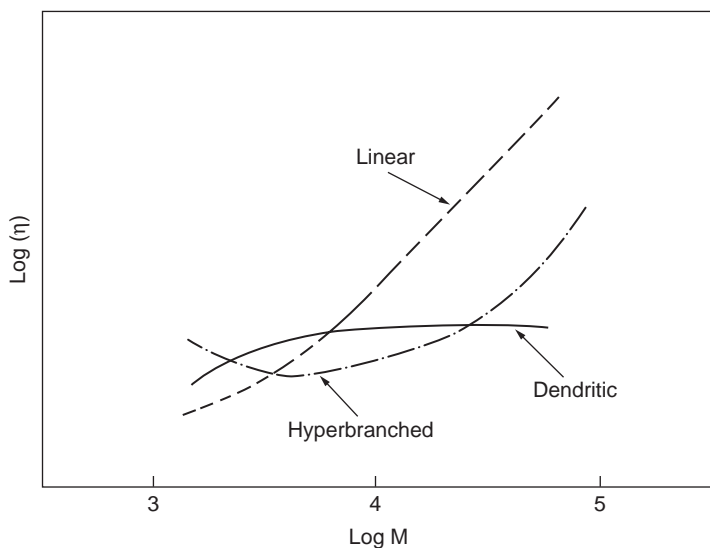

FIGURE 8.12
A log-log plot of the intrinsic viscosity, $[\eta]$, against molecule weight for a comparison of convergent polyether dendrimers, linear polystyrene, and hyperbranched polyesters. (From Frechet, J.M.J. and Hawker, C.J., 1995, *Reactive and Functional Polymers,* 26, 127–136. With permission.)

linear analogues. Due to different types of polymer architectures, regular dendrimers do not obey the Mark–Houwink relationship for intrinsic viscosity, while hyperbranched polymers are reported to still follow it.[27] In addition, no critical molar mass has been found for dendrimers, indicating that few chain entanglements occur.[2]

Dendritic and hyperbranched macromolecules demonstrate comparative solubilities that are much greater than those found for linear analogues, indicating that molecular shape has a pronounced effect on solubility. For example, Wooley et al.[48] reported that the benzyl ether-terminated dendritic polyester had a solubility of 1.15 g/ml in THF, while the benzyl ether-terminated linear polyester had a solubility of only 0.025 g/ml in THF (approximately 50 times less). This study clearly confirms that the highly branched dendritic structure dramatically affects solubility. It can be concluded that the increased solubility of dendritic macrololecules is due both to their branched architecture and to the solubilizing contributions of their large number of end groups. Furthermore, the hyperbranched polyester may have a less-packed structure than dendrimers according to their very small intrinsic viscosities and their hydrodynamic radius scales, as R_h is proportional to $M^{0.39}$.

8.11   General Aspects of Rheology

Rheological properties of polymer solutions or melts are an extremely important aspect of processing behavior. By definition, rheology deals with the science of deformation and flow of liquids. The resistance to flow when a stress is applied determines the viscosity of the solution or polymer melt, depending on chemical architecture and composition, molecular weight, temperature, and the shear rate. Polymeric fluids show a unique behavior due to their long-chain, molecular structure. Macromolecular chains are usually entangled in the case of common commercial polymers in the molten state, and the flow phenomenon involves movement of the chains, which involves a dynamic network of entanglements. Since rheology depends on the molecular features, it also represents a powerful analytical tool for determination of many aspects of molecular structure.

Oscillatory tests belong to the general framework of dynamic measurements in which both stress and strain are varied harmonically with time. In most cases, the relevant strain or strain rates are small enough to remain within the limits of linear viscoelasticity. The complex shear modulus, $G^*(\omega)$,

$$G^*(\omega) = \text{complex stress}/\text{complex strain} = \sigma^*/\gamma^* = G'(\omega) + G''(\omega) \quad (8.8)$$

may be experimentally determined from oscillatory measurements at a given strain amplitude. The real part $G'(\omega)$ of this function is called the storage modulus, and it gives the measure of the average energy stored in a defor-
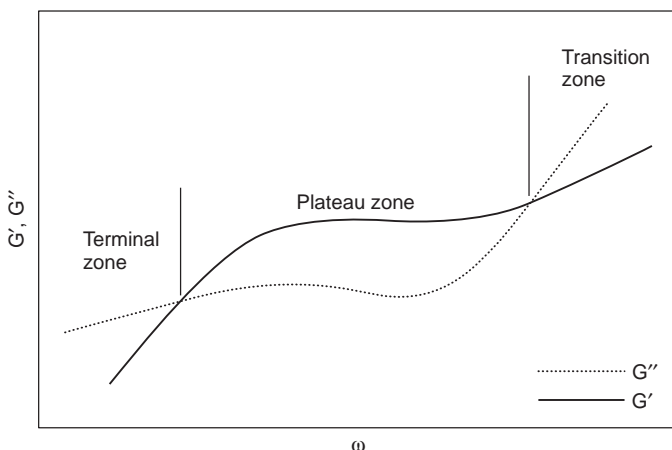
FIGURE 8.13
The three-zone model behavior of polymeric liquids.

mation cycle, and thus is an indication of a material melt elasticity. By contrast, the imaginary part of the complex modulus, $G''(\omega)$, is the measure of the average energy lost in a cycle of deformation.[61]

A three-zone model has been proposed to describe the viscoelastic behavior of polymeric melts as measured by dynamic rheology.[61,62] According to the relative magnitude of G' and G'', a logarithmic plot of G' and G'' as a function of frequency consists of three zones: terminal, plateau, and transition zones, which are shown in Figure 8.13. For conventional polymers with flexible chains, such variation in behavior with frequency is thought to arise from the influence of molecular weight of polymers or entanglements between macromolecules.

At the lowest frequencies (terminal zone), the double logarithmic plot of $G'(\omega)$ and $G''(\omega)$ give limiting slopes of 2 and 1, respectively. Within this domain of relaxation, the behavior of the materials is mainly that of a viscous liquid in nature ($G' \ll G''$). At intermediate frequencies, the real part of the complex modulus is nearly constant, showing quasi-elastic behavior; the dynamic network of entanglements formed in a melt of long macromolecular chains appears to be permanent in that time (or frequency) scale. At frequencies related to the plateau-to-transition zone, and within the transition zone itself, the glass transition comes into play and the G'' can eventually show a maximum (not shown in Figure 8.13).

8.12 Dynamic Solution Rheology of Dendritic Polymers

The above Ferry model is mainly intended for modeling rheology in the molten state and will be further applied in the next section. In this section,

results from dynamic solution rheometry of (reasonably high concentration) dendritic polymer/solvent mixtures are discussed. It is usually reported that solutions of dendrimers show Newtonian flow behavior. For example, Uppuluri et al.[45] reported the Newtonian flow behavior of medium and highly concentrated solutions of polyamidoamine dendrimers in ethylene-diamine solvent. Bodnar et al.[63] found that both the acetylated and poly(propyleneimine) (PPI) dendrimers exhibited Newtonian rheology in solution (water and D_2O) over a range of concentrations. Furthermore, rheological results of measurements at higher concentrations suggest dendrimer clustering and interpenetration, leading to a lower viscosity than expected when behavior is extrapolated from dilute solution viscosity data. This is explained by assuming that there is interpenetration and association between dendrimers at high concentrations. However, the study of Sendi-jarevic and McHugh[13] on flow rheological behaviors of several poly(propylenimine) dendrimers, hyperbranched polyesters, and poly(ether-imide) (PEI) HBPs illustrated that the higher-molecular-weight solutions showed shear thinning and normal stress effects, both of which increase with a decrease in the degree of branching.

Nunez et al.[64] recently also found that the hyperbranched polyester solutions exhibit Newtonian behavior, with steady viscosities independent of shear rate, also likely due to the absence of physical entanglements in these systems (HBPs being less highly branched). In addition, they found that solution viscosities are only slightly affected by the different generations of the hyperbranched polymers.

8.13   Dynamic Melt Rheology of Dendritic Polymers

Unlike the solution rheology, melt rheology investigates the flow properties of materials under deformation in the melt state. The relationship between zero-shear melt viscosity, η_0, and molecular weight of linear polymers is usually described by the power law:

$$\eta_0 = KM_w^\alpha \tag{8.9}$$

where the value of the exponent, α, is approximately 1.0 for low-molecular-weight polymers, but approaches a value of 3.4 as the molecular weight increases beyond a critical value, M_{cr} or M_c. This transition around M_c is quite sharp and is believed to be associated with the onset of entanglements. While this relationship holds for all linear polymer systems, the unique nature of dendritic macromolecules, where entanglements are not expected to be a dominant process, may result in no observed change in α from the initial value of 1.0. Indeed, no critical molecular weight, M_c, is expected or

observed in dendrimers[2,65] as generation number is increased. This phenomenon is due to the unique structures of these three-dimensional dendritic polymers. Their surface congestion, coupled with the high degree of branching, is expected to contribute greatly to the prevention of entanglements between dendrimer molecules.

Hawker et al.[2] reported detailed studies of the melt viscosity behavior of dendritic macromolecules for the first time, which showed that melt viscosity was a function of molecular weight, with no critical molecular weight being observed, even for molecules having a molecular weight as high as 85,000 amu. Their studies also found that the viscosity of mono- and tridendrons yielded a master curve when the viscosity was plotted against molecular mass rather than generation number (Figure 8.14). Thus, there is no big difference in behavior for mono- and tridendrons; their viscosity lies in a continuous, monotonic line, as long as it is total molecular weight that is plotted. Even though the Rouse prediction is that $\alpha = 1$ in such unentangled system, in lower-molecular-weight polymers there is the issue that there is very high free volume due to a large concentration of chain ends, which leads to a departure from linearity at low molecular weights. This has also been seen for low-molecular-weight linear polymers in the nonentangled regime.[66,67] For lower-molecular-weight dendrimers, there is a negative deviation from the linear proportionality due to the density and monomeric friction coefficient being mass dependent. If the data are recalculated at a constant fractional free volume, then the data shows the linear dependence expected for lower-molecular-weight, unentangled systems.[65]
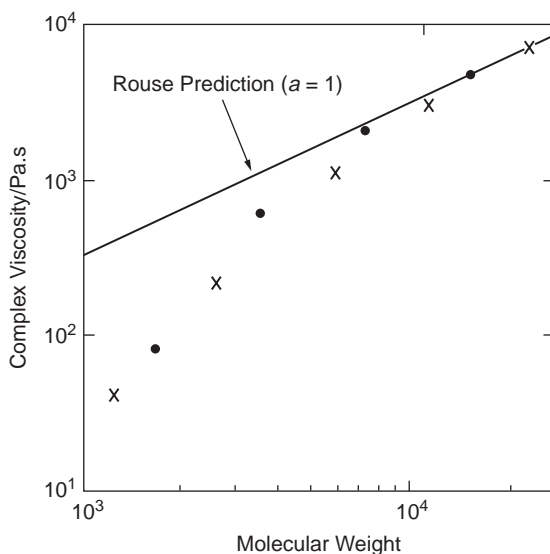

FIGURE 8.14
Melt viscosity vs. molecular weight for monodendrons (●) and dendritic polyether macromolecules (×), based on 3,5-dihydroxybenzyl alcohol at 80°C. (From Hawker, C.J. et al., 1995, *J. Am. Chem. Soc.*, 117, 4409–4410. With permission.)

A more recent study by Farrington et al.[65] found that the fractional free volume and zero-shear melt viscosity (η_0) at the reference temperature all scale with molecular mass (M), rather than generation number or number of ends per M, for mono- and tridendrons. It was concluded that an (almost) linear relation between η_0 and M is obtained in agreement with the Rouse model, and end groups influence the viscosity to a much greater extent than the bulk of the core.

Both dendrimers and hyperbranched polymers have been found to show mainly Newtonian melt flow behaviors, with some deviation from this at higher shear rates or frequencies.[49] Recently, Sendijarevic and McHugh[13] compared the simple shear, oscillatory, and creep flow rheological behaviors of several poly(propylenimine) dendrimers (DAB), hyperbranched polyesters, and poly(ether-imide) HBPs with different variables, including molecular weight, degree of branching, nature of peripheral groups, and molecular architecture. They found that in oscillatory experiments, amine end-capped DAB dendrimers and HBPs exhibited Newtonian behavior, while the nitrile end-capped DAB dendrimers showed a Rouse-like frequency dependence of both moduli. This is likely due to the more open structure of PEI HBPs, which apparently promotes a significant degree of coil overlap and entanglement coupling. Thus, it is suggested that the rheological properties of PEI HBPs are closer to those of linear polymers than perfect dendrimers.

Uppuluri et al.[49] investigated the rheological behavior of the first eight generations of bulk polyamidoamine dendrimers under steady shear, shear creep, and dynamic oscillatory shear. It was found that (1) these dendrimers exhibit a constant viscosity at small deformations, regardless of the type of stress applied; and (2) a temperature-/generation-dependent non-Newtonian response occurs at higher shear rates/frequencies. The latter was characterized by finite moduli of elasticity at all generations and by the onset of complex viscosity thinning at some generation-dependent critical temperature and shear frequency. Uppuluri et al. suggested that this might be caused by approaching the generation-dependent T_g, rather than by interdendrimer interactions of the entanglement type. Nevertheless, this did not preclude some sort of supramolecular microorganization of deformed (i.e., flattened or collapsed) dendrimers in the state of rest. Such an organization may result from compositionally dependent secondary interactions that, in the case of PAMAMs, may involve interdendrimer hydrogen bonding.

Others have also reported that dendritic end groups play a very important role in determining the rheological properties of dendritic polymers. Jahromi et al.[68] studied rheological behaviors of a series of side-chain dendritic polymers (SCDPs) produced by copolymerization of dendritic diols with various diisocyanates. Their results suggest that the dendritic end groups have a distinct effect on the elastic part of the complex modulus, whereas the effect on the viscous component appears to be small. Furthermore, the viscosity increased with the generation number for the dendritic macromonomers. However, for the dendritic polymers, the reverse trend was observed: the relative increase of the viscosity upon polymerization is smaller for dendritic

polymers of higher-generation side groups. It seems that the dendritic side groups can shield the polyurethane main chain and discourage intermolecular interaction.

Sendijarevic and McHugh[13] found that a fit of Fox and Flory theory to the fractional free volume data obtained by Williams–Landel–Ferry (WLF) analysis of DAB dendrimer viscosity suggests that the volume fraction of end groups is independent of generation number. They found that the fractional free volume exhibits a linear relationship with the $1/M_n$ consistent with the Fox and Flory equation. It is found that the fractional free volume due to the end groups is the same with the increase in generation, despite there being more end groups. This was explained by backfolding of the end groups into the void space in the interior of the molecules, thereby creating more uniform density profiles throughout molecules of higher-generation dendrimers.

It is interesting to note that there have been several research works that indicate that there might be a structural transition occurring at the fourth or fifth generation of dendrimers. In their study, Uppuluri et al.[49] revealed a distinct change from a single-relaxation-mode to a multi-relaxation-mode Maxwell-type behavior at generation four, which is consistent with the closure of the dendrimer molecular surface upon itself and the earlier mentioned soft interior–dense shell model of intramolecular dendrimer morphology. The behavior of higher-generation dendrimers suggests the existence of more than one submolecular mode of stress relaxation, which seems to indicate that for the fourth generation, the dendrimer molecule may become too large to move coherently through the bulk as a single unit.

There is other evidence that reinforces the idea of a structural rearrangement of the dendrimers as they increase in size, with some transition occurring at a molecular mass close to the fourth generation.[69] Measurements of pressure–volume–temperature (P–V–T), oscillatory shear rheology, and differential scanning calorimetry (DSC) results demonstrated that the third-generation dendrimer undergoes an irreversible crystallization phase transition. It was suggested that the crystallization phenomena could be caused by the compression molding step in the sample preparation procedure. This solution polymerization-created physical structure could be completely eliminated after achieving a sufficient temperature. The fourth- to sixth-generation dendrimers did not exhibit similar behavior, suggesting that larger dendritic structures discourage such a phenomenon.

8.14 Dielectric Relaxation of Hyperbranched Polymers and Dendrimers

Dielectric relaxation spectroscopy (DRS) is a potent technique capable of probing the molecular motion and electrical properties of polymeric materials. It involves the measurement of the response of dipoles on the polymeric

main or side chain to an electric perturbation to a sinusoidally varying voltage. The basis of the dielectric properties of polymers is their ability to experience polarization when placed in an electrical field. Polarization within the polymer sample occurs as a response to an electrical field and can arise from a range of mechanisms, each occurring with a different strength, response time, and frequency. These include electronic, atomic, and dipole orientation and space-charge or interfacial polarizations.

Generally, the highest temperature peak seen in DRS (α-relaxation) relates to the large-scale, cooperative Brownian motion of the main chains associated with the glass transition and the relaxation of dipoles associated with it. The α-relaxation occurs at temperatures above T_g (as determined by techniques such as differential scanning calorimetry) when the kinetic units of the chains have sufficient free volume and mobility to rotate. At temperatures below the α-relaxation, the mobility of the polymer chain is reduced and sub-T_g relaxations (labeled β, γ, etc., as a function of decreasing temperature) in the glassy state may be observed due to local motions of the chains. For example, dielectric spectroscopy on hyperbranched polymers with the same backbone but different terminal groups allows determination of the glass transition (α-relaxation), which agrees well with those obtained in DSC measurements and dynamic mechanical analyses when the frequency of measurement is taken into account.

DRS has a number of advantages over other techniques in measuring relaxation phenomena. Its ability to cover a wide range of frequencies (some 10^{-5} to 10^9 Hz) compares favorably with its mechanical analogue, dynamic mechanical thermal analysis (DMTA), which monitors the response of a polymer to a sinusoidal stress–strain deformation and determines materials modulus in a frequency range between 0.01 and 100 Hz. This often means that data can be presented and readily analyzed for phenomenological parameters such as relaxation time, relaxation strength, and broadness. A limitation for DRS can be that if the materials are highly conductive due to presence of impurities, dust, ions, catalyst, or water, the relaxation peaks can be masked by the DC conductivity curve.[70] In addition, since thin films are used and can be supported on electrodes, more brittle samples can be examined. Because of the lack of entanglements in dendrimers and HBPs, they are indeed brittle and DRS is an ideally-suited technique.

To date, only a few papers have been published on the dielectric relaxation behaviors of hyperbranched polymers and dendrimers. The main features seems to be a secondary β- and γ-relaxation, which shows Arrhenius behavior in the reciprocal temperature–frequency plots,[71–73] with the α-relaxation often being overwhelmed by the dielectric loss due to DC conductivity of impurities and ions present. A strong correlation between the degree of branching and the nature of the terminal groups of dendrimers and hyperbranched polymers to their dielectric relaxation properties has been observed.[71]

Malmström et al.[71] reported on permittivity and loss measurements of hyperbranched polyesters of 2,2-bis(hydroxymethyl)propionic acid in a five-

generation hydroxy-functional (5G-OH) hyperbranched polyester; they observed three relaxation transitions: α, the glass–rubber transition, which was indicated according to a second-order phase transformation by DSC; and two subglass processes, denoted β- and γ-relaxation, both with an Arrhenius temperature dependence and an activation energy of 96 ± 2 kJ mol^{-1}. The similarity in activation energies of β- and γ-processes does not necessarily prove that the processes are of the same origin, but are related due to the fact that the relatively short HBP arm length (compared to a linear polymer) means that the β- and γ-motion must be highly coupled with each other. The β-relaxation process was assigned to a reorientation of the internal ester groups, and the low-temperature γ-relaxation process to motions of the terminal hydroxyl groups. A third-generation hyperbranched polyester with the terminal –CO–CH$_2$CH$_3$ groups exhibited, in addition to the glass transition (α), only one subglass process (β), presumably because it had no hydroxyl groups as terminal groups. Malmström et al.'s further studies of three hyperbranched polyesters with the same backbone structure but with different terminal groups — hydroxyl, benzoate, or acetate groups — show that the relaxation strengths of the hyperbranched polymers are considerably lower than those for the linear analogues.[74] The activation energies of the β-process in the polymers studied increased in the order of hydroxyl, acetate, and benzoate, indicating that the benzoated-terminated polymer is the most constrained.

Emran et al.[72] studied the relaxation of ester-terminated, amide-based dendrimers. The identification of the glass transition was characterized and demonstrated by the relaxation time–temperature dependence being of the Vogel–Fulcher–Tammann form. The dendrimers also showed secondary β-relaxations, with an Arrhenius-type temperature dependence and activation energies between 37.7 and 85.8 kJ/mol for three generations (1 ~ 3) of *tert*-butyl and methyl ester, amide-based dendrimers. They found that secondary transitions of these dendrimers increased in temperature location with generation number. Dielectric relaxation responses were analyzed to yield dielectric strengths of the molecular relaxation, which increased with generation number and were comparable for both *tert*-butyl and methyl esters in the glass transition region. Two possible contributing mechanisms were suggested. One is that secondary β-relaxations in polyamides were assigned to the motions of dipolar (e.g., CH$_2$NH$_2$ and CH$_2$OH) chain-end groups and the motions of chain segments, including end groups, which are not H-bonded to neighboring chains. A second possible mechanism could involve molecular motion of the bulky terminal ester groups, which hinder the rotation of particular ester side groups in poly(*tert*-butyl methacrylate).

Trahasch et al.[73] dielectrically investigated a series of carbosilane dendrimers, generations G$_x$RF6 (x = 1, 2, 3), with perfluorohexyl end groups (–C$_6$F$_{13}$). The dendrimers demonstrate a β-relaxation, with an Arrhenius-like temperature dependence and an activation energy of 17 kJ/mol. The dominant α-process was observed in all G$_x$RF6 dendrimers and was itself split into slow and fast components. It was suggested that the microscopic origin of this

relaxation is in the relaxation of the component of the dipole moment parallel to the helical axis of the end groups.

Huwe et al.[75] investigated a set of dendritic poly(ether amides) of three different generations. For the amorphous materials, an α-relaxation (dynamic glass transition) was found to agree well with calorimetrically measured values. For the β-relaxation, a molecular assignment to the motion of ester, amide, and *tert*-butoxycarbonyl(Boc)-protected amine groups is suggested. The observed relaxation strength fits well to the results obtained by numerical calculations of the dipole moments involved.

Recently, Zhu et al.[76] studied the dielectric relaxations in hyperbranched polyesters. The α- and β-relaxations of these HBPs were not observed due to the high level of sample conductivity, while the γ-relaxation displayed was due to the motion of polar, terminal hydroxyl groups. The experimental results of γ-relaxation implied that the motion of these hydroxyl chain ends could be coupled with the branch motion related to the α-relaxation to some degree. It was found that the γ-relaxation temperature is almost independent of molecular weight (generation), while the β-relaxation temperature increases with the increasing generation number. Thus, the chain ends were expected to change from an ordering state at lower generations to an isotropically disordered state at high generations.

In summary, dielectric spectroscopic investigations examine and explain different molecular dynamic processes (α-, β-, γ-, and δ-relaxation) of dendritic polymers. The application of dielectric spectroscopy on dendrimers can provide a deeper understanding of molecular dynamics and relaxational properties of these materials.

8.15 General Concepts of Polymer Blends

Over the last 50 years, many multicomponent systems have been developed ranging from glass-reinforced thermosets to rubber-toughened plastics and thermoplastic polymer blends. It is thus possible to greatly enhance the properties of a given polymer or, alternatively, to achieve a given performance at a lower cost. In this section, some of the basic concepts of polymer blends and thermodynamic aspects of their compatibility or miscibility are outlined.

Mixing two or more polymers together to produce blends or alloys is a well-established strategy to achieve novel properties, either an intermediate or (preferably) synergistic combination of physical properties. The term *polymer blend* (PB) is used to describe multicomponent polymeric materials consisting primarily of two or more polymers. It is mainly used to describe combinations (or mixtures) of two or more polymers that are not bonded chemically to each other. Polymer blend systems are often intended to meet requirements of a particular application more cheaply or effectively. On the

other hand, some provide novel combinations of properties that can lead to new applications. A major driving force for the growth of the polymer blend industry is the relative ease of mixing and blending. Thus, the development of a new blend or compound from existing materials is generally more rapid to commercialization than discovering and commercializing an entirely new polymer.

Two-phase blends are less like to have properties that vary monotonically with composition. Mixing immiscible polymers can often produce properties inferior to either component, especially if the interface is poor. However, very desirable combinations of properties may also be obtained. A particularly successful family of two-phase blends is that of rubber-toughened polymers. In these materials the rubbery component imparts very considerable toughness without, at low concentrations, significant loss of stiffness due to a range of mechanisms, such as entanglement of yielding due to stress concentration, crack blocking, and so on.

The question of whether a given polymer will mix with another polymer on a molecular level, i.e., form a miscible blend, is of prime importance. According to thermodynamics, the free energy at equilibrium must be a minimum. This means that the free energy change upon mixing the items, i.e., a polymer or a solvent, must be negative. If we let the change in Gibbs free energy upon mixing be ΔG_m, it can be written as

$$\Delta G_m < 0 \tag{8.10}$$

The free energy change at a given temperature is related to the enthalpy, H, and entropy, S, change by the equation

$$\Delta G_m = \Delta H_m - T\Delta S_m \tag{8.11}$$

so that we need to determine if the right-hand side of this equation is negative. For spontaneous mixing, ΔG_m must be negative, and so

$$\Delta H_m - T\Delta S_m < 0 \tag{8.12}$$

This implies that exothermic mixtures ($\Delta H_m < 0$) will mix spontaneously, whereas for endothermic mixtures, miscibility will only occur at high temperatures. The statistical thermodynamic theory of mixing starts with Boltzmann's relation:

$$\Delta S_m = k \ln \Omega \tag{8.13}$$

where Ω is the number of possible arrangements in space that the molecules may assume. Briefly, it is recognized that miscibility between polymers is determined by the balance of enthalpic and entropic contributions to the free energy of mixing. While for small molecules the entropy is high enough to

encourage miscibility, for polymers, the entropy is almost zero, causing enthalpy to be decisive in determining miscibility.

An interesting aspect of blends of dendrimers and thermoplastics is whether the solubility of dendrimers in linear thermoplastics is enhanced compared to blends of two different linear macromolecules. One aspect could relate to the fact that dendrimers are small molecules compared to linear polymers, and thus entropy of mixing with polymer molecules is higher ($\Delta S_m > 0$) since the number of possible arrangements (Ω) may be higher than that for solely linear polymer blends. This allows for the possibility that small dendritic molecules can accommodate themselves within the coiled, linear polymer chains. Alternatively, the relatively short-chained arms of the dendrimers could discourage entanglement and thus reduce the chance of miscibility. The fact that dendrimers have large numbers of functional groups on the surface due to their special three-dimensional structures may strongly influence and encourage miscibility, aiding ΔH_m to be less than zero, if there are appropriate interactions.

8.16 Blends of Dendritic Polymers with Thermoplastics

There are few reported polymer blends to date that involve mixtures of hyperbranched polymers and dendrimers with thermoplastics. This is partially due to the relative recent discovery of these materials. In addition, the detailed and painstaking synthesis of the materials outlined above (of dendrimers especially) means that there are limited quantities. There are a slightly greater number of reports of hyperbranched polymers in blends with linear thermoplastics, and these will be presented first.

Massa et al.[77] studied the phase behavior and other physical properties of blends of hydroxyphenyl- and acetoxyphenyl-terminated hyperbranched polyesters with linear polymers such as polycarbonate, polyesters, and polyamides. They found that the miscibility of hydroxy-terminated hyperbranched polyesters with linear polymers was identical to that of poly(vinylphenol) (PVPh), independent of the hyperbranched polyester synthetic method. This indicates that strong interactions due to hydrogen bonding (rather than chain architecture) dominate blend miscibility in these blends, although highly branched materials with plentiful end groups facilitate such interactions. Their mechanical properties indicate that blending with all-aromatic hyperbranched polymers should lead to greater hardness and elevated heat-deflection temperatures, when compared with unmodified polymers.

Huber et al.[78] studied the influence of 0.1 to 10 wt% hyperbranched poly(ether amide) in a polyamide-6 (PA-6) matrix. All the blends show full miscibility due to the possibility of the hyperbranched polymer to form hydrogen bonding with the thermoplastic matrix. Furthermore, the hyperbranched polymer had no significant influence on the melting and crystal-

lization behavior of the polyamide-6 matrix. The fact that hyperbranched poly(ether amide) (even 0.1 wt% additions) reduced the melt viscosity of the blend system without loss of mechanical properties shows its promise in the use of hyperbranched polymers as a processing aid without compromising other properties.

As mentioned in Section 8.14, dielectric relaxation spectroscopy is a potent technique capable of probing the molecular motion and electrical properties of polymeric materials. One of the principal interests that dielectric relaxation has is its ability to detect, in dendritic polymers, the effects of the macromolecule topology and chemical functionality on relaxation dynamics and blend miscibility behavior. This can be assessed by examining the effect of dendrimer incorporation on the relaxation processes of the linear polymer in these blends, and hence to determine structure–property relationships. At the time of writing, only two papers to date have discussed the dielectric relaxation of dendritic blends. Connolly et al.[79] reported dielectric characterization of miscible blends of dendritic polyester and bisphenol-A polycarbonate (BPA-PC), showing that with increasing dendrimer content, the polycarbonate glass transition temperature was progressively reduced (as well its activation energy). The magnitude, width, and temperature of the subambient β-transition associated with motions of the carbonate group were greatly enhanced by the addition of the branched polyesters. These effects were attributed to the large increase in free volume of the blends due to the branched nature of the dendritic polymers. It increased with the dendrimer concentration in the blend, becoming stronger for interactions between the nearest neighbor of PC carbonate moiety and the dendrimer phenyl ester groups.

Carr et al.[80] studied the dielectric properties of miscible blends of two aryl ester dendrimers with poly(ethylene terephthalate) (PET). As illustrated in Figure 8.15, they revealed that lowering of the α-peak temperature for dendrimer blends is equivalent to a T_g depression. Such an effect is commonly
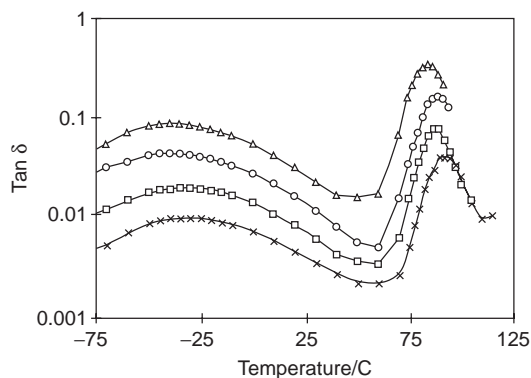

FIGURE 8.15
Dielectric loss at 1 kHz vs. temperature for dendrimer/PET blends. ×, PET; □, 5% dendrimer/PET; ○, 10% dendrimer/PET; △, 20% dendrimer/PET. (From Carr, P.L. et al., 1996, *Polymer*, 37, 2395–2401. With permission.)

associated with plasticization, and was explained on the basis that small molecules separate the polymer chains and increase the free volume of the system, disrupting interchain interaction and make local motion easier. Furthermore, the observed effect was dependent on the size or shape of the added dendrimer. The smaller of the two dendrimers investigated acted as a plasticizer, reducing the chain entanglement density of the blend, whereas the larger dendrimer acts as an antiplasticizing agent and increases entanglement density.

8.17 Rheological Properties of Dendritic-Thermoplastic Blends

Due to the close relationship between rheology and processing properties, the study of the rheological flow behavior of dendritic polymer blends is of much interest. Such studies can provide valuable insights into the effects that molecular variables such as generation number, nature of peripheral functional groups, and degree of branching of the dendrimers and hyperbranched polymers have on bulk blend properties. As mentioned before, due to low amounts of samples, only a few studies of rheological behavior of dendrimer and hyperbranched blend systems can be found.

Generally, it has been shown that the addition of dendritic polymers to solutions or melts of linear polymers has the effect of strongly lowering the viscosity of the blends. Kim and Webster[56] reported the addition of a small amount of hyperbranched polyphenylene in polystyrene, the result being decreased melt viscosity, and thus improved thermal stability compared to pure polystyrene.

Hong et al.[81] investigated the use of hyperbranched polymers as a processing aid for linear low-density polyethylene (LLDPE). Various-generation HBPs were used that had either 16 carbon atom alkanes or a mixture of 20 ~ 22 carbon atom alkanes attached to the end groups. It was found that the HBP with a greater degree of end-group substitution acted more effectively as a processing or rheological property aid (Figure 8.16). Hong et al. also found that the power requirement for extrusion was significantly decreased as a result of reduced blend viscosity, and thus the mass flow rate for a given extruder speed was greater than that of virgin LLDPE for all HBP blends. It is hypothesized that the HBP-rich phase acted as a lubricating layer at the polymer–die wall interface.

Huber et al.[78] found that the complex viscosity of blends of polyamide-6 changed significantly with only small amounts of a hyperbranched poly(ether amide) (0.1 ~ 10wt%), although the mechanical properties of the blends remained very similar to that of pure PA-6. The blended systems showed a homogeneous morphology, even at high concentrations of the
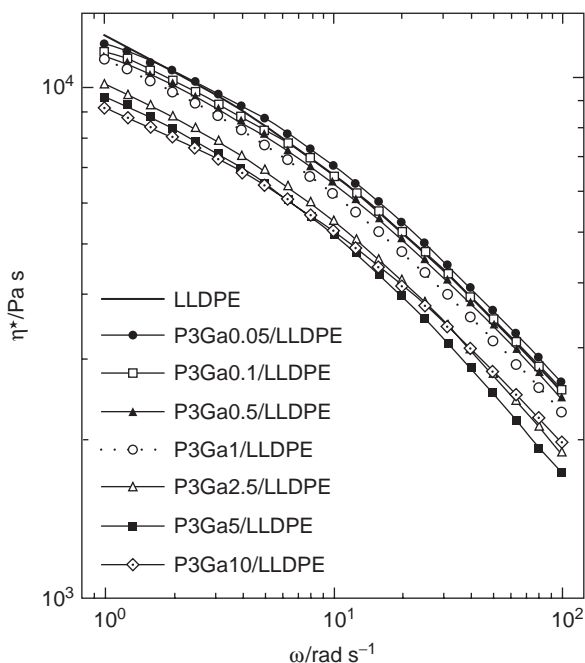
FIGURE 8.16

Effect of hyperbranched polymer concentration on the complex viscostiy of P3Ga (90% of third generation hyperbranched polymer esterified with C-20/22 fatty acid) blends at 170°C. The concentration varies from 0 to 10 wt%. Ninety percent of the end groups for this HBP are terminated with C-20/22 alkanes. (From Hong, Y. et al., 1999, *J. Rheology,* 43(3), 781–793. With permission.)

poly(ether amide). It was found that a small amount of hyperbranched polymer was able to strongly reduce the complex viscosity of the blends.

In the recent work of Tande et al.,[82] a series of hyperbranched poly(siloxysilanes) were synthesized and modified by derivatizing their end groups, and their shear rheology determined as homopolymers, as well as in blends with linear, atactic polystyrene. Complete functionalization (phenylization of the end groups for HBPs) was found to be less effective at reducing blend viscosity at high shear rates, and was found to increase the zero-shear blend viscosity. This suggested that a higher degree of functionalization may be acting as weak, physical cross-links.

References

1. Frechet, J.M.J. 1994, *Science*, 263, 1710–1715.
2. Hawker, C.J., Farrington, P.J., Mckay, M.E., Wooley, K.L., and Frechet, J.M.J. 1995, *J. Am. Chem. Soc.*, 117, 4409.
3. Buhleier, E., Wehner, W., and Vogtle, F. 1978, *Synthesis*, 155–158.

4. Tomalia, D.A., Baker, H., Dewald, J., Hall, M., Kallos, G., Martin, S., Roeck, J., Ryder, J., and Smith, P. 1985, *Polym. J.*, 17, 117.
5. Newkome, G.R., Yao, Z., Baker, G.R., and Gupta, V.K. 1985, *J. Org. Chem.*, 50, 2003.
6. Tomalia, D.A., Naylor, A.M., Goddard, W.A., III. 1990, *Angew. Chem. Int. Ed. Engl.*, 29, 138–175.
7. Tomalia, D.A. and Durst, H.D. 1993, *Top. Curr. Chem.*, 165, 193–313.
8. Newkome, G.R., Moorefield, C.N., and Baker, G.R. 1992, *Aldrichim. Acta*, 25, 31–38.
9. Voit, B.I. 1995, *Acta Polymer*, 46, 87–99.
10. Malmström, E. 1996, Hyperbranched Aliphatic Polyesters, thesis, Royal Institute of Stockholm, Sweden.
11. Hudson, R.H.E. and Damha, M.J. 1993, *J. Am. Chem. Soc.*, 115, 2119–2124.
12. Achar, S. and Puddephatt, R.J. 1995, *Organometallics*, 14, 1681–1687.
13. Sendijarevic, I. and McHugh, A.J. 2000, *Macromolecules*, 33, 590–596.
14. Launay, N., Caminade, A.-M., and Majoral, J.-P. 1995, *J. Am. Chem. Soc.*, 117, 3282–3283.
15. Rajca, A. and Utampanya, S. 1993, *J. Am. Chem. Soc.*, 115, 10688–10694.
16. Denkewalter, R.G., Kolc, J., and Lukasavage, W.L. 1981, U.S. Patent 4,289,872.
17. Tomalia, D.A. August 1984, paper presented at 1st International Polymers Conference, Society Polymer Science Japan, Kyoto, Japan.
18. Matthews, O.A., Shipway, A.N., and Stoddart J.F. 1998, *Prog. Polym. Sci.*, 23, 1–56.
19. Frechet, J.M.J. and Hawker, C.J. 1996, in *Comprehensive Polymer Science*, 2nd Supplement, Pergamon Press, Oxford, chap. 3.
20. Hawker, C.J. and Frechet, J.M.J. 1990, *J. Am. Chem. Soc.*, 112, 7638.
21. Hawker, C.J. and Frechet, J.M.J. 1990, *J. Chem. Soc. Chem. Commun.*, 1010.
22. Hawker, C.J. 1999, *Adv. Polym. Sci.*, 147, 114–160.
23. Flory, P.J. 1952, *J. Am. Chem. Soc.*, 75, 2718–2723.
24. Kim, Y.H. and Webster, O.W. 1990, *J. Am. Chem. Soc.*, 112, 4592–4593.
25. Malmström, E. and Hult, A. 1997, *JMS Rev. Macromol. Chem. Phys.*, C37, 555–579.
26. Johansson, M., Malmstrom, E., and Hult, A. 1993, *J. Polym. Sci. Polym. Chem.*, 31, 619.
27. Malmström, E., Johansson, M., and Hult, A. 1995, *Macromolecules*, 28, 1698–1703.
28. Kim, Y.H. and Webster, O.W. 1988, *Polym. Prepr.*, 29, 310.
29. Kim, Y.H. 1989, U.S. Patent 4,857,630.
30. Frechet, J.M.J., Hemmi, M., Gitsov, I., Aoshima, S., Leduc, M.R., and Grubbs, R.B. 1995, *Science*, 269, 1080.
31. Hawker, C.J., Frechet, J.M.J., Grubbs, R.B., and Dao, J. 1995, *J. Am. Chem. Soc.*, 117, 10763.
32. Hawker, C.J. 1995, *Angew. Chem. Ins. Ed. Engl.*, 34, 1465.
33. Zhu, L., Tong, X., Li, M., and Wang, E. 2001, *J. Phys. Chem.*, 105B, 2461–2464.
34. Hawker, C.J., Wooley, K.L., Lee, R., and Frechet, J.M.J. 1991a, *Polym. Mater. Sci. Eng.*, 64, 73.
35. Hawker, C.J. and Frechet, J.M.J. 1992, *Polymer*, 33, 1507.
36. Claussen, W., Schulte, N., and Schluter, A.D. 1995, *Macromol. Rapid Commun.*, 16, 89.
37. Wooley, K.L. and Frechet, J.M.J. 1992, *Polym. Mater. Sci. Eng.*, 67, 90.
38. Leduc, M.R., Jawker, C.J., Dao, J., and Frechet, M.J. 1996, *J. Am. Chem. Soc.*, 118, 11111–11118.

39. Hawker, C.J. 1994, paper presented at the 35th IIUPAC International Symposium on Macromolecules, Akron, Ohio.
40. Hawker, C.J., Lee, R., and Frechet, J.M.J. 1991, *J. Am. Chem. Soc.*, 113, 4583.
41. Kambouris, P. and Hawker, C.J. 1993, *J. Chem. Soc. Perkin Trans.*, 1, 2717.
42. Hawker, C.J. and Chu, F. 1996, *Macromolecules*, 29, 4370.
43. Percec, V., Chu, P., and Kawasumi, M. 1994, *Macromolecules*, 257, 4441.
44. Mourey, T.H., Turner, S.R., Rubinstein, M., Frechet, J.M.J., Hawker, C.J., and Wooley, K.L. 1992, *Macromolecules*, 25, 2401.
45. Uppuluri, S., Keinath, S.E., Tomalia, D.A., and Dvornic, P.R. 1998, *Macromolecules*, 31, 4498–4510.
46. De Gennes, P.G. and Hervet, H.J. 1983, *J. Phys. Lett.*, 44, 351.
47. Lescanec, R.L. and Muthukumar, M. 1990, *Macromolecules*, 23, 2280.
48. Wooley, K.L., Frechet, J.M.J., and Hawker, C.J. 1994, *Polymer*, 35, 4489.
49. Uppuluri, S., Morrison, F.A., and Dvornic, P.R. 2000, *Macromolecules*, 33, 2551–2560.
50. Lyulin, A.V., Davies, G.R., and Adolf D.B. 2000, *Macromolecules*, 33, 3294.
51. Kao, H.-M., Stefanesco, A.D., and Wooley, K.L. 2000, *Macromolecules*, 33, 3294.
52. Sperling, L.H. 1986, The crystalline state, in *Introduction to Physical Polymer Science*, John Wiley & Sons, New York, chap. 6.
53. Moreno-Bondi, M.C., Orellana, G., Turro, N.J., and Tomalia, D.A. 1990, *Macromolecules*, 23, 910.
54. Hawker, C.J., Wooley, K.L., and Frechet, J.M.J. 1993, *J. Am. Chem. Soc.*, 115, 4375.
55. Wooley, K.L., Hawker, C.J., Pochan, J.M., and Frechet, J.M.J. 1993, *Macromolecules*, 26, 1514.
56. Kim, Y.H. and Webster, O.W. 1992, *Macromolecules*, 25, 5561.
57. Stutz, H., Illers, K.-H., and Mertes, J. 1995, *J. Pol. Sci. Polym. Phys.*, 33B, 333.
58. Kim, Y.H. and Becherbauer, R. 1994, *Macromolecules*, 27, 1968.
59. Jayakannan, M. and Ramakrishnan, S. 2000, *J. Polym. Sci. Polym. Chem. Ed.*, 38, 261–268.
60. Dealy, J.M. and Wissbrun, K.F. 1989, *Melt Rheology and Its Role in Plastics Processing: Theory and Applications*, Van Nostrand Reinhold, New York.
61. Ferry, J.D. 1980, *Viscoelastic Properties of Polymers*, 3rd ed., Wiley, New York.
62. Kim, S.S. and Han, C.D. 1994, *Polymer*, 35, 93.
63. Bodnar, I., Silva, A.S., Deitcher, R.W., Weisman, N.E., Kim, Y.H., and Wagner, N.J. 2000, *J. Polym. Sci. Polym. Phys.*, 38B, 857–873.
64. Nunez, C.M., Chiou, B.-S., Andrady, A.L., and Khan, S.A. 2000, *Macromolecules*, 33, 1720–1726.
65. Farrington, P.J., Hawker, C.J., Frechet, J.M.J., and Machay, M.E. 1998, *Macromolecules*, 31, 5043–5050.
66. Colby, R.H., Fetters, L.J., and Graessley, W.W. 1987, *Macromolecules*, 20, 2226.
67. Ohko, Y., Uedono, A., and Ujihara, Y. 1995, *J. Polym. Sci. Polym. Phys.*, 33B, 1183.
68. Jahromi, S., Palmen, J.H., and Steeman, P.A.M. 2000, *Macromolecules*, 33, 577–581.
69. Hay, G., Hawker, C.J., and Mackay, M.E. 2000, paper presented at XIIIth International Congress on Rheology, Cambridge, U.K.
70. McCrum, N.G., Read, B.E., and Williams, G. 1967 and 1991, *Anelastic and Dielectric Effects in Polymeric Solids*, Dover, New York.
71. Malmström, E., Liu, F., Boyd, R.H., Hult, A., and Gedde, U.W. 1994, *Polym. Bull.*, 32, 697.

72. Emran, S.K., Newkome, G.R., Weis, C.D., and Harmon, J.P. 1999, *J. Polym. Sci. Polym. Phys.*, 37B, 2025–2038.
73. Trahasch, B., Stühn, B., Frey, H., and Lorenz, K. 1999, *Macromolecules*, 32, 1962–1966.
74. Malmström, E., Hult, A., Gedde, U.W., Liu, F., and Boyd, R.H. 1997, *Polymer*, 38, 4873–4879.
75. Huwe, A., Appelhans, D., Prigann, J., Voit, B.I., and Kremer F. 2000, *Macromolecules*, 33, 3762–3766.
76. Zhu, P.W., Zheng, S., and Simon, G.P. 2001, *Macromol. Chem. Phys.*, 15, 202.
77. Massa, D.J., Shriner, K.A., Turner, S.R., and Voit, B.I. 1995, *Macromolecules*, 28, 3214.
78. Huber, T., Pötschke, P., Pompe, G., Häßler, R., Voit, B., Grutke, S., and Gruber, F. 2000, *Macromol. Mater. Eng.*, 280/281, 33–40.
79. Connolly, M., Ma, B., and Karasz, F.E. 1993, *PMSE Prepr.*, 69, 82.
80. Carr, P.L., Davies, G.R., Feast, W.J., Stainton, N.M., and Ward, I.M. 1996, *Polymer*, 37, 2395.
81. Hong, Y., Cooper-White, J.J., and Mackay, M.E. 1999, *J. Rheology*, 43, 781–793.
82. Tande, B., Sadowsky, R., Wagner, N.J., and Kim, Y.H. 2000, paper presented at XIII International Congress on Rheology, Cambridge, U.K.

9

Gas Barrier Properties of Polymeric Materials

Gabriel O. Shonaike

CONTENTS

9.1   Introduction

Within the last few decades, barrier polymers have been increasingly in demand, especially in packaging industries. They are polymers with low permeability coefficients capable of restricting the passage of gases, vapors, and organic liquids. In comparison with glass and metal food containers, plastic packages are more permeable to gases, water vapor, and aroma compounds;[1] i.e., in some cases, where long shelf life is required, they failed by allowing oxygen to migrate through the wall and ruin the flavor or safety of

the food products.[2] This aspect is a direct result of interaction between the food and the film.[3,4] Thus, migration of flavor would greatly affect the quality of food because it has been in direct contact with the film after a long period of storage.[5] Therefore, a good barrier plastic must be able to protect the food from transmission of oxygen, carbon dioxide, and other gases. Although there are some food products such as freshly packed meat that require at least moderate gas transmission, all in all they must conform to some requirements that will maintain the freshness of the food. Consequently, an ideal packaging polymer would exhibit the following characteristics:[5–8]

- High oxygen and water vapor barrier
- Retention of barrier properties during manufacturing
- Flexibility for various packaging needs
- Optical transparency
- Low thickness
- Relatively appealing in order to motivate consumers to buy and increase the manufacturer's turnover
- Reduced volume and weight
- Good storage potential
- Low cost
- Easy disposability of the packaging waste
- Easy recyclability of the packaging materials
- Environmentally friendly

Studies on barrier properties of polymers have been the subject of various investigations in order to understand the transport phenomena of gases and vapors through polymeric materials. Both theoretical and experimental explanations on the diffusion, solubility, and permeability of organic penetrants through polymer structures have been reported in various industrial and academic institutions. These investigations are due to the need to shift from the expensive traditional materials to less-expensive polymers. Figure 9.1 shows the complexity of the high-barrier film industry, including such participants as raw material producers, equipment suppliers, film producers, packaging converters, product producers, and retailers.[9] The sales of high-barrier films in 1998 was about \$2.8 billion and is forecast to grow at an average annual growth rate of 6.3% a year to \$3.8 billion in 2003.[9] Several high-barrier polymers have been developed. These include polyvinyl alcohol (PVA), ethylene vinyl alcohol (EVOH) copolymers, polyacrylonitrile (PAN), polyvinylidene chloride (PVDC), polyethylene naphthalate (PEN), oriented polypropylene (OPP), liquid crystalline polymer (LCP), oriented polyethylene terephthalate (o-PET), polychloro-fluoro-ethylene (PCTFE), polyamide 6 (PA6), etc.
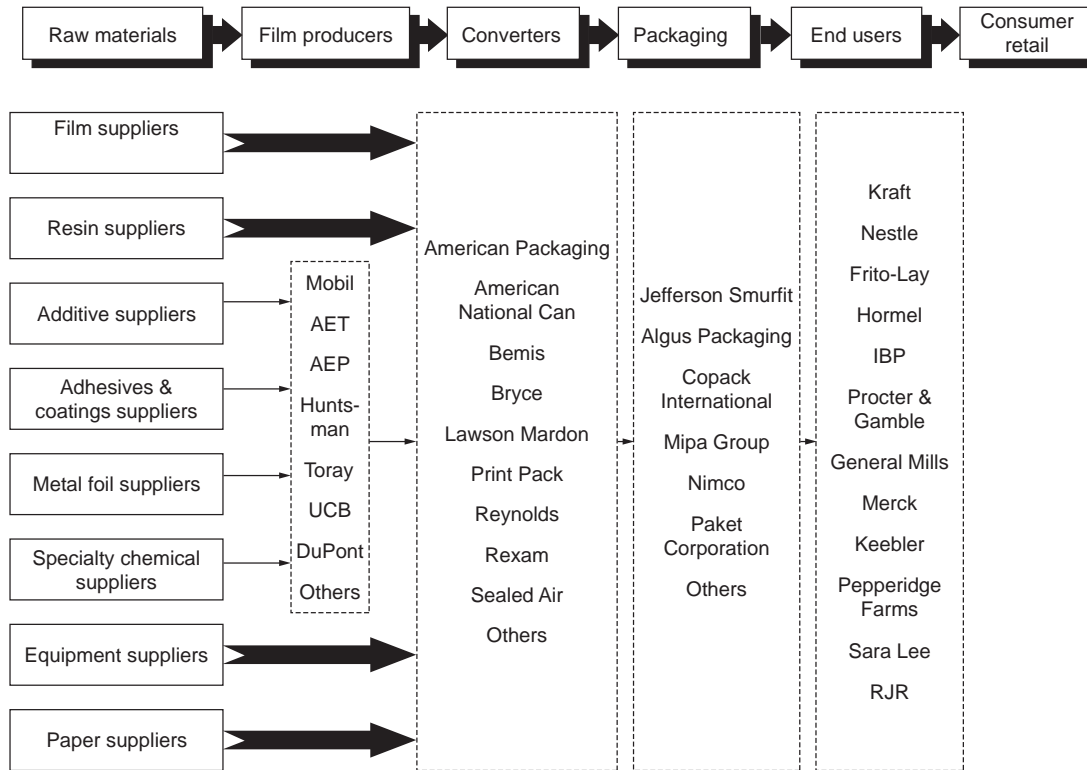
FIGURE 9.1
High-performance-barrier film industry structure. (From Gee, G.L., Value Chain Dynamics in the High-Performance Barrier Films Industry, paper presented at Proceedings at Future-Pak '99, Houston, TX, November 1999. With permission.)

In this chapter, a general survey of barrier properties covering a wide range is reviewed. These include information on synthesis of selected barrier thermoplastics and general physical properties, i.e., oxygen transmission rate, permeability, effect of polymer modifications, etc.

9.2   Barrier Polymers

Polymeric materials may be classified into high-, medium-, and low-barrier polymers. In this review, only representative polymers will be highlighted.

9.2.1   Polyvinylidene Chloride

PVDC is the first known gas barrier polymer that was developed several decades ago. A commercial grade of PVDC known as SARAN is produced by Dow Chemical. Saran is a generic name for polymers with high vinylidene chloride (VDC) content. It is produced by free radical polymerization of 1,1,2-trichloroethene with aqueous alkali:

$$2CH_2ClCHCl_2 + Ca(OH)_2 \rightarrow 2CH_2=CCl_2 + CaCl_2 + 2H_2O$$
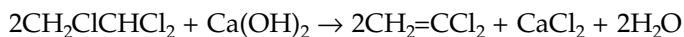
Properties of the VDC monomer is shown in Table 9.1.[10,11]

Polymerization of VDC to PVDC leads to long-chain molecules that are tightly bound together and resist permeation of gas and water vapor. This characteristic of PVDC results in a high-barrier polymer suitable for protecting foods and industrial products. PVDC is a high crystalline polymer with a melting point of 220°C and a high density of around 1.9 g cm^{-3}. It does not dissolve in most solvents at ambient temperatures but dissolves in some solvents above 130°C.[12] The key properties of PVDC include a high barrier, heat sealability, a high transparency, and a gloss; PVDC can be blended with a wide variety of materials and can be processed using liquid extrusion coating and extrusion. Processing of PVDC is difficult, and as a result, direct measurement of the mechanical properties is difficult. In Table 9.2, the mechanical properties of high VDC, unplasticized copolymers are shown.[13]
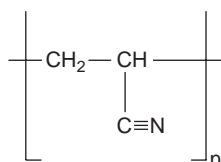
9.2.2   Polyacrylonitrile

TABLE 9.1

Properties of Vinylidene Chloride Monomer

Property	Value
Molecular weight	96,944
Odor	Pleasant, sweet
Appearance	Clear, liquid
Color (APHA)	0–10
Solubility of monomer in water (at 25°C), wt%	0.25
Solubility of water in monomer (at 25°C), wt%	0.035
Normal boiling point, °C	31.56
Freezing point, °C	−122.56
Flash point (tag closed-cup), °C	−28
Flash point (tag open-cup), °C	−16
Flammable limits in air (ambient conditions), vol%	6.5–15.5
Autoignition temperature, °C	513[a]
Latent heat of vaporization, ΔH_v^o, kJ/mol[b]	
At 25°C	26.48 ± 0.08
At normal boiling point	26.14 ± 0.08
Latent heat of fusion (at freezing point), ΔH_m^o, J/mol[b]	6514 ± 8
Heat of polymerization (at 25°C), ΔH_p^o, kJ/mol[b]	−75.3 ± 3.8
Heat of combustion, liquid monomer (at 25°C), ΔH_c^o, kJ/mol[b]	1095.9
Heat of formation	
Liquid monomer (at 25°C), ΔH_f^o, kJ/mol[b]	−25.1 ± 1.3
Gaseous monomer (at 25°C), ΔH_f^o, kJ/mol[b]	1.26 ± 1.26
Heat capacity	
Liquid monomer (at 25°C), C_p^o, J/(mol·K)[b]	111.27
Gaseous monomer (at 25°C), C_p^o, J/(mol·K)[b]	67.03
Critical temperature, T_c, °C	220.8
Critical pressure, P_c, MPa[c]	5.21
Critical volume, V_c, cm³/mol	218
Liquid density, g/cm³	
−20°C	1.2852
0°C	1.24998
20°C	1.2137
Index of refraction, n_D	
10°C	1.43062
15°C	1.42777
20°C	1.42468
Absolute viscosity, mPa·s (= cP)	
−20°C	0.4478
0°C	0.3939
20°C	0.3302
Vapor pressure, T, °C (P measured from 6.7–104.7 kPa)[d]	$\log P_{kPa} = 6.1070 - 1104.29/(T + 237.69)$

[a] Inhibited with methyl ether of hydroquinone.
[b] To convert J to cal. divide by 4.184.
[c] To convert MPa to atm divide by 0.101.
[d] To convert kPa to mmHg, multiply by 7.5.

Source: Vinylidene Chloride Monomer Safe Handling Guide, No. 100-6339-88-SAL, Dow Chemical Co., Midland, MI, 1988. With permission.

TABLE 9.2

Properties of Poly(vinylidene) Chloride

Property	Value
Melting temperature (°C)	220
Glass transition temperature (°C)	–17
Crystallization temperature (°C)	150°C
Density at 15°C	
Amorphous	1.775
Crystalline	1.96
Refractive index (crystalline), n_D	1.63
Tensile strength (MPa)	
Unoriented	34.5–69.0
Oriented	207–414
Elongation (%)	
Unoriented	10–20
Oriented	15–40
Softening range (heat distortion), (°C)	100–150
Flow temperature (°C)	>185
Brittle temperature (°C)	–10 to 10
Impact strength (J/m)	26.7–53.4

Source: Shelton, L.G. et al., *Vinly and Diene Monomers, High Polymers*, Vol. 24, Leonard, E.C., Ed., Wiley Interscience, New York, 1971, p. 1205. With permission.

PAN is virtually one of the high-barrier polymers. It is produced by free radical polymerization of acrylonitrile in solution or in suspension. It may be synthesized from hydrogen cyanide with acetylene, ethylene oxide, or acetaldehyde; nitric acid with propylene; and ammonia and oxygen with propylene (ammoxidation process).[14] The ammoxidation process has been adopted commercially due to a dramatic price reduction and an increased supply.[15,16]

$$CH_2{=}CH + NH_3 + 1.5O_2 \rightarrow CH_2{-}CH + 3H_2O$$
$$\underset{CH_3}{|} \qquad\qquad\qquad \underset{C{\equiv}N}{|}$$
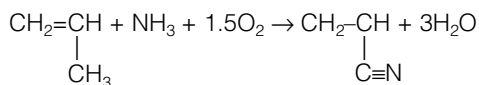
The basic importance of PAN is felt in the textile industries, where it is spun directly from solution into fibers. According to Billmeyer,[17] during the time that other polymers were being developed as plastics, PAN was considered a useless material for two major reasons: it could neither be dissolved nor plasticized, and it softens only slightly below its decomposition temperature. However, acrylic fiber was introduced in the early 1940s by DuPont under the trade name Orlon. Since then, other companies have produced PAN fibers with various trade names.

PAN cannot be easily melt-processed like other thermoplastics because of its insolubility in common solvents and its higher melting point, which is just in the neighborhood of its thermal decomposition. Some of the physical properties of PAN are:[18–20]

Density: 1.17
Glass transition temperature: 100°C
Tensile strength: 4000 kp/cm³
Elongation at break: 8 to 20%
Maximum temperature for permanent use: 200°C
Maximum moisture uptake: 2.5 to 3%

The melting temperature of PAN cannot be easily determined because it degrades before reaching the melting point. However, a melting temperature of 317°C has been reported by Krigbaunn and Tokita[21] using dilatometry at a heating rate of 40°C/min. This is sufficiently fast to achieve melting before reaching a value of 326°C, which was recorded as the degradation temperature by Dunn and Ennis.[22] PAN is highly resistant to common solvents by hydrolysis; hot alkali solution leads to the formation of poly(acrylic acid), and hydration with concentrated sulfuric acid leads to solution.

9.2.3 Polyesters

Polyethylene terephthalate (PET) is one of the most successful medium-range engineering polymers. PET, discovered in Britain,[23] possesses excellent properties that make it suitable for fiber production. Injection-molded PET was commercialized after the Second World War. A rapid growth of engineering-grade PET, especially in the packaging industry, was energized by the need for beverage bottles as well as containers. Synthesis of PET is based on the condensation reaction between ethylene glycol (EG) and terephthalic acid:[24]
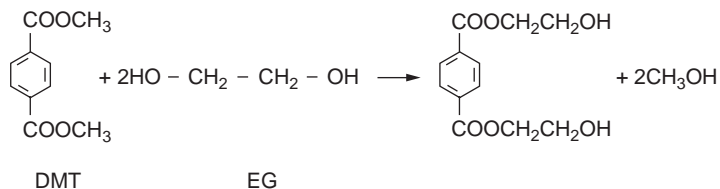
However, commercial production is by ester interchange and there are two steps involved. The first step is an ester interchange of dimethyl terephthalate (DMT) and ethylene glycol carried out at 150 to 195°C, from which methanol is removed.[25]
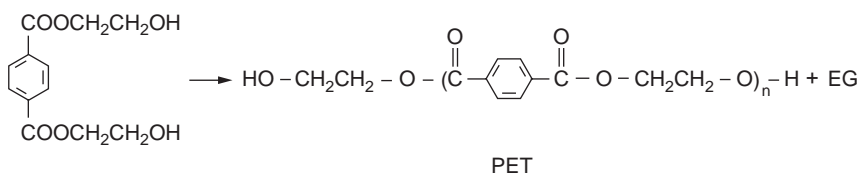
TABLE 9.3

Properties of PET

| Property	Value
Specific gravity	1.37
Melting temperature (°C)	255–265
Glass transition temperature (°C)	67–140
Heat deflection temperature (°C)	
At 0.46 MPa	115
At 1.82 MPa	85
Water absorption at 23°C (%)	
After 24 h	0.08
At equilibrium	0.60
Tensile strength (MPa)	53
Tensile elongation (%)	300
Flexural strength (MPa)	114
Compressive strength (MPa)	128
Shear strength (MPa)	55
Izod impact strength (notched) J/m^2	43
Izod impact strength (unnotched) J/m^2	No break
Rockwell hardness	M106

The second stage is carried out at elevated temperature (about 290°C), and ethylene glycol from the second ester exchange is distilled off.

The thermal property measurements[26-28] have shown that virgin PET has a melting temperature at 280°C, but for commercial PET, it is between 255 and 265°C. This reduction is due to the chemical impurities during production. Thus the impurity, usually a by-product, resulted from diethylene glycol, which acts as a comonomer in further stages of polymerization.[29] The heat of fusion of PET is 166 J/g, and the specific gravity is 1.33 for normal and 1.39 for highly oriented crystalline PET.[30] The average molecular weight (Mw) of injection-mold PET is around 80,000, which is higher than the range for fiber production. High-molecular-weight PET improves the mechanical properties, especially the impact strength.[31] Other physical properties are shown in Table 9.3.[32,33] As for the chemical properties, PET is one of the thermoplastic polymers that are highly resistant to a wide range of organic solvents, such as alcohol, water, ketones, etc.

Apart from its various applications in the packaging industry, it is also used for applications that require high levels of rigidity and dimensional stability, particularly at elevated temperatures.[33] The widespread commercial application of PET in the packaging industry is due to its low cost, clarity, and good barrier properties. When biaxially oriented, it is suitable for various applications, including blow-molded containers. Recently, a new monomer was added to the polyester family with improved barrier properties. This new monomer, known as naphthalene dicarboxylate (NDC),
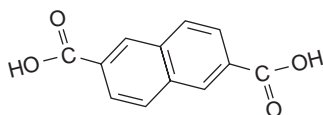
can be polymerized with dimethyl terephthalate to yield poly(ethylene naphthalate) PEN.[25]
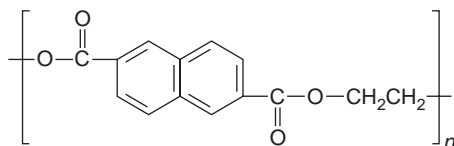
PEN, which is produced from NDC (homopolymer), has properties that make it suitable for various applications, including high-performance polyester films, fibers, and specialty packaging applications. PEN can be extruded and blow-molded with improved properties, e.g., chemical resistance and ultraviolet (UV), thermal, and dimensional stability. Above all, the barrier properties, in comparison with PET, are overwhelming. The property comparison of PET and PEN is shown in Table 9.4.[34] A low-molecular-weight PEN with the trade name HYPERTUF was recently introduced by Shell Chemical Company. It is designed to provide very good container properties, including high clarity, thermal properties, and good water and UV barrier properties.
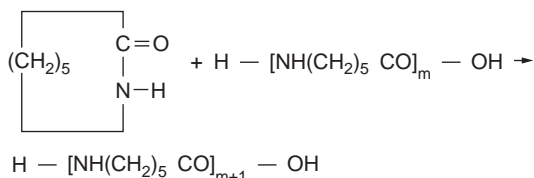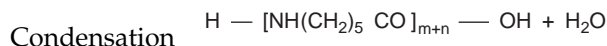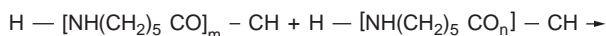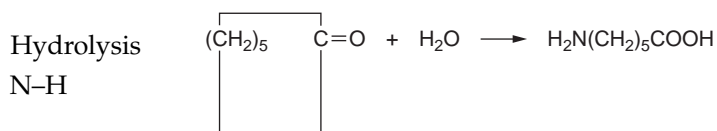
9.2.4 Polyamide 6

Polyamide 6 (nylon 6) is the best gas and aroma barrier of all nylons.[35] A nylon is any long-chain synthetic polymeric amide that has a recurring amide group as an integral part of the main chain.[36] The commercial viability of nylon 6 commenced in 1938 when it was discovered that ε-caprolactam polymerizes by heating with water[37] or with amine salts of carboxylic acids. Nylon 6 is made from caprolactam in three stages: hydrolysis, condensation, and addition. Dry caprolactam cannot polymerize,[38] but in the presence of water, a reaction occurs:

TABLE 9.4

Property Comparison of PET and PEN

Property	PET	PEN
Tensile strength (MPa)	195	200
Glass transition temperature, T_g (°C)	70	120
Continuous-use temperature (°C)	120–130	160
H_2O transmission (g/100 in.²/day)	1.3	0.23
O_2 transmission (cc/100 in.²/day)	10–40	2–10

Source: Bonis, L.J., Property Comparison of PET and PEN Polyesters in Packaging, presented at Future-Pak 96, 13th International Schroeder Conference on Packaging, Chicago, IL, November 20–21, 1996. With permission.

Hydrolysis
N–H

$(CH_2)_5$ C=O + H_2O ⟶ $H_2N(CH_2)_5COOH$

H — $[NH(CH_2)_5 CO]_m$ – CH + H — $[NH(CH_2)_5 CO_n]$ – CH ➤

Condensation   H — $[NH(CH_2)_5 CO]_{m+n}$ —— OH + H_2O

$(CH_2)_5$ C=O
           |
           N–H   + H — $[NH(CH_2)_5 CO]_m$ — OH ➤

H — $[NH(CH_2)_5 CO]_{m+1}$ — OH

Addition

The process is that addition of water opens the ring to give ε-amino acid, which reacts with the second molecule of the lactam to give a dimetric acid, which in turn reacts with a third molecule of the lactam, and so on.

Nylon 6 is known to be strong, having good impact, tensile, and flexural strengths. Its solvent resistance is also good, but solvents such as phenols, cresols, and formic acid may dissolve the polymer at room temperature. Discoloration of nylon 6 in air may occur at a temperature of about 130°C and is degraded by hydrolysis at elevated temperatures.[39,40] Other properties of nylon 6 are shown in Table 9.5.[35]

A comparison of the gas barriers of various polyamides is shown in Table 9.6.[36] As can be seen in the table, nylon 6 has the best gas and aroma barrier. As you go down the chart, the gas barrier decreases and the moisture barrier increases. Another advantage is that nylon 6 is the least costly of the nylons.

9.2.5 Ethylene Vinyl Alcohol

Ethylene vinyl alcohol, a modified polyvinyl alcohol (PVOH), has been the most successful of all barrier polymers. Since its inception in the early seventies, EVOH has been enjoying a rapid growth due to its high solvent and gas barrier properties, which make it suitable for various applications in the packaging industry. Other important properties include excellent resistance to solvents, flavor and aroma retention, moderate cost, and easy processability.[41,42] EVOH was first commercialized by Kuraray in 1972 under the trade name EVAL. Two years later, Nippon Gohsei (Osaka, Japan) commercialized it as Soarnol. In the United States, EVOH is produced by Noltex, which is a joint venture between Mitsubishi and Nippon Gohsei, and EVALCA, owned by Kuraray.

TABLE 9.5

Properties of Nylon 6b

Property	Value
Density (g/cm³)	
Amorphous	1.09
Crystalline	1.12–1.14
Heat of fusion (kJ/kg)	230
Melting point (°C)	225
Glass transition temperature (°C)	~45
Melt viscosity	
Coefficient K of zero shear	9.5×10^{-14}
Rate melt viscosity (Pa·s)	(250°C)
Specific volume (cm³/g) at 20°C	
Amorphous	0.917
Crystalline	0.813
Water absorption (%)	9–11
Dielectric constant, 10^3 Hz (dry)	8.0
Dissipation factor, 10^3 Hz (dry)	0.10
Coefficient of linear thermal expansion (°C^{-1})	8×10^{-5}
Tensile strength at beak (MPa)	94
Elongation at break (%)	30–100
Tensile yield strength (MPa)	80.7
Tensile modulus (GPa)	2.6
Compressive strength (MPa)	90–110
Flexural strength (MPa)	108
Flexural modulus (MPa)	2.7
Izod impact, 3.2 mm, notched (J/m)	32–53
Rockwell hardness	R119

Source: Kohan, M.I., *Eng. Plast.*, 2, 125, 1995. With permission.)

TABLE 9.6

Comparison of Some Properties of Polyamides

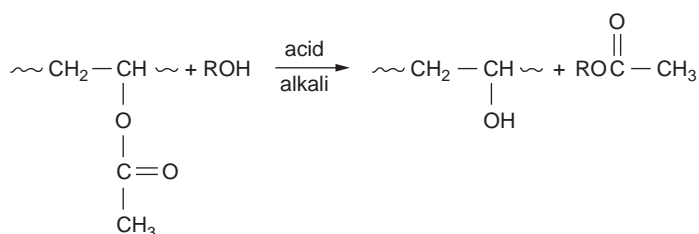|	Density	Melt Point, 0°C	H₂O Absorption, Max	Gas and Aroma Barrier	Cost (Relative)
PA 6	1.13	220	9.5%	Best	1.0
PA 6/6,6	1.13	204	9.0%	↑	1.2
PA 6,6	1.14	255	8.5%		1.3
PA 6,10	1.07	215	3.3%		1.4
PA 6,12	1.07	210	3.3%		1.5
PA 11	1.04	186	1.8%	↓	1.8
PA 12	1.01	178	1.6%	Poorest	1.7

Source: Levy, J.H., Polyamide 6 Resins for Co-Extruded Films, presented at 13th Annual World Congress in Specialty Plastic Films 97, Zurich, Switzerland, 1997. With permission.

EVOH is a copolymer containing both ethylene and vinyl alcohol repeat units. The copolymer is produced by hydrolysis of ethylene vinyl acetate copolymers. Copolymers containing about 20 to 35% ethylene are crystalline and are useful as barrier polymers having very low permeabilities to many vapors and odors, but not to water vapor.[43] The unit cell of EVOH with a vinyl alcohol content higher than 27% mol is monoclinic[44]; i.e., the two planar zigzag chains are statistically packed in a mode similar to that of PVOH. When the alcohol content is between 14 and 27 mol%, the unit cells are hexagonal; below 7 mol%, they are orthorhombic, similar to those of poly-ethylene. It has recently been reported by Cerrada et al.[45] that the crystalline structure depends on the cooling rate. For the samples slowly crystallized from the melt, a monoclinic lattice is obtained for copolymers with 71 and 68 mol% vinyl alcohol, while an orthorhombic lattice resulted in copolymers with 56 mol% VA. However, when both copolymers with 71 and 60 mol% VA content are quenched from the melt, orthorhombic lattices are formed.
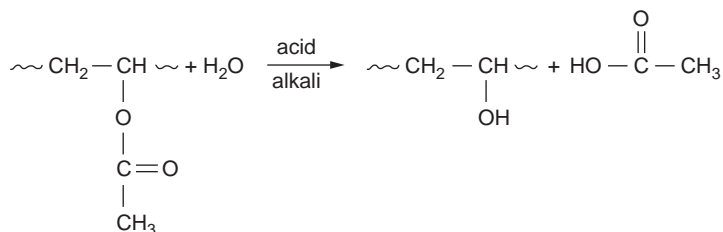
In this chapter, it may be worthwhile to spend more time reviewing the polymerization and production of EVOH.

EVOH is an ethylene-modified polyvinyl alcohol, and PVOH is produced through the hydrolysis of polyvinyl acetate (PVAc). Production of a PVOH monomer is not easy, due to instability as well as problems in obtaining quantities and purity that make free radical polymerization feasible.[46,47] Mar-ten and Zeanut[48] have reviewed the various methods of converting PVAc to PVOH. These methods include transesterification (also known as saponifi-cation reaction), hydrolysis, and aminolysis. Since this chapter is only to highlight the method adopted commercially, other methods may be found elsewhere.[48] Industrially, transesterification reaction is most common; it involves the use of a small acid or base to catalyze the reaction.
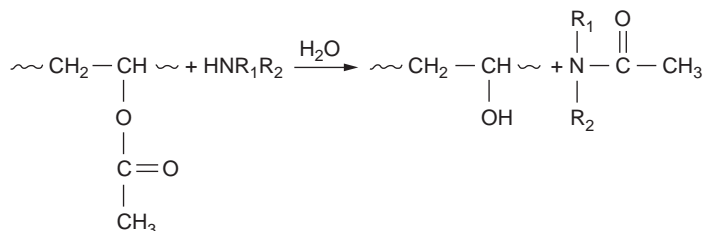
Transesterification:

$$\sim\!\!\sim CH_2\!-\!CH\!\sim\!\!\sim\ +\ ROH \quad \xrightarrow[\text{alkali}]{\text{acid}} \quad \sim\!\!\sim CH_2\!-\!CH\!\sim\!\!\sim\ +\ ROC\!-\!CH_3$$

(side group on left reactant: CH attached to O—C=O—CH₃; right product: CH attached to OH; ROC—CH₃ has O double-bonded)

Hydrolysis:

$$\sim\!\!\sim CH_2\!-\!CH\!\sim\!\!\sim\ +\ H_2O \quad \xrightarrow[\text{alkali}]{\text{acid}} \quad \sim\!\!\sim CH_2\!-\!CH\!\sim\!\!\sim\ +\ HO\!-\!C\!-\!CH_3$$

(side group on left reactant: CH attached to O—C=O—CH₃; right product: CH attached to OH; HO—C—CH₃ has O double-bonded)

Aminolysis:

$$\sim\!\!\sim CH_2\!-\!CH\!\sim\!\!\sim + HNR_1R_2 \xrightarrow{H_2O} \sim\!\!\sim CH_2\!-\!CH\!\sim\!\!\sim + \underset{R_2}{\overset{R_1}{N}}\!-\!\overset{O}{\overset{\|}{C}}\!-\!CH_3$$

(with the left CH bearing an O—$C{=}O$—CH_3 ester group and the right CH bearing OH)

There are various methods of converting PVAc to PVOH, but all are based on an ester exchange reaction between PVAc and methanol. The reaction is catalyzed by sodium hydroxide or sodium methoxide, and this results in sodium acetate as a by-product. However, mixing of the PVAc and sodium hydroxide is the most important step because the quality of the final product depends on the mixing process.[48] The saponification process may be by belt, screw, slurry, etc.[49] Whichever process is used, it involves mixing the PVAc with the base of choice in a high-intensity mixer. The slurry method consists of two stirred tanks. The mixture is transferred from the first to the second reactor for full conversion. During conversion, both alkyl acetate and alcohol are continuously distilled off, and the product precipitates without forming a gel. The final product yields a very fine polyvinyl alcohol. In the case of the screw process, the PVAc and catalyst are mixed in a high-intensity mixer and continuously introduced to a screw-type saponification and system, schematically represented in Figure 9.2.

Commercially produced EVOH has an ethylene content of between 29 and 44 mol%. The properties of EVOH, which vary with the relative composition of the two components (PVOH and polyethylene (PE)), are represented in Figure 9.3.[2] The monolytic region that represents the commercially available grades has a monolithic crystal structure up to 42 mol% of ethylene. In this case, the crystals are dense and closely packed, resembling those of PVOH, and have higher barrier properties to gases and higher thermoforming temperatures than PE.[2] On the other hand, the hexagonal crystals between 42 and 80 mol% are larger and less dense, resulting in lower gas barrier properties and thermoformability.

Nippon Gohsei and Noltex have commercialized various EVOH grades known as Soarnol. The activities of each grade depend on the ethylene content and other physical properties, as shown in Table 9.7. With increasing ethylene content, the oxygen permeability increases. Other physical properties such as density and thermal properties, and melting, crystallization, and glass transition temperatures all reduce with increasing ethylene content. The increase in ethylene content leads to a more porous material due to increase in free volume. All the Soarnol grades have been found to be suitable for various applications in the packaging industry. Soarnol D, DT, and DC with high oxygen barriers are excellent for packaging both wet and dry foods, especially if they are used for multilayer packages under low humid-
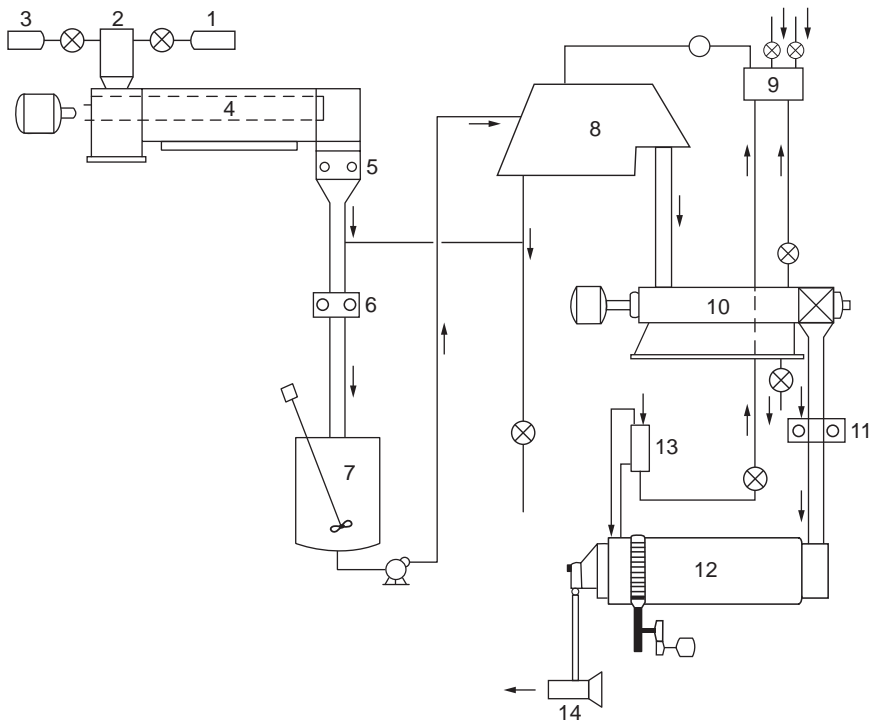
FIGURE 9.2
Poly(vinyl acetate) saponification system. 1. Paste dilution tank. 2. Catalyst and paste mixer. 3. Sodium hydroxide storage. 4. Saponifier. 5. Crusher. 6. Grinder. 7. Slurry tank. 8. Vacuum filter. 9. Methanol reservoir. 10. Screw press. 11. Grinder. 12. Rotary dryer. 13. Methanol condenser. 14. Poly(vinyl alcohol) storage. (From Marten, F.L., *Encyclopedia Polym. Sci. Eng.*, 17, 167, 1989. With permission.)

ity. Soarnol E, ET, A, and AT with high ethylene contents are suitable for wet foods meant for sterilization and can also be thermoformed.

Lastly, those with the highest ethylene content (Soarnol A and AT) are more important for the packages that need to be thermoformed. The mechanical properties also depend on ethylene content (Figure 9.4). Except for elongation, which increases with increasing ethylene content, other properties such as modulus, strength, and impact are all reduced. (Soarnol can be extruded and coextruded with other polymers without any problem.) Apart from the food industry, various Soarnol grades have established themselves for packaging agricultural chemicals, pharmaceuticals, cosmetics, etc.

9.2.6 Liquid Crystalline Polymer

Do we call it fiber-reinforced composite? No, it is a self-reinforced thermoplastic polymer that contains primarily benzene rings as the backbone. Liquid crystalline compounds have been in existence for more than 100 years, but
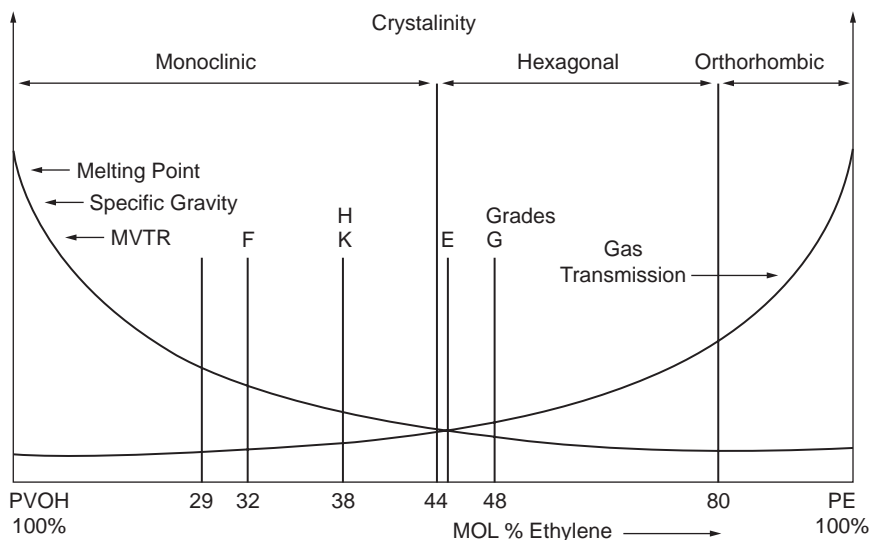
FIGURE 9.3
Effect of ethylene concentration on properties of EVOH resins. Grades refer to designations used for EVAL-EVOH resins. (From Blackwell, A.L., in *Plastic Film Technology*, Vol. 1, Finlayson, K.M., Ed., Technomic Publishers, Lancaster, PA, 1989, chap. 5. With permission.)

commercial viability was not realized until the discovery of aramid fiber by DuPont in 1974. Since then, various grades, most of which are copolyester, copolyamides, or polyesteramides, have been developed. Most of the LCPs display liquid crystalline behavior either in solution or in the melt. Polymers that form a liquid crystal organization in solution are termed *lyotropic*, while those that form from the melt are *thermotropic*. LCP chains tend to organize themselves into domains with preferred directions of orientation.[50,51] They contain three main mesophasic structures, shown in Figure 9.5.[52] The cholestic structure contains rigid molecules (mesogens) oriented parallel to one another, with the direction varying from one layer to another. The smetic structure results when all the mesogens are arranged in a parallel and lateral order. In the nematic state, the mesogens are arranged parallel, but not in lateral order. All commercial LCPs show nematic, one-dimensional order, which results from the semirigid architecture of the aggregate.[53] The chemical structures of commercial LCPs are shown in Figure 9.6. The first category (Figure 9.6(a)) is the general-purpose LCP, which has exceptional ease of processing, dimensional stability, molded-part repeatability, chemical resistance, flame resistance, and strength. The LCPs in Figure 9.6(b) are a more temperature-resistant variant and are not easy to process, but they have good chemical resistance, excellent frame resistance, and very good strength and stiffness. The structure of a less-expensive and easy-to-process LCP is shown in Figure 9.6(c). It has good dimensional stability but less chemical resistance, moderate flame resistance, and good strength and stiffness. All grades of LCPs have a flexible–rigid structure where the rigid-rod nature of the LCP tends to stack together like

TABLE 9.7

Properties of Various Grades of Soarnol

	Unit	D2908	DT2903	DC3212	DC3203	E3808	ET3803	A4412	AT4403
Ethylene content	mol%	2.9		32		38		44	
Density	g/cm^3	1.21		1.19		1.17		1.14	
Melting temperature[a]	°C	188		183		173		164	
Crystallization temperature	°C	163		160		152		144	
Glass transition temperature	°C	62		61		58		55	
MFI (210°C, 2160 g)	g/10 min	8	3.2	12	3.2	8	3.2	12	3.5
Apparent melt viscosity	poise								
(210°C)		9,000	24,000	5,500	24,000	9,000	24,000	5,500	20,000
(230°C)		5,000	13,000	2,500	13,000	5,000	12,000	2,500	10,000
Oxygen permeability (20°C, 60% RH)	cc·20 μ/m^2 · 24 h · atm	0.4		0.5		0.7		1.5	
	cc·ml/100 in^2 · 24 h · atm	0.021		0.024		0.037		0.074	

[a] measured by DSC.

Source: Nippon Gohsei Soarnol Data Sheet, Okayama, Japan, 1998. With permission.
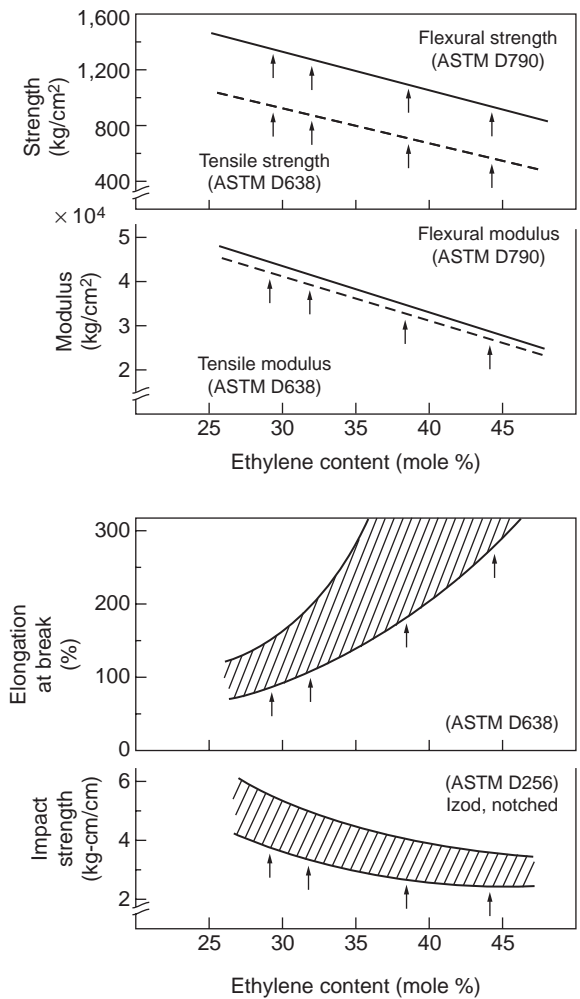
FIGURE 9.4
The mechanical properties vs. ethylene content of Soarnol EVOH. (From Nippon Gohsei Soarnol Data Sheet, Okayama, Japan, 1998. With permission.)

woods. Thus, when the LCP flows in the liquid crystal state, molecular alignment in the shear flow direction occurs, creating locally oriented domains that in turn create macroscopic-oriented regions. The rigid component imparts high temperature capability, while the flexible region enhances processability. LCP is melt processible with high orientation during molding having improved mechanical properties as well as high temperature capability. Shonaike et al.[54] have attributed the improved mechanical properties of LCP to skin-core morphology. Under short-term loading, the LCP fibrils on the skin layer orient in a way similar to that in a traditional reinforcing agent, such as glass fiber. This alignment of LCP fibrils enhances its stiffness.
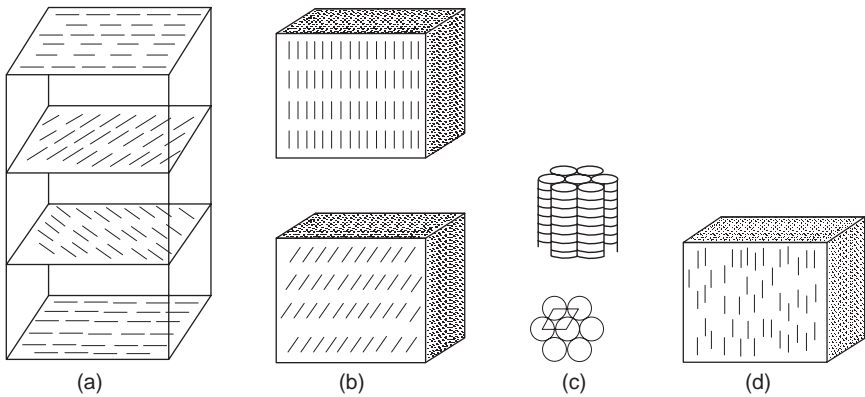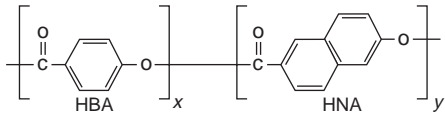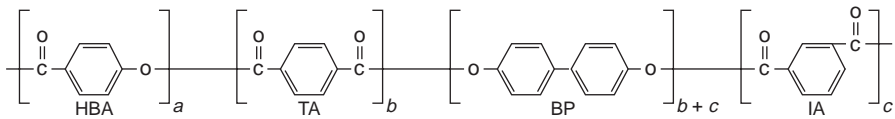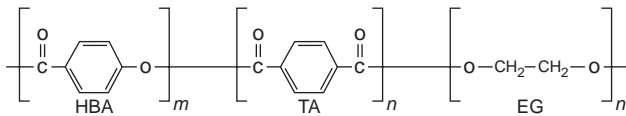
FIGURE 9.5
Mesophasic structures of LCP: (a) cholesteric; (b) smectic A (top) and smectic C (bottom); (c) discotic; (d) nematic. (From Brown, G.H. and Crooker, P.C., *Chem. Eng. News*, 61, 25, 1983. With permission.)

FIGURE 9.6
Principal LCP structures and sources. BP, biphenol; EG, ethylene glycol; HBA, hydroxy benzoic acid; HNA, hydroxy napthoic acid; IA, isophthalic acid; TA, terephthalic acid. (a) Produced by Hoeechst Celanese Corporation and Polyplastics Inc. as Vectra A and C resins. (b) Produced by Dartco Manufacturing Inc. (Amoco Performance Products) and Nippon Petrochemical as Xydar SRT 300 and 500, by Sumitomo as Ekonol, and by Toyo Soda MA as HB. (c) Produced by Eastman Kodak Company as X7G and X7H, by Unitika as Rodrum, by Mitsubushi Chemical as EPE, and by Idemitsu as LCP2000J. (From McChesney, C.E., *Eng. Plast.*, 2, 179, 1995. With permission.)

9.3 Permeability of Gases

The permeability of a polymer to a gas or vapor is the product of the solubility of the gas or vapor in the polymer and its diffusion coefficient.[17] It is a property that is directly measured as the rate of transfer of vapor or gas through the thickness of the film per unit area and pressure difference across the film. Permeability may be viewed as a product of solubility and diffusivity coefficients.

Diffusion is the net transport of the environment into the samples. Gases pass through a polymeric material by dissolving into the polymer. After a steady rate of flow is established in the polymer, diffusion can be described by Fick's law,[55] which states that the flux of penetrant through a membrane is proportional to the local concentration gradient:

$$J = -D\frac{\partial c}{\partial x} \tag{9.1}$$

where J is the diffusion rate or the amount of the diffusing substance per unit time (unit is g ml/m^2 day), D is the diffusion coefficient or diffusivity (expressed in cm^2/sec), and $^1c/^1x$ is the concentration gradient of the diffusing molecule across the membrane. If the polymer is thin in one dimension when compared with its in-plane dimensions, Fick's second law is applicable:

$$\frac{\partial c}{\partial t} = D\frac{\partial^2 c}{\partial x} \tag{9.2}$$

Consider diffusion of a small molecule through a thin film at steady state; the one-dimensional concentration gradient across the film is given as[56]

$$(c - c_1)/(c_2 - c_1) = x/L \tag{9.3}$$

where c is the concentration at position x, and c_1 and c_2 are the concentrations at x = 0 and x = L, respectively. The rate of mass transfer is given as

$$J = -D\,dc/dx = D(c_1 - c_2)/L \tag{9.4}$$

If the values of L, c_1, and c_2 are known, the rate of mass transfer can be written as

$$J = P(\rho_1 - \rho_2)/L \tag{9.5}$$

where ρ_1 and ρ_2 are the vapor pressure on each side of the film and P is the permeability coefficient. The relationship between P and D may be based on Henry's law:

$$c = Sp \qquad (9.6)$$

where S is the solubility coefficient. If diffusivity is assumed to be constant, then

$$P = DS \qquad (9.7)$$

Thus, P may be expressed as

$$cc(STP) \cdot cm/m^2 \cdot 24\ h \cdot atm$$

$$cc(STP) \cdot cm/cm^2 \cdot sec \cdot cm\ Hg$$

$$D = cm^2/sec$$

$$S = cc(STP)/cc \cdot atm$$

Henry's law indicates that the permeation rate of a material is affected by the product of D and S.

The diffusion rate of gases such as O_2, CO_2, etc., through a polymeric material is necessary, especially where food packaging is concerned. For example, if CO_2 diffuses rapidly through the PET bottle, the content may go flat too soon. On the other hand, if O_2 diffuses rapidly into a container, e.g., beer container, the beer may become sour. Therefore, the rate at which these gases or vapors penetrate polymeric materials is important. It was shown recently by Salame[57] that O_2 permeability can be regarded as a measure of barrier because any material that possesses inherent good barriers to oxygen is also a good barrier to CO_2, with the exception of material that contains specific O_2 scavengers. The flavor-scalping capabilities of a polymer are related to S, and P determines the loss of permeant from the total package.[58] Permeability of a polymer by a gas depends on the size and solubility of the gas; i.e., it increases with decreasing size and increasing solubility of the gas.[58] Thus the transmission rate is given in the order of

$$H_2 > He > H_2S > CO_2 > O_2 > Ar > CO \cdot CH_4 \cdot N_2$$
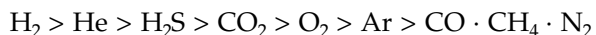
The size and (Lennard–Jones) collision parameters which determine how easy it is for a gas to condense have shown that the higher the value, the easier it is for the gas to penetrate the polymer.[59] The permeabilities for several polymers are shown in Table 9.8.[60] The barrier property of EVOH is seen to be the highest of all the listed polymers. Brown[61] has shown that oxygen permeabilities of EVOH with 29 mol% ethylene and EVOH with 38

TABLE 9.8

Gas Permeability of Various Polymers

| Polymer | Gas Permeability, 23°C, nmol/m·sec·GPA | | |
	O_2	N_2	CO_2
High-barrier vinylidene chloride copolymers	0.04–0.3	0.01–0.1	0.1–0.5
Nitrile barrier resin	1.6		6
Nylon 6,6; nylon 6	2–5		3–9
Polypropylene	300	60	1200
Poly(ethylene terephthalate)	10–18	2–4	30–50
Rigid poly(vinyl chloride)	10–40		40–100
High-density polyethylene	300		1200
Low-density polyethylene	500–700	200–400	2000–4000
Polystyrene	600–800	40–50	2000–3000
Ethylene vinyl alcohol			
32 mol% ethylene			
0% RH	0.02	0.002	0.09
100% RH	2.3		
44 mol% ethylene			
0% RH	0.18	0.015	0.8
100% RH	1.3		

Source: Demorest, R.L., New Developments in Testing the Permeability, Solubility and Diffusivity of Polymers, paper presented at Proceedings of Future-Pak '96, Chicago, IL, November 20, 1996. With permission.

mol% ethylene are 100 times less than those of polyamide, about 1000 times less than those of polyethylene, and approximately 10,000 times less than those of polypropylene.

With EVOH, the oxygen transmission rate (OTR) depends on the ethylene content. Thus, with increasing ethylene content, the OTR increases. The OTR of various grades of Soarnol EVOH as a function of ethylene content is shown in . Salame[57] has shown that materials with an O_2 permeation rate of much more than about 10 (cc·ml/100 in² day.atm) measured in pure O_2 at 73°F, 50% relative humidity (RH) have not been generally successful in packaging many foods and beverages. In addition, materials with an O_2 above this level are usually not good flavor barriers. The success of EVOH as shown in our laboratory by Iwanami and Hirai[62] is due to high intermolecular and intramolecular cohesive energy, which limits diffusion of oxygen through EVOH. This is one of the main reasons why EVOH has dominated the packaging industry for various applications.

The transportation of gases through polymers depends on the morphology of the polymers, i.e., amorphous or semicrystalline. The amorphous polymer is permeable by gases. The semicrystalline polymers contain a two-phase structure: crystalline and amorphous. The crystalline is an impermeable region, and diffusion of the environments occurs in the amorphous region.[63–65] Recent studies by Paul and collaborators[66,67] and Guadagno et al.[68] showed that absorption may occur in the crystalline region of some polymers. There are various factors influencing gas trans-
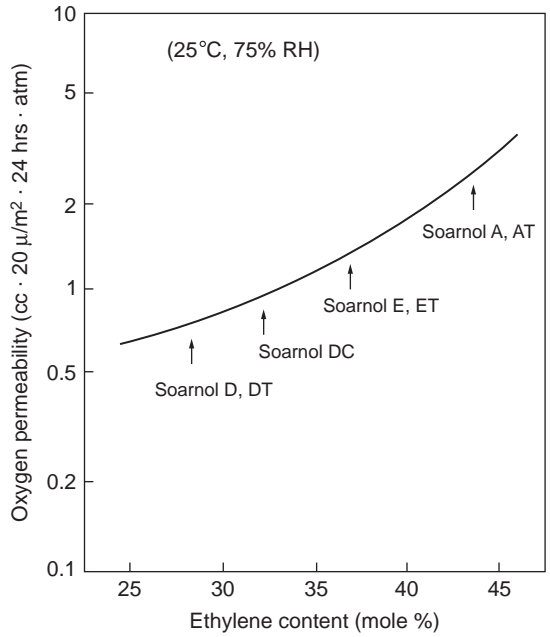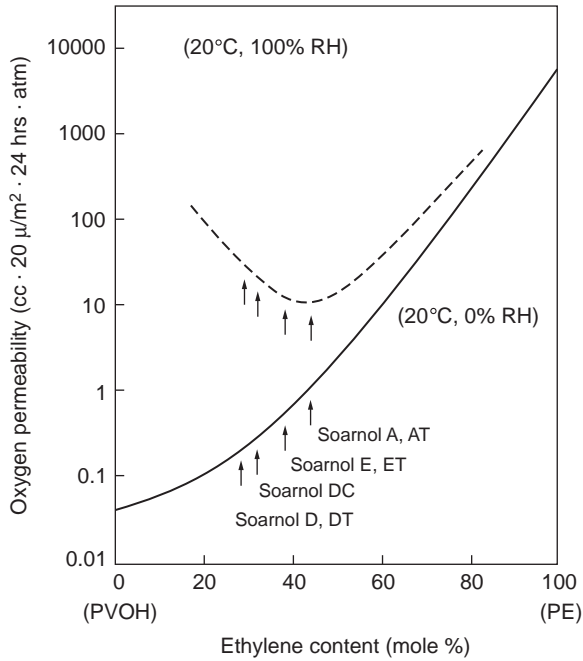
FIGURE 9.7
Oxygen transmission rate as a function of ethylene content of various grades of Soarnol. (From Nippon Gohsei Soarnol Data Sheet, Okayma, Japan, 1998. With permission.)

port properties; these include tightness of molecular packing and forces restricting its movement; crystalline size, shape, and orientation; and regularity of chain branching.[69,70] The effect of polymer structure was shown by Salame[71] several years ago. In his studies, he correlated the permeability coefficient of gases with several polymers using the parameter "permachor," π, for the structural unit, and the permeability coefficients are expressed as follows:

$$P_{N2} = 1.52 \times 10^{-9} \exp(-0.115\pi)$$

$$P_{O2} = 6.1 \times 10^{-9} \exp(-0.115\pi)$$

$$P_{CO2} = 2.2 \times 10^{-8} \exp(-0.115\pi)$$

The permachor values for some selected polymers are:

Polypropylene	15
Silicone elastomer	−23
Polycarbonate	31
PET	70
Nylon 6	80
PVDC	97
PAN	109
PVOH	157

The higher the permachor, the better the barrier properties. Okaya and Ikari[72] in their extensive studies on EVOH asserted that the permachor method may not be applicable to most polymers, e.g., EVOH. Recently, the effect of polymer structure on gas permeability was further advanced.[67,73–77] Mogri and Paul[76] on poly(alkyl acrylate)s showed that penetrant permeability in the amorphous state increases as the side-chain length becomes longer, and shows a mixed trend in the crystalline state. Thus the mixed trend in the crystalline state is an indication that permeability that actually occurs in the crystalline region is very low. Various investigators have reported different effects, including:

1. Decreased permeability of poly(silyi propyne)s with increasing side-chain length[78]
2. Increased permeability with increasing side-chain length[79]
3. No change in gas permeability for the poly(1-(n-alkylthio)-1-propyne) series up to 10 methylene units in the alkyl side chain

Figure 9.8 shows the results of work conducted by Mogri and Paul[76] on the gas permeability of poly(alkyl acetate)s as a function of the length of
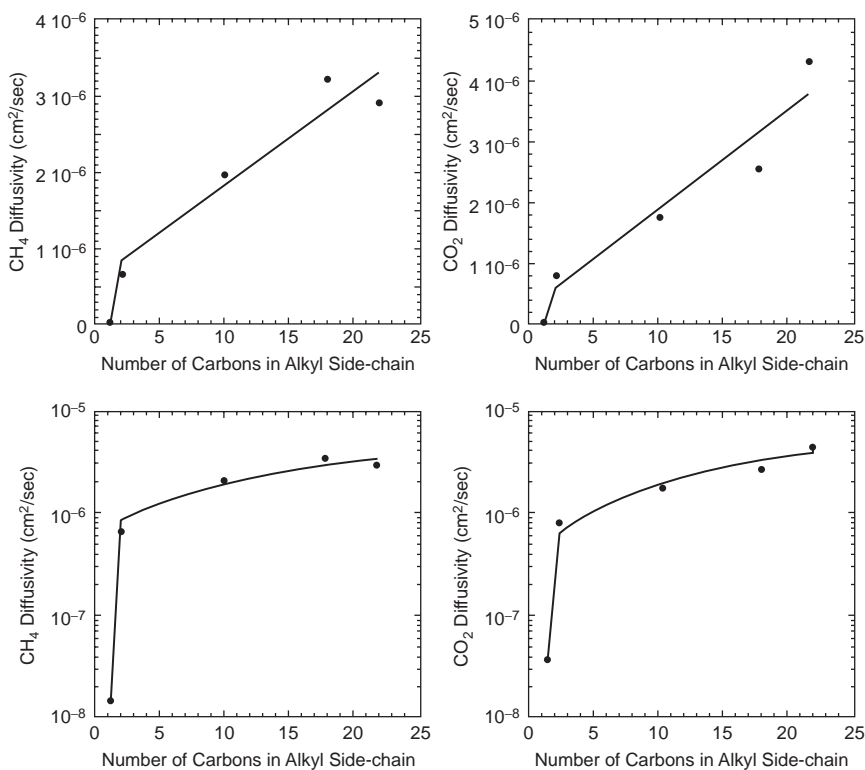
FIGURE 9.8
CH_4 and CO_2 diffusion coefficients (cm^2/sec) (on arithmetic and logarithmic scales) of amorphous poly(alkyl acrylate) as a function of side-chain length. (From Mogri, Z. and Paul, D.R., *Polymer*, 42, 7781, 2001. With permission.)

chain. As can be seen in the figure, the permeability of each gas increases as the side chain is lengthened. The authors attributed the increase to the increase in free volume as additional methylenes are added in the amorphous state. Recently, Ito et al.[80] used positronium lifetime measurement on EVOH to establish an increase of the free volume EVOH. They ascribed the increase of free volume to a reduced interaction between the hydroxy monomers due to the hydrogen bonding. Huige,[81] on a beer package, identified five contributing factors to total package oxygen:

1. Oxygen dissolved in the incoming beer
2. Oxygen pickup during filling
3. Oxygen permeation through closure
4. Oxygen desorbed from the plastic bottle wall
5. Oxygen permeation through the plastic bottle wall

Also, the amount of oxygen that enters a three-layered beer bottle by desorption from the bottle wall, and permeation through the bottle wall may simply be estimated as follows:[81]

For inside layer:

$$F = (P_{1,2}/d_{1,2}) * (X_2 - X_1) \qquad (9.8)$$

For middle layer:

$$F = (P_{2,3}/d_{2,3}) * (X_2 - X_1) \qquad (9.9)$$

For outside layer:

$$F = (P_{3,4}/d_{3,4}) * (X_4 - X_3) \qquad (9.10)$$

where F is the flux in cc/(100 in.^{2} · day), P is the permeability in cc · ml (100 in.^{2} · day · atm), d is the thickness of layer in milliliters, and X is the concentration of permeating gas or vapor in partial pressure (atm), RH, etc.

Rearranging Equations (9.8) to (9.10) will give

$$X_4 - X_1 = F(d_{1,2}/P_{1,2} + d_{2,3}/P_{2,3} + d_{3,4}/P_{3,4}) \qquad (9.11)$$

For all layers,

$$F = (P_{1,4}/d_{1,4}) * (X_4 - X_1) \qquad (9.12)$$

Thus, the overall permeability can be calculated as follows:

$$P_{1,4} = d_{1,4}(d_{1,2}/P_{1,2} + d_{2,3}/P_{2,3} + d_{3,4}/P_{3,4}) \qquad (9.13)$$

Some materials such as EVOH are strongly affected by the relative humidity. Therefore, the RH value of the layer must be considered.

9.3.1 Effect of Humidity and Crystallinity on Gas Permeability

Gas permeability of various polymers is affected by humidity and crystallinity of the polymer. The oxygen permeability in various grades of Soarnol[82] is shown in Figure 9.9. The oxygen transmission rate remains unchanged below 50% RH. However, above this value, a rapid increase occurs. Recently, Khanna[83] reported an initial reduction on casted nylon 6 film with increasing RH up to around 35% (Figure 9.10) before a rapid increase. A similar trend was noted on nylon 6 film by Gavara and Hernandez[84] and Krizan et al.[85] on amorphous polyamide. This reduction was attributed to absorbed water, which reduces free volume, hence increasing the density. The density of Selar
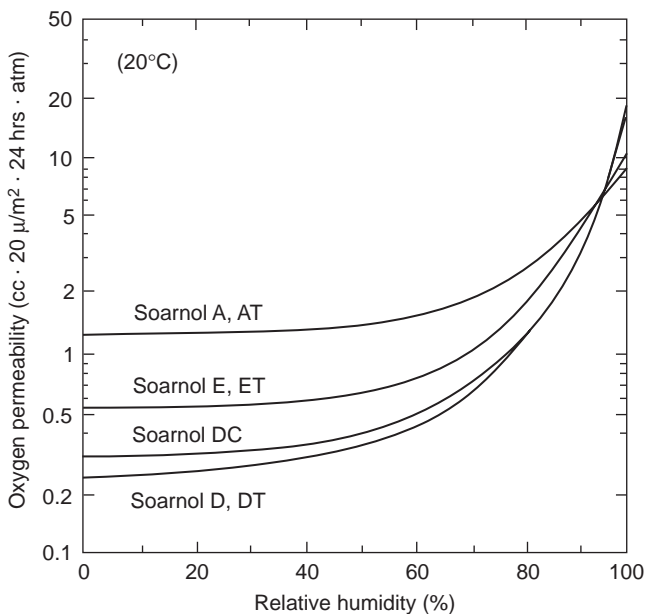
FIGURE 9.9
Oxygen permeability vs. relative humidity of quenched Soarnol cast film. (From Nippon Gohsei Soarnol Data Sheet, Okayama, Japan, 1998. With permission.)

PA, developed by Du Pont,[85] on immersion in water increased from 1.178 to 1.189. Thus the consequence of occupation of excess free volume by water is reduction of oxygen transmission. Pye et al.[86] and Chern et al.[87] also noted reduction of CH_4 and CO_2 in polyimide films with increasing RH. The oxygen permeability rate of some polymers is not affected by humidity, e.g., PVDC and PET (Figure 9.11).[88] Recently, Chou and Lee[89] on EVOH blended with amorphous nylon showed that 30% nylon content in the blend had no effect on the oxygen barrier of EVOH at low relative humidities. At high humidities, the blends demonstrated an improved oxygen barrier over the unblended EVOH.

Barrier properties of polymeric materials are affected by the degree of crystallinity. In crystalline polymers, the well-aligned molecular chains educe permeation of gases. Thus, an increase in crystallinity enhances gas barrier. It is seen in Figure 9.12, where the OTR of two Soarnol EVOH grades reduces with increasing crystallinity, irrespective of the grade type. The effect of crystallinity on OTR vs. %RH of cast nylon 6 where the crystallinity is varied between 18 and 43% is shown in Figure 9.13.[2] The figure suggests that at 65% RH, the OTR of cast nylon 6 films will decrease by 0.04 cc·ml/ 100 in.$_2$/day at 23°C for every 1% increase in crystallinity. Khanna[83] also discussed that based on the processing history, change of crystallinity from about 10 to 35% can improve the OTR of the cast nylon 6 film.
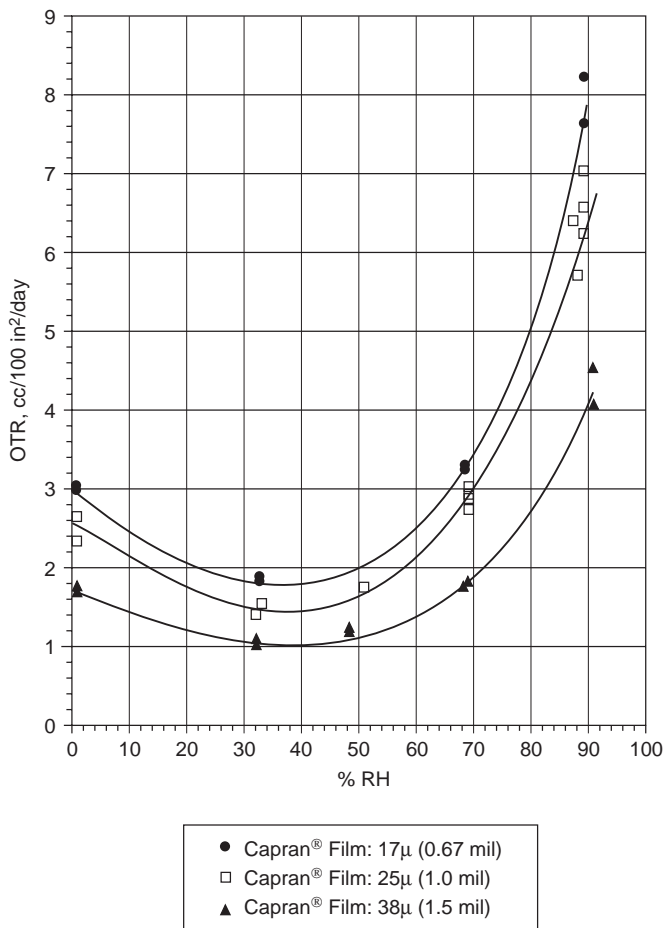
FIGURE 9.10
Effect of RH on OTR of cast nylon 6 film ($OTR_{0\%RH}/OTR_{35\%RH} = 1.7$). (From Khanna, Y.P., New Understanding of the Oxygen Barrier of Nylon 6 in Packaging Applications, Proceedings of the 13th International Conference on Packaging Innovations, Future-Pak '96, Chicago, IL, November 1996. With permission.)

9.3.2 Measurement of Oxygen Transmission Rate

The oxygen transmission rate can be measured based on ISO/DIS 14663-1.[90] This method was developed for the evaluation of the oxygen gas transmission rate in EVOH. However, the method is suitable for other polymers. The method involves measuring the volume of oxygen gas that passes through a unit area of the parallel surfaces of a film per unit time under the conditions of test. The rate is usually expressed in cubic centimeters (at 0°C under standard atmospheric pressure) per square meter per 24 h under a pressure difference of 1 atm ($cm^3/m^2/24$ h/atm).
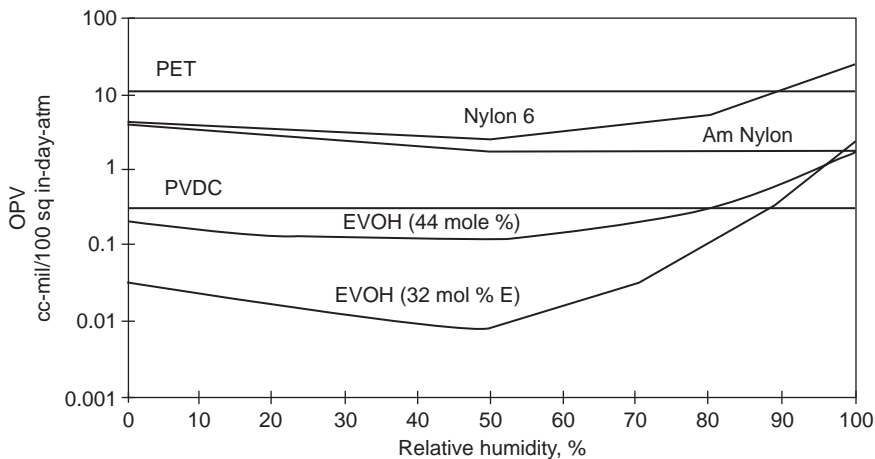
FIGURE 9.11
Oxygen permeability rate as a function of relative humidity of various polymers. (From Perdikoulias, J. and Hoegy, L., Blown Film Coextrusion, paper presented at Future-Pak '95, Chicago, IL, September 1995. With permission.)
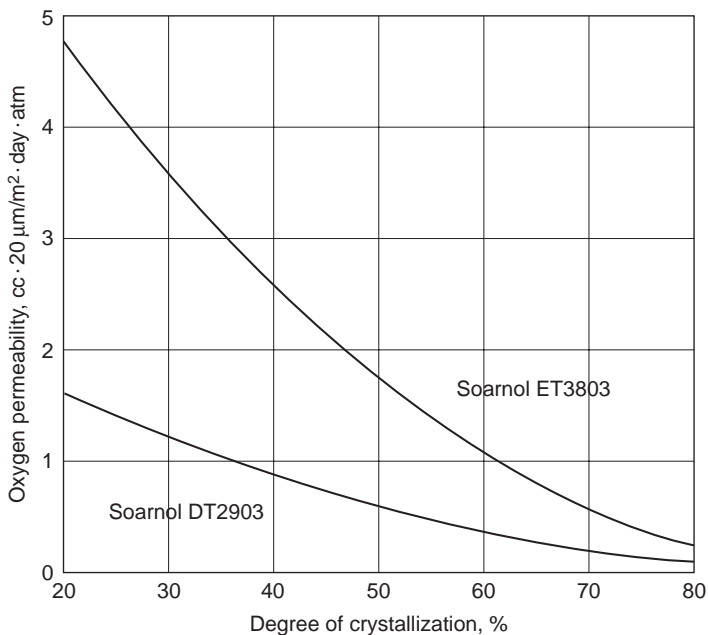

FIGURE 9.12
Relationship between oxygen permeability and degree of crystallinity of Soarnol EVOH grades. (From Nippon Gohsei Soarnol Data Sheet, Osaka, Japan, 1998. With permission.)
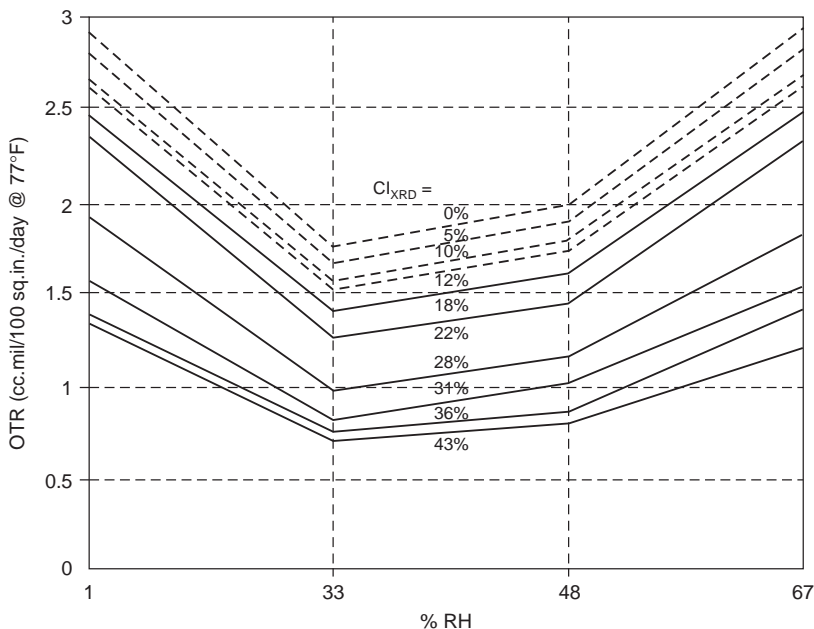
FIGURE 9.13
OTR vs. RH of nylon 6 with varying crystallinity. (From Khanna, Y.P., New Understanding of the Oxygen Barrier of Nylon 6 in Packaging Applications, presented at Proceedings of the 13th International Conference on Packaging Innovations, Future-Pak '96, Chicago, IL, November, 1996. With permission.)

Schematic representation of OTR equipment is shown in Figure 9.14. The sample is mounted in a diffusion cell composed of two chambers. One chamber is slowly purged at a definite rate of nitrogen stream (carrier gas); the other chamber, by oxygen. Oxygen permeated through the film into the nitrogen carrier gas is determined by the coulometric sensor, where the magnitude of an electrical current is proportional to the amount of oxygen flowing into the sensor per unit time. Care should be taken during measurement because the presence of certain interfering substances in the carrier gas stream may give rise to unwanted electrical output and error factors. Interfering substances may be chlorine and some strong oxidizing agents. The transmission rate is determined as follows:

$$OTR = (E_c - E_o)C/A \tag{9.14}$$

where E_c is the steady-state voltage level, E_o is the zero voltage level, C is the calibration constant, and A is the specimen area.
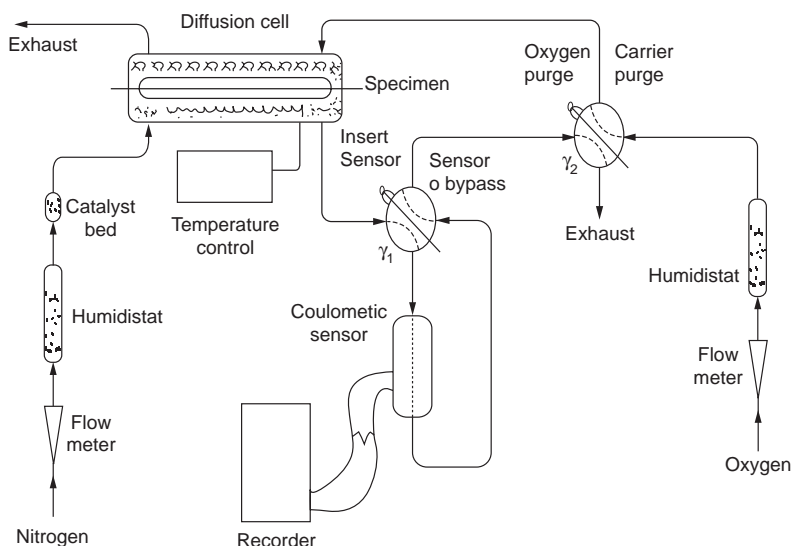
FIGURE 9.14
Schematic representation of OTR equipment. (From Chou, R. and Lee, I.-H., *J. Plast. Films Sheeting*, 13, 94, 1997. With permission.)

9.4 Polymer Modification

With increasing demand in barrier polymers for various applications, particularly in the packaging industry, various research activities have been carried out for further improvement. These include polymer modification via blending, orientation, coextrusion, solution coating, etc. Due to the limitation of this chapter, only improvement of barrier properties by orientation and blending will be highlighted.

9.4.1 Orientation

In a simple way, molecular orientation is the alignment of the crystal structure in polymeric materials. The molecules are stretched in such a manner that they are lined up in a predetermined direction. It is a means of improving the strength and durability of polymers in particular directions in order to broaden the scope of applications. Among the properties of polymers that can be significantly improved are gas barrier, tensile and impact strengths, stiffness, clarity, and resistance to crazing.[39] During orientation, three forces must be overcome:[91]

1. The strong covalent forces within the molecular chain itself, hooking carbon to carbon on the backbone and to any side chains that are present

2. The frictional constraining force caused by the intertwining of the molecules

3. The attraction existing between the molecules

Orientation may be either uniaxial or biaxial. In uniaxial orientation, the polymer is stretched in one direction, thereby causing the alignment of the chain molecules parallel to the direction of stretching. In most cases, uniaxial orientation upsets the balance of properties, i.e., sacrificing the dimensional stability on the one hand, and on the other gaining tear strength in the transverse direction and superior tensile strength in the machine direction. Consequently, the barrier properties of the oriented film are improved. Biaxial orientation is accomplished by stretching the sheet in both directions at right angles to each other. The chain segments tend to line up parallel to the plane of the sheet, but randomly within that plane. The higher the orientation, the more nearly parallel are the molecules and the smaller is the angle formed by them with the chain axis. The mechanism of reduced gas permeation through a polymeric material was explained by Williams and Peterlin.[92] They clarified that reduction of gas permeability was due to gradual transformation of the spherulitic structure to a densely packed microfibrillar structure.

Orientation of polymeric materials, especially biaxial-oriented polypropylene (BOPP) for the packaging industry, has been well documented in the literature. A recent investigation by Shonaike[39] on the diffusion of nitrogen into preoriented PA6 has shown that in the unoriented state, the presence of crystallites restricts permeation of the gas. However, after preorientation, achieved by cold-rolling, the restriction is further enhanced up to a certain level, after which the PA6 becomes porous to the nitrogen due to the breakup of crystallites. This was supported by the reduction of density and crystallinity of the PA6. However, it corroborated the earliest investigation by Geil[93] and later by Bahadur and Henkin,[94] who explained that deformation in the lamellar region would result in the slipping and unfolding of chains within the lamellar. This breakup of the lamellar and the disorder that occurs in the crystallographic arrangement of those blocks would give rise to loose packing, thereby reducing the density.

Due to space limitations in this chapter, the discussion here will be brief and the reader is referred to standard textbooks.

Biaxial orientation, which is a common process to improve gas barrier properties, may be simultaneous or sequential. In the sequential process, which is more common than the simultaneous process, the film is first stretched in the machine direction, and then in the transverse direction. This is schematically represented in Figure 9.15. As for the simultaneous process, the film is stretched in both directions at the same time.

9.4.2 Polymer Blend

Barrier properties of polymeric materials may be improved by blending two or more components together. This system of creating new material
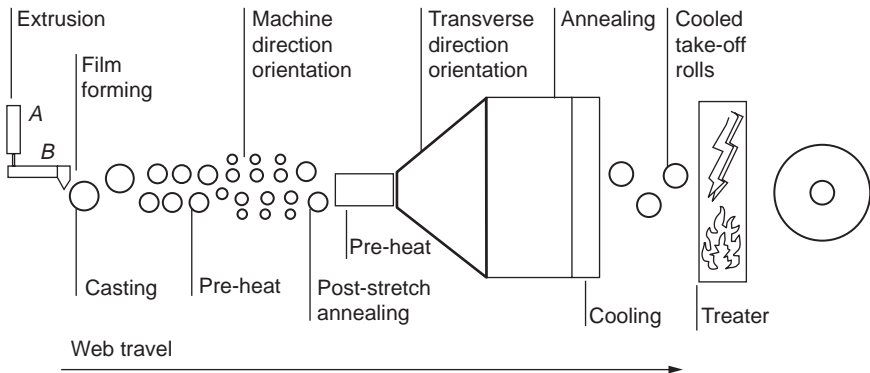
FIGURE 9.15
Schematic representation of biaxial orientation process.

with improved properties has been in existence for the past decades. Properties other than barrier that can be improved by blending include stiffness, thermal stability, processability, chemical resistance, and heat distortion temperature.[95–98] One of the major setbacks in blending is miscibility of the two components because most polymers are immiscible. Miscibility is the tendency or capacity of the components to form a uniform blend[99]; i.e., the blend is homogeneous down to the molecular level. With the present state of art, immiscible blend can now be made partially miscible with the addition of a compatibilizer. The effect of compatibilization is to provide morphological stability, homogeneity, and specific interactions at the interface of the two components.[100–105] Blending improves barrier properties when the free volume of the main component is reduced. This reduction of free volume is accompanied by improved density of the new component.

Various factors that contribute to the miscibility or immiscibility of polymer blends include:[104,106–111]

Polarity — Miscibility is likely to occur when two polymers of similar structures are blended.

Specific group interaction — Miscibility is likely to be achieved when polymers are drawn together by hydrogen bonding; acid–base, charge transfer, ion–dipole, or donor–acceptor adducts; or transition metal complexes.

Molecular weight — Lower molecular weight permits greater randomization on mixing, and therefore greater gain of entropy, which favors miscibility. Polymers of similar molecular weights are more miscible, while polymers of very different molecular weights may be immiscible, even when they both have the same composition.[112]

Ratio — A small amount of one polymer may be soluble in a large amount of the other polymer.

Crystallinity — In a polymer blend, both polymers will crystallize and form two separate phases; it is quite rare for the two polymers to co-crystallize in a single crystalline phase.

The barrier properties of several blends have been reported in the literature.[113–116] The oxygen permeabilities of PET/EVOH blends as well as PEN/EVOH blends recently reported by Kit and collaborators[116] are shown in Figure 9.16. In both cases, the barrier properties improved with increasing EVOH content. Although, by blending, one component takes advantage of the other, recent studies on EVOH/nylon blends[111] show that excellent barrier properties of EVOH are maintained in the blended material. When
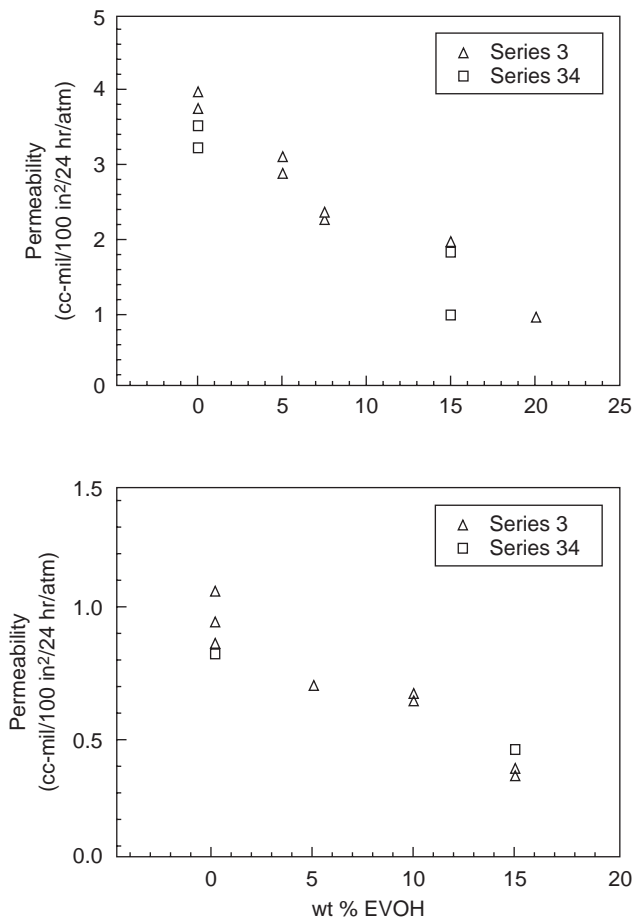

FIGURE 9.16
Oxygen permeability of (a) PET/EVOH blends; (b) PEN/EVOH blends (series 3: barrel temperature = 258°C, die temperature = 274°C; series 34: barrel temperature = 282°C, die temperature = 294°C). (From Kit, K.M. and Schultz, J.M., *Polym. Eng. Sci.*, 35, 680, 1995. With permission.)

EVOH is coextruded with another polymeric material, its excellent barrier properties always remain unaffected.

Polymeric materials, with their excellent gas barrier properties, transparency, low cost, flexibility, etc., will continue to attract various packaging applications. Ultra-high-barrier polymers are suitable for packaging pharmaceutical products, soup, pet foods, and milk. High-barrier polymers, on the other hand, are suitable for packaging mashed potatoes, dry fruits, coffee, etc. Finally, the barrier polymers are good for packaging snacks, biscuits, chips, and confectioneries.

Acknowledgments

References

1. Zhang, Z., Lim, L.T., and Tung, M.A., *J. Appl. Polym. Sci.*, 79, 1949, 2001.
2. Blackwell, A.L., Ethylene vinyl alcohol resin as a barrier material in multi-layer packages, in *Plastic Film Technology*, Vol. 1, Finlayson, K.M., Ed., Technomic Publishers, Lancaster, PA, 1989, chap. 5.
3. Shimoda, M., Nitanda, T., Kadota, N., Ohta, H., Suetsuma, K., and Osajima, Y., *Jpn. Soc. Food Sci. Technol.*, 31, 1984.
4. Sadler, G.I. and Bradock, R.J., Absorption of citrus flavor volatiles by low density polyethylene, *J. Food Sci.*, 56, 35, 1991.
5. Fukamichi, M., Matsui, T., Shimoda, M., Nakashima, M., and Osajima, Y., *J. Agric. Food Chem.*, 41, 929, 1993.
6. Flieger, D., New Packaging Development from DuPont, paper presented at 13th Annual World Congress on Specialty Plastic Films, Zurich, Switzerland, 1997.
7. Pasqui, S., Technology for Cost Reduction of a High Performing Clear Barrier Coating, paper presented at 13th Annual World Congress on Specialty Plastic Films, Zurich, Switzerland, 1997.
8. Ang, P.G., The Scale-Up of QLF Barrier Coating Process, paper presented at Proceedings of the 12th International Schroeder Conference on Packaging Innovation.
9. Gee, G.L., Value Chain Dynamics in the High-Performance Barrier Films Industry, paper presented at Proceedings at Future-Pak '99, Houston, TX, November 1999.
10. *Vinylidene Chloride Monomer Safe Handling Guide*, No. 100-6339-88-SAI, Dow Chemical Co., Midland, MI, 1988.
11. Shelton, L.G., Hamilton, D.E., and Fisackerly, R.H., in *Vinly and Diene Monomers, High Polymers*, Vol. 24, Leonard, E.C., Ed., Wiley Interscience, New York, 1971, p. 1205.

12. Wessling, R.A., *J. Appl. Polym. Sci.*, 14, 1531, 1970.
13. Wessling, R.A., Gibbs, D.S., and Delassus, P.T., Vinylidene chloride polymers, *Encyclopedia Polym. Sci. Eng.*, 17, 531, 1989.
14. Roberts, D.R. and Beavers, R.H., *J. Polym. Sci. Polym. Lett. Ed.*, 17, 155, 1979.
15. Morse, P.L., Acrylonitrile, Report No. 17, Process Economics Program, SRI International, Menlo Park, CA, November 1966, p. 26.
16. Peng, F.M., Acrylonitrile polymers, *Encyclopedia Polym. Sci. Eng.*, 1, 470, 1985.
17. Billmeyer, F.W., Jr., *Textbook of Polymer Science*, Wiley Interscience, Toronto, Canada, 1984, chap. 14, p. 390.
18. Fester, W., Physical constants of poly(acrylonitrile), in *Polymer Handbook*, Brandrup, J. and Immergut, E.H., Eds., John Wiley & Sons, New York, 1975, pp. V-37–V-40.
19. Davies, C.W. and Shapiro, P., *Encyclopedia Polym. Sci. Technol.*, 1, 342, 1964.
20. Beevers, R.B., The physical properties of polyacrylonitrile and its copolymers, *Macromol. Rev.*, 3, 113, 1968.
21. Krigbaun, W.R. and Tokita, N., *J. Polym. Sci.*, 43, 467, 1960.
22. Dunn, P. and Ennis, B.C., *J. Appl. Polym. Sci.*, 14, 1795, 1979.
23. Whinfield, J.R. and Dickson, J.T., Fibers from Glycol, Terephthalate Polymers, British Patent 578,079, 1946.
24. Billmeyer, Jr., *Textbook of Polymer Science*, Wiley Interscience, New York, 1962, p. 237.
25. Fried, J.R., *Polymer Science and Technology*, Prentice Hall, Englewood Cliffs, NJ, 1995, p. 300.
26. Buxbaun, L.H., *J. Appl. Polym. Sci.*, 35, 59, 1979.
27. Drescher, M., *Makromol. Chem.*, 181, 789, 1980.
28. Farrone, G., McIntosh, J., and Ward, I.M., *Makromol. Chem.*, 38, 147, 1960.
29. Jadhav, J.Y. and Kantor, S.W., Polyester thermoplastics, *Encycopedia Polym. Sci. Eng.*, 12, 217, 1988.
30. Hall, I.H., *Structure of Crystalline Polymers*, Elsevier Applied Science Publishers, Barking, U.K., 1984, p. 39.
31. Galanty, P.G. and Richardson, J.J., Polyethylene terephthalate, *Eng. Plast.*, 2, 172, 1995.
32. Gozenick, N.J., in *Modern Plastics Encyclopedia*, McGraw-Hill, New York, 1968–1987, p. 464.
33. *Plastic Technology Manufacturing Handbook and Buyer's Guide*, Vol. 31, No. 7, Bill Communications, New York, 1995, p. 518.
34. Bonis, L.J., paper presented at Future-Pak 96, 13th International Schroeder Conference on Packaging, Chicago, IL, November 20–21, 1996.
35. Kohan, M.I., Polyamides, *Eng. Plast.*, 2, 125, 1995.
36. Levy, J.H., Polyamide 6 Resins for Coextruded Films, paper presented at 13th Annual World Congress in Specialty Plastic Films 97, Zurich, Switzerland, 1997.
37. Perkins, H.J., and Porter, R.S., *J. Mater. Sci.*, 12, 2355, 1977.
38. Schlack, P., U.S. Patent 2,241,321, May 6, 1941.
39. Shonaike, G.O., Ph.D. thesis, University of London, 1986.
40. Wunderlich, B., Equilibrium melting of flexible linear macromolecules, *Polym. Eng. Sci.*, 19, 431, 1978.
41. Nippon Gohsei, Soarnol Data Sheet, Okayama, Japan, 1998.
42. Moriyama, T., private communication.
43. Alger, M.S.M., *Polymer Science Dictionary*, Elsevier Publishers, Essex, England, 1980, p. 157.

44. Takahashi, M., Tashiro, K., and Amiya, S., *Macromolecules*, 39, 5860, 1999.
45. Cerrada, M.L., Perez, E., Perena, J.M., and Benavente, R., *Macromolecules*, 31, 2559, 1999.
46. Hay, J.M. and Lyon, D., *Nature*, 216, 790, 1967.
47. Kapon, B., Watson, D.S., and Zucco, C., *J. Am. Chem. Soc.*, 103, 1761, 1987.
48. Marten, F.L. and Zeanut, C.W., Hydrolysis of polyvinyl acetate to polyvinyl alcohol, in *Polyvinyl Alcohols Developments*, Finch, C.A., Ed., John Wiley Publishers, Chichester, U.K., 1992, p. 57.
49. Marten, F.L., Vinyl alcohols, *Encyclopedia Polym. Sci. Eng.*, 17, 167, 1989.
50. Cifveri, A., Krigbaum, W.R., and Meyer, R.B., *Polymer Liquid Crystals*, Academic Press, New York, 1982.
51. Donald, A.M. and Windle, A.H., *Liquid Crystalline Polymers*, Cambridge Press, London, 1982.
52. Brown, G.H. and Crooker, P.C., *Chem. Eng. News*, 61, 25, 1983.
53. McChesney, C.E., *Eng. Plast.*, 2, 179, 1995.
54. Shonaike, G.O., Hamada, H., Yamaguchi, S., Nakamichi, M., and Maekawa, Z., *J. Appl. Polym. Sci.*, 54, 881, 1994.
55. Fick, A., *Ann. Phys. Chem.*, 94, 56, 1855.
56. Progelhof, R.C. and Throne, J.L., *Polymer Engineering Principles*, Hanser Publishers, Munich, 1993, chap. 4.
57. Salame, M., The Latest Developments in High Barrier Plastic Packaging for Foods & Beverages, paper presented at Future-Pak '93, 10th Annual Ryder Conference on Food Packaging Innovations, Atlanta, GA, October 4–6, 1993.
58. Demorest, R.L., New Developments in Testing the Permeability, Solubility, and Diffusivity of Polymers, paper presented at Proceedings of Future-Pak '96, Chicago, IL, November 20, 1996.
59. Fried, J.R., *Polymer Science and Technology*, Prentice Hall, Englewood Cliffs, NJ, 1995, chap. 12.
60. Steingiser, S., Memphos, S.P., and Salame, M., in *Kirk/Othmer Encyclopedia of Chemical Technology*, 3rd ed., Vol. 3, Grayson, M., Ed., 1980, p. 480.
61. Brown, W.E., *Plastics in Food Packaging*, Marcel Dekker, New York, 1992, p. 62.
62. Iwanami, T. and Hirai, Y., *TAPPI J.*, 66, 85, 1983.
63. Michael, A.S. and Parker, R.B., *J. Polym. Sci.*, 41, 53, 1959.
64. Michael, A.S. and Bixler, H.J., *J. Polym. Sci.*, 50, 393, 1961.
65. Michael, A.S. and Bixler, H.J., *J. Polym. Sci.*, 50, 413, 1961.
66. Puleo, A.C., Paul, D.R., and Wong, P.K., *Polymer*, 30, 1357, 1988.
67. Chiou, J.S., Barlow, J.W., and Paul, D.R., *J. Appl. Polym. Sci.*, 30, 1173, 1985.
68. Guadagno, L., Baldi, P., Vittoria, V., and Guerra, G., *Macromol. Chem. Phys.*, 199, 1357, 1999.
69. Mogri, Z. and Paul, D.R., *Polymer*, 42, 7765, 2001.
70. Murray, L.J., *An Organic Vapor Permeation Rate Determination for Flexible Packaging Materials in Plastic Films Technology*, Vol. 1, Finlayson, K.M., Ed., Technomic Publishers, Lancaster, PA, 1989, pp. 21–31.
71. Salame, M., *ACS Polym. Prepr.*, 8, 1967, 137.
72. Okaya, T. and Ikari, K., Ethylene-vinyl alcohol copolymers, in *Polyvinyl Alcohol-Developments*, Finch, C.A., Ed., Wiley, Chichester, England, 1992, chap. 8.
73. Paul, D.R. and Yampol'skii, Y.P., Eds., *Polymeric Gas Separation Membranes*, CRC Press, Boca Raton, FL, 1994.
74. Koros, W.J., Ed., *Barrier Polymers and Structures*, American Chemical Society, Washington, D.C., 1990.

75. Sweeting, R.E. and Fritzsche, A.K., *Polymeric Gas Separation Membranes*, Wiley, New York, 1993.
76. Mogri, Z. and Paul, D.R., *Polymer*, 42, 7781, 2001.
77. Savoca, A.C., Surnamer, A.D., and Tien, T.P., *Macromolecules*, 26, 6211, 1993.
78. Morisato, A., He, Z., and Pinnau, L., *Polym. Prepr. ACS Polym. Mater. Sci. Eng.*, 81, 529, 1999.
79. Masuda, T., Matsumoto, T., Yoshimura, T., and Higashimura, T., *Macromolecules*, 23, 4902, 1990.
80. Ito, K., Saito, Y., Yamamoto, T., Ujihara, Y., and Nomura, K., *Macromolecules*, 34, 6153, 2001.
81. Huige, N.J., Requirements for Plastic Beer Packages, paper presented at Future-Pak '96, 13th Schroeder Conference on Packaging, Chicago, IL, November 20–21, 1996.
82. Nippon Gohsei's Soarnol Data Catalog, Osaka, Japan.
83. Khanna, Y.P., New Understanding of the Oxygen Barrier of Nylon 6 in Packaging Applications, paper presented at Proceedings of the 13th International Conference on Packaging Innovations, Future-Pak '96, Chicago, IL, November 1996.
84. Gavara, R. and Hernandez, R., *J. Polym. Sci. Phys.*, 32, 2375, 1994.
85. Krizan, T.D., Coburn, J.C., and Blatz, P.S., Structure of amorphous polyamides, in *Barrier Polymers and Structures*, Koros, W.J., Ed., chap. 5, pp. 111–125, 1984.
86. Pye, D.G., Hoehn, H.H., and Panar, M., *J. Appl. Polym. Sci.*, 20, 287, 1976.
87. Chern, R.T., Koros, W.J., Sanders, E., and Yui, R., *J. Membr. Sci.*, 15, 157, 1983.
88. Perdikoulias, J. and Hoegy, L., Blown Film Coextrusion, paper presented at Future-Pak '95, Chicago, IL, September 1995.
89. Chou, R. and Lee, I.-H., *J. Plast. Films Sheeting*, 13, 94, 1997.
90. International Organization for Standardization, ISO/DIS 14663-1, 1996.
91. Mauro, J.B., *Science and Technology of Polymer Fiber*, Vol. 1, Sweeting, O.J., Ed., Wiley Interscience, New York, 1968, p. 459.
92. Williams, J.L. and Peterlin, A., *J. Polym. Sci.*, A2, 1483, 1971.
93. Geil, P.H., *Am. Chem. Soc. Polym. Prepr.*, 15, 35, 1974.
94. Bahadur, S. and Henkin, A., *Polym. Eng. Sci.*, 18, 255, 1978.
95. Birley, A.W. and Chen, X.Y., *Br. Polym. J.*, 16, 77, 1984.
96. Robeson, L.M., *Polym. Eng. Sci.*, 24, 587, 1984.
97. Laverty, J.J., *Polym. Eng. Sci.*, 28, 260, 1988.
98. Nishi, T. and Kwei, T.K., *Polymer*, 10, 285, 1975.
99. Shonaike, G.O., Hayase, T., and Takenaka, Y., *Omron Technics*, 32, 195, 1992.
100. Heikens, D. and Barentsen, W., *Polymer*, 18, 69, 1979.
101. Gelles, R. and Fank, C.W., *Macromolecules*, 15, 741, 1982.
102. Garcia, J.D., *J. Polym. Sci. Polym. Phys. Ed.*, 22, 1773, 1984.
103. Utracki, L., *SPE Tech. Pap.*, 33, 1339, 1987.
104. Utracki, L., Introduction to polymer alloys and blends, *Polymer Alloys and Blends*, Hanser, New York, 1988, chap. 1.
105. Ougizawa, T., Kitano, T., Lee, Y., and Kim, J., Morphology and impact strength in high density polyethylene/nylon 6 blend, *Proceedings of the SAMPE Meeting*, Vol. 1, Kishi, I., Takeda, N., and Kagawa, Y., Eds., Tokyo, Japan, 1993, p. 751.
106. Paul, D.R., Interfacial agents for polymer blends, in *Polymer Blends*, Vol. 2, Paul, D.R. and Newman, S., Eds., Academic Press, New York, 1978, pp. 35–62.
107. Gaylaord, N.G., *Macromol. Sci. Chem.*, A26, 8, 1989.
108. Markam, R.L., *Adv. Polym. Tech.*, 10, 3, 1991.
109. Xanthios, M. and Dagli, S.S., *Polym. Eng. Sci.*, 31, 13, 1991.

110. Chen, C.C. and White, J.L., *Polym. Eng. Sci.*, 33, 14, 1993.
111. Deanin, R.D. and Manion, M.A., Compatibilization of polymer blends, in *Polymer Blends and Alloys*, Shonaike, G.O. and Simon, G.P., Eds., Marcel Dekker, New York, 1999, chap. 1.
112. Althal, U.S., Balundgiand, R.H., and Shukla, S.S., *Polym. Plast. Technol. Eng.*, 30, 299, 1991.
113. Hopfenberg, H.B. and Paul, D.R., in *Polymer Blends*, Vol. 1, Paul, D.R. and Newman, S., Eds., Academic Press, NY, 1978.
114. Shepherd, F.A., Gonzales, H., and Hess, S.L., U.S. Patent No. 4,835,214, June 1989.
115. Kamal, M.R., Jinnah, I.A., and Utracki, L.A., *Polym. Eng. Sci.*, 24, 1337, 1984.
116. Kit, K.M. and Schultz, J.M., *Polym. Eng. Sci.*, 35, 680, 1995.

10

Polymer–Clay Nanocomposites

Kathleen A. Carrado

CONTENTS

10.1 Introduction

Within the fascinating world of nanomaterials in general, polymer–clay nanocomposites more than carry their weight in terms of intrigue and applicability. Consider all the factors that must be involved in the dramatic modification and improvement of a polymer's behavior upon the addition of just a few weight percent (wt%) of a nano-size inorganic sheet compound. Tensile modulus and strength can be doubled and the heat distortion temperature dramatically increased (by 100°C), without any sacrifice in impact resistance, upon the addition of just 2% by volume of this compound to nylon, for

example. These inorganic, layered silicate species are clays, and the wealth of chemistry involved in the polymer–sheet silicate interaction shall comprise the contents of this chapter.

For the most part, it is so-called smectite clays that are exploited in polymer–clay nanocomposite (PCN) synthesis. Smectites are a class of layered clays that are swellable in water and contain a significant cation exchange capacity at about 80 meq/100 g (this means that there are 80 meq of exchangeable cation per 100 g of clay). The fundamental inorganic unit is comprised of two tetrahedral silicate layers that sandwich a central metal octahedral layer (see Figure 10.1). Idealized formulas for montmorillonite, the aluminum-based version, and hectorite, the magnesium-based version, are $Ex_{0.66}[Si_8Al_{3.34}Mg_{0.66}O_{20}(OH)_4] \cdot H_2O$ and $Ex_{0.66}[Si_8Mg_{5.34}Li_{0.66}O_{20}(OH,F)_4] \cdot H_2O$, respectively.[1] Notice the isomorphous substitution of these clays, primarily within the octahedral layer, which gives rise to a net negative charge on the basal oxygen surfaces. This is compensated for by the presence of hydrated exchangeable cations in the interlayer or gallery regions, which in nature are usually alkali or alkaline earth cations. These cations are easily exchanged by larger species such as long-chain alkylammonium ions, whose importance will become clear later. The distance from one basal surface to the next in registry is called the basal spacing and is measured as the lowest-angle peak in x-ray powder diffraction spectra. Natural clays have basal spacings in the range of 1.2 to 2.0 nm, depending on the type of cation and the amount of water present. This ability to swell is one of the most important characteristics of a smectite clay. They can, in fact, swell so greatly in some situations, such as in the presence of large concentrations of macromolecules, that the sheets can lose interaction with each other, the registry is lost, no basal spacing is observed, and the system is said to be exfoliated.

Other clays have been exploited in PCN research as well, including saponite, beidellite, and a synthetic swelling fluorine–mica. All are smectites, with differences primarily in elemental composition, cation exchange capacity, abundance, aspect ratio, and particle size. The interactions of smectite clays with polymeric molecules both in nature and for industrial applications have been exploited for quite some time,[2] although the development of polymeric nanocomposites has occurred fairly recently.

Since several excellent review articles have been published quite recently on the burgeoning field of polymer–clay nanocomposites,[3–21] a thorough review of this information would be redundant. Instead, this chapter hopes to provide a fairly comprehensive survey of the literature available to date (excluding for the most part the patent literature) as a reference guide, along with (1) an introduction and general overview; (2) the various methods of PCN synthesis (intercalation compounds, *in situ* polymerization, melt methods, the polymer–clay gel formation method) and most frequently used characterization tools; (3) PCN properties and applications such as toughness, tensile strength, rheology, flame retardancy, gas barriers, and separations; and (4) advances in the fundamental understanding of PCNs via molecular modeling techniques.
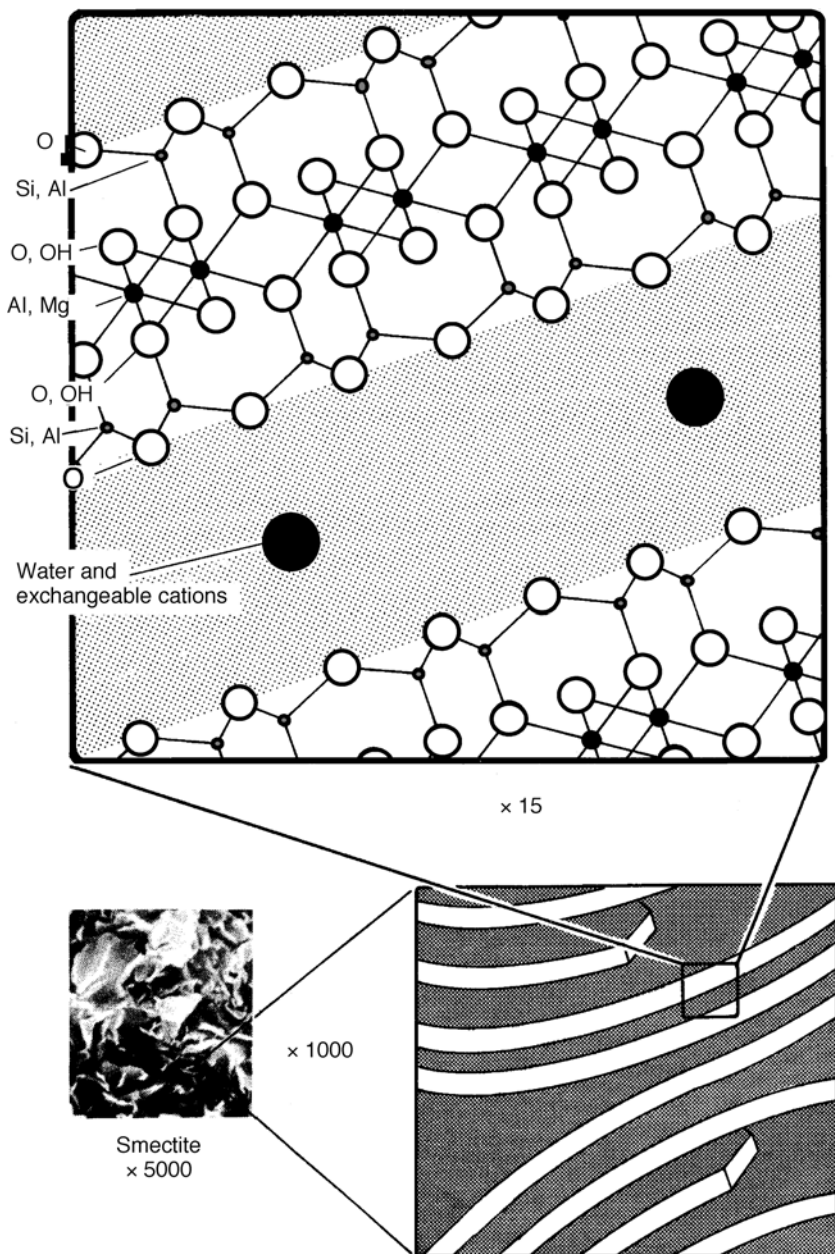
FIGURE 10.1
Schematic representation of a montmorillonite smectite clay structure, from an SEM of the flexible "cornflakes" plate morphology to stacked individual plates to atomic assignments. The height of a 2:1 clay layer is about 1 nm. The height of the gallery region is variable depending on the type of cation and the amount of water present, and is generally 1 nm or less for natural clays. (From *Clay Minerals and the Origin of Life*, Cairns-Smith, A.G. and Hartman, H., Eds., Cambridge, U.K.: Cambridge University Press, 1986. With permission.)

10.2 Polymer–Clay Nanocomposite Synthesis and Characterization

Table 10.1 is provided as a reference guide to many of the most commonly used polymers in PCNs, their acronyms and trade names, and their general repeating structures. Table 10.2 is provided as a fairly comprehensive literature survey (not including patents) to polymers, types of clay used, and whether synthesis or application is the primary focus of the reference. Scrutiny of this guide reveals the exponential rise in publication rate within the past few years, reflecting the explosively growing interest of late in this topic.

10.2.1 Introduction to PCN Architectures

There are two end members that delineate the realm of structures possible in polymer–clay nanocomposites. At one end of the spectrum are well-ordered, stacked multilayers that result from intercalated polymer chains within host silicate clay layers. At the other end of the spectrum are exfoliated materials, wherein the host clay layers have lost their entire registry and are well dispersed within a continuous polymer matrix. These two cases are shown schematically in Figures 10.2(a) and (b). Exfoliated (also called delaminated) polymer–clay nanocomposites display acceptable stiffness, strength, and barrier properties with far lower ceramic content than is achieved for more conventional particulate-filled (e.g., glass fibers) polymer composites. Generally, the larger the degree of exfoliation in polymer–clay nanocomposites, the greater the enhancement of these properties. Figure 10.2(c) provides an idealized view of a mixed intercalated–exfoliated structure. All three of these morphologies have been observed, and representative transmission electron microscopy (TEM) images of each are provided in Figure 10.2(d) to (f) as well.

10.2.2 Intercalation Compounds

Often, there are occasions where retention of the layered nature of a polymer–clay nanocomposite is the desired outcome. Such regular nanoassemblies have the following unique characteristics and applications:[302]

1. There are a wide variety of both host materials (clay and nonclay) and polymers.
2. Anisotropic arrangements of polymers in two-dimensional microenvironments occur.
3. The variable gallery spacing is adaptable to polymer size.
4. Microenvironments can induce spatial chemistry and host surface chemistry effects.
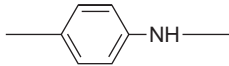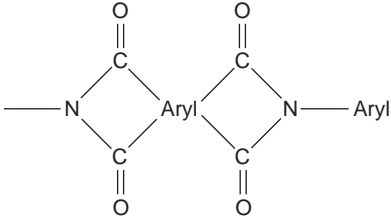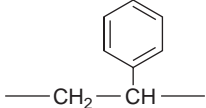
TABLE 10.1

Some Polymers Used in PCNs
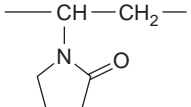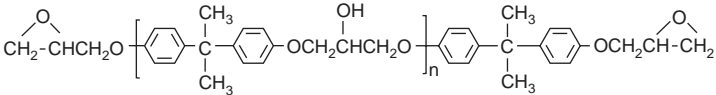
Name	General Repeating Structure
Polyacrylamides (PAAM)	$$\begin{array}{c} NH_2 \\ | \\ C=O \\ | \\ -CH_2-C- \\ | \\ CH_3 \end{array}$$
Polyacrylonitrile (PACN, Orlon, Creslan)	$$\begin{array}{c} C\equiv N \\ | \\ -CH_2-CH- \end{array}$$
Polyamides (nylon)	$$-\overset{O}{\overset{||}{C}}-R-\overset{O}{\overset{||}{C}}-\overset{H}{\overset{|}{N}}-R'-\overset{H}{\overset{|}{N}}-$$
Polyaniline (PAN)	$$-\langle\bigcirc\rangle-NH-$$
Polyimides (PI)	$$-N\langle\overset{\overset{O}{||}}{\underset{\underset{O}{||}}{C}}\rangle Aryl \langle\overset{\overset{O}{||}}{\underset{\underset{O}{||}}{C}}\rangle N-Aryl$$
Poly(methyl methacrylate) (PMMA, Lucite, Plexiglas)	$$\begin{array}{c} OCH_3 \\ | \\ C=O \\ | \\ -CH_2-C- \\ | \\ CH_3 \end{array}$$
Polystyrene (PS)	$$\begin{array}{c} \bigcirc \\ | \\ -CH_2-CH- \end{array}$$
Polyurethanes	$$-C(O)-O-R-O-C(O)-N(H)-R'-N(H)-$$
Poly(vinylpyrrolidone) (PVP)	$$-CH-CH_2-$$
Epoxy monomer (Epon-828)	$$CH_2-CHCH_2O-\left[\langle\bigcirc\rangle\overset{CH_3}{\underset{CH_3}{C}}\langle\bigcirc\rangle-OCH_2\overset{OH}{CHCH_2}O\right]_n\langle\bigcirc\rangle\overset{CH_3}{\underset{CH_3}{C}}\langle\bigcirc\rangle-OCH_2CH-CH_2$$

TABLE 10.2

Polymer–Clay Nanocomposite Literature Survey

Polymer	Clay	Synthesis References	Properties References
Polyacrylamide	Montmorillonite	22–26	
Polyacrylamide	Kaolinite	22, 27	
Polyacrylamide	Hectorite/laponite	28	
Polyacrylic acid	Montmorillonite	29–31	
Polyacrylic acid	Kaolinite	30, 32	
Polyacrylic acid	Vermiculite	33	
Polyacrylonitrile (PACN)	Montmorillonite	34	
Polyacrylonitrile	Hectorite	35	
Polyamide-6 (nylon)	Montmorillonite	36–49	50–70
Polyamide-6	Saponite	71	50
Polyamide-6	Swelling mica	72	
Polyamide-6	Kaolinite	73	
Polyamide-12	Montmorillonite	74	
Polyamide-12	Synthetic smectite	75	76
Polyaniline	Montmorillonite	77–85	86–90
Polyaniline	Hectorite	35, 91	
Poly(ε-caprolactone)	Montmorillonite	92	
Poly(ε-caprolactone)	Hectorite	93	93b
Polydimethylsiloxane (PDMS)	Montmorillonite	94	
Polydimethylsiloxane	Fluorohectorite	95	
Polydimethylsiloxane	Kaolinite	94b	
Polyetherimide	Montmorillonite	96	
Poly(ethylene)	Montmorillonite	97–101	102
Poly(ethylene)	Palygorskite	103	
Poly(ethylene oxide) (PEO)	Montmorillonite	104–112	102, 113–115
Poly(ethylene oxide)	Hectorite/laponite	105, 110, 111	114, 116
Poly(ethylene oxide)	Vermiculite	33, 117	
Poly(ethylene oxide)	Saponite Beidellite Nontronite	109, 118	
Polyethylene terephthalates (PETs)	Various	119–123	124
Polyimide	Montmorillonite	125–138	139–143
Polyimide	Synthetic mica	127, 135	
Polyimide	Hectorite	127	
Polyimide	Saponite	127	
Poly(methyl methacrylate)	Montmorillonite	144–157	157–164
Poly(methyl methacrylate)	Hectorite/laponite	151, 165	
Poly(phenylene vinylene)	Montmorillonite	166, 167	168
Polypropylene	Montmorillonite	169–185	54, 59, 171, 186–193
Polypropylene	Hectorite	175, 176	169, 175
Polypropylene	Swelling mica	171, 176, 194	
Polypropylene	Vermiculite	195	
Polystyrene	Montmorillonite	147, 152, 196–211	54, 161, 186, 212–218
Polystyrene	Hectorite	219	186
Polystyrene	Swelling mica	220	
Styrene copolymers and rubber	Montmorillonite	221–232	224, 227, 233–236

TABLE 10.2 *(Continued)*

Polymer–Clay Nanocomposite Literature Survey

Polymer	Clay	Synthesis References	Properties References
Styrene copolymers	Kaolinite	237	
Styrene/butylene copolymer	Vermiculite	238	
Ethylene/propylene rubber	Sepiolite	239	
Polyurethane	Montmorillonite	240–245	246
Polyurethane	Swelling mica	247	
Poly(vinyl alcohol) (PVA)	Montmorillonite	108, 248–250	251
Poly(vinyl alcohol)	Hectorite	252	
Poly(vinyl pyrrolidone)	Montmorillonite	31, 253–258	
Poly(vinyl pyrrolidone)	Kaolinite	259	
Poly(vinyl pyrrolidone)	Hectorite/laponite	35, 260	
Poly(vinyl pyrrolidone)	Swelling mica	261	
Epoxy	Montmorillonite	126, 262–273	62, 275–280
Epoxy	Hectorite/laponite	264, 266	276
Epoxy	Vermiculite	264, 266	
Block copolymers	Montmorillonite Hectorite Saponite	281–283	
Miscellaneous	Montmorillonite	284–301	

5. Rigid host layers provide enhancements to structural, chemical, and thermal stabilities to more fragile guest polymers.

Two primary methods are utilized to prepare intercalated polymer–clay materials. These are shown schematically in Figure 10.3 as direct intercalation and as *in situ* polymerization of preintercalated monomers. The former route is limited because the types of polymers that can be intercalated directly are limited. The latter route, while more universal, results in a loss of control over the molecular weight of the final polymer. The polymers reported to form well-ordered intercalated assemblies from clay suspensions of dissolved polymer in solution are poly(vinyl alcohol) (PVA),[248,252] poly(ethylene oxide) (PEO),[104,105,107,109–111,113,115,116] polypyrrole,[303] poly(vinyl pyrrolidone),[31,35,253–261] poly(acrylic acid),[29–33] polycaprolactone,[92] polyethylene terephthalate,[121,122,124] poly(phenylene vinylene),[166–168] and polystyrene (PS).[220,224,238] Polyaniline is intercalated via an "emulsion polymerization" method in solution.[85] In addition, an intercalated polyimide PCN was reported to form upon intercalating poly(amic acid) precursors from solution and subsequent thermal transformation by heating to decompose water.[126] Some of the above PCN systems are created in a unique way wherein the clay layers are crystallized from a silicate sol-gel in direct contact with a polymer solution, including poly(vinyl alcohol),[252] and poly(vinyl pyrrolidone), polyaniline, cellulose, and polydimethyldiallyl ammonium chloride.[35] In the majority of intercalated PCN cases, the linear macromolecules are in
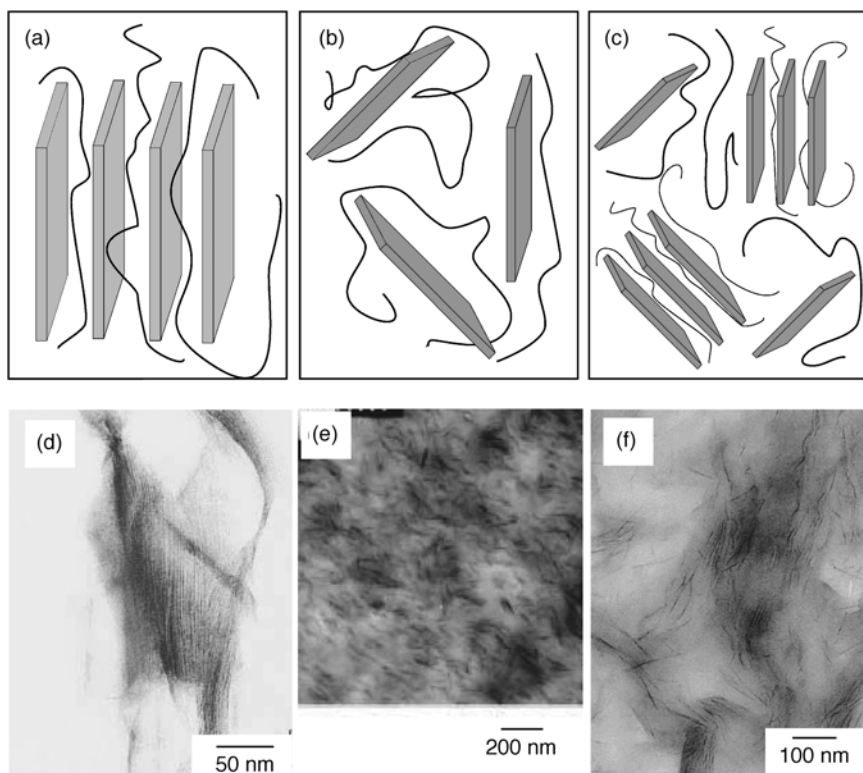
FIGURE 10.2
Schematic representation of the various PCN architectures: (a) intercalated, (b) exfoliated, and (c) mixed intercalated–exfoliated. TEM images of actual PCN hybrids assigned to these various structures: (d) intercalated polystyrene–fluorohectorite showing 2.9-nm registry, (Vaia et al., *Chem. Mater.*, 1996, 8, 2628. With permission), (e) exfoliated nylon–montmorillonite, (Cho and Paul, *Polymer*, 2001, 42, 1083. With permission), and (f) a mixed intercalated–exfoliated epoxy–montmorillonite (10% clay) (Brown et al., *Chem. Mater.*, 2000, 12, 3376. With permission).

nearly fully extended conformation. In a few cases, for example, poly(ethylene oxide),[105,107] helical conformations of the macromolecules are proposed.

Another way to intercalate polymers directly is through a melt method, where the polymers are heated with a preexfoliated (in most cases) clay. In this way, a conventional polymer extrusion process can often be utilized. The formation of PCNs via melt intercalation depends on the thermodynamic interaction between polymer chains and host layers, and also on the diffusion of polymer chains from bulk to interlayers.[41] For PEO, direct melt intercalation into sodium and lithium clays is possible.[106,107,111,114,115] For more hydrophobic polymers, however, the clays must be rendered more organophilic to enhance their compatibility. The most common method for this purpose is to preexchange the clay with alkylammonium ions, often of substantial chain length. There are, in fact, various commercial sources of such modified clays due to the demand of applications such as this. Examples of well-intercalated PCNs
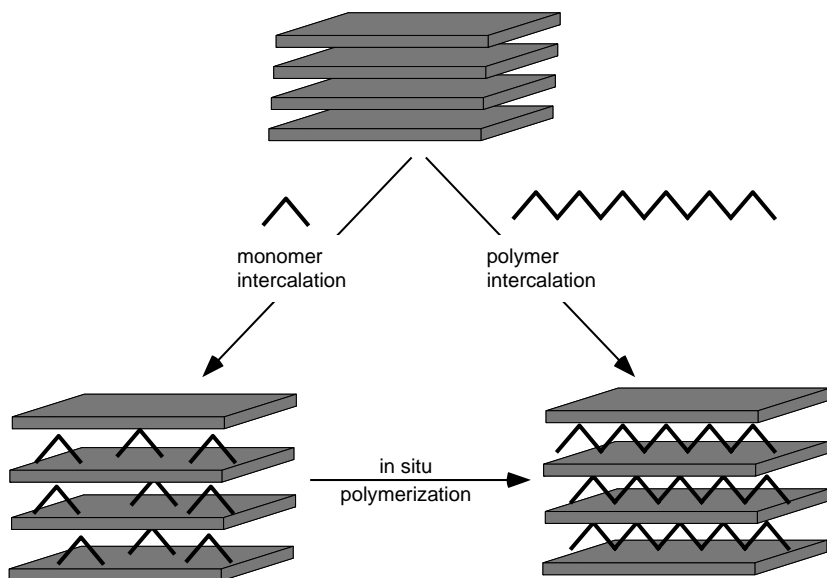
FIGURE 10.3
Methods for creating intercalated polymer–clay architectures via direct polymer contact (usually in solution) and via *in situ* polymerization of preintercalated monomers.

derived from organophilic clays and melt processing include nylon (although here it is concentration dependent; at < 10% clay the system exfoliates),[41] polymethyl methacrylate (PMMA),[148] polypropylene,[170–172,175,179,189] polyvinyl chloride (PVC),[294] and various polystyrenes.[197,206,219a,226] In the case of polypropylene, the polarity mismatch between clay and polymer is so great that the PCN is actually mediated by a maleic anhydride-modified polypropylene oligomer preloaded clay. This system is much more amenable to polypropylene incorporation via melt processing, although a mixed polymeric phase naturally results. An ethylene vinyl acetate copolymer was intercalated via the melt method, whether starting from a pure clay or an organoclay.[282]

Probably the most successful route to creating PCNs in general has been the *in situ* process, wherein monomers are polymerized in the presence of clay mineral layers. In terms of well-ordered polymer–clay intercalates, reports using *in situ* polymerization have included polyacrylamide,[27b,28] nylon,[36,37,42,72,75] polyaniline,[83,84,86,88,91a] polycaprolactone,[93] polyimide,[130,131,133,139] PMMA,[150] polystyrene,[147,198,200,227,228] polyurethane,[243–245] polyethynylpyridine,[295] and epoxy resins.[269–271,273]

If conditions are varied, many of these polymers can also be induced to form exfoliated PCN architectures, as shall be discussed in the next section.

10.2.3 Exfoliated Compounds

Before delving into the details of PCN exfoliated systems, a brief discussion is warranted as to why the *nano* in the term *nanocomposite* is critical for this

application. The dispersion of mineral reinforcing components to a polymeric matrix has been utilized for many decades. Inactive fillers or extenders act to simply reduce costs, and their chemistry is less important than factors such as particle size, shape, morphology, distribution, and, of course, cost. Active fillers are reinforcing materials and require at least some compatibility between polymer and inorganic, and they must often undergo a surface modification process to insure this. In contrast to conventionally scaled composites on the micrometer level, nanocomposites exhibit changes in composition and structure over the nanometer length scale.[9] Individual clay layers fall into this realm because they have a thickness on the order of 1 nm. Clays such as kaolinite, mica, and talc have been important plate-shaped conventional fillers in the past. However, preparation of a true nanocomposite requires complete dispersion, or exfoliation, of the elementary clay layers within the polymer matrix, without any aggregation into larger units such as tactoids or intercalation products. This is a serious challenge that has been addressed well since the first pioneering research was published in 1987 from Toyota workers.[37–39] As was done in Section 10.2.2 for intercalated structures, we shall discuss the various methods of making exfoliated PCNs from solution, from melts, and via *in situ* polymerization.

There are very few successful reports of making fully exfoliated PCNs from dissolved polymer solutions. This is because even when dispersions of fully exfoliated clays are exposed to macromolecular solutions, the strong interactions between macromolecules and silicate layers often just reaggregate the layers.[9] There is a report that polysulfone exfoliates organoclays via a "solution dispersion" technique.[301] For PVA,[108,249,250] exfoliation occurs only when the system has undergone simple mild air-drying. After drying at higher temperatures for longer times, or in vacuum, the silicate layers reaggregate to a spacing of 13.6 Å, indicating monolayer intercalation of PVA. A well-dispersed nanocomposite forms from solution blending of a syndiotactic polystyrene with a surfactant-modified clay in a solvent.[211]

More success for making exfoliated PCNs has occurred using the melt method, including the polymers nylon,[41,44,47,49,70,71] polydimethylsiloxane (PDMS),[94a] polyetherimide,[96a] poly(ethylene terephthalate) (PET),[120,124] polystyrene,[206,212,219a,220] an ethylene vinyl alcohol copolymer,[283] and various PS hybrids.[221,222,226] In a study of nylon–PCN synthesis, higher-molecular-weight polyamides were found to yield superior composite properties, including more exfoliation, which was attributed to differences in melt rheology.[49] In another recent development concerning nylon–PCN studies, focus has been on the crystalline morphology of the nylon (specifically, changes between the alpha and gamma phases[66,68,69]). The effects of preparative variables on the extent of exfoliation of poly(butyleneterephthalate)–organoclays formed via the melt method were investigated.[123] As in the case for intercalated materials, the clays need to be premodified by reaction with alkylammonium ions in order to make them more compatible with the hydrophobic polymers. This includes polypropylene, where the

polarity mismatch requires use of a maleic anhydride-modified polypropylene oligomer preloaded clay.[180,195]

The most successful process for making exfoliated PCNs has been through the polymerization of monomers that are in the presence of clay minerals. Conditions must be optimized to promote a polymerization that causes the uniform dispersion of silicate layers within the polymer matrix. The heat of reaction evolved (enthalpy) during polymerization provides an essential component to the exfoliation.[9] Therefore, exfoliation is enhanced with increasing amounts of intercalated monomers and with decreasing layer charge on the clay surface.[264] The seminal contribution to this research involved nylon–PCNs. Specifically, ε-caprolactam was intercalated into a montmorillonite preexchanged and preswelled with undecylammonium cations, and was subsequently polymerized to poly-6-amide by heating at 250°C under nitrogen.[38,39] Others have since reviewed this work,[42] and similar nylon–PCN preparations have been studied using saponite[71] and swelling mica[72] clays. The various forms of nylon (α and γ) in a PCN have been examined using ^{15}N nuclear magnetic resonance (NMR).[40] More recently, proton and ^{13}C NMR have been employed to study crystallinity, morphology, clay dispersion, crystal stratification, and stability of organic modifiers in nylon–montmorillonite and –laponite exfoliated PCNs, by making use of the effect of iron(III) paramagnetism on the nuclear spins.[63,64]

Other *in situ* polymerizations (emulsion, thermal, photo, free radical, etc.) that employ organoclays and lead to truly exfoliated PCNs include polyacrylamide,[28] polyacrylonitrile (PACN),[34a] PET,[120,124] polyimides,[125,127–129,131–135,137,140,141] PMMA,[147,148,150–152,154–156,163] polypropylene,[169,182] polystyrene,[152,201,203,233] polyurethane,[241,242] and epoxy resins,[126,262–280] among others. An intercalated PDMS–hectorite can be exfoliated upon cross-linking using tetraethyl orthosilicate and tin(II) octoate catalyst.[95] In a very new method, clays (some of them organo-modified) are preloaded with Ziegler–Natta polymerization catalysts (metallocenes), and ethylene or propylene[185] is subsequently polymerized; exfoliated products via the melt method also have been reported.[99,101]

10.2.4 Mixed Intercalated–Exfoliated Systems

As might be expected, there are many reports of PCNs that are perhaps considered to be partially successful preparations in that exfoliation occurs only to some degree. These mixed systems in many cases contain units of just a few intercalated clay layers, rather than an entire extended registry, that are themselves randomly oriented within the polymeric matrix. In most of these cases, conditions can be varied to foster full exfoliation. Examples of mixed intercalated–exfoliated (I-E) systems made using various methods (solution, melt, or *in situ*) include the polymers polyacrylamide,[25] PACN,[35] polyaniline,[35,80] polyetherimide,[96a] polyimide (for montmorillonite,[141,143] saponite, and hectorite clays[127] and mica[135]),

PMMA,[155,156] polypropylene,[169–194] polyurethane,[247] poly(vinyl alcohol),[250] poly(vinyl chloride),[293] polyurethane,[240,247] and epoxy.[268] There is also a report detailing a new method, the living anionic polymerization of styrene, to yield a mixed I-E product.[209] As stated previously, the polarity mismatch between clay and polypropylene is so great that this PCN needs to be mediated by a maleic anhydride-modified polypropylene oligomer preloaded clay. By doing this, a larger fraction of layers are exfoliated, but complete exfoliation has not been very successful. Some of the above PCN systems are created in a unique way wherein the clay layers are crystallized from a silicate sol-gel in direct contact with a polymer solution, including polyaniline and polyacrylonitrile.[35] There is a tendency for the clay layers to aggregate here as they are crystallizing and growing, but it is impressive that a product consisting of up to 88% of a water-soluble polymer (polyacrylonitrile, in this case) is able to crystallize into a polymer–clay nanocomposite from an aqueous solution. They are also insoluble upon resuspension in water.[35b]

10.3 Polymer–Clay Nanocomposite Properties and Applications

Once true clay nanolayer exfoliation is achieved, improvements in a polymer's performance can be manifested in increased tensile properties, enhanced barrier properties, decreased solvent uptake, increased thermal stability, and increased flame retardance. Complete dispersion optimizes the number of reinforcing elements (individual plates) for carrying an applied load and for deflecting cracks. Although conventional polymer–clay composites that contain aggregated clay tactoids, or many associated sheets in registry, show improved rigidity characteristics, they also often display diminished strength, toughness, and elongation properties. On the other hand, truly exfoliated PCN systems, like those for nylon-6 and epoxy, for example, show improvements in nearly all aspects of their mechanical performance.[8] The high-aspect-ratio nanoplates (up to 0.5 microns in length and width, but only 1 nm in thickness) also make possible certain applications that cannot be considered for the larger-scaled composites. Figure 10.4 shows schematically how the tortuous pathways through an exfoliated PCN can improve barrier properties, chemical resistance, and flammability, and reduce solvent permeability because of the hindered diffusion.[8] Figure 10.4 concerns the case of an oriented, exfoliated PCN system. Orientation of plates along a plane normally occurs due to processing conditions (melt extrusion, for example). Yano et al.[127] have developed a permeability coefficient based on this model. However, one also can envision a case where the plates are randomly oriented, and in this latter system, the tortuous path is even greater.
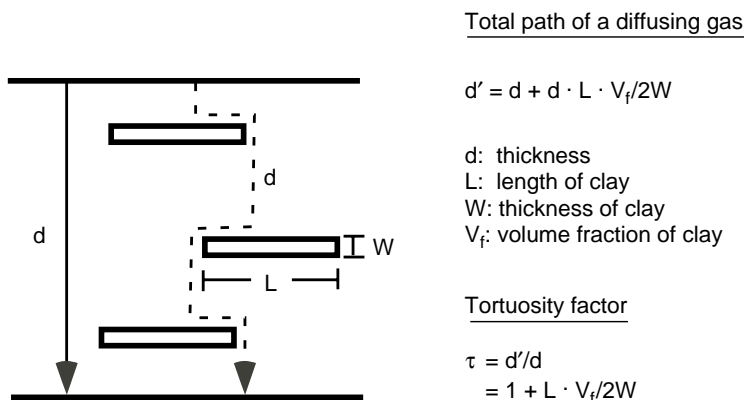
Total path of a diffusing gas

$$d' = d + d \cdot L \cdot V_f/2W$$

d: thickness
L: length of clay
W: thickness of clay
V_f: volume fraction of clay

Tortuosity factor

$$\tau = d'/d$$
$$= 1 + L \cdot V_f/2W$$

FIGURE 10.4
Model for the path of a gas diffusing through an exfoliated polymer–clay nanocomposite matrix.
(From Lan et al., *Chem. Mater.*, 1994, 6, 573.)

10.3.1 Mechanical Properties

One of the most striking examples of increasing the mechanical properties of a polymer upon incorporation of exfoliated clay nanolayers is the first reported PCN system, that of nylon-6 montmorillonite.[37–39] At loadings of just 4.7% clay, the modulus doubles, its strength increases by over 50%, and the heat distortion temperature increases by 87°C when compared to the pure nylon (see Table 10.3). Table 10.3 also shows the advantages of clay nanolayer

TABLE 10.3

Mechanical and Thermal Properties of Various Polymers and Polymer–Clay
Composites (Nylon,[42,50] Polypropylene[175])

System	Wt% Clay	Tensile Strength (MPa)	Tensile Modulus (GPa)	Flexural Strength (MPa)	Flexural Modulus (GPa)	HDT (°C)[a] at 1.82 MPa
Pure nylon-6	0	69	1.1	89	1.9	65
Nylon-6–talc[b]	4.0	n.r.	n.r.	125	3.0	70
Nylon-6–mont.[c]	4.7	97	1.9	143	4.3	152
Pure PP	0	31	1.6	40	1.5	120
PP–talc[b]	3	35	n.r.	45	1.9	n.r.
PP–hectorite, intercalated	3	39	n.r.	53	2.1	130
PP–hectorite, mixed[d]	3	35	n.r.	49	2.0	125

Note: n.r. = not reported.

[a] Heat distortion temperature.
[b] Conventional microcomposite.
[c] Exfoliated montmorillonite PCN.
[d] Mixed intercalated–exfoliated.

exfoliation over a more conventional composite made using a clay (talc) filler that neither intercalates nor exfoliates. Montmorillonite and talc share similar rigidity characteristics, but the former has a larger aspect ratio. Compared with the popular, conventional glass fibers, the aspect ratios are similar, but montmorillonite is much more rigid. Further, nylon–PCN does not exhibit nearly as great a decrease in flexural modulus at the glass transition temperature as does nylon–talc, and it has better creep resistance. It has been proposed that these features are due to the interactions and microstructure between the matrix polymer and its nanofiller.[42] In terms of appearance and specific gravity, nylon–PCN is similar to pure nylon-6, making the PCN a strong but lightweight material. Nylon–PCN materials have in fact been used in actual under-the-hood applications in the automobile industry (as engine covers, timing belt covers, oil reservoir tanks, and fuel hoses), in the construction field (as floor adjusters and handrails), and in electrical applications (various connectors).[42] A recent comprehensive study comparing intercalated and exfoliated nylon–PCNs shows that in low-deformation tests there are no significant differences between them;[67] however, the elastic modulus and flow strain did demonstrate a sensitivity to clay platelet orientation.

The epoxy–clay PCN system has also demonstrated significant enhancements in mechanical properties. As seen in Table 10.4, the presence of exfoliated montmorillonite clay nanolayers substantially increases both the tensile strength and modulus relative to the pure epoxy elastomer. The reinforcement effect in this system is clearly dependent upon clay loading, but substantial improvements are observed at loadings as low as 5 to 10 wt%.[270] The tensile properties of several epoxy nanocomposites using various types of clays (organo-montmorillonite, synthetic swellable fluoromica, and synthetic hectorite) have recently been compared.[266] Different types of functionality on the organocations that are used to premodify the clay are found to have profound effects on degrees of exfoliation. The best balance between increased stiffness and toughness at 5 to 10 wt% clay loadings was observed for fluoromicas preintercalated with specific ammonium cations. In addition, while larger anisotropic intercalated particles led to increased toughness, exfoliated nanoplates best led to increased stiffness properties.[266] Overall, clay nanolayers are more effective in mechanical improvement when the polymer is in its rubbery state than when it is in the glassy state.[3f] The first

TABLE 10.4

Mechanical Properties of Epoxy and Epoxy–Clay Nanocomposites[270]

System	Wt% Clay	Tensile Strength (MPa)	Tensile Modulus (MPa)	Compressive Yield Strength (MPa)	Compressive Yield Modulus (GPa)
Pure epoxy	0	1.1	3.8	75	1.40
Epoxy–PCN[a]	5.0	1.5–3.5	6.0–9.5	79–81	1.50–1.56
Epoxy–PCN[a]	10.0	2.8–6.0	8.5–17	83–88	1.68–1.76

[a] Ranges in data occur because various premodified montmorillonites were used.

TABLE 10.5

Storage Modulus (E') Data for Epoxy–Clay PCNs

Reference	Wt% Clay	E' below Tg, % Higher Than Epoxy	E' above Tg, % Higher Than Epoxy
270	5	72	76
270	10	80	164
262	4	58	450

Note: Tg = glass transition temperature of epoxy (82°C).

evidence for clay nanolayer reinforcement of a glassy epoxy matrix under compressive strain is also detailed in Table 10.4. The compressive yield strengths and moduli are found to increase as a function of clay loading, whereas intercalated nanocomposites were found to display no enhancement whatsoever.[270] Dynamic mechanical analysis (DMA) is often employed in PCN characterization to determine temperature dependence of the storage modulus. Table 10.5 presents thermomechanical data from various researchers for epoxy PCNs. Others have also shown that epoxy PCNs display improvements in glass transition temperature, dynamic behavior, and a lowering of residual stress.[262]

Table 10.3 also contains mechanical data for the polypropylene (PP) system. Fillers do not tend to enhance the tensile properties in this system no matter what the architecture may be (microcomposites, intercalated, or mixed intercalated–exfoliated clays). In contrast, the flexural properties are increased somewhat. Inexplicably, it turns out that the more intercalated systems actually display better performance than the more exfoliated PCN systems. Workers have tentatively attributed this to better stiffness characteristics of the clay layers rather than to exfoliation.[175] The effects of exfoliation on dynamic storage modulus (E') have been investigated in detail by other researchers. Although complete exfoliation was not possible, a mixed intercalate–exfoliate containing 5% clay demonstrated an E' value 2.4 times higher than pure PP at 90°C.[171] Overall, the significance of nanolayer reinforcement in the PP system is not as great as for nylon-6 due to the lower degree of exfoliation and the introduction of a large amount of oligomer. PP-PCNs remain attractive for other applications,[178] however, such as for packaging materials where enhanced barrier properties are desired.

Benefits from the nanolayer dispersal of clays in the polyurethane thermoset system have also been realized recently. In most of these materials, there is a basal spacing at very high values on the order of 50 to 90 Å.[240,247] One group has reported exfoliation, but since the x-ray powder diffraction (XRD) spectra did not go to low enough angles, it is possible that an unobserved basal spacing in fact exists.[241] In any event, these mixed intercalated–exfoliated systems have a great enough distance between the nanolayers, with a high enough tactoid dispersion within the polymeric matrix, that the materials are in the range where nanocomposite-type reinforcement is expected. Wang and Pinnavaia[240] found that at a loading of 10

wt% organoclay, the strength, modulus, and strain-at-break were all

TABLE 10.6

Mechanical Properties for the Polyurethane Thermoset System

Sample	Wt% Filler	Tensile Strength (MPa)	Young's Modulus (MPa)	Elongation at Break (%)
PU	0	0.8	3.6	65
PU–mica microcomposite[247]	10.0	1.4	4.2	95
PU–mica nanocomposite[247]	10.0	2.7	2.8	200
PU–montmorillonite nanocomposite[241]	1.4	0.9	n.r.	690
PU–montmorillonite nanocomposite[241]	4.2	1.7	n.r.	3

Note: n.r. = not reported.

increased by more than 100% of pristine polymer. They report that it is unusual to have improvements in modulus, strength, and toughness all in the same system and attribute the improved elasticity to the plasticizing effect of the gallery onium ions in the organoclay. Table 10.6 summarizes the work of Chen et al.[241,242] and Zilg et al.[247] for their polyurethane (PU)–clays. In contrast to conventional mica-filled polyurethanes, PU nanocomposites exhibit substantially higher elongation-at-break combined with a much higher tensile strength.[247] The Young's modulus, a measure of polymer stiffness, decreased slightly in the nanocomposite, which was attributed to "softer" nanolayers, compared to the pure mica. The high matrix reinforcement and tear resistance was assigned to orientation of the anisotropic nanolayers and to interfacial coupling between intercalated mica and polymer (between isocyanate groups and hydroxy groups in the organoclay). For the montmorillonite system,[241] tensile strength increased with clay content from 1.4 to 4.2 wt%, but the elongation decreased drastically. This behavior was attributed to a transformation in the polymer phase from elastomer to thermoplastic. In addition, the lap shear stress increased by three times over pure PU.

The mechanical properties of a polyimide–montmorillonite nanocomposite have recently been reported. Agag et al.[140] prepared two different polyimides as 2 wt% montmorillonite exfoliated PCNs, and both showed significant improvements in tensile modulus (42 and 110% higher than their respective pure polyimides). Tyan et al.[139] also report such enhancements in a similar system, along with increased elongation-at-break. For a 5 wt% clay material, Zhu et al.[128] show that the tensile strength increased from 79 to 95 MPa and the elongation-at-break increased from 15 to 20%; however, the degree of clay nanoplate dispersion (intercalation vs. exfoliation) is unclear. The primary benefits of polyimide–PCNs lie in barrier properties and thermal stability, as will be discussed later.

Only very recently have mechanical data for polystyrene–PCNs been reported. Park et al.[206] used the unique approach of melt-intercalating amorphous polystyrene (aPS) into organoclay, followed by blending with syndiotactic polystyrene (sPS). sPS is crystalline with a high melting point, and therefore has heat and chemical resistance along with dimensional stability. Both aPS and sPS have a low specific gravity, electrical properties, and hydrolytic stability. All of these properties make sPS an important engineering thermoplastic. Variables studied were the types of amorphous styrenic polymer and their wt%, clay wt%, and simultaneous or stepwise fabrication methods. These yielded either intercalated or exfoliated products. Increases in tensile strength and flexural modulus were not significant; however, the Izod impact strengths could be dramatically improved, especially for the exfoliated structures (from 1 to 4 kgf.cm/cm).[206]

A few isolated reports of the mechanical performance of styrene-based copolymer rubbers exist. Laus et al.[221] discovered an increasing storage modulus with increasing clay content (from 3.8 to 40 GPa as clay increased from 0 to 30 wt%) for a poly(styrene-*b*-butadiene) (SBR) copolymer–PCN. Zhang et al.[224] report that some mechanical properties of SBR-PCN exceed those of conventional carbon black-filled composites, and that careful attention to preparing nanocomposites offers the same advantages over simple mixing of SBR and clay.

10.3.2 Gas Barrier Properties

There is an enormous and varied use of plastics in the food packaging industry, where they have replaced much traditional glass, metal, and paper packaging. There are limitations, however. For example, certain foods, such as tomato-based products and wine, are sensitive to oxygen and cannot be stored in plastic containers due to oxygen permeability. Poly(ethylene terephthalate) (PET) has become the mainstay of packaging materials for products such as soft drinks, water, fruit juice, and peanut butter. It too suffers from oxygen permeability, especially at high surface–volume ratios (small containers), leading to unacceptable shelf life. Currently, multilayer processing techniques (high-barrier specialty polymer sandwiched between PET layers) are being utilized to provide barrier enhancements,[120,124] but the ability for exfoliated clays to improve PET gas barrier characteristics is beginning to receive attention as a lower-cost alternative.[119,120,124] An extensive description of PET-PCNs exists, and the reader is referred to this for synthetic details, mechanical properties, and a thorough patent literature review.[120]

Recall from Figure 10.4 that the tortuous path model (TPM) is used to calculate parameters such as tortuosity factor, τ. From this model, the permeability coefficient Pc of a PCN is equal to Pp/τ, where Pp is the permeability coefficient of pure PET. Figure 10.5 displays the oxygen permeability data for a variety of polyesters, including PET, as a function of wt% clay.[124] Note that for PET it decreases by a factor of 3 at just 5 wt% clay. The
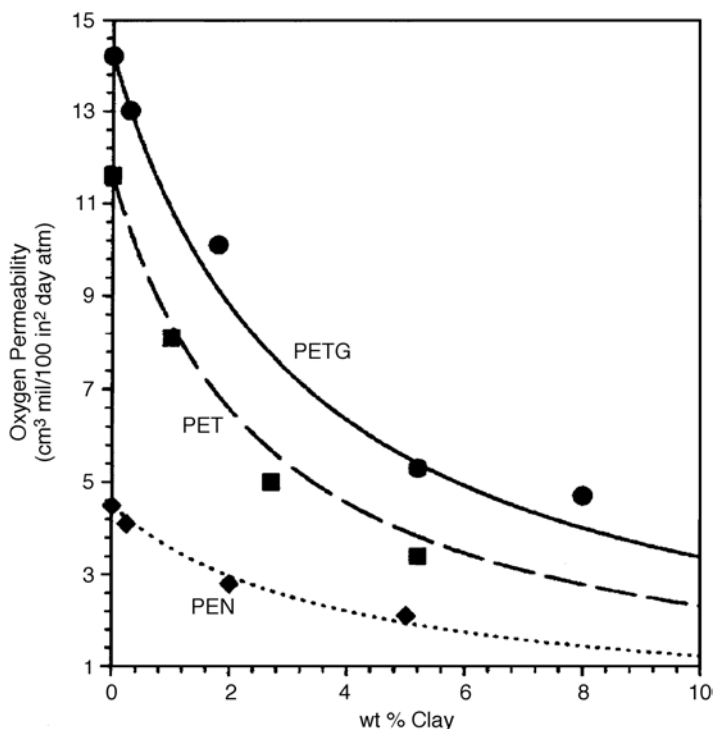
FIGURE 10.5
Plot of the oxygen permeability of 10-mil-thick amorphous, compression-molded polyester–PCN films vs. clay loading. PETG = glycol-modified PET; PEN = poly(ethylene naphthalate). Data are fit to Pc = Pp/τ, as described in the text. (From Matayabas, J.C. and Turner, S.R., in *Polymer-Clay Nanocomposites*, Pinnavaia, T.J. and Beall, G.W., Eds., New York: John Wiley & Sons, 2000, chap. 11. With permission.)

importance of obtaining an exfoliated system is highlighted by the use of an effective aspect ratio term, which can be calculated by fitting the curves of Figure 10.5 to the equation in Figure 10.4. Typical values are 150 to 200 for amorphous PET nanocomposites. The effective aspect ratio has proven, therefore, to be a good relative indicator for the extent of clay exfoliation.[124]

The use of PET-PCNs as the internal layer of a multilayer container has been assessed as well.[32] Advantages to using them this way, rather than as the pure container material, include (1) neat PET is the food contact surface, (2) recyclability, and (3) less haze than the pure PET-PCNs. The disadvantage is that at the same container thickness, this arrangement dilutes the barrier improvement achieved by the clay. Nylon–PCNs have been similarly investigated for use in multilayer containers.[124] Their advantages are (1) a high gas barrier, (2) similar processing to PET, and (3) good adherence to PET. They are a much more effective oxygen barrier than conventional nylon materials at lower weights (see Table 10.7), but they have negative hazing

characteristics. Nylon–PCNs are also reported to be excellent barriers against water vapor, nitrogen, carbon dioxide, and gasoline.[42]

TABLE 10.7

Gas Permeability Data for Nylon-6 and Nylon-6/ Montmorillonite PCN (4 Wt% Clay) Unstretched Films (150 μm thickness)[42]

Gas Permeability (cm³/m² (24 h · atm))	Pure Nylon-6	Nylon-6/Clay
H_2O[a]	130	55
O_2[b]	30	5

 [a] 40°C, 90% relative humidity.
 [b] 20°C, 100% relative humidity.

Polyimide–clay nanocomposite systems demonstrate dramatically improved barrier properties. Chang et al.[138] have shown a 95% reduction in oxygen gas permeability upon the addition of just 2 wt% organoclay to polyimide. Yano et al.[127] studied different clays and discovered that montmorillonite and synthetic mica produce exfoliated PCNs, whereas hectorite and saponite are intercalated. Regardless of the degree of dispersal of the clay layers, mass transport studies reveal a several-fold reduction in the permeability of small gases such as O_2, H_2O, He, and CO_2.[125,127] For example, a 2 wt% polyimide–mica has a water vapor permeability coefficient (Pc) that is ten times lower than that of the pure polyimide.[127] A comparison of Pc with the aspect ratio of these various clays shows that permeability decreases with increasing aspect ratio in a nonlinear fashion.

The potential applications of rubber–clay PCNs as tire inner liners and inner tubes depend, naturally, on their barrier ability. Various workers have reported reductions in the permeability of oxygen,[304] and hydrogen and water vapor[233] for such systems. Another system showing enhancements in barrier properties is poly(ε-caprolactone)–PCN. Messersmith and Giannelis[93b] used cast films to monitor water vapor permeation; at 4.8 vol% clay, a fivefold reduction in permeability, compared to the pure polymer, was observed. Another exfoliated PCN system that demonstrates a reduction (by 60%) in water permeability, compared to pure polymer, occurs for poly(vinyl alcohol)–montmorillonite, and this cast film containing 5 wt% clay retains optical clarity.[250] Applications here may lie in water-soluble food packaging.

Recently, a new conceptual model for predicting nanocomposite barrier behavior was proposed by Beall[305] because the tortuous path model appears to hold well only at very low clay loadings (< 1 wt%), with significant deviations at higher loadings (1 to 5 wt%) and with changes in humidity and temperature. The TPM also does not explain the observation of better barrier properties for the less-exfoliated samples in the polyimide–clay systems,[127] for example. Beall's constrained polymer model (CPM) is based on treating

the clay–polymer interface as the dominating factor. It assumes that a montmorillonite particle has an aspect ratio of 250 (250 nm in two directions, 1 nm in the other), a total surface area over 700 m^2/g, and a molecular weight of over 100 million. In this sense, it is treated as a true macromolecule. Four distinct phases are then defined: (1) the clay itself, (2) a 1- to 2-nm well-defined clay surface compatibilized with an organic modifier, (3) an ill-defined region up to 50 to 100 nm away containing constrained polymer, and (4) an unconstrained polymer region not affected by clay. There is substantial direct and inferred experimental evidence for the existence of all of these phases. With respect to permeability, the important parameters are the diffusion coefficients of the three latter regions and their relative volume fractions. This model is quite versatile in that it allows for variations in relative diffusion coefficients for various permeant gases. The CPM predicts that:[305]

1. Actual permeabilities can be higher or lower than those predicted by the TPM, depending on relative diffusion coefficients of the phases.
2. The permeability for a particular PCN can vary considerably for different permeants.
3. Nematic polymer phases often predominate at > 5 wt% clay.
4. A mineral's aspect ratio is not a good predictor of a given polymer's permeability.
5. Many PCN mechanical property changes can be modeled as well.

All of this said, Bharadwaj[306] has recently published a useful detailed report describing the effects of sheet length, concentration, orientation, and degree of delamination on relative permeability by modifying the simple tortuosity-based model.

10.3.3 Rheological Properties

Knowledge of the rheological properties of PCNs is fundamental to understanding their processability and structure–property relationships. A recent review focuses on the linear and nonlinear viscoelastic rheological properties of PCNs in the melt state.[307] Three detailed examples are used to highlight the assumption that the melt rheological properties are dependent upon a combination of the overall, long-range (mesoscopic) structure and the strength of the nanoscale interaction between polymer and clay. The specific examples used are an exfoliated end-tethered poly(ε-caprolactone), an exfoliated nylon-6, and intercalated polystyrene–polyisoprene diblock copolymer PCNs. A pseudo-solid-like behavior that is observed at long times in the linear viscoelastic response is attributed to the percolation of locally correlated layers that are treated as randomly oriented grains. Nonlinear viscoelastic behavior is strongly dependent on the physical connectivity or interaction between the polymer and the clay layer. Strong end-tethering

interactions result in strain hardening, while weaker interactions lead to shear thinning.

10.3.4   Flame Retardance and Ablative Performance

Most of the flame retardant approaches for polymers come at the expense of physical properties. Exploration of various PCNs for flame retardance have proven fruitful, however, especially since this approach can simultaneously improve the mechanical strength and other properties of the polymer. Reviews of PCNs with respect to flammability characteristics and thermal stability have begun to appear,[308] along with studies specific to polystyrene,[54,186,217] polypropylene,[54,178,186,191,193] nylon-6,[54,70] epoxy,[276,279] and polycarbonate[309] PCNs.

Serious evaluation of the flammability properties of PCNs began with Giannelis et al. regarding the self-extinguishing flammability of polyetherimide[310] and polycaprolactone[5] PCNs. Gilman et al.[311] first observed reduced flammability as a lower-peak heat release rate (HRR) for exfoliated nylon-6 PCNs. Soon thereafter, reduced flammability was found to be a general phenomenon for both thermoplastics — polypropylene (see Figure 10.6) and polystyrene — and thermoset resins such as epoxies and vinyl esters.[308b] Further, this was true whether the PCN was exfoliated or intercalated. Table 10.8 summarizes cone calorimetric data for some examples of these results. Flammabilities are reduced from 25 to 75% at low clay loadings (2 to 6%) without increasing carbon monoxide or smoke yields. The cone calorimeter is an effective bench-scale method for studying flammability properties.[308a] One parameter that this method yields, peak HRR, has been determined as the most relevant in evaluating fire safety.[312]

By studying PCN combustion residues using TEM and XRD, Gilman et al. have deduced that during combustion, the PCN architecture collapses and the resulting multilayered carbonaceous-silicate structure appears to enhance the performance of the char through structural reinforcement.[308b] Apparently this silicate-rich char also acts as an insulator and mass transport barrier, slowing the escape of volatile decomposition products, in that the mass loss rate (MLR) decreases along with HRR. Another group studying the flammability properties of polystyrene PCNs has reported similar results.[217] Specifically, a clay pretreated with a phosphonium salt was found to be more thermally stable than one pretreated with ammonium salts. Decomposition was retarded by 50°C; the peak HRR decreased by 27 to 58%, depending upon wt% clay loading; and the MLR decreased in the presence of clay.

Because of promising results such as these, researchers have explored the use of PCNs with conventional flame retardants in the hopes of improving their physical properties. The general approach is to incorporate a portion of premade PCN to a conventional flame retardant formulation. Improvements occur due to a reduction in the amount of conventional flame retardant
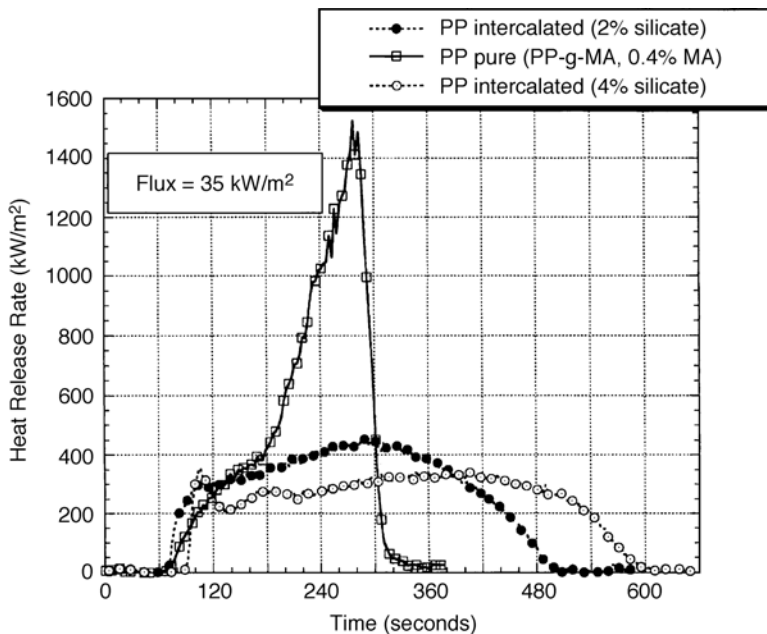
FIGURE 10.6
Heat release rate plots for pure polypropylene (PP) and two PP–montmorillonite PCNs, showing a 70 to 80% reduction for PCNs at only 2 and 4 wt% clay, respectively. (From Gilman, J.W., *Appl. Clay Sci.*, 1999, 15, 31. With permission.)

TABLE 10.8

Cone Calorimetry Data for Various Polymers and Their Montmorillonite Nanocomposite Counterparts (Heat Flux 35 kW/m^2)[308]

Sample (*structure*)	Residue Yield, %	Peak HRR, kW/m^2 (Δ%)	Mean MLR g/sec m^2 (Δ%)
Nylon-6	1	1010	29
Nylon-6, 2% clay, *exfoliated*	3	686 (32%)	17 (41%)
Nylon-6, 5% clay, *exfoliated*	6	378 (63%)	12 (58%)
Polystyrene (PS)	0	1120	29
PS, 3% clay, *mixed I-E*	4	567 (48%)	17 (41%)
Polypropylene (PP)	5	1525	13
PP, 2% clay, *mixed I-E*	6	450 (70%)	8 (38%)
PP, 4% clay, *mixed I-E*	12	381 (75%)	6 (46%)
Mod-bis-A vinyl ester	0	879	26
Above, 6% clay, *intercalated*	8	656 (25%)	18 (30%)
Bis-A/novolac vinyl ester	2	977	29
Above, 6% clay, *intercalated*	9	596 (39%)	18 (39%)
DGEBA/BDMA epoxy resin	3	1336	34
Above, 6% clay, *intercalated*	10	769 (42%)	21 (38%)

Note: HRR = heat release rate; MLR = mass loss rate; mixed I-E = mixed inter-calated–exfoliated.

used, which often degrades properties, and from the normal reinforcement effects of the nanodispersed silicate layers. Some examples studied thus far, all of which demonstrate enhanced physical properties, include (1) nylon-6 PCN (2 wt% montmorillonite) substitution for pentaerythritol in a typical ammonium polyphospate intumescent flame retardant formulation (using ethylene vinyl acetate); (2) polytetrafluoroethylene–clay dispersed in a styrene–acrylonitrile copolymer to replace 40% of the brominated polycarabonate/Sb_2O_3 flame retardant in polybutylene terephthalate; (3) polyethylene PCN, compared with decabromodiphenyl oxide/Sb_2O_3; and (4) melamine PCNs.[308b]

In a related vein, materials with high ablation properties are critical for insulation against the severe effects of very high temperatures and incident heating rates. High-performance applications include aerodynamic surface protection and insulation for space and launch systems, propulsion structures, payloads, and ground equipment. During the firing of a solid rocket motor, for example, insulation is subjected to temperatures in excess of 2000°C; pressures of 1000 psi or greater; compressive, tensile, and shear stresses; and oxidizing atmospheres.[53] Vaia et al.[53] at Wright-Patterson Air Force Base have begun to examine various PCNs for these applications. Exfoliated nylon-6 montmorillonites were found to yield a tough, inorganic char during ablation. For PCNs with as little as 2 wt% clay, at least an order of magnitude decrease in mass loss rate (erosion) relative to pure nylon was observed. It was deduced that the nanoscopic distribution of silicate layers leads to a uniform char layer that enhances the ablative performance.[53] The length scale of this nanoscopic morphology is comparable to the diffusivities of the decomposition reactants and products, so that a uniform supply of silicate to the char is available during decomposition. In contrast, traditionally filled systems on the micron scale require a higher inorganic loading for the formation of a uniform char layer. Layer concentration, size, and degree of dispersion were found to be the dominant factors over such details as clay organic modifier or specific clay–polymer interactions.[53]

A related study concerns the self-passivation (char layer) response of nylon-6 and epoxy PCNs to aggressive oxidative environments, specifically an oxygen plasma.[62] The self-passivation layer was found to retard penetration of the plasma and to prevent further polymer degradation, as demonstrated in Figure 10.7. Erosion profiles show an induction phase that is consistent with required oxidation of the polymer to form the passivated silicate layer. After this layer forms, degradation of the underlying polymer is significantly retarded (up to an order of magnitude). A so-called self-healing feature is inherent to this material as well, since failure of the passivation layer in an aggressive environment exposes bulk PCN that is capable of re-forming the char region. The structure of the inorganic char layer was found to be turbostratic from careful XRD measurements, which agrees with qualitative observations from TEM images. Figure 10.8 contains a TEM image of a nylon-6 montmorillonite PCN, showing the exfoliated nature of the material, and two images of the material after exposure to an oxygen plasma.
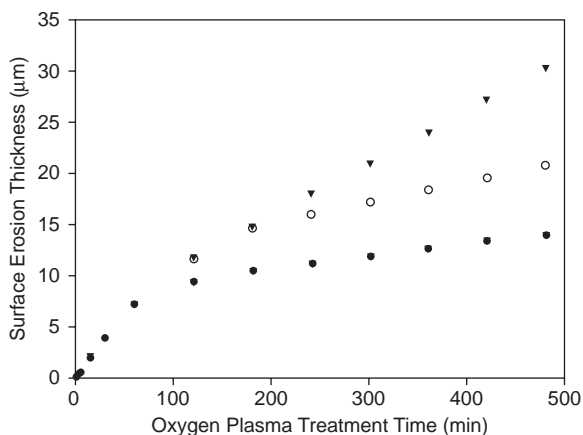
FIGURE 10.7
Oxygen plasma surface erosion rates for pure nylon-6 (triangles) and nylon–montmorillonite PCNs at 5 wt% clay (open circles) and 7.5 wt% clay (closed circles). (From Fong et al., *Chem. Mater.*, 2001, 13, 3781. With permission.)

After treatment, an inorganic char layer from 0.1 to 0.5 μm thick is clearly evident parallel to the surface. Formation of the layer is due to the preferential oxidation of the polymer and the corresponding enrichment of nanoscale silicate layers on the surface.[62]

10.4   Molecular Modeling

It is by now apparent that all PNCs have a common feature: an interphase polymer layer near the inorganic clay surface that has dramatically different properties from the bulk polymer phase. Nanocomposite properties are therefore due to more than the sum of their bulk phases. A fundamental understanding of this interfacial region is one goal of recent molecular modeling research.[19] Loring and coworkers have utilized coarse-grained molecular dynamics simulations to provide insight into the intercalation process.[313] For example, an effective diffusion coefficient (D_{eff}) for intercalation of block copolymer melts was found to be twice the value of the bulk self-diffusion coefficient.[313b,c] Increasing the affinity of the polymer for the silicate caused a decrease in D_{eff}, in accordance with actual results. Molecular dynamics simulations also provide insight into the complex dynamic behavior of a "confined" polymer–clay structure, wherein the polymers actually have a higher mobility than they do in the bulk.[314,315] When confined to the nanoregion near a clay surface, the polymer chains are found to order into discrete subnanometer layers (see Figure 10.9). This imparts a strong density inhomogeneity in the direction normal to the surface. Fast dynamics occur in the
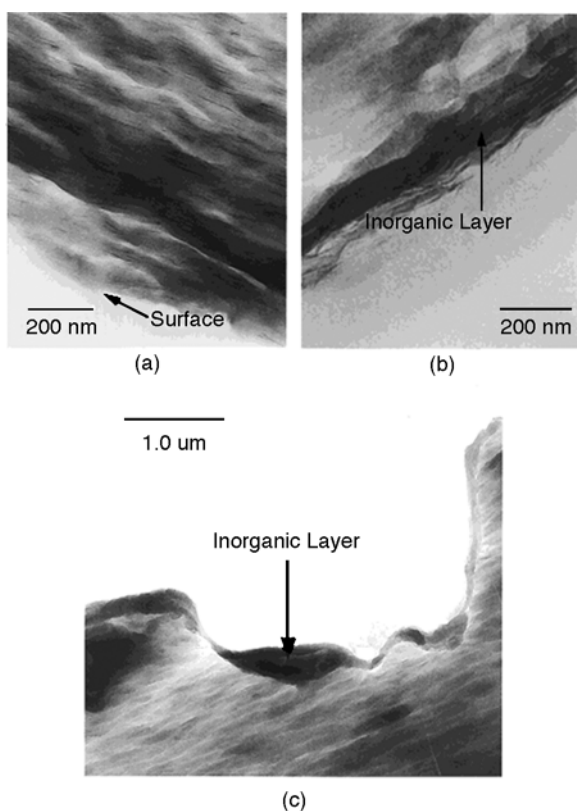
FIGURE 10.8
TEM images of nylon-6 PCN (7.5 wt% montmorillonite) before (a) and after (b and c) oxygen plasma treatment for 1 h. (From Fong, D.L. et al., *Chem. Mater.*, 2001, 13, 3781. With permission.)

lower density regions, whereas slower dynamics occur in high-segment-density regions close to the surface.[19,314,315] This heterogenous mobility combined with an observed persistence of mobility below the bulk glass transition temperature (Tg) has implications to PCN properties.[19]

The labs of Balazs et al. have been prolific in modeling the equilibrium phase behavior of polymer–clay nanocomposites.[316–325] They argue that conditions for creating a uniform clay layer dispersion depend on both processing conditions and thermodynamic considerations. Describing the stability and morphology of PCN mixtures is divided into two parts: (1) determining the polymer-mediated interactions between silicate layers, and (2) calculating phase diagrams as a function of the composition of the mixture once these interactions are known.[325] Together, they comprise nanoscale and macroscale interactions, respectively. On the nanoscale, interactions between organic modifiers and polymer chains are modeled with clay sheets treated as infinitely planar silicate surfaces. This therefore concerns properties of polymers confined between clay surfaces. On the macroscale level, the clay
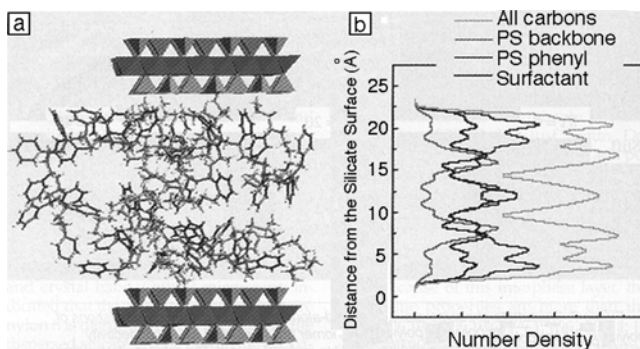
FIGURE 10.9
(a) Molecular dynamics simulation "snapshot" of a silicate–surfactant–polystyrene PCN, giving an atomistic view of the various system components. (b) The corresponding ensemble-averaged number density of carbon atoms as a function of distance, offset from the lower clay surface. (From Vaia, R.A. and Giannelis, E.P., *MRS Bull.*, Vol. 36, 2001, 394. With permission.)

layers are treated as rigid particles dispersed in an incompressible fluid with interactions via excluded-volume and effective long-range potentials. This behavior concerns the thermodynamics of anisotropic colloidal particles in a melt or solution.

Vaia and Giannelis[326] have used a lattice model, and Balazs et al.[317–319,325] have used both numerical and analytical self-consistent field (SCF) theories to calculate free energy profiles as two clay layers are pulled apart in the presence of molten polymer. Results show whether systems will be intercalated, exfoliated, or phase separated. Theoretical models that describe the macroscopic behavior are needed to account for free energy (including the translational and orientational entropy of the clay particles) and excluded-volume interactions. Balazs et al. have developed models[325] to describe the liquid crystalline ordering of a polymer–clay system that takes into account the strong anisotropy in the shape of the clay sheets (see Figure 10.10). Since these models only approximate the long-range clay interactions, a more recent study combined the density functional theory (DFT) approach for silicate-layer ordering with the SCF-calculated potentials; this model was used to describe phase diagrams for clays with organic modifiers (surfactants) dispersed in a polymer melt.[320]

A recent review summarizes studies on the phase behavior of polymer–clay mixtures.[325] Shapes of SCF-derived profiles reveal whether a polymer–clay interaction is favorable and if the mixture is miscible. If so, the curves further indicate whether the PCNs are intercalated or exfoliated structures. The calculations allow for modification of surfactant, polymer, and clay characteristics and can therefore identify factors that enhance polymer permeation into clay galleries. Employing DFT allows one to take into account clay ordering, to pinpoint boundaries for the various phases shown in Figure 10.9, and to generate the complete phase diagram. Then the com-
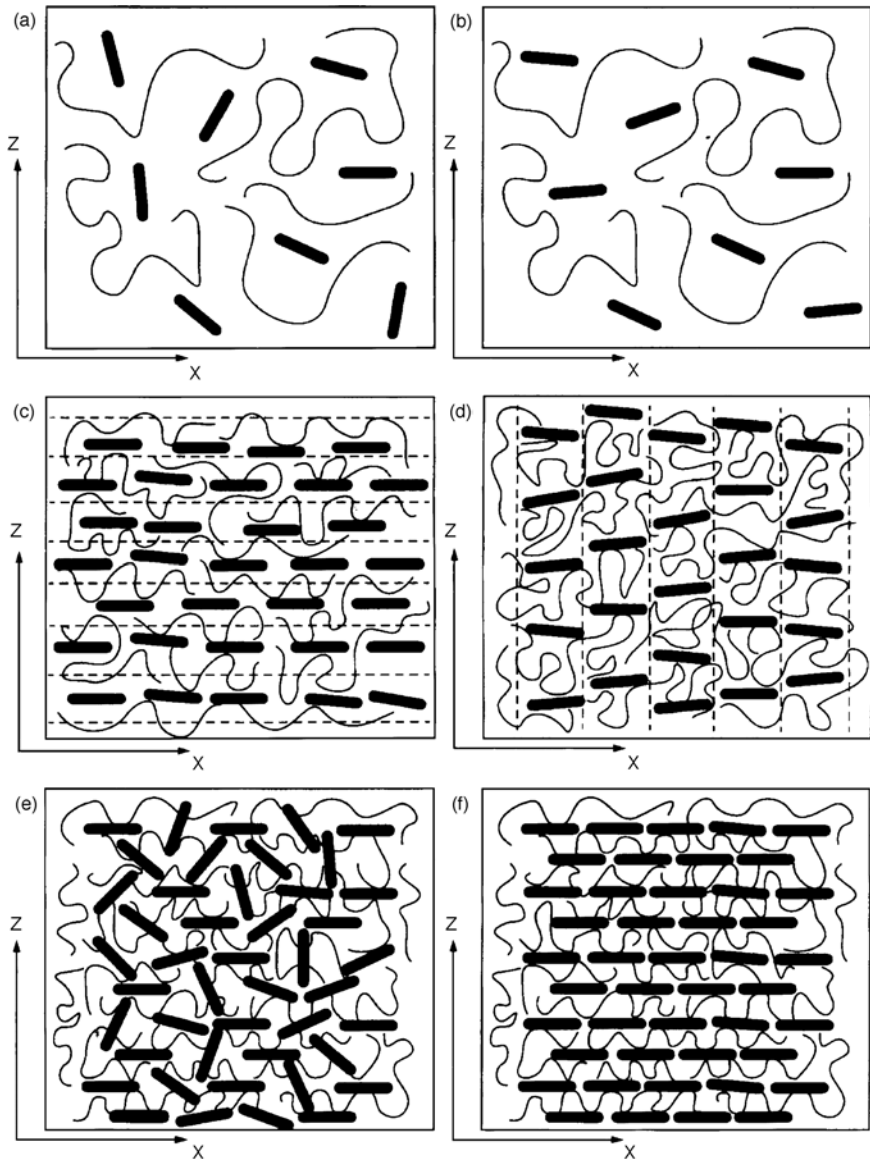
FIGURE 10.10
Mesophases of oblate uniaxial particles (i.e., clay sheets or disks) dispersed in a polymer: (a) isotropic, (b) nematic, (c) smectic A, (d) columnar, (e) plastic solid, and (f) crystal. The nematic director n in ordered phases is aligned along the Z axis, and the disks lie in the XY plane. Dashed lines show smectic layers (c) and columns (d). (From Balazs, A. et al., in *Polymer-Clay Nanocomposites*, Pinnavaia, T.J. and Beall, G.W., Eds., New York: John Wiley & Sons, 2000, chap. 14. With permission.)

bined DFT-SFC approach is used to obtain phase diagrams for several values of surfactant grafting density and length. Results offer quantitative estimates of the volume fractions of clay that correspond to the different phases. In addition, a combined kinetic and equilibrium analysis provides insight into factors that affect morphological aspects of the PCN.[316] One prediction, for example, is that under certain conditions (large N, $\chi < 0$, where N is the number of monomeric units in a polymer and χ is the polymer–surfactant interaction parameter), a stable hybrid will exhibit only intercalated morphology. Another prediction is that optimal polymers for creating stable exfoliated PCNs are those that would sterically optimize colloidal suspensions.

Farmer et al.[327] have developed a coarse-grained molecular dynamics model for investigating the early stages of intercalation and exfoliation in order to derive the operative processes and interactions. They further extended the model to study the infusion process of a fluid into a layered nanostructure. Infusion rates were found to depend on overall fluid composition and on the absolute and relative magnitudes of attraction between beads of fluid and the clay sheets.[327] Initially, fluid infusion causes a metastable, intercalated condition with sheets separated by a single layer of fluid beads. Progression to exfoliation is found to involve a much slower process with a much lower driving force.

Monte Carlo and molecular dynamics computer simulations have been used to explore the atomic scale structure and dynamics of intercalated PEO/montmorillonite PCNs, with particular attention given to polymer configuration within the clay galleries.[315] In this system, a layered, though disordered and liquid-like, structure is observed, with cations residing primarily near the silicate surface. Interlayer mobility of Li(I) cations was found to be related to the ionic conductivity.

Beall and Tsipursky[328] utilize molecular modeling to demonstrate certain facets of a novel ion–dipole clay surface modification. First, montmorillonite is modeled. Then, to illustrate ion–dipole bonding, caprolactam bonded to the sodium ions of a clay surface is modeled. Another small and hydrophobic molecule modeled is dodecylpyrrolidone on a clay surface, with carbonyl groups bonded to sodium ions and alkyl chains projected into the clay gallery. This mimics a clay ion-exchanged with the acid salt of an alkyl amine, and relative bond strengths are in fact found to be similar. Finally, a polymer intercalate of polyvinyl pyrrolidone is modeled, with carbonyl groups again bound to sodium ions.

Very recently, molecular modeling techniques were applied to predict the binding energies of nylon–exfoliated clays, and pure clay (rather than ammonium–clay) was found to yield the highest binding strength to nylon.[329] Plane-wave density functional theory was applied to study *in situ* polymerization of ethylenediamine and methanal in montmorillonite,[330] and catalysis was shown to occur at the clay mineral lattice edge where hydroxyl groups and exposed aluminum ions act as the acid sites. Finally, one recent paper

discusses the modeling of the "micromechanics," including tensile and elastic moduli as a function of exfoliation.[331]

10.5 Summary

Clearly, from the enormous volume of very current literature references in the field of polymer–clay nanocomposites, intense interest remains in understanding the synthesis and properties of these versatile materials. One could separately do a patent literature search and find a similarly overwhelming amount of applications, showing the industrial relevance of PCNs. As of this writing, a few of the most up-to-date areas of research are (1) *in situ* polymerization via metallocenes (see, for example, Rong et al.[103] to make polyethylene); (2) grafted surfactants (where surfactants are covalently attached to the clay surfaces; see, e.g., Seckin et al.[34b] and Agag et al.[140]); and (3) in-depth studies of the surfactant–clays themselves.[332] No doubt the future will continue to provide new insights, materials, and applications, and promises to be very exciting indeed.

Acknowledgment

References

1. (a) *Clay Mineralogy,* Grim, R.E., McGraw-Hill: New York, 1968. (b) *Clay Minerals and the Origin of Life*, Cairns-Smith, A.G. and Hartman, H., Cambridge, U.K.: University Press, 1986.
2. *Formation and Properties of Clay-Polymer Complexes*, Theng, B.K.G., New York: Elsevier Scientific, 1979.
3. Giannelis, E.P. A new strategy for synthesizing polymer-ceramic nanocomposites, *J. Miner. Met. Mater. Soc.*, 1992, 44, 28.
4. Okada, A. and Usuki, A. The chemistry of polymer-clay hybrids, *Mater. Sci. Eng.*, 1995, C3, 109.
5. Giannelis, E.P. Polymer layered silicate nanocomposites, *Adv. Mater.*, 1996, 8, 29.
6. Ogawa, M. and Kuroda, K. Preparation of inorganic-organic nanocomposites through intercalation of organoammonium ions into layered silicates, *Bull. Chem. Soc. Jpn.*, 1997, 70, 2593.

7. Giannelis, E.P. Polymer-layered silicate nanocomposites: synthesis, properties, and applications, *Appl. Organomet. Chem.*, 1998, 12, 675.
8. LeBaron, P.C., Wang, Z., and Pinnavaia, T.J. Polymer-layered silicate nano-composites: an overview, *Appl. Clay Sci.*, 1999, 15, 11.
9. Lagaly, G. Introduction: from clay mineral-polymer interactions to clay mineral-polymer nanocomposites, *Appl. Clay Sci.*, 1999, 15, 1.
10. Dagani, R. Putting the 'nano' into composites, *Chem. Eng. News*, 1999, 77, 25.
11. Rothon, R.N. Mineral fillers in thermoplastics: filler manufacture and characterization, *Adv. Polym. Sci.*, 1999, 139, 67.
12. Garces, J.M., Moll, D.J., Bicerano, J., Fibiger, R., and McLeod, D.G. Polymeric nanocomposites for automotive applications, *Adv. Mater.*, 2000, 12, 1835.
13. *Polymer-Clay Nanocomposites*, Pinnavaia, T.J. and Beall, G.W., Eds., New York: John Wiley & Sons, 2000.
14. Zanetti, M., Lomakin, S., and Camino, G. Polymer layered silicate nanocomposites, *Macromol. Mater. Eng.*, 2000, 279, 1.
15. Ishida, H., Campbell, S., and Blackwell, J. General approach to nanocomposite preparation, *Chem. Mater.*, 2000, 12, 1260.
16. Alexandre, M. and Dubois, P., Polymer-layered silicate nanocomposites: preparation, properties and uses of a new class of materials, *Mater. Sci. Eng. R-Rep.*, 2000, 28, 1.
17. Oriakhi, C.O. Polymer nanocomposition approach to advanced materials, *J. Chem. Ed.*, 2000, 77, 1138.
18. Groenewold, J. and Fredrickson, G.H. Elastic interactions and stability of clay-filled lamellar phases, *Eur. Phys. J. E: Soft Matter*, 2001, 5, 171.
19. Vaia, R.A. and Giannelis, E.P. Polymer nanocomposites: status and opportunities, *MRS Bull.*, 2001, 36, 394.
20. Dennis, H.R., Hunter, D.L., Chang, D., Kim, S., White, J.L., and Cho, J.W. Nanocomposites: the importance of processing, *Plast. Eng.*, 2001, 57, 56.
21. Zilg, C., Dietsche, F., Hoffmann, B., Dietrich, C., and Mulhaupt, R. Nanofillers based upon organophilic layered silicates, *Macromol. Symp.*, 2001, 169, 65.
22. Schamp, N. and Huylebroeck, J. Adsorption of polymers on clays, *J. Polym. Sci.*, 1973, 42, 553.
23. Bera, P. and Saha, S.K. Redox polymerization of acrylamide on aqueous montmorillonite surface: kinetics and mechanism of enhanced chain growth, *Polymer*, 1998, 39, 1461.
24. Volpert, E., Selb, J., Candau, F., Green, N., Argillier, J.F., and Audibert, A. Adsorption of hydrophobically associating polyacrylamides on clay, *Langmuir*, 1998, 14, 1870.
25. Liang, L., Liu, J., and Gong, X. Thermosensitive poly(N-isopropylacrylamide)-clay nanocomposites with enhanced temperature response, *Langmuir*, 2000, 16, 9895.
26. Gungor, N. and Karaoglan, S., Interactions of polyacrylamide polymer with bentonite in aqueous systems, *Mater. Lett.*, 2001, 48, 168.
27. (a) Graveling, G.J., Ragnarsdottir, K.V., Allen, G.C., Eastman, J., Brady, P.V., Balsley, S.D., and Skuse, D.R. Controls on polyacrylamide adsorption to quartz, kaolinite, and feldspar, *Geochim. Cosmochim. Acta*, 1997, 61, 3515. (b) Komori, Y., Sugahara, Y., and Kuroda, K. Thermal transformation of a kaolinite-poly(acrylamide) intercalation compound, *J. Mater. Chem.*, 1999, 9, 3081.
28. Muzny, C.D., Butler, B.D., Hanley, H.J.M., Tsvetkov, F., and Peiffer, D.G. Clay platelet dispersion in a polymer matrix, *Mater. Lett.*, 1996, 28, 379.

29. Billingham, J., Breen, C., and Yarwood, C. Adsorption of polyamine, polyacrylic acid and polyethylene glycol on montmorillonite: an in situ study using ATR-FTIR, *Vib. Spect.*, 1997, 14, 19.

30. Blockhaus, F., Sequaris, J.M., Narres, H.D., and Schwuger, M.J. Adsorption-desorption behavior of acrylic-maleic acid copolymer at clay minerals, *J. Coll. Interf. Sci.*, 1997, 186, 234.

31. Sequaris, J.M. Hexacyanoferrate(II) transport in coated montmorillonite clay films: effects of water-soluble polymers, *Langmuir*, 2000, 16, 1368.

32. Jarnstrom, L. and Stenius, P. Adsorption of polyacrylate and carboxy methyl cellulose on kaolinite: salt effects and competitive adsorption, *Coll. Surf.*, 1990, 50, 47.

33. Smalley, M.V., Hinnai, H., Hashimoto, T., and Koizumi, S. The effect of added polymers on n-butylammonium vermiculite swelling, *Clays Clay Miner.*, 1997, 45, 745.

34. (a) Bastow, T., Hardin, S.G., and Turney T.W. The formation of beta-sialon from a montmorillonite-polyacrylonitrile composite by carbothermal reduction, *J. Mater. Sci.*, 1991, 26, 1443. (b) Seckin, T., Gultek, A., Icduygu, M.G., and Onal, Y. Polymerization and characterization of acrylonitrile with gamma-methacry-loxypropyltrimethoxy-silane grafted bentonite clay, *J. Appl. Polym. Sci.*, 2002, 84, 164.

35. (a) Carrado, K.A. and Xu, L. In situ synthesis of polymer-clay nanocomposites from silicate gels, *Chem. Mater.*, 1998, 10, 1440. (b) Carrado, K.A., Xu, L., Seifert, S., Csencsits, R., and Bloomquist, C.A. Polymer-clay nanocomposites derived from polymer-silicate gels, in *Polymer-Clay Nanocomposites*, Pinnavaia, T.J. and Beall, G.W., Eds., New York: John Wiley & Sons, 2000, chap. 3.

36. Kato, C., Kuroda, K., and Misawa, M. Preparation of montmorillonite-nylon complexes and their thermal properties, *Clays Clay Miner.*, 1979, 27, 129.

37. Fukushima, Y. and Inagaki, S. Synthesis of an intercalated compound of mont-morillonite and 6-polyamide, *J. Inclu. Phenom.*, 1987, 5, 473.

38. Fukushima, Y., Okada, A., Kawasumi, M., Kurauchi, T., and Kamigaito, O. Swelling behaviour of montmorillonite by poly-6-amide, *Clay Miner.*, 1988, 23, 27.

39. Usuki, A., Kojima, Y., Kawasumi, M., Okada, A., Fukushima, Y., Kurauchi, T., and Kamigaito, O. Synthesis of nylon 6-clay hybrid, *J. Mater. Res.*, 1993, 8, 117.

40. Mathias, L.J., Davis, R.D., and Jarrett, W.L. Observation of α and γ crystal forms and amorphous regions of nylon 6-clay nanocomposites using solid-state ^{15}N NMR, *Macromolecules*, 1999, 32, 7958.

41. Liu, L., Qi, Z., and Zhu, X. Studies on nylon 6/clay nanocomposites by melt-intercalation process, *J. Appl. Polym. Sci.*, 1999, 71, 1133.

42. Yasue, K., Katahira, S., Yoshikawa, M., and Fujimoto, K. In situ polymerization route to nylon 6-clay nanocomposites, in *Polymer-Clay Nanocomposites*, Pinnava-ia, T.J. and Beall, G.W., Eds., New York: John Wiley & Sons, 2000, chap. 6.

43. Varlot, K., Reynaud, E., Kloppfer, M.H., Vigier, G., and Varlet, J. Clay-reinforced polyamide: preferential orientation of the montmorillonite sheets and the polyamide crystalline lamellae, *J. Polym. Sci. Polym. Phys.*, 2001, 39B, 1360.

44. Cho, J.W. and Paul, D.R. Nylon 6 nanocomposites by melt compounding, *Polymer*, 2001, 42, 1083.

45. Lincoln, D.M., Vaia, R.A., Wang, Z.G., Hsiao, G.S., and Krishnamoorti, R. Structure model for nylon 6/montmorillonite nanocomposites, *Am. Chem. Soc. Polym. Prepr.*, 2001, 42, 55.

46. Zhang, G., Li, Y., Yan, D., Yang, X., and Zhou, E. The kinetics of nylon 10 melt intercalation in montmorillonite, *Am. Chem. Soc. Polym. Prepr.*, 2001, 42, 322.
47. Fong, H., Liu, W.D., Wang, C.S., and Vaia, R.A. Generation of electrospun fibers of nylon 6 and nylon 6-montmorillonite nanocomposite, *Polymer*, 2002, 43, 775.
48. Wu, Q.J., Liu, X.H., and Berglund, L.A. An unusual crystallization behavior in polyamid 6/montmorillonite nanocomposites, *Macromol. Rapid Commun*. 2001, 22, 1438.
49. Fornes, T.D., Yoon, P.J., Keskkula, H., and Paul, D.R. Nylon 6 nanocomposites: the effect of matrix molecular weight, *Polymer*, 2001, 42, 9929.
50. Kojima, Y., Usuki, A., Kawasumi, M., Okada, A., Fukushima, Y., Kurauchi, T., and Kamigaito, O. Mechanical properties of nylon 6-clay hybrid, *J. Mater. Res.*, 1993, 8, 1185.
51. Liu, X.H., Wu, Q.J., Zhang, Q.X., Berglund, L.A., and Mo, Z.S., High temperature x-ray diffraction studies on polyamide 6 clay nanocomposites upon annealing, *Polymer Bull.*, 2002, 48, 381.
52. Yamashita, A., Takahara, A., and Kajiyama, T. Aggregation structure and fatigue characteristics of nylon 6/clay hybrid, *Composite Interf.*, 1999, 6, 247.
53. Vaia, R.A., Price, G., Ruth, P.N., Nguyen, H.T., and Lichtenhan, J. Polymer/layered silicate nanocomposites as high performance ablative materials, *Appl. Clay Sci.*, 1999, 15, 67.
54. Gilman, J.W., Jackson, C.L., Morgan, A.B., Harris, R., Manias, E., Giannelis, E.P., Wuthenow, M., Hilton, D., and Phillips, S. Flammability studies of polymer layered-silicate (clay) nanocomposites: polypropylene, polystyrene and polyamide-6, in *Flame Retard.*, London: Interscience Comm. Ltd., 2000, p. 49.
55. Dabrowski, F., Bourbigot, S., Delobel, R., and LeBras, M. Kinetic modelling of the thermal degradation of polyamide-6 nanocomposite, *Eur. Polym. J.*, 2000, 36, 273.
56. Akkapeddi, M.K. Glass fiber reinforced polyamide-6 nanocomposites, *Polym. Composites*, 2000, 21, 576.
57. Wu, S.H., Wang, F.Y., Ma, C.M., Chang, W.C., Cuo, C.T., Kuan, H.C., and Chen, W.J. Mechanical, thermal and morphological properties of glass fiber and carbon fiber reinforced polyamide-6 and polyamide-6/clay nanocomposites, *Mater. Lett.*, 2001, 49, 327.
58. Shelley, J.S., Mather, P.T., and DeVries, K.L. Reinforcement and environmental degradation of nylon-6/clay nanocomposites, *Polymer*, 2001, 42, 5849.
59. Gloaguen, J.M. and Lefebvre, J.M. Plastic deformation behaviour of thermoplastic/clay nanocomposite, *Polymer*, 2001, 42, 5841.
60. Liu, X., Wu, Q., Berglund, L.A., Fan, J., and Qi, Z.N. Polyamide 6-clay nanocomposites/polypropylene-grafted-maleic anhydride alloys, *Polymer*, 2001, 42, 8235.
61. VanderHart, D.L., Asano, A., and Gilman, J.W. NMR measurements related to clay-dispersion quality and organic-modifier stability in nylon-6/clay nanocomposites, *Macromolecules*, 2001, 34, 3819.
62. Fong, H., Vaia, R.A., Sanders, J.H., Lincoln, D., Vreugdenhil, A.J., Liu, W., Bultman, J., and Chen, C. Self-passivation of polymer-layered silicate nanocomposites, *Chem. Mater.*, 2001, 13, 4123.
63. VanderHart, D.L., Asano, A., and Gilman, J.W. Solid-state NMR investigation of paramagnetic nylon-6 clay nanocomposites: 1. Crystallinity, morphology, and direct influence of Fe^{3+} on nuclear spins, *Chem. Mater.*, 2001, 13, 3781.

64. VanderHart, D.L., Asano, A., and Gilman, J.W. Solid-state NMR investigation of paramagnetic nylon-6 clay nanocomposites: 2. Measurement of clay dispersion, crystal stratification, and stability of organic modifiers, *Chem. Mater.*, 2001, 13, 3796.

65. Usuki, A., Hasegawa, N., Kadoura, H., and Okamoto, T. Three-dimensional observation of structure and morphology in nylon-6/clay nanocomposite, *Nano Lett.*, 2001, 1, 271.

66. Lincoln, D.M., Vaia, R.A., Wang, Z.G., Hsiao, B.S., and Krishnamoorti, R. Temperatue dependence of polymer crystalline morphology in nylon 6/montmorillonite nanocomposites, *Polymer*, 2001, 42, 9975.

67. Masenelli-Varlot, K., Reynaud, E., Vigier, G., and Verlet, J. Mechanical properties of clay-reinforced polyamide, *J. Polym. Sci. Polym. Phys.*, 2002, 40B, 272.

68. Liu, X.H. and Wu, Q.J., Phase transition in nylon 6/clay nanocomposites on annealing, *Polymer*, 2002, 43, 1933.

69. Murase, S., Inoue, A., Miyashita, Y., Kimura, N., and Nishio, Y. Structural characteristics and moisture sorption behavior of nylon-6/clay hybrid films, *J. Polym. Sci. Polym. Phys.*, 2002, 40B, 479.

70. Bourbigot, S., Devaux, E., and Flambard, X. Flammability of polyamide-6/clay hybrid nanocomposite textiles, *Polym. Degrad. Stabil.*, 2002, 75, 397.

71. Wu, T.M. and Liao, C.S. Polymorphism in nylon 6/clay nanocomposites, *Macromol. Chem. Phys.*, 2000, 201, 2820.

72. Watari, T., Yamane, T., Moriyama, S., Torikai, T., Imaoka, Y., and Suehiro, K. Fabrication of (expandable mica)/nylon 6 composites, *Mater. Res. Bull.*, 1997, 32, 719.

73. Itagaki, T., Matsumura, A., Kato, M., Usuki, A., and Kuroda, K. Preparation of kaolinite-nylon 6 composites by blending nylon 6 and a kaolinite-nylon 6 intercalation compound, *J. Mater. Sci. Lett.*, 2001, 16, 1483.

74. Wu, Z.G., Zhou, C.X., Zi, R.R., and Zhang, H.B. Synthesis and characterization of nylon 10,12/clay nanocomposite, *J. Appl. Polym. Sci.*, 2002, 11, 2403.

75. Reichert, P., Kressler, J., Thomann, R., Mulhaupt, R., and Stoppelmann, G. Nanocomposites based on a synthetic layer silicate and polyamide-12, *Acta Polym.*, 1998, 49, 116.

76. (a) Hoffmann, B., Kressler, J., Stoppelmann, G., Friedrich, C., and Kim, G.M. Rheology of nanocomposites based on layered silicates and polyamide-12, *Coll. Polym. Sci.*, 2000, 278, 629. (b) Kim, G.M., Lee, D.H., Hoffmann, B., Kressler, J., and Stoppelmann, G. Influence of nanofillers on the deformation process in layered silicate/polyamide-12 nanocomposites, *Polymer*, 2001, 42, 1095.

77. Wu, Q., Zue, Z., Qi, Z., and Wang, F. Synthesis and characterization of PAN/clay nanocomposite with extended chain conformation of polyaniline, *Polymer*, 2000, 41, 2029.

78. Frisch, H.L., Zi, B.W., Qin, Y.C., Failovich, M., Yang, N.L., and Yan, X.Z. Synthesis and characterization of a conductive polyaniline/clay hybrid system, *High Perform. Polym.*, 2000, 12, 543.

79. Ilic, M., Koglin, E., Pohlmeier, A., Narres, H.D., and Schwuger, M.J. Adsorption and polymerization of aniline on Cu(II)-montmorillonite: vibrational spectroscopy and ab initio calculation, *Langmuir*, 2000, 16, 8946.

80. Yeh, J.M., Liou, S.J., Lai, C.Y., and Wu, P.C. Enhancement of corrosion protection effect in polyaniline via the formation of polyaniline-clay nanocomposite materials, *Chem. Mater.*, 2001, 13, 1131.

81. Feng, B., Su, Y.Z., Song, J.H., and Kong, K.C. Electropolymerization of polyaniline/montmorillonite nanocomposite, *J. Mater. Sci. Lett.*, 2001, 20, 293.
82. Kim, J.W., Kim, S.G., Choi, H.J., Suh, M.S., Shin, M.J., and Jhon, M.S. Synthesis and electrorheological characterization of polyaniline and Na-montmorillonite clay nanocomposite, *Int. J. Mod. Phys.*, 2001, 15B, 657.
83. Kim, B.H., Jung, J.H., Joo, J., Kim, J.W., and Choi, H.J. Charge transport and structure of nanocomposites of polyaniline and inorganic clay, *J. Kor. Phys. Soc.*, 2000, 36, 366.
84. Kim, B.H., Jung, J.H., Kim, J.W., Choi, H.J., and Joo, J. Effect of dopant and clay on nanocomposites of polyaniline intercalated into Na-montmorillonite, *Synth. Metals*, 2001, 121, 1311.
85. Kim, B.H., Jung, J.H., Hong, S.H., Joo, J., Epstein, A.J., Mizoguchi, K., Kim, J.W., and Choi, H.J. Nanocomposite of polyaniline and Na-montmorillonite clay, *Macromolecules*, 2002, 35, 1419.
86. Orata, D. and David, S.K. A comparative study of the electrochemical/electrodegradation of polyaniline from aniline loaded in a clay mineral/polyaniline composite matrix, *React. Funct. Polym.*, 2000, 43, 133.
87. Dai, L.M., Wang, Q., and Wan, M.X. Direct observation of conformational transitions for polyaniline chains intercalated in clay particles upon secondary doping, *J. Mater. Sci. Lett.*, 2000, 19, 1645.
88. Kim, B.H., Jung, J.H., Kim, J.W., Choi, H.J., and Joo, J. Physical characterization of polyaniline-Na-montmorillonite nanocomposite intercalated by emulsion polymerization, *Synth. Metals*, 2001, 117, 115.
89. Park, J.H., Lim, Y.T., and Park, O.O. New approach to enhance the yield stress of electro-rheological fluids by polyaniline-coated layered silicate nanocomposites, *Macromol. Rapid Commun.*, 2001, 22, 616.
90. Lim, Y.T., Park, J.H., and Park, O.O. Improved electrorheological effect in polyaniline nanocomposite suspensions, *J. Coll. Interf. Sci.*, 2002, 245, 198.
91. (a) Mehrotra, V. and Giannelis, E.P. Metal-insulator molecular multilayers of electroactive polymers: intercalation of polyaniline in mica-type layered silicates, *Solid State Commun.*, 1991, 77, 155. (b) Uemura, S., Yoshie, M., Kobayashi, N., and Nakahira, T. Photopolymerization of aniline dimer by photocatalytic reaction of ruthenium trisbipyridyl in the interlayer of hectorite clay, *Polym. J.*, 2000, 32, 987.
92. Jimenez, G., Ogata, N., Kawai, H., and Ogihara, T. Structure and thermal/mechanical properties of poly(ε-caprolactone)-clay blend, *J. Appl. Polym. Sci.*, 1997, 64, 2211.
93. (a) Messersmith, P.B. and Giannelis, E.P. Polymer-layered silicate nanocomposites: in situ intercalative polymerization of ε-caprolactone in layered silicates, *Chem. Mater.*, 1993, 5, 1064. (b) Messersmith, P.B. and Giannelis, E.P. Synthesis and barrier properties of poly(ε-caprolactone)-layered silicate nanocomposites, *J. Polym. Sci. Polym. Chem.*, 1995, 33A, 1047.
94. (a) Burnside, S.D. and Giannelis, E.P. Synthesis and properties of new poly(dimethylsiloxane) nanocomposites, *Chem. Mater.*, 1995, 7, 1597. (b) Xu, S.H. Hydrolysis of poly(dimethylsiloxanes) on clay minerals as influenced by exchangeable cations and moisture, *Environ. Sci. Technol.*, 1998, 32, 3162. (c) Takeuchi, H. and Cohen, C. Reinforcement of poly(dimethylsiloxane) elastomers by chain-end anchoring to clay particles, *Macromolecules*, 1999, 32, 6792.
95. LeBaron, P.C. and Pinnavaia, T.J. Clay nanolayer reinforcement of a silicone elastomer, *Chem. Mater.*, 2001, 13, 3760.

96. (a) Morgan, A.B., Gilman, J.W., and Jackson, C.L. Characterization of the dispersion of clay in a polyetherimide nanocomposite, *Macromolecules*, 2001, 34, 2735. (b) Huang, J.C., Zhu, Z.K., Yin, J., Qian, X.F., and Sun, Y.Y. Poly(etherimide)/montmorillonite nanocomposites prepared by melt intercalation: morphology, solvent resistance and thermal properties, *Polymer*, 2001, 42, 873.
97. Jeon, H.G., Jung, H.T., Lee, S.W., and Hudson, S.D. Morphology of polymer-silicate nanocomposites: high density polyethylene and a nitrile copolymer, *Polym. Bull.*, 1998, 41, 107.
98. Wang, K.H., Xu, M., Choi, Y.S., and Chung, I.J. Effect of aspect ratio of clay on melt extensional process of maleated polyethylene/clay nanocomposites, *Polym. Bull.*, 2001, 46, 499.
99. Jin, Y.H., Park, H.J., Im, S.S., Kwak, S.Y., and Kwak, S. Polyethylene/clay nanocomposite by in situ exfoliation of montmorillonite during Ziegler-Natta polymerization of ethylene, *Macromol. Rapid Commun.*, 2002, 23, 135.
100. Wang, J., Liu, Z.Y., Guo, C.Y., Chen, Y.J., and Wang, D. Preparation of a PE/MT composite by copolymerization of ethylene with in situ produced ethylene oligomers under a dual functional catalyst system intercalated into MT layer, *Macromol. Rapid Commun.*, 2001, 22, 1422.
101. Wang, K.H., Choi, M.H., Koo, C.M., Choi, Y.S., and Chung, I.J. Synthesis and characterization of maleated polyethylene/clay nanocomposites, *Polymer*, 2001, 42, 9819.
102. Liao, B., Song, M., Liang, H.J., and Pang, Y.X. A study of PEO/Na-montmorillonite nanocomposites as polyelectrolytes and PE-PEG copolymer/Na-montmorillonite nanocomposites as fillers for reinforcement of polyethylene, *Polymer*, 2001, 42, 10007.
103. Rong, J.F., Li, H.Q., Jing, Z.H., Hong, X.Y., and Shing, M. Novel organic/inorganic nanocomposite of polyethylene: 1. Preparation via an in situ polymerization approach, *J. Appl. Polym. Sci.*, 2001, 82, 1829.
104. Ruiz-Hitzky, E. and Aranda, P. Polymer-salt intercalation complexes in layer silicates, *Adv. Mater.*, 1990, 2, 545.
105. Aranda, P. and Ruiz-Hitzky, E. Poly(ethylene oxide)-silicate intercalation materials, *Chem. Mater.*, 1992, 4, 1395.
106. Vaia, R.A., Vasudevan, S., Krawiec, W., Scanlon, L.G., and Giannelis, E.P. New polymer electrolyte nanocomposites: melt intercalation of poly(ethylene oxide) in mica-type silicates, *Adv. Mater.*, 1995, 7, 154.
107. Ruiz-Hitzky, E., Aranda, P., Casal, B., and Galvan, J.C. Nanocomposite materials with controlled ion mobility, *Adv. Mater.*, 1995, 7, 180.
108. Ogata, N., Kawakage, S., and Ogihara, T. Poly(vinyl alcohol)-clay and poly(ethylene oxide)-clay blends prepared using water as a solvent, *J. Appl. Polym. Sci.*, 1997, 66, 573.
109. Aranda, P., Galvan, J.C., and Ruiz-Hitzky, E. Microwave assisted blending: intercalation of ion-conductor polymers into layered silicates, *Mater. Res. Soc. Symp. Proc.*, 1998, 519, 375.
110. Aranda, P. and Ruiz-Hitzky, E. Poly(ethylene oxide)/NH_4^+-smectite nanocomposites, *Appl. Clay Sci.*, 1999, 15, 119.
111. Bujdak, J., Hackett, E., and Giannelis, E.P. Effect of layer charge on the intercalation of poly(ethylene oxide) in layered silicates: implications on nanocomposite polymer electrolytes, *Chem. Mater.*, 2000, 12, 2168.

112. Choi, H.J., Kim, S.G., Hyun, Y.H., and Jhon, M.S. Preparation and rheological characteristics of solvent-cast poly(ethylene-oxide)/montmorillonite nanocomposites, *Macro. Rapid Commun.*, 2001, 22, 320.

113. Wu, J. and Lerner, M.M. Structural, thermal, and electrical characterization of layered nanocomposites derived from Na-montmorillonite and polyethers, *Chem. Mater.*, 1993, 5, 835.

114. Wong, S., Vaia, R.A., Giannelis, E.P., and Zax, D.B. Dynamics in a poly(ethylene oxide)-based nanocomposite polymer electrolyte probed by solid state NMR, *Solid State Ionics*, 1996, 86, 547.

115. Vaia, R.A., Sauer, B.B., Tse, O.K., and Giannelis, E.P. Relaxations of confined chains in polymer nanocomposites: glass transition properties of poly(ethylene oxide) intercalated in montmorillonite, *J. Polym. Sci. Polym. Phys.*, 1997, 35B, 59.

116. (a) Doeff, M.M. and Reed, J.S. Li ion conductors based on laponite/poly(ethylene oxide) composites, *Solid State Ionics*, 1998, 115, 109. (b) Harris, D.J., Bonagamba, T.J., and Schmidt-Rohr, K. Conformation of poly(ethylene oxide) intercalated in clay and MoS2 studied by two-dimensional double-quantum NMR, *Macromolecules*, 1999, 32, 6718.

117. Swenson, J., Smalley, M.V., Hatharasinghe, H.L.M., and Fragneto, G. Interlayer structure of a clay-polymer-salt-water system, *Langmuir*, 2001, 17, 3813.

118. Hecht, E. and Hoffmann, H. Adsorption of EOxPOyEOx block copolymers onto saponite, *Tensile Surf. Det.*, 1998, 35, 185.

119. Ke, Y.C., Long, C.F., and Qi, Z.N. Crystallization, properties, and crystal and nanoscale morphology of PET-clay nanocomposites, *J. Appl. Polym. Sci.*, 1999, 71, 1139.

120. Tsai, T.Y. Polyethylene terephthalate-clay nanocomposites, in *Polymer-Clay Nanocomposites*, Pinnavaia, T.J. and Beall, G.W., Eds., New York: John Wiley & Sons, 2000, chap. 9.

121. Imai, Y., Nishimura, S., Abe, E., Tateyama, H., Akimasa, A., Yamaguchi, A., Aoyama, T., and Taguchi, H. High-modulus poly(ethylene terephthalate)/expandable fluorine mica nanocomposites with a novel reactive compatibilizer, *Chem. Mater.*, 2002, 14, 477.

122. Chang, J.H. and Park, D.K. Nanocomposites of poly(ethylene terephthalate-co-ethylene napththalate) with organoclay, *J. Polym Sci. Polym. Phys.*, 2001, 39B, 2581.

123. Li, X.C., Kang, T.Y., Cho, W.J., Lee, J.K., and Ha, C.S. Preparation and characterization of poly(butylene terephthalate)/organoclay nanocomposite, *Macromol. Rapid Commun.*, 2001, 22, 1306.

124. Matayabas, J.C. and Turner, S.R. Nanocomposite technology for enhancing the gas barrier of polyethylene terephthalate, in *Polymer-Clay Nanocomposites*, Pinnavaia, T.J. and Beall, G.W., Eds., New York: John Wiley & Sons, 2000, chap. 11.

125. Lan, T., Kaviratna, P.D., and Pinnavaia, T.J. On the nature of polyimide-clay hybrid composites, *Chem. Mater.*, 1994, 6, 573.

126. Pinnavaia, T.J., Lan, T., Kaviratna, P.D., and Wang, M.S. Clay-polymer nanocomposites: polyether and polyimide systems, *Mater. Res. Soc. Symp. Proc.*, 1994, 346, 81.

127. Yano, K., Usuki, A., and Okada, A. Synthesis and properties of polyimide-clay hybrid films, *J. Polym. Sci. Polym. Chem.*, 1997, 11A, 2289.

128. Zhu, Z.K., Yang, Y., Yin, J., Wang, X.Y., Ke, Y.C., and Qi, Z.N. Preparation and properties of organosoluble montmorillonite/polyimide hybrid materials, *J. Appl. Polym. Sci.*, 1999, 73, 2063.

129. Tyan, H.L., Liu, Y.C., and Wei, K.H. Enhancement of imidization of poly(amic acid) through forming poly(amic acid)/organoclay nanocomposites, *Polymer*, 1999, 40, 4877.
130. Tyan, H.L., Liu, Y.C., and Wei, K.H. Thermally and mechanically enhanced clay/polyimide nanocomposite via reactive organoclay, *Chem. Mater.*, 1999, 11, 1942.
131. Yang, Y., Zhu, Z.K., Yin, J., Wang, X.Y., and Qi, Z.E. Preparation and properties of hybrids of organo-soluble polyimide and montmorillonite with various chemical surface modification methods, *Polymer*, 1999, 40, 4407.
132. Gu, A.J. and Chang, F.C. A novel preparation of polyimide/clay hybrid films with low coefficient of thermal expansion, *J. Appl. Polym. Sci.*, 2001, 79, 289.
133. Tyan, H.L., Leu, C.M., and Wei, K.H. Effect of reactivity of organic-modified montmorillonite on the thermal and mechanical properties of montmorillonite/polyimide nanocomposites, *Chem. Mater.*, 2001, 13, 222.
134. Huang, J.C., Zhu, Z.K., Ma, X.D., Qian, X.F., and Yin, J. Preparation and properties of montmorillonite organo-soluble polyimide hybrid materials prepared by a one-step approach, *J. Mater. Sci.*, 2001, 36, 871.
135. Hsiao, S.H., Liou, G.S., and Chang, L.M. Synthesis and properties of organo-soluble polyimide/clay hybrids, *J. Appl. Polym. Sci.*, 2001, 80, 2067.
136. Gu, A., Kuo, S.W., and Chang, F.C. Syntheses and properties of PI/clay hybrids, *J. Appl. Polym. Sci.*, 2001, 79, 1902.
137. Delozier, D.M., Orwoll, R.A., Cahoon, J.F., Johnston, N.J., Smith, J.G., and Connell, J.W. Preparation and characterization of polyimide/organoclay nanocomposites, *Polymer*, 2002, 43, 813.
138. Chang, J.H., Park, K.M., Cho, D.H., Yang, H.S., and Ihn, K.J. Preparation and characterization of polyimide nanocomposites with different organo-montmorillonites, *Polym. Eng. Sci.*, 2001, 41, 1514.
139. Tyan, H.L., Wei, K.H., and Hsieh, T.E. Mechanical properties of clay-polyimide (BTDA-ODA) nanocomposites via ODA-modified organoclay, *J. Polym. Sci. Polym. Phys.*, 2000, 38B, 2873.
140. Agag, T., Koga, T., and Takeichi, T. Studies on thermal and mechanical properties of polyimide-clay nanocomposites, *Polymer*, 2001, 42, 3399.
141. Magaraphan, R., Lilayuthalert, W., Sirivat, A., and Schwank, J.W. Preparation, structure, properties and thermal behavior of rigid-rod polyimide/montmorillonite nanocomposites, *Composite Sci. Technol.*, 2001, 61, 1253.
142. Tyan, H.L., Wu, C.Y., and Wei, K.H. Effect of montmorillonite on thermal and moisture absorption properties of polyimide of different chemical structures, *J. Appl. Polym. Sci.*, 2001, 81, 1742.
143. Chang, J.H. and Park, K.M. Polyimide nanocomposites: comparison of their properties with precursor polymer nanocomposites, *Polym. Eng. Sci.*, 2001, 41, 2226.
144. Chen, G.H., Chen, X.Q., Lin, Z.Y., Ye, W., and Yao, K.D. Preparation and properties of PMMA/clay nanocomposite, *J. Mater. Sci. Lett.*, 1999, 18, 1761.
145. Limary, R., Swinnea, S., and Green, P.F. Stability of diblock copolymer/layered silicate nanocomposite thin films, *Macromolecules*, 2000, 33, 5227.
146. Dietsche, F., Thomann, Y., Thomann, R., and Mulhaupt, R. Translucent acrylic nanocomposites containing anisotropic laminated nanoparticles derived from intercalated layered silicates, *J. Appl. Polym. Sci.*, 2000, 75, 396.

147. Okamoto, M., Morita, S., Taguchi, H., Kim, Y.H., Kotaka, T., and Tateyama, H. Synthesis and structure of smectic clay/poly(methyl methacrylate) and clay/polystyrene nanocomposites via in situ intercalative polymerization, *Polymer*, 2000, 41, 3887.

148. Tabtiang, A., Lumlong, S., and Venables, R.A. The influence of preparation method upon the structure and relaxation characteristics of poly(methyl methacrylate)/clay composites, *Eur. Polym. J.*, 2000, 36, 2559.

149. Salahuddin, N. and Shehata, M. Polymethylmethacrylate-montmorillonite composites: preparation, characterization and properties, *Polymer*, 2001, 42, 8379.

150. Okamoto, M., Morita, S., Kim, Y.H., Kotaka, T., and Tateyama, H. Dispersed structure change of smectic clay/poly(methyl methacrylate) nanocomposites by copolymerization with polar comonomers, *Polymer*, 2001, 42, 1201.

151. Huang, X.Y. and Brittain, W.J. Synthesis and characterization of PMMA nanocomposites by suspension and emulsion polymerization, *Macromolecules*, 2001, 34, 3255.

152. Zeng, C.C. and Lee, J. Poly(methyl methacrylate) and polystyrene/clay nanocomposites prepared by in situ polymerization, *Macromolecules*, 2001, 34, 4098.

153. Gao, Z., Xie, W., Hwu, J.M., Wells, L., and Pan, W.P. The characterization of organic modified montmorillonite and its filled PMMA nanocomposite, *J. Thermal Anal. Calor.*, 2001, 64, 467.

154. Choi, Y.S., Choi, M.H., Wang, K.H., Kim, S.O., Kim, Y.K., and Chung, I.J. Synthesis of exfoliated PMMA/Na-MMT nanocomposites via soap-free emulsion polymerization, *Macromolecules*, 2001, 34, 8978.

155. Meneghetti, P. and Qutubuddin, S. Synthesis of poly(methyl methacrylate)-clay nanocomposites, *Chem. Eng. Commun.*, 2001, 188, 81.

156. Yeh, J.M., Liou, S.J., Lin, C.Y., Cheng, C.Y., Chang, Y.W., and Lee, K.R. Anticorrosively enhanced PMMA-clay nanocomposite materials with quaternary alkylphosphonium salt as an intercalating agent, *Chem. Mater.*, 2002, 14, 154.

157. Wang, H.M., Mei, M.H., Jiang, J.C., Li, Q.S., Zhang, X.H., and Wu, S.K. A study on the preparation of polymer/montmorillonite nanocomposite materials by photo-polymerization, *Polym. Int.*, 2002, 51, 7.

158. Chen, G.H., Yao, K.D., and Zhao, J.T. Montmorillonite clay/poly(methyl methacrylate) hybrid resin and its barrier property to the plasticizer within poly(vinyl chloride) composite, *J. Appl. Polym. Sci.*, 1999, 73, 425.

159. Dietsche, F. and Mulhaupt, R. Thermal properties and flammability of acrylic nanocomposites based upon organophilic layered silicates, *Polym. Bull.*, 1999, 43, 395.

160. Tabtiang, A., Lumlong, S., and Venables, R.A. Effects of shear and thermal history on the microstructure of solution polymerized poly(methyl methacrylate)-clay composites, *Polym. Plast. Technol. Eng.*, 2000, 39, 293.

161. Okamoto, M., Morita, S., and Kotaka, T. Dispersed structure and ionic conductivity of smectite clay/polymer nanocomposites, *Polymer*, 2001, 42, 2685.

162. Dortmans, A., Fischer, H., Batenburg, L., and Dominicus-van der Acker, M. Reinforcement of a porous PMMA filter material by nanodispersed clay, *Adv. Eng. Mater.*, 2001, 3, 717.

163. Hwu, J.Y., Jiang, G.J., Gao, Z.M., Xie, W., and Pan, W.P. The characterization of organic modified clay and clay-filled PMMA nanocomposites, *J. Appl. Polym. Sci.*, 2002, 83, 1702.

164. Salahuddin, N. and Shehata, M.M. Reduction of polymerization shrinkage in methyl methacrylate-montmorillonite composites, *Mater. Lett.*, 2002, 52, 289.

165. Eastman, M.P., Bain, E., Porter, T.L., Manygoats K., Whitehorse, R., Parnell, R.A., and Hagerman, M.E. The formation of poly(methyl methylacrylate) on transition metal-exchanged hectorite, *Appl. Clay Sci.*, 1999, 15, 173.

166. Oriakhi, C.O., Zhang, X., and Lerner, M.M. Synthesis and luminescence properties of a poly(p-phenylenevinylene)/montmorillonite layered nanocomposite, *Appl. Clay Sci.*, 1999, 15, 109.

167. Winkler, B., Dai, L., and Mau, A.W.H. Organic-inorganic hybrid light-emitting composites: poly(p-phenylene vinylene) intercalated clay nanoparticles, *J. Mater. Sci. Lett.*, 1999, 18, 1539.

168. (a) Lee, T.W., Park, O.O., Yoon, J., and Kim, J.J. Polymer-layered silicate nanocomposite light-emitting devices, *Adv. Mater.*, 2001, 13, 211. (b) Lee, T.W., Park, O.O., Kim, J.J., Hong, J.M., and Kim, Y.C. Efficient photoluminescence and electroluminescence from environmentally stable polymer/clay nanocomposites, *Chem. Mater.*, 2001, 13, 2217.

169. Usuki, A., Kato, M., Okada, A., and Kurauchi, T. Synthesis of polypropylene-clay hybrid, *J. Appl. Polym. Sci.*, 1997, 63, 137.

170. Kato, M., Usuki, A., and Okada, A. Synthesis of polypropylene oligomer-clay intercalation compounds, *J. Appl. Polym. Sci.*, 1997, 66, 1781.

171. Kawasumi, M., Hasegawa, N., Kato, M., Usuki, A., and Okada, A. Preparation and mechanical properties of polypropylene-clay hybrids, *Macromolecules*, 1997, 30, 6333.

172. Walter, P., Mader, D., Reichert, P., and Mulhaupt, R. Novel polypropylene materials, *J. Macromol. Sci. Pure Appl. Chem.*, 1999, A36, 1613.

173. Lee, J.W., Lim, Y.T., and Park, O.O. Thermal characteristics of organoclay and their effects upon the formation of polypropylene/organoclay nanocomposites, *Polym. Bull.*, 2000, 45, 191.

174. Hasegawa, N., Okamoto, H., Kato, M., and Usuki, A. Preparation and mechanical properties of polypropylene-clay hybrids based on modified polypropylene and organophilic clay, *J. Appl. Polym. Sci.*, 2000, 78, 1918.

175. Oya, A. Polypropylene-clay nanocomposites, in *Polymer-Clay Nanocomposites*, Pinnavaia, T.J. and Beall, G.W., Eds., New York: John Wiley & Sons, 2000, chap. 8.

176. Oya, A., Kurokawa, Y., and Yasuda, H. Factors controlling mechanical properties of clay mineral/polypropylene nanocomposites, *J. Mater. Sci.*, 2000, 35, 1045.

177. Reichert, P., Nitz, H., Klinke, S., Thomann, R., Brandsch, R., Zilg, C., and Mulhaupt, R. Polypropylene nanocomposites based upon organophilic layered silicates, *Polym. Mater. Sci. Eng.*, 2000, 82, 251.

178. Manias, E., Touny, A., Wu, L., Strawhecker, K., Lu, B., and Chung, T.C. Polypropylene/montmorillonite nanocomposites: review of the synthetic routes and materials properties, *Chem. Mater.*, 2001, 13, 3516.

179. Nam, P.H., Maiti, P., Okamot, M., Kotaka, T., Hasegawa, N., and Usuki, A. A hierarchical structure and properties of intercalated polypropylene/clay nanocomposites, *Polymer*, 2001, 42, 9633.

180. Okamoto, M., Nam, P.H., Maiti, P., Kotaka, T., Hasegawa, N., and Usuki, A. A house of cards structure in polypropylene/clay nanocomposites under elongational flow, *Nano Lett.*, 2001, 1, 295.

181. Okamoto, M., Nam, P.H., Maiti, P., Kotka, T., Nakayama, T., Takada, M., Ohshima, M., Usuki, A., Hasegawa, N., and Okamoto, H. Biaxial flow-induced alignment of silicate layers in polypropylene/clay nanocomposite foam, *Nano Lett.*, 2001, 1, 503.

182. Ma, J.S., Qi, Z.N., and Hum Y.L. Synthesis and characterization of polypropylene/clay nanocomposites, *J. Appl. Polym. Sci.*, 2001, 82, 3611.

183. Liu, X.H. and Wu, Q.J. PP/clay nanocomposites prepared by grafting-melt intercalation, *Polymer*, 2001, 42, 10013.

184. Ma, J.S., Zhang, S.M., Qi, Z.N., Li, G., and Hu, Y.L. Crystallization behaviors of polypropylene/montmorillonite nanocomposites, *J. Appl. Polym. Sci.*, 2002, 83, 1978.

185. Sun, T. and Garces, J.M. High-performance polypropylene-clay nanocomposites by in situ polymerization with metallocene/clay catalysts, *Adv. Mater.*, 2002, 14, 128.

186. Gilman, J.W., Jackson, C.L., Morgan, A.B., Harris, R., Manias, E., Giannelis, E.P., Wuthenow, M., Hilton, D., and Phillips, S.H. Flammability properties of polymer-layered-silicate nanocomposites: polypropylene and polystyrene, *Chem. Mater.*, 2000, 12, 1866.

187. Solomon, M.J., Almusallam, A.S., Seefeldt, K.F., Somwangthanaroj, A., and Varadan, P. Rheology of polypropylene/clay hybrid materials, *Macromolecules*, 2001, 34, 1864.

188. Hambir, S., Bulakh, N., Kodgire, R., Kalgaonkar, R., and Jog, J.P. PP/clay nanocomposites: a study of crystallization and dynamic mechanical behavior, *J. Polym. Sci. Polym. Phys.*, 2001, 39B, 446.

189. Kodgire, P., Kalgaonkar, R., Hambir, S., Bulakh, N., and Jog, J.P. PP/clay nanocomposites: effect of clay treatment on morphology and dynamic mechanical properties, *J. Appl. Polym. Sci.*, 2001, 81, 1786.

190. Kim, K.N., Kim, H., and Lee, J.W. Effect of interlayer structure, matrix viscosity and composition of a functionalized polymer on the phase structure of polypropylene-montmorillonite nanocomposite, *Polym. Eng. Sci.*, 2001, 41, 1963.

191. Zanetti, M., Camino, G., Canavese, D., Morgan, A.B., Lamelas, F.J., and Wilkie, C.A. Fire retardant halogen-antimony-clay synergism in polypropylene layered silicate nanocomposites, *Chem. Mater.*, 2002, 14, 189.

192. Xu, W.B., Ge, M.L., and He, P.S. Nonisothermal crystallization kinetics of PP/montmorillonite nanocomposites, *J. Polym. Sci. Polym. Phys.*, 2002, 40B, 408.

193. Tidjani, A. and Wilkie, C.A. Photooxidation of polymeric-inorganic nanocomposites: chemical, thermal stability and fire retardancy investigations, *Polym. Degrad. Stabil.*, 2001, 74, 33.

194. Reichert, P., Nitz, H., Klinke, S., Brandsch, R., Thomann, R., and Mulhaupt, R. Poly(propylene)/organoclay nanocomposite formation: influence of compatibilizer functionality and organoclay modification, *Macromol. Mater. Eng.*, 2000, 275, 8.

195. Tjong, S.C., Meng, Y.Z., and Jay, A.S. Novel preparation and properties of polypropylene-vermiculite nanocomposites, *Chem. Mater.*, 2002, 42, 44.

196. Kato, C., Kuroda, K., and Takahara, H. Preparation and electrical properties of quaternary ammonium montmorillonite-polystyrene complexes, *Clays Clay Miner.*, 1981, 29, 294.

197. Vaia, R.A., Ishii, H., and Giannelis, E.P. Synthesis and properties of two-dimensional nanostructures by direct intercalation of polymer melts in layered silicates, *Chem. Mater.*, 1993, 5, 1694.

198. Doh, J.G. and Cho, I. Synthesis and properties of polystyrene-organoammonium montmorillonite hybrid, *Polym. Bull.*, 1998, 41, 511.
199. Laus, M., Camerani, M., Lelli, M., Sparnacci, K., Sandrolini, F., and Francescangli, O. Hybrid nanocomposites based on polystyrene and a reactive organophilic clay, *J. Mater. Sci.*, 1998, 33, 2883.
200. Noh, M.W. and Lee, D.C. Synthesis and characterization of PS-clay nanocomposite by emulsion polymerization, *Polym. Bull.*, 1999, 42, 619.
201. Weimer, M.W., Chen, H., Giannelis, E.P., and Sogah, D.Y. Direct synthesis of dispersed nanocomposites by in situ living free radical polymerization using a silicate-anchored initiator, *J. Am. Chem. Soc.*, 1999, 121, 1615.
202. Chen, G.M., Liu, S.H., Zhang, S.F., and Qi, Z.N. Self-assembly in a polystyrene/montmorillonite nanocomposite, *Macromol. Rapid Commun.*, 2000, 21, 746.
203. Jung, M., German, A.L., and Fischer, H.R. Polymerization in supported bilayers, *Coll. Polym. Sci.*, 2000, 278, 1114.
204. Fu, X. and Qutubuddin, S. Polymer-clay nanocomposites: exfoliation of organophilic montmorillonite nanolayers in polystyrene, *Polymer*, 2001, 42, 807.
205. Wu, H.D., Tseng, C.R., and Chang, F.C. Chain conformation and crystallization behavior of the syndiotactic polystyrene nanocomposites studied using FTIR, *Macromolecules*, 2001, 34, 2992.
206. Park, C.I., Park, O.O., Lim, J.G., and Kim, H.J. The fabrication of syndiotactic polystyrene/organophilic clay nanocomposites and their properties, *Polymer*, 2001, 42, 7465.
207. Ko, M.B. and Jho, J.Y. Ion exchange reaction in preparation of clay-dispersed polystyrene nanocomposite by emulsion polymerization-coagulation technique, *Polym. Bull.*, 2001, 46, 315.
208. Tseng, C.R., Lee, N.Y., and Chang, F.C. Crystallization kinetics and behavior of syndiotactic polystyrene/clay nanocomposites, *J. Polym. Sci.*, 2001, 39B, 2097.
209. Zhou, Q., Fan, X., Xia, C., Mays, J., and Advincula, R. Living anionic surface initiated polymerization of styrene from clay surfaces, *Chem. Mater.*, 2001, 13, 2465.
210. Zhu, J., Uhl, F.M., Morgan, A.B., and Wilkie, C.A. Studies on the mechanism by which the formation of nanocomposites enhances thermal stability, *Chem. Mater.*, 2001, 13, 4649.
211. Tseng, C.R., Wu, J.Y., Lee, H.Y., and Chang, F.C. Preparation and crystallization behavior of syndiotactic polystyrene-clay nanocomposites, *Polymer*, 2001, 42, 10063.
212. Hasegawa, N., Okamoto, H., Kawasumi, M., and Usuki, A. Preparation and mechanical properties of polystyrene-clay hybrids, *J. Appl. Polym. Sci.*, 1999, 74, 3359.
213. Chen, G.M., Qi, Z.N., and Shen, D.Y. Shear-induced ordered structure in polystyrene/clay nanocomposite, *J. Mater. Res.*, 2000, 15, 351.
214. Zhu, J. and Wilkie, C.A. Thermal and fire studies on polystyrene-clay nanocomposites, *Polym. Int.*, 2000, 49, 1158.
215. Yoon, J.T., Jo, W.H., Lee, N.S., and Ko, M.B. Effects of comonomers and shear on the melt intercalation of styrenics/clay nanocomposites, *Polymer*, 2001, 42, 329.
216. Chen, G.M., Liu, S.H., Chen, S.J., and Qi, Z.N. FTIR spectra, thermal properties, and dispersibility of a polystyrene/montmorillonite nanocomposite, *Macromol. Chem. Phys.*, 2001, 202, 1189.

217. Zhu, J., Morgan, A.B., Lamelas, F.J., and Wilkie, C.A. Fire properties of polystyrene-clay nanocomposites, *Chem. Mater.*, 2001, 13, 3774.

218. Fan, J.Q., Liu, S.H., Chen, G.M., and Qi, Z.N. SEM study of a polystyrene/clay nanocomposite, *J. Appl. Polym. Sci.*, 2002, 83, 66.

219. (a) Vaia, R.A., Jandt, K.D., Kramer, E.J., and Giannelis, E.P. Microstructural evolution of melt intercalated polymer-organically modified layered silicate nanocomposites, *Chem. Mater.*, 1996, 8, 2628. (b) Porter, T.L., Haterman, M.E., Reynolds, B.P., Eastman, M.P., and Parnell, R.A. Inorganic/organic host-guest materials: surface and interclay reactions of styrene with copper(II)-exchanged hectorite, *J. Polym. Sci. Polym. Phys.*, 1998, 36B, 673.

220. Hoffmann, B., Dietrich, C., Thomann, R., Friedrich, C., and Mulhaupt, R. Morphology and rheology of polystyrene nanocomposites based upon organoclay, *Macromol. Rapid Commun.*, 2000, 21, 57.

221. Laus, M., Francescangeli, O., and Sandrolini, F. New hybrid nanocomposites based on an organophilic clay and poly(styrene-b-butadiene) copolymers, *J. Mater. Res.*, 1997, 12, 3134.

222. Noh, M.H., Jang, L.W., and Lee, D.C. Intercalation of styrene-acrylonitrile copolymer in layered silicate by emulsion polymerization, *J. Appl. Polym. Sci.*, 1999, 74, 179.

223. Dai, J.C. and Huang, J.T. Surface modification of clays and clay-rubber composite, *Appl. Clay Sci.*, 1999, 15, 51.

224. Zhang, L.Q., Wang, Y.Z., Wang, Y.Q., Sui, Y., and Yu, D.S. Morphology and mechanical properties of clay/styrene-butadiene rubber nanocomposites, *J. Appl. Polym. Sci.*, 2000, 78, 1873.

225. Wang, Y.Z., Zhang, L.W., Tang, C.H., and Yu, D.S. Preparation and characterization of rubber-clay nanocomposites, *J. Appl. Polym. Sci.*, 2000, 78, 1879.

226. Ko, M.B. Effects of acrylonitrile content on the properties of clay-dispersed poly(styrene-co-acrylonitrile) copolymer nanocomposites, *Polym. Bull.*, 2000, 45, 183.

227. Kim, J.W., Noh, M.H., Choi, H.J., Lee, D.C., and Jhon, M.S. Synthesis and electrorheological characteristics of SAN-clay composite suspensions, *Polymer*, 2000, 41, 1229.

228. Jang, L.W., Kang, C.M., and Lee, D.C. A new hybrid nanocomposite prepared by emulsion copolymerization of ABS in the presence of clay, *J. Polym. Sci. Polym. Phys.*, 2001, 39B, 719.

229. Kim, S.W., Jo, W.H., Lee, M.S., Ko, M.B., and Jho, J.Y. Preparation of clay-dispersed poly(styrene-co-acrylonitrile) nanocomposites using poly(ε-caprolactone) as a compatibilizer, *Polymer*, 2001, 42, 9837.

230. Lee, S.S., Lee, C.S., Kim, M.H., Kwak, S.Y., Park, M., Lim, S., Choe, C.R., and Kim, J. Specific interaction governing the melt intercalation of clay with poly(styrene-co-acrylonitrile) copolymers, *J. Polym. Sci. Polym. Phys.*, 2001, 39B, 2430.

231. Vu, Y.T., Mark, J.E., Pham, L.H., and Engelhardt, M. Clay nanolayer reinforcement of cis-1,4-polyisoprene and epoxidized natural rubber, *J. Appl. Polym. Sci.*, 2001, 82, 1391.

232. Wu, Y.P., Zhang, L.Q., Wang, Y.Q., Liang, Y., and Yu, D.S. Structure of carboxylated acrylonitrile-butadiene rubber (CNBR)-clay nanocomposites by co-coagulating rubber latex and clay aqueous suspension, *J. Appl. Polym. Sci.*, 2001, 82, 2842.

233. Kojima, Y., Fukumori, K., Usuki, A., Okada, A., and Kurauchi, T. Gas permeabilities in rubber-clay hybrid, *J. Mater. Sci. Lett.*, 1993, 12, 889.

234. Ren, J.X., Silva, A.S., and Krishnamoorti, R. Linear viscoelasticity of disordered polystyrene-polyisoprene block copolymer based layered silicate nanocomposites, *Macromolecules*, 2000, 33, 3739.

235. Varghese, H., Bhagawan, S.S., and Thomas, S. Thermogravimetric analysis and thermal aging of crosslinked nitrile rubber/poly(ethylene-co-vinyl acetate) blends, *J. Thermal Anal. Calor.*, 2000, 63, 749.

236. Lim, Y.T. and Park, O.O. Microstructure and rheological behavior of block copolymer/clay nanocomposites, *Kor. J. Chem. Eng.*, 2001, 18, 21.

237. Wang, T.L., Lee, H.M., and Kuo, P.L. Functional polymers for colloidal applications: XIV. Syntheses of styrene-maleic anhydride copolymers with different charges and their ability to disperse kaolinite particles, *J. Appl. Polym. Sci.*, 2000, 78, 592.

238. Burnside, S.D., Wang, H.C., and Giannelis, E.P. Direct polymer intercalation in single crystal vermiculite, *Chem. Mater.*, 1999, 11, 1055.

239. Gonzales, L., Rodriguez, A., Maracos-Fernandez, A., and Del-Campo, A. Reinforcing effect and electrical properties of ethylene-propylene rubber filled with calcined sepiolite, *J. Appl. Polym. Sci.*, 2001, 79, 714.

240. Wang, Z. and Pinnavaia, T.J. Nanolayer reinforcement of elastomeric polyurethane, *Chem. Mater.*, 1998, 10, 3769.

241. Chen, T.K., Tien, Y.I., and Wei, K.H. Synthesis and characterization of novel segmented polyurethane/clay nanocomposite via poly(e-caprolactone)/clay, *J. Polym. Sci. Polym. Chem.*, 1999, 37A, 2225.

242. Chen, T.K., Tien, Y.I., and Wei, K.H. Synthesis and characterization of novel segmented polyurethane/clay nanocomposites, *Polymer*, 2000, 41, 1345.

243. Hu, Y., Song, L., Xu, J., Yang, L., Chen, Z., and Fan, W. Synthesis of polyurethane/clay intercalated nanocomposites, *Coll. Polym. Sci.*, 2001, 279, 819.

244. Yao, K.J., Song, M., Hourston, D.J., and Luo, D.Z. Polymer/layered clay nanocomposites: 2 polyurethane nanocomposites, *Polymer*, 2002, 43, 1017.

245. Ma, J.S., Zhang, S.F., and Qi, Z.N. Synthesis and characterization of elastomeric polyurethane/clay nanocomposites, *J. Appl. Polym. Sci.*, 2001, 82, 1444.

246. (a) Tien, Y.I. and Wei, K.H. Thermal transitions of montmorillonite/polyurethane nanocomposites, *J. Polym. Res. Taiwan*, 2000, 7, 245. (b) Tien, Y.I. and Wei, K.H. Hydrogen bonding and mechanical properties in segmented montmorillonite/polyurethane nanocomposites of different hard segment ratios, *Polymer*, 2001, 42, 3213.

247. Zilg, C., Thomann, R., Mulhaupt, R., and Finter, J. Polyurethane nanocomposites containing laminated anisotropic nanoparticles derived from organophilic layered silicates, *Adv. Mater.*, 1999, 11, 49.

248. Greenland, D.J. Adsorption of polyvinyl alcohols by montmorillonite, *J. Coll. Sci.*, 1963, 18, 647.

249. Lagaly, G. Smectic clays as ionic macromolecules, in *Developments in Ionic Polymers*, Wilson, A.D. and Prosser, H.J., Eds., London: Elsevier, 1986, p. 77.

250. Strawhecker, K.E. and Manias, E. Structure and properties of poly(vinyl alcohol)/Na-montmorillonite nanocomposites, *Chem. Mater.*, 2000, 12, 2943.

251. Strawhecker, K.E. and Manias, E. AFM of poly(vinyl alcohol) crystals next to an inorganic surface, *Macromolecules*, 2001, 34, 8475.

252. Carrado, K.A., Thiyagarajan, P., and Elder, D.L. Polyvinyl alcohol-clay complexes formed by direct synthesis, *Clays Clay Miner.*, 1996, 44, 506.

253. Levy, R. and Francis, C.W. Interlayer adsorption of polyvinylpyrrolidone on montmorillonite, *J. Coll. Interf. Sci.*, 1975, 50, 442.

254. Miyata, H., Sugahara, Y., Kuroda, K., and Kato, C. Synthesis of montmorillonite-viologen intercalation compounds and their photochromic behaviour, *J. Chem. Soc. Far. Trans.*, 1987, 83, 1851.

255. Bassmann, F., Sequaris, J.M., Narres, H.D., and Schwuger, M.J. Adsorption of nonionic and anionic polymers on gamma-alumina and Na-montmorillonite and their mixtures, *J. Disp. Sci. Technol.*, 1999, 20, 607.

256. Sequaris, J.M., Bassmann, F., Hild, A., Narres, H.D., and Schwuger, M.J. Characterization of polyvinylpyrrolidone adsorption at inorganic soil components by a microelectrophoretic method, *Coll. Surf. Phys. Eng. Asp.*, 1999, 159A, 503.

257. Sequaris, J.M., Hild, A., Narres, H.D., and Schwuger, M.J. Polyvinylpyrrolidone adsorption on Na-montmorillonite: effect of the polymer interfacial conformation on the colloidal behavior and binding of chemicals, *J. Coll. Interf. Sci.*, 2000, 230, 73.

258. Uhlik, P., Sucha, V., Elsass, F., and Caplovicova, M. High-resolution transmission electron microscopy of mixed-layer clays dispersed in PVP-10, *Clay Miner.*, 2000, 35, 781.

259. (a) Hild, A., Sequaris, J.M., Narres, H.D., and Schwuger, M. Adsorption of polyvinyl pyrrolidone on kaolinite, *Coll. Surf. Phys. Eng. Asp.*, 1997, 123/124A, 515. (b) Komori, Y., Sugahara, Y., and Kuroda, K. Direct intercalation of poly(vinyl pyrrolidone) into kaolinite by a refined guest displacement method, *Chem. Mater.*, 1999, 11, 3.

260. Senillou, A., Jaffrezic, N., Martelet, C., and Cosnier, S. A laponite clay-poly(pyrrole-pyridinium) matrix for the fabrication of conductimetric microbiosensors, *Anal. Chim. Acta*, 1999, 401, 117.

261. (a) Ogawa, M., Inagaki, M., Kodama, N., Kuroda, K., and Kato, C. Novel controlled luminescence of tris(2,2-bipyridine) ruthenium(II) intercalated in a fluortetrasilicic mica with poly(vinyl pyrrolidone), *J. Phys. Chem.*, 1993, 97, 3819. (b) Ogawa, M., Tsujimura, M., and Kuroda, K. Incorporation of tris(2,2-bipyridine)ruthenium(II) in a synthetic swelling mica with poly(vinyl pyrrolidone), *Langmuir*, 2000, 16, 4202.

262. Messersmith, P.B. and Giannelis, E.P. Synthesis and characterization of layered silicate-epoxy nanocomposites, *Chem. Mater.*, 1994, 6, 1719.

263. Lan, T. and Pinnavaia, T.J. Clay-reinforced epoxy nanocomposites, *Chem. Mater.*, 1994, 6, 2216.

264. Lan, T., Kaviratna, P.D., and Pinnavaia, T.J. Mechanism of clay tactoid exfoliation in epoxy-clay nanocomposites, *Chem. Mater.*, 1995, 7, 2144.

265. Shi, H., Lan, T., and Pinnavaia, T.J. Interfacial effects on the reinforcement properties of polymer-organoclay nanocomposites, *Chem. Mater.*, 1996, 8, 1584.

266. Zilg, C., Mulhaupt, R., and Finter, J. Morphology and toughness/stiffness balance of nanocomposites based upon anhydride-cured epoxy resins and layered silicates, *Macromol. Chem. Phys.*, 1999, 200, 661.

267. Ke, Y.C., Lu, J.K., Yi, X.S., Zhao, J., and Qi, Z.N. The effects of promoter and curing process on exfoliation behavior of epoxy/clay nanocomposites, *J. Appl. Polym. Sci.*, 2000, 78, 808.

268. Brown, J.M., Curliss, D., and Vaia, R.A. Thermoset-layered silicate nanocomposites: quaternary ammonium montmorillonite with primary diamine cured epoxies, *Chem. Mater.*, 2000, 12, 3376.

269. Lu, J.K., Ke, Y.C., Qi, Z.N., and Yi, X.S. Study on intercalation and exfoliation behavior of organoclays in epoxy resin, *J. Polym. Sci. Polym. Phys.*, 2001, 39B, 115.

270. Wang, Z., Massam, J., and Pinnavaia, T.J. Epoxy-clay nanocomposites, in *Polymer-Clay Nanocomposites*, Pinnavaia, T.J. and Beall, G.W., Eds., New York: John Wiley & Sons, 2000, chap. 7.

271. Chin, I.J., Thurn-Albrecht, T., Kim, H.C., Russell, T.P., and Wang, J. On exfoliation of montmorillonite in epoxy, *Polymer*, 2001, 42, 5947.

272. Kornmann, X., Lindberg, H., and Berglund, L.A. Synthesis of epoxy-clay nanocomposites: influence of the nature of the clay on structure, *Polymer*, 2001, 42, 1303.

273. Kornmann, X., Lindberg, H., and Berglund, L.A. Synthesis of epoxy-clay nanocomposites: influence of the nature of the curing agent on structure, *Polymer*, 2001, 42, 4493.

274. Kelly, P., Akelah, A., Qutubuddin, S., and Moet, A. Reduction of residual stress in montmorillonite/epoxy compounds, *J. Mater. Sci.*, 1994, 29, 2274.

275. Lee, A. and Lichtenhan, J.D. Thermal and viscoelastic property of epoxy-clay and hybrid inorganic-organic epoxy nanocomposites, *J. Appl. Polym. Sci.*, 1999, 73, 1993.

276. Gilman, J.W., Kashiwagi, T., Nyden, M., Brown, J.E.T., Jackson, C.L., Lomakin, S., Giannelis, E.P., and Manias, E. Flammability studies of polymer layered silicate nanocomposites: polyolefin, epoxy, and vinyl ester resins, in *Chemistry and Technology of Polymer Additives*, Al-Malaika, S., Golovoy, A., and Wilkie, C.A., Eds., Oxford: Blackwell, 1999, p. 249.

277. Zilg, C., Thomann, R., Finter, J., and Mulhaupt, R. The influence of silicate modification and compatibilizers on mechanical properties and morphology of anhydride-cured epoxy nanocomposites, *Macromol. Mater. Eng.*, 2000 280/281, 41.

278. Zilg, C., Mulhaupt, R., Thomann, R., and Finter, J. Epoxy nanocomposites based upon organophilic layered silicates: improving toughness/stiffness/strength balance, *Polym. Mater. Sci. Eng.*, 2000, 82, 249.

279. Hsiue, G.H., Liu, Y.L., and Liao, H.H. Flame-retardant epoxy resins: an approach from organic-inorganic hybrid nanocomposites, *J. Polym. Sci. Polym. Chem.*, 2001, 39A, 986.

280. Zerda, A.S. and Lesser, A.J. Intercalated clay nanocomposites: morphology, mechanics, and fracture behavior, *J. Polym. Sci. Polym. Phys.*, 2001, 39B, 1137.

281. (a) Fischer, H.R., Gielgens, L.H., and Koster, T.P.M. Nanocomposites from polymers and layered minerals, *Mater. Res. Soc. Symp. Proc.*, 1998, 519, 117. (b) Fischer, H.R., Gielgens, L.H., and Koster, T.P.M. Nanocomposites from polymers and layered minerals, *Acta Polym.*, 1999, 50, 122.

282. Alexandre, M., Beyer, G., Henrist, C., Cloots, R., Rulmont, A., Jerome, R., and Dubois, P. One-pot preparation of polymer/clay nanocomposites starting from Na-montmorillonite: 1. Melt intercalation of ethylene-vinyl acetate copolymer, *Chem. Mater.*, 2001, 13, 3830.

283. Artzi, N., Nir, Y., Wang, D., Narkis, M., and Siegmann, A. EVOH/clay nanocomposites produced by melt processing, *Polym. Composites*, 2001, 22, 710.

284. Oriakhi, C.O. and Lerner, M.M. Poly(pyrrole) and poly(thiophene)/clay nanocomposites via latex-colloid interaction, *Mater. Res. Bull.*, 1995, 30, 723.

285. Kawasumi, M., Hasegawa, N., Usuki, A., and Okada, A. Liquid crystal/clay mineral composites, *Appl. Clay Sci.*, 1999, 15, 93.

286. Fournaris, K.G., Karakassides, M.A., Petridis, D., and Yiannakopoulou, K. Clay-polyvinylpyridine nanocomposites, *Chem. Mater.*, 1999, 11, 2372.

287. Agag, T. and Takeichi, T. Polybenzoxazine-montmorillonite hybrid nanocomposites: synthesis and characterization, *Polymer*, 2000, 41, 7083.

288. Huang, X.Y., Lewis, S., Brittain, W.J., and Vaia, R.A. Synthesis of polycarbonate-layered silicate nanocomposites via cyclic oligomers, *Macromolecules*, 2000, 33, 2000.

289. Suh, D.J., Lim, Y.T., and Park, O.O. The property and formation mechanism of unsaturated polyester-layered silicate nanocomposite depending on the fabrication methods, *Polymer*, 2000, 41, 8557.

290. Hasegawa, N., Okamoto, H., Kawasumi, M., Kato, M., Tsukigase, A., and Usuki, A. Polyolefin-clay hybrids based on modified polyolefins and organophilic clay, *Macromol. Mater. Eng.*, 2000, 280, 76.

291. Choi, M.H., Chung, I.J., and Lee, J.D. Morphology and curing behaviors of phenolic resin-layered silicate nanocomposites prepared by melt intercalation, *Chem. Mater.*, 2000, 12, 2977.

292. Zhou, W., Mark, J.E., Unroe, M.R., and Arnold, F.E. Some clay nanocomposites based on a high-temperature, high-performance polymer, *J. Macrmol. Sci. Pure Appl. Chem.*, 2001, 38, 1.

293. Alexandre, M., Beyer, G., Henrist, C., Cloots, R., Rulmont, A., Jerome, R., and Dubois, P. Preparation and properties of layered silicate nanocomposites based on ethylene vinyl acetate copolymers, *Macromol. Rapid Commun.*, 2001, 22, 643.

294. Wang, D., Parlow, D., Yao, Q., and Wilkie, C.A. PVC-clay nanocomposites: preparation, thermal and mechanical properties, *J. Vinyl Addit. Technol.*, 2001, 7, 203.

295. Liu, H., Kim, D.W., Blumstein, A., Kumar, J., and Tripathy, S.K. Nanocomposite derived from intercalative spontaneous polymerization of 2-ethynylpyridine within layered aluminosilicate: montmorillonite, *Chem. Mater.*, 2001, 13, 2756.

296. Byun, H.Y., Choi, M.H., and Chung, I.J. Synthesis and characterization of resol type phenolic resin/layered silicate nanocomposites, *Chem. Mater.*, 2001, 13, 4221.

297. Dabrowski, F., Le Bras, M., Cartier, L., and Bourbigot, S. The use of clay in an EVA-based intumescent formulation, *J. Fire Sci.*, 2001, 19, 219.

298. Wang, H.S., Zhao, T., Zhi, L.J., Yan, Y.H., and Yu, Y.Z. Synthesis of novolac/layered silicate nanocomposites by reaction exfoliation using acid-modified montmorillonite, *Macromol. Rapid Commun.*, 2002, 23, 44.

299. Takeichi, T., Zeidam, R., and Agag, T. Polybenzoxazine/clay hybrid nanocomposites: influence of preparation method on the curing behavior and properties, *Polymer*, 2002, 43, 45.

300. Xu, W., Ge, M., and He, P. Nonisothermal crystallization kinetics of polyoxymethylene/montmorillonite nanocomposite, *J. Appl. Polym. Sci.*, 2001, 82, 2281.

301. Sur, G.S., Sun, H.L., Lyu, S.G., and Mark, J.E. Synthesis, structure, mechanical properties, and thermal stability of some polysulfone/organoclay nanocomposites, *Polymer*, 2001, 42, 9783.

302. Komori, Y. and Kuroda, K. Layered silicate-polymer intercalation compounds, in *Polymer-Clay Nanocomposites*, Pinnavaia, T.J. and Beall, G.W., Eds., New York: John Wiley & Sons, 2000, chap. 1.

303. Ramachandran, K. and Lerner, M.M. Electrochemical characterization of a polypyrrole/montmorillonite nanocomposite, *J. Electrochem. Soc.*, 1997, 144, 3739.

304. Kresge, E.N. and Lohse, D.J. Composite Tire Innerliners and Inner Tubes, U.S. Patent 5,576,372, 1996.

305. Beall, G.W. New conceptual model for interpreting nanocomposite behavior, in *Polymer-Clay Nanocomposites*, Pinnavaia, T.J. and Beall, G.W., Eds., New York: John Wiley & Sons, 2000, chap. 13.

306. Bharadwaj, R.K. Modeling the barrier properties of polymer-layered silicate nanocomposites, *Macromolecules*, 2001, 34, 9189.

307. (a) Krishnamoorti, R. and Silva, S. Rheological properties of polymer-layered silicate nanocomposites, in *Polymer-Clay Nanocomposites*, Pinnavaia, T.J. and Beall, G.W., Eds., New York: John Wiley & Sons, 2000, chap. 15. (b) Krishnamoorti, R. and Yurekli, K. Rheology of polymer layered silicate nanocomposites, *Curr. Opin. Coll. Interf. Sci.*, 2001, 6, 464.

308. (a) Gilman, J.W. Flammability and thermal stability studies of polymer layered-silicate (clay) nanocomposites, *Appl. Clay Sci.*, 1999, 15, 31. (b) Gilman, J.W. and Kashiwagi, T. Polymer-layered silicate nanocomposites with conventional flame retardants, in *Polymer-Clay Nanocomposites*, Pinnavaia, T.J. and Beall, G.W., Eds., New York: John Wiley & Sons, 2000, chap. 10. (c) Nyden, M.R., Gilman, J.W., Davis, R.D., Harris, R.H., and Awad, W.H. Development of high-throughput approaches to materials flammability research, *Am. Chem. Soc. Polym. Prepr.*, 2001, 42, 658.

309. Stretz, H.A., Koo, J.H., Dimas, V.M., and Zhang, Y. Flame retardant properties of polycarbonate/montmorillonite clay nanocomposite blends, *Am. Chem. Soc. Polym. Prepr.*, 2001, 42, 50.

310. Lee, J., Takekoshi, T., and Giannelis, E. Fire retardant polyetherimide nanocomposites, *Mater. Res. Soc. Symp. Proc.*, 1997, 457, 513.

311. Gilman, J.W., Kashiwagi, T., and Lichtenhan, J.D. Nanocomposites: a revolutionary new flame retardant approach, *SAMPE J.*, 1997, 33, 40.

312. Babrauskas, V. and Peacock, R.D. Heat release rate: the single most important variable in fire hazard, *Fire Safety J.*, 1992, 18, 255.

313. (a) Lee, J.Y., Baljon, A.R.C., Loring, R.F., and Panagiotopoulos, A.Z. Modeling intercalation kinetics of polymer silicate nanocomposites, *Mater. Res. Soc. Symp. Proc.*, 1999, 543, 131. (b) Lee, J.Y., Baljon, A.R.C., and Loring, R.F. Spontaneous swelling of layered nanostructures by a polymer melt, *J. Chem. Phys.*, 1999, 111, 9754. (c) Lee, J.Y., Baljon, A.R.C., Sogah, D.Y., and Loring, R.F. Molecular dynamics study of the intercalation of diblock copolymers into layered silicates, *J. Chem. Phys.*, 2000, 112, 9112. (d) Lee, J.Y. and Loring, R.F. Driven diffusion of confined polymers, *Macromolecules*, 2001, 34, 5727.

314. Zax, D.B., Yang, D.K., Santos, R.A., Hegemann, H., Giannelis, E.P., and Manias, E. Dynamical heterogeneity in nanoconfined polystyrene chains, *J. Chem. Phys.*, 2000, 112, 2945.

315. Hackett, E., Manias, E., and Giannelis, E.P. Computer simulation studies of PEO/layer silicate nanocomposites, *Chem. Mater.*, 2000, 12, 2161.

316. Lyatskaya, Y. and Balazs, A.C. Modeling the phase behavior of polymer-clay composites, *Macromolecules*, 1998, 31, 6676.

317. Balazs, A.C., Sing, C., and Zhulina, E. Modeling the interactions between polymers and clay surfaces through self-consistent field theory, *Macromolecules*, 1998, 31, 8370.

318. Zhulina, E., Singh, C., and Balazs, A.C. Attraction between surfaces in a polymer melt containing telechelic chains, *Langmuir*, 1999, 15, 3935.

319. Balazs, A.C., Singh, C., Zhulina, E., and Lyatskaya, Y. Modeling the phase behavior of polymer-clay nanocomposites, *Acc. Chem. Res.*, 1999, 32, 651.
320. Ginzburg, V.V., Singh, C., and Balazs, A.C. Theoretical phase diagrams of polymer/clay composites: role of grafted organic modifiers, *Macromolecules*, 2000, 33, 1089.
321. Kuznetsov, D.V. and Balazs, A.C. Scaling theory for end-functionalized polymers confined between two surfaces, *J. Chem. Phys.*, 2000, 9, 4365.
322. Sing, C. and Balazs, A.C. Effect of polymer architecture on the miscibility of polymer/clay mixtures, *Polym. Int.*, 2000, 49, 469.
323. Kuznetsov, D.V. and Balazs, A.C. Phase behavior of end-functionalized polymers confined between two surfaces, *J. Chem. Phys.*, 2000, 113, 2479.
324. Ginzburg, V.V. and Balazs, A.C. Calculating phase diagrams for nanocomposites, *Adv. Mater.*, 2000, 12, 1805.
325. Balazs, A., Ginzburg, V.V., Lyatskaya, Y., Singh, C., and Zhulina, E. Modeling the phase behavior of polymer-clay nanocomposites, in *Polymer-Clay Nanocomposites*, Pinnavaia, T.J. and Beall, G.W., Eds., New York: John Wiley & Sons, 2000, chap. 14.
326. (a) Vaia, R.A. and Giannelis, E.P. Lattice model of polymer melt intercalation in organically-modified layered silicates, *Macromolecules*, 1997, 30, 7990. (b) Vaia, R.A. and Giannelis, E.P. Polymer melt intercalation in organically-modified layered silicates: model predictions and experiment, *Macromolecules*, 1997, 30, 8000.
327. Farmer, B.L., Vaia, R.A., and Bharadwaj, R.K. Modeling of organically-modified layered silicates in binary solvents, *Am. Chem. Soc. Polym. Prepr.*, 2001, 42, 21.
328. Beall, G.W. and Tsipursky, S.J. Nanocomposites produced utilizing a novel ion-dipole clay surface modification, in *Chemistry and Technology of Polymer Additives*, Al-Malaika, S., Golovoy, A., and Wilkie, C.A., Eds., Malden, MA: Blackwell Science Ltd., 1999, chap. 15.
329. Tanaka, G. and Goettler, L.A. Predicting the binding energy for nylon 6,6/clay nanocomposites by molecular modeling, *Polymer*, 2002, 43, 541.
330. Stackhouse, S., Coveney, P.V., and Sandre, E. Plane-wave density functional theoretic study of formation of clay-polymer nanocomposite materials by self-catalyzed in situ intercalative polymerization, *J. Am. Chem. Soc.*, 2001, 123, 1764.
331. Brune, D.A. and Bicerano, J. Micromechanics of nanocomposites: comparison of tensile and compressive elastic moduli, and prediction of effects of incomplete exfoliation and imperfect alignment on modulus, *Polymer,* 2002, 43, 369.
332. (a) Suh, D.J. and Park, O.O. Nanocomposite structure depending on the degree of surface treatment of layered silicate, *J. Appl. Polym. Sci.*, 2002, 83, 2143. (b) Xie, W., Gao, Z.M., Pan, W.P., Hunter, D., Sing, A., and Vaia, R. Thermal degradation chemistry of alkyl quaternary ammonium montmorillonite, *Chem. Mater.*, 2001, 13, 2979.

11

Review of Polymer Composites with Carbon Nanotubes

Vincenza Antonucci, Kuang-Ting Hsiao, and Suresh G. Advani

CONTENTS

11.1 Carbon Nanotubes

11.1.1 Nanostructure Science and Technology

In the last two decades, progress in material science has led to explosive development of a broad and interdisciplinary research area: the *nanostructure science and technology*. In fact, due to the potential of realizing new materials with novel and improved properties and functionality, this research field has been growing and attracting the interest of scientists and engineers all over the world. Significant resources are being allocated worldwide for research and development in nanostructure science and technology with specific aims to:

- Control the nanoscale size and synthesis
- Characterize the materials, in terms of electrical, optical, magnetic, and chemical properties
- Understand the relationship between the nanostructure and properties
- Develop techniques to process these materials

Table 11.1 shows the distribution of government funding in 1997, which approached over half a billion dollars.[1]

The potential uses and benefits of nano-materials and nano-devices should lead to breakthroughs of many frontiers, including materials manufacturing, nanoelectronics and computer technology, medicine and health, aeronautics and space exploration, environment and energy, biotechnology and agriculture, and security.

Table 11.2 shows some examples of innovative applications as outlined by the American National Science and Technology Council in the National Nanotechnology Initiative report.[2]

Therefore, due to the potentially immense impact both on the economics and on the quality of life, further investment in nanotechnology is being made to explore further applications and uses, such as:[2]

TABLE 11.1

Government Funding for Nanotechnology Science in 1997

Region	Government Funding, Million $
Western Europe	128
Japan	120
United States	116
China, Canada, Australia, Korea, Taiwan, Singapore, countries of the former Soviet Union	70

TABLE 11.2

Examples of Nanotechnology Applications

Materials and Manufacturing	Nanoelectronics	Medicine and Health	Environment and Energy
Nanostructured metals, ceramics, and polymers net shape manufacturing without machining	Nanostructured microprocessor devices	Rapid and more efficient genome sequencing	Removal of ultrafine contaminants with mesoporous materials
Improved printing	Higher-transmission-frequency communications system	New formulations and routes for drug delivery	Metallic automotive components replacement by nanoparticle/polymer systems
Nanocoatings	Small-mass storage devices with multiterabit capacities	Sensor systems able to detect emerging diseases in the body	Replacement of carbon black in tires by clay/polymer nanocomposites

- Containing the entire contents of the Library of Congress in a device the size of a sugar cube
- Making materials and products from atoms and molecules
- Developing materials that are ten times stronger than steel and, at the same time, lighter, to improve the fuel efficiency of vehicles
- Improving the computer speed and efficiency of transistors and memory chips by a factor of millions
- Detecting cancerous tumors by nanoengineered contrast agents
- Removing the finest contaminant from water and air and promoting a cleaner environment and potable water at affordable cost
- Doubling the energy efficiency of solar cells

But what is nanotechnology? And why is the nanometer length scale so important?

Nanotechnology involves the creation and utilization of structures with at least one dimension in the nanometer length scale that creates novel properties and phenomena otherwise not displayed by either isolated molecules or bulk materials. The recent discovery of organized structures (such as carbon nanotubes, molecular motors, DNA-based assemblies, quantum dots, and molecular switches) and new intrinsic nanoscale phenomena (size confinement, magnetoresistance, and predominance of interfacial phenomena) offers fertile research areas for future development.[2] For example, since variations at the nanometer scale affect electronic and atomic interactions, the nanoscale material design should enable one to control the material properties (magnetization, catalytic activity) without changes in chemical composition. Further, in the medicinal field, nanoscience and technology

could allow one to place artificial components and assemblies inside the cells and to pattern new materials by imitating the self-assembly rules of nature. Finally, nanoscale structures display a high surface-to-volume ratio, which is ideal for applications that involve composite materials, chemical reactions, drug delivery, and energy storage.

11.1.2 Carbon Nanotubes

Recently, great effort has been devoted to the synthesis and characterization of carbon nanotubes, due to the very high aspect ratio and promising physical properties for many applications. They are fullerene-based structures that can be viewed as a single sheet of graphite rolled into a cylinder of several microns in length and 1 nm in diameter.[3–9] In 1991, Iijima[10] discovered them while studying the material deposited on the cathode during the arc evaporation synthesis of fullerene (see Figure 11.1). Since the performing of a large-scale synthesis method by Ebbesen and Ajaian in 1992,[11] systematic investigations and attempts have been made to understand their chemical structure, to improve the synthesis techniques, and to analyze the relationship between structure and properties.

Currently, the high cost of producing carbon nanotubes limits their use in the industrial market, but as new techniques to fabricate carbon nanotubes on a large scale emerge, it is expected that they will find their way in many applications. In fact, due to their remarkable properties, they could be used potentially in several applications, including electronics, reinforcement, and biological.[10]

The main focus of this chapter is to present the use of carbon nanotubes as reinforcements in polymer matrices and to summarize the developments
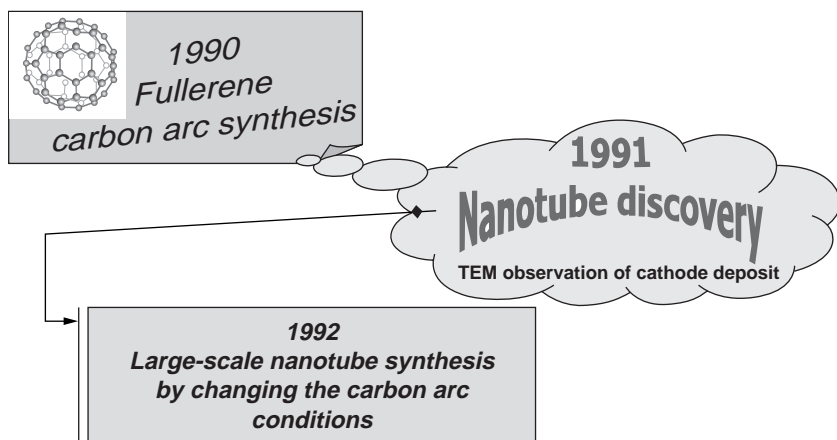
FIGURE 11.1
Schematic of the nanotube history.

in the characterization of structure, properties, and processing of polymer carbon nanotubes composites.

11.1.2.1 Structure

A nanotube can be conceptualized as a tubular microcrystal of graphite. It consists of one or more cylinders of graphitic shells where trivalent carbon atoms form a hexagonal network; i.e., each carbon atom is bonded to three neighboring carbon atoms through sp^2 hybridization.[3–9,12,13] Figure 11.2 shows a schematic of a graphite sheet.

By folding the graphite sheet, an open cylinder can be formed. The nanotube is typically closed at each end by hemispherical caps that are constituted by at least 12 pentagons. According to the Euler theorem,[3] which relates the number of vertices, edges, and faces, a convex structure can be created by introducing a positive curvature and, therefore, pentagons to close up the hexagonal lattice of the tube (see Figure 11.3).

Due to the hexagonal symmetry of the carbon atoms in the graphitic sheet, different structural isomers are possible depending on how the planar graphite sheet is folded. The rolling up can be accomplished in several different ways requiring only the matching of the dangling bonds at each end. However, the nanotubes can present a different helicity degree with respect to the tube axis. Figure 11.4 shows the three different possible nanotubes: armchair, zigzag, and chiral (for more details, see references 3, 5, and 9).

The characteristic of helicity in nanotubes has a great relevance affecting the physical properties that depend also on the tube diameter.[5] For example, it has been shown that all the armchair tubes are metallic, whereas the zigzag and chiral tubes are either metallic or semiconducting.
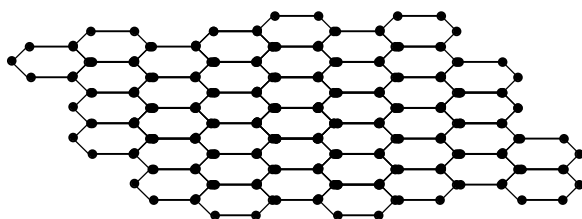
FIGURE 11.2
Schematic of the graphite sheet.
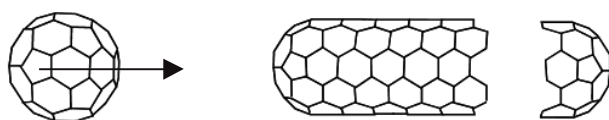
FIGURE 11.3
Schematic of the nanotube formation.
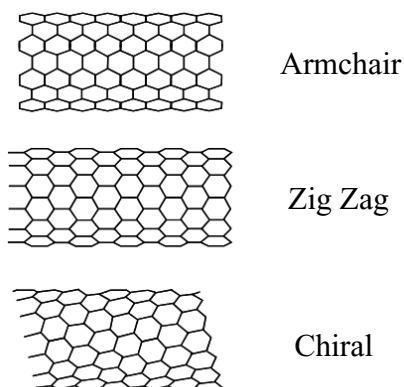
FIGURE 11.4
Schematic of the three different nanotubes structures.

The nanotubes can exist in two forms: multiwalled and single layer (see Figure 11.5).

The multiwall carbon nanotubes were the first to be discovered. They consist of concentric cylinders placed around a common central hollow area with a constant separation between the layers close to the graphite interlayer spacing (0.34 nm). Each individual cylinder can be characterized by a different helicity and has a diameter ranging from 2 to 25 nm and a length of several microns.

The single-walled nanotubes were synthesized in 1993 when it was found that the addition of metals such as cobalt to the graphite electrodes in the arc evaporation method resulted in tubes with single-layer walls.[7] A single-walled nanotube is close to an ideal fullerene fiber and consists of a single-layer cylinder extending from end to end with a narrow distribution in diameter range (1 to 2 nm). When produced in vapor phase, the single-wall nanotube can self-assemble into larger bundles, called ropes, consisting of several tens of nanotubes arranged in a one-dimensional triangular lattice.
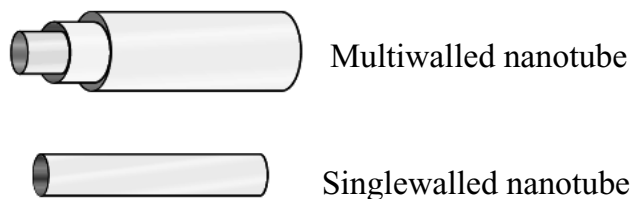
FIGURE 11.5
Multiwalled and single nanotubes.

It is important to observe that the discovery of single-wall tubes has been very significant, allowing researchers to verify and test some of the theoretical predictions about nanotube properties.

11.1.2.2 Material Properties

Due to the combination of size, structure, and topology, the nanotubes display remarkable features. In particular, the graphitic nature of the nanotube lattice contributes to provide high conductivity, high strength and stiffness, chemical specificity, and inertness, while the lattice helicity and elasticity provide optimal electronic properties. Further, the nanoscale size and the high aspect ratio are advantageous for many applications that require a large surface area-to-volume ratio. However, due to their very small size and often the presence of defects, mechanical property characterization is a challenge. Nevertheless, it is possible to imagine that their stiffness and strength are very high if one uses graphite as a reference. The in-plane elastic modulus of graphite is estimated to be 1.06 TPa ($1.06*10^{12}$ Pa) and the tensile stiffness as 0.8 TPa, due to the very strong covalent C-C bonds in the plane.[5]

The elastic properties evaluation of carbon nanotubes has been performed by:

- Measurement of their thermal vibration amplitudes
- Atomic force microscopy measurement during bending

The first technique provided the Young's modulus equal to 1.8 TPa, while a modulus close to 1 TPa has been determined by the second method. Further, the maximum tensile strength has been determined close to 30 GPa ($30*10^9$ Pa).[5] Many other observations have shown that carbon nanotubes have other intriguing properties, such as:

- High flexibility, related to the ability of the carbon atoms to rehybridize, with the degree of rehybridization depending on the strain
- High capability to sustain strain in tension (40%) without brittleness, plastic deformation, or bond rupture

These features make the carbon nanotubes ideal candidates for reinforcing fibers in polymer-based composites. In particular, due to their ability to sustain high deformations, they have a significant advantage over carbon fibers in composites for structural and strength applications. However, the effective reinforcement action due to the nanotubes hinges on the success of the preparation techniques and stable dispersion of the nanotubes in the polymer matrix. In most cases, since the nanotubes have many entanglements, it is a challenge and an unresolved issue to disperse them effectively with polymer systems to make strong and stiff components.

11.1.3 Preparation Techniques

The evaluation and characterization of the nanotubes properties are related to the synthesis of pure samples in reasonable quantities. In 1991, when the nanotubes were discovered by the carbon arc technique, the product contained a high content of impurities, making it difficult to verify any theoretical prediction about the nanotube features.[7] Therefore, in order to attain high levels of yields and purity, in the last few years great effort has been devoted to the development and improvement of the carbon nanotubes synthesis techniques. However, today the high price of purification and very small yields from the technique still limit the commercial applications of the nanotubes. The most common methods for producing the nanotubes include carbon arc, catalytic vapor deposition (CVD), catalytic arc method, laser ablation, and hot-filament plasma-enhanced CVD. They produce nanotubes that are multiwalled or single walled.

11.1.3.1 Multiwalled Nanotubes

Multiwalled nanotubes are commonly produced by the carbon arc method, which is also used to synthesize other carbon materials such as carbon whiskers and fullerenes.[7,17] The fullerene molecules are formed in the carbon soot generated by the evaporation of the graphite electrodes. However, in the case of the multiwalled nanotubes production, the soot generation and the arc conditions affect the final quality and, consequently, have to be controlled. In fact, it is important to optimize the preparation conditions minimizing the amount of soot production and maximizing the amount of cathode deposit.

Figure 11.6 shows a schematic of the carbon arc apparatus.[7] The growth of multiwalled nanotubes on the cathode surface (1 mm/min) is obtained
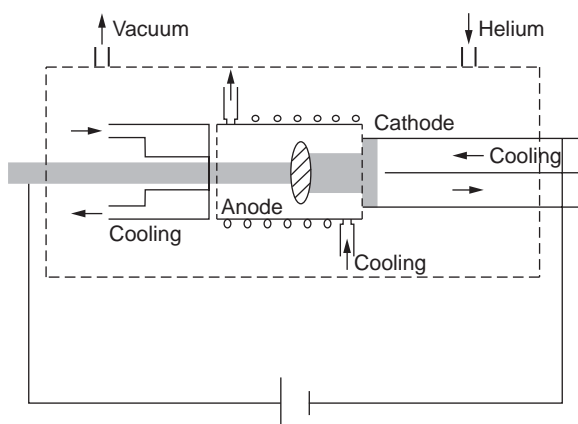
FIGURE 11.6
Schematic of the carbon arc apparatus.

by generating a plasma arc in an inert atmosphere (usually helium at 500 torr). This is done by applying a DC current of 150 A cm^{-2} and a voltage of 20 V between two carbon rods kept at a constant distance of 1 mm. Both the anode (6 mm) and the negative electrode are water cooled. The average temperature in the interelectrode region is around 3500°C.

The deposit has the same shape of the consumed positive electrode and shows two different microstructures: an outer hard region and an inner core region. The outer region consists of nanotubes and nanoparticles fused together and is not of much use, while the inner core region is formed by a highly porous network of randomly oriented nanotubes that are arranged into columns aligned along the axial direction of the deposit[5] (see Figure 11.7).

Scanning electron microscopy (SEM) and scanning tunneling microscope (STM) images have shown that the deposit generated by the arc has a fractal structure consisting of aligned 50-μm fibers that are themselves made of aligned nanotubes and aligned nanotube bundles. The alignment, the yield, and the quality of the nanotubes depend on the arc conditions. The inert gas pressure, the cooling rate, the current density, and the plasma stability between the two electrodes are the most critical parameters. Recently, Zhang et al.[17] studied the effect of the two inert gases, argon and helium, on the nanotubes preparation and found that the gas pressure had a significant influence on the growth rate of the cathode deposit and on the nanotube
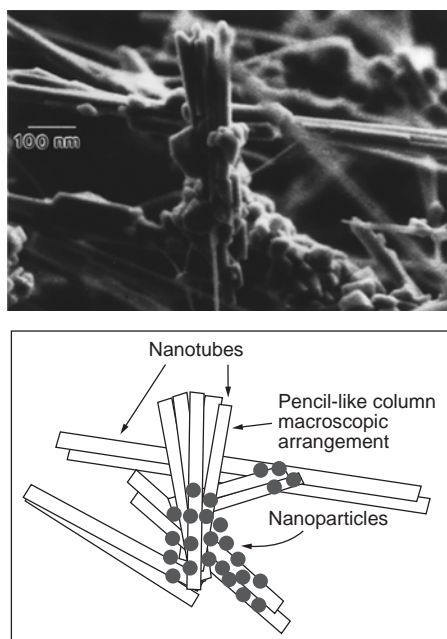
FIGURE 11.7
SEM image of multiwalled nanotubes generated by the electric arc (top). (With permission from Ajayan, P.M., *Chem. Rev.*, 99, 1787–1799, 1999.) The schematic on the bottom displays the porous network formed by the aligned nanotubes.

yield. In particular, at high pressure, argon gas showed a larger yield of nanotubes than helium gas, all other conditions being the same. The carbon arc should enable the production of carbon nanotubes with better properties than those of nanotubes produced by other techniques, due to the high arc temperatures. However, it provides only a limited quantity of material that must be purified from a significant amount of polyhedral-shaped nanoparticles that are low in aspect ratio.

Catalytic vapor deposition could overcome some of these problems, allowing one to obtain a higher yield and production of carbon nanotubes from the raw product.[5] The CVD is a common technique used to transform gaseous molecules, called precursors, into a solid material in the form of thin films or powders. It consists of a series of steps, such as:

- Vaporization of the precursor molecules into a reactor
- Diffusion and adsorption of the gaseous molecules on a substrate
- Decomposition and incorporation of the precursors into solid films
- Desorption of the reaction products into a gaseous phase

The synthesis of nanotubes by CVD consists of the catalytic decomposition of hydrocarbon gases (benzene or acetylene) over substrates: carbon black or silica or graphite covered by transition metals (Co, Fe, Ni)[18–21] or mesoporous silica embedded with iron particles.[22,23] Since the reactions are carried out at lower temperatures (700 to 1500°C) than those of the carbon arc, the nanotubes produced by CVD are not straight, but curved and entangled in a conglomeration containing also catalyst particles and other carbon products (soot, fibers). This is shown in the transmission electron microscopy (TEM) image in Figure 11.8, in which the nanotubes were produced with Ni-based substrates.

It should be observed that the nanotubes are randomly oriented with size and shape depending on the growth conditions. However, the CVD method enables one to obtain large amounts of nanotubes with good uniformity of the tube size by controlling the size of the catalyst particles. Further, the use of mesoporous substrates embedded with iron particles allows the production of aligned nanotubes.[22,23] In this case, the mesoscopic pores of the membrane act as templates and can direct the nanotube formation in terms of size and growth direction. As an example, Figure 11.9 shows a high-magnification SEM image of a carbon nanotube growing from a mesoporous iron/silica substrate.[23]

The carbon nanotubes sprout separately from the substrates, forming an array with spacing consistent with the substrate pore distance. Further, most of nanotubes were approximately perpendicular to the silica surface. Similar results were also found by Xie et al.[22] They prepared large arrays of aligned nanotubes by decomposition of acetylene at 700°C on mesoporous iron/silica substrates. Since the mesoporous silica could have a large, flat surface with a uniform distribution of the pores, large areas of nanotube arrays can be
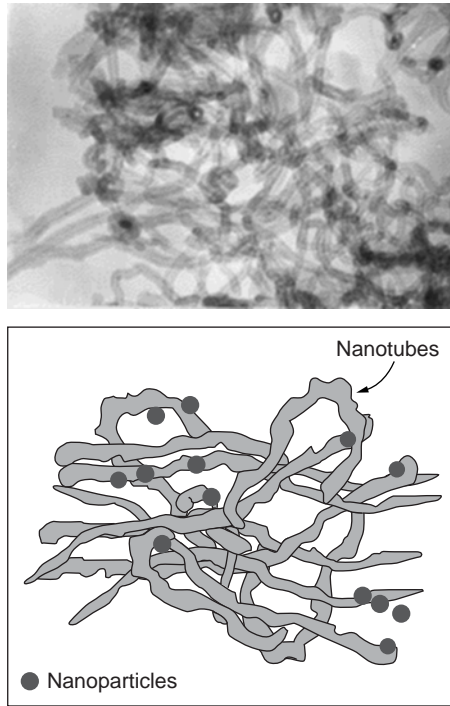
FIGURE 11.8
TEM image of CVD carbon nanotubes along with a schematic on the following page. (With permission from Hernadi, K. et al., *Synth. Metals,* 77, 31–34, 1996.)

obtained compared to other methods, such as chemical vapor deposition over laser-patterned catalyst.

Growing aligned carbon nanotubes on large-scale surfaces is crucial for electronic applications such as scanning probes, sensors, field emitters, and nano-devices. Therefore, to produce organized arrays of nanotubes, improvements in the chemical vapor deposition technique have been achieved by employing different types of substrates such as Fe-patterned
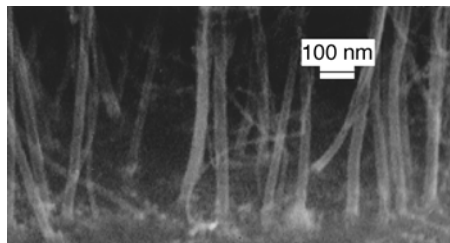
FIGURE 11.9
SEM image of CVD carbon nanotube growing from a mesoporous iron/silica substrate. (With permissino from Li, W.Z. et al., *Science*, 274, 1701–1703, 1996.)

porous silicon[24] and quartz glass plates.[25] In particular, large arrays of oriented and micropatterned nanotubes have been produced by the pyrolysis of ethylene and iron phthalocyanine for the case of the light-emitting porous silicon substrate and the quartz glass plates, respectively. Further, the prepared nanotube films could be transferred onto various substrates of specific interest, for example, electrodes for electrochemistry and polymer films for organic optoelectronic devices.

Aligned multiwalled carbon nanotubes have also been grown by other approaches, including microwave plasma-enhanced CVD[26–28] and hot-filament plasma-enhanced CVD.[29,30] In particular, by using the microwave plasma-enhanced CVD, Bower et al.[27,28] showed that the alignment of nanotubes, in a direction perpendicular to the substrate, is mainly induced by the electrical self-bias field imposed on the substrate surface from the microwave plasma. Turning off the plasma source turned off the alignment mechanism. It was observed that when the plasma was on, aligned nanotubes emerged, while the nanotubes appeared to be randomly oriented when the plasma was off, as shown in Figure 11.10. It displays a bundle of straight and curled nanotubes obtained by thermal CVD and microwave plasma-enhanced CVD, respectively.

It was observed that the nanotubes grew up initially with a rapid and constant rate (around 100 nm/sec) and decreased rapidly after the catalyst particles were encapsulated by the nanotubes. The high growth rate is crucial for large-scale productions.
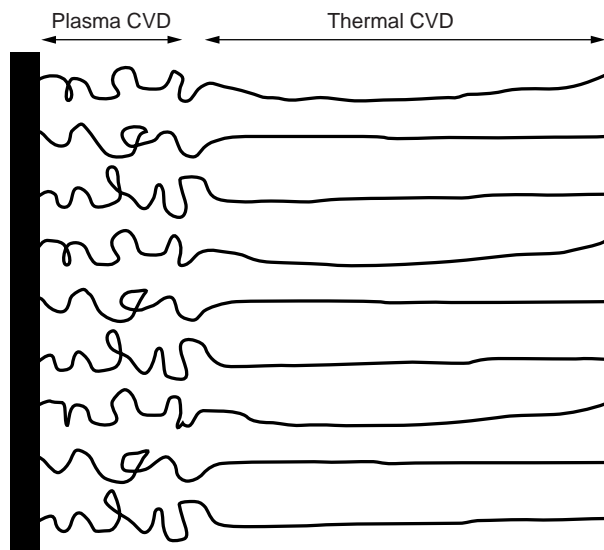
FIGURE 11.10
Schematic of the TEM image of CVD. (With permission from Bower et al., *Appl. Phys. Lett.*, 77, 830–832, 2000.)

Both the microwave plasma-enhanced CVD and the hot-filament plasma-enhanced CVD techniques occur at low temperature. In particular, Ren et al.[31] reported the growth of large-scale aligned nanotube arrays on nickel-coated glass at temperatures below 666°C by using the hot-filament plasma-enhanced CVD method. The use of low temperature is suitable for electron emission applications (cold-cathode flat-panel displays) requiring carbon nanotube emitters to grow perpendicular to the glass surface. In this case, the nanotube nucleation and growth was found to depend on the catalytic centers (ammonia and nickel); in particular, the alignment and thickness are affected by the orientation and size of the initial catalytic sites, respectively.

11.1.3.2 Single-Wall Nanotubes

Various methods have been investigated to synthesize single-wall nanotubes, including electric arc,[7] laser ablation,[32–37] and more recently solar energy vaporization.[38–40] In all cases, the vaporization of a graphite and catalyst mixing under an inert gas atmosphere is involved.

The electric arc was the first technique explored, as it is a catalytic variant of the carbon arc method used for the multiwalled nanotube synthesis. To produce single-wall nanotubes, the carbon arc apparatus was modified by drilling a hole in the anode and filling it with a mixture of the metal catalyst and the graphite powder. Several metal catalysts (Co, Fe, Ni) were investigated to increase the nanotube yield, which was found to be the highest when a mixture of Ni, Y, and graphite was used in the weight ratio of 15:5:80. The single-wall nanotubes were produced in a weblike structure, consisting of tens of tubes, in a chamber and not on the anode as in the case of the multiwalled tubes. The higher density of the nanotubes is observed around the cathode (> 50 wt%), where the nanotubes are arranged in a collar form.[5]

In the laser ablation technique,[32–37] single-wall nanotubes are formed in a carbon plasma generated by the laser ablation of a metal (Ni/Co) composite carbon rod at a temperature of 1200°C under inert atmosphere (argon). A very high yield is obtained by using two successive laser pulses generating 70 to 90 vol% single-walled nanotubes organized in hexagonal ropes. A scaling up of the dual-pulsed laser vaporization technique was recently developed by Rinzler et al.[36] that enabled them to synthesize 10 g/day, which was 45% by volume of the material.

Single-wall nanotubes have also been produced by employing solar energy.[38–40] To understand the nanotube mechanism formation as a function of temperature, pressure, and flow rate of inert gas and target composition, small-scale experiments have been performed with a 2-kW solar furnace (3000 K) consisting of a flat tracking mirror that reflects the sunlight toward a parabolic mirror. Figure 11.11 shows a schematic of the vertical solar reaction chamber.

A Pyrex balloon flask surrounds a water-cooled cylinder supporting a cellulose filter that collects the soot. The target is a graphite crucible filled with a graphite powder and catalyst, which is placed in a graphite pipe that cana-
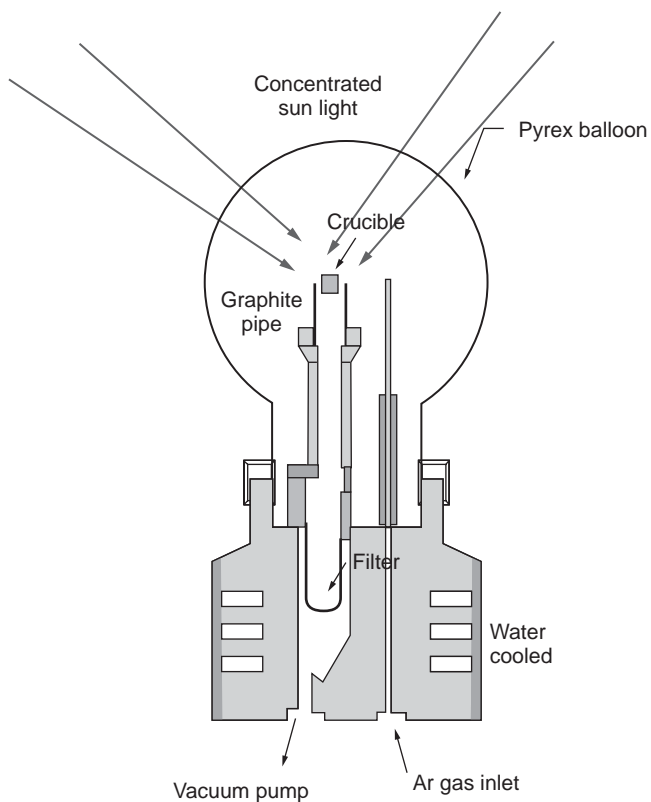
FIGURE 11.11
Solar reactor used for the single-wall nanotube synthesis.[38,39]

lizes the carbon vapor and is heated by the sunlight acting as a thermal screen
and an annealing zone. Most of the nanotubes are formed in the graphite pipe
where the temperature is the highest. The nanotube formation is strongly
affected by the pressure and the inert gas flow rate. Nanotubes have been
observed for pressures higher than 400 mbar from a mixture of graphite, cobalt
(2%), and nickel (2%) in an argon atmosphere. The nanotubes' presence was
detected by TEM images displaying single-wall nanotube bundles, with sizes
increasing as the flow rates decreased. Figure 11.12 shows a TEM image of
nanotube bundles produced by solar energy at pressures above 400 mbar.

The structure of the nanotubes produced by a 2-kW solar furnace is similar
to those observed for nanotubes formed by other common techniques, such
as laser ablation and electric arc. However, as the vaporization temperature
in the solar furnace method is lower than that in the other methods, the
material that grows in addition to nanotubes contains other undesired par-
ticles, such as carbon-coated metal nanoparticles, amorphous carbon, and
carbon nanospheres. Employing more powerful solar furnaces can raise the
purity level, as they increase the vaporization temperature.
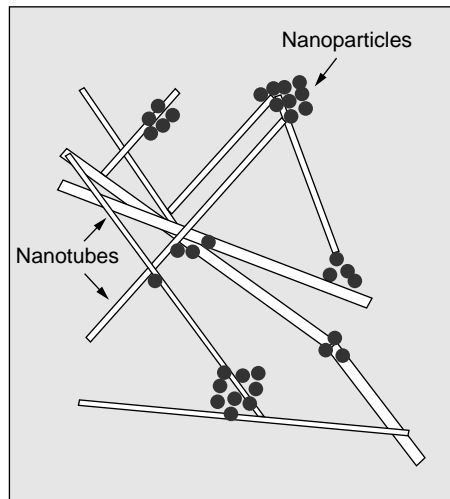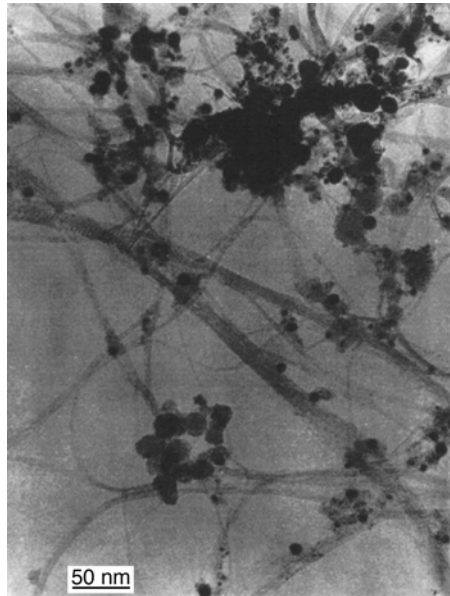
FIGURE 11.12
TEM image of single-wall nanotubes (schematic on the bottom) produced by solar energy. (With permission from Guillard, T. et al., *J. Mater. Sci.*, 419–425, 2000.)

Single-wall nanotubes have also been synthesized under high pressures (about 5.5 GPa) by annealing carbon nanofibers produced with the catalytic chemical vapor deposition technique.[41] Straight and open-ended short nanotubes were obtained from structural transformation of nanofibers in the condensed phase and not in the gaseous phase, as is the case for other techniques, indicating that the high pressure may play an important role in their formation.

11.1.3.3 Purification Methods

The nanotubes produced with all of the above preparation methods contain a large amount of impurities, including carbon nanoparticles, fullerenes, and hydrocarbons. In addition, for the case of the single-wall nanotubes, metal impurities (Ni, Co, Fe) derived from the catalyst may be attached at the end of the formed nanotube ropes. Therefore, the raw material needs to be purified and separated from these impurities. The most common technique to eliminate the nanoparticles is to burn the material at a high temperature (750°C). However, this will also destroy many of the nanotubes, resulting in low yield (about 1%).[7] Other purification methods have been developed more recently based on:

- Chemical oxidation
- Filtration
- Chromatography

Table 11.3 summarizes the procedures of the most common purification techniques for multiwalled nanotubes.[42,43]

Chemical oxidation is a technique that is inexpensive and easy to use. However, even if very pure samples are obtained, the yield is very low (~1%). In addition, depending on the tube curvature and helicity, the oxidation treatment results in thinner and shorter nanotubes with open caps and chemical functionalities on the outer shell.

On the other hand, filtration and chromatography methods are nondestructive. In particular, in the case of size exclusion chromatography, different nanotube fractions with high purity are collected and separated by size.

TABLE 11.3

Purification Techniques of Multiwalled Nanotubes

Purification Technique	Procedure	Yield
Chemical oxidation	Dispersion of the raw sample (1 g) in acid solutions (200 ml of 1 N H_2SO_4 or HNO_3), refluxing for 5 h with 20 g of $KMnO_4$ and heating to 150°C, cooling, filtering, washing with water, washing with HCl to remove manganese oxide, and washing with water to remove HCl_7	Low yield, short and thin nanotubes
Filtration	Nanotube dispersion with the aid of ultrasound in an aqueous surfactant solution, followed by centrifugation and filtration[42,43]	90% of nanotubes
Size exclusion chromatography	Dispersion of the raw material in an aqueous solution with 1 wt% surfactant (sodium dodecylsulfate), followed by sanitation for 5 min and elution through two columns filled with controlled pore glasses[43]	Material loss 10%

The purification methods for single-wall nanotubes are based on the same principles. However, especially in the case of chemical oxidation, researchers have developed several procedures by using different reaction times, temperatures, and acid concentrations.[17,44-46] For example, Hernadi et al.[19] combined chemical and ultrasound treatments to purify single-wall nanotubes synthesized by decomposition of acetylene over supported Co/silica and Fe/silica catalysts. In particular, since the nanotubes were strongly attached to the catalyst particles, the samples were immersed in acidic solution (30% HNO_3) for 4 h. They were filtered, washed with distilled water, and finally washed with acetone. The second step of the purification involved ultrasound treatments for 10 min in an equal mixture of n-hexane, acetone, and ethanol allowed to sediment for 20 min. This last treatment was repeated several times. To remove the amorphous carbon, hydrogenation was performed at 900°C for 4.5 h.

Dillon et al.[44] employed different times and temperatures for the acid treatment. The single-wall nanotubes (80 mg) obtained by laser ablation were refluxed in 60 ml of HNO_3 at 120°C. The suspension was filtered through a 0.2-μm (polytetra-fluoroethiliene-coated polypropylene) filter, washed with deionized water, and then dried. After this treatment, TEM images showed that nanotubes were encased in a carbon matrix, which was removed completely by oxidation at 550°C for 30 min. The final purity of the samples was estimated to be greater than 98% by weight.

Thus, the oxidation method has the advantage to remove almost all the metal catalyst and amorphous carbon particles easily. However, the nanotube bundles could be damaged if they are exposed to higher concentration or longer times of the acid solution.

Li et al.[45] developed an oxidation method able to purify single-wall nanotubes synthesized by the catalytic decomposition of carbon hydrocarbons without damaging the nanotube bundles. In particular, 200 mg of raw samples was suspended in benzene for 1 week and filtered to extract benzene-soluble materials, such as catalyst precursor and fullerenes. After washing with deionized water, ultrasound treatment at 1000 W cm^{-2} for 1 h was carried out in 37 wt% HCl. The mixture was stirred for 10 min, which caused the acid dissolution of the Fe catalyst. Finally, the sample was washed with deionized water and dried, obtaining 75 mg of purified single-wall nanotubes. Figure 11.13 shows SEM images of the single-wall nanotubes before and after the purification, displaying the effectiveness of the procedure. In fact, after the purification one can easily identify nanotube ropes.

Filtration methods have also been used to purify single-wall nanotubes. However, filtration of single-wall nanotubes could become very slow due to the blocking of the filter pores. To overcome this problem, Rinzler et al.[36] reported a macroscale purification technique based on a cross-flow filtration system that may be scaled to industrial levels with a yield of 10 to 20% by weight. The developed method consisted of refluxing (45 h) in nitric acid (2 to 3 M), centrifugation, and washing with deionized water. After the acid treatment, the sample was dispersed, by ultrasonic agitation, in 1.8 l of NaOH solution (pH 10) with the aid of a surfactant and then filtered by the cross-
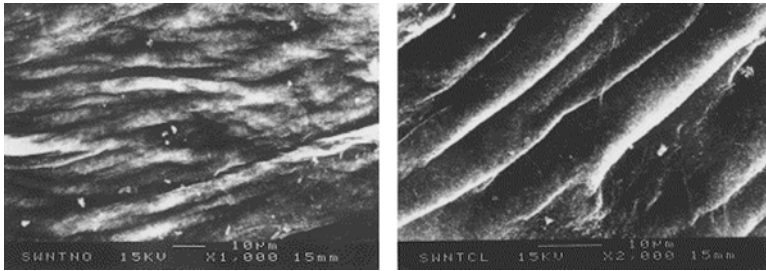
FIGURE 11.13
SEM image of single-walled nanotubes before and after purification. (With permission from Li, F. et al., *Carbon*, 38, 2041-2045, 2000.)

flow filtration system. Finally, to remove the surfactant and residual impurities, the solids were washed with methanol, treated with acid (sulfuric/nitric mixture), and filtered.

A microscale purification procedure for single-wall nanotubes has also been developed. For example, Bandow et al.[37] developed a purification method based on:

- Preliminary filtration to remove fullerenes and polyaromatic carbons
- Sonication in aqueous solution with a surfactant followed by micro-filtration

Starting with 30 mg, the raw sample was filtrated and dispersed in 150 cm^3 of aqueous solution with a cationic surfactant (0.1%). After sonication for 2 h, the nanotube suspension was filtrated through a microfiltration cell using overpressure (about 2 atm of N_2). The filtration step was repeated three times obtaining high levels of purity (90% by weight).

Finally, a yield larger than 90% was found by Shi and coworkers[47,48] by combining burning in air at 350°C with the microfiltration technique. The purification procedure consisted of three steps:

- Heating to 350°C for 2 h to remove amorphous carbon
- Soaking in 36% HCl for 1 day and centrifuging to remove metal catalyst in the sample
- Washing with deionized water (several times), dispersion in 0.2% benzalkonium chloride solution, filtration through a 1-micron-pore polytetrafluoroethylene (PTFE) membrane, and refiltration through a 0.2-micron membrane under vacuum

11.1.3.4 Summary

Recently, several nanotube synthetic techniques (see Table 11.4) have been developed, allowing the production of reasonable pure carbon nanotubes. In particular, great effort has been devoted to the development of preparation

TABLE 11.4

Preparation Techniques of Carbon Nanotubes

Nanotubes	Technique	Final Product Characteristics
Multiwalled	Carbon arc[7,17]	Fractal structure consisting of aligned fibers made of aligned nanotubes and nanotube bundles (low yield)
Multiwalled	Catalytic vapor deposition[18–21] Mesoscopic substrates[22,23]	Curved and entangled nanotubes with good uniformity of size (higher yield than carbon arc) Aligned nanotubes
Multiwalled	Microwave plasma-enhanced CVD[26–28]	Aligned nanotubes
Multiwalled	Hot-filament-enhanced CVD[29,30]	Aligned nanotubes
Single wall	Electric arc[7]	Weblike structure
Single wall	Laser ablation[32–37]	Hexagonal ropes arrangement (70–90 vol%)
Single wall	Solar furnace[38–40]	Structure similar to the electric arc with purity level depending on the furnace power
Single wall	Catalytic CVD[41]	Straight and open-ended short nanotubes

methods able to make organized nanotube structures that could have a great impact on the applications. However, there is still the need to improve and optimize the processing techniques in terms of final yield, which could provide effectively commercial large-scale uses. Further, more investigations are required on the purification procedures of the raw nanotubes. In fact, at this stage, the available purification techniques do not satisfy all requirements displaying the following characteristics:[42]

- Oxidative methods: cheap, easy to apply, low yield, chemical alteration of the tubes
- Filtration and sedimentation: good yield, slow process (time-consuming)
- Chromatography: high purity, low yield

11.1.4 Dispersion and Rheological Behavior

The study of the preparation methods of how nanotubes disperse in aqueous solution and their relative motion represents the first step in understanding their behavior for application as fillers. Since the starting material often consists of curved and intertwined carbon nanotubes, the formation of stable dispersions is achieved by chemical treatments that provide suspensions with a more significant concentration than the use of ultrasounds. In particular, Shaffer and coworkers[49,50] used oxidation treatments based on a mixture of concentrated nitric and sulfuric acid. To characterize nanotube dispersion with different length distributions, they also performed bromine pretreatment, providing a short tube suspension. The two dispersions were charac-
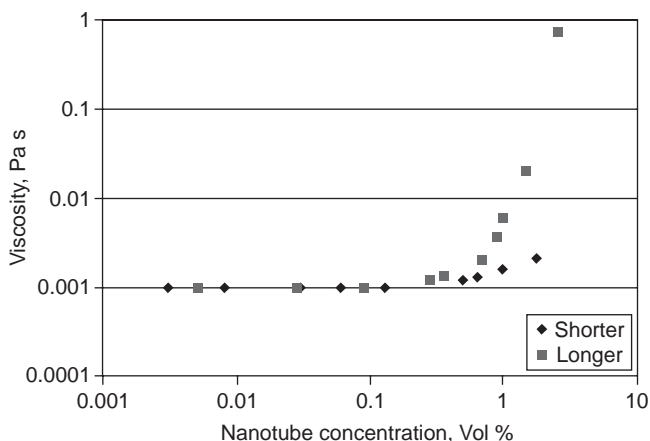
FIGURE 11.14
Nanotube dispersion viscosity as a function of the concentration.[49]

terized in terms of length distribution by TEM image analysis and viscosity measurements by capillary rheometry. The viscosity of both dispersions displayed the same behavior as a function of the tube concentration: a slight increase at low concentrations and an abrupt increase above a critical concentration, estimated around 0.5 and 1% by volume for the longer and shorter nanotube suspensions, respectively (see Figure 11.14).

The rapid increase of the viscosity is observed typically in polymer solution and is named as entanglement transition. A good fitting of the viscosity data was found by using the Schulz–Blaschke equation for polymer solutions:

$$\frac{\eta_{sp}}{c} = [\eta] + k[\eta]\eta_{sp} \tag{11.1}$$

where η_{sp} is the specific viscosity, $[\eta]$ is the intrinsic viscosity, k is a constant, and c is the concentration of the nanotubes.

A viscoelastic gel was formed by increasing the nanotube concentration above 5% by volume. The gel density was measured, which enabled the evaluation of the packing fraction that was found to be significantly high (around 50%). It was also observed that the water readdition to the solid not only redispersed the tubes, but also resulted in a reversible swelling.

Moreover, to study the nanotube alignment, films were prepared by filtration of dispersions. SEM images and x-ray diffraction provided information on the tube orientation and alignment degree. The tube arrangement was found to be a function of concentrations. Dispersions with a concentration above the critical value of 0.3% by volume formed random tube films (see Figure 11.15A), while a significant local alignment was observed from dispersions with lower tube concentrations (Figure 11.15B).
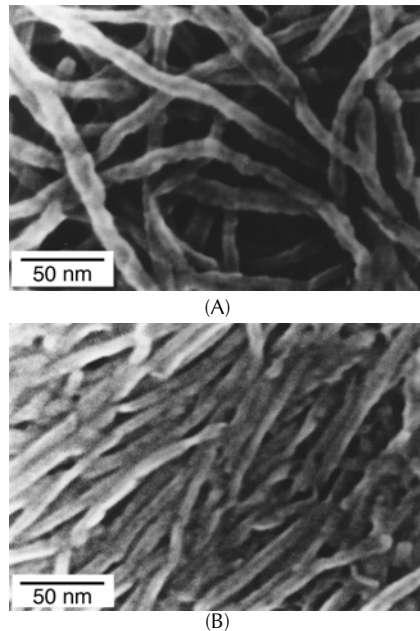
FIGURE 11.15
SEM image displaying a random arrangement (A) and a local alignment (B) for nanotube concentrations above and below a critical value. (With permission from Shaffer, M.S.P. and Windle, A.H., *Macromolecules*, 32, 6864–6866, 1999.)

11.1.4.1 Summary

The carbon nanotube is an important discovery of the new era of nanotechnology revolution. However, if the advantages of these tubes is to be fully realized one must overcome some of the barriers that are precluding their use on a large scale. The challenges are to (1) obtain high yields from the current preparation methods or to invent new methods to produce them on a large scale; (2) explore purification techniques that are simple, relatively inexpensive, do not damage or change the structure of the nanotubes, and can be automated; and (3) develop the ability to disperse them effectively as fillers in a matrix with good adhesion and bonding properties. The next section will discuss the state of our understanding about the uses of carbon nanotubes in polymeric composites.

11.2 Polymer Nanotube Composites

11.2.1 Introduction

Carbon nanotubes have extraordinary properties that have attracted the attention of several researchers from diverse fields. Substantial effort has

been devoted to the experimental evaluation and theoretical calculation of their physical, electronic, magnetic, electrical, and mechanical properties. For example, recently good electrical transport properties (ballistic conductance) have been noted.[5] In particular, due to the different helicities of the cylinder, a range of electronic behaviors (metallic, semiconducting, and semimetallic) has been observed by four-probe measurements on several multiple-wall nanotubes, while the single-wall nanotubes have a well-defined behavior and can be regarded as quantum wires.[5]

Because of their promising physical and mechanical properties, the most common commercial application of carbon nanotubes is based on their use as filler elements for metals, ceramic, or polymers matrix. In particular, carbon nanotubes may exhibit characteristics that can be beneficial. For example, they can be used as:

- Reinforcement of polymer-based composite materials, which improve structural properties
- Polymer modifiers for high-temperature uses
- Conductive filler in insulating polymer matrices to provide electrostatic discharge and electromagnetic radio frequency interference protection
- Doping of conjugated luminescent polymers to produce active materials for electronic applications

The use of carbon nanotubes as reinforcing systems of polymer matrix would offer several advantages over the conventional reinforcements, including continuous and short fibers (glass, carbon). In the case of continuous-fiber reinforcements, the advanced composite material has much higher mechanical properties in the direction parallel to the fibers or in the plane of the lamina than it does in the transverse direction. Further, since the conventional polymer processing equipment cannot process the long continuous fibers, their use is limited to simple shapes and limited production. On the other hand, it is established that the fiber aspect ratio represents the critical factor affecting the resulting structural properties of short-fiber composites. As the aspect ratio increases, the composite stiffness and strength increase. However, the packing of short fibers in a polymer matrix is a percolation phenomenon, so the maximum packing decreases with increasing aspect ratio (see Figure 11.16) and may not be sufficient to manufacture a very strong material.[12]

Carbon nanotubes could overcome these problems by combining their high aspect ratio (around 1000), small size, and greater strength and stiffness than the corresponding macroscopic forms. Further, since they do not break as easily during processing (due to their ability to withstand large strains) as the carbon fibers, they have a substantial advantage in composite processing and manufacturing.[4]

The addition of carbon nanotubes to polymers could improve not only the mechanical properties, but also the thermal stability and the electrical
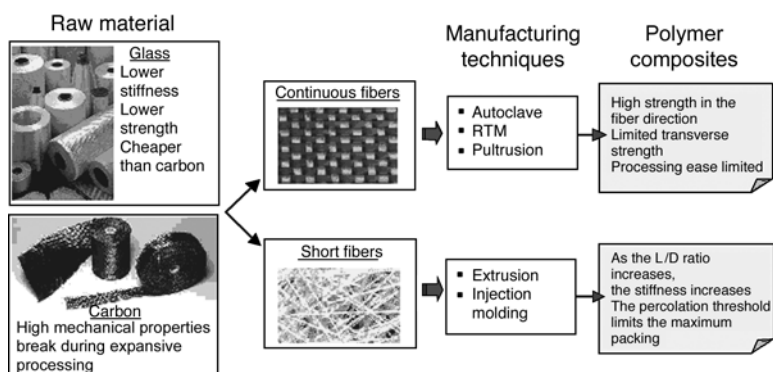
FIGURE 11.16
The use of conventional fiber systems in polymer composites.

conductivity of the resulting composite. In particular, due to high thermal resistance, carbon nanotubes could improve the composite performance, allowing applications at high temperatures. Moreover, the dispersion of the carbon nanotubes into insulating polymer systems induces substantial increases of the electrical conductivity, enabling other applications in aeronautical (vertical stabilizers of the aircraft), automotive (antistatic coating of exterior parts), and consumer goods (computer housings) fields.[51] Therefore, the high aspect ratio and the small size of the carbon nanotubes make them interesting as valid alternatives to the common conductive fillers, such as carbon black. In fact, even if the conductive filler is useful to provide a conductive path through an insulating component, its content has to be minimized due to the possible reduction of the mechanical properties of the matrix and the increase in the viscosity, which affects the processing ease. Finally, the combination of carbon nanotubes and polymer materials also has promising potential for the development and design of electronic devices, such as light-emitting diodes (LEDs)[71,73] and photovoltaic devices,[70] giving better performance and greater efficiency, respectively.

In recent years, many researchers have manufactured composite films from carbon nanotubes and polymer matrices, which may be either thermoset or thermoplastic. Table 11.5 reports samples made by various researchers to form this new class of composites. It should be noted that in most cases, multiwalled tubes were used. Further, it is important to outline that the effective use of the carbon nanotubes in composite applications depends strongly on the ability to uniformly disperse and orient the nanotubes and on the interfacial bond with the polymer matrix. In fact, the achievement of homogeneous dispersions has a significant impact on the final properties of the composite material affecting the fiber–matrix stress transfer ability and, as a consequence, the efficiency and the quality of the composite interface.

To attain stable dispersions before the composite preparation, since the carbon nanotubes had many entanglements as supplied, chemical

TABLE 11.5

Polymer-Based Carbon Nanotube Systems and Corresponding Dispersion Methods

Nanotubes	Polymer	Preparation Method
Single wall	Epoxy (Epon 828)	Ultrasonic dispersion[53]
Single wall; multiwalled	PMMA	Mixing in ultrasonic bath and spin coating,[54] ultrasonic dispersion,[55] mixing followed by *in situ* polymerization[56]
Single wall	Polypropylene	Electrochemical method,[57] mixing, and ultrasonic treatment[58]
Single wall; multiwalled	Epoxy (Araldite LY556)	Tube sonication followed by mixing with the polymer[59,60]
Multiwalled	Epoxy (Epon 828)	Ultrasonic dispersion before the curing[61]
Multiwalled	Polystyrene	Solution evaporation assisted by high-energy sonication[62]
Multiwalled	Epoxy (Araldite LY564)	Tube sonication, drying, and dispersion on a glass surface, spreading of the polymer by blade[63,64]
Multiwalled	Poly(vinyl alcohol)	Mixing with the polymer, casting, and controlled water evaporation after chemical treatment of the tubes[65]
Multiwalled	PHAE	Casting of nanotube suspension, polymer, and chloroform after sonication[66,67]
Multiwalled	Urethane/diacrylate EBECRYL 4858	Tube sonication in ethanol, drying, and dispersion on a glass surface, polymer spreading by blade[68]
Multiwalled	Epoxy (Epon 812)	Tube sonication and mixing with polymer[69]
Multiwalled	PPV	Chemical oxidation and spin coating[70]
Multiwalled	PmPV	Mixing and sonication[71–73]

(oxidation) or ultrasonic treatments were performed (see Table 11.5). Different solvents (ethanol, toluene, chloroform) and times were employed for the sonication treatment. For example, multiwalled carbon nanotube polystyrene composites[62] were produced by a solution evaporation method assisted by high-energy sonication. The process consisted of separate dispersion and high-energy sonication of the polymer and the nanotubes in toluene (from half a minute to 120 min), followed by mixing, casting into a culture dish, and solvent evaporation. Also, single-wall nanotube epoxy composites[59] have been produced by ethanol sonication of the nanotubes for 2 h, followed by mechanical mixing with the polymer resin, solvent evaporation in a vacuum oven (50°C), and curing at 72°C (3 h).

The homogeneity of the composite films and the nanotube dispersion is often investigated by using scanning electron microscopy[53–56,60,61,65] and transmission electron microscopy.[59,62,66,69,71] Uniform distributions of carbon nanotubes into the polymer matrices are usually attained for low values (1 wt%) of the nanotube concentrations, as in the case of polystyrene[62] and polymethyl methacrylate (PMMA).[54] Due to the greater interfacial wetting, the thermoplastic polyhydroxyaminoether (PHAE)[66] and the conjugated luminescent polymer poly(m-phenylenevinylene-co-2,5-dioctoxy-p-pnenylenevinylene) (PMPV)[71] gave better results for higher values of the nanotube concentrations. In particular, in the case of PHAE, the analysis of the fracture surface by TEM

showed that the nanotubes did not aggregate significantly and were well wetted by the polymer. The TEM image of multiwalled/PMPV composite film displayed a thin membrane of the polymer enveloping the nanotubes, suggesting good wetting and mechanical strengthening. A good interfacial bond was also found with the urethane/diacrylate system,[68] which was characterized by a stress transfer efficiency one order of magnitude higher than the conventional fiber-reinforced composites. On the other hand, the epoxy matrices[53,60] did not seem to be compatible with the carbon nanotubes, forming a weak interfacial bond between the two phases. In fact, in the case of the Araldite LY556,[60] although the ultrasonic treatment and the strong stirring led to an improvement of the dispersion, the resulting composite films exhibited the presence of many entanglements.

Recently, to improve the nanotube dispersion in an epoxy matrix and modify the interfacial bonding, a surfactant was used by Gong et al.[52] The surfactant addition was found to influence both the composite thermomechanical properties and the interfacial adhesion. In particular, the authors hypothesize that the surfactant can introduce a steric repulsive force between the carbon nanotubes that appear distributed and those aligned along one direction. Conversely, when the surfactant is not used, SEM images display high agglomerations of carbon nanotubes clustered and lumped together.

11.2.2 Properties of Manufactured Nanotube Polymer Composites

11.2.2.1 Physical and Mechanical Properties

The study of the influence of the carbon nanotubes on the properties of the polymer matrix can shed light on both the potential of nanocomposite processing techniques and possible nanotube applications. To date, very few researchers have focused on the effect of the carbon nanotubes on the thermomechanical properties of the resulting composite. There have been two studies: one of multiwalled carbon nanotubes (range: 10 to 50 wt%) in the matrix of poly(vinyl alcohol),[65] and the other one on multiwalled carbon nanotubes (1 wt%) and an epoxy matrix.[52] These studies indicated that the nanotube addition moderately increases the glass transition temperature (Tg) measured by dynamic mechanical analysis (tan δ), but when a good dispersion is achieved with the use of a surfactant, the addition of 1 wt% nanotubes could increase the glass transition temperature by a substantial amount (the Tg increased from 63 to 88°C). In addition, the presence of nanotubes stiffened the polymer matrix, especially at high temperatures,[65] and increased the temperature at which the onset of degradation initiates.[58,65] These results suggest that the nanotubes could find applications both as reinforcing systems and as polymer modifiers for high-temperature uses.

Several authors have investigated the mechanical behavior of carbon nanotube polymer composites. Their goal has been to characterize both their tension and the compression properties and to understand their fracture modes. It was observed that the effective reinforcement of the polymer

TABLE 11.6

Tensile and Compression Modulus of Carbon Nanotube Polymer Composites

Multiwalled Content	Polymer	Tensile Modulus	Compression Modulus	Measurement Method
5 wt%	Epoxy[61]	Composite: 3.71 ± 0.2 GPa Pure polymer: 3.1 ± 0.2 GPa	Composite: 4.5 ± 1.5 GPa Pure polymer: 3.63 ± 0.25 GPa	ASTM and Raman spectrum
V_f = 0.25 thin	Epoxy[63]	—	99.8–139.8 GPa 116.7–151 GPa	TEM
V_f = 0.25 thick	Epoxy[63]	—	135–147 GPa	TEM
1 wt% ($l/2\,r$ = 446)	Polystyrene (PS)[62]	Composite: 1620 ± 130 MPa Pure polymer: 1190 ± 130 MPa	—	Macroscopic tensile test
1 wt% ($l/2\,r$ = 1167)	PS[62]	1690 ± 130 MPa	—	Macroscopic tensile test
1, 5, 8 wt%	PMMA[55]	Composite: 3.3, 5, 6 GPa Pure polymer: 3.1 GPa	—	Macroscopic tensile test

matrix and the improvement in the composite mechanical properties was a function of the interfacial shear stress between the two phases. It is the shear stress that determines the load transfer efficiency from the matrix to the carbon nanotubes. Table 11.6 reports the tensile and compression modulus of different multiwalled carbon nanotube polymer composites, where $l/2\,r$ indicates the ratio between the average length and diameter tube (an average of the aspect ratio).

As reported, only in the case of the epoxy matrix (EPON 828),[61] both the tensile and compression data are available displaying a different value: the maximum compression modulus is significantly higher than the tensile elastic modulus. These data were obtained by the linear region of the stress–strain curves that are compared to the stress–strain curve of pure epoxy in Figure 11.17.

The introduction of nanotubes into the epoxy matrix affected the tensile modulus less than the compression modulus, which was 3.63 ± 0.25 GPa and 4.5 ± 1.5 GPa for the epoxy and the nanotube composite, respectively. The qualitative measurement of the strain was performed by using micro-Raman spectroscopy during the American Society for Testing and Materials (ASTM) test. Raman spectroscopy is a common technique used to characterize carbon materials. It gives information about the amount of ordering, the degree of sp^2-to-sp^3 bonding, and the size of the graphitic crystallites in the material. In particular, when a strain is applied to the material, a Raman peak shift is observed due to the changing of the interatomic distances and the vibration frequencies of the normal modes. By observing a larger shift in compression than in tension, it was deduced that the nanotubes carry less strain in tension than in compression due to the poor load transfer between
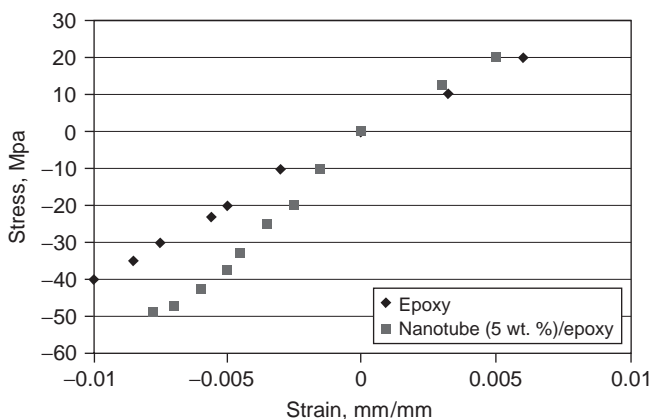
FIGURE 11.17
Stress–strain curves from the tension and compression test on pure epoxy and 5 wt% nanotube/
epoxy composites. (With permission from Schandler, L.S., Giannans, S.C., and Ajaian, P.M.,
Appl. Phys. Lett., 73, 3842–3844, 1998.)

the outer and inner layers. However, in compression, the load was trans-
ferred to the inner layers through nanotube bent sections and the slipping
was prevented due to the tube structure and geometrical constraint.

A high compressive strength was found by Lourie et al.[63] by TEM exami-
nation of nanotubes/epoxy (Araldite LY564) composite samples. They ana-
lyzed two groups of samples having different ratios between the tube wall h
and the average outer radius r. The groups were divided into thick walled
and thin walled, depending on if the h/d ratio was greater than 0.6 or less than
0.6, respectively. The compressive stress was induced by the polymerization
shrinkage (5.4 ± 1.4%) and the thermal effect associated with the electron beam
in the TEM cell. Depending on the h/d ratio and the quality of the interface
with the polymer matrix, different compressive strength values and behavior
were calculated. In general, the thicker-walled nanotubes deformed by
buckling as an elastic medium and bent laterally, while the thinner-walled
ones collapsed or fractured, showing a progressive fragmentation.

For the polystyrene composite,[62] Qian et al. found that the tensile modulus
increases as $l/2\,r$ increases. For the two analyzed systems (see Table 11.6),
the modulus increased by 35 and 42% compared to the neat polystyrene.
These experimental data were validated by theoretical calculations consid-
ering the composite films as random-oriented discontinuous-fiber lamina.
Good agreement between the data suggested that the external tensile load
was transferred successfully to the nanotubes across the interface.

Complementary deformation investigations inside the TEM were performed
to understand the tensile fracture and the crack propagation mode. By taking
TEM images at different points along the crack wake, it was observed that the
cracks nucleate at low-density nanotube areas and then propagate along weak
interfaces or low-density nanotube zones[62] (see Figure 11.18).
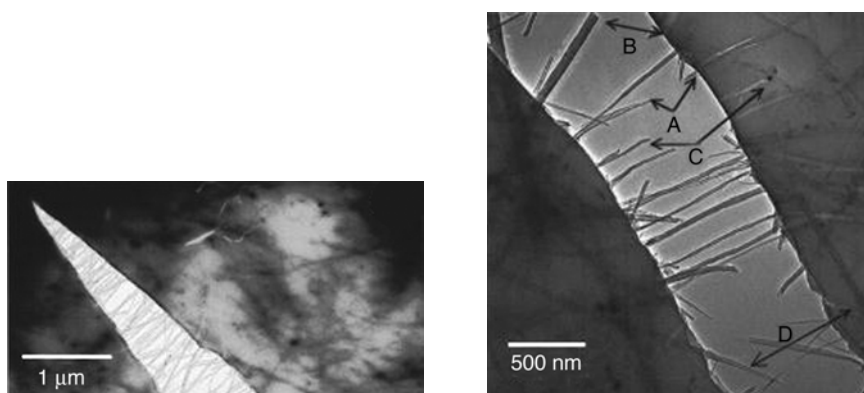
FIGURE 11.18

TEM image of crack nucleation and propagation in multiwalled polystyrene composites. (A) Nanotube alignment perpendicular to the crack direction. (B) Nanotube breaking and pulling out of the matrix. (C) Broken nanotubes with defects. (D) Nanotubes breaking between the crack faces. (With permission from Qian, D. et al., *Appl. Phys. Lett.*, 76, 2868–2870, 2000.)

To bridge the crack faces, the nanotubes aligned perpendicular to the crack direction and pulled out of the matrix at a crack-opening displacement of 800 nm. The fracture stress increased by 25% compared to the neat polystyrene value.

The analysis of the failure was performed also for other composite systems by observing the fracture surface with TEM and, in some cases, measuring the interfacial shear stress (Raman spectroscopy, Kelly–Tyson approach). Bower et al.[67] reported that, depending on the r/h ratio, the uniaxially oriented nanotubes embedded within the thermoplastic polyhydroxyaminoether displayed a bending deformation with multiple or single buckles. The multiwalled nanotubes that had an r/h of less than 2 showed multiple buckling, while the thin-walled nanotubes ($r/h > 2$) formed single buckles. The onset buckling strain and the fracture strain were estimated around 4.7 and 18%, respectively. This is at least one order of magnitude higher than those of the high-modulus carbon fibers. The TEM observation of the fracture surface showing the polymer wetting of the nanotubes and their pullout suggests that the composite failure was induced by the nanotube pullout and the mechanical fracture of the polymer matrix.

The pullout was observed also in the case of single-wall nanotubes (5 wt%) embedded in an epoxy matrix.[53] The TEM observations of the fracture surface showed a network of nanotube bundles covering the surface. Depending on the crack size (d, distance between the crack surface) and the average nanotube length (l), three different configurations of the nanotubes across the crack were observed:

- In the case of a large crack (> 3 μm, $l/d < 1$), all nanotubes were completely pulled out and no nanotubes were displayed between the crack surfaces.

- For a crack separation close to 1 μm, aligned nanotubes and stretched bundles bridging the crack were observed.
- For a crack size ranging from several tens to several hundreds of nanometers, most nanotubes were curved and looped, and few were stretched.

In the last case, the crack first separated and stretched the nanotubes and then relaxed the load. This behavior exhibits the high flexibility and the elastic properties of the single-walled nanotubes that can effectively increase the composite toughness having reversible deformations.[53]

However, to take advantage of the promising nanotube properties, the load must be transferred from the matrix to tubes. In this case, by Raman spectroscopy it was found that the load transfer was limited by the nanotube slipping within the bundles. As a consequence, the composite strength was controlled by the modulus of the bundles that is less than the individual nanotube modulus.[53] On the other hand, a high degree of interfacial shear stress was obtained by Wagner et al.[68] for a multiwalled carbon urethane/diacrylate composite consolidated by ultraviolet (UV) action. As in the single-fiber fragmentation phenomenon of macroscopic composites, TEM image analysis showed a progressive fragmentation of single nanotubes parallel to the tensile stress direction. Since the fragmentation was observed only in the stressed samples, it was attributed to the stress induced during the tensile testing and not to possible compressive thermal stress resulting from the polymer shrinkage. The interfacial shear stress τ_{NT} was evaluated by assuming that the applied stress was transferred to the nanotubes through an interfacial shear mechanism at a molecular level and, consequently, using a generalization of the classical model of Kelly and Tyson:[68]

$$\tau_{NT} = \left[\frac{\sigma_{NT}(l_c)}{2(1_c / D_{NT})} \right] \left(1 - \frac{d_{NT}^2}{D_{NT}^2} \right) \qquad (11.2)$$

where $\sigma_{NT}(l_c)$ is the strength of a nanotube fragment of length l_c, and d_{NT} and D_{NT} are the inner and outer tube diameters, respectively. A very high interfacial shear strength was found to be of the order of 500 MPa, which is an order of magnitude higher than the stress transfer ability of the conventional composites.[68] This high value was explained as a consequence of the strong nanotube curvature and the presence of multiple concentric graphitic sheets that can increase the reactivity of the nanotubes during the UV cure.

Finally, for well-aligned multiwalled nanotubes dispersed in an epoxy matrix, Lourie et al.[63] observed doublets of breaks in close thin-walled tubes (see Figure 11.19). The authors claim that similar behavior is usually observed in the conventional composites, where the interaction between the fibers leads to the formation of progressive larger break clusters and to final failure.

Moreover, they suggested that the fundamental concepts of the continuum mechanics of traditional fiber composites could be applied at the
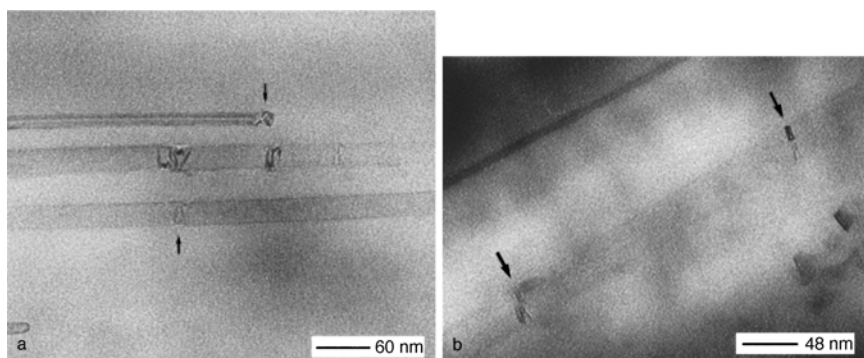
FIGURE 11.19
TEM image of doublets of breaks in multiwalled epoxy composites. (From Lourie, O., Cox, D.M., and Wagner, H.D., *Phys. Rev. Lett.*, 81(8), 1638–1641, 1998. With permission from the American Physical Society.)

nanometric level to understand the load transfer mechanisms from the matrix to the nanotubes.

11.2.2.2 Electrical and Electronic Properties

The addition of the carbon nanotubes to a polymer matrix also strongly affects the electrical properties of the composites. This effect can be used for several applications, including optoelectronic, electromagnetic induction shielding, and membrane technologies.[63]

Table 11.7 reports some examples of nanotube polymer composites and the corresponding electrical conductivity.

These types of systems typically show a percolation behavior. The percolation phenomenon is characterized by the presence of a conductive path through the matrix due to the formation of a three-dimensional network of conductive fillers, which are the nanotubes. A sharp drop characterizes the percolation threshold in the electrical resistance.

As an example, Figure 11.20 shows the conductivity data obtained by Coleman et al.[72] for the nanotube PMPV system that can be used for optoelectronic applications.

TABLE 11.7

Electrical Conductivity of Nanotube Polymer Composites

Nanotube Content	Polymer	Composite Electrical Conductivity, S m^{-1}	Pure Polymer Electrical Conductivity, S m^{-1}
0.1 vol%	Epoxy[60]	10^{-2}	$5 \cdot 10^{-8}$
20 wt%	Polypyrrole[58]	$1.4 \cdot 10^{-1}$	$2.6 \cdot 10^{-2}$
20 wt%	PVOH[62]	10^{-1}	$2.9 \cdot 10^{-9}$
7–11 wt%	PMPV[72]	$1.5 \cdot 10^{-9}$ to $1 \cdot 10^{-1}$	$2 \cdot 10^{-10}$
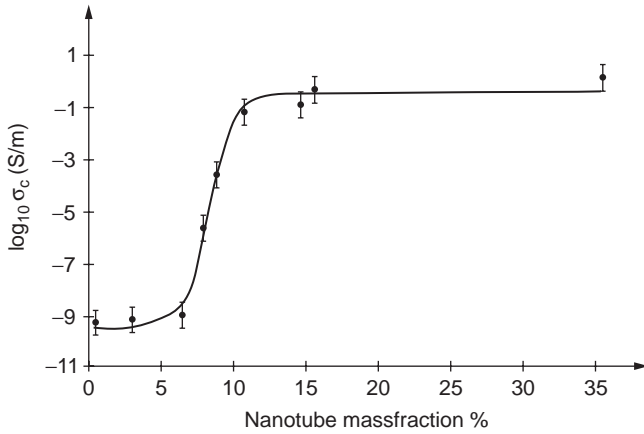
FIGURE 11.20
Composite conductivity as a function of the nanotube mass fraction. (From Coleman, J.N. et al., *Phys. Rev. B*, 58(12), 7492–7495, 1998. With permission from the American Physical Society.)

As reported, the electrical conductivity increases ten orders of magnitude starting from the value of $2 \cdot 10^{-10}$ S/m of the pure polymer PMPV. The fitting of the experimental data was performed by using the analytical model, based on the Fermi–Dirac distribution:[72]

$$\log(\sigma_c) = \log(\sigma_n) + \left[\log(\sigma_p) - \log(\sigma_n)\right] / \left[1 + \exp(b(p - p_c))\right] \quad (11.3)$$

where σ_c, σ_n, and σ_p are the composite, nanotube, and polymer conductivity, respectively; p is the mass fraction; b is an empirical parameter; and p_c is the percolation threshold. The best fit of the data reported in Figure 11.21 gave a percolation threshold of 8.4%.

A significant increase of the electrical conductivity was found also for the nanotube epoxy composite. The polymer matrix (Araldite LY556), investigated by Sandler et al.,[60] is usually used for aircraft applications where high electrical conductivity is required to avoid electrostatic charging and electromagnetic radio frequency interference. For this type of applications the carbon black is commonly used as the conductive filler; its percolation threshold is attained at the concentration of 0.5 vol%. The doping with a carbon nanotube in place of carbon black reduced the concentration required from 5 to 0.04% and increased the overall conductivity. Finally, it should be observed that no negative influence was observed on the processing and on the finished surface of samples corresponding to this low filler content of nanotubes.[60]

The dispersion of carbon nanotubes in polymer systems attracted research interests not only to reinforce the polymer, but also to improve the electronic properties based on the morphological interactions between the two constit-
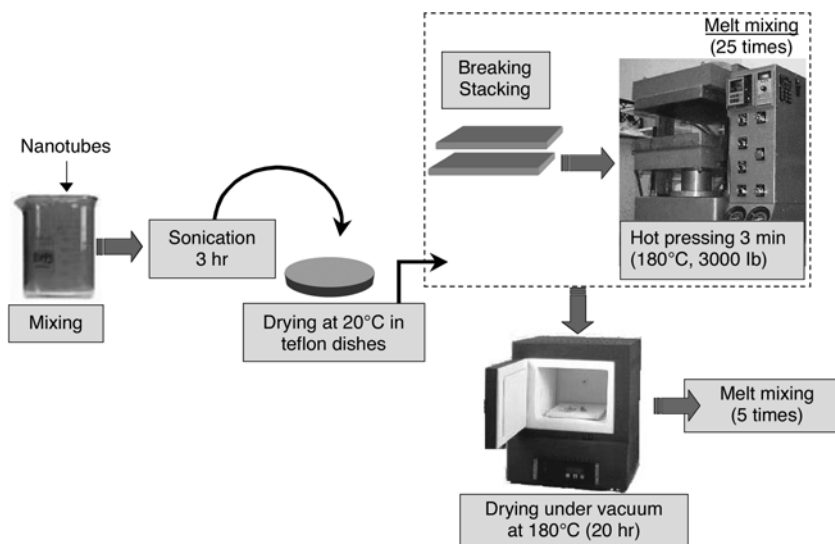
FIGURE 11.21
Schematic of the melt-mixing technique.[55]

uents. In particular, combining the nanotubes and the conjugate polymers, active materials have been obtained for light-emitting diodes,[71,73] field effect transistors, and photovoltaic devices.[70]

Curran et al.[71] investigated the optical properties of a nanotube/PMPV composite that was then used as an emissive layer to fabricate an organic light-emitting diode. The addition of the nanotube to the PMPV polymer caused a gradual decrease of the luminescence intensity due to absorbing, quenching, and scattering phenomena from the nanotubes. Further, the nanotubes acted as a heat sink, avoiding the polymer degradation that can occur at high laser intensities. The LED device showed a better stability in air than that of the polymer. Since, the polymer was chemically undoped, the big advantage of using the nanotube in conjugated polymers was the resulting unchanged electronic processes, which, on the other hand, led to higher mobility of charge carriers due to the increase of the electrical conductivity.

Multiwalled nanotube/poly(p-phenylenevinylene) (PPV) composites were used to fabricate a photovoltaic device by Ago et al.[70] The multiwalled nanotubes acted as a hole-collecting electrode and allowed one to obtain a good quantum efficiency, 1.8% at 2.9 to 3.2 eV, which is twice the quantum efficiency of the standard device with an indium-tin oxide electrode. The high efficiency was attributed to the formation of an interpenetrating network of PPV polymer chains and the nanotubes, and the high work function of the nanotubes. Further, the addition of nanotubes to the PPV caused a significant reduction of the photoluminescence efficiency and affected the photoluminescence spectrum.

11.2.3 Processing and Manufacturing

11.2.3.1 Processing Techniques

As outlined above, the improvement of the final properties of the composite material depends on the dispersion degree and the alignment of the carbon nanotubes into the polymer matrix. In fact, as the orientation is critical in the carbon nanotube composites, an important issue is the study and development of the processing techniques able to manufacture and control the microstructure of this new nanocomposites class. Currently, after the ultrasonic treatment on the carbon nanotubes, the composites are produced by mixing the polymer matrix with the nanotubes and sonication, followed by solvent evaporation and casting[62,65] or curing into molds or a vacuum oven for the case of thermoset matrices.[52,53,59–61,63]

More recently, in order to facilitate the dispersion of the nanotubes, different techniques have been used, including:

- *In situ* polymerization of PMMA in the presence of multiwalled carbon nanotubes[56]
- Electrochemical method in the case of polypropylene by growing the conducting polymer film on an electrode surface using the carbon nanotube as a dopant[57]
- Spin coating of the nanotube suspension onto substrates[54,70]
- Casting of the nanotube/urethane–diacrylate mixture and polymerization by UV[68]
- Combination of solvent casting and melt mixing[55]

In particular, the last technique allowed the production of single-wall nanotubes/PMMA composite films with anisotropic properties. It consisted of several steps:

- Mixing and sonication (3 h) of nanotubes in a 10 wt% solution of PMMA and dimethylformamide (DMF)
- Pouring of the dispersion into Teflon dishes and drying at 20°C
- Folding, breaking into pieces of 1 to 1.5 cm^2, and stacking between two polished metal plates
- Hot pressing at 180°C and 3000 lb for 3 min
- Breaking and hot pressing (melt mixing) repeatedly 25 times
- Drying under vacuum at 180°C for 20 h
- Melt mixing (5 times) at 180°C and 3000 lb for 3 min

The resulting composite films were characterized by higher electrical conductivity along the flow direction of melt pressing than along the perpendicular direction. This effect confirms that a strong relationship exists

between the flow direction of the melt-mixing process, the nanotube alignment, and the physical properties. Moreover, starting from these composite films, nanotubes/PMMA composite fibers were produced by melt spinning with high alignment along the flow direction. Due to the use of a large draw ratio, the carbon nanotubes were aligned along the fiber axis and showed improved tensile mechanical properties as a function of the nanotube loading and the draw ratio.

11.2.3.2 Alignment Techniques

The study of the carbon nanotube orientation methods represents an important area of investigation. In fact, the macroscopic alignment would offer several advantages in terms of properties and applications. At this stage, some alignment techniques have been developed with and without the presence of a polymer matrix.

Aligned nanotube films have been produced and characterized by using the following techniques:

1. Dispersion of the nanotubes in a solvent followed by the pulling through a ceramic filter and the pressing of the remaining deposit onto the filter on a Teflon surface to transfer a film of nanotube (see Figure 11.22). In this case, the preferential orientation of the tubes is normal to the surface; it can be changed in parallel by rubbing the film along the surface with aluminum foil.[74]

2. Filtration/deposition from suspension in a strong magnetic field. A high alignment was achieved in the magnetic field direction.[75,76]
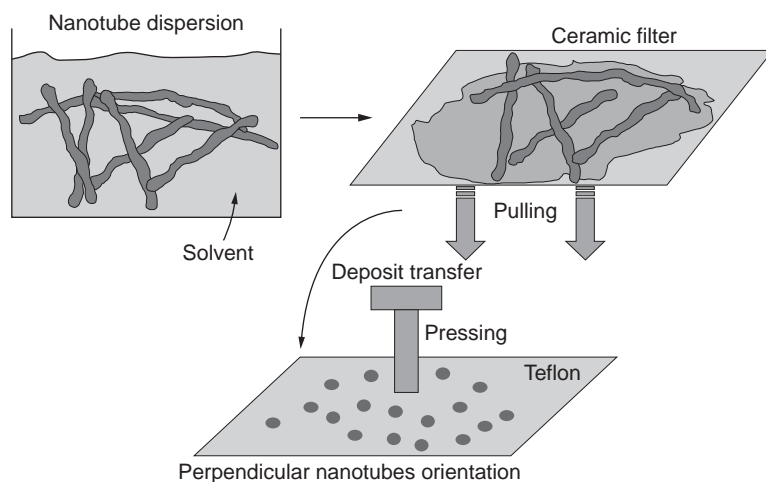
FIGURE 11.22
Schematic of nanotube alignment technique.[74]
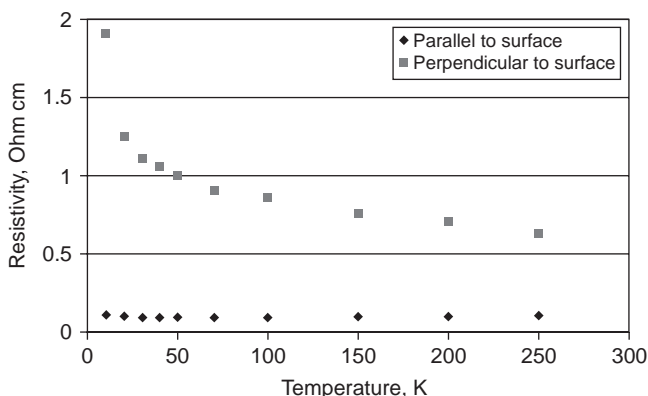
FIGURE 11.23
Resistivity of nanotube films.[74]

The orientation of the tubes was observed by SEM images. Further, some physical properties, such as optical, electrical, and thermal, exhibited anisotropy. In particular, de Heer et al.[74] measured the optical properties and the resistivity of carbon nanotube films prepared with the first technique. Figure 11.23 shows the resistivities of nanotube films as a function of the temperature depending on the tube orientation.

The films that have the tubes oriented in the plane of the surface show a high degree of anisotropy, while the ones with nanotubes normal to the surface exhibited isotropic behavior in the plane. Further, it was found that the thickness did not affect the anisotropy for samples thinner than 1 μm.

Hone et al.[76] found that the single-wall nanotube alignment increases the parallel components of both the electrical and thermal conductivities with respect to the unoriented material. In particular, the room temperature electrical conductivity was found to be of the same order as for individual single nanotube ropes, while the thermal conductivity value was over 200 W/m K, within an order of magnitude of graphite.

The literature also reports some methods to align carbon nanotubes in polymer matrix, including epoxy resins[69] and a thermoplastic polymer (PHAE).[66] In the first case, the alignment of multiwalled tubes was achieved by dispersing the nanotubes in the polymer matrix and making thin slices of the polymer composite with a diamond knife.[69] During the cutting the tubes displayed an alignment along the cutting direction. TEM image analysis showed that longer and thinner nanotubes were oriented, while the thicker and shorter ones were randomly dispersed. This behavior was attributed[69] to the action of the directional cutting that created shear within the material: the tubes in contact with the knife were pulled out or deformed from the matrix and oriented unidirectionally. After cutting, the lengths of the aligned tubes were found not to be different from the lengths of the original tubes, indicating that either the tubes were very strong or the interfacial bond with the polymer matrix was weak. Further, the matrix defor-
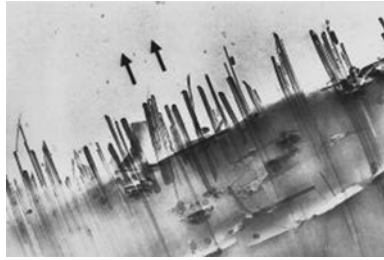
FIGURE 11.24
TEM image of a composite fracture surface obtained by slicing along the stretching direction. (With permission from Jin, L., Bower, C., and Zhou, O., *Appl. Phys. Lett.*, 73, 1197–1199, 1998.)

mation caused a separation of the individual tubes that did not break, suggesting strong mechanical properties.

The alignment of multiwalled nanotubes in the thermoplastic polymer (PHAE) was performed by applying a uniaxial stretching at 100°C.[66] After the stretching, the samples were cooled at room temperature and then the load was released. The orientation and the degree of alignment were determined by x-ray diffraction and TEM images.

X-ray diffraction analysis showed that:

- The fraction of nanotubes aligned increased with increasing stretching ratio, while the mosaic angle increased with decreasing stretching ratio.
- Since necking and fracture occurred at lower strains, it was more difficult to stretch thick samples to the same maximum elongation of the thin samples.
- The degree of alignment is not affected by the thickness of the sample; i.e., it was the same at a given stretching ratio.

Further, preliminary studies suggested that the alignment was better in multiwalled nanotubes than in single-walled ones, which are more flexible and have higher aspect ratios. Moreover, TEM analysis showed that the nanotube alignment direction is not affected by slicing, performed to prepare the samples. In fact, due to the stronger interface with the thermoplastic polymer matrix, the nanotube alignment was found to be along the stretching direction, suggesting that the cutting did not realign the nanotubes along the cutting direction, as observed for the epoxy/nanotube composite (see Figure 11.24).

11.2.4 Outlook

The use of carbon nanotubes as reinforcement of polymer systems could offer several advantages over the conventional structural composite mate-

rials in terms of the resulting final properties and processing. Since the carbon nanotubes have superior mechanical properties and a small size, their incorporation into polymer matrices could be performed easily, through extruders without fiber breakage. Further, the high aspect ratio of the nanotubes should enable one to obtain a stronger and more lightweight composite material that could be used in several fields, including automotive, aerospace, infrastructure, and military. For example, while the conventional aeronautical composites have high in-plane mechanical properties and limited transverse strength, the carbon nanotube polymer composites could gain a greater strength in the third dimension. This benefit supports the insight to apply the carbon nanotubes as fillers not only in pure polymer systems, but also in the traditional composite materials, which have not been experimented with yet.

However, since the reinforcement action depends on the nanotube dispersion into the polymer matrix, more investigations on the dispersion techniques and on the identification of the better-dispersing polymer systems are needed. In addition, to characterize the mechanical behavior of the resulting composite material, a better understanding of the fracture modes at the nanoscale level of the mechanisms of the load transfer from the matrix to the nanotubes and the corresponding analytical models are desired.

Due the high thermal and electrical conductivity of the carbon nanotubes, several other potential applications of the carbon nanotube polymer composites can be identified, including electromagnetic shields, antistatic coatings, transistors, light-emitting diodes, battery electrodes, and nonlinear optical devices.[7] However, the realization of large-scale application of carbon nanotubes will require good synthesis methods to obtain pure and uniform material in a cost-effective way. In conclusion, if synthesis and processing techniques for carbon nanotubes are improved, they will spur the growth of innovative applications in diverse fields due to their superior and versatile properties.

References

1. WTEC Panel Report on Nanostrcuture Science and Technology, 1997; website: http://itri.loyola.edu/nano/00_es.htm.
2. National Nanotechnology Initiative: The Initiative and Its Implementation Plan, report, 2000.
3. Ebbesen, W.T., Carbon nanotubes, *Physics Today*, 49(6), pp. 26–32, 1996.
4. Ebbesen, W.T., Carbon nanotubes, *Ann. Rev. Mater. Sci.*, 24, 235–264, 1994.
5. Ajayan, P.M., Nanotubes from carbon, *Chem. Rev.*, 99, 1787–1799, 1999.
6. Ajayan, P.M. and W.T. Ebbesen, Nanometre-size tubes of carbon, *Rep. Prog. Phys.*, 60, 1025–1062, 1997.
7. Ebbesen, W.T., *Carbon Nanotubes Preparation and Properties*, CRC Press, Boca Raton, FL, 1997.

8. Andrews, R., Jacques, D., Rao, A.M., Rantell, T., Derbyshire, F., Chen, Y., Chen, J., and Haddon, R.C., Nanotube composite carbon fibers, *Appl. Physics Lett.*, 75(9), 1329–1331, 1999.

9. Dresselhaus, M., Dresselhaus, G., Eklund, P., and Saito, R., Carbon nanotubes, *Physicsweb*, 11, 1, 1998.

10. Iijima, S., Helical microtubules of graphitic carbon, *Nature*, 354, 56–58, 1991.

11. Ebbesen, T.W. and P.M. Ajaian, Large scale synthesis of carbon nanotubes, *Nature*, 358, 220–222, 1992.

12. Calvert, P., A recipe for strength, *Nature*, 399, 210–211, 1999.

13. Ajayan, P.M., J.C. Charlier, and A.G. Rinzler, Carbon nanotubes: from macro-molecules to nanotechnology, *Science*, 96, 14199–14200, 1999.

14. Smalley, R.E., Discovering the fullerenes, Nobel lecture, *Rev. Mod. Phys.*, 69, 723–729, 1997.

15. Saito, R., M. Fujita, G. Dresselhaus, and M.S. Dresselhaus, Electrical structure of chiral graphene tubules, *Appl. Phys. Lett.*, 60, 2204–2206, 1992.

16. Dresselhaus, M.S., G.F. Dresselhaus, and P.C. Eklund, *Science of Fullerenes and Carbon Nanotubes*, Academic Press, New York, 1996.

17. Zhang, H., X. Xue, D. Wang, Y. He, and S. Peng, The effect of different kinds of inert gases and their pressures on the preparation of carbon nanotubes by carbon arc method, *Mater. Chem. Phys.*, 58, 1–5, 1999.

18. Yudasaka, M., R. Kikuchi, T. Matsui, Y. Ohki, S. Yoshimura, and E. Ota, Specific conditions for Ni catalyzed carbon nanotube growth by chemical vapor deposition, *Appl. Phys. Lett.*, 67, 2477–2479, 1995.

19. Hernadi, K., A. Fonseca, J.B. Nagy, D. Bernaertz, J. Riga, and A. Lucas, Catalytic synthesis and purification of carbon nanotubes, *Synth. Metals*, 77, 31–34, 1996.

20. Chen, P., H.-B. Zhang, G.D. Lin, Q. Hong, and K.R. Tsai, Growth of carbon nanotubes by catalytic decomposition of CH_4 or CO on a Ni-MgO catalyst, *Carbon*, 35, 1495–1501, 1997.

21. Jia, Z., Z. Wang, J. Liang, B. Wei, and D. Wu, Production of short multi-walled carbon nanotubes, *Carbon*, 37, 903–906, 1999.

22. Xie, S.S., B.H. Change, W.Z. Li, Z.W. Pan, L.F. Sun, J.M. Mao, X.H. Chen, L.X. Qian, and W.Y. Zhou, Synthesis and characterization of aligned carbon nanotube arrays, *Adv. Mater.*, 11, 1135–1138, 1999.

23. Li, W.Z., S.S. Xie, L.X. Qian, B.H. Chang, B.S. Zou, W.Y. Zhou, R.A. Zhao, and G. Wang, Large-scale synthesis of aligned carbon nanotubes, *Science*, 274, 1701–1703, 1996.

24. Fan, S., M.G. Chapline, N.R. Franklin, T.W. Tombler, A.M. Cassell, and H. Dai, Self-oriented regular arrays of carbon nanotubes and their field emission properties, *Science*, 283, 512–514, 1999.

25. Huang, S., L. Dai, and A.W.H. Mau, Patterned growth and contact transfer of well-aligned carbon nanotube films, *J. Phys. Chem. B*, 103, 4223–4227, 1999.

26. Choi, Y.C., D.J. Bae, Y.H. Lee, B.S. Lee, I.T. Han, W.B. Choi, N.S. Lee, and J.M. Kim, Low temperature synthesis of carbon nanotubes by microwave plasma-enhanced chemical vapor deposition, *Synth. Metals*, 108, 159–163, 2000.

27. Bower, C., W. Zhu, S. Jin, and O. Zhou, Plasma-induced alignment of carbon nanotubes, *Appl. Phys. Lett.*, 77, 830–832, 2000.

28. Bower, C., O. Zhou, W. Zhu, D.J. Werder, and S. Jin, Nucleation and growth of carbon nanotubes by microwave plasma chemical vapor deposition, *Appl. Phys. Lett.*, 77, 2767–2769, 2000.

29. Chen, Y., L. Guo, S. Patel, and D.T. Shaw, Aligned conical carbon nanotubes, *J. Mater. Sci.*, 35, 5517–5521, 2000.
30. Chen, Y., S. Patel, Y. Ye, D.T. Shaw, and L. Guo, Field emission from aligned high-density graphitic nanofibers, *Appl. Phys. Lett.*, 73, 2119–2121, 1998.
31. Ren, Z.F., Z.P. Huang, J.W. Xu, J.H. Wang, P. Bush, M.P. Siegal, and P.N. Provencio, Synthesis of large arrays of well-aligned carbon nanotubes on glass, *Science*, 282, 1105–1107, 1998.
32. Liu, J., A.G. Rinzler, H. Dai, J.H. Hafner, R.K. Bradley, P.J. Boul, A. Lu, T. Iverson, K. Shelimov, C.B. Huffman, F. Rodriguez-Macias, Y.S. Sheon, T. Randall Lee, D.T. Colbert, and R.E. Smalley, Fullerene pipes, *Science*, 280, 1253, 1998.
33. Thess, A., R. Lee, P. Nikolaev, H. Dai, P. Petit, J. Robert, C. Xu, Y.H. Lee, S.G. Kim, D.T. Colbert, G. Scuseria, D. Tomanek, J.E. Fischer, and R.E. Smalley, Crystalline ropes of metallic carbon nanotubes, *Science*, 273, 483–487, 1996.
34. Yudasaka, M., T. Komatsu, T. Ichinashi, Y. Achiba, and S. Iijima, Pressure dependence of the structures of carbonaceous deposits formed by laser ablation on targets composed of carbon, nickel and cobalt, *J. Phys. Chem.*, 102B, 4892–4896, 1998.
35. Kokay, F., K. Takahashi, M. Yudasaka, R. Yamada, T. Ichihashi, and S. Iijima, Growth dynamics of single-wall carbon nanotubes synthetized by CO_2 laser vaporization, *J. Phys. Chem.*, 103B, 4346–4351, 1999.
36. Rinzler, A.G., J. Liu, H. Dai, P. Nikolaev, C.B. Huffman, F.J. Rodriguez-Macias, P.J. Boul, A. Lu, D. Heymann, D.T. Colbert, R.S. Lee, J.E. Fischer, A.M. Rao, P.C. Eklund, and R.E. Smalley, Large scale purification of single-wall carbon nanotubes: process, product and characterization, *Appl. Phys.*, 67A, 29–37, 1998.
37. Bandow, S., A.M. Rao, K.A. Williams, A. Thess, R.E. Smalley, and P.C. Eklund, Purification of single-wall carbon nanotubes by microfiltration, *J. Phys. Chem.*, 101B, 8839–8842, 1997.
38. Flamant, G., A. Ferriere, D. LaPlaze, and C. Monty, Solar processing of materials: opportunities and new frontiers, *Solar Energy*, 66, 117–132, 1999.
39. Guillard, T., S. Cetout, G. Flamant, and D. Laplaze, Solar production of carbon nanotubes: structure evolution with experimental conditions, *J. Mater. Sci.*, 35, 419–425, 2000.
40. Anglaret, E., N. Bendiab, T. Guillard, C. Journet, G. Flamant, D. LaPlaze, P. Bernier, and J.L. Sauvajol, Raman characterization of single-wall carbon nanotubes prepared by the solar energy route, *Carbon*, 36, 1815–1820, 1998.
41. Zhang, M., C.L. Xu, D.H. Wu, L.M. Cao, and W.K. Wang, A new method for synthesizing single wall carbon nanotubes, *J. Mater. Sci. Lett.*, 19, 511–514, 2000.
42. Duesberg, G.S., J. Muster, H.J. Byrne, S. Roth, and M. Burghard, Toward processing of carbon nanotubes for technical applications, *Appl. Phys.*, 69A, 269–274, 1999.
43. Duesberg, G.S., M. Burghard, J. Muster, G. Philipp, and S. Roth, Separation of carbon nanotubes by size exclusion chromatography, *Chem. Commun.*, 435–438, 1998.
44. Dillon, A.C., T. Gennett, K.M. Jones, J.L. Alleman, P.A. Parilla, and M.J. Heben, A simple and complete purification of single walled carbon nanotube materials, *Adv. Mater.*, 11, 1354–1358, 1999.
45. Li, F., H.M. Cheng, Y.T. Xing, P.H. Tan, and G. Su, Purification of single-wall carbon nanotubes synthesized by the catalytic decomposition of hydrocarbons, *Carbon*, 38, 2041–2045, 2000.

46. Tohji, K., H. Takahashi, Y. Shinoda, N. Shimizu, B. Jeyadevan, I. Matsuoka, Y. Saito, A. Kasuya, S. Ito, and Y. Nishina, Purification procedure for single wall nanotubes, *J. Phys. Chem.*, 101B, 1974–1978, 1997.
47. Shi, Z., Y. Lian, F. Liao, X. Zhou, Z. Gu, Y. Zhang, and S. Iijima, Purification of single-wall carbon nanotubes, *Solid State Commun.*, 112, 35–37, 1999.
48. Zhang, Y., Z. Shi, Z. Gu, and S. Iijima, Structure modification of single-wall carbon nanotubes, *Carbon*, 38, 2055–2059, 2000.
49. Shaffer, M.S.P. and A.H. Windle, Analogies between polymer solutions and carbon nanotube dispersions, *Macromolecules*, 32, 6864–6866, 1999.
50. Shaffer, M.S.P., X. Fan, and A.H. Windle, Dispersion and packing of carbon nanotubes, *Carbon*, 36, 1603–1612, 1998.
51. Lahr, B. and J. Sandler, Carbon nanotubes, high strength reinforcing compounds for composites, *Kunststoffe Plast.*, 90(1), 94–96, 2000.
52. Gong, X., J. Liu, S. Baskaran, R.D. Voise, and J. Young, Surfactant-assisted processing of carbon nanotube/polymer composites, *Chem. Mater.*, 12, 1049–1062, 2000.
53. Ajayan, P.M. and L.S. Schandler, Single-walled carbon nanotube-polymer composites: strength and weakness, *Adv. Mater.*, 12, 750–753, 2000.
54. Stephan, C., T.P. Nguyen, M. Lamy de la Chapelle, S. Lefrant, C. Journet, and P. Bernier, Characterization of single walled carbon nanotubes-PMMA composites, *Synth. Metals*, 108, 139–149, 2000.
55. Haggenmueller, R., H.H. Gommans, A.G. Rinzler, J.E. Fischer, and K.I. Winey, Aligned single-wall carbon nanotubes in composites by melt processing methods, *Chem. Phys. Lett.*, 330, 219–225, 2000.
56. Jia, Z., Z. Wang, C. Xu, J. Liang, B. Wei, D. Wu, and S. Zu, Study on polymethylmethacrylate/carbon nanotube composites, *Mater. Sci. Eng.*, 271A, 395–400, 1999.
57. Chen, G.Z., M.S.P. Shaffer, D. Coleby, G. Dixon, W. Zhou, D.J. Fray, and A.H. Windle, Carbon nanotubes and polypirrole composites: coating and doping, *Adv. Mater.*, 12, 522–525, 2000.
58. Chang, B.H., Z.Q. Liu, L.F. Sun, D.S. Tang, W.Y. Zhou, G. Wang, L.X. Qian, S.S. Xie, J.H. Fen, and M.X. Wan, Conductivity and magnetic susceptibility of nanotube/polypyrrole nanocomposites, *J. Low Temp. Phys.*, 119, 41–48, 2000.
59. Lourie, O. and H.D. Wagner, Evaluation of Young's modulus of carbon nanotubes by micro-Raman spectroscopy, *J. Mater. Res.*, 13, 2418–2422, 1998.
60. Sandler, J., M.S.P. Shaffer, T. Prasse, W. Bauhofer, K. Schulte, and A.H. Windle, Development of a dispersion process for carbon nanotubes in an epoxy matrix and the resulting electrical properties, *Polymer*, 40, 5967–5971, 1999.
61. Schandler, L.S., S.C. Giannaris, and P.M. Ajaian, Load transfer in carbon nanotube epoxy composites, *Appl. Phys. Lett.*, 73, 3842–3844, 1998.
62. Qian, D., E.C. Dickey, R. Andrews, and T. Rantell, Load transfer and deformation mechanisms in carbon nanotube-polystyrene composites, *Appl. Phys. Lett.*, 76, 2868–2870, 2000.
63. Lourie, O., D.M. Cox, and H.D. Wagner, Buckling and collapse of embedded carbon nanotubes, *Phys. Rev. Lett.*, 81(8), 1638–1641, 1998.
64. Lourie, O. and H.D. Wagner, Evidence of stress transfer and formation of fracture clusters in carbon nanotube-based composites, *Composite Sci. Technol.*, 59, 975–977, 1999.
65. Shaffer, M.S.P and A.H. Windle, Fabrication and characterization of carbon nanotube/poly(vinyl alcohol) composites, *Adv. Mater.*, 11, 937–941, 1999.

66. Jin, L., C. Bower, and O. Zhou, Alignment of carbon nanotubes in a polymer matrix by mechanical stretching, *Appl. Phys. Lett.*, 73, 1197–1199, 1998.
67. Bower, C., R. Rosen, L. Jin, J. Han, and O. Zhou, Deformation of carbon nanotubes in nanotube-polymer composites, *Appl. Phys. Lett.*, 74, 3317–3319, 1999.
68. Wagner, H.D., O. Lourie, Y. Feldman, and R. Tenne, Stress-induced fragmentation of multiwall carbon nanotubes in a polymer matrix, *Appl. Phys. Lett.*, 72, 188–190, 1998.
69. Ajayan, P.M., O. Stephan, C. Colliex, and D. Trauth, Aligned carbon nanotube arrays formed by cutting a polymer resin-nanotube composite, *Science*, 26, 1212–1214, 1994.
70. Ago, H., K. Petritsch, M.S.P. Shaffer, A. Windle, and R.H. Friend, Composites of carbon nanotubes and conjugated polymers for photovoltaic devices, *Adv. Mater.*, 11, 1281, 1999.
71. Curran, S., P.M. Ajaian, W.J. Blau, D.L. Carroll, J.N. Coleman, A.B. Dalton, A.P. Davey, A. Drury, B. McCarthy, S. Maier, and S. Strevens, A composite from poly(m-phenylenevinylene-co-2,5-dioctoxy-p-pnenylenevinylene) and carbon nanotubes: a novel material for molecular optoelectronics, *Adv. Mater.*, 10, 1091–1093, 1998.
72. Coleman, J.N., S. Curran, A.B. Dalton, A.P. Davey, B. McCarthy, W.J. Blau, and R.C. Barklie, Percolation-dominated conductivity in a conjugated polymer carbon nanotube composite, *Phys. Rev. B*, 58(12), 7492–7495, 1998.
73. Woo, H.S., R. Czerw, S. Webster, D.L. Carroll, J. Ballato, A.E. Strevens, D. O'Brien, and W.J. Blau, Hole blocking in carbon nanotube-polymer composite organic light emitting diodes based on poly(m-phenylenevinylene-co-2,5-dioctoxy-p-pnenylenevinylene), *Appl. Phys. Lett.*, 77, 1393–1395, 2000.
74. De Heer, W.A., W.S. Bacsa, A. Chatelain, T. Gerfin, R. Humphrey-Baker, L. Forro, and D. Ugarte, Aligned carbon nanotube films: production and optical and electronic properties, *Science*, 268, 845–847, 1995.
75. Smith, B.W., Z. Benes, D.E. Luzzi, J.E. Fischer, D.A. Walters, M.J. Casavant, J. Schmidt, and R.E. Smalley, Structural anisotropy of magnetically aligned single wall carbon nanotubes films, *Appl. Phys. Lett.*, 77, 663–665, 2000.
76. Hone, J., M.C. Llaguno, N.M. Nemes, A.T. Johnson, J.E. Fischer, D.A. Walters, M.J. Casavant, J. Schmidt, and R.E. Smalley, Electrical and thermal transport properties of magnetically aligned single wall carbon nanotube films, *Appl. Phys. Lett.*, 77, 666–668, 2000.

12

Performance Synergism in Polymer-Based Hybrid Materials

Shing-Chung Wong and Yiu-Wing Mai*

CONTENTS

---

* Author to whom all correspondence should be addressed.

12.1 Introduction

High-specific-strength and -modulus, cost-effective fabrication and multi-functional characteristics have made high-performance polymers the materials of choice for engineering, defense, electronics, and medical applications. Most engineering polymers can be improved on either their mechanical strength or their impact toughness, or both. For those thermoplastics that exhibit notch sensitivity and brittle behavior under impact conditions, a compliant heterogeneity phase or particles have been introduced into the matrices since 1940s.[1,2] The generic scheme of toughening rigid polymers with a second elastomeric phase was a great success in the plastics industry. However, toughening thermoplastics with a soft rubbery phase would inadvertently reduce the materials' inherent strength and stiffness, which are important benchmark properties for acceptable material performance. It is now understood that not all materials systems can be toughened by means of elastomeric inclusions, particularly for those highly cross-linked thermosetting polymers, whose intrinsic yielding capability may be lacking. It is also an attractive idea to introduce a second rigid phase[3-5] or inorganic fillers[6-24] for toughening thermoplastic matrices. To compensate for the loss of strength and stiffness of rubber-toughened plastics, manufacturers in recent years produced glass fiber-reinforced toughened grades of high-performance semicrystalline resins such as nylons, polybutylene terephthalate (PBT), and polypropylene (PP). Such composites are in fact hybrid systems. Some products arising from hybridization turned out to be concomitantly strong and tough. The potential of delivering synergistic performance in hybrid material systems is attractive.

Development of novel polymeric materials in the future points toward hybrid systems. Hence, new combinations, such as ternary alloys,[25-31] hybrid particulate composites,[24,32-37] glass fiber-containing toughened plastics,[6,7,16-18,38-40] liquid crystalline polymer (LCP) hybrid composites,[41-43] and nanocomposites,[23,44-60] have been investigated. These hybrid systems, if carefully engineered, not only provide linear additive properties unavailable in single- or binary-phase composites, but also impart synergistic interactions among different heterogeneities for multiplicative enhancement in material properties and cost dilution. Evidence of performance nonlinearity or multiplicative properties in hybrid systems has been noted.[4,6,25,26,35] While the synergistic effect was reported from time to time, few studies were focused on the mechanisms that promote synergism among different components. To this end, it is required that the interplay of each independent component in a hybrid system be identified. Positive materials performance often does not exist in all mixtures. However, limited success has been achieved in identifying the essential elements of such behavior. In this chapter, we shall review different polymer-based hybrid materials. Emphasis is on the mechanical properties and toughness enhancement as a function of material

composition in selected hybrid systems. Materials processability and functional enhancement are also considered as parts of performance synergism in this review.

12.2 Concepts of Synergistic Properties for Composites

For property synergism in hybrid composites, toughness,[6,61] strength,[11,12,62–65] and stiffness[41] often operate distinctively, and they warrant specific investigation into each of their synergistic mechanisms.

12.2.1 Mechanical Properties

Figure 12.1 shows the linear additive behavior vs. synergistic behavior for a binary mixture. Note that from left to right, the property increases from component A to that pertaining to component B in a volume-averaged relationship:

$$P_c = \sum_{i=1}^{n} P_i v_i \tag{12.1}$$

where P_i is the material property and v_i is the volume fraction of the i-th component in the composite. Equation (12.1) is the optimal value for the
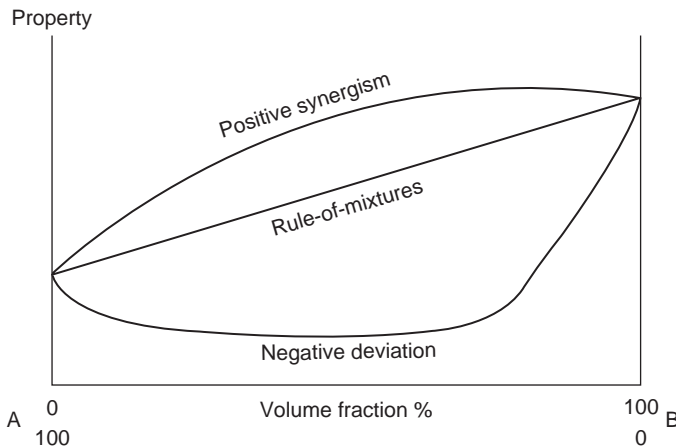
FIGURE 12.1
A schematic showing performance synergism in composite materials. The typical observations are positive synergism, rule-of-mixtures, and negative deviation from the rule-of-mixtures.

composite property provided the components' structural integrity remains unchanged after mixing. Stiffness models that describe the optimization of asymptotic behavior as functions of filler concentration, orientation, distribution, and geometry are well established[11,12,62–65] for glass fiber-reinforced thermoplastics. Ideal assumptions include uniform filler distribution; perfect bonding at the filler–matrix interface, so that no slip occurs during stress transfer between fiber and matrix materials; and linear elastic deformation. Filler aspect ratio, dimensions, and orientations are also critical to effective stress transfer for discontinuous composites. Some specific examples for different hybrid material systems will be provided in the discussion that follows.

To achieve synergistic behavior that deviates positively from a volume-averaged relationship for strength and stiffness, it is required that either of the ideal assumptions is not satisfied or the materials have undergone microstructure or property changes. A good example is a polymer filled with a thermotropic liquid crystalline polymer. There is evidence showing that molecular alignment of LCP in the composite is better than LCP processed alone.[41] The processing conditions alter the microstructure of LCP and its properties. This effect produces a positive synergism in the composite stiffness.

Materials strength cannot be predicted by the volume-averaged rule in most circumstances. This is because strength depends on the localized deformation prior to failure, whereas stiffness is dependent on the global deformation at the beginning of loading. It is necessary to understand the failure mechanisms before composite strength can be applied.

12.2.2   Synergism for Fracture Toughness

Many, if not all, polymers are intrinsically brittle in the presence of sharp cracks and will behave as such at low temperatures and high strain rates. Fracture of polymers is a complex phenomenon that provides the basis for multiplicative performance. A composite toughness value is commonly defined as the work dissipated per unit *planar* crack area (ignoring those other surface areas created by debonding at the fiber–matrix interfaces). But by definition, fracture toughness includes the localized matrix plastic deformation in addition to the fracture works involved with fiber–matrix debonding, fiber bridging, breakage and pullout, etc., which are embodied by a fracture process zone (FPZ). Hence, the total essential work consumed on fracture is more than breaking the interatomic bonds between two surfaces in molecular scale and is directly related to the FPZ width. Contrary to other mechanical and physical properties, the toughness of composites in many instances seldom follows a volume-average rule and is often greater (or less) than the sum of the toughness of all composite components. The operative fracture mechanisms control multiplicative toughening (or embrittlement)[6,61] as the crack advances. While the inherent toughness of each component is

essential to the combined composite toughness, the toughening mechanisms of each component could be unique and their interactions would generate unpredictable behavior using the volume-average rule. As a result, it is often necessary to identify the mechanisms of fracture so that the component toughening can be activated to its fullest potential.

One classical example of synergistic toughness is rubber toughening of epoxies.[66-68] Rubber particles possess low fracture toughness due to their low elastic modulus and poor mechanical strength. The cross-linked thermosetting epoxy is capable of shear deformation only under critical deviatoric stresses. The presence of hydrostatic stresses due to plane-strain conditions severely limits the deformation capability of epoxies. Plane strain is often exacerbated by the presence of a sharp crack, an inherent or machining flaw, or under impact and low-temperature environments. Upon introduction of rubber particles of controlled sizes,[68-70] the stress states of the epoxy matrix could be modified. The mechanism is primarily attributed to the stress concentration around the rubber particles, which leads to cavitation, whereby hydrostatic stresses can be relieved and deviatoric stresses remain to promote volume-conserving deformation. The latter absorbs a tremendous amount of energy prior to fracture. Clearly, the toughness of rubber-toughened epoxy cannot be estimated independently by summing up the component toughness of rubber particles and epoxy resins. The way the two components interact with each other must be taken into account.

12.3 Mechanical Behavior of Hybrid Materials

The ultimate objective of hybridization is to create and combine an engineered proportion of material components for a range of applications. The hybrid materials so obtained must meet the stringent requirements for materials performance and cost-effectiveness. Mechanical behavior sets the benchmark for acceptable materials performance. In the discussion that follows, we shall investigate examples of polymer-based hybrid materials, which deliver some potential for synergistic toughness or enhanced load-bearing applications. These include ternary polymer blends, glass-filled rubber-toughened polymers, LCP hybrid composites, and nanocomposites.

12.3.1 Ternary Polymer Blends

The major drawback in toughened plastics is reduced strength, stiffness, and heat deflection temperature, all of which are important properties for high-performance polymers. In the last decade, a series of studies focused on rigid–rigid polymer blends[4-7] were successfully carried out. The advantage of blending one thermoplastic polymer with another thermoplastic to form

a rigid–rigid blend is to minimize the reduction in tensile strength, tensile and flexural stiffness, and other important engineering properties, as in rubber-toughened plastics. Some prominent toughening mechanisms include crazing prior to massive shear yielding in polyamide/polyphenylene oxide (PA/PPO)[71] and debonding-shear yielding-crack bridging in polycarbonate/polybutylene terephthalate (PC/PBT).[4] In the latter, a coordination of several toughening mechanisms was involved. Cavitation stresses of a rigid phase are too high, and the crack-tip triaxial stresses would first promote crazing in one component; in this case, crazing occurs in PBT.[4] At 60/40 PBT/PC, the crazes are stabilized by PC domains, which raise the interfacial stress between PBT and PC until debonding occurs. The voids so obtained at the interface relieve the triaxial stresses and enhance shear yielding in the component phases. Further increase in the applied stress would fracture the PBT, but the PC fibrils stretch and bridge the crack faces. Other rigid–rigid blends include polyethylene terephthalate/polycarbonate (PET/PC),[72–75] polycarbonate/polymethyl methacrylate (PC/PMMA),[76] polystyrene/polymethyl methacrylate (PS/PMMA),[77] and polystyrene/polyethylene (PS/PE).[78] The results of these studies show that it is possible to toughen brittle polymers by the inclusion of another rigid phase.

Some recent studies[25–27] showed that synergistic toughness could also be achieved using ternary blend systems. Figure 12.2 shows the J-integral fracture toughness of 75/25 nylon 6,6/PP blends containing 20% styrene-ethylene-butylene-styrene (SEBS) copolymer grafted with varied maleic anhydride (MA) content from a master batch. In this study, it was found that the fracture toughness of nylon 6,6/PP/SEBS-g-MA blends shows an unambiguous dependence on the rubber functionality given by the grafted MA content. In a nylon-rich matrix, it is observed that the variation of J_c with MA closely matches that of the tensile ductility, which also produces optimal elongation at break when both maleated and nonmaleated SEBS copolymers are in equal proportions.[26] J_c reaches a maximum value at 0.92% MA content with an optimal combination of tensile strength and ductility as shown in Figure 12.3. It was also shown that at this MA level, the blend has well-dispersed SEBS inclusions in the continuous-nylon phase, effectively toughening the matrix. In addition, there are PP inclusions surrounded by SEBS fringes forming a core-shell morphology. The dispersed SEBS/PP inclusions allow plastic yielding followed by debonding and subsequent matrix deformation to take place, giving rise to maximum ductility. The results point to the fact that 75/25 nylon 6,6/PP blends can be tailored to possess high fracture toughness with good tensile strength and high stiffness by properly controlling the phase morphology in a ternary system.

Wu et al.[25] recently reported synergistic performance in a polystyrene/high-density polyethylene/styrene-butadiene-styrene (PS/HDPE/SBS) system. It was found that both binary blends, viz., PS/HDPE and PS/SBS, showed deteriorated mechanical properties at all compositions due to the extremely poor interfacial adhesion between HDPE and PS, while the SBS particles were too small to stabilize the crazes formed in PS before fracture.
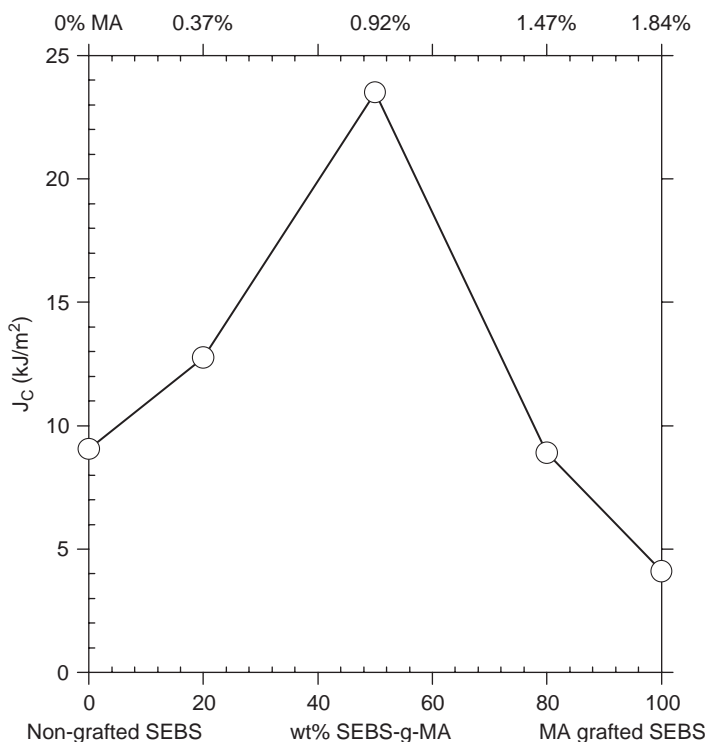
FIGURE 12.2
J-integral fracture toughness of 75/25 PA66/PP blends modified with different levels of MA-grafted SEBS copolymers. The total content of SEBS (nongrafted and grafted) remains 20 wt%.

But the ternary blend (PS/HDPE/SBS) gives rise to synergistic toughening. The enhancement in toughness was attributed to the ability of SBS to form a thin layer covering the HDPE fibers, which significantly improves the PS/HDPE interfacial strength and mechanical properties of blends. The debonding–cavitation at the PS/HDPE interface releases the triaxial stresses and enables shear deformation at the crack tip. It was also noted that the encapsulated HDPE fiber pulled out from the PS domains, contributing to significant toughness improvement.

It is clear from these previous studies[25–27] that a ternary blend can deliver synergistic toughness performance in comparison to binary systems. The mechanisms of toughening are often the central issue to be addressed. With established understanding of toughening in ternary blends, more new materials can be designed to meet a variety of end-use requirements.

12.3.2   Glass-Containing Rubber-Toughened Polymers

Hybridization of toughened plastics using glass fillers has recently received extensive attention.[6,7,14,16–18] One clear advantage of such a design scheme is
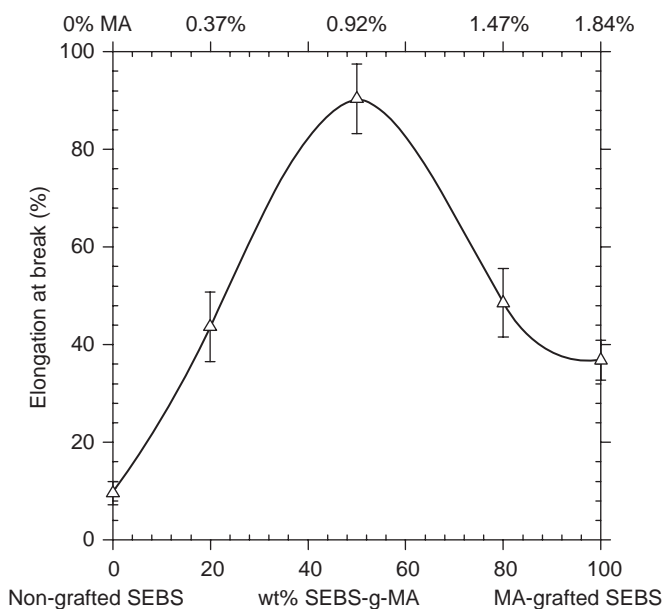
FIGURE 12.3
Ductility of 75/25 PA66/PP blends modified with different levels of MA-grafted SEBS copolymers.

the cost-effective fabrication by means of conventional processing equipment, such as regular compounders and injection-molding machines, etc., and the primary motivation is to strengthen the toughened matrix with inorganic glass fillers. The ideal scenario is one that can accomplish concomitant toughening derived from the matrix and strengthening derived from the glass reinforcement. This scenario often does not hold because of the complex stress interactions between the impact modifiers and the reinforcing phase. However, success in obtaining high-strength and high-toughness blends with glass fiber reinforcement was nevertheless reported.[6,16–17] It is also evident that positive synergism exists in hybridization of toughened plastics with glass beads.[34–37]

Little is understood on the distinctive roles of components in fiber-reinforced toughened plastics. It is simplistic to assume that the fracture mechanisms in fiber-reinforced single polymers are identical to those for hybrid composites. This approach ignores the distinctive role of the second-phase rubber particles and assumes the rubber-toughened matrix to possess certain effective properties in the presence of glass fibers. However, the actual fracture events as to whether there is a need for both fibers and rubbery phase to be present for toughening remain unclear. For short glass fiber-containing toughened plastics, it is evident that a transition from matrix-dominant failure to fiber-dominant failure takes place as the fiber volume fraction increases. In the presence of mechanisms such as fiber debonding, fiber
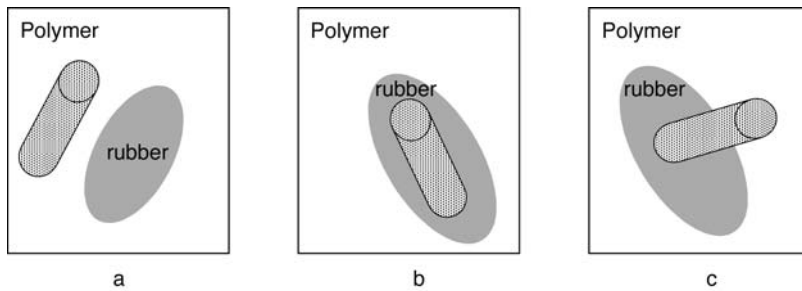
FIGURE 12.4
A schematic showing the three distributions of glass fibers in a rubber-toughened polymer. (a) Glass fiber is located in the polymer matrix. (b) The fiber is encapsulated by functionalized rubber enclosed by the polymer matrix. (c) The fiber is spanning across both the polymer and rubbery phases.

bridging, and fiber pullout, the matrix-borne stress could be severely curtailed. Conversely, the short fibers could also induce matrix plasticity due to fiber-end debonding.

12.3.2.1 Microstructures

Microstructures of hybrid systems are often very complex. This complexity is caused by a number of possible combinations, the thermodynamics and chemistry of mixing, and the processing conditions under which steady-state products are formed. It is instructive to make some simple assumptions for the possible array of heterogeneous microstructures. Figure 12.4 compares the possible microstructures of short glass fiber-reinforced toughened polymers. The fibers could be distributed in the engineering polymeric matrix or the rubbery phase, or they could be spanning across both phases. To reveal the general microstructures and fiber distributions for fiber-reinforced toughened nylon 6,6, we polished the specimen cross sections with different fiber volume fractions for scanning electron microscopy (SEM) examination to be followed by image analysis. Figure 12.5 illustrates the fiber distribution and orientation for the 10, 20, 30, and 40 wt% fiber-reinforced hybrid composites by extrusion compounding, followed by injection molding. The conversion of weight fraction to fiber volume fraction is given in Table 12.1. In the 10 wt% case (Figure 12.5(a)), the fiber distribution appears sparse, but the density of fiber distribution gradually increases as the fiber weight fraction increases. A relatively thin skin layer is present in all the compositions. Scanning from the surface layer across the in-plane width of a dog bone specimen, it is noted that there is a distinctive skin-core morphology, as is common in injection-molded fiber-reinforced thermoplastics. The skin layer shows fibers transverse to the mold filling direction (MFD), whereas fibers near the core are lying on the plane parallel to the MFD. The core region also shows more random alignments on the plane. As fiber concentration increases, more fibers are distributed in the core layer, wherein increasing
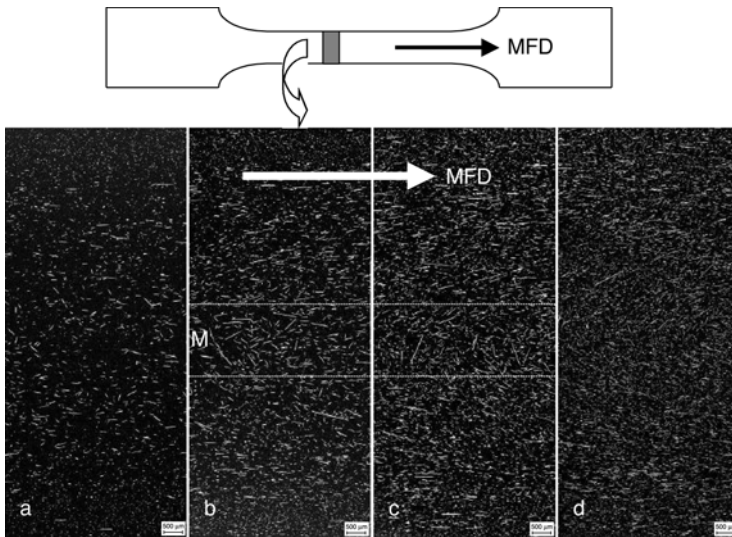
FIGURE 12.5
SEM photomicrograph of a polished middle section of rubber-toughened nylon 6,6 reinforced with (a) 10 wt%, (b) 20 wt%, (c) 30 wt%, and (d) 40 wt% short glass fibers. M is the midlayer. (From S.C. Wong, G.X. Sui, C.Y. Yue, and Y.-W. Mai, *J. Mater. Sci.*, 37, 2659–2667, 2002. Reprinted with permission from Kluwer Academic Publishers.)

TABLE 12.1

Conversion of Fiber Volume Fraction from Weight Fraction of Short Glass Fiber-Reinforced Toughened Nylon 6,6

Fiber weight fraction (wt%)	0	10	20	30	40
Fiber volume fraction (vol%)	0	4.43	9.41	15.18	21.80

alignment of the fibers parallel to the mold filling direction can be observed. The microstructural results are consistent with Friedrich's model,[79] whereby fiber orientation increases as a function of fiber volume fraction in injection-molded reinforced plastics. It is noted that a middle layer (M) with fibers aligned transverse to the MFD can be seen in 20 and 30 wt% compositions (Figures 12.5(b) and (c)), whereas the M layer disappears in 40 wt% composition (Figure 12.5(d)).

Fiber orientation is studied using image analysis software and is shown in Figure 12.6. The measurement of counts made on in-plane fiber alignment is plotted against the angle between fiber and MFD, excluding the ones lying out of plane. A general trend of counts decreasing with increase of angle between the fiber alignment and MFD exists in all concentrations. Figure 12.7 plots the fiber length distribution as measured in the burnt-off injection-molded specimens. According to the model established by Karger-Kocsis and Friedrich,[80] the average fiber length decreases slightly with an increase of fiber volume fraction. Based on the results given in Figure 12.7, the fiber
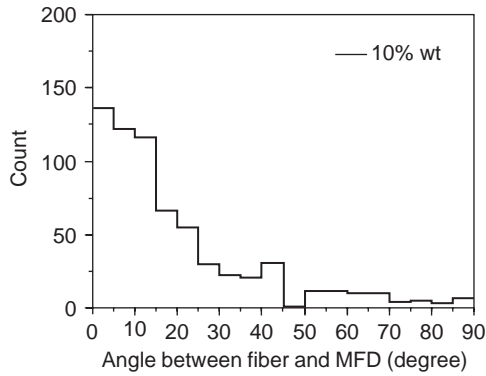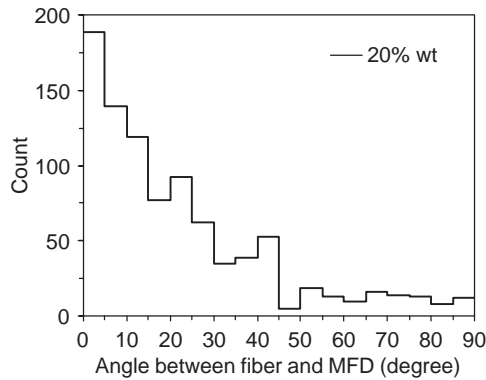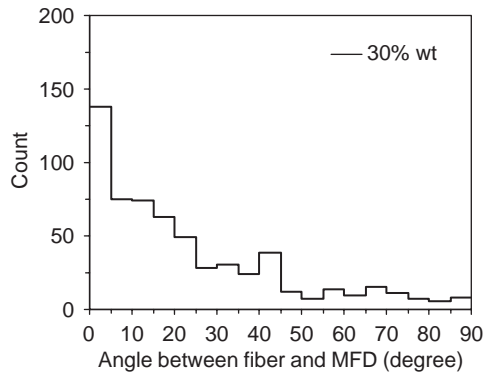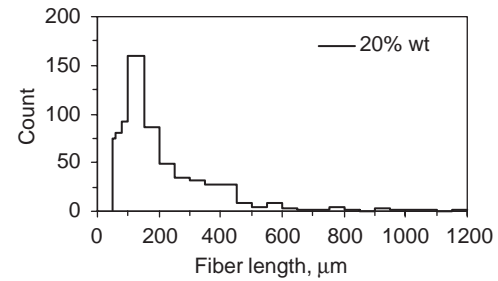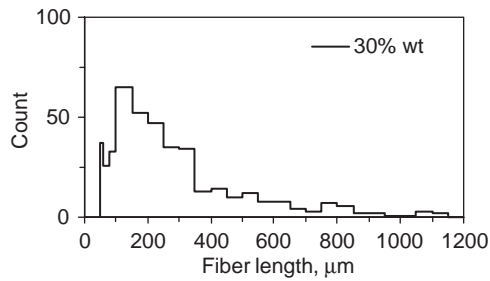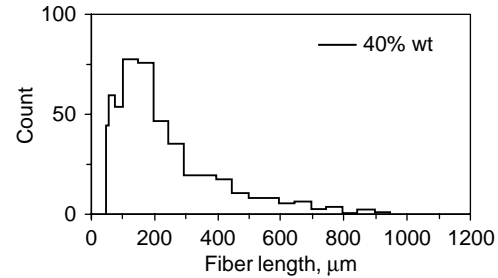
FIGURE 12.6
Counts made on in-plane cross section vs. the angle between fiber and MFD on a polished middle section of a toughened nylon 6,6 reinforced with (a) 10 wt%, (b) 20 wt%, and (c) 30 wt%. (From S.C. Wong, G.X. Sui, C.Y. Yue, and Y.-W. Mai, *J. Mater. Sci.*, 37, 2659–2667, 2002. Reprinted with permission from Kluwer Academic Publishers.)
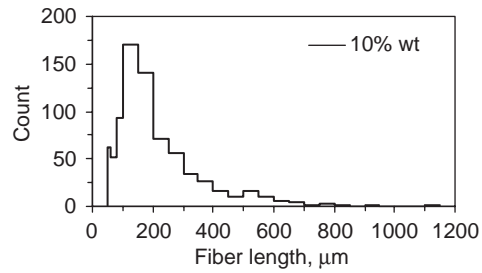
FIGURE 12.7
Glass fiber length distributions measured on the fibers extracted from the injection-molded bars of (a) 10 wt%, (b) 20 wt%, (c) 30 wt%, and (d) 40 wt% short glass fiber-reinforced toughened nylon 6,6. (From S.C. Wong, G.X. Sui, C.Y. Yue, and Y.-W. Mai, *J. Mater. Sci.*, 37, 2659–2667, 2002. Reprinted with permission from Kluwer Academic Publishers.)

length distribution appears rather consistent for all compositions. The average fiber lengths in the materials studied fall in between 220 and 260 μm for all compositions. A simple estimation of the critical fiber transfer length based on composite theory shows that it is greater than the measured average fiber length after processing. This is consistent with other extruded and injection-molded short-fiber-reinforced polymers.[9,10] Clearly, stress transfer from the matrix to the fiber is not optimized in this case, and most fibers will be pulled out rather than broken.

12.3.2.2 Toughening Mechanisms

The technique of essential work of fracture (EWF) provides fruitful insights on the mechanisms of deformation for fiber-reinforced toughened polymers. The technique separates the FPZ toughness from the geometry-dependent plastic work.[40] Figure 12.8 plots the specific essential and nonessential fracture work against fiber weight fraction. The plot indicates the transformation of matrix-dominant to fiber-dominant toughening mechanisms. For the unreinforced toughened matrix, the specific essential fracture work, w_e, is the lowest (~7 kJ/m^2) among all compositions, while the specific nonessential fracture work, βw_p, is the highest (~8 kJ/m^3). It is clear the major deformation of the matrix comes from massive shear yielding surrounding the crack tip. Note that this shear plasticity is nonessential, and it varies according to the specimen and loading geometry. w_e is, however, directly related to the fracture process, which only depends on material microstructures and specimen thickness. In this case, rubber-toughened nylon is well known to deform by rubber cavitation followed by matrix shear yielding.

We first examine the essential fracture work and its implications on the roles of rubber toughening and fiber-related process zone toughening in a hybrid system. In Figure 12.8, we can see that w_e rises upon introduction of
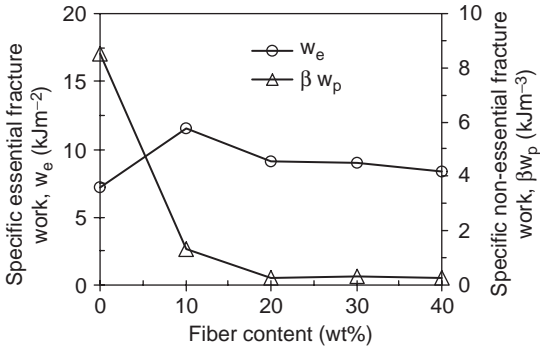

FIGURE 12.8
Specific essential and nonessential work of fracture vs. fiber weight content. (From S.C. Wong, G.X. Sui, C.Y. Yue, and Y.-W. Mai, *J. Mater. Sci.*, 37, 2659–2667, 2002. Reprinted with permission from Kluwer Academic Publishers.)

short glass fibers. The increase is attributed to a combination of fiber-related process zone toughening and the matrix being able to sustain potent rubber toughening promoted by rubber cavitation. Continued increase in fiber weight fraction reduces w_e, which suggests the occurrence of a transition from rubber toughening to fiber-related process zone toughening. It seems that there is an optimal fracture toughness at a particular blend composition that invokes both toughening mechanisms. This occurs somewhere between 0 and 20 wt% fiber reinforcement. When the fiber weight fraction continues to increase, the load borne by the fibers increases and the stress on the matrix decreases. The stress reduction on the matrix would severely limit the shear yielding promoted by rubber cavitation. As a result, plastic yielding is constrained and the role of rubber toughening gradually diminishes. Much of the load is now borne by the fibers, and toughening is primarily derived from fiber-related process zone mechanisms such as fiber debonding, bridging, and pullout.

To verify our proposal, we will illustrate the reduction in matrix-borne stress using a simple composites mechanics theory. The effect of load shedding from the matrix onto the fibers can be demonstrated by recognizing that in a short-fiber composite, the average matrix stress σ_{ms} can be estimated by

$$\sigma_{ms} = \frac{\sigma_c - \overline{\sigma}_f v_f}{\left(1 - v_f\right)} \tag{12.2}$$

where σ_c is the composite stress, $\overline{\sigma}_f$ is the average fiber stress, and v_f is the fiber volume fraction. In this system, the fiber lengths are less than the critical transfer length, l_c, as discussed above. Therefore,

$$\overline{\sigma}_f = \frac{l \times \tau}{d} = \sigma_m \times \frac{s}{2} \tag{12.3}$$

where s is the fiber aspect ratio and τ is the shear bond strength taken to be half the matrix yield strength σ_m. Accordingly, the ratio of matrix stress with fibers (σ_{ms}) to the composite stress ($\approx \sigma_c$) is

$$\frac{\sigma_{ms}}{\sigma_c} = \frac{\sigma_c - \sigma_m s \dfrac{v_f}{2}}{\sigma_c\left(1 - v_f\right)} \tag{12.4}$$

Substituting the values given in Table 12.2 and using Equation (12.4), we could calculate σ_{ms}/σ_c Ý 0.73, 0.57, 0.52, and 0.42 for 10, 20, 30, and 40 wt% fiber-reinforced toughened nylon 6,6, respectively. For Equation (12.4) we assume that the fibers are perfectly aligned parallel to the mold filling direction and the applied stress acts on a cross section containing fibers and matrix

TABLE 12.2

Mechanical Properties of Short Glass Fiber-Reinforced Toughened
Nylon 6,6

Fiber content (wt%)	0	10	20	30	40
Tensile strength (MPa)	42.71	41.08	53.88	75.16	90.23
Tensile modulus (GPa)	1.83	2.24	3.48	5.46	7.74
Average fiber aspect ratio	N/A	~13	~13	~13	~13

Note: N/A = not applicable.

as in a uniformly loaded tensile specimen. Hence the fiber orientation effect
and the nonuniform crack-tip stress field have been ignored. If we assume
the short fibers are two-dimensional and randomly aligned, then the effective
length, $\bar{l}$, for reinforcement is given by

$$\bar{l} = \frac{N \int_0^{\pi/2} l \cos \theta \, d\theta}{N(\pi/2)} = 0.637l \tag{12.5}$$

where N is the total number of fibers and θ is the projected angle of fibers
from the plane parallel to the MFD. Hence, Equation (12.4) can be modified to

$$\frac{\sigma_{ms}}{\sigma_c} = \frac{\sigma_c - \eta \sigma_m s \frac{v_f}{2}}{\sigma_c (1 - v_f)} \tag{12.6}$$

where the fiber orientation efficiency factor, η, is 0.637.

From Equation (12.4), even though the fiber length is smaller than the
critical transfer length, the matrix stress could be substantially reduced by
as much as 27 to 58%. Thus, the role of stress shedding in constraining the
matrix deformation appears very plausible and may play a key role in the
mechanics of fracture in composites containing second phases distributed
among the fiber-reinforced hybrid materials. Plots of Equations (12.4) and
(12.6) vs. fiber weight fraction are given in Figure 12.9. Similar trends are
shown for the data obtained for the specific nonessential plastic work in
Figure 12.8. There appears to be an interesting correlation between the reduc-
tion in nonessential plastic work and the reduction in matrix-borne stress.
Equation (12.6), which takes into account the effect of two-dimensional ran-
dom orientation, shows a greater resemblance of the trend in Figure 12.8,
particularly toward high fiber content. The reduction in the specific nones-
sential work levels off at higher fiber content. The reduction in matrix stress
critically influences the sequence of events upon fracture and decreases the
nonessential plastic work during crack growth. This is an interesting result,
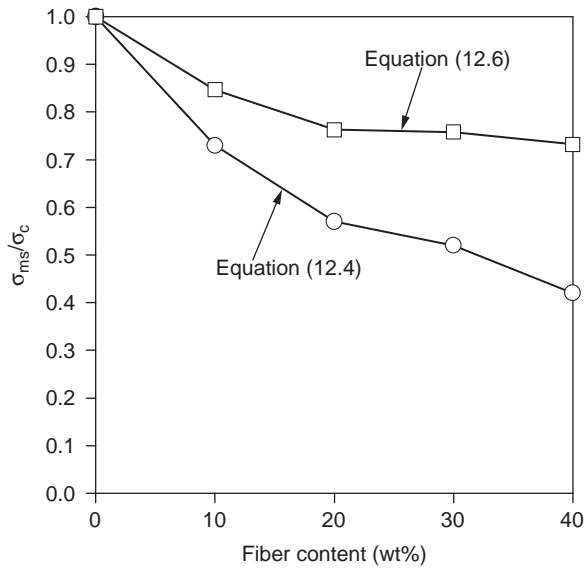and further study on the correlations observed is warranted.

FIGURE 12.9
The ratio of matrix stress to composite stress, σ_{ms}/σ_c, vs. fiber weight content. Equation (12.4) is derived from the assumptions of uniform alignment and uniformly applied load. Equation (12.6) is derived from the assumption of two-dimensional random orientation. (From S.C. Wong, G.X. Sui, C.Y. Yue, and Y.-W. Mai, *J. Mater. Sci.*, 37, 2659–2667, 2002. Reprinted with permission from Kluwer Academic Publishers.)

Figure 12.10 shows the crack-tip deformation zones of fractured specimens of different fiber weight fractions. Clearly, the large flame-shaped stress whitened zone associated with the unreinforced rubber-toughened sample (Figure 12.10(a)) is quenched upon addition of 10 wt% fibers (Figure 12.10(b)). Nevertheless, the latter still exhibits some substantial amount of matrix shear yielding. This is because, prior to fiber–matrix debonding, there is still sufficient matrix triaxial stress to cavitate the embedded rubber particles, and hence matrix plastic deformation is enhanced. An increase in fiber content generates tortuous fracture paths that are indicative of pervasive crack deflections at the fiber–matrix interface and near fiber ends. This once again reiterates the transition from matrix-dominant to fiber-dominant mechanisms in fiber-reinforced toughened plastics. Further increase in fiber weight fractions, viz., 20, 30, and 40 wt% in Figures 12.10(c) to (e), drastically decreases matrix deformation.

The specific essential fracture work is the total work per unit area of crack growth that is dissipated in the fracture process zone and required to debond and pull out the fibers, as well as to deform and tear the matrix ligament. When the matrix-borne stress is low, such as in high-fiber volume systems, the FPZ is dominated by fiber-related mechanisms, viz., fiber debonding, bridging, and pullout. However, outside the FPZ, the size of the plastic/ damage zone is small due to the low matrix stress there. For low-fiber
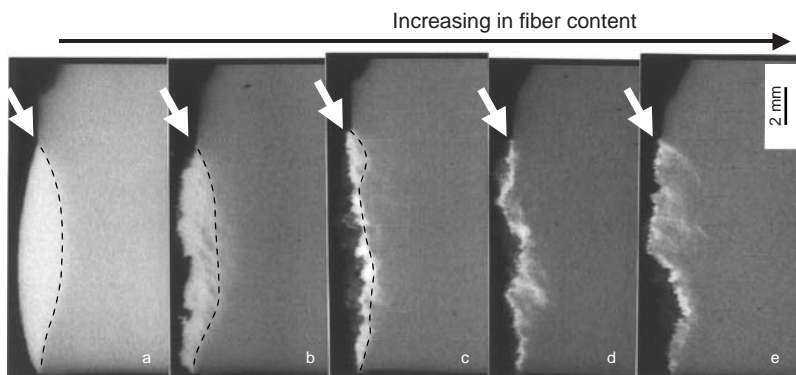
Increasing in fiber content

FIGURE 12.10
Optical photographs showing the plastic deformation zone beneath the fracture surface. The white arrows on the photographs indicate the onset of the crack. (a) Unreinforced toughened nylon 6,6; (b) 10 wt%, (c) 20 wt%, (d) 30 wt%, and (e) 40 wt% fiber-reinforced toughened nylon 6,6. (From S.C. Wong, G.X. Sui, C.Y. Yue, and Y.-W. Mai, *J. Mater. Sci.*, 37, 2659–2667, 2002. Reprinted with permission from Kluwer Academic Publishers.)

volume systems (< 20%), the dominant failure mechanisms will be rubber cavitation, which enhances matrix shear deformation. There will still be some contributions due to fiber-related mechanisms. To obtain a synergistic effect, it appears that we need to sustain sufficient hydrostatic stresses to cavitate the rubber particles prior to the activation of fiber-related debonding, bridging, and pullout. Under such circumstances, the hybrid system will benefit from both rubber and fiber toughening in a sequence of energy absorption events.

It appears from the presented results that too high a fiber content will suppress matrix toughening and only retain those fiber-related toughness contributions. Vice versa, too low a fiber content will be dominated by matrix toughening as activated by rubber cavitation. Also, the fiber–matrix adhesion will control the debonding mechanism and fiber end-induced plasticity. Further studies could focus on the effect of interfacial adhesion on fiber toughening in the presence of the rubbery phase.

12.3.2.3   *Glass Sphere-Containing Polymers*

Particulate-reinforced thermosets[34–37] or thermoplastics[19,24,32,33] often lead to brittle failure behavior. Martinatti and Ricco[24] studied the fracture toughness of polypropylene-based hybrid particulate composites. The dispersed phases included rubber particles, talc, and calcium carbonate. It was found that hybridization of the secondary phases produced synergistic effects in comparison to the corresponding binary systems. In a range of compositions, the hybrid particulate composites being filled by both talc and rubber or by $CaCO_3$ and rubber possess better impact fracture properties than the binary systems, viz., rubber-toughened PP, talc-reinforced PP, and $CaCO_3$-reinforced

PP alone. The micromechanical deformation and fracture mechanism of epoxy-based hybrid particulate composites were studied recently by a few research groups.[34–37] Zhang and Berglund[34] showed that the presence of glass beads not only promoted stiffening in the carboxyl-terminated butadiene-acrylonitrile rubber (CTBN)-toughened epoxy, but also played a toughening role. The addition of glass beads to the unmodified epoxy caused a significant increase in the fracture resistance G_{Ic}. Toughening was attributed to crack pinning. While the increase in toughness as CTBN content increased was apparent, addition of glass beads gave rise to further increases in the plane-strain fracture toughness, K_{Ic} and G_{Ic}. Nevertheless, glass beads did not appear to strengthen the toughened matrix. An increase in glass bead content left the yield strength of CTBN-toughened epoxy more or less unchanged, probably due to the weak glass–epoxy interface. How the energy absorption mechanisms on fracture interplayed with one another remained unclear. However, the glass bead/CTBN/epoxy led to concomitantly stiff and tough particulate hybrid composites.

Lee and Yee[36,37] critically examined the interactions between two particulate modifiers, viz., glass beads and CTBN, and the transition in micromechanical deformation of the hybrid composites. The toughening mechanisms were found to be more complex than the so-called crack bowing/pinning mechanism, as commonly known for particulate composites. Microscopy studies[81,82] showed that debonding of glass beads, which promotes matrix shear yielding, step formation on fracture surface, birefringence due to thermal residual misfit between glass beads and matrix, and microshear banding, operated in glass-filled epoxies without rubbery inclusions. Within a certain range of composition, however, rubber encapsulation could alter the interactions between rubber and CTBN particles, resulting in an increase in fracture toughness. Based on varied contents and subsequent toughening effects of glass beads and rubber, the hybrid composites could be divided into two groups, viz., glass bead dominant and CTBN dominant. Without the presence of CTBN, the major energy absorption source in the fracture of glass bead-filled epoxies was primarily the crack-front bowing mechanism and microshear banding.[36,37,81,82] As the CTBN content increased in the hybrid–particulate composites, the major micromechanical deformation observed at the crack tip changed from microshear banding to cavitation of the CTBN particles followed by matrix shear yielding.[37] In the case whereby the glass beads were encapsulated by the rubbery layer through the solution/evaporation technique, the transition of such a major deformation mechanism seems to occur at a lower CTBN content. It was shown[37] that the encapsulated systems induced significantly larger cavities than the nonencapsulated system. The larger cavities promoted shear yielding at a lower rubbery content. The results clearly indicated that with proper control of the interphase between glass beads and epoxy matrix, toughness comparable to that of conventional rubber-toughened thermosets is plausible without sacrificing much of the intrinsic stiffness and strength in a hybrid system.

12.3.3   LCP Hybrid Composites

Performance synergism can also be affirmed when there is value added to the material performance in addition to mechanical strength, stiffness, and toughness. Enhanced processability coupled with a sustained mechanical profile also contributes toward performance synergism.

The presence of inorganic fillers inadvertently raises the melt viscosity of thermoplastics, whereby high-energy consumption and constrained processability incur additional fabrication costs. Reinforcements using glass fibers, beads, or spheres and clay particles also catalyze the tear and wear of processing equipment. The high volume of inorganic fillers leads to heavier products. The reinforcement effect arising from fiber inclusions critically depends upon the retention of fiber length and its orientation. Unfortunately, shearing during the compounding and injection-molding processes often leads to fiber breakage. It is thus desirable to optimize fiber lengths and to promote good mixing during the compounding process.

Addition of LCPs to a thermoplastic matrix demonstrates the promise to reduce the viscosity of the compounding process, and hence processability could be improved. The LCP/thermoplastic blends also have other advantages over glass fiber-reinforced systems in addition to reduced melt viscosity and lower energy consumption in processing. Most injection-molded LCP-containing thermoplastics produce a smooth surface finish because of their propensity for a skin-core morphology. LCP also imparts good recycle characteristics to glass fiber-reinforced thermoplastics because glass fiber breakage is less severe in the presence of LCP during processing. Being an organic component by itself, LCP can form *in situ* fibers, offering lightweight substitutes for inorganic glass. Of critical importance is that the mechanical properties of hybrid composites are potentially superior to the glass-filled composites[83] via synergistic interactions. Previous studies by He et al.[84,85] reported attractive properties for LCP/glass/thermoplastic hybrid composites. They also showed good processability using polyether etherketone (PEEK), PC, and polyethersufone (PES) as matrices for LCP-containing systems. We shall examine the benefits of LCP addition in processing glass fiber-containing hybrid materials below.

12.3.3.1   Processability

Figure 12.11 shows the variation of torque with time for the extrusion of the glass fiber-reinforced composites. As expected, the torque increases with glass fiber content. This is due to the increase in the melt viscosity of the composite with increasing amount of glass fiber. It is, however, noted that the melt viscosities of glass fiber composites decrease with time and soon become lower than those of toughened nylon. This result is attributed to the fact that during increasingly elongational flow experienced by the melt in the converging section of the extrusion die, fibers in the composites oriented in the flow field direction. Thus, a reduction in viscosity and hence decreasing torque with time occurs.
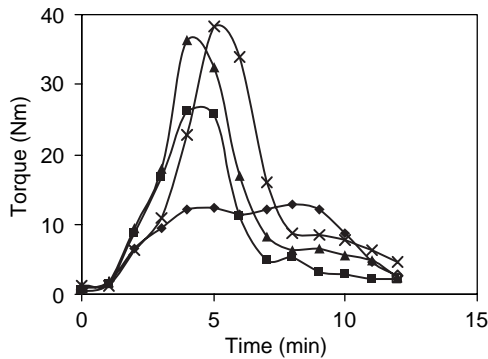
FIGURE 12.11
Variation of torque with time for toughened nylon 6,6 reinforced by different weight fractions of short glass fibers. (♦) Unreinforced; (■) 10 wt% glass fiber reinforced; (▲) 20 wt% glass fiber reinforced; (✕) 30 wt% glass fiber reinforced. (From S. Pisharath and S.C. Wong, *Polym. Composites*, in press. Reprinted with permission from Society of Plastics Engineers.)

In extrusion and injection molding, the flow fields generated always promote some degree of fiber orientation. The extent of fiber orientation depends on the intensity of the flow field and the response characteristics of the fiber.[86] Concentrated fiber suspensions are found to be more sensitive to elongational flows in promoting fiber orientation. Crowson et al.[87] studied glass fiber-reinforced polypropylene subjected to converging and shearing flows. Using a contact radiography technique, they found a high degree of fiber orientation parallel to the converging flow direction when the polymer melt entered the capillary die through a small cone angle from the reservoir. But much of this orientation was found to be lost during shear flow. Greene and Wilkes[88] examined the rheological properties of short-fiber-reinforced plastics using steady-state shear measurements. They found that at low shear rates the steady-state shear viscosity increased with fiber concentration. With extended shearing time, the viscosity became almost the same as the neat resin, regardless of the glass fiber content. Previous studies are consistent with our observation, which indicates decreasing torque with time and fiber alignment in the direction of flow.

Figure 12.12 shows the variation in the total torque with glass fiber content for reinforced toughened nylon. The information generated from the total torque could be rather complex. It represents the resistance of the solids in the conveying region of and the melt resistance throughout the extruder, and this torque is integrated with respect to time. The total torque is clearly indicative of the energy consumed for blending, and it increases with glass fiber content. A steep rise in the total torque is observed between 10 and 20 wt% of glass fibers. It appears that there exists a critical fiber volume fraction, above which the viscosity increases more markedly with fiber content. Clearly, inclusion of glass fibers has greatly increased the energy consumption during processing.
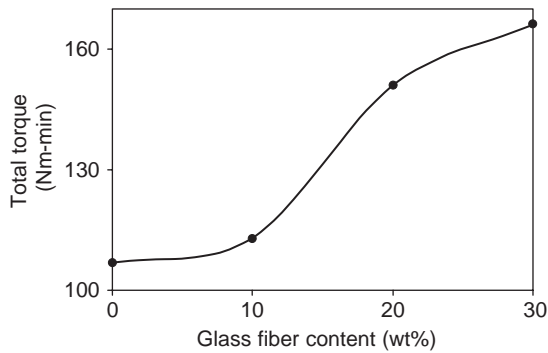
FIGURE 12.12
Variation of total torque of toughened nylon 6,6 with short glass fiber content. (From S. Pisharath and S.C. Wong, *Polym. Composites*, in press. Reprinted with permission from Society of Plastics Engineers.)

A change in the trend of instantaneous torque and the total torque profile arises upon addition of the LCP to the glass fiber-reinforced materials. The torque during extrusion for all hybrid compositions with a varied content of LCP is lower than that experienced during the processing of rubber-toughened nylon 6,6 reinforced with 20 wt% glass fiber, as shown in Figure 12.13. When the total torque is plotted against the LCP content in Figure 12.14, the decrease in accumulated torque appears to follow a volume-average rule. In contrast to Figure 12.12, Figure 12.14 clearly shows that the total torque for LCP-containing hybrid composites decreases with increasing LCP content. Hence, addition of LCP to glass fiber-reinforced toughened nylon reduces the energy consumption in processing. The low energy consumption can be envisaged in light of the reduction in the viscosity owing to the addition of LCP.
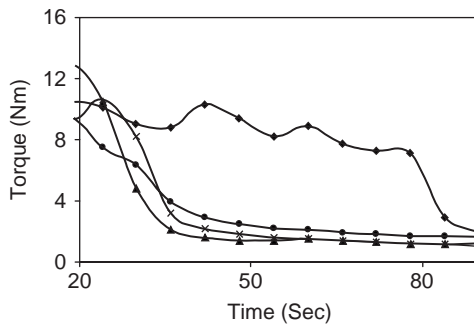
FIGURE 12.13
Variation of torque with time for LCP-containing hybrid composites. (♦) 0 wt% LCP; (●) 5 wt% LCP; (▲) 10 wt% LCP; (✕) 20 wt% LCP. (From S. Pisharath and S.C. Wong, *Polym. Composites*, in press. Reprinted with permission from Society of Plastics Engineers.)
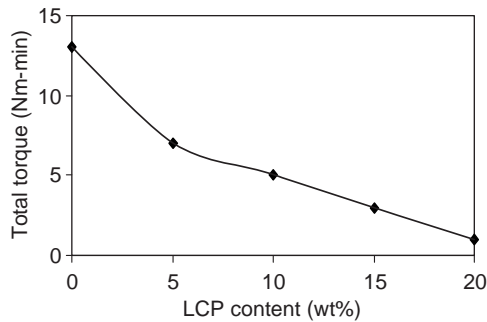
FIGURE 12.14
Variation of total torque of hybrid composites with LCP content. (From S. Pisharath and S.C. Wong, *Polym. Composites*, in press. Reprinted with permission from Society of Plastics Engineers.)

The role of LCP as a processing aid for thermoplastics is well established.[89] Seigmann et al.,[90] studying the blends of amorphous polyamide and liquid crystalline polyester, observed a marked decrease in viscosity for all the blends with the addition of as little as 5% LCP. This viscosity drop was attributed to the characteristic melt orientation of the LCP domains. Malik et al.[91] found that blends of LCP with polycarbonate had lower viscosities and exhibited more shear thinning than that of PC alone. Blizard and Baird[92] also observed a significant reduction in viscosity when they studied blends of an LCP with nylon 6,6. Investigating the torque during extrusion of nylon 6/LCP blends, La Mantia et al.[93] observed a pronounced decrease in the torque with addition of LCP. Nevertheless, little work has been done on the effect of LCP on the processability of fiber-reinforced hybrids. Based on these previous studies[90–93] on LCP-containing thermoplastics, we conjecture that LCP domains orient themselves in the direction of flow so that this interlayered alignment could facilitate the flow of polymer, thereby reducing the viscosity of the short glass fiber-reinforced matrix. Evidence to this end awaits further investigation.

To facilitate LCP fibrillation in hybrid composites, the viscosity of the dispersed phase (LCP) should be lower than that of the continuous phase.[94] It was interesting that Berry et al.[94] could barely observe the deformation of Vectra A950 in a nylon 6 matrix even at a high shear rate of 2500 sec^{-1}. At this shear rate, the ratio of viscosity of LCP to that of nylon 6 was found to be 4. In contrast, Wang et al.[95] investigated the dynamic rheological behavior of Vectra A950-reinforced nylon and observed that the viscosity ratio of Vectra A950 to nylon 66 was less than 1 at processing temperatures higher than 290°C. Their optical micrographs of blends of Vectra A950 and nylon 66 showed good fibrillation of the LCP above 290°C, but it could not fibrillate well at 280°C.

Figure 12.15 compares the torque profile of toughened nylon containing 20 wt% glass fibers and that of Vectra A950 at 290°C. The torque in the extrusion process of Vectra A950 is much lower than that for the fiber-
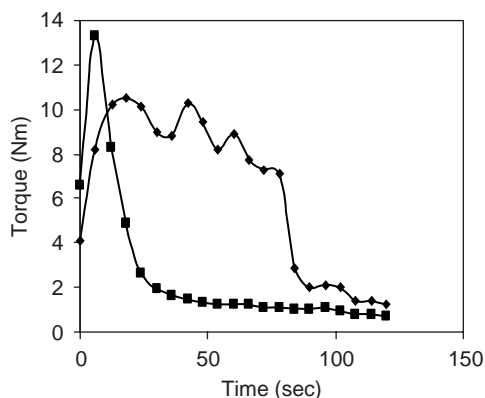
FIGURE 12.15
Variation of torque with time for glass fiber-reinforced toughened nylon 6,6 (♦) and Vectra A950 (■). (From S. Pisharath and S.C. Wong, *Polym. Composites*, in press. Reprinted with permission from Society of Plastics Engineers.)

containing nylon. This condition appears to satisfy Wang et al.'s observation[95] that the melt viscosity of Vectra A950 is lower than that of the matrix. Under this condition, LCP fibrillation should be enhanced during melt processing.

12.3.3.2 Extrudate Morphology

The morphology of the extrudates was observed under SEM after they were cryo-fractured following immersion in liquid nitrogen. Figure 12.16 compares the fracture surface morphologies of the extrudate from 5 wt% (Figures 12.16(a) and (b)) and 20 wt% (Figure 12.16(c)) LCP-containing hybrid composites. The micrographs show two main features. The continuous phase is toughened nylon reinforced with 20 wt% short glass fibers, and the LCP fibrils appear sparsely drawn out from the surface in Figure 12.16(b). The LCP phase is not completely distinctive from the predominant nylon matrix even though some individual LCP fibrils are visible. Such surface morphology suggests that some degree of complex interchange reactions[96] between LCP and nylon may take place at the molecular level. Further evidence of the interchange reactions is discussed elsewhere.[96,97] At 5 wt% LCP (Figure 12.16(b)), the fibrils seem to be uniformly and sparsely distributed all over the surface, but as the LCP content increases to 20 wt% (Figure 12.16(c)), the LCP phase seems to coalesce and forms some sheet-like structures. This fibril formation and orientation of the LCP phase are the primary driving forces behind enhanced processability and hybrid effects for LCP composites.

12.3.3.3 Thermal Properties
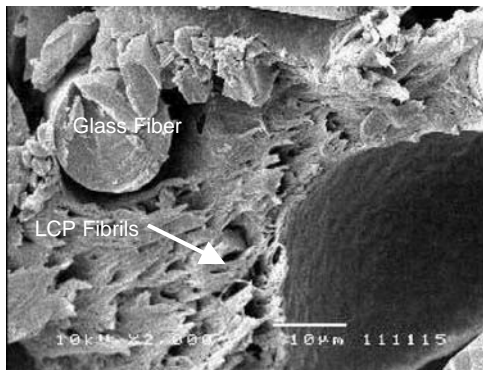
Thermogravimetry analysis (TGA) results are summarized in Table 12.3. Blending of glass fiber-reinforced nylon 6,6 with Vectra A950 has improved
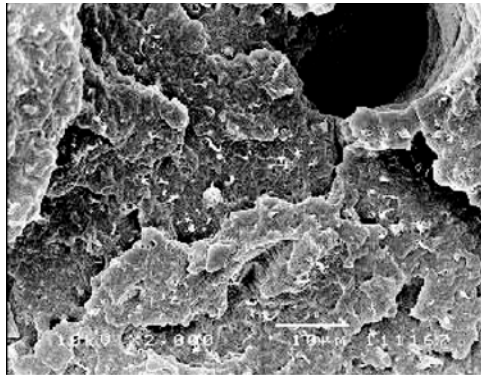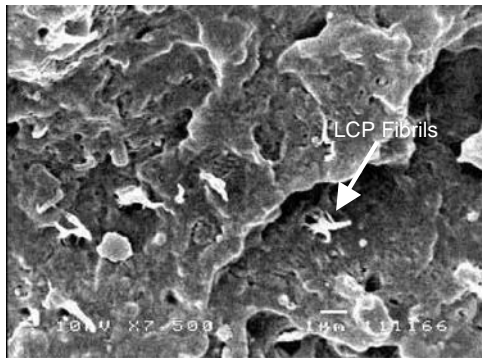
FIGURE 12.16

SEM photomicrograph of cryo-fractured surface of an extrudate from hybrid composites with (a) 5 wt% LCP (low magnification), (b) 5 wt% LCP (high magnification), and (c) 20 wt% LCP. (From S. Pisharath and S.C. Wong, *Polym. Composites*, in press. Reprinted with permission from Society of Plastics Engineers.)

TABLE 12.3

TGA Results of LCP Hybrid Composites

Sample Description	Degradation Temperature, T_d (C°)	Residue at 450°C (%)
Toughened nylon reinforced with 20 wt% short glass fibers	382.59	42.8
Toughened nylon reinforced with 20 wt% short glass fibers and 15 wt% LCP	397.06	63.8
Toughened nylon reinforced with 20 wt% short glass fibers and 20 wt% LCP	400	64.5

Note: Degradation temperature was determined by TGA at 5% weight loss.

the thermal stability of the blends. LCPs having better thermal properties than the flexible chain polymers impart improved thermal stabilities to the reinforced matrix. The results indicate that the thermal stabilities of glass fiber-reinforced composites could be considerably improved by inclusion of LCP, and these are consistent with those reported by other researchers[98–100] on nonhybrid systems.

12.3.3.4   Mechanical Properties

The plots of tensile strength and modulus vs. LCP content are shown in Figure 12.17. The trends of variation of both strength and stiffness with respect to LCP content appear to be similar. With the addition of 5 wt% of LCP, there is a slight drop in strength and stiffness. A further increase in LCP content enhances both properties. At 20 wt% LCP, there is a rapid rise in the tensile strength and stiffness. Figure 12.18 compares the tensile modulus and strength of unreinforced, glass fiber-reinforced, and LCP-containing hybrid material. The tensile strength of the hybrid composite at 20 wt% LCP (70 MPa) is higher than that of a rubber-toughened nylon 6,6 reinforced with 30 wt% glass fiber (67 MPa). Clearly, the presence of LCP not only provided good processability, but also a strengthening role for the glass fiber-reinforced polymer matrix.

12.3.4   Polymer Nanocomposites: Potential Synergistic Properties

In the emerging area of polymer nanocomposites, extensive research[44–60] has been undertaken to evaluate the possibility of significant weight reduction in high-performance, high-barrier, and recyclable materials primarily for the packaging and automotive industries. While many nanocomposites appear to provide enhanced strength, stiffness, and barrier and thermal properties, some of them are found to be quite brittle. The embrittlement effect arising from nano reinforcements has severely limited the applications of such nanocomposites. Efforts to establish toughening strategies for nanocomposites have been pioneered by Yee and others.[22,44] In the discussion that follows, we highlight the mechanical properties and toughening
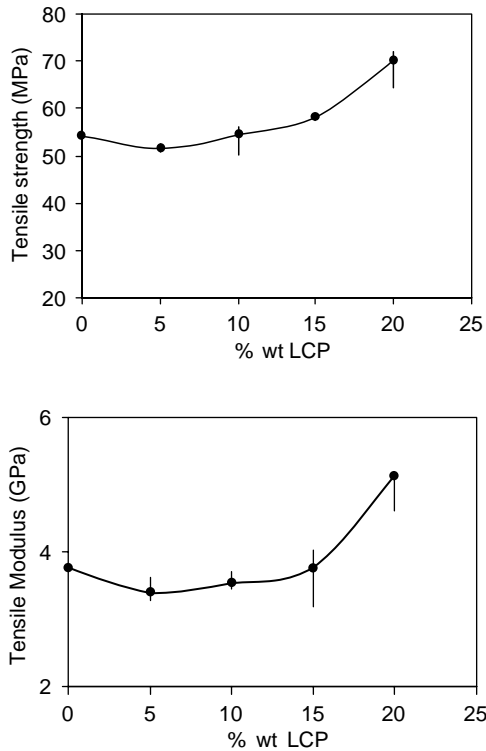
FIGURE 12.17
Variation of tensile strength and modulus of hybrid composites with LCP content. (From S. Pisharath and S.C. Wong, *Polym. Composites*, in press. Reprinted with permission from Society of Plastics Engineers.)

behavior in polymer-based nanocomposites. Readers are referred to Chapter 10 in this book for discussions on synthesis, processing, and physical properties of nanocomposites.

12.3.4.1 Toughening of Nylon-Based Nanocomposites

Figure 12.19 shows a typical mechanical response of nanocomposites as a function of clay content.[44] Here, the polymer matrix used was nylon 6 (grade SF1018A) from UBE. Surface-modified montmorillonite (I30TC) was supplied by Nanocor Inc. The clay platelets were well exfoliated, as evident, using wide-angle x-ray scattering (WAXS). While modulus increases with clay content, the strain-at-break decreases sharply in Figure 12.19. Fracture toughness also decreases in the same fashion as the strain-at-break. Embrittling factors are classified into intrinsic and extrinsic ones. The extrinsic factors, such as degradation of polymer chains, aggregation of clay and air bubble, etc., may result from processing of nanocomposites. The intrinsic factors, such as crystalline morphology, chain confinement, crazing, and
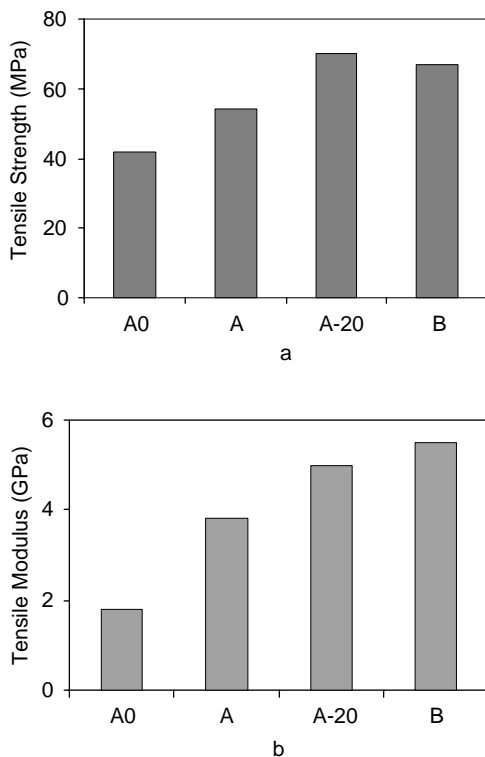
FIGURE 12.18
Comparison of tensile strength and modulus of unreinforced, glass fiber-reinforced, and hybrid composite materials. A0: Rubber-toughened nylon 6,6. A: Rubber-toughened nylon 6,6 reinforced with 20 wt% glass fiber. A-20: Rubber-toughened nylon 6,6 reinforced with 20 wt% glass fiber and 20 wt% LCP. B: Rubber-toughened nylon 6,6 reinforced with 30 wt% glass fiber. (From S. Pisharath and S.C. Wong, *Polym. Composites*, in press. Reprinted with permission from Society of Plastics Engineers.)

microcracking, are mainly due to the transformation of morphology upon introduction of nanoclay and the onset of deformation. He and Yee[44] showed that for nylon-based nanocomposites, extrinsic embrittlement factors could not be established on the basis of their results from molecular weight measurements, melt viscosities, WAXS, and small-angle x-ray scattering (SAXS). The use of SAXS in examining the exfoliated morphology is novel and interesting. WAXS is a technique widely used to examine whether modified clay has been properly exfoliated.[45,50–57,60] There are, however, limitations with this method. First, the clay may still exhibit an intercalated morphology with a longer interlayer distance that could not be accessed by WAXS since WAXS is normally limited to about 2° (2 q). Second, there is a possibility that the scattering peak due to the intercalated clay (modified clay) disappears, yet the clay still exhibits an aggregate morphology. This may occur when the shearing force disrupts the layer packing arrangement during
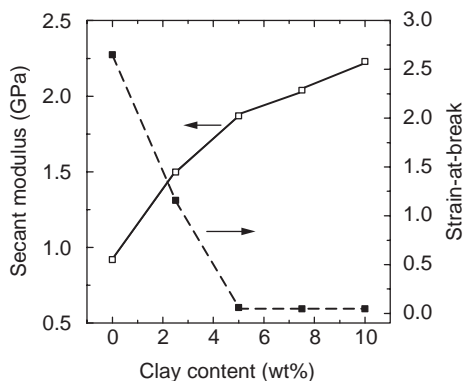
FIGURE 12.19
Tensile modulus and strain-at-break vs. clay content for nanoclay-reinforced nylon 6–clay. (From C.B. He and A.F. Yee, unpublished report, 2001. Reprinted with permission from He and Yee.)

compounding, but does not fully disperse the aggregated clay. To address this problem, SAXS is preferred, and it can probe a longer length scale.

Figure 12.20 gives the SAXS of nylon 6 containing 2.5% clay.[44] The scattering pattern is dominated by a peak at $q \sim 0.08$ Å^{-1}, where $q = 4\pi \sin \theta/\lambda$; θ is Bragg's angle, and λ is the wavelength. This peak corresponds to a d spacing of 8 nm. Except for this peak, there is no significant scattering up to 80 nm. Given the evidence that WAXS showed exfoliated morphology in the polymer matrix and SAXS showed insignificant concentration of aggregates up to the length scale of 80 nm, it was concluded that clay aggregation was not a contributing factor to the brittle response of the nanocomposites.

Figure 12.21 compares the undeformed and deformed tensile specimens of unfilled nylon 6,6 and 2.5% nanocomposites under SAXS.[44] Figure 12.21(a)
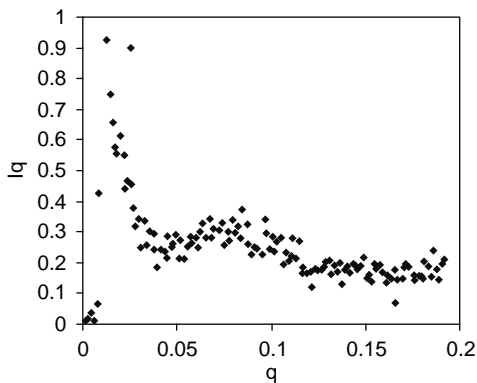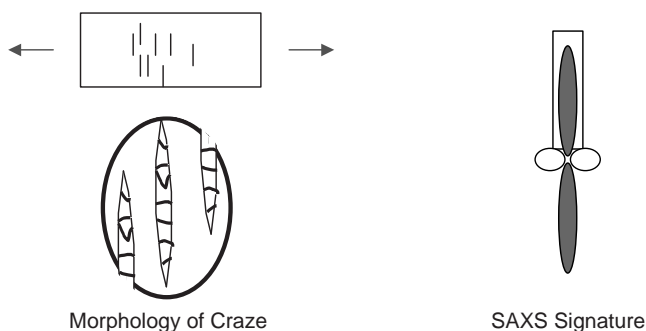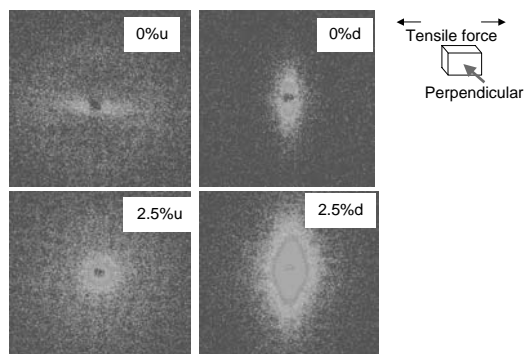

FIGURE 12.20
SAXS of nylon 6 containing 2.5% of clay. Experiment was performed on a NanoStar small-angle x-ray diffractometer. Cu Kα: $\lambda = 1.5418$ Å. (From C.B. He and A.F. Yee, unpublished report, 2001. Reprinted with permission from He and Yee.)

Morphology of Craze

SAXS Signature

(a)

(b)

FIGURE 12.21
SAXS of deformed and undeformed nylon nanocomposites. (a) Theoretical SAXS imaging from crazes. (b) Comparison of undeformed (u) and deformed (d) nylon and 2.5 wt% nanocomposites. The x-ray direction is given in the inserted figure. (From C.B. He and A.F. Yee, unpublished report, 2001. Reprinted with permission from He and Yee.)

shows the expected feature of SAXS arising from polymer crazing. The meridional scattering was attributed to scattering from fibrils of the crazes, which can be quantitatively related to craze concentration through invariant analysis. In Figure 12.21(b), equatorial scattering is hardly seen, and it could be related to the scattering from the interference of the polymer matrix and the crack when craze fibrils break apart. The results suggest that premature microcracking overrides any intrinsic deformation mechanisms from the nylon matrix. The report[44] appears to be the first of it kind in deformation studies of nanocomposites, and they warrant more detailed investigation using microscopic techniques.

12.3.4.2   *Synergistic Toughening Using PVDF*

Apart from using rubber toughening for nylon nanocomposites, the consequence of which inevitably reduces the desired strength and stiffness, syn-
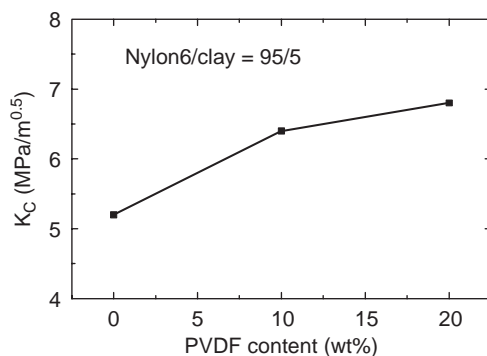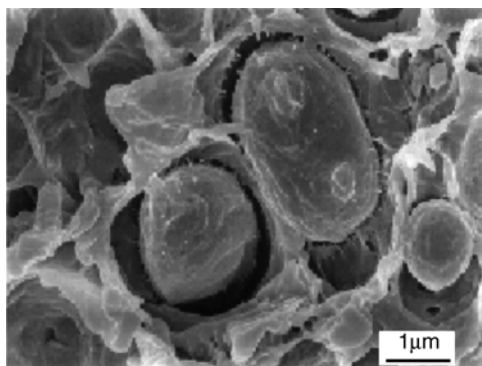
FIGURE 12.22
(a) Fracture toughness, K_c, of nylon 6–clay–PVDF hybrid nanocomposites vs. PVDF content. The weight ratio of nylon 6 to clay is fixed at 95 to 5. (b) SEM fractograph of nylon 6–clay–PVDF hybrid nanocomposites containing 20 wt% PVDF.

ergistic toughening by means of crack bridging mechanisms was also attempted.[44] Figure 12.22(a) plots K_{Ic} of polyvinylidiene fluoride (PVDF)-containing nylon nanocomposites. It is clear that addition of PVDF could effectively toughen the nanocomposites. Figure 12.22(b) shows the bridging PVDF particles in 20 wt% PVDF-toughened nanocomposites under SEM. Debonding-bridging mechanisms[4] appear to stabilize the premature crazes and microcracks and lead to enhanced fracture toughness.

12.3.4.3 Toughening of Silsesquioxane Epoxy[101,102]

Silsesquioxane epoxy (POSS) resin[101,102] is a new polymer nanomaterial for functional and high-performance applications. It has been shown that organic/inorganic hybrid polymers made of POSS possess several attractive properties such as increased thermal stability, high glass transition temperature, better flame and heat resistance, and enhancements in mechanical and melt strengths. The organic/inorganic hybrid material studied[44] was octa cyclohexenyl silses-
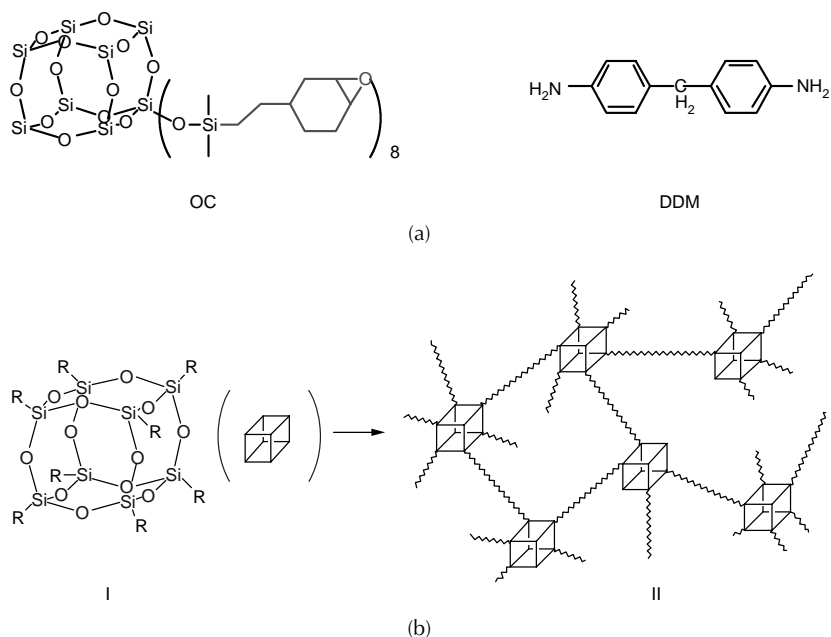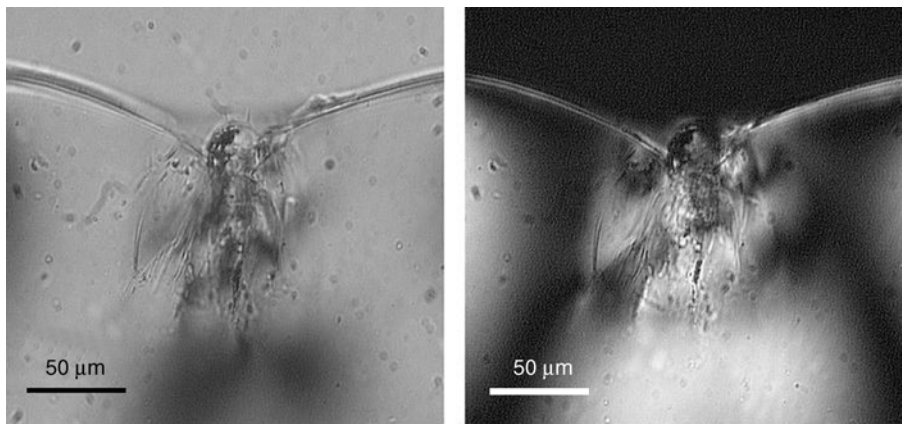
FIGURE 12.23
(a) Chemical formulations of silsesquioxane epoxide cube (OC) and curing agent, diamino-diphenyl methane (DDM). (b) Formation of nanocomposites from cubic silsesquioxane: OC/DDM invented by Laine et al.[101,102]

quioxane epoxide cube (OC),[101,102] while diamino-diphenyl methane (DDM) served as the curing agent. The chemical structures of OC/DDM and their nanocomposites are shown in Figure 12.23.[101,102] Figure 12.23(a) gives the basic chemical formulations, while Figure 12.23(b) shows the three-dimensional structure. It was found that indentation on the specimen surface using a diamond stylus showed cracks propagating underneath the indentation surface, as shown in Figure 12.24(a). Birefringence imaging suggested that both elastic and plastic deformation existed. When the specimen was sliced into halves to relieve the residual stress, birefringence patterns arising from the half cross sections (Figure 12.24(b)) confirmed that plastic deformation was plausible with OC/DDM nanocomposites. These recent findings suggested that toughening of such organic/inorganic hybrid materials could be accomplished by using hybridization strategies, e.g., the inclusion of an elastomeric phase.

12.4 Conclusions

We could envisage great potential and variation arising from the development of hybrid materials at micrometer and nanometer scales. We reviewed a number of hybridization strategies, including rigid–rigid polymer blends
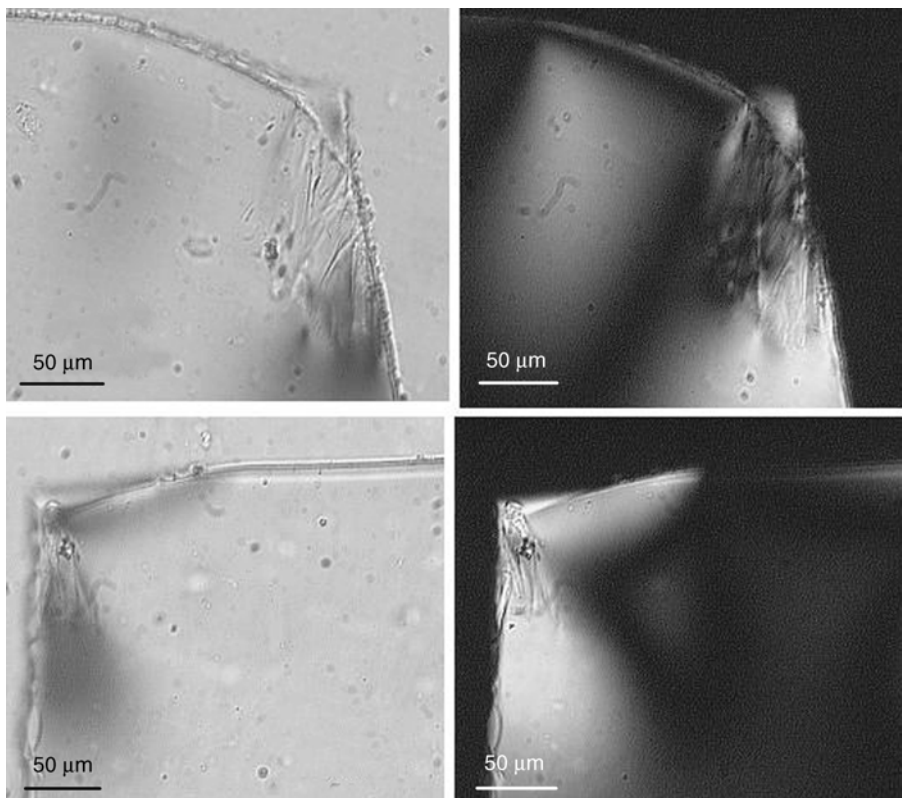
FIGURE 12.24
(a) Deformation of POSS created by indentation with a diamond stylus, arbitrary load, ×400. Note the birefringence under the indented crack. (b) Relief of elastic stress by halving the indented crack. Note the plastic deformation beneath the crack. (From C.B. He and A.F. Yee, unpublished report, 2001. Reprinted with permission from He and Yee.)

TABLE 12.4

Summary of Hybrid Effects

Hybrid Systems	Synergistic Properties	Related References
Ternary polymer blends	Strength, toughness	25–27
Glass-containing toughened polymers	Strength, stiffness, toughness	6, 16–18, 34–37
LCP hybrid composites	Strength, stiffness, toughness, processability, thermal stability	83–85, 91–93, 96, 97
Nanocomposites containing PVDF and POSS	Toughness, shear deformation	44

and ternary alloys, glass-containing rubber-toughened polymers, LCP-containing glass-filled polymers, and polymer nanocomposites, with an emphasis on their fracture mechanisms and toughenability and the understanding of synergistic performance. The hybrid effects in load-bearing capability, processability, and materials functionality were reviewed. The synergistic performance is summarized in Table 12.4. It was clear that with proper design of the micro- and nanostructures, particularly the interfacial properties, and precise control of stress state and failure mechanisms, hybridization could often deliver exciting engineered properties. Much of the control demands an understanding of how the heterogeneities interact with one another. Such understanding is not yet complete, but novel experimental studies coupled with advances in modeling capability have promised every prospect of placing the unique hybridization of materials on a quantitative basis. Synergistic hybridization of polymer-based composites appears to remain the focus of intensive research in the next decade.

Acknowledgments

References

1. C.B. Bucknall. *Toughened Plastics*. Applied Science Publishers, London, 1977.
2. L.A. Utracki. *Polymer Alloys and Blends: Thermodynamics and Rheology*. Hanser, New York, 1990.

3. J. Rösch and R. Mülhaupt. Deformation behavior of PP/PA blends. *J. Appl. Polym. Sci.*, 56, 1607–1613, 1995.

4. J. Wu, Y.-W. Mai, and A.F. Yee. Fracture toughness and fracture mechanisms of polybutylene-terephthalate/polycarbonate/impact-modifier blends: Part III. Fracture toughness and mechanisms of PBT/PC blends without impact modifiers. *J. Mater. Sci.*, 29, 4510–4522, 1994.

5. J. Wu, D.-M. Yu, Y.-W. Mai, and A.F. Yee. Fracture toughness and fracture mechanisms of PBT/PC/IM blends: Part IV. Impact toughness and failure mechanisms of PBT/PC blends without impact modifier. *J. Mater. Sci.*, 35, 307–315, 2000.

6. S.V. Nair, S.-C. Wong, and L.A. Goettler. Fracture resistance of polyblends and polyblend matrix composites: Part I. Unreinforced and fiber-reinforced nylon 6,6/ABS polyblends. *J. Mater. Sci.*, 32, 5335–5346, 1997.

7. S.V. Nair, A. Subramaniam, and L.A. Goettler. Fracture resistance of polyblends and polyblend matrix composites: Part II. Role of the rubber phase in nylon 6,6/ABS alloys. *J. Mater. Sci.*, 32, 5347–5354, 1997.

8. M.-L. Shiao, S.V. Nair, P.D. Garrett, and R.E. Pollard. Deformation mechanism and fiber toughening of nylon 6,6. *Polymer*, 35, 306–314, 1994.

9. M.-L. Shiao, S.V. Nair, P.D. Garrett, and R.E. Pollard. Effect of glass-fiber reinforcement and annealing on microstructure and mechanical behavior of nylon 6,6: Part I. Microstructure and morphology. *J. Mater. Sci.*, 29, 1973–1981, 1994.

10. M.-L. Shiao, S.V. Nair, P.D. Garrett, and R.E. Pollard. Effect of glass-fiber reinforcement and annealing on microstructure and mechanical behavior of nylon 6,6: Part II. Mechanical behavior. *J. Mater. Sci.*, 29, 1739–1752, 1994.

11. J. Karger-Kocsis. Part IIB. Fracture of short-fiber reinforced thermoplastics: microstructure and fracture mechanical performance of short-fiber reinforced thermoplastics, in *Application of Fracture Mechanics to Composite Materials*, Friedrich, K., Ed. Elsevier, Oxford, 1989, chap. 6, pp. 189–247.

12. J. Karger-Kocsis. Microstructural aspects of fracture in polypropylene and in its filled, chopped fiber and fiber mat reinforced composites, in *Polypropylene: Structure, Blends and Composites*, Vol. 3, *Composites*, Karger-Kocsis, J., Ed. Chapman & Hall, London, 1995, chap. 4, pp. 142–201.

13. K. Friedrich. Microstructure and fracture mechanical performance of discontinuous fiber reinforced thermoplastic composites, in *Proceedings of the International Symposium on Polymer Alloys and Composites* (Hong Kong, December 1992), Choy, C.L. and Shin, F.G. Eds. Hong Kong Polytechnic, Hong Kong, 1994, pp. 121–144.

14. D.E. Mouzakis, F. Stricker, R. Mülhaupt, and J. Karger-Kocsis. Fracture behavior of polypropylene/glass bead elastomer composites by using the essential-work-of-fracture method. *J. Mater. Sci.*, 33, 2551–2562, 1998.

15. Z.A. Mohd Ishak, U.S. Ishiaku, and J. Karger-Kocsis. Hygrothermal aging and fracture behavior of short-glass-fiber-reinforced rubber-toughened PBT composites. *Composite Sci. Technol.*, 60, 803–815, 2000.

16. D.M. Laura, H. Keskkula, J.W. Barlow, and D.R. Paul. Effect of glass fiber and maleated ethylene-propylene rubber content on tensile and impact properties of nylon 6. *Polymer*, 41, 7165–7174, 2000.

17. D.M. Laura, H. Keskkula, J.W. Barlow, and D.R. Paul. Effect of glass fiber and maleated ethylene-propylene rubber content on the impact fracture parameters of nylon 6. *Polymer*, 42, 6161–6172, 2001.

18. K. Wang, J. Wu, and H. Zeng. Microstructures and fracture behavior of glass-fiber reinforced PBT/PC/E-GMA elastomer blends: 1. Microstructures. *Composite Sci. Technol.*, 61, 1529–1538, 2001.

19. M.W.L. Wilbrink, A.S. Argon, R.E. Cohen, and M. Weinberg. Toughen-ability of nylon-6 with $CaCO_3$ filler particles: new findings and general principles. *Polymer*, 42, 10155–10180, 2001.

20. B. Lauke and W. Pompe. Fracture toughness of short fiber reinforced thermo-plastics. *Composite Sci. Technol.*, 26, 37–57, 1986.

21. B. Lauke and W. Pompe. Relation between work of fracture and fracture toughness of short-fibre reinforced polymers. *Composite Sci. Technol.*, 31, 25–33, 1988.

22. S.C. Wong and L. Chen. Mechanical and fracture properties of nanoclay filled polypropylene, in *Proceedings of the Society of Plastics Engineers ANTEC 2002* (San Francisco, CA) Brookfield, CT, 2002, 2, 1466–1469.

23. Y. Ou, F. Yang, and Z.Z. Yu. A new conception on the toughness of nylon 6/silica nanocomposite prepared via *in situ* polymerization. *J. Polym. Sci. Polym. Phys.*, 36B, 789–795, 1988.

24. F. Martinatti and T. Ricco. High-rate fracture toughness of polypropylene-based, hybrid, particulate composites. *J. Mater. Sci.*, 29, 442–448, 1994.

25. J. Wu, B. Guo, C.-M. Chan, J. Li, and H.-S. Tang. Synergistic toughening effect of SBS and HDPE on the fracture of the PS/HDPE/SBS blends. *Polymer*, 42, 8857–8865, 2001.

26. S.-C. Wong and Y.-W. Mai. Effect of rubber functionality on microstructures and fracture toughness of impact-modified nylon 6,6/polypropylene blends: I. Structure-property relationships. *Polymer*, 40, 1553–1566, 1999.

27. S.-C. Wong and Y.-W. Mai. Effect of rubber functionality on microstructures and fracture toughness of impact-modified nylon 6,6/polypropylene blends: II. Toughening mechanisms. *Polymer*, 41, 5471–5483, 2000.

28. C.R. Lindsey, D.R. Paul, and J. W. Barlow. Mechanical properties of HDPE-PS-SEBS blends. *J. Appl. Polym. Sci.*, 26, 1–8, 1981.

29. J. Rösch. Modeling the mechanical properties in polypropylene/polyamide 6 blends with core shell morphology. *Polym. Eng. Sci.*, 35, 1917–1922, 1995.

30. J. Rösch and R. Mülhaupt. The role of core/shell-microparticle dispersions in polypropylene/polyamide-6 blends. *Polym. Bull.*, 32, 697–704, 1994.

31. J. Wu and Y.-W. Mai. Fracture toughness and fracture mechanisms of PBT/PC/IM blend: Part II. Toughening mechanisms. *J. Mater. Sci.*, 28, 6167–6177, 1993.

32. D. Benderly, A. Siegmann, and M. Narkis. Preferential distribution of glass particles in reinforced polypropylene/polyamide immiscible blends. *J. Mater. Sci. Lett.*, 14, 132–134, 1995.

33. S.C. Tjong and S.A. Xu. Ternary polymer composites: PA6,6/maleated SEBS/glass beads. *J. Appl. Polym. Sci.*, 81, 3231–3237, 2001.

34. H. Zhang and L.A. Berglund. Deformation and fracture of glass bead/CTBN-rubber/epoxy composites. *Polym. Eng. Sci.*, 33, 100–107, 1993.

35. H.R. Azimi, R.A. Pearson, and R.W. Hertzberg. Fatigue of hybrid epoxy com-posites: epoxies containing rubber and hollow glass spheres. *Polym. Eng. Sci.*, 36, 2352–2365, 1996.

36. J. Lee and A.F. Yee. Micro-mechanical deformation mechanisms in the fracture of hybrid particulate composites based on glass beads, rubber and epoxies. *Polym. Eng. Sci.*, 40, 2457–2470, 2000.

37. J. Lee and A.F. Yee. Effect of rubber interlayers on the fracture of glass bead/epoxy composites. *J. Mater. Sci.*, 36, 7–20, 2001.
38. T.J. Pecorini and R.W. Hertzberg. The fracture behavior of rubber-toughened short fiber composites of nylon 6,6. *Polym. Composites*, 15, 174–183, 1994.
39. S.-C. Wong and Y.-W. Mai. Essential fracture work of short fiber reinforced polymer blends. *Polym. Eng. Sci.*, 39, 356–364, 1999.
40. G.X. Sui, S.C. Wong, and C.Y. Yue. The effect of fiber inclusions in toughened plastics: Part I. Fracture characterization by essential fracture work. *Composite Sci. Technol.*, 61, 2481–2490, 2001.
41. Q. Xu, Y. Leng, and Y.-W. Mai. Injection molding of PC/PBT/LCP ternary *in situ* composite. *Polym. Eng. Sci.*, 36, 769–777, 1996.
42. S.-C. Wong and Y.-W. Mai. Fiber reinforcement and fracture resistance of PC/PBT/LCP ternary *in situ* composite. *Polym. Eng. Sci.*, 38, 156–168, 1998.
43. S. Pisharath and S.C. Wong. Processability of LCP-nylon-glass hybrid composites. *Polym. Composite*, in press.
44. C.B. He and A.F. Yee. Fracture and toughening of composites of polymers and nanoscale inorganic and organic fillers. Unpublished report, 2001.
45. E. Manias, A. Touny, L. Wu, K. Strawhecker, B. Lu, and T.C. Chung. Polypropylene/montmorillonite nanocomposites: review of the synthetic routes and materials properties. *Chem. Mater.*, 13, 3516–3523, 2001.
46. R.A. Vaia, B.B. Sauer, O.K. Tse, and E.P. Giannelis. Relaxation of confined chains in polymer nanocomposites: glass transition properties of poly(ethylene oxide) intercalated in montmorillonite. *J. Polym. Sci. Polym. Phys.*, 35B, 59–67, 1997.
47. R.A. Vaia and E.P. Giannelis. Lattice model of polymer melt intercalation in organically modified layered silicates. *Macromolecules*, 30, 7990–7999, 1997.
48. R.A. Vaia and E.P. Giannelis. Polymer melt intercalation in organically modified layered silicates: model predictions and experiment. *Macromolecules*, 30, 8000–8009, 1997.
49. R. Krishnamoorti and E.P. Giannelis. Rheology of end-tethered polymer layered silicate nanocomposites. *Macromolecules*, 30, 4097–4102, 1997.
50. P. Reichert, J. Kressler, R. Thomann, R. Mülhaupt, and G. Stöppelmann. Nanocomposites based on a synthetic layer silicate and polyamide-12. *Acta Polym.*, 49, 116–123, 1998.
51. N. Hasegawa, H. Okamoto, M. Kawasumi, M. Kato, A. Tsukigase, and A. Usuki. Polyolefin-clay hybrids based on modified polyolefins and organophilic clay. *Macromol. Mater. Eng.*, 280/281, 76–79, 2000.
52. X. Huang, S. Lewis, W.J. Brittain, and R.A. Vaia. Synthesis of polycarbonate-layered silicate nanocomposites via cyclic oligomers. *Macromolecules*, 33, 2000–2004, 2000.
53. M. Kato, A. Usuki, and A. Okada. Synthesis of polypropylene oligomer-clay intercalation compounds. *J. Appl. Polym. Sci.*, 66, 1781–1785, 1997.
54. X. Fu and S. Qutubuddin. Polymer-clay nanocomposites: exfoliation of organophilic montmorillonite nanolayers in polystyrene. *Polymer*, 42, 807–813, 2001.
55. J. W. Cho and D.R. Paul. Nylon 6 nanocomposites by melt compounding. *Polymer*, 42, 1083–1094, 2001.
56. L. Liu, Z. Qi, and X. Zhu. Studies on nylon 6/clay nanocomposites by melt-intercalation process. *J. Appl. Polym. Sci.*, 71, 1133–1138, 1999.

57. H.R. Dennis, D.L. Hunter, D. Chang, S. Kim, J.L. White, J.W. Cho, and D.R. Paul. Effect of melt processing conditions on the extent of exfoliation in organoclay-based nanocomposites. *Polymer*, 42, 9513–9522, 2001.

58. T. Lan and G. Qian. Preparation of high performance polypropylene nanocomposites, in *Proceeding of Additives 2000* (Clearwater Beach, FL, April 10–12, 2000).

59. G. Qian, J.W. Cho, and T. Lan. Preparation and properties of polyolefin nanocomposites, in *Proceedings of Polyolefins 2001* (Houston, TX, February 25–28, 2001).

60. H. Wang, M. Elkovitch, L.J. Lee, and K.W. Koelling. Processing and properties of polymer nanocomposites, in *Proceedings of SPE ANTEC* 2000. Brookfield, CT, 2000, 2402–2406.

61. A.G. Evans, Z.B. Ahmad, D.G. Gilbert, and P.W.R. Beaumont. Mechanisms of toughening in rubber toughened polymers. *Acta Metall.*, 34, 79–87, 1986.

62. J.C. Halpin and J.L. Kardos. The Halpin-Tsai equations: a review. *Polym. Eng. Sci.*, 16, 344–352, 1976.

63. S.-Y. Fu and B. Lauke. Characterization of tensile behavior of hybrid short glass fibre/calcite particle/ABS composites. *Composites*, 29A, 575–583, 1998.

64. S.Y. Fu, X. Hu, and C.-Y. Yue. A new model for the transverse modulus of unidirectional fiber composites. *J. Mater. Sci.*, 33, 4953–4960, 1998.

65. R.M. Jones. Micromechanical behavior of a lamina, in *Mechanics of Composite Materials*. Scripta Book Company, Washington D.C., 1975, chap. 3, pp. 85–146.

66. A.F. Yee and R.A. Pearson. Toughening mechanisms in elastomer-modified epoxies: Part I. Mechanical studies. *J. Mater. Sci.*, 21, 2462–2473, 1986.

67. R.A. Pearson and A.F. Yee. Toughening mechanisms in elastomer-modified epoxies: Part II. Microscopy studies. *J. Mater. Sci.*, 21, 2475–2488, 1986.

68. R.A. Pearson and A.F. Yee. Influence of particle size and particle size distribution on toughening mechanisms in rubber-modified epoxies. *J. Mater. Sci.*, 26, 3828–3844, 1991.

69. R.J. Gaymans. Toughening of semicrystalline thermoplastics, in *Polymer Blends*, Vol. 2, *Performance*, D.R. Paul and C.B. Bucknall, Eds. John Wiley & Sons, New York, 2000, chap. 25, pp. 177–224.

70. A.C. Steenbrink, V.M. Litvinov, and R.J. Gaymans. Toughening of SAN with acrylic core-shell rubber particles: particle size effect or cross-link density? *Polymer*, 39, 4817–4825, 1998.

71. H.-J. Sue and A.F. Yee. Toughening mechanisms in a multi-phase alloy of nylon 6,6/polyphenylene oxide. *J. Mater. Sci.*, 24, 1447–1457, 1989.

72. S.R. Murff, J.W. Barlow, and D.R. Paul. *J. Appl. Polym. Sci.*, 29, 3231, 1984.

73. Z.-L. Liao and F.-C. Chang. Mechanical properties of the rubber-toughened polymer blends of polycarbonate (PC) and poly(ethylene terephthalate) (PET). *J. Appl. Polym. Sci.*, 52, 1115–1127, 1994.

74. J.-S. Wu and Y.-W. Mai. Effect of blending sequence on the impact strength of PET/PC blends. *Key Eng. Mater.*, 145–149, 787–792, 1998.

75. J.-S. Wu, P. Xue, and Y.-W. Mai. Effect of blending sequence on the morphology and impact toughness of poly(ethylene terephthalate)/polycarbonate blends. *Polym. Eng. Sci.*, 40, 786–797, 2000.

76. T.W. Cheng, H. Keskkula, and D.R. Paul. Property and morphology relationships for ternary blends of polycarbonate, brittle polymers and impact modifier. *Polymer*, 33, 1606–1619, 1992.

77. M.E. Fowler, H. Keskkula, and D.R. Paul. Synergistic toughening in rubber modified blends. *Polymer*, 28, 1703–1711, 1987.

78. Z. Wang, C.M. Chan, S.H. Zhu, and J. Shen. Compatibilization of polystyrene and low density polyethylene blends by a two-step crosslinking process. *Polymer*, 39, 6801–6806, 1998.
79. K. Friedrich. Microstructural efficiency and fracture toughness of short fiber/thermoplastic matrix composites. *Composite Sci. Technol.*, 22, 43–74, 1985.
80. J. Karger-Kocsis and K. Friedrich. Fracture behavior of injection molded short and long glass fiber polyamide 6,6 composites. *Composite Sci. Technol.*, 32, 293–325, 1988.
81. J. Lee and A.F. Yee. Fracture of glass bead/epoxy composites: on micro-mechanical deformations. *Polymer*, 41, 8363–8373, 2000.
82. J. Lee and A.F. Yee. Inorganic particle toughening II: toughening mechanisms of glass bead filled epoxies. *Polymer*, 42, 589–597, 2001.
83. S.S. Bafna, J.P. De Souza, T. Sun, and D.G. Baird. Mechanical properties of *in situ* composites based on partially miscible blends of glass filled polyetherimide and liquid crystalline polymers. *Polym. Eng. Sci.*, 33, 808–818, 1987.
84. J. He, H. Zhang, and Y. Wang. In-situ hybrid composites containing reinforcements at two orders of magnitude. *Polymer*, 38, 4279–4283, 1997.
85. J. He, H. Zhang, and Y. Wang. In-situ hybrid composites of thermoplastic poly(ether ether ketone), poly(ether sulphone) and polycarbonate. *Composite Sci. Technol.*, 60, 1919–1930, 2000.
86. L.A. Goettler. The effects of processing variables on the mechanical properties of reinforced thermoplastics, in *Mechanical Properties of Reinforced Plastics*, D.W. Clegg and A.A. Collyer, Eds. Elsevier Applied Science Publishers, London, 1986. p. 151.
87. R.J. Crowson, M.J. Folkes, and P.F. Bright. Rheology of short glass fiber reinforced thermoplastics and its application to injection moldings: Part 1. Fiber motion and viscosity measurement. *Polym. Eng. Sci.*, 20, 925–933, 1980.
88. J.P. Greene and J.O. Wilkes. Steady state and dynamic properties of concentrated fiber-filled thermoplastics. *Polym. Eng. Sci.*, 35, 1670–1681, 1995.
89. D. Dutta and R.A. Weiss. Rheological behavior of liquid crystalline polymer-polymer blends, in *Polymers as Rheology Modifiers*, D.N. Schulz and J.E. Glass, Eds. American Chemical Society, Washington, D.C., 1991, p. 145.
90. A. Seigmann, A. Dagan, and S. Kenig. Polyblends containing a liquid crystalline polymer. *Polymer*, 26, 1325–1330, 1985.
91. T.M. Malik, P.J. Carreau, and N. Chapleau. Characteristics of liquid crystalline polyester polycarbonate blends. *Polym. Eng. Sci.*, 29, 600, 1990.
92. K.G. Blizard and D.G. Baird. The morphology and rheology of polymer blends containing liquid crystalline copolyester. *Polym. Eng. Sci.*, 27, 653–662, 1987.
93. F.P. La Mantia, A. Valenza, M. Paci, and P.L. Maganini. Rheology-morphology relationships in nylon 6/liquid crystalline polymer blends. *Polym. Eng. Sci.*, 30, 7–12, 1990.
94. D. Berry, S. Kenig, and A. Seigmann. Structure development during flow of polyblends containing liquid crystalline polymers. *Polym. Eng. Sci.*, 31, 451–458, 1991.
95. H. Wang, K.W. Lee, and T.S. Chung. Rheological behavior and prediction for blending conditions of thermotropic liquid crystalline polyester with nylon. *Polym. Adv. Technol.*, 11, 153–158, 2000.
96. G. Costa, D. Meli, Y. Song, A. Turturro, B. Valenti, M. Castellano, and L. Falqui. Reactive blending of polyamide 6,6 and Vectra A. *Polymer*, 42, 8035–8042, 2001.

97. S.-C. Wong, S. Pisharath, and W.-G. Zheng. Fracture properties and microstructures of injection molded LCP hybrid composites. In preparation.
98. I. Campoy, M.A. Gomez, and C. Marco. Thermogravimetric analysis of blends based on nylon 6 and a thermotropic liquid crystal copolyester. *J. Thermal Anal.*, 52, 711–715, 1998.
99. S.C. Tjong, S.L. Liu, and R.K.Y. Li. Mechanical properties of injection molded blends of polypropylene with thermotropic liquid crystalline polymer. *J. Mater. Sci.*, 31, 479–484, 1996.
100. D. Berry, S. Kenig, and A. Seigmann. Structure and properties of molded polyblends containing liquid crystalline polymers. *Polym. Eng. Sci.*, 31, 459–466, 1991.
101. R.M. Laine, J. Choi, and R.O.R. Costa. Organic/inorganic nanocomposites with completely defined interfacial interactions from cubic silsesquioxanes. *Polym. Prepr. Div. Polym. Chem. Am. Chem. Soc.*, 41, 524–525, 2000.
102. R M. Laine, M. Asuncion, S. Baliat, N.L. Dias Filho, J. Harcup, A.C. Sutorik, L. Viculis, A.F. Yee, C. Zhang, and Q. Zhu. Organic/inorganic molecular hybrid materials from cubic silsesquioxanes. *Mater. Res. Soc. Symp. Proc.*, 576, 3–14, 1999.

13

Synthetic Biomedical Polymers for Tissue Engineering and Drug Delivery

Dhirendra S. Katti and Cato T. Laurencin

CONTENTS

13.1 Introduction

This chapter provides an overview of the chemical, physical, and biological aspects of three families of polymers: poly(α-hydroxyesters), poly(anhydrides), and polyphosphazenes. In addition, the latter part of the chapter will focus on the application of these polymers in tissue engineering and drug delivery systems. Although individual characteristics and applications of these polymers has been the subject of a number of reviews, original articles, and patents, this chapter provides an integrated broad coverage of the same.

13.1.1   Polymers as Biomaterials

Biomaterials can be broadly defined as natural or synthetic materials that are biocompatible and/or biodegradable and can be used for biological applications without leading to any undesired side effects. Among the large variety of materials available for biological applications, polymeric materials have received great attention in the past few decades.[1] This may be attributed to the fact that properties of polymeric materials can be manipulated to fit desired needs, thereby making them favorable candidates for most biological applications.

Polymers are available from both synthetic and natural origins. Natural polymers intuitively seem to be a better choice for biological applications; however, they may not be the best choice for property manipulation and could face the problem of limited availability. Further, with the growing awareness for the conservation of natural resources, natural polymers may not be a prudent choice for the future. Therefore, synthetic polymers, which may be obtained by the calculated manipulation of chemical reagents, have received a lot of attention in the recent past for a wide variety of applications, ranging from engineering plastics for aerospace application to artificial valves for the human heart. The major advantage that synthetic polymers possess over most other materials is that their physical, chemical, and in some cases biological properties can be tailored for a desired end use. This, along with many other factors, has made the synthetic polymer a very attractive class of materials.

13.1.2   Biomedical Applications of Synthetic Polymers

Some of the impressive and more recent applications of synthetic polymers have been in the area of biomedical sciences.[2] To be used in biomedical applications, these polymers need to possess certain properties such as biocompatibility and biodegradability. Biocompatibility of a polymer implies that it will not elicit any adverse response once inside the body.[2] Biodegradability of a polymer implies that the polymer degrades in an *in vivo* environment and that the degradation products are metabolizable by the body. Most biomedical applications would require either one or both of these properties. Some of the prominent biomedical applications that have needed both of these properties are the areas of drug delivery and, more recently, tissue engineering.[3,4] The development of controlled drug delivery systems has been the goal of researchers for the past two to three decades. The advances in the area of drug delivery have led to an increase in the development of synthetic polymers suitable for biomedical applications. Recently, these polymers have been used for tissue engineering purposes. The development of these biomaterials and their ability to be tailored to particular end uses have led to their use in the area of tissue engineering. Drug delivery and tissue engineering are two areas where there has been an extensive usage of biomaterials. The application of synthetic polymers to the areas of drug delivery and tissue engineering shall be discussed at greater lengths in Sections 13.4 and 13.5.

13.2 Synthetic Polymers for Biomedical Applications

Synthetic polymers have now come to form a major class of biomaterials being used for a variety of biomedical applications. Of these, three families,

namely, poly(α-hydroxyesters), poly(anhydrides), and poly(phosphazenes), have received greater attention and will be discussed further in this chapter.

13.2.1 Poly(α-hydroxyesters)

Poly(hydroxyacid) polymers derived from α-hydroxyacids are degraded more easily than those polymers of β-, γ-, δ-, and ε-hydroxy analogues.[5] Therefore, poly(α-hydroxyesters) are one of the most widely used classes of biodegradable polymers in medicine. The polymers of lactic and glycolic acid and their copolymers are perhaps the most popular polymers of this class. Since their introduction as sutures (poly(glycolic acid)),[6,7] these polymers have been used in humans for almost three decades and have been approved by the Food and Drug Administration for use in humans for many applications.[8] The advantage of these polymers is that the copolymer ratios and molecular weight of the polymer can be tailored to obtain materials with desired crystallinity, solubility, rates of degradation, and hydrophobicity. The biocompatibility, biodegradability, and ability to tailor properties for desired end uses have made these polymers a very popular choice of the medical researcher. The homopolymers of lactic acid, glycolic acid, and their copolymers will be further discussed in the following sections.

13.2.1.1 Glycolic Acid

Glycolic acid (GA), chemically known as hydroxyacetic acid or 2-hydroxyethanoic acid (structure shown in Figure 13.1), is usually prepared by the hydrolysis of molten monochloroacetic acid with 50% aqueous sodium hydroxide at 90 to 130°C.[9] For the lack of chiral centers (Figure 13.1), both glycolic acid and its cyclic ester glycolide (Figure 13.2) are optically inactive. In the U.S., glycolic acid is commercially produced (Du Pont) by treating formaldehyde or trioxymethylene with carbon monoxide and water in the presence of an acid catalyst at > 30 Mpa pressure.[10] Glycolic acid is available commercially as either a 57% (Hoechst) or a 70% (Du Pont) aqueous solution. The total annual consumption worldwide is approximately 2000 to 3000 tonnes of solution.[11]

13.2.1.2 Polymers of Glycolic Acid (Poly(glycolic acid))

Polymers of α-hydroxyacids (glycolic acid and lactic acid) may be synthesized by polycondensation reactions directly from their respective α-hydroxyacid monomers. However, polycondensation is a high-temperature reaction accompanied by side reactions that can result in low molecular weight, impurities, and discolored products.[12] The low molecular weight and impurities could cause the polymer to have undesired properties that in turn can lead to an undesired biological response when used as a biomaterial. Hence, polycondensation may not be a favorable method for the synthesis of polymers of glycolic acid and lactic acid. Alternatively, ring-opening poly-
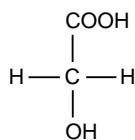
FIGURE 13.1
Structure of glycolic acid.

Glycolic Acid Monomer   Polyglycolic Acid (PGA)   Glycolide
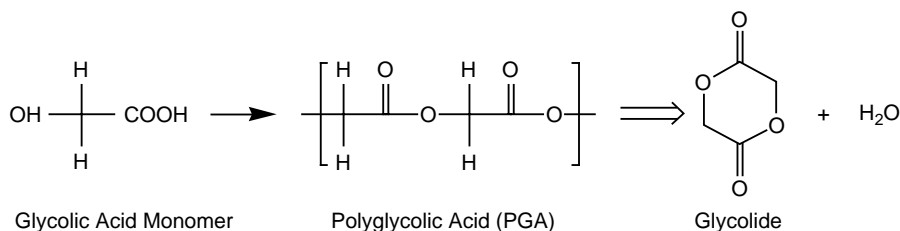
FIGURE 13.2
Formation of poly(glycolic acid) and glycolide from glycolic acid monomer.

merization of the corresponding cyclic diester, glycolide, or lactide is favored for biomedical polymer synthesis.

Glycolic acid udergoes thermal degradation to form a low-molecular-weight polymer. This low-molecular-weight polymer can be pyrolized to form glycolide (1,4 dioxan-2,5 dione), as shown in Figure 13.2. The glycolide can easily be polymerized by ring-opening melt polymerization using a tin catalyst to form a semicrystalline polymer of glycolic acid. Poly(glycolic acid) (PGA) can also be synthesized by ring-opening polymerization using initiators such as protonic and Lewis acids, amines and phosphines, hydrides, alkoxides, alkyl derivatives of alkali and alkaline earth metals, and hydrogen-donor substances such as carboxylic acids, alcohols, glycols, and alkanolamines.[13]

Poly(glycolic acid) is insoluble in most common solvents, has a melting point of 224 to 226°C, and has a glass transition temperature of 36°C.[14] Melt-extruded fibers can be obtained using poly(glycolic acid) with molecular weights ranging from 20,000 to 145,000.[14]

13.2.1.3   Lactic Acid

Lactic acid (LA), 2-hydroxypropionic acid, was discovered in 1780 by the Swedish chemist Scheele; he isolated it from sour milk as an impure brownish syrup.[15] Substituting methyl groups in glycolic acid and its cyclic dimer creates chiral centers in the corresponding products, lactic acid and lactide, respectively. Molecules containing a chiral carbon can polarize light. Enantiomers rotate the plane of polarized light to an equal extent but in opposite directions. The symbols + and – are used to denote rotation to the right or left, respectively. Lactic acid is found in two nonequivalent optical isomers,

```
            COOH                        COOH
              |                            |
   H —— C —— OH            OH —— C —— H
              |                            |
            CH₃                         CH₃

Structure 1: D(–) Lactic Acid      Structure 2: L(+) Lactic Acid
```
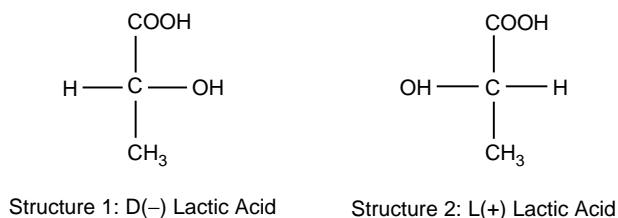
FIGURE 13.3
Enantiomers of lactic acid. Structure 1: D(–) lactic acid. Structure 2: L(+) lactic acid.

D(–) lactic acid and L(+) lactic acid, and as a racemate (DL), one being the enantiomer (mirror image) of the other (Figure 13.3). Both enantionmers of lactic acid have the same chemical properties, but they differ in their physical and, more importantly, physiological properties.

Lactic acid is synthesized by the lactic acid fermentation of carbohydrates such as glucose, sucrose, and lactose with *Bacillus acidi lacti* or related organisms such as *Lactobacillus delbrueckii*, *L. bugaricus*, etc.[16] Lactic acid can also be obtained as a biomass intermediate from acetaldehyde or the fermentation of hexose polymers, such as cellulose or starch. Commercially, lactic acid produced using the fermentation technique is accomplished by the fermentation of whey, cornstarch, potatoes, or molasses.[16] Lactic acid produced by fermentation is optically active, and the specific production of the L(+) and D(–) forms of lactic acid can be determined by using the appropriate lactobacillus. Synthetically produced lactic acid is optically inactive, i.e., a racemic mixture.

Dimerization of L(+)-LA or D(–)-LA to six-membered lactide rings produces a unique change. It causes the L-lactide to rotate polarized light to the left (–) and the D-lactide to the right (+). Both L(–)-lactide and D(+)-lactide have their methyl groups on the same side of the plane of the six-membered ring. However, the side of the plane having the methyl groups differs in each (Figure 13.4). The dimerization of L(+)-LA and D(–)-LA together results in the formation of the optically inactive meso-lactide along with the formation of L(–)-lactide and D(+)-lactide (due to the possibility of L(+)-LA reacting with itself and D(–)-LA reacting with itself). The properties (physical and chemical) of each of these lactides are different, thereby indicating that these precursor monomers when polymerized will produce polymers having disparate properties. Selective synthesis protocols are highly relevant to yielding a predictable polymer.

13.2.1.4   Polymers of Lactic Acid (Poly(lactic acid))

Poly(lactic acid) (PLA) is a semicrystalline, thermoplastic poly(ester) formed by the homopolymerization of lactic acid. The polymerization of lactic acid can be achieved by using different techniques. Low-molecular-weight poly(lactic acid) (< 3000) can be synthesized by direct polycondensation of lactic acid using acid catalysts (phosphoric acid, p-toluene sulfonic acid, and
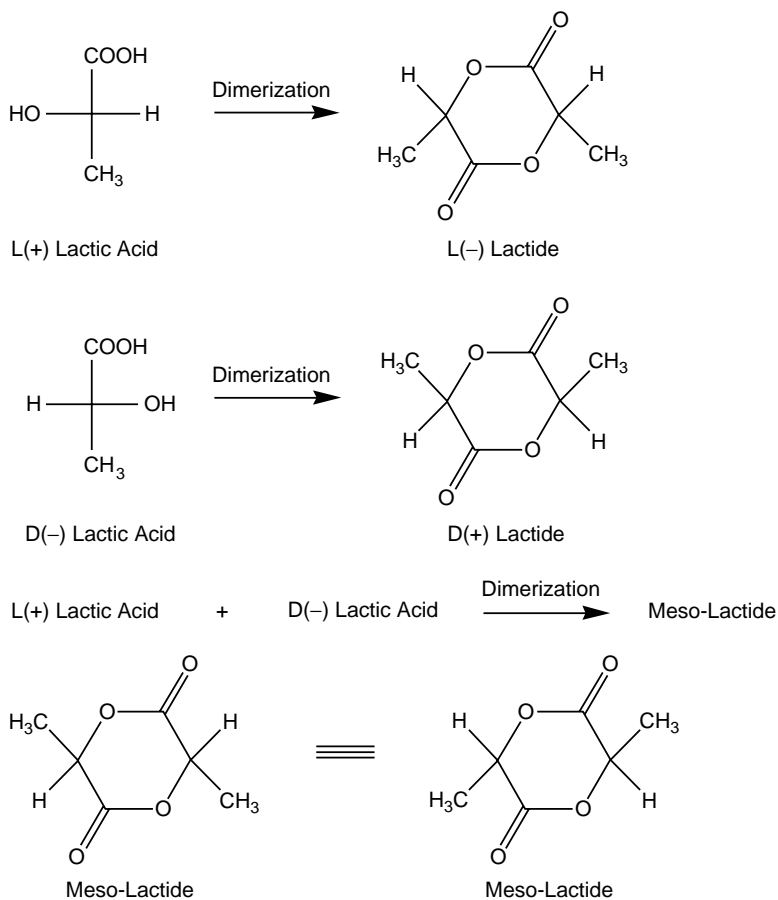
FIGURE 13.4
Dimerization of L(+) and D(−) forms of lactic acid.

antimony trifloride).[17] High-molecular-weight polymers can be synthesized by ring-opening polymerization of lactide (cyclic diester of lactic acid) at 140 to 180°C for 2 to 10 h using a catalyst (stannous-ocatate).[18] Lactide (2,5 dimethyl-1,4 dioxan-3,6 dione) can be synthesized by the internal esterification of lactic acid, as shown in Figure 13.5. The term *lactone* denotes internal mono-, di-, or higher esters of hydroxy carboxylic acids. Cyclic diesters of hydroxyacetic acids are often described generally as glycolides, or in older literature as lactides. Although a few lactones and cyclic esters apparently polymerize spontaneously on standing or when heated, most do so only under the influence of initiators. Lactide in its racemic, meso, and optically active forms undergoes polymerization in the presence of alkylaluminium, -magnesium, and -zinc initiators and with tin (II) and tin (III) compounds.[19] L-lactic acid (enantiomer) occurs naturally in the human body and is also the only degradation product after hydrolysis of the polymer. Since the L(+)
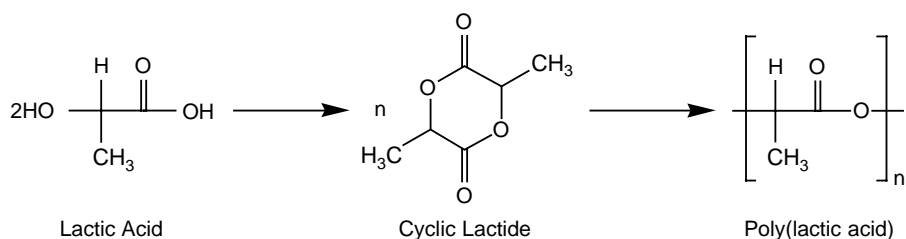
FIGURE 13.5
Conversion of lactic acid to poly(lactic acid) through the formation of lactide.

form of lactic acid is metabolized by the human body, poly(L-lactic acid) (PLLA) is used more commonly than poly(D-lactic acid) (PDLA).

Poly(L-lactic acid) has a glass transition temperature of 55 to 60°C and a melting temerature of 170 to 178°C for a molecular weight of the polymer ranging from 50,000 to 300,000, respectively. Polymers of lactic acid can be synthesized in a broad range of molecular weights depending on the end use sought. For example, lower-molecular-weight polymers in the range of 2000 to 100,000 are used for microparticle fabrication for drug delivery systems; polymers in the range of 180,000 to 250,000 are good for melt spinning of fibers; and higher-molecular-weight polymers in the range of 250,000 to 530,000 are suitable for solution-spun fibers.

13.2.1.5 Copolymers of Lactic Acid and Glycolic Acid (Poly(lactide-co-glycolide))

Copolymers of lactic acid and glycolic acid can be synthesized by melt polymerization of a mixture of the cyclic glycolide and lactide in the presence of catalysts such as Lewis acids or metal salts (as shwon schematically in Figure 13.6).[20]

The ratio of the monomers (lactic acid:glycolic acid or lactide:glycolide) during the polymerization determines the properties of the copolymer, i.e., poly(lactide-co-glycolide) (PLAGA). For example, the crystallinity of PLAGA polymers depends on the molar ratio of the two monomers. PLAGA copolymers with less than 70% of the glycolide component are almost completely amorphous. Although PLAGA is synthesized as a random copolymer, differences of monomer substitution along the PLAGA polymer has resulted in copolymers with similer overall compositions but dissimilar mechanical properties. As the sterically hindered PLA is more slowly degraded than PGA, it is obvious that the degradation rates of the copolymer of lactic acid and glycolic acid, namely, PLAGA, would be determined by the relative proportions of the GA and LA components, respectively. Therefore, a 70:30 poly(lactide-co-glycolide) denotes a 7:3 molar ratio of latide to glycolide comprising the copolymer. However, 70:30 PLAGA may contain various combinations of optically active PLA or the racemate, thereby meaning that
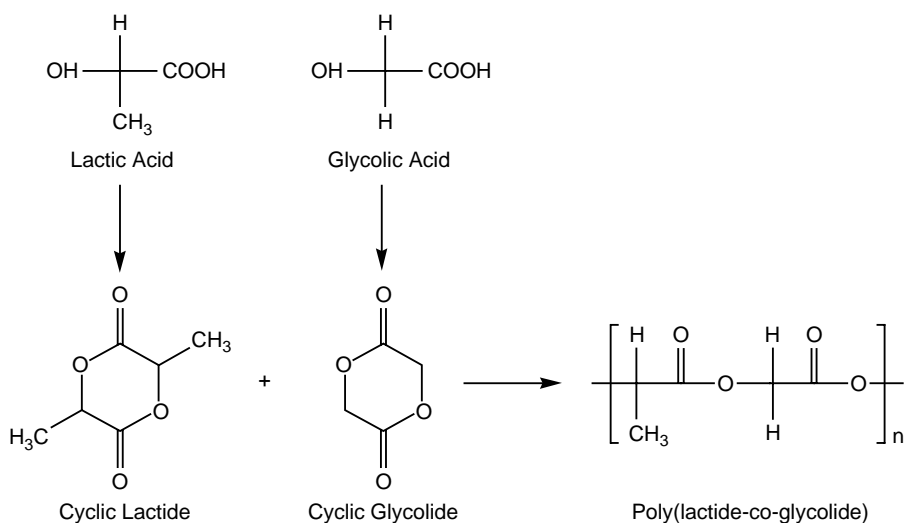
FIGURE 13.6
Copolymerization of lactic acid and glycolic acid to form poly(lactide-*co*-glycolide).

one could synthesize 70:30 poly(D,L-lactide-*co*-glycolide), 70:30 poly(D-lactide-*co*-glycolide), or 70:30 poly(L-lactide-*co*-glycolide). Thus, synthesizing homopolymers and copolymers with desired properties and identifying them correctly via proper characterization are of great importance for these materials to be used successfully in biomedical applications.

13.2.2   Poly(anhydrides)

The rapid growth in the area of controlled drug delivery systems in the past two decades has been driven by the need to deliver biologically active molecules efficiently to a desired site and at a desired rate. The developments in the area of drug delivery in turn have led to the development of a large variety of biodegradable polymers. Biodegradable polymers enable researchers to fabricate vehicles for drug delivery that eliminate the need for subsequent removal from the implant site. A large number of biodegradable polymers have been synthesized and applied for the purpose of drug delivery, including poly(esters), poly(aliphatic esters), poly(orthoesters), poly(phosphazenes), poly(amino acids), poly(anhydride-*co*-imides), and poly(saccharides). Some of these polymers will be discussed at length in this chapter.

The synthesis of poly(anhydrides) can be traced to a report in 1909 by Bucher and Slade.[21] They synthesized the polymer by heating isophthalic acid or terephthalic acid in acid anhydrides. In the early 1930s, Hill and Carothers developed and synthesized poly(anhydrides) from aliphatic dicarboxylic acids for applications in the textile industry.[22,23] However, it was found that these polymers were hydrolytically unstable and degraded at room temperature,

thereby making them unsuitable for textiles. Further, they showed that when heated to high temperatures, these polymers were unstable and formed cyclic dimers and polymer rings. Later, Conix and Yoda, in the 1950s and 1960s, synthesized poly(anhydrides) that were polymers and copolymers containing aromatic, aliphatic, and hetrocyclic diacid monomers.[24–26] It was not until the 1980s and 1990s when researchers at the Massachusetts Institute of Technology proposed the use of poly(anhydrides) in biomedical applications, especially in drug delivery systems.[27–29] These polymers were originally found to be unsuitable for textiles for their hydrolytic unstability. This inherent instability was found to be useful for the development of drug delivery work.

13.2.2.1   Synthesis of Poly(anhydrides)

In the past, there have been a number of ways reported for the synthesis of poly(anhydrides), namely, melt polycondensation, dechlorination, ring-opening polymerization, solution polymerization, and interfacial polymerization.[22,30–32] These polymers have been synthesized using a wide variety of aromatic and heterocyclic moities. Similarly, a large variety of copolymers have been synthesized using aliphatic and aromatic diacid monomers.

13.2.2.1.1   Melt Condensation

The melt condensation technique involves the reaction of aliphatic and aromatic dicarboxylic acid monomers with excess anhydride to form an acetyl anhydride prepolymer, which can then be polymerized at higher temperatures under vacuum to obtain the anhydride polymer. The melt condensation process commences readily under low pressure and is completed in a few hours (as shown schematically in Figure 13.7).

The molecular weight of the polymer can be increased by purification of the prepolymer via crystallization. It is important to monitor the prepolymer reaction carefully to prevent the formation of high oligomers, which are high melting and difficult to purify.

The optimal reaction time at high reaction temperatures is several hours. However, excessive heating may cause decarboxylation or decarbonylation.[30] As the polymerization reaction is weekly exothermic, the equilibrium constants for the reaction decrease with temperature, thereby meaning that a higher-molecular-weight polymer could be obtained at lower polymerization temperatures.

In an attempt to increase the molecular weight of poly(anhydrides) and to arrive at a better reaction condition, Domb and Langer proposed the use of coordination catalysts to enhance the nucleophilicity of the carbonyl carbon and to facilitate the anhydride interchange in the polymerization.[33] The use of catalysts such as cadmium acetate, alkaline earth metal oxides, and zinc etherate resulted in shorter reaction times and higher-molecular-weight polymers. However, the polymerization reactions were inhibited by iron, titanium, and basic catalysts (4-dimethylaminopyridine), and acid catalysts did not seem to have any effect on the polymerization reaction.

FIGURE 13.7
Synthesis of poly(anhydrides) by melt condensation.

To improve the solubility and thermal processing characteristics of poly(anhydrides), Anastasiou et al. have synthesized via melt condensation a family of aromatic poly(anhydrides) based on ortho-, meta-, and para-substituted xylenes as derived from o- and p-hydroxybenzoic acids to replace the alkyl chain (sebacic acid (SA)) of previously reported poly(anhydrides).[34]

13.2.2.1.2 Solution Polymerization

For heat-sensitive polymers that would be difficult to synthesize by melt polymerization, it is desirable to have milder reaction conditions. Solution polymerization schemes were therefore proposed to obtain poly(anhydrides) that were heat sensitive. The dehydrochorination reaction between a diacid chloride and a dicarboxylic acid at room temperature leads to the formation of poly(anhydride), as shown in Figure 13.8.

Polymerization was then proposed in a combination of organic solvents such as pyridine–benzene and pyridine–ether with the intention of synthesizing copoly(anhydrides) of regular structure. For example, to a solution of terephthalic acid in pyridine, a solution of adipic acid chloride in ether when added dropwise results in the formation of poly(anhydride). Similarly, polymerizations conducted in single solvents such as chloroform, ethyl ether,
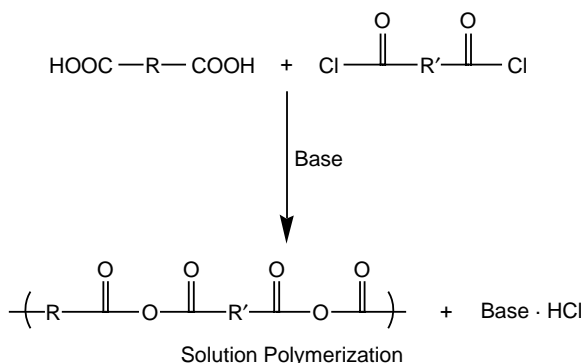
FIGURE 13.8
Synthesis of poly(anhydrides) by solution polymerization.

dichloromethane (DCM), and benzene in the presence of an acid acceptor gave good results in terms of molecular weights and yields.

13.2.2.1.3 Interfacial Polymerization

The success of synthesizing other polymers (polyamides, poly(esters), and polycarbonates) using the interfacial polymerization technique led to the testing of this method for the synthesis of poly(anhydrides). Using sebacic acid as the model monomer, the feasibility of this method was confirmed.[30] The problem of decomposition can be alleviated by avoiding the use of water. In a nonaqueous system, the anhydride polymer was obtained in close to quantitative yields and the number average molecular weight range was 4000 to 5000. However, the choice of organic solvents that are immisible is very limited. Dimethylformamide (DMF) with 1,4-dicynobutane and DMF with hexane are some of the best-suited solvent systems studied for this reaction.

13.2.2.2 Types of Poly(anhydrides)

1. **Unsaturated poly(anhydrides):** These polymers have been synthesized mainly using unsaturated monomers like fumaric acid, acetylene-dicarboxylic acid, and 4,4'stilbenedicarboxylic acid. These poly(anhydrides) could be either homopolymers of the unsaturated monomers or copolymers of the unsaturated monomer and sebacic acid. The homopolymers have been shown to be crystalline and insoluble in common organic solvents; however, the copolymers have been shown to be less crystalline and soluble in chlorinated organic solvents.

2. **Amino acid-based poly(anhydrides):** These poly(anhydrides) have been synthesized by the amidation of the amino group of an amino acid with a cyclic anhydride, or by the amide coupling of two amino

acids with a diacidchloride. Staubli et al. reported the use of trimel-lido–amino acid as a monomer to synthesize both homo- and copol-ymers.[35] These polymers, by virtue of their functionality, came to be know as poly(anhydride-*co*-imides). Poly(anhydride-*co*-imides) are erodible polymers and form a large subgroup in the family of poly(anhydrides). These polymers will be discussed seperately later in this section.

3. **Aliphatic-aromatic homopoly(anhydrides):** These are polymers synthesized from diacid monomers containing aliphatic and aro-matic moities.

4. **Soluble aromatic poly(anhydrides):** Homopoly(anhydrides) syn-thesized from monomers containing aromatic moities are generally insoluble in organic solvents and have a high melting point. There-fore, the synthesis of soluble aromatic poly(anhydrides), by virtue of their solubility, enabled researchers to fabricate drug delivery systems such as microspheres, films, etc., using these polymers.

5. **Poly(ester-anhydrides):** These polymers were synthesized using 4,4'dialkaline- and oxaalkanedioxydibenzoic acids.

6. **Fatty acid-based poly(anhydrides):** Poly(anhydrides) were synthe-sized from dimers and trimers of unsaturated fatty acids. Oleic and erucic acid dimers containing two carboxylic acids were synthesized using the technique of radical coupling via double bonds. The com-position of fatty acid-based poly(anhydrides) could be changed eas-ily by altering the fatty acid used, thereby making it possible to tailor them for specific end uses. For example, incorporation of long-chain fatty acids such as stearic acid altered hydrophobicity and decreased degradation rates.

7. **Modified poly(anhydrides):** Poly(anhydrides) were modified for their physical and mechanical properties by either blending, branching, or cross-linking the polymer or partial hydrogenation. Domb et al. reported the blending of poly(anhydrides) with poly(esters) — poly(lactic acid), poly(caprolactone), and poly(hydroxybutyrate).[36] Branching or cross-linking of poly(anhy-drides) was accomplished by reacting the diacid monomer with tri- or poly(carboxylic acid)-branching monomers, and the reaction was allowed until gel formation.

13.2.2.3 Poly(anhydride-co-imides)

Poly(anhydrides) have been the basis for the development of poly(anhydride-*co*-imide). Poly(anhydrides) are biocompatible, have well-defined degradation characteristics, and have been successfully utilized clinically as drug delivery systems. However, in spite of their desirable properties, they have limited mechanical properties that restrict their use in load-bearing applications. For example, the Young's modulus of the homopolymer of the carboxyphenoxy-

hexane (CPH) monomer was reported as 1.3 MPa; that is well below the modulus of human bone (40 to 60 MPa).[37,38] It was then proposed by Uhrich et al. that the mechanical strength of these biodegradable polymers can be increased by the incorporation of rigid units, such as imides in the backbone of the poly(anhydrides).[39] This idea was supported and strengthened by a study in which several polyimides were shown to be biocompatible.[40] Poly(anhydride-co-imides) were reported initially by Abajo et al.[41a] and Gonzalez et al.[41b] in 1971 and were shown to have high thermal stability (thermally unstable above 350°C).[41] However, these polymers suffered from the drawback of needing strong polar solvents (dimethylformamide and m-cresol) for dissolution.

13.2.2.3.1 Synthesis of Poly(anhydride-co-imides)

The poly(anhydride-co-imide) synthesis involves a technique that is similar to the melt condensation technique. Briefly, the synthesis involves the reaction of an amino acid with an anhydride monomer to give a diacid. The diacid is then activated with acetic anhydride to get the imide–anhydride monomer. The imide–anhydride monomer is then polymerized by melt condensation to arrive at the final poly(anhydride-co-imides). A typical example of the poly(anhydride-co-imide) synthesis is the polymerization of poly(pyromellitylimidoalanine-co-bis(carboxyphenoxy)hexane) (PMA-ala:CPH) (Figure 13.9).[39]

As shown in Figure 13.9, the process involves the reaction of pyromellitic anhydride with alanine refluxed in a mixture of m-cresol and dimethylformamide to give the diacid. The diacid is then reacted with excess of acetic anhydride to give the imide-anhydride monomer, which is then reacted with acetylated CPM to get the final polymer (PMA-ala:CPH).

13.2.3   Poly(phosphazenes)

In most biomedical applications, organic polymers are most commonly the polymers of choice; however, one type of inorganic polymer that shows promise is a relatively new class of polymers called poly(phosphazenes). Poly(phosphazenes) are generally high-molecular-weight polymers with an inorganic backbone consisting of alternating phosphorus and nitrogen atoms.

13.2.3.1   Synthesis of Poly(phosphazenes)

In the late 1800s, Stokes initially reported the polymerization of the cyclic trimer {(NPCl$_2$)$_3$} to form poly(phosphazenes).[42,43] However, these polymers that were then referred to as inorganic rubber were found to be insoluble in most common solvents and hydrolytically unstable.[44-46] It was not until recently that Allcock and coworkers reported the first soluble form of poly(dichlorophosphazene). They accomplished this task by using a highly purified trimer {(NPCl$_2$)$_3$} and by excluding moisture and controlling the
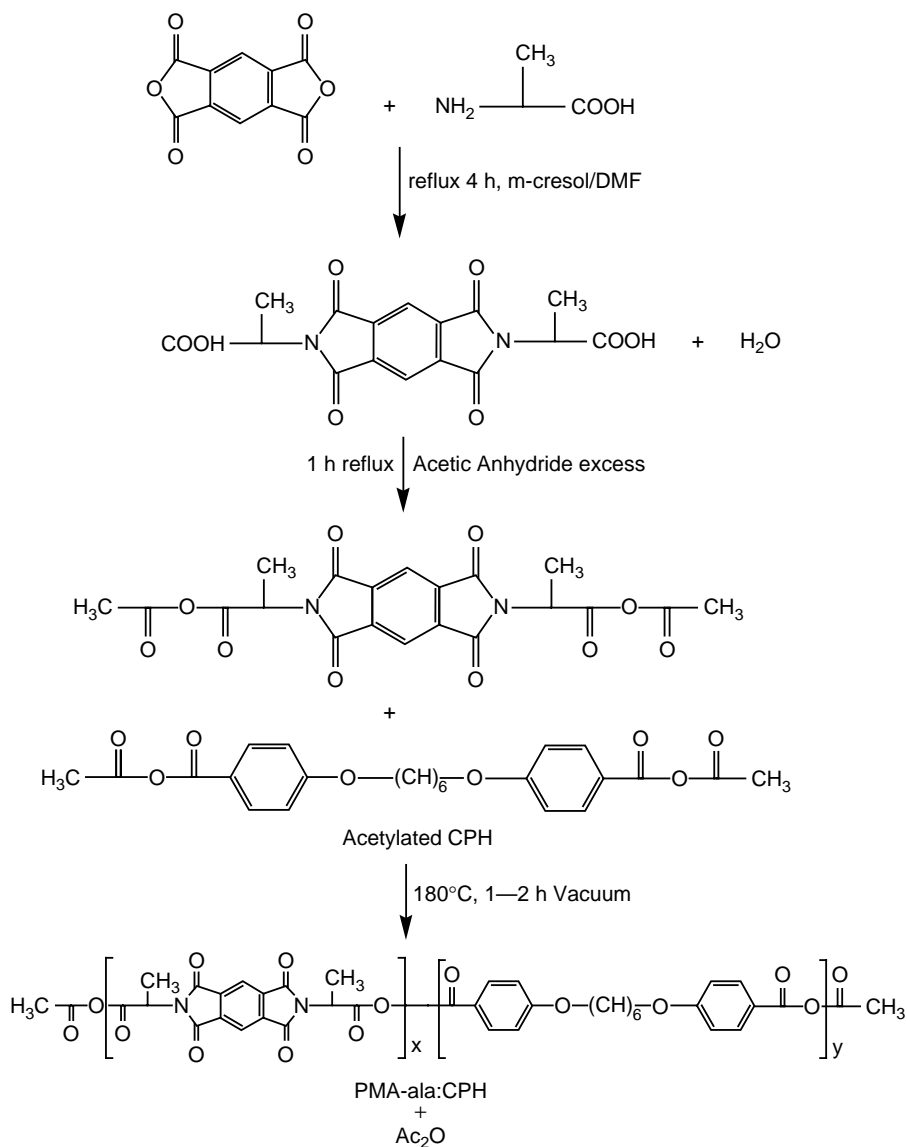
FIGURE 13.9
Synthesis of poly(anhydride-*co*-imide) (poly(pyromellitylimidoalanine-*co*-bis(carboxyphen-oxy)hexane) (PMA-ala:CPH)).

time and temperature of polymerization. This discovery by Allcock and coworkers has led to a renewed interest in poly(phosphazenes).[47–49]

Although there now exists more than one way to synthesize poly(phosphazenes), the largely preferred method is based on the thermal ring-opening polymerization of the cyclic trimer, hexachlorocyclotriphosphazene (NPCl$_2$)$_3$.
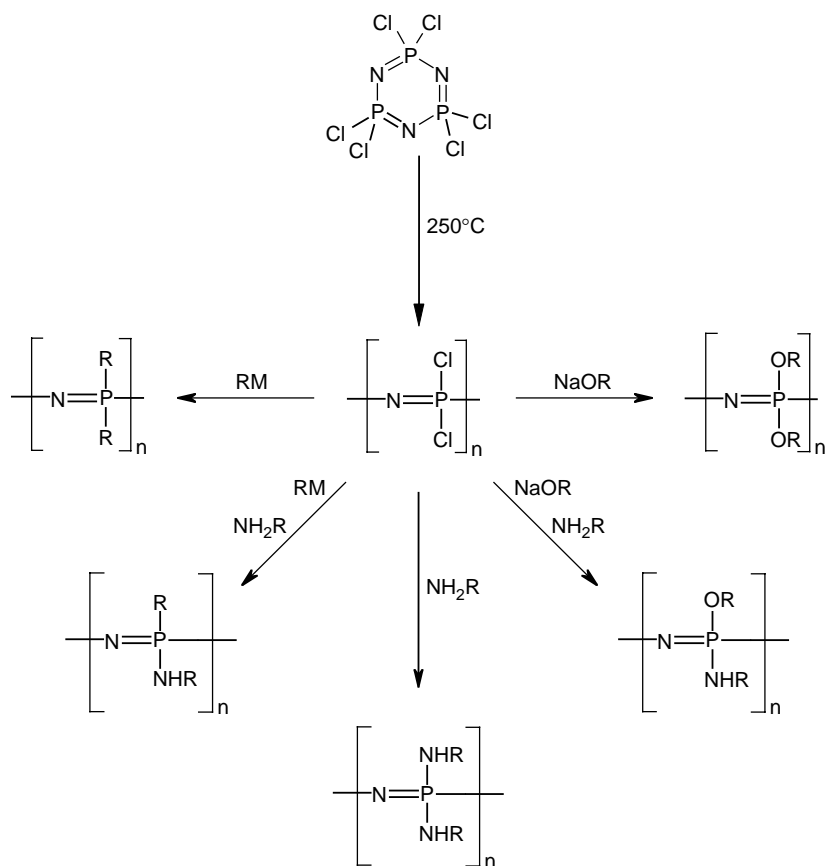
FIGURE 13.10
Synthesis of poly(phosphazene).

The synthesis involves the ring-opening polymerization of $(NPCl_2)_3$ at 250°C to give the poly(dichlorophosphazene) $(NPCl_2)_n$. This reaction takes place as shown in Figure 13.10.[50–52]

The mechanism of the reaction involves the ionization of the cyclic trimer hexachlorocyclotriphosphazene (P-Cl bond) to yield a cationic trimer that then reacts with a lone pair of electrons from another cyclic trimer. This mechanism is supported by a study reported by Allcock and Best wherein they showed that the ionic conductivity of the molten $(NPCl_2)_3$ significantly increases as the temperature approaches 250°C (polymerization tempera- ture), thereby confirming the ionic nature of this reaction. Additionally, Allcock and Best did not detect any free radicals in the molten trimer, indi- cating that the mechanism of polymerization was not via free radical poly- merization.[53,54] This reaction initially leads to the opening of the ring of one of the cyclic trimers and its attachment to the ionized phosphorus of the other cyclic trimer. This simultaneously causes the ionization of the terminal
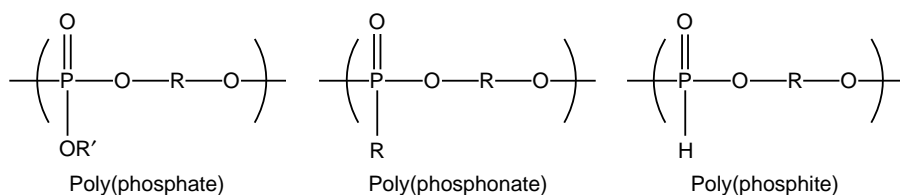
FIGURE 13.11
Structure of poly(phosphoesters), poly(phosphates) (P-O-C), poly(phosphonates) (P-C), and poly(phosphites) (P-H).

P-Cl bond of the opened trimer. The ionized bond of the opened trimer then initiates a similar reaction with another cyclic trimer molecule. This reaction then propogates in a similar fashion until a high-molecular-weight polymer is formed, as shown in Figure 13.10.

The availability of the labile P-Cl bond in the poly(dichlorophosphazenes) makes it easy to conduct a nucleophilic substitution reaction. The linear un-cross-linked poly(dichlorophosphazene) readily dissolves in organic solvents and can react with molecules having groups such as alkoxy, aryloxy, amino, and alkyl to form either a mono- or di-substituted poly(organophosphazene). A combination of two of these side groups in varying ratios may also be incorporated into the polymer backbone to generate specific properties. This ablility to vary the substituted side group enables the synthetic polymer chemist to design or tailor poly(phosphazenes) having specific properties. It is this flexibility that has allowed for the use of these polymers in a range of applications, from inert biomaterials for dental applications to polymers for drug delivery and tissue engineering.

13.2.3.2   Poly(phosphoesters)

Poly(phosphoesters), as the name suggests, are polymers having a phosphorus atom and an ester group in the backbone of the polymer chain. The initial interest in these phosphorus-containing polymers was because of their flame retardation property. But, because of their hydrolytic instablility and relatively higher cost of manufacture, there had not been extensive research done on this class of polymers. However, the recent discovery of their potential in biomedical application has instigated researchers to restudy this class of polymers in further depth.

These polymers can be broadly classified into three main types, depending on the side chain attached to the phosphorus: poly(phosphites) (P-H), poly(phosphonates) (P-C), and poly(phosphates) (P-O-C). General structures of these three classes are shown in Figure 13.11.

13.2.3.2.1   Poly(phosphates)

One of the most popular methods of synthesizing poly(phosphates) is by reacting a phosphorodichloridate with a diol to undergo dehydrochlorina-
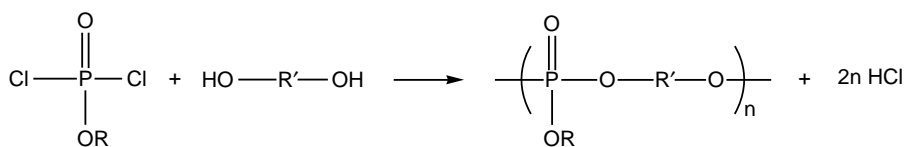
FIGURE 13.12
Synthesis of poly(phosphates).
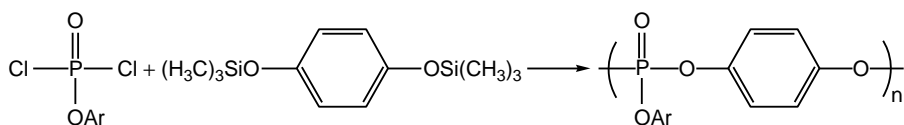
Poly(phosphate) synthesis using Friedel-Crafts reaction
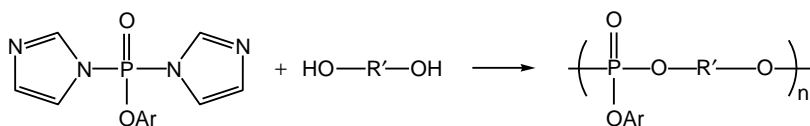
Poly(phosphate) synthesis using polycondensation reaction

FIGURE 13.13
Other methods of poly(phosphate) synthesis.

tion and yield the polymer.[55,56] The reaction is as shown in Figure 13.12. This reaction can be carried out either in bulk, solution, or interfacially.

There are two other methods that have been reported for the synthesis of poly(phosphates): a Friedel–Crafts reaction and a polycondensation reaction. The Friedel–Crafts reaction involves the reaction of aromatic hydrocarbons with bischloromethyl compounds, as shown in Figure 13.13.[57] The second method involves a condensation between aromatic diols and phosphorus diimidazolides under a nitrogen atmosphere.[58] The bulk condensation process avoids the need for solvents and additives, thereby making it easy to purify the final product.

13.2.3.2.2 Poly(phosphites)

Poly(phosphites) have been most commonly prepared by a method reported by Pretula and Penczek that involves a condensation reacting between a dimethylphosphite and a glycol, followed by removal of the methoxyphosphonyl end groups in the oligomers using higher temperatures.[59] The generic reaction is as shown in Figure 13.14.

Penczek and coworkers have also synthesized poly(phosphites) by ringopening polymerization of five- and six-membered cyclic phosphates (Figure 13.15).[60,61]
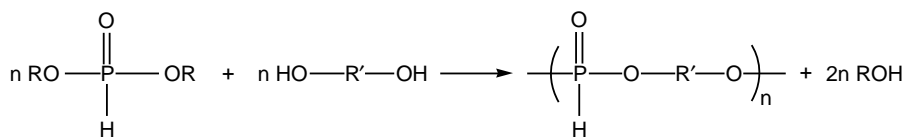
FIGURE 13.14
Synthesis of poly(phosphites) by a two-step condensation process.
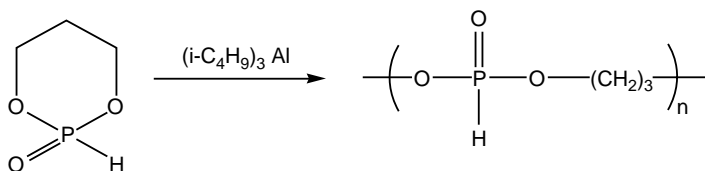
FIGURE 13.15
Synthesis of poly(phosphites) by ring-opening polymerization.

13.2.3.2.3 Poly(phosphonates)

Most poly(phosphonates) are obtained by a condensation reaction between dichlorides and diols, as shown in Figure 13.16.[62,63] Another common method used for poly(phosphonates) synthesis is transesterification of phosphonates with diols.[64]

Other methods of synthesis that have been reported include the condensation of bis(β-chloroethyl)phosphonates and the condensation of dimethylphosphonates with dihalides.[65]
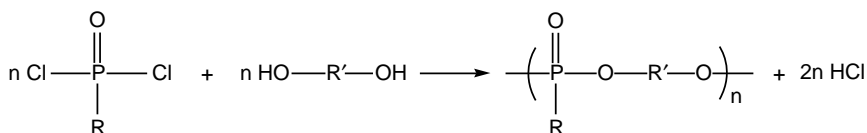
Synthesis of poly(phosphonates) by condensation process
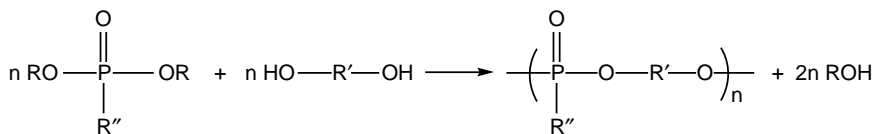
Synthesis of poly(phosphonates) by transesterification

FIGURE 13.16
Synthesis of poly(phosphonates).

13.3 Polymer Properties and Their Modifications for Biomedical Applications

13.3.1 Poly(esters)

13.3.1.1 Degradation

Degradation of polymers can involve different processes such as physical degradation, degradation controlled by biological mechanisms, and chemically controlled degradation. Physical degradation involves the physical loss of the polymer, although the total quantity and composition may still be the same. Degradation due to biological processes is relatively more complex and difficult to control because of the complex mechanisms involved. However, in chemical-controlled degradation the rate of degradation is predictable and controllable and is generally the preferred choice for degrading biomaterials. Biodegradable polymers such as poly(esters) and poly(anhydrides) degrade by hydrolytic cleavage of chemical bonds in the backbone of the polymer, resulting in water-soluble degradation products.

The poly(α-hydroxyesters), including PLA, PGA, and PLAGA, degrade primarily through hydrolysis. PLA, for example, degrades by nonspecific hydrolytic scission to form lactic acid that undergoes dehydrogenation to pyruvate and then to acetyl coenzyme A for incorporation into the citric acid cycle.[66,67] Similarly, poly(glycolic acid) degrades to its monomer glycolic acid that can be excreted in the urine or can undergo further enzymatic reactions with glycolate oxidase and glycine transaminase to form serine, which ultimately can be transformed to pyruvate for use in the citric acid cycle.[67–69] The copolymers of lactic acid and glycolic acid also undergo degradation in a similar fashion to form the respective monomers that form pyruvates by the above-mentioned processes, which in turn are finally used in the citric acid cycle.

Although the degradation products of poly(α-hydroxyesters) are metabolized by the body, the rates of degradation of the polymer depend on a number of factors, such as crystalline or amorphous nature of the polymer, molecular weight of the polymer, and, in the case of copolymers, the ratio between the comonomers.

13.3.1.1.1 Crystalline or Amorphous Nature of the Polymer

It has been found that the semicrystalline homopolymers in the family of poly(α-hydroxyesters) degrade at a slower rate than amorphous homopolymers.[70] The degradation of the copolymer PLAGA has been reported to depend on the relative amounts of crystalline and amorphous polymer domains. Here again the amorphous domains have been found to degrade faster than the crystalline domains.[66,71–72]

13.3.1.1.2 Composition of the Polymer

As mentioned above, the poly(α-hydroxyesters) degrade by hydrolysis. Therefore, polymer hydration is the first step of biodegradation. The hydration of the polymer depends on the hydrophobicity/hydrophilicity and wettability of the polymer. Since the composition of the polymer determines its hydrophobicity and wettability, its influence on hydration and hence degradation will be detrimental. It has been reported by many investigators that the rates of degradation for PLAGAs with a higher content of lactic acid moiety are slower than those with lower lactic acid content.[73,74] This has been attributed to the fact that polymers with higher lactic acid moiety are less susceptible to hydrolysis because the pendant methyl group on the lactic acid moiety sterically hinders the attack of water molecules, in addition to its effect on hydrophobicity and wettability of the polymers. Recently, Wu and coworkers reported that the degradation of PLAGA follows a first-order kinetics, wherein the absolute value of the biodegradation reaction rate constants increases with increasing glycolic acid moiety in the polymers, which indicates an increase in the rate of degradation of the polymers.[75,76] Therefore, the observations made by researchers in the past agree with the theory that hydrolysis of the poly(α-hydroxyesters) is determined by the accessibility of water molecules to the backbone ester bond of the polymer chain.

13.3.1.1.3 Molecular Weight of the Polymer

The molecular weight of the poly(α-hydroxyesters) affects both the mechanical properties and the degradation of the polymers. The effect of molecular weight of the poly(α-hydroxyesters) on these properties is now fairly well understood. Wu and Wang studied the *in vitro* degradation of a range of molecular weights (weight average molecular weight (Mw) of ~10,000 to 166,000) for PLAGA.[75] They found that irrespective of molecular weight, PLAGA degrades via three phases. In the first phase (first week), there is a slow hydration of the polymer that leads to a slow degradation rate. In the second phase (second to fifth week), there is a high rate of degradation, followed by a third phase (sixth week to complete degradation) associated with a low rate of degradation attributed to the low Mw of the remaining polymer. It was observed that the rate of degradation is higher for the higher-molecular-weight polymers. Wu and Wang performed a linear regression analysis of the data to calculate the degradation rate constants. A decrease in the absolute value of the rate constant with a decrease in molecular weight reconfirmed the above observation. A possible explanation for this behavior could be as follows. The higher-molecular-weight polymers have longer polymer chains than the lower-molecular-weight ones. Therefore, the probability of a long-chain polymer being attacked by a water molecule is higher. This higher probability can lead to a faster cleavage of the polymer backbone, thereby causing higher degradation rates. This is further supported by the newly formed carboxylic end groups that act as catalysts for polymer chain

scission.[77,78] Therefore, high-molecular-weight poly(α-hydroxyesters) degrade faster than low-molecular-weight polymers.

13.3.1.1.4 Type of Copolymer

In the case of copolymers, i.e., PLAGA, the type of the copolymer also plays an important role in the degradation of the polymer. As mentioned earlier, the lactic acid component of the copolymer degrades slower than the glycolic acid moieties. In addition to the molar ratios, the sequence of the comonomers in the chain may influence the rate of degradation. For example, it is possible to have a copolymer with the same ratio of lactic acid to glycolic acid content that could be a random copolymer, a block copolymer, an alternating copolymer, or a graft copolymer. Block copolymers can produce a degradation rate that is quite different from random copolymers or alternating copolymers. Block copolymers may be formed due to the higher reaction rate of glycolic acid, compared to lactic acid, during bulk polymerization. However, the unintentional formation of a block copolymer is rare, and more often the monomer sequences are random. This change in polymer type could be one of the reasons why copolymers of the same ratios and levels of crystallinity may have different rates of degradation.[79,80]

13.3.2 Poly(anhydrides)

13.3.2.1 Degradation

One of the most desirable properties for a polymer to be used in drug delivery and tissue engineering applications is its biodegradability. The poly(α-hydroxyesters) discussed above degrade by bulk erosion, i.e., the simultaneous cleavage of the hydrolytic bonds throughout the polymer matrix. Though biodegradation is a desirable property, the mechanism of degradation of a polymer could play a major role for its application in drug delivery and tissue engineering. It would therefore be desirable to have a polymeric system that degrades from the surface. This could potentially lead to a greater level of control over the release process of the bioactive molecule in case of delivery systems. However, achieving such a surface-degrading polymer would require the rate of hydrolytic degradation at the polymer surface to be faster than the rate of penetration of water into the polymer. Because of the presence of the highly labile anhydride bond, the poly(anhydrides) form a class of surface-degrading polymers that have been widely studied for their use in drug delivery and, to some extent, in tissue engineering. In surface erosion, the rate of degradation is directly proportional to the external surface area, as degradation is always occurring at the outer surface of the polymer matrix. The major advantage of this form of degradation is that both the length of time the polymer erodes and the rate of erosion can be controlled by altering the chemical properties of the polymer during its synthesis. Further control over the degradation process can be brought about by altering the geometry of the matrix, i.e., controlling the

external surface area of the matrix. This ability to tailor the polymer to have desired degradation rates and times make the poly(anhydrides) a very attractive polymer for drug delivery and tissue engineering applications.

13.3.2.1.1 Monomer Composition

For a single type of copolymer such as poly((carboxyphenoxy)propane:sebacic acid) (P(CPP:SA)), the relative ratios of the two monomers can greatly influence the rate of degradation of the resulting polymer. The sebacic acid component of the polymer contributes to a faster degradation rate, whereas the CPP component contributes to a slower degradation rate. The ratios of SA to CPP could be altered to obtain polymers having a degradation time of between 1 day and 3 years.[81]

13.3.2.1.2 Type of Polymer Backbone

Similarly, the type of the poly(anhydride) backbone was shown to influence its degradation rate. This was illustrated by studying the degradation of a homologous series of poly((p-carboxyphenoxy) alkane), wherein with an increase in the number of methylene groups in the alkane, the resulting polymer was increasingly hydrophobic, thereby decreasing the rates of degradation. It was reported that the degradation rates decreased by three orders of magnitude with an increase in the number of methylene groups to six (hexane).[81]

13.3.2.1.3 pH of Environment

The effect of pH of degradation media on rates of degradation was studied by Leong et al. In general, they found that the rate of degradation of poly(anhydrides) increased rapidly with an increase in pH of the degradation medium above a pH of 7.4. It was also seen that the rates of degradation were very low in the acidic pH range, and that many of the poly(anhydrides) did not show any degradation in acidic pH.[81]

13.3.2.1.4 Molecular Weight

One initial drawback for poly(anhydrides) was their low molecular weight, which made them impractical for many applications. However, Domb and Langer studied the mechanism of polymerization and factors influencing molecular weight and were thereby able to synthesize high-molecular-weight poly(anhydrides).[82] From the degradation perspective too, the problem of crumbling is aggravated by the low-molecular-weight polymers. However, the duration of degradation can be increased or decreased by alterations in molecular weight. Further, an increase in molecular weight showed a corresponding improvement in mechanical properties (tensile strength) that is desirable for weight-bearing applications.[82]

13.3.2.2 Composition of Polymer

As seen above, depending on the method of synthesis and the type of monomer, or comonomers in case of copolymers, the properties of the

poly(anhydride) obtained could be different. The solution polymerization technique yielded relatively lower-molecular-weight polymers than did polymers synthesized using the melt condensation technique.[82] For all the different classes of polymers discussed above, there was a broad range of properties that were obtained.

For the unsaturated poly(anhydrides) (fumaric acid, acetylene–carboxylicacid, and 4,4'stilbenecarboxylic acid), it was seen that the homopolymers were more crystalline and therefore less soluble in common organic solvents. However, the copolymers of the unsaturated monomers with aliphatic diacids (sebacic acid) were less crystalline and soluble in chlorinated organic hydrocarbons.[83]

Staubli et al.,[84] Domb,[85] and Hartmann and Schultz[86] studied the amino acid-containing poly(anhydrides). Hartmann et al. showed that low-molecular-weight amido-containing poly(anhydrides) could be synthesized using a variety of aliphatic groups on the carboxyl end of p-aminobenzoic acid. This yielded poly(anhydrides) having a broad range of glass transition temperatures (Tg) ranging from 20 to 150°C.[86] Similarly, Staubli et al. synthesized low-molecular-weight trimellitic anhydride-based amino acid-containing poly(anhydrides).[84] In their studies, Staubli et al. found that the use of catalysts and aliphatic spacers such as sebacic acid enable the synthesis of high-molecular-weight polymers. However, increasing the content of the aliphatic spacer produced polymers with lower melting temperatures (Tm).

Similarly, for the aliphatic-aromatic homopolymers an increase in the spacer length produced polymers with Tm values ranging from 40 to 200°C (the Tm being proportional to the molecular weight of the polymer).[87] To enable the use of insoluble aromatic poly(anhydrides), Domb et al. reported the synthesis of aromatic homo- and copoly(anhydrides) based on terephthalic acid and iso-phthalic acid, showing improved solubility properties that could be altered via the ratio of the respective comonomers.[87]

The unsaturated fatty acid dimers and trimers have been used in combination with aliphatic diacids (sebacic acid) for poly(anhydride) synthesis, and depending on the ratio of the comonomer used, a range of molecular weights (25,000 to 280,000) could be obtained. Further, the changes in the composition of the copolymer using long-chain fatty acids altered the hydrophobicity and hence decreased the degradation rate of the copolymer.[88]

Lastly, the composition of the poly(anhydrides) was altered by modifications of the backbone of the polymer, such as branching or cross-linking, partial hydrogenation, and physical blending of different polymers. Maniar et al. showed that the type and extent of branching agent used could influence the molecular weight and hence the rate of degradation and drug release.[89]

13.3.3 Poly(anhydride-*co*-imide)

13.3.3.1 *Composition of Polymer*

Staubli et al. initially investigated poly(anhydride-*co*-imides) for biomedical applications.[90] This work was then carried forward by Uhrich et al., who

synthesized poly(anhydride-*co*-imides) based on pyromellitic acid (PMA) and trimellitic acid (TMA) derivatives for its potential use as a degradable, high-compressive strength. They also studied the effect of the ratio of imide monomer to anhydride monomer in poly(anhydride-*co*-imide) and the effect of type of imide monomer (PMA and TMA derivatives) and anhydride monomer (CPH and SA) on the properties of poly(anhydride-*co*-imide).

As can be expected, the incorporation of the imide group into the poly(anhydrides) led to an increase in the mechanical and thermal stability of the copolymers.[91] It was observed that the hydrophobicity of the poly(anhydride-*co*-imide) increased with an increase in the imide content of the copolymer and that the polymers containing PMA derivatives have thermal transition temperatures that are higher than those observed for polymers containing TMA derivatives.[91] It was also seen that for all the systems studied by Uhrich et al., the molecular weight of the poly(anhydride-*co*-imides) decreased with an increase in the amount of imide in the backbone of the polymer.[91] This was attributed to the increased viscosity of the reaction medium due to the imide monomer that might lead to decreased polymer chain interactions and hence molecular weight buildup.

The choice of the anhydride monomer also influenced the properties of the resulting copolymers. Copolymers containing CPH are more hydrophobic, have higher compressive strengths, have higher glass transition and decomposition temperatures, and exhibit no melting transitions compared to polymer-containing SA.[91]

13.3.3.2 Poly(anhydride-co-imide) Terpolymers

Hanes et al. studied the synthesis of poly(anhydride-*co*-imide) consisting of more than two monomers (terpolymers) and discussed their usefulness as drug carrier systems.[92] A careful selection of three monomers allowed for a series of amorphous polymers with a wide range of polymer erosion. All the polymers studied by Hanes et al. contained a tyrosine derivative of trimellitylimido, as it improved the immunostimulatory effects of poly(anhydride-*co*-imides).[92] Their study revealed that the monomers of the terpolymers are randomly distributed throughout the polymer backbone, thereby allowing for uniform degradation of the polymer, a property that is highly desirable for drug delivery applications. Further, these polymers show good stability in the solid state at room temperature, making them more desirable for drug delivery applications.

13.3.3.3 Degradation of Poly(anhydride-co-imide)

Uhrich et al. initially studied the degradation of pyromellitylimidoalanine (PMA-ala)- and trimellitylimidoglycine (TMA-gly)-containing poly(anhydride-*co*-imides).[93,94] They found that for both these types of polymers the degradation was pH sensitive, being enhanced under basic conditions. As in the case of poly(anhydrides), the degradation times of the poly(anhydride-

co-imide) could be altered from 1 day to 2 months by appropriate selection of monomer units in the backbone of the polymer.[93,94] They also showed that increasing the imide content in the polymer (PMA-ala, TMA-gly) increases the hydrophilicity of the polymers and hence degradation rate. Overall, it was seen that increasing the imide monomer (PMA-ala, TMA-gly) and use of SA rather than CPH as the comonomer increased the degradation rate of the poly(anhydride-*co*-imides).[93,94]

13.3.4 Poly(phosphazenes)

13.3.4.1 Composition of Polymer

In the case of poly(phosphazenes), the type of side group attached to the backbone has a profound effect on the chemical and physical properties of the polymer, thereby enabling the tailoring of polymers for desired properties.

The usually high degree of flexibility of the poly(phosphazene) backbone is due to the low torsional barrier about the P-N bond. This translates into low glass transitional temperatures for most poly(phosphazenes). However, the Tg can be altered by proper choice of the side group attached to the backbone. For example, the Tg of a poly(phosphazene) with a benzyl glycolate side group is 43°C. When benzyl lactate is introduced as the side group, the Tg is increased to 84°C. This is because benzyl lactate is bulkier and therefore restricts skeletal motion.[95]

The hydrophilicity/hydrophobicity of the poly(phosphazene) can also be controlled depending on the side group on the backbone. The hydrophilicity of the polymer would contribute toward enhanced biocompatibility and degradation effects, whereas a hydrophobic polymer would reduce these effects, while giving a certain level of control when desired. It is reasonable to expect that a hydrophilic side group would result in a hydrophilic polymer and a hydrophobic side group would result in a hydrophobic polymer. This effect was reported by Allcock and coworkers, wherein they demonstrated that a polymer with a trifluoroethoxy side group is hydrophobic and insoluble in water, while a polymer with an alkyl ether side group is hydrophilic and water soluble.[96,97] This effect was further demonstrated by Laurencin et al. via contact angle measurements for different poly(phosphazenes). They studied side groups such as the p-methylphenoxy group and ethyl glycinato group and found that in either case, an increase in the content of side group led to a corresponding increase in contact angle, thereby indicating an increase in hydrophobicity of the polymer.[98]

13.3.4.2 Degradation

Allcock et al. were amongst the first to develop biodegradable poly(phosphazenes) containing a variety of amino acid esters.[99] They studied the degradation of poly(phosphazenes) and proposed and presented initial evidence for more than one mechanism of polymer degradation. One of the mecha-

nisms for the ethyl glycinato-contained polymers involves the hydrolysis of the ester linkage to yield carboxylic acid, which then protonates a skeletal nitrogen atom. The resulting phosphazene undergoes further hydrolysis to yield phosphate and ammonia. Another mechanism involves the attack on the backbone by the carbonyl group by the side unit to produce a phosphazene. Yet another mechanism occurs through hydrolytic cleavage of the P-N bond linking the side group to the polymer backbone. Although evidence for all three mechanisms was provided, it was suggested that all three could occur simultaneously; however, it is not clear which mechanism predominates, if at all.

Biodegradable poly(phosphazenes) can be synthesized by introducing side groups that are susceptible to hydrolytic degradation, such as ethyl glycinato and other amino acid alkyl esters, glycolate and lactate esters, imidazolyl, glucosyl, and glyceryl.[95,99–102] The rates of degradation can be controlled by the type and extent of loading of a particular side group. However, in recent times poly(phosphazene)-containing ethyl glycinate side chains are the preferred biodegradable polymers because they lend an enhanced ability to tailor the polymer for desired end uses. Laurencin et al. have demonstrated that a higher percentage of loading of a hydrophilic group like ethyl glycinato group or imidazolyl unit will result in a faster degrading polymer. Similarly, an increase in the percentage incorporation of the p-methylphenoxy group led to an increase in hydrophobicity and hence slower degradation rates.[98]

While the preceding discussion of degradation was based on the composition of the poly(phosphazene), there are other external factors that can affect the rate of degradation, such as pH. Ibim et al. studied the influence of pH (2.0 to 10.0) of degrading media on rates of degradation.[103] They demonstrated that a deviation from neutral pH increased mass loss of the polymer, indicating that hydrolysis could either be acid or base catalyzed. This was in accordance with studies by Allcock et al.[99] on poly((amino acid alkyl ester)phosphazenes) and Crommen et al.[104] on the degradation of poly((organo)phosphazenes).

13.4 Synthetic Polymers for Tissue Engineering

13.4.1 Tissue Engineering

Tissue engineering is a relatively new and emerging interdisciplinary field that aims at solving the critical medical problems of tissue loss and organ failure. With the development of bioresorbable materials having a broad range of properties and characteristics, implants can be engineered to stimulate or assist in tissue regeneration. This area of research is called tissue engineering and can be defined as the application of biological, chemical,

and engineering principles toward the repair, restoration, and regeneration of living tissue using biomaterials, cells, and factors alone or in combination.[105] By participating in the growth and regeneration of natural tissue, the role of implants is not limited to one that is static; that is, if biodegradable, they can serve as a scaffold that can eventually be replaced by natural tissue.

13.4.2 Rationale for Tissue Engineering

The need for tissue (hard and soft) is acute, and therefore, there exists a large gap between the demand and supply of tissue. The present-day treatment for tissue loss, although fairly successful, does not provide optimal therapy. These treatments rely on donor tissue obtained either from a patient (autografts) or from another source (allografts). Donor tissue obtained from a patient is limited due to shortage of supply and donor site morbidity, in which the remaining tissue at the harvest site is damaged by removal of the graft. Donor tissue from another source poses the risk of rejection due to immunogenic response and holds the risk of disease transfer. These limitations have initiated the search for synthetic biocompatible substitutes to autografts and allografts. This area of research, now better known as tissue engineering, has as one of its goals the bridging of the gap between demand and supply of tissue, while providing optimal repair, restoration, or regeneration of tissue.

13.4.3 Methods of Tissue Engineering

13.4.3.1 *Polymeric Microspheres*

Polymeric microspheres have been used as a vehicle for the delivery of bioactive molecules for more than two decades now. Recently, Laurencin and coworkers reported the use of microspheres to design scaffolds for tissue engineering of bone.[120,121] However, it is their biodegradable aspect that makes them especially attractive. The biodegradable property of the polymer circumvents the need for surgical removal of the implant after the completion of the desired function. In addition, the ability to alter and control the rates of degradation of the polymer in turn enables control over the release kinetics of a drug or bioactive molecule. Therefore, synthetic biodegradable polymers such as poly(α-hydroxyesters), poly(anhydrides), and poly(phosphazenes) have been extensively used for the purpose of tissue engineering and drug delivery.

13.4.3.1.1 *Microsphere Fabrication Technique*

Since the fabrication techniques for microspheres have been reviewed by a number of researchers previously, they shall only be briefly discussed in this section.[106,107] There are number of methods for fabrication of microspheres that have been reported.[106–110] Some of them include complex coacervation,

interfacial polymerization (at liquid–liquid or solid–liquid interfaces), solvent evaporation or spray drying, aggregation by pH adjustment or heat, fluidized-bed method, and modifications of the same.[106,107] However, the most commonly reported laboratory technique for encapsulation of bioactive molecules in microspheres is the solvent evaporation technique. The solvent evaporation technique involves the preparation of an emulsion: oil in water (O/W) if the drug is lipophilic (water insoluble) and oil in oil (O/O) if the drug is hydrophilic (water soluble). Briefly, the technique involves preparation of a solution of polymer in an organic solvent to which the drug is added. When the drug is soluble in the polymer solution, a O/O emulsion is used; when the drug is insoluble in the polymer solution, a suspension is formed and a O/W emulsion is used. Depending on the choice of drug, the above polymer solution with drug is mixed with the external phase of the emulsion that contains a surfactant. The emulsion formed (O/W, W/O, or O/O) is then stirred at a constant speed in a hood, at room temperature, until complete solvent evaporation takes place. This process yields a suspension of the solidified microspheres loaded with the drug. The microspheres are then separated by filteration and washed with an inert solvent to remove any residual organic solvent or surfactant. Finally, the microspheres are dried by lyophilization and stored until they are needed. The encapsulation efficiency is calculated as the ratio of the actual drug content in the microspheres over the theoretical drug loading.

13.4.3.2 Scaffolds for Tissue Engineering

One of the major methods of causing the body to regenerate or repair tissue that fails to repair spontaneously is through the use of three-dimensional, synthetic, biodegradable, polymeric scaffolds. The scaffolds can provide for mechanical support at the defect site while providing a three-dimensional framework for the attachment and proliferation of cells. The scaffolds can also serve as a carrier for other cells, growth factors, and other bioactive molecules. In an ideal case, the rate of degradation of the scaffold should match the rate at which cells grow or proliferate, and thereby cause a complete replacement of the three-dimensional space previously occupied by the scaffold. One of the key issues of scaffold design is the technique used for the fabrication of the scaffold. In the following section, some of the most commonly used techniques are discussed.

13.4.3.2.1 Fabrication Technique

An ideal polymeric scaffold should have desired porosity, mechanical properties, surface properties, degradation properties, biocompatibility properties, and three-dimensional structure. Depending on the type of tissue being engineered, there could be a fair amount of difference between the desired properties. However, for most tissues one would desire high porosity, high surface area, a highly biocompatible system, good mechanical strength for load-bearing applications, and degradation rates that can be tailored to fit a

specific end use. High porosity is desired, as it would enable cell seeding and migration. It is the pore size that will determine the ability of the scaffold to allow for cell ingrowth and the internal surface area available for cell attachment. Therefore, high porosity with the correct pore size would be the ideally desired property. A high surface area allows for enhanced cell attachment, proliferation, and migration, and hence is very desirable. Further, a specific three-dimensional structure of the scaffold is detrimental to its function. To achieve the above-mentioned properties, researchers have proposed a number of fabrication techniques for scaffolds. The following section briefly describes some of these techniques:

1. **Fiber bonding:** This technique was developed using two well-known degradable polymers, poly(lactic acid) and poly(glycolic acid).[111] It involves the use of a solution of PLA in chloroform that is poured into a nonwoven mesh of PGA fibers. The chloroform is then removed by evaporation, and the resulting composite of PLA-PGA can then be heated at temperatures nearing the melting temperature of PGA (~195°C for 1.5 h), causing the PGA fibers to bond. The PLA from the composite is then selectively removed by dissolving in dichloromethane, as PGA is insoluble in DCM. The resulting scaffold is a mesh of bonded PGA fibers with a three-dimensional structure.

2. **Solvent-casting and particulate leaching:** This technique involves the use of a fast-evaporating solvent such as dichloromethane, methanol, acetone, chloroform, etc. Typically, a biodegradable polymer, for example, poly(lactide-*co*-glycolide), is dissolved in chloroform, and sieved sodium chloride particles are added to this solution. The solution is then allowed to air dry for a few hours, and the residual solvent is removed by vacuum drying. The salt particles are then leached out by immersing the dry film in deionized water at 25°C for 48 h. This final structure is then redried to eliminate any residual water to yield a porous membrane-like structure.[112] Three-dimensional scaffolds can be obtained using the membrane lamination process.

   Particulate leaching, very similar to the above technique, can also be used to design scaffolds. In this technique, the polymer and sodium chloride particles are fused together by heating above the melting temperature of the polymer. The heat treatment causes the polymer to form the continuous phase with the salt particles entrapped in it. The resulting composite is then immersed in deionized water to leach out the salt particles to yield a three-dimensional macroporous structure.[112]

3. **Membrane lamination:** This method uses the membrane-like porous structures prepared using the solvent casting and particulate leaching technique to design three-dimensional scaffolds. For example, a contour plot of three-dimensional anatomical shapes is first

prepared, and membranes having shapes of the contour are then manufactured. The adjacent membranes are then bonded together by coating with a suitable solvent (e.g., chloroform for PLAGA membranes) at the contacting surface. This method can yield three-dimensional structures having very accurately fitting shapes.[113]

Other techniques that have been reported are membrane lamination processing using the phase inversion technique or diffusion-induced precipitation.[114]

4. **Melt molding:** In this method, fine PLAGA powder and previously sieved gelatin microspheres are mixed in a desired proportion and the dry mixture is poured into a mold. The mold is then heated above the glass transition temperature of the polymer to cause bonding of the polymer particles. The PLAGA–gelatin microspheres composite, having the shape of the mold, is then immersed in a solvent to selectively dissolve the gelatin. This procedure yields a porous PLAGA matrix, whose pore size is determined by the diameter of the geletin microspheres and whose porosity is determined by the ratio of polymer:gelatin microspheres.[115]

5. **Polymer–ceramic composite foams:** Polymer–ceramic composites can be formed by either the solvent casting method, solvent aggregation method, or gel microsphere method.[116]

The solvent casting method involves dissolving the polymer in a desired solvent and adding the ceramic particles to the polymer solution to get a uniform dispersion. The dispersion is then poured into a Teflon mold and allowed to air dry in a chemical hood to yield a porous membrane-like structure. The porosity can be increased by accelerated solvent evaporation.

The solvent aggregation method involves making a dry mixture of polymeric microspheres (prepared using the solvent evaporation method), sodium chloride particles, and ceramic particles in a desired weight ratio. While stirring the dry mixture, very small amounts of the solvent (just enough to dissolve the outer surface of the microspheres) are added. The mixture is then poured into a Teflon mold and compressed to cause fusion between the microspheres. The composite is then lyophilized and immersed in deionized water to leach out the sodium chloride and yield a three-dimensional porous scaffold.

The gel microsphere method involves incomplete formation of polymeric microspheres via the solvent evaporation method. The microspheres in the gel state are isolated and mixed with sodium chloride particles and ceramic particles. The mixture is allowed to air dry in a Teflon mold. The dried composite is then immersed in deionized water to leach out the salt particles to yield a three-dimensional porous scaffold similar to that obtained by the solvent aggregation method.

6. **Phase separation:** In this technique the polymer is dissolved in a solvent (for example, dioxane, naphthalene, benzene, and methanol). Liquid–liquid or solid–liquid phase separation is performed by lowering of the solution temperature to cause the formation of a polymer-rich phase and a polymer-lean phase. The polymer-rich phase is then dried to yield a porous polymer scaffold.[117] The advantage of this method is that it can easily be used for the incorporation of bioactive molecules as no harsh conditions (temperature or chemicals) are used.

7. **Polymerization:** This method involves the preparation of a formulation (consisting of a monomer, initiator, solvent, nonsolvent, cross-linking agent, accelerator, etc.) that is injected into a previously prepared mold and allowed to polymerize to form a scaffold. The scaffold is then subject to soxhlet extraction to remove any residual reactant and eventually dried and sterilized to yield a three-dimensional porous scaffold.

8. **Gas foam processing:** This technique can be used for any synthetic biodegradable polymers to form three-dimensional porous scaffolds. The process involves saturation of polymeric disks with CO_2 using high pressure (5.5 MPa) for approximately 3 days. The pressure of the gas is then rapidly decreased to atmospheric pressure. This drop in pressure causes a thermodynamic instability of the CO_2 inside the disks and leads to nucleation and growth of gas cells within the polymer matrix to yield a porous three-dimensional polymer scaffold. This technique could also be used in combination with sodium chloride particles that can be leached out later to yield enhanced porosity.[118]

9. **Freeze-drying:** Whang et al. reported this technique, which involves using two immiscible phases, an aqueous phase, and an organic phase that is necessarily a solution of the polymer in an organic solvent, for example, PLAGA in dichloromethane.[119] The immiscible layers are then homogenized together and poured into a mold (made of copper) that is quenched in liquid nitrogen (–196°C) and freeze-dried at 20 milli-torr pressure and –110°C and slowly warmed to room temperature over 12 h. The resulting structure is a three-dimensional porous structure, with the porosity being due to the aqueous droplets dispersed in the polymer phase.

10. **Microsphere sintering:** Laurencin and coworkers reported this novel technique, which involves the use of polymeric microspheres using the solvent evaporation technique and sintering them at temperatures above the melting temperature of the polymer to cause bonding between the microspheres.[120,121] This yields a porous three-dimensional matrix with good mechanical properties. This technique is especially useful to engineering scaffolds for load-bearing application such as in the case of bone. The size of the microspheres and

the extent of bonding control the porosity of the scaffold and, to some extent, the mechanical properties of the three-dimensional scaffold.

In addition to the above-mentioned techniques, there are other techniques, such as the vibrating particle technique, the nonwoven fiber constructs, and techniques involving the use of polymer–ceramic composites.[122,123] Therefore, there is a plethora of scaffold fabrication techniques that can lead to a wide variety of scaffold architecture. Depending on the type of tissue, a proper choice of fabrication technique can enable engineer scaffolds having a desired architecture.

13.4.3.2.2   Scaffold Characterization

1. ***In vitro* characterization:**[120,121] The *in vitro* development and characterization of a three-dimensional scaffold for the purpose of tissue engineering prior to cell studies normally involves properties such as polymer type, polymer chemical structure, polymer molecular weight, polymer mechanical properties, mechanical properties of scaffold, porosity of scaffold (pore size, pore volume, pore size distribution), surface area of scaffold, degradation mechanism of the polymer and scaffold, and degradation products of the polymer. Some of the properties will be briefly discussed in this section. The chemistry of the polymer, i.e., polymer type, and polymer molecular weight are two important properties having an influence on the degradation properties of the polymer. The polymer type determines the products of degradation, which in turn determine the kind of response the polymer may produce in the presence of cells or when implanted in an animal model. The molecular weight of the polymer influences to a degree the time required for degradation of the scaffold and the mechanical properties of the scaffold.

    The porosity of the scaffold is another important property that allows for cell penetration and cell mobility. The size of the pores influences the penetrability of cells, and the interconnectivity of pores influences the ability of cells to move inside the pores. In addition, the porosity of a scaffold adversely affects the mechanical properties of the scaffold; i.e., with an increase in porosity of the scaffold, there is a decrease in mechanical strength of the scaffold. This is of importance in load-bearing applications, wherein one would typically try to strike a compromise between porosity and mechanical strength, i.e., an optimal value for both properties that can satisfy the requirements for the regeneration of tissue.

2. ***In vivo* characterization:**[124] The *in vivo* testing of polymeric scaffolds involves an animal model that is normally dependent on the type of tissue being studied and the stage of development of the tissue-engineered scaffold. The mouse and rat models are the most

commonly studied among small animal models, and the rabbit among medium to large animals. However, dog, sheep, pig, and monkey models have also been studied by many researchers.

Very briefly, the *in vivo* testing of a polymeric scaffold would involve the surgical creation of a defect in the tissue of interest and implanting the scaffold at the defect site. The animal and site of implantation will then be studied for a desired duration of time (normally equal to or little longer than the healing time of the tissue), with time points at designated intervals to study the progress of regeneration of tissue with time in the presence of scaffold. The polymeric scaffold can be tested at the designated time points for mechanical strength, degradation (via molecular weight or mass loss), and histology (tissue ingrowth or any unfavorable responses such as inflammation).

13.5 Synthetic Polymers for Drug Delivery

13.5.1 Controlled Drug Delivery

Controlled drug delivery is one of the most rapidly growing areas of research that has led to the development of several biodegradable polymers. The general goal of research in this area is to develop delivery vehicles and systems that can hold biologically active molecules and deliver them at desired times, for desired durations, at desired rates, and in many cases targeted to a desired tissue or organ, while maintaining their biological activity. Most of the attempts at developing such systems have made use of synthetic polymers, and it is the physical and chemical properties of these polymers that mainly influence their performance clinically. All the synthetic biodegradable polymers discussed earlier in this chapter have been studied and used successfully for the development of drug delivery systems.[125–127]

13.5.2 Rationale for Drug Delivery

The general goal of all controlled drug delivery systems is to improve the effectiveness of drug therapy. These improvements can be either to decrease the number of times a drug needs to be administered (i.e., sustained delivery) or to increase the bioavailability of the drug (i.e., decrease loss) or to decrease side effects while increasing therapeutic effects. These improvements can be brought about using different methods of drug delivery. The two most commonly studied methods are the temporal control method and the distribution control method.

The temporal control method is used to deliver drugs for specific time periods or longer durations of time. The delivery of drugs over extended
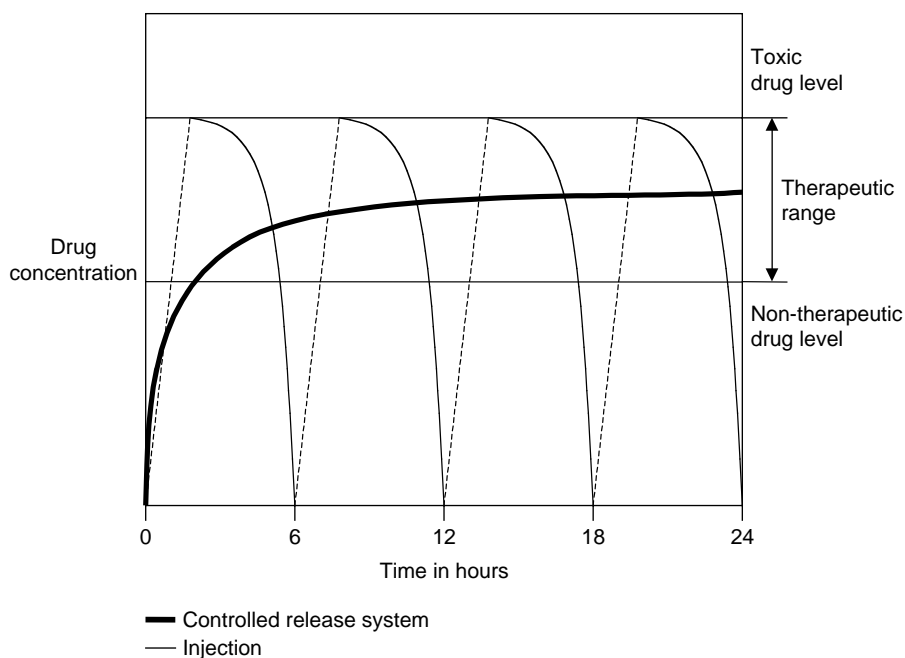
FIGURE 13.17
Drug concentration profile for conventional delivery system (injection) vs. controlled drug delivery system.

durations is especially useful for drugs that need to be administered repeatedly because of their rapid elimination from the body. When a drug is administered orally in the form of a tablet or administered as an injection, the plasma concentration of the drug would increase from zero to a peak value and then decrease back to zero, when it would be time for the second dose to be administered. As shown in Figure 13.17, the plasma concentration of the drug has a large fluctuation, with a substantial portion being in the nontherapeutic range.[128] However, with the controlled drug delivery systems, the rate of elimination of the drug is matched with the rate of release of the drug, thereby maintaining the drug concentration to remain in the therapeutic range for a long duration.

The distribution control method is used to deliver drugs to a specific site of the body. This method is especially useful when the drug is known to produce side effects or adverse effects on parts of the body that it is not intended for. In such cases, the targeting of the drug to specific sites of the body can exclude any adverse effects that the drug may have on other tissues. Another application of the distribution control method is when biologically active molecules cannot naturally reach the site they are meant for. For example, the brain tissue is difficult to access because of the blood–brain barrier. In such cases, the use of nano-size delivery systems has shown

promise in crossing the blood–brain barrier and successfully delivering the biologically active molecule to the brain tissue.[129]

13.5.3 Methods of Drug Delivery

A diverse range of devices fabricated using synthetic polymers has been developed for the purpose of controlled drug delivery. Some of them include micron-size delivery devices (microspheres and microparticles), nano-size delivery devices (nanospheres and nanoparticles), disks or wafers, macrosize solid implants such as films or patches (for transdermal delivery), and inserts (for ocular and vaginal delivery).[130] Most of these applications use synthetic polymers that degrade with time, and the rate of degradation along with diffusion parameters determine the release kinetics of the drug molecule from the delivery device. The advantage of using degradable materials is that when used on humans, there is no need for a second surgery for their removal. In addition, as the rates of degradation depend on the chemical content of the polymer, there is a direct structure property relationship between the chemical properties or the type of polymer and rate of degradation. In the following section, we will briefly discuss some of the delivery systems fabricated using synthetic degradable polymers.

13.5.3.1 Microsphere-Based Delivery Systems

The technique for microsphere fabrication was discussed earlier in Section 13.4.3.1, "Polymeric Microspheres."[120]

Using the solvent evaporation technique, microspheres of varying sizes (10 to 1000 μm) can be fabricated. The size of microsphere can greatly impact the duration of drug release and the rate of drug release. Further, this technique allows for flexibility of drug loading into the microspheres, thereby enabling additional control on the system. Therefore, the microsphere-based delivery systems have been used for a number of drugs, such as anesthetics, antibiotics, anti-inflammatory agents, anticancer agents, hormones, steroids, and vaccines.[125,131–135] In addition, these systems have been extensively used in the agricultural, cosmetic, and food industries.

13.5.3.2 Nanosphere-Based Delivery Systems

The nano-size delivery systems have been studied for more than two decades now, and until recently, the most extensively studied systems have been liposomal in nature. However, sensitivity to environmental degradation, rapid drug leakage across the phospholipid bilayer, and difficulty to scale up have limited their development and commercialization. Degradable polymer-based nanoparticulate delivery systems offer an interesting alternative because of their greater stability in biological fluids, and their preparation is more amenable to scale-up. Synthetic degradable polymers have been used to fabricate nanoparticulate delivery systems using techniques such as emul-

sion evaporation, solvent displacement, salting-out, and emulsification diffusion.[136] Of these, the emulsion evaporation technique has been the most extensively studied and commonly used technique. The emulsion evaporation technique can be considered an alteration of the solvent evaporation technique used for fabricating microspheres (Section 13.4.3.1.1).

13.5.3.2.1 *Emulsification Evaporation*

This technique is based on a procedure originally patented by Vanderhoff et al. for the preparation of artificial latexes.[137] It involves the dissolution of the synthetic polymer and the drug into an organic solvent that is immiscible with water. This solution is then emulsified in an aqueous solution of a protective colloid (such as polyvinylalcohol, gelatin, or albumin). The emulsion is then subject to a high-energy source such as ultrasonic devices, homogenizers, or microfluidizers. Subsequently, the solvent is removed by evaporation using heat or vacuum, resulting in the formation of fine aqueous dispersion of nanospheres. The nanospheres are then filtered and dried in a lyophilizer and stored in a cool, dry place until further use.

13.5.3.3 **Characterization of Drug Delivery Systems**

1. ***In vitro* characterization:** One of the main goals of *in vitro* development and characterization of a delivery system is to release the drug at a controlled rate. The rate of release of a drug from a delivery system is controlled by the diffusion of the drug through the delivery device or the rate of degradation of the delivery system. For degradable systems, the major controlling factor of release kinetics of the drug is the degradation rate of the polymer. As the type and chemistry of the polymer influence its degradation properties, it is possible to alter the chemistry of the polymer to arrive at desired degradation rates. This ability to alter degradation rates of the polymer enables tailoring of release kinetics of the drug, making the degradable polymers attractive materials for the purpose of drug delivery. In addition, as stated earlier, the degradable polymers have the advantage of not needing to be surgically removed after the completion of their function. The disadvantage of some of the degradable systems is that the products of degradation are acidic in nature. Hence, if used in sufficiently large quantities, there could be a buildup of the acidic degradation products in the microenvironment of the implant that may potentially lead to undesirable tissue reaction.

2. ***In vivo* characterization:** The *in vivo* testing of drug delivery systems is most commonly used either to study the delivery kinetics of the drug or to determine the therapeutic effect of the controlled drug delivery system on the disease being treated. In the latter case, there is normally a need for the animal model to be pretreated for the

induction of the disease, e.g., diabetis, cancer, arthritis, etc.

The animal models used for drug delivery experiments vary from small animals such as mice and rats to medium–large animals such as rabbits to large animals such as sheep, dogs, pigs, and monkeys. The choice of the animal model depends on the type of drug delivery system, its therapeutic effect, the disease being studied, and the ease of performance of study on the animal model.

The *in vivo* study would involve the pretreatment of the animal model for the induction of the disease being studied, followed by the implantation of the delivery system. The animal would then be studied at specific time points, wherein at each time point the animal would be euthanized and studied for the amount of drug released, the degradation of the delivery system, and histology (for detecting therapeutic effects and undesired reactions to the degradation products of the polymer). There could, however, be other characterization techniques specific to the requirements of the study.

13.6 Future Directions for Synthetic Biomedical Polymers

13.6.1 Tissue Engineering

Tissue engineering is a young area of research and has great scope for future development. Tissue engineering, as mentioned earlier, is defined as "the application of biological, chemical, and engineering principles toward the repair, restoration, and regeneration of living tissue using biomaterials, cells, and factors alone or in combination." From the definition, it can be inferred that developments in the area of biological and chemical sciences, coupled with advances made in engineering, will greatly contribute toward the development and future of this area of research. Specifically, tissue engineering mainly involves the use of biomaterials, cells, and factors; therefore, advances made in either one of these areas, i.e., material science (including chemistry and polymer science), cell biology, or molecular biology, can initiate development of better biomaterials, engineered cells, and genetically engineered factors.

An important aspect of tissue engineering that has great potential for growth is the design and architecture of the scaffold. Every tissue in the human body is unique and therefore has specific requirements for it to be engineered. Some of the specific physical requirements to be considered for design of scaffold architecture are size, shape, porosity, and mechanical strength. There are a number of existing techniques available for fabricating scaffolds (Section 13.4.3.2.1). However, there is scope for the development of newer methods for fabricating scaffolds that are either universal in their approach or specifically meant for a target tissue. In addition, a better under-

standing of the mechanism at the molecular level for the process of tissue regeneration can potentially increase the ability of researchers to manipulate it to work in the favor of tissue reconstruction.

Recent advances in the area of nanotechnology have led to the development of nanostructured biomaterials for the purposes of tissue engineering. This is an area that is largely unexplored and is receiving a lot of attention. The advances in this aspect of tissue engineering largely depend on understanding the behavior of cells at the nano-level and the ability to fabricate nanostructured materials,[138] including fabrication of nano-size building blocks for scaffolds or macrosize scaffolds with nano-patterned surfaces.

Another direction that shows potential is the engineering of whole organs, wherein the ultimate aim would be to build or grow complete organs and use them for the purpose of transplantation. This seemingly far-fetched goal, because of the exponential rate of development in tissue engineering, is not too far from reality.

13.6.2   Drug Delivery

The area of drug delivery, though relatively older than the area of tissue engineering, is still young and growing at a fast rate. Since the inception of drug delivery more than three decades ago, it has made great progress. There are many commercially available drug delivery systems that are based on biodegradable polymers. However, there still remains a big scope for the development of new and better drug delivery systems.

This chapter has focused on some of the more widely used synthetic biodegradable polymers. However, some of the future challenges of drug delivery involve the development of new biomaterials with unique requirements for specific applications. There are many research groups actively involved in designing new biomaterials. Although there has been a fair amount of success through the use of combinatorial techniques, there still exists the need for newer biomaterials.

An important area of drug delivery that has received a lot of attention in the recent past is targeted delivery, wherein the bioactive molecule or drug is delivered selectively to a target tissue. The targeting to specific tissue involves the ability for the delivery system to distinguish between desired and undesired tissue. This is achieved via the understanding of delivery system and cell behavior, i.e., cell adhesion molecules, cell attachment, cell mobility, cell–delivery system interactions, and cell–bioactive molecule interactions. This understanding enables the development of smart delivery systems that can deliver drugs to target tissue only.

Another method of drug delivery has been the use of external or internal stimuli to effect drug delivery. Studies in the past have attempted to use external stimuli such as pH, temperature, electric current, magnetic field, ultrasound, or enzymes to cause the release of drug from the delivery system. Studies using internal stimuli have been limited to effecting delivery by

engineering alterations in osmotic pressure. Future studies in this area aim at developing a delivery system that can respond to changes in stimuli within the *in vivo* environment. This is a challenging area of research and can potentially lead to intelligent delivery systems that can respond only to specific stimuli.

Finally, gene therapy is probably the most exciting and exponentially growing area of delivery systems.[127] One of the future challenges of gene therapy may be the need to design new degradable polymer systems that can be used for specific applications. Advances in the area of genetics and cell biology, combined with polymer technology, will contribute to the future of this area of research.

References

1. *Polymeric Biomaterials*, Dumitriu, S., Ed., Marcel Dekker, New York, 1994.
2. *Human Biomaterials Applications*, Wise, D.L., Trantolo, D.J., Altobelli, D.E., and Yaszemski, M.J., Eds., Humana Press, Totowa, NJ, 1996.
3. *Biomedical Materials: Drug Delivery, Implants and Tissue Engineering*, Neeman, T., Marcolongo, M., and Valentini, R.F., Eds., Material Research Society, Warrendale, PA, 1999.
4. *Biomedical Applications of Synthetic Biodegradable Polymers*, Hollinger, J.E., Ed., CRC Press, Boca Raton, FL, 1995.
5. Miller, R.A., Brady, J.M., and Cutright, D.E., Degradation rates of oral resorbable implants (polylactates and polyglycolates): rate modification with changes in PLA/PGA copolymer ratios, *J. Biomed. Mater. Res.*, 11, 711–719, 1977.
6. Eibert, J.G., McKinney, P.W., Conn, J., Jr., Binder, P., and Beal, J.M., Polyglycolic acid synthetic absorbable sutures, *Am. J. Surg.*, 121, 561–565, 1971.
7. Frazza, E.J. and Schmitt, E.E., A new absorbable suture, *J. Biomed. Mater. Res.*, 5, 43–58, 1971.
8. Jain, R., Shah, N.H., Malick, A.W., and Rhodes, C.T., Controlled drug delivery by biodegradable poly(ester) devices: different preparative approaches, *Drug Dev. Ind. Pharm.*, 24, 703–27, 1998.
9. Hoechst, DE-OS 2,812,682, 1979 (Leupold, E.I., Wojtech, B., and Arpe, H.J.).
10. DuPont, U.S. 2,152,852, 1939 (D.J. Loder); U.S. 2,153,064, 1939 (A.T. Larson); U.S. 2,443,482, 1948 (M.T. Shattuck).
11. Miltenberger, K., Hydroxycarboxylic acids, aliphatic: specific aliphatic hydroxycarboxylic acids of commercial significance, in *Ullmann's Encyclopedia of Industrial Chemistry*, Wiley-VCH Verlag GmbH, Weinheim, Germany, 2002.
12. Hollinger, J.O., Jamiolkowski, B.S., and Shalaby, S.W., Bone repair and a unique class of biodegradable polymers: the poly(α-esters), in *Biomedical Applications of Synthetic Polymers*, Hollinger, J.O., Ed., CRC Press, Boca Raton, FL, 1995, pp. 197–222.
13. Goodman, I. and Haward, R.N., Eds., *Development in Polymerization-2*, Applied Science Publishers, London, 1979, chap. 4.
14. Laurencin, C.T. and Lane, J.M., Poly(lactic acid) and poly(glycolic acid): orthopaedic surgery application, in *Bone Formation and Repair*, Reddi, H., Ed., American Academy of Orthopaedic Surgeons, Rosemont, IL, 1994, pp. 325–339.

15. Scheele, C.W., Om Mjolk: *Kgl.* Vetenskaps-Academiens nya Handlingar, 1, Stockholm 1780, pp. 116 –124.
16. Cox, G.C. and Macbean, R.D., Lactic acid production by *Lactobacillus vulgaris* is supplemented whey ultrafilterate, *Aust. J. Dairy Technol.,* 32, 19–22, 1977.
17. Kulkarni, R.K., Pani, K.C., Neuman, C., and Leonard, F., Polylactic acid for surgical implants, *Arch. Surg.*, 93, 839–843, 1966.
18. Kulkarni, R.K., Moore, E.G., Hegyeli, A.F., and Leonard, F., Biodegradable poly(lactic acid) polymers, *J. Biomed. Mater. Res.*, 5, 169–81, 1971.
19. Goodman, I., Polyesters, in *Encyclopaedia of Polymer Science and Engineering*, 2nd ed., Vol. 12, Kroschwitz, J.I., Ed., John Wiley & Sons, New York, 1985, pp. 1–75.
20. Kohn, F.I., van den Bergh, J.W.A., van de Ridder, C.T., and Feijen, J., The ring-opening polymerization of D,L-lactide in the melt initiated with tetraphenyltin, *J. Appl. Polym. Sci.,* 29, 4265, 1984.
21. Bucher, J.E. and Slade, W.C., The anhydrides of isophthalic and terepthalic acids, *J. Am. Chem. Soc.*, 31, 1319, 1909.
22. Hill, J.W. and Carothers, H.W., Studies on polymerization and ring formation: XIV. A linear super poly(anhydride) and a cyclic dimeric anhydride from sebacic acid, *J. Am. Chem. Soc.*, 54, 5169, 1932.
23. Hill, J.W. and Carothers, H.W., Studies of polymerization and ring formation: many membered cyclic anhydrides, *J. Am. Chem. Soc.*, 55, 5023, 1933.
24. Conix, A., Aromatic poly(anhydrides): a new class of high melting fiber-forming polymers, *J. Polym. Sci.*, 29, 343, 1958.
25. Yoda, N., Synthesis of poly(anhydrides): poly(anhydrides) of five-membered heterocyclic dibasic acids, *Makromol. Chem.*, 55, 174, 1962.
26. Yoda, N. and Miyake, A., Synthesis of poly(anhydrides): I. Mixed anhydrides of aromatic and dibasic acids, *Bull. Chem. Soc. Jpn.*, 32, 1120, 1959.
27. Rosen, H.B., Chang, J., Wnek, G.E., Lindhardt, R.J., and Langer R., Biodegradable poly(anhydrides) for controlled drug delivery, *Biomaterials*, 4, 131, 1983.
28. Chasin, M., Lewis, D., and Langer R., Poly(anhydrides) for controlled drug delivery, *Biopharm. Manuf.*, 1, 33, 1988.
29. D'Amore, P., Leong, K., and Langer, R., Bioerodable Articles Useful in Implants and Prostheses Having Predictable Degradation Rates, U.S. Patent 4,886,870, 1989.
30. Leong, K.W., Simonte, V., and Langer, R., Synthesis of poly(anhydrides): melt-polycondensation, dehydrochlorination, and dehydrative coupling, *Macromolecules*, 20, 705, 1987.
31. Poly(anhydrides), in *Encyclopedia of Polymer Science and Technology*, supplemental volume, Mark, H.F. et al., Eds., John Wiley & Sons, New York, 1989, pp. 648–665.
32. Laurencin, C.T., Ibim, S.E.M., and Langer, R.S., Poly(anhydrides), in *Biomedical Applications of Synthetic Polymers*, Hollinger, J.O., Ed., CRC Press, Boca Raton, FL, 1995, pp. 59–102.
33. Domb, A. and Langer, R., Poly(anhydrides): I. Preparation of high molecular weight polyanhydrides, *J. Polym. Sci. Polym. Chem.*, 25, 3373, 1987.
34. Anastasiou, T.J. and Uhrich, K.E., Novel polyanhydrides with enhanced thermal and solubility properties, *Macromolecules*, 33, 6217–6221, 2000.
35. Staubi, A., Ron, E., and Langer, R., Hydrolytically degradable amino acid containing polymers, *J. Am. Chem. Soc.*, 112, 4419, 1990.
36. Domb, A., Biodegradable polymers derived from amino acids, *Biomaterials*, 11, 680, 1990.

37. Leong, K.W., Brott, B.C., and Langer, R., Bioerodible polyanhydrides as drug-carrier matrices. I: Characterization, degradation, and release characteristics, *J. Biomed. Mater. Res*., 19, 941, 1985.

38. Jarcho, M., Calcium phosphate ceramics as hard tissue prosthetics, *Clin. Orthop. Rel. Res*., 157, 259, 1981.

39. Uhrich, K.E., Gupta, A., Thomas, T.T., Laurencin, C.T., and Langer, R., Synthesis and characterization of degradable poly(anhydride-co-imide), *Macromolecules*, 28, 2184, 1995.

40. Richardson, R.R., Miller, J.A., and Reichert, W.M., Polyimides as biomaterials: preliminary biocompatibility testing, *Biomaterials*, 14, 627, 1993.

41a. Abajo, J., Babe, S.G., and Fontan, J., *Angew. Makromol. Chem.*, 19, 121, 1971.

41b. Gonzalez, J.I., Abajo, J., Babe, S.G., and Fontan, J., *Angew. Makromol. Chem.*, 55, 85, 1976.

42. Stokes, H.N., On the chloronitrides of phosphorus, *Am. Chem. J.*, 17, 275, 1895.

43. Stokes, H.N., On trimetaphosphinic acid and its decomposition products, *Am. Chem. J.*, 18, 629, 1896.

44. Stokes, H.N., On tetrametaphosphinic acid, *Am. Chem. J.*, 18, 780, 1896.

45. Stokes, H.N., On the chloronitrides of phosphorus (II), *Am. Chem. J.*, 19, 782, 1897.

46. Stokes, H.N., On the metaphosphinic acids (III), *Am. Chem. J.*, 20, 740, 1898.

47. Allcock, H.R. and Kugel, R.L., Synthesis of high polymeric alkoxy and aryloxy phosphonitriles, *J. Am. Chem. Soc.*, 87, 4216, 1965.

48. Allcock, H.R., Kugel, R.L., and Valan, K.J., Phosphonitrilic compounds (VI): high molecular weight poly(alkoxy- and aryloxy-phosphazenes), *Inorg. Chem.*, 5, 1709, 1966.

49. Allcock, H.R. and Kugel, R.L., Phosphonitrilic compounds (VII): high molecular weight poly(diaminophosphazenes), *Inorg. Chem.*, 5, 1716, 1966.

50. Allcock, H.R., *Phosphorus-Nitrogen Compounds: Cyclic, Linear and High Polymeric Systems*, Academic Press, New York, 1972.

51. Hagnauer, G.L., Polydichlorophosphazene polymerization studies, *J. Macromol. Sci. Chem.*, A16, 385, 1981.

52. Allcock, H.R., Polymerization of cyclic phosphazenes and other inorganic systems, *Polymer*, 21, 673, 1980.

53. Allcock, H.R. and Best, R.J., Phosphonitrile compounds I: mechanism of phosphonitrile chloride polymerization, capacitance, conductance, and electo-spin resonance, *Can. J. Chem.*, 42, 447, 1964.

54. Konecny, J.O., Douglas, C.M., and Gray, M.Y., Polymerization of dichlorophosphinic nitrides, *J. Polym. Sci.*, 36, 195, 1959.

55. Oomae, I. and Takeuchi, Y., Polyphosphate, *Chemical Abstracts*, 83, 132282, 1975.

56. Cass, W.E., Organophosphorus resin compositions, *Chemical Abstracts*, 47, 1977i, 1953.

57. Okada, N., Yanagimoto, A., Koto, N., Kamaki, S., and Kumazawa, S., High molecular weight phosphorus-containing polyesters, *Chemical Abstracts*, 87, 68883, 1977.

58. Nielsen, M.L., Polyarylene Phosphonates and Phosphates, U.S. Patent 3,354,242, 1967; *Chemical Abstracts*, 68, 13593, 1968.

59. Pretula, J. and Penczek, S., Poly(ethylene glycol) ionomers with phosphate diester linkages, *Makromol. Chem. Rapid Commun.*, 9, 731, 1988.

60. Kaluzynski, K., Libiszowski, J., and Penczek, S., A new class of synthetic poly-electrolytes: acidic polyesters of phosphoric acid, poly(hydroxyalkylene phosphates), *Macromolecules*, 9, 365–367, 1976.
61. Klosinski, P. and Penczek, S., Synthesis of models of teichoic acids by ring-opening polymerization, *Macromolecules*, 16, 316, 1983.
62. Perec, S., Natansohn, A., Galea, D., and Dima, M., Polycondensation of bisphenol A and chloromethylphosphonic dichloride, *Angew. Makromol. Chem.*, 72, 1, 1978.
63. Natansohn, A., Synthesis and characterization of some aromatic polyphosphonates, *J. Appl. Polym. Sci.*, 32, 2691, 1986.
64. Schmidt, M., Greitag, D., and Bottenbruch, L., Thermoplastic aromatic polyphosphonates with improved thermal aging resistance, *Chemical Abstracts*, 95, 81795z, 1981.
65. Baran, J., Klosinski, P., and Penczek, S., Poly(alkylene phosphate)s by poly-condensation of phosphonic diamides with diols, *Makromol. Chem.*, 190, 1903, 1989.
66. Brady, J.M., Cutright, D.E., Miller R.A., et al. Resorption rate, route of elimination and ultrastructure of the implant site of polylactic acid in the abdominal wall of the rat, *J. Biomed. Mater. Res.*, 7, 155–166, 1973.
67. Hollinger, J.O., Preliminary report on the osteogenic potential of a biodegradable copolymer of polylactide (PLA) and polyglycolide (PGA), *J. Biomed. Mater. Res.*, 17, 71–82, 1983.
68. Frazza, E.J. and Schmitt, E.E., A new absorbable suture, *J. Biomed. Mater. Res.*, 5, 43–58, 1971.
69. Gilding, D.K. and Reed, A.M., Biodegradable polymers for use in surgery: poly(glycolic)-poly(lactic acid) homopolymers and copolymers, *Polymer*, 20, 1459–1464, 1979.
70. Kulkarni, R.K., Moore, E.G., Hegyeli, H.F., et al. Biodegradable poly(lactic acid) polymers, *J. Biomed. Mater. Res.*, 5, 169–181, 1971.
71. Cutright, D.E., Perez, B., Beasley, J.D., III et al., Degradation rates of polymers and copolymers of polylactic and polyglycolic acids, *Oral Surg. Oral Med. Oral Pathol.*, 37, 142–152, 1974.
72. Miller, R.A., Brady, J.M., and Cutright D.E., Degradation rates of oral resorbable implants (polylactates and polyglycolates): Rae modification with changes in PLA/PGA co-polymer ratios, *J. Biomed. Mater. Res.*, 11, 711–719, 1977.
73. Kaetsu, I., Yoshida, M., Asano, M., Yamanaka, H., Imai, K., Yuasa, H., Mashimo, T., Suzuki, K., Katakai, R., and Oya, M., *J. Control. Release*, 4, 283, 1987.
74. Lewis, D.H., Controlled release of bioactive agents from lactide/glycolide polymers, in *Biodegradable Polymers as Drug Delivery System*, Chasin, M. and Langer, R.S., Eds., Marcel Dekker, New York, 1990, p. 1.
75. Wu, X.S. and Wang, N., Synthesis, characterization, biodegradation, and drug delivery application of biodegradable lactic/glycolic acid polymers: Part II. Biodegradation, *J. Biomater. Sci. Polymer Ed.*, 12, 21–34, 2001.
76. Pitt, C.G. and Gu, Z.W., *J. Control. Release*, 19, 189–95, 1987.
77. Pitt, C.G., Gratzl, M.M., Kimmel, G.L., Surles, J., and Schindler, A., Aliphatic polyesters II: the degradation of poly (DL-lactide), poly (epsilon-caprolactone), and their copolymers in vivo, *Biomaterials*, 2, 215–220, 1981.
78. Fukuzaki, H., Yoshida, M., Asano, M., Kumakura, M., Mashimo, T., Yuasa, H., Imai, K., and Yamanaka, H., In vivo characteristics of high molecular weight copoly(L-lactide/glycolide) with S-type degradation pattern for application in drug delivery systems, *Biomaterials*, 12, 433–437, 1991.

79. Jalil, R. and Nixon, J.R., Biodegradable poly(lactic acid) and poly(lactide-co-glycolide) microcapsules: problems associated with preparative techniques and release properties, *J. Microencapsulation*, 7, 297–325, 1990.
80. Hollinger, J.O. and Battistone, G.C., Biodegradable bone repair materials: synthetic polymers and ceramics, *Clin. Orthop.*, 207, 290–305, 1986.
81. Leong, K.W., Brott, B.C., and Langer, R., Bioerodible poly(anhydrides) as drug-carrier matrices I: characterization, degradation and release characteristics, *J. Biomed. Mater. Res.*, 19, 941–955, 1985.
82. Domb, A. and Langer, R., Polyanhydrides I: preparation of high molecular weight polyanhydrides, *J. Polym. Sci.*, 25, 3373–3386, 1987.
83. Domb, A., Mathiowitz, E., Ron, E., Giannos, S., and Langer, R., Polyanhydrides IV: unsaturated and cross-linked poly(anhydrides), *J. Polym. Sci. Polym. Chem.*, 29A, 571, 1991.
84. Staubli, A., Mathiowitz, E., Lucarelli, M., and Langer, R., Characterization of hydrolytically degradable amino acid containing poly(anhydride-co-imides), *Macromolecules*, 24, 2283, 1991.
85. Domb, A., Biodegradable polymers derived from amino acids, *Biomaterials*, 11, 680, 1990.
86. Hartmann, M. and Schultz, V., Synthesis of poly(anhydrides) containing amido groups, *Macromol. Chem.*, 190, 2133, 1989.
87. Domb, A., Gallardo, C.F., and Langer, R., Poly(anhydrides) 3: poly(anhydrides) based on aliphatic-aromatic diacids, *Macromolecules*, 22, 3200–3204, 1989.
88. Domb, A., Amselem, S., Shah, J., and Maniar, M., Poly(anhydrides): synthesis and characterization, in *Advances in Polymer Science*, Peppas, N.A. and Langer, R.S., Eds., Springer-Verlag, Heidelberg, 1992/1993.
89. Maniar, M., Xie, X., and Domb, A., Poly(anhydrides): V. Branched poly(anhydrides), *Biomaterials*, 11, 690, 1990.
90. Staubli, A., Ron, E., and Langer, R., Hydrolytically degradable amino acid containing polymers, *J. Am. Chem. Soc.*, 112, 4419, 1990.
91. Uhrich, K.E., Gupta, A., Thomas, T.T., Laurencin, C.T., and Langer, R., Synthesis and characterization of degradable poly(anhydride-co-imide), *Macromolecules*, 28, 2184–2193, 1995.
92. Hanes, J., Chiba, M., and Langer, R., Synthesis and characterization of degradable anhydride-co-imide terpolymers containing trimellitylimido-L-tyrosine: novel polymers for drug delivery, *Macromolecules*, 29, 5279–5287, 1996.
93. Uhrich, K.E., Larrier, D.R., Laurencin, C.T., and Langer, R., *In vitro* degradation characteristics of poly(anhydride-imides) containing pyromellitylimidoanaline, *J. Polym. Sci. Polym. Chem.*, 34A, 1261–1269, 1996.
94. Uhrich, K.E., Thomas, T.T., Laurencin, C.T., and Langer, R., *In vitro* degradation characteristics of poly(anhydride-imides) containing trimellitylimidoglycine, *J. Appl. Polym. Sci.*, 63, 1401–1411, 1997.
95. Allcock, H.R., Pucher, S.R., and Scopelianos, A.G., Synthesis of poly(organophosphazenes) with glycolic acid ester and lactic acid ester side groups: prototypes for new bioerodible polymers, *Macromolecules*, 27, 1–4, 1994.
96. Allcock, H.R. and Cook, W.J., Thermolysis of poly[bis(trifluoroethoxy)phosphazene], *Macromolecules*, 7, 284–290, 1974.
97. Allcock, H.R., Austin, P.E., Neenan, T.X., Sisko, J.T., Blonsky, P.M., and Shriver, D.F., Polyphosphazenes with etheric side groups: prospective biomedical and solid electrolyte polymers, *Macromolecules*, 19, 1508–1512, 1986.

98. Laurencin, C.T., Norman, M.E., Elgendy, H.M., El-Amin, S.F., Allcock, H.R., Pucher, S.R., and Ambrosio, A.A., Use of polyphosphazenes for skeletal tissue regeneration, *J. Biomed. Mater. Res*., 27, 963–973, 1993.

99. Allcock, H.R., Fuller, T.J., Mack, D.P., Matsumura, K., and Smeltz, K.M., Synthesis of poly[(amino acid alkyl ester)phosphazenes], *Macromolecules*, 10, 824–830, 1977.

100. Allcock, H.R. and Fuller, T.J., The synthesis and hydrolysis of hexa[(imidazolyl)cyclotriphosphazenes], *J. Am. Chem. Soc*., 103, 2250–2256, 1981.

101. Allcock, H.R. and Scopelianos, A.G., Synthesis of sugar-substituted cyclic and polymeric phosphazenes and their oxidation, reduction, and acetylation, and acetylation reactions, *Macromolecules*, 16, 719–722, 1983.

102. Allcock, H.R. and Kwon, S., Glyceryl polyphosphazenes: synthesis, properties and hydrolysis, *Macromolecules*, 21, 1980–1985, 1988.

103. Ibim, S.M., Ambrosio, A.A., Larrier, D., Allcock, H.R., and Laurencin, C.T., Controlled macromolecule release from poly(phosphazene) matrices, *J. Control. Release*, 40, 31–39, 1996.

104. Crommen, J.H., Schact, L.E.H., and Mense, E.H.G., Biodegradable polymers II: degradation characteristics of hydrolysis-sensitive poly[(organo)phosphazenes], *Biomaterials*, 13, 601–611, 1992.

105. Laurencin, C.T., Ambrosio, A.M.A., Borden, M.D., and Cooper, J.A., Jr., Tissue engineering: orthopedic applications, in *Annu. Rev. Biomed. Eng.,* Vol. 1, Annual Reviews, Yarmush, M.L., Diller, K.R., and Toner, M., Eds., Palo Alto, CA, 1999, pp. 19–46.

106. Thies, C., Microencapsulation, in *Encyclopaedia of Polymer Science and Engineering*, 2nd ed., Vol. 9, Kroschwitz, J.I., Ed., John Wiley & Sons, New York, 1985, pp. 724–745.

107. Thies, C., Microencapsulation, in *Encyclopaedia of Chemical Technology*, 4th ed., Vol. 16, Kroschwitz, J.I., Ed., John Wiley & Sons, New York, 1992, pp. 628–651.

108. Zimmer, A. and Kreuter, J., Microspheres and nanoparticles used in ocular delivery systems, *Adv. Drug Delivery Rev.*, 16, 61–63, 1995.

109. Herrero-Vanrell, R. and Refojo, M.F., Biodegradable microspheres for vitreoretinal drug delivery, *Adv. Drug Delivery Rev.*, 52, 5–16, 2001.

110. Deasy, P.B., *Microencapsulation and Related Drug Processes*, Marcel Dekker, New York, 1984.

111. Mikos, A.G., Bao, Y., Cima, L.G., Ingber, D.E., Vacanti, J.P., and Langer, R., Preparation of poly(glycolic acid) bonded fiber structures for cell attachment and transplantation, *J. Biomed. Mater. Res.*, 27, 183–189, 1993.

112. Mikos, A.G., Sarakinos, G., Leite, S.M., Vacanti, J.P., and Langer, R., Laminated three-dimensional biodegradable foams for use in tissue engineering, *Biomaterials*, 14, 323–330, 1993.

113. Mikos, A.G., Sarakinos, G., Vacanti, J.P., Langer, R., and Cima, L.G., Biocompatible Polymer Membranes and Methods of Preparation of Three-Dimensional Membrane Structures, U.S. Patent 5,514,378.

114. Kesting, R.E., Phase inversion membranes, in *Material Science of Synthetic Membranes*, American Chemical Society, Washington, D.C., 1985, pp. 65–195.

115. Thomson, R.C., Yaszemski, M.J., Powers, J.M., and Mikos, A.G., Fabrication of biodegradable polymer scaffolds to engineer trabecular bone, *J. Biomater. Sci. Polym. Ed.*, 7, 23–28, 1995.

116. Laurencin, C.T., Lu, H.H., and Khan, Y., Processing of polymer scaffolds: polymer-ceramic composite foams, in *Methods of Tissue Engineering*, Atala, A. and Lanza, R.P., Eds., Academic Press, New York, 2002, pp. 705–714.

117. Zhang, R. and Ma, P.X., Processing of polymer scaffolds: phase seperation, in *Methods of Tissue Engineering*, Atala, A. and Lanza, R.P., Eds., Academic Press, New York, 2002, pp. 715–724.

118. Mooney, D.J., Baldwin, D.F., Suh, N.P., Vacanti, J.P., and Langer, R., Novel approach to fabricate porous sponges of poly(D,L-lactic-co-glycolic acid) without the use of organic solvents, *Biomaterials*, 17, 1417–1422, 1996.

119. Whang, K., Thomas, C.K., Nuber, G., and Healy, K.E., A novel method to fabricate bioabsorbable scaffolds, *Polymer*, 36, 837–842, 1995.

120. Borden, M.D., Attawia, M.A., Khan, Y.M., and Laurencin, C.T., Tissue engineered microsphere-based matrices for bone repair: design and evaluation, *Biomaterials*, 23, 551–559, 2002.

121. Laurencin, C.T. and Borden, M.D., Methods for Using Microsphere Polymers in Bone Replacement Matrices and Composition Produced Thereby, U.S. Patent 5,866,155, 1999.

122. Li, W.J., Laurencin, C.T., Caterson, E.J., Tuan, R.S., and Ko, F.K., Electrospun nanofibrous structure: a novel scaffold for tissue engineering, *J. Biomed. Mater. Res.*, 60, 613–621, 2002.

123. Ambrosio, A.M., Sahota, J.S., Khan, Y., and Laurencin, C.T., A novel amorphous calcium phosphate polymer ceramic for bone repair: I. Synthesis and characterization, *J. Biomed. Mater. Res.*, 58, 295–301, 2001.

124. *Animal Models in Orthopaedic Research*, An, Y.H. and Friedman, R.J., Eds., CRC Press, Boca Raton, FL, 1999.

125. Attawia, M.A., Borden, M.D., Herbert, K.M., Katti, D.S., Asrari, F., Uhrich, K.E., and Laurencin, C.T., Regional drug delivery with radiation for the treatment of Ewing's sarcoma: in vitro development of a taxol release system, *J. Control. Release*, 71, 193–202, 2001.

126. Ibim, S.M., El-Amin, S.F., Goad, M.E., Ambrosio, A.M., Allcock, H.R., and Laurencin, C.T., In vitro release of colchicine using poly(phosphazenes): the development of delivery systems for musculoskeletal use, *Pharm. Dev. Technol.*, 3, 55–62, 1998.

127. Laurencin, C.T., Attawia, M.A., Lu, L.Q., Borden, M.D., Lu, H.H., Gorum, W.J., and Lieberman, J.R., Poly(lactide-co-glycolide)/hydroxyapatite delivery of BMP-2-producing cells: a regional gene therapy approach to bone regeneration, *Biomaterials*, 22, 1271–1277, 2001.

128. Uhrich, K.E., Cannizzaro, S.M., Langer, R.S., and Shakesheff, K.M., Polymeric systems for controlled drug release, *Chem. Rev.*, 99, 3181–3198, 1999.

129. Kreuter, J., Nanoparticulate systems for brain delivery of drugs, *Adv. Drug Delivery Rev.*, 47, 65–81, 2001.

130. Ottenbrite, R.M., Controlled release technology, in *Encyclopedia of Polymer Science and Engineering*, 2nd ed., Kroschwitz, J.I., Ed., John Wiley & Sons, New York, 1989, pp. 164–187.

131. Maniar, M., Domb, A., Haffer, A., and Shah, J., Controlled release of a local anesthetic from fatty acid dimer based polyanhydride, *J. Control. Release*, 30, 233–239, 1994.

132. Laurencin, C.T., Gerhart, T., Witschger, P., Satcher, R., Domb, A., Rosenberg, A.E., Hanff, P., Edsberg, L., Hayes, W., and Langer, R., Bioerodible polyanhydrides for antibiotic drug delivery: in vivo osteomyelitis treatment in a rat model system, *J. Orthop. Res.*, 11, 256–62, 1993.

133. Johnson, O.L., Cleland, J.L., Lee, H.J., Charnis, M., Duenas, E., Jaworowicz, W., Shepard, D., Shahzamani, A., Jones, A.J., and Putney, S.D., A month-long effect from a single injection of microencapsulated human growth hormone, *Nat. Med.*, 2, 795–799, 1996.
134. Ye, W.P. and Chien, Y.W., Dual-controlled drug delivery across biodegradable copolymer: I. Delivery kinetics of levonorgestrel and estradiol through (caprolactone/lactide) block copolymer, *Pharm. Dev. Technol.*, 1, 1–9, 1996.
135. O'Hagan, D.T., Jeffery, H., Roberts, M.J., McGee, J.P., and Davis, S.S., Controlled release microparticles for vaccine development, *Vaccine*, 9, 768–771, 1991.
136. Quintanar-Guerrero, D., Allemann, E., Fessi, H., and Doelker, E., Preparation techniques and mechanisms of formation of biodegradable nanoparticles from preformed polymers, *Drug Dev. Ind. Pharm.*, 24, 1113–1128, 1998.
137. Vanderhoff, J.W., El-Aasser, M.S., and Ugelstad, J., U.S. Patent 4,177,177, 1979.
138. Laurencin, C.T., Katti, D.S., Ko, F.K., Li, W.J., Khan, Y.M., El-Amin, S.F., and Cooper, J., Nanotechnology and tissue engineering, in *Proceedings of the International Conference on Nanocomputing: Technology Trends*, December 2001, pp. 155–162.

14

An Introduction to Absorbable and Degradable Systems and Their Biomedical Application

Karen J.L. Burg

CONTENTS

14.1 Introduction

14.1.1 Evolution of Absorbable Biomaterials

As early as 3500 B.C., the Egyptians developed polymeric sutures from animal tissue and plants. These early biomedical devices were used for wound closure to facilitate wound repair. It was not until the late 1960s that synthetic, absorbable materials became a large-scale focus in biomedicine. Indeed, many of the innovations in absorbable materials research have been derived from established industries that produce, for example, textile products, packaging, and filters. Indeed, absorbable polymer technology, while relatively new to biomedical application, has earlier roots in the packaging and environmental industries. The concept of packaging that breaks down on exposure to water was initially designed to reduce waste in landfills. This concept of a temporary product was applied in the early 1960s to create "temporary" biomedical devices. Rather than leaving a foreign material implanted and susceptible to wear and degradation, the absorbable biomedical device eliminates the need for a second surgery and may be better designed to suit given mechanical and chemical constraints of the particular surrounding environment. As the absorbable material slowly breaks down and diminishes in strength and mass, the wounded tissue gradually repairs, gaining in strength and mass (Figure 14.1). Because the absorbable devices are dynamic systems, their interaction with the surrounding environment is constantly changing; thus, their biocompatibility (i.e., their positive or negative influence on surrounding tissues) may shift. The characteristics of the degradant therefore enormously affect local response to the material. So not only must the material bulk chemistry and texture be carefully assessed, but so must that of the absorption products.
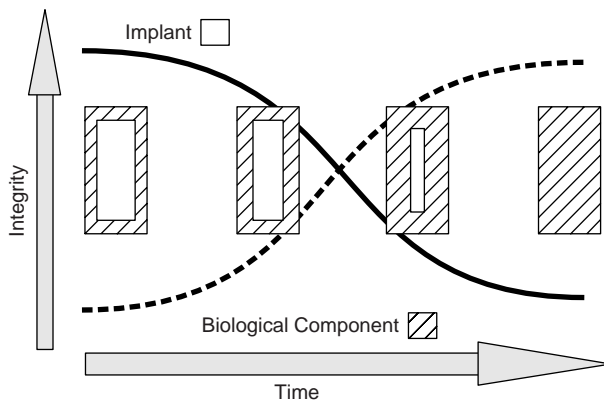

FIGURE 14.1
The mass or strength of an absorbable material diminishes with time as the tissue repairs and increases in strength.
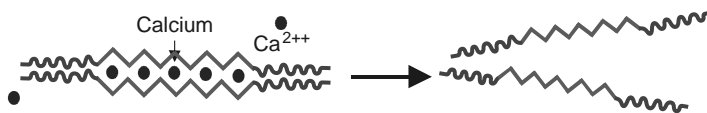
FIGURE 14.2
Alginate chains separate with shifts in ionic concentrations. The chains remain the same length.

14.2   Definitions and Terminology

14.2.1   Mechanisms of Degradation

The term *absorbable* characterizes those materials that are solubilized in the body and removed through the kidneys. Thus, an absorbable material absorbs *in vivo*, but degrades *in vitro*. There are, however, materials that degrade in the body. Several of the natural materials, e.g., collagens, are remodeled in the body and therefore not absorbed. Alginate, a naturally derived material gelled in the presence of a divalent cation, is degraded by shifts in local ion concentrations. In this manner, the cationic species migrate from the biomaterial, causing the gel to decompose into the individual alginate chains (Figure 14.2). The human body does not contain alginases, the enzymes that cleave the alginate chain, and thus newly independent backbone chains are not cleaved and, depending on their size, may not absorb.

The two major mechanisms of degradation are enzymatic and hydrolytic. Absorbables may be largely degraded by enzymes, water, or a combination of the two. Select polymers may be affected by both. Natural materials are generally degraded via enzymatic processes, whereas synthetic materials may be custom designed to degrade via hydrolysis. Biodegradation via enzymatic means is less predictable, as enzyme presence may vary with location in the body and with the patient profile. Natural materials tend to illicit much stronger tissue responses postimplantation.

Polyester materials such as polylactide and polyglycolide degrade via bulk degradation. For this reason, polylactide devices have demonstrated variable success clinically. When implanted in areas of low transport, the acidic products may overpower the local transport capabilities, if sufficiently prolonged, causing tissue necrosis and bone resorption (van der Elst et al., 1999; Bostman and Pihlajamaki, 2000). The initial tissue response may have subsided long before the bulk mass loss is apparent and, in fact, the initial insult may have healed. Instead, the device will gradually degrade at the central region, eventually resulting in a bulk release of acidic products when the outer shell is fragmented.

There are two physical types of degradation: surface erosion (as exhibited by poly (ortho esters), for example) and bulk degradation (as exhibited by polyesters, for example). Surface erosion is the most obvious, in which the material is gradually broken down from the outer regions to the inner (Figure

Bulk Degradation (section)

Surface Erosion

FIGURE 14.3
Top schematic shows bulk degradation, moving from the inside to the outside. Bottom schematic indicates degradation from the outside.

14.3). Bulk degradation occurs when degradation occurs at the inner region first, eventually resulting in a breach of the outer shell of the material. Bulk degradation may be detrimental to the surrounding environment, depending on the by-product, the local fluid transport, and the sensitivity of surrounding tissues. Bulk degradation therefore results in a so-called surface–center differential. This is a phenomenon that occurs because of processing, for example, due to a "shell" caused by compression molding or other processing method. As a result, the occurrence is dependent on the size of the device and generally is not an issue for thicknesses less than 3 mm (Li et al., 1990). It has been shown that orientation of a polymer, i.e., the ordered arrangements of the molecular chains, may change the degradation pattern of the polymeric material (Burg et al., 2000). For example, extrusion of a polymer may cause it to acquire more order, more crystallinity, and hence degrade in a manner more characteristic of surface erosion. The absorption time or time required for the material to completely solubilize may be controlled by manipulating the chemistry, morphology, molecular weight, and percent crystallinity of the plastic.

14.3 Examples of Absorbable and Degradable Biomaterials

Only a handful of synthetic absorbable polymers have been approved for clinical use by the U.S. Food and Drug Administration. The three most common are polyglycolide (a polyester), polylactide (a polyester), and polydioxanone (a polyetherester). Polymers of potential future use in the clinic and subjects of current studies include polyamides, polyanhydrides,

polyesters, polyiminocarbonates, poly(ortho esters), polyphosphazenes, and polyphosphonates.

Class (Chemical Name)	Current Applications
Polyester 　Polylactide 　Polyglycolide 　Polycaprolactone 　Polyhydroxybutyrate	Sutures, drug delivery patches, anchors, plates, screws, tissue engineering scaffolds (Kulkarni et al., 1966, 1971; see also Pitt et al., 1990; Gilding, 1981; Burg and Shalaby, 1999)
Poly(ortho ester)	Drug delivery patches (Heller et al., 1990)
Polysaccharide 　Alginate	Injectable bulking agents, tissue engineering scaffolds (see Burg et al., 2000; Loebsack et al., 2001)
Protein 　Collagen	Hemostatic mesh, tissue engineering scaffold
Substituted polyanhydrides	Drug delivery patches (Chasin et al., 1990)
Substituted polyphosphazene	Drug delivery patches, tissue engineering scaffolds (Allcock, 1990)

14.4 Biocompatibility of Absorbable Materials and Relationship to Processing

Absorbable materials are particularly intriguing as they are dynamic, constantly changing with exposure to the surrounding elements. Because the material–tissue interface is constantly changing, evaluation of biocompatibility is quite complex. The natural response of the host to an implanted material, denoted a foreign body response, involves the appearance of transient vessels and cells directed to rid the material from the body, as well as the deposition of collagen intended to wall the foreign material from the body. The response to a "permanent," nonabsorbable material generally occurs for a defined amount of time and subsides. Absorbable or degradable materials, however, will release low-molecular-weight entities in stages, so the response will be cyclic as the material gradually disappears. A detailed explanation of histological assessment and methods of diagnosing a biomaterial response is given by Woodward and Salthouse (1986).

Processing of absorbable materials generally results in a decrease in molecular weight and an increase in lower-molecular-weight moieties. This increases the potential for leachables that can plasticize the material, creating shifts in modulus and other mechanical properties. These lower-molecular-weight species will be quick to solubilize and will have an immediate effect on the surrounding host tissue if not extracted from the device prior to implantation. To minimize this problem, the device may be "cleaned" postprocessing, to remove any low-molecular-weight particulate. This may be accomplished using supercritical fluid extraction (Fages et al., 1998) or a vacuum and low-

level heat treatment. The latter should be carefully controlled, respecting the thermal transitions to avoid crystallization by annealing.

Processing with solvents results in solvent residuals. Many solvents have a toxic effect on tissues and therefore cannot be left in the bulk material. A series of extraction processes, in conjunction with characterization tests, may be used to eliminate residuals. Nonsolvent processing techniques have been used for many nonbiomedical applications and, more recently, applied to absorbable polymer processing for biomedical application. DePonti and coworkers (1991) developed the concept of producing porous, absorbable foams for biomedical application using supercritical fluids. In this manner, no solvent is required for processing; therefore, there is no concern about residual solvent, and the mechanical integrity of the material is preserved since there is no exposure to heat or solvent. This method of processing is not suitable for all material types; namely, highly crystalline polymers may not be processed using this technique as the tight packing may inhibit permeation of fluids into the polymer.

14.5 Processing of Absorbable Biomaterials: Forms and Applications

Absorbable polymers may be produced into many types of forms, including fibers, mesh, composites, foams, beads, gels, and films.

14.5.1 Fibers

Thousands of years ago, the Egyptians were among the first to use fibrous materials as biomedical devices, using naturally derived materials for wound closure. Today, fibers found in the textile industry have a variety of applications in bioengineering. Contributions from the textile industry to implantable materials include improvements in sutures, hernia mesh, vascular graft, composite rods, screws, plates, and fibrous tissue engineering scaffolds. The simplest example of a fibrous biomedical device is a suture. Sutures are used for wound closure, to close cuts and incisions, and thus prevent infection. Critical features in suture design parameters include absorption/degradation rate and potential; surface roughness (as this will affect tissue drag, the frictional forces associated with the suture–tissue interface); compliance (this will affect general handling as well as slippage of knots made with the fiber, therefore how tightly the wound is closed); knot strength; suture tensile strength; elongation; and general dimensional requirements. With modern advances in synthetic filaments, sutures are the most common implant material today. The suture market currently exceeds $1.3 billion annually. Monofilament suture compliance may be reduced by braiding; however,

braids are typically more susceptible to bacterial invasion. As some sutures will be blood contacting, the suture should not cause blood clotting and, as with any biomedical device, should behave favorably with surrounding tissues. Examples of absorbable sutures (see Burg and Shalaby, 1999a) include polyesters (polydioxanone, polyglycolide, poly(glycolide-co-lactide), segmented glycolide -caprolactone, and segmented glycolide trimethylene carbonate) and proteins (catgut, regenerated collagen).

Absorbable sutures are advantageous in many internal applications, where a second surgery for suture removal is not desired. Absorbable sutures are generally not used for external applications where removal is easy; nor are they used for applications where prolonged high strength is required. Products have been developed combining absorbable sutures with absorbable anchors in order to reattach soft tissue to bone.

14.5.2   Mesh

Fibers can also be woven or knitted into mesh. Mesh finds use in such procedures as hernia repair and abdominal wall replacement, where mechanical strength and fixation are very important. Mesh may be designed to display a heterogeneous pore size distribution, each side of which may be designed with a specific porosity and texture in order to optimize its long-term function.

There are 1.4 million surgeries in the U.S. annually associated with vascular diseases. Approximately 750,000 of vascular surgeries are coronary artery bypass graft surgeries (the purpose of which is to bypass occluded coronary arteries and supply the necessary flow to the heart). The traditional method of treatment is to use a blood vessel from another location in the patient (this vessel is then called an autograft), for example, from the leg. Autograft procedures require multiple surgeries and increased risk and cost to the patient. Suitable vessels are not always available; for example, if the patient has had a similar, previous surgery or is an amputee, or has other influencing health conditions, the vessels may not be suitable for the procedure. Thirty percent of bypass patients lack suitable vessels. Synthetic grafts, therefore, are of interest to provide a feasible alternative, and absorbable grafts are of interest to eliminate the need for surgical revisions.

There are several factors to consider in absorbable graft production, including permeability, since it is a fluid-containing device, and flexibility, since it must be readily handled and sutured securely into place by the surgeon. The absorbable material must be carefully designed to allow complete tissue reformation prior to loss of graft mechanical integrity. Also, there are many clinical requirements to consider. Braided fibers are relatively compliant and easily handled. Weft-knits are also easily handled; however, they have high radial elasticity and, since the same yarn is continuous throughout the structure, any localized damage or rupture will propagate. This phenomenon is catastrophic for a vessel. Warp-knit fabrics are comprised of a series of

interlocking loops, but the loops are associated with separate yarns, thus minimizing the opportunity for catastrophic failure. The mechanical properties of a warp-knit may be varied to range from weave to weft-knit properties, so they are advantageous for this reason. The warp-knit is more loosely arranged than a weave, thus increasing permeability; however, this may be modulated with surface coatings and other topical treatments.

Partially absorbable grafts, comprised of polyglycolide and polyethylene terephthalate yarns, appear to promote tissue ingrowth and mechanical stability, attributed to the continued stimulus of the absorbing component (Greisler et al., 1986). The porosity of the mesh will influence cellular attachment and long-term stability of the implant, so the type of weave or knit and its dimensional parameters are crucial. The mesh permeability will also be important, since the intended application is blood contacting.

14.5.3 Composites

Fracture of a bone may result in the implantation of a fixation device, such as a plate, screw, pin, or rod, to temporarily stabilize or "fix" the bone in the correct position for healing to occur. These implants not only must be physically stable in order to meet the necessary mechanical requirements of the implant site, but also must be comprised of materials that are accepted by the body. The fixation devices currently in clinical use are metals that are extremely rigid and, as a result, can sometimes cause damage to the bone. Absorbable plastic materials may be manufactured with varying compliances similar to that of bone, but they generally have insufficient strength compared with similar metal devices. Plastics can also undergo creep with the continual high stresses often found in orthopedic applications. By adding fibers to reinforce the absorbable plastic and create a so-called fiber-reinforced plastic (FRP), both the creep resistance and the strength of the device may be improved (Vainionpää et al., 1987). This concept has yet to become a clinical reality; however, improvements in polymer synthesis as well as fiber processing and postprocessing (providing new combinations of fibers and new reinforcing structures and arrangements of fibers) will render these devices clinically appealing. Polymeric screws are used with or without a fracture fixation plate to hold bone fragments in place. Unlike their metallic counterparts, they have low strength and require a pretapped hole in the bone. Improvements in a new composite system to increase strength and cutting ability will eliminate time in the operating room and increase the use of these plastics. Currently, absorbable screws are used in non-load-bearing applications such as craniofacial repair.

Composite technology is of great interest in orthopedics, the field related to bone repair. Composites may be comprised of many configurations, the most basic comprised of a fibrous reinforcement in a polymer resin. Fiber reinforcement of plastics can enhance mechanical properties of devices, and this is of particular interest in the orthopedic industry for such devices that

are used in bone repair and where typically high mechanical loads (due to walking, running, bending, kicking, etc.) are applied. Even though fiber-reinforced materials have not demonstrated success in the past for total joint replacements, such as the hip and the knee joints, they offer tremendous potential if optimized. Permanent implants, such as the knee and hip, are replaced using nonabsorbable materials, while fracture plates and pins, which are used to splice broken bones together and allow the repair process to commence, have potential as absorbables.

Absorbable materials have never enjoyed widespread use in load-bearing applications due to their poor strengths. With improvements in composite technologies and the development of new absorbables and surface treatments to allow greater interfacial adhesion, it will be possible to enhance the mechanical properties of absorbable systems. An absorbable fixation device has a lower modulus than the traditional metallic implants and therefore may avoid so-called stress shielding of the bone. Several studies have assessed the potential of self-reinforced composite fracture fixation pins, in which the fibrous reinforcement is comprised of the same material as the resin. Bone pins have been manufactured using this process, typically with polyester systems where the goal is to allow ester–ester interchange, and therefore a strong covalent interfacial bond. Candidate systems may be evaluated and compared using a variety of tests to critique the relative interfacial bond strengths. One method employed in our laboratory is a microdroplet test, in which a droplet of the matrix material is placed onto a reinforcement fiber and sheared from the fiber to determine the debonding strength (Figure 14.4). Although this does not allow an absolute evaluation of interfacial bond strength, it does allow comparison of various systems and will be important in the development of new absorbable systems. One day, the so-called permanent implants may even have absorbable components, particularly with the advent of tissue engineering or biologically based solutions.

14.5.4 Foams

Over 8 million surgical procedures are performed annually in the U.S. to treat people with organ failure or tissue loss. For example, in 1996 there were approximately 20,000 donor organs for 50,000 patients. Tissue engineering is the replacement of damaged tissues or organs with biologically based systems. One approach to tissue engineering is taking a small number of healthy cells from a patient, allowing the cells to multiply in laboratory culture, and then combining them with an absorbable polymer (Figure 14.5). The polymer may be shaped to mirror the target organ or tissue shape and is generally porous. This may be fabricated in a number of ways, including the three-dimensional arrangement of fibers into a scaffold. The cells are added to the scaffold and allowed to adhere and grow on and within the plastic material. The cell/scaffold is implanted into the patient and, as the cells develop and form tissue, the plastic breaks
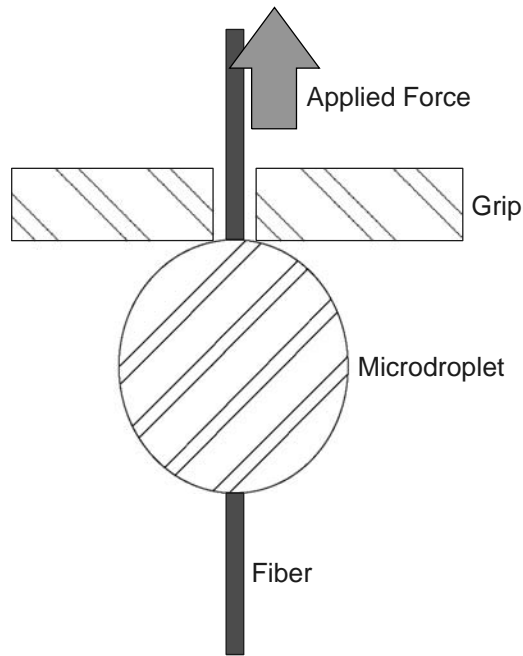
FIGURE 14.4
Relative comparisons of adhesion strengths may be made by using a microdroplet system.

down (by hydrolysis and/or enzymatic means) and is removed from the body. The tissue fills the space that the polymer initially maintained. Because the cells are retrieved from the patient, issues and complications that are commonly found with organ recipients should be minimized. Tissue engineering is an emerging field that can benefit tremendously from improved absorbable biomaterial technologies.

There are a number of processing methods used to create absorbable, porous scaffolds for tissue engineering. These methods are adapted from standard processing techniques (largely from the textiles, plastics, filter, and
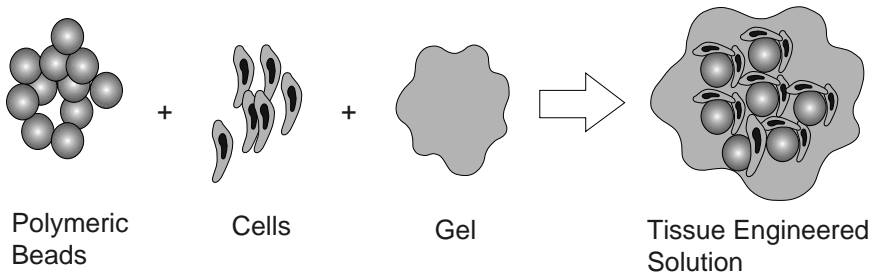

| Polymeric Beads | Cells | Gel | Tissue Engineered Solution |

FIGURE 14.5
The concept of tissue engineering: combining cells with an absorbable polymeric scaffold to eventually create a completely biological replacement.

packaging industries) to tissue engineering. A list of select processing methods is given in Table 14.1, with reference to tissue engineering applications (for more detail, see Burg and Shalaby, 1999b). The first formalized tissue engineering research was based on fibrous systems (sutures); these concepts have evolved considerably. Researchers have investigated random fibrous arrays, which are formed through either mechanical or chemical interlocking. Typically these constructs, while stable in laboratory conditions, have very low compressive strengths at body conditions of 37°C in an aqueous like environment. Further studies have attempted to improve this by "bonding" or gluing the interlock points using a polymer/solvent solution as the glue. This, while enhancing compressive strength, confounds the biocompatibility problem, by providing an additional solvent-based component. Fibers with enhanced mechanical integrities and improved methods of combining the fibers will be critical in furthering the success of fabric-based scaffolds. Development of fibers with specialized properties will also be important. Conductive fibers, for example, are attractive to orthopedic tissue engineering since current and magnetic fields have been shown to affect bone cell behavior in culture. Thus the bone cells, after placement on a polymeric fiber, may be stimulated in a laboratory environment and prompted to grow along a surface in a given configuration or direction. Tissue-engineered possibilities encompass any damaged organs or tissues, so the possibilities are wide and varied.

Currently there are no absorbable fibrous scaffolds that have sufficient mechanical integrity to allow tissue ingrowth once implanted; rather, the scaffolds will readily compress when placed in the moist, 37°C environment, even under simple loading conditions. This may be improved by the introduction of new processing and postprocessing techniques. Various tissue-engineered skin options are currently available clinically, including cells cultivated on a thin, fibrous mesh. Although any tissue or organ is a reasonable tissue engineering target, specific tissue engineering applications that lend readily to fiber-based systems include tendons and ligaments.

Traditional tissue engineering approaches address either three-dimensional, relatively thick porous systems or nonporous injectable gels. The major limiting issues facing the former are the difficulties associated with vascularizing a large volume of material in order to support implanted cells and also the risks and costs associated with an operative implant procedure. A series of smaller porous constructs may avoid this issue; however, there still remains the issue of implanting multiple, easily dispersed materials as well as avoiding their compression once implanted. The major limiting issue facing the latter approach is the nonporous, low-modulus nature of gels, generally not conducive to tissue proliferation, and therefore not optimal as cell carriers. Previous studies by Burg and coworkers (2000a) have suggested that combining a gel with a series of smaller, porous cellular constructs is a potentially clinically effective method for delivery of a tissue-engineered material (Figure 14.6). These studies were completed using porous collagen beads with an alginate gel to demonstrate proof of

TABLE 14.1

Absorbable Materials Processing for Tissue Engineering

Scaffold Processing Method	Select Advantages	Select Disadvantages	Citation Pertinent to Biomedical Absorbable Materials Literature
Physical and chemical aggregation: Formation of interconnected network by binding random array of particles or fibers. Binding may be by entanglement, heat, or chemical treatment.	High, defined porosity. Relatively simple method.	Diminished mechanical properties. Limited use of biological agents due to chemical, heat.	Schugens et al., 1995; Mikos et al., 1993
Cryofabrication: Formation of injectable scaffolds via treatment with liquid nitrogen, solvent extraction.	Relatively simple method.	Difficulty of mass production. Use of solvent.	McGlohorn, in press
Emulsion freeze-drying: Formation of scaffolds by emulsion; pore size controlled by ratio of components.	Ability to manufacture thicker constructs.	Use of solvent. High pore size distribution.	Whang et al., 2000
Supercritical fluid extraction: Application of very high-pressure gas to polymer granules, followed by sharp pressure reduction.	Removal of lower-molecular-weight species. No solvents. Maintenance of mechanical properties. High pore interconnectivity.	Limited by percent crystalline component.	DePonti et al., 1991

|			
Gelation: Formation of injectable scaffolds via cross-linking.	Relatively simple. No solvent.	Variable absorption or degradation. Lower modulus resulting in select cellular attachment.	Loebsack et al., 2001
Solid free-form fabrication: Application of solvent to defined arrays of polymeric granules.	Intricate microarchitecture.	Time, cost intensive. Mechanical properties diminished. Use of solvent.	Park et al., 1998
Crystallization-induced microphase separation: Addition of solid solvent to polymer followed by low heat and sublimation.	Low temperatures allow incorporation of biological components. Pore size distribution tightly controlled by ratio of components.	Use of solvent.	Roweton, 1994; Shalaby and Roweton, 1997
Solid and liquid dispersion: Casting of polymeric solution over bed of leachables.	Relatively simple procedure. Allows highly porous scaffold.	Use of solvent. Diminished mechanical properties. Heterogeneous pore structure.	Mikos et al., 1994
Gas dispersion: Application of high-pressure gas to polymer granules, followed by sharp pressure reduction.	No solvents. Maintenance of mechanical properties.	Limited by percent crystalline component. Additional processing required to achieve interconnectivity of pores.	Mooney et al., 1996
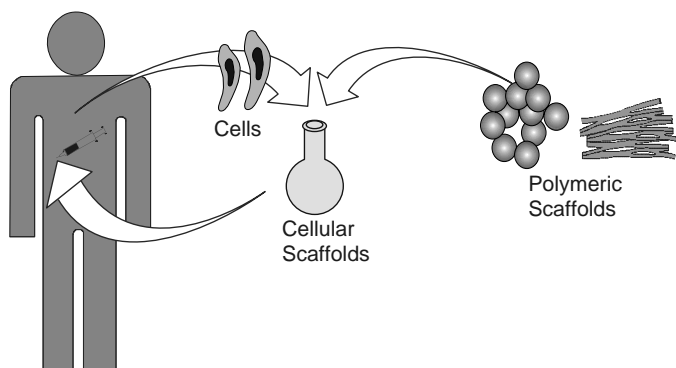
FIGURE 14.6
Formation of an injectable tissue-engineered device.

principle. This work has evolved into the development and investigation of alternate absorbable cell carriers. Low-temperature casting, for example, is a feasible method to make synthetic polylactide beads with surface topography attractive to cells. Beads may be produced on the order of 1.5 to 2.0 mm, a "large" size that is difficult to produce using traditional emulsion techniques. The beads were irregular in shape, providing cracks and surface roughness conducive to cellular attachment, and contained a hollow core, approximately 0.5 mm in diameter. The morphology of the carriers was readily modified by porogen selection, thus modifying cellular behavior. It is possible to combine beads of differing morphologies within a composite in order to address coculture systems.

14.5.5 Beads, Gels, and Films

Temporary drug delivery patches are the simplest biomedical devices, requiring minimal mechanical integrity. These two-dimensional devices may be loaded with antibiotics, growth factors, or other drugs to provide a controlled release system. The release profile may be modulated by changing the physicochemical properties of the patch or by creating "zones" of polymer that absorb at specific times. Therapeutic value may also be achieved by incorporation of the growth factor into microspheres or gels. The release mechanisms in these devices vary. The most common is diffusion control, where the drug is incorporated on the surface or throughout a microporous matrix, or within a reservoir. In the former, the release profile will diminish with time as the drug has increasingly farther to travel to reach the surrounding environment. A drug incorporated in a solid matrix without micropores will be trapped and will await absorption of the polymer for subsequent release. Hydrogels may be used in diffusion-controlled release, wherein the release is controlled by a swelling mechanism (see Spargo et al., 1994; Paige et al., 1995, 1996; Atala et al., 1993; Schuman et al., 1995).

14.6 Processing of Biodegradables and Absorbables

There are a variety of traditional processing methods that may be adapted for use in developing absorbable devices. Depending on the desired form, extrusion, compression molding, and casting are among the possible processing methods. The major difference in the handling of absorbable materials hinges on their sensitivity to heat, chemicals, and air. These factors individually, and combined, may cause decreases in molecular weight and premature degradation of the devices. Therefore, new processes must be carefully designed and the absorbable materials must be characterized prior to as well as postprocessing in order to track changes in physicochemical properties.

14.6.1 Considerations for Incorporation of Biological Component

The processing method must be carefully selected if a growth factor, drug, or cellular component is to be incorporated in a given absorbable device. Processes involving elevated temperature and solvents will be less desirable in these cases. Additionally, the morphology, crystallinity, and molecular weight must be carefully selected, as these will influence the drug release profile (Burg and Shalaby, 1999b).

14.6.2 Key Considerations for Hard and Soft Tissue Applications

The degradation profile of a given absorbable polymer will in part determine whether it is suitable for hard or soft tissue application. Longer-lasting materials are necessary for load-bearing applications, where the mechanical requirements are more stringent. The modulus of a hard tissue replacement will be higher in order to match that of the surrounding tissue. The crystallinity and molecular weight are influencing factors determining mass and strength retention. Crystallinity may be adjusted to an extent via processing, e.g., by annealing or by controlled cooling following a heating cycle (Burg et al., 1999).

Plastics are susceptible to swelling in the presence of lipids and may plasticize at elevated temperatures such as 37°C. Certainly wear debris from an absorbable material will not be of as much concern as that from a nonabsorbable material; however, if an absorbable material wears, it will expose a new surface to the surrounding tissues that may or may not be of similar charactistics to the original. Parameters that may change include surface charge, chemistry, and topography.

14.6.3 Sterilization and Effect on Polymer Properties

Before implantation in the body, an implant must be sterilized to rid the device of microorganisms. Typically, metallic devices are sterilized with dry

or moist heat. An important point to consider in processing implantable absorbable biomaterials is the effect of sterilization on these properties and on absorption. Packaging, shelf life, and handling are of the utmost importance, since many of these materials break down hydrolytically. Sterilization by gamma irradiation is generally detrimental to absorbable materials, reducing their molecular weight by chain cleavage. Ethylene oxide is currently the method of choice, using appropriate degassing times, but may rapidly be phased out as more environmentally friendly methods are developed.

Absorbable and degradable implants can deform, hydrolyze, or melt under these extreme conditions. Ethylene oxide sterilization may be used; however, it is necessary to impose strict regulations governing removal of gases post-sterilization in order to avoid tissue necrosis due to residual ethylene oxide. With the continuing pressures to find environmentally friendly alternatives, other sterilization processes are necessary to consider. Gamma or electron beam sterilization are other options, particularly for select natural materials such as bone graft, but may cause cross-linking, chain scission, or gas evolution in select polymers, in particular synthetics. It is suspected that the radiation causes the production of excited atoms and free radicals. The microorganism survival level deemed acceptable for medical sterilization was set by the Association for the Advancement of Medical Instrumentation (1984) at 10^{-6} (or 1 colony forming unit per million).

New sterilization methods have been developed to combat the problems associated with gas sterilization and gamma sterilization. Chemical agents are considered surface sterilants, while radiation is considered a volume sterilant. Radiochemical methods have been developed in which a low level of irradiation is combined with low levels of chemical sterilization (Shalaby and Linden, 1996). Preliminary studies have shown that subthreshold levels of the chemical agent and the ionizing radiation act cooperatively to accomplish sterilization without the undesirable side effects.

14.7   Future Trends in Absorbable Development

14.7.1   Nerve Guidance Channels

Paralysis due to nerve damage debilitates an additional 11,000 Americans each year; the associated costs are approximately $7 billion annually, and usually these are lifelong disabilities. Nerve damage may be centrally or peripherally located. Acute spinal cord injury is extremely resistant to effective treatment. Peripheral nerve damage is even more common and can be caused by a variety of mechanisms, including mechanical, thermal, chemical, or pathological ones. Autografting in both cases is often an insufficient remedy since the resulting regeneration may be incomplete and the damage considered irreversible. Additionally, autografting can cause loss of function
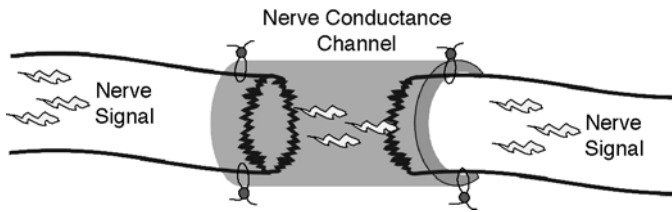
FIGURE 14.7
A nerve guidance channel is an area of evolving interest in tissue engineering research.

at the donor site. A developing area of research interest is in the fabrication of nerve guidance channels (Figure 14.7) that are used to bridge damaged nerve endings, facilitate the passage of molecules secreted by the nerve, and bar fibrous tissue from infiltrating the area and thus preventing repair. A new innovation is the use of electrically conducting polymers (e.g., polypyrrole) to promote nerve regeneration by allowing a locally applied electrical stimulus. Electrical fields have been found to enhance the regeneration of nerve. This is a blossoming field of research interest; the guidance channel may be a single, continuous hollow tube, or it may be a hollow tube comprised of fibers. Eventually it will be of interest to develop an absorbable material that may serve this purpose.

14.7.2 Minimally Invasive Surgeries

The increasing interest of minimally invasive surgery will shift the research areas of interest in absorbable polymer development. Traditional surgical procedures involve a large incision. Minimally invasive surgeries use multiple small incisions to allow camera access and visibility of the surgical site via video monitor. Minimally invasive surgeries can decrease operating room time, chance of infection, cost of surgical procedure, and healing time. A material that is delivered by minimally invasive means vs. one delivered by standard mechanisms will have different features. The mechanical loads applied to the implant will have different qualities because of different points of focus. The size of the implant is obviously restricted in a minimally invasive option. There may be use for foaming materials that swell with exposure to fluid, for example, and that may be implanted in a small volume, but which grow to a larger volume *in vivo*. Materials may be lyophilized to a reduced volume, implanted in this compact form, and then expanded with exposure to fluids. Also, materials may be implanted in liquid or gel form and then cured *in situ*. There are several polymers that are light curing and may be used in these applications.

14.7.3 Necessary Advances in Biomedical Textiles Technology

Biomedical engineering, or bioengineering, is at the intersection of many research fields, including engineering, biological sciences, and medicine. In

order for biomedical device technology to progress, it will be necessary for the contributing fields to progress individually and collectively. Textiles and biology are two such fields. The ability to produce fiber-based scaffolds for tissue engineering will be a milestone. This may mean shifts in development of new materials that better withstand the body's harsh environment; new methods of carefully processing and handling absorbable fibers; and the weaving or knitting of the fibers in order to create scaffolds that will withstand normal loading in the body. The ability to understand the attachment and growth of cells on these new and dynamic three-dimensional surfaces will be crucial. The manufacturing of new conductive fibers will also enhance tissue engineering research, since electric fields are suspected to influence both bone and nerve growth. Rapid progress of this technology will also have a large impact on nerve regeneration devices. The development of biologically friendly and predictable absorbable fibers will be of great interest, both as suture materials and as the basis for tissue-engineered constructs. The surface texturing and coating of fibers will be extremely important, as this governs cell adhesion. New noninvasive mechanisms of assessing the cell–material interface, as it shifts with time, will be an area of exploding interest. Improved absorbable and nonabsorbable fibers with greater resistance to various modes of sterilization will be necessary as new sterilization technologies are introduced to meet evolving environmental specifications. Methods of combining fiber types will be influential to the advancement of all biomedical devices in order to more tightly control mechanical, physical, and chemical properties. Advances in other keystone fields will clearly bring a new and improved group of biomedical devices.

14.8   Summary

As interest in tissue-engineered organs grows, so too will the advancement of absorbable material technologies. Although interest has shifted toward the development of cellular constructs, it will be of continued interest to develop novel absorbable materials that have superior mechanical integrity for use in orthopedics. In order to hone widespread confidence in absorbable materials clinically, it will be necessary to comprehensively evaluate degradation patterns in a variety of clinically relevant environments.

References

Allcock, H.R. 1990. Polyphosphazenes as new biomedical and bioactive materials, in *Biodegradable Polymers as Drug Delivery Systems*, M. Chasin and R. Langer, Eds. New York: Dekker, pp. 163–193.

Association for the Advancement of Medical Instrumentation. 1984. Guideline for Gamma Radiation Sterilization of Medical Devices. Arlington, VA: AAMI.

Atala, A., L.G. Cima, W. Kim, K.T. Paige, J.P. Vacanti, A.B. Retik, and C.A. Vacanti. 1993. Injectable alginate seeded with chondrocytes as a potential treatment for vesicoureteral reflux, *J. Urol.*, 150:745–747.

Bostman, O.M. and H.K. Pihlajamaki. 2000. Adverse tissue reactions to bioabsorbable fixation devices, *Clin. Orthop.*, 371:216–227.

Burg, K.J.L., C.E. Austin, C.R. Culberson, K.G. Greene, C.R. Halberstadt, W.D. Holder, Jr., A.B. Loebsack, and W.D. Roland. 2000a. A Novel Approach to Tissue Engineering: Injectable Composites, Transactions of the 2000 World Biomaterials Congress.

Burg, K.J.L., C.E. Austin, D.J. Mooney, P. Eiselt, J. Yeh, J.A. Rowley, C.R. Culberson, K.G. Greene, W.D. Holder, Jr., A.B. Loebsack, S. Wyatt, and C.R. Halberstadt. 2000. Optimizing Microstructure of Porous Alginate-RGD Beads for Tissue Engineering Application, Transactions of the 2000 World Biomaterials Congress.

Burg, K.J.L., M. LaBerge, D.L. Powers, and S.W. Shalaby. 1999. Image analysis and the effect of molecular orientation on degrading lactide polymer films, *Cells Mater.*, 9:127–134.

Burg, K.J.L. and S.W. Shalaby. 1999a. Absorbable materials and pertinent devices, in *Handbook of Biomaterials Evaluation*, A.F. von Recum, Ed. Ann Arbor, MI: Taylor and Francis, pp. 99–110.

Burg, K.J.L. and S.W. Shalaby. 1999b. Biodegradable materials, in *Tissue Engineering of Prosthetic Vascular Grafts*. Austin, TX: R.G. Landes, pp. 505–512.

Chasin, M., A. Domb, E. Ron, E. Mathiowitz, R. Langer, K. Leong, C. Laurencin, H. Brem, and S. Grossman. 1990. Polyanhydrides as drug delivery systems, in *Biodegradable Polymers as Drug Delivery Systems*, M. Chasin and R. Langer, Eds. New York: Dekker, pp. 43–70.

DePonti, R., C. Torricelli, and A. Martini. 1991. Use of Supercritical Fluids to Obtain Porous Sponges of Biodegradable Polymers, International Patent WO 91/09079.

Fages, J., N. Poddevin, M.W. King, Y. Marois, J. Bronner, B. Jakubiec, R. Roy, D. Mainard, G. Laroche, J.P. Delagoutte, and R. Guidoin. 1998. Use of supercritical fluid extraction as a method of cleaning anterior cruciate ligament prostheses: in vitro and in vivo validation, *ASAIO J.*, 44:278–288.

Gilding, D.K. 1981. Biodegradable polymers, in *Biocompatibility of Clinical Implant Materials*. Boca Raton, FL: CRC Press, pp. 209–232.

Greisler, H.P., T.H. Schwarcz, J. Ellinger, and D.U. Kim. 1986. Dacron inhibition of arterial regenerative activity, *J. Vasc. Surg.*, 3:747–756.

Heller, J., R.V. Sparer, and G.M. Zentner. 1990. Poly(ortho esters), in *Biodegradable Polymers as Drug Delivery Systems*, M. Chasin and R. Langer, Eds. New York: Dekker, pp. 121–162.

Kulkarni, R.K., E.G. Moore, A.F. Hegyeli, and F. Leonard. 1971. Biodegradable poly(lactic acid) polymers, *J. Biomed. Mater. Res.*, 5:169–181.

Kulkarni, R.K., K.C. Pani, C. Neuman, and F. Leonard. 1966. Polylactic acid for surgical implants, *Arch. Surg.*, 93:839–843.

Li, S.M., H. Garreau, and M. Vert. 1990. Structure-property relationships in the case of the degradation of massive poly-(-hydroxy acids) in aqueous media: Part 2. Degradation of lactide-glycolide copolymers: PLA37.5GA25 and PLA75GA25, *J. Mater. Sci. Mater. Med.*, 1:131–139.

Loebsack, A., K. Greene, S. Wyatt, C. Culberson, C. Austin, R. Beiler, W. Roland, P. Eiselt, J. Rowley, K. Burg, D. Mooney, W. Holder, and C. Halberstadt. 2001. In vivo characterization of a porous hydrogel material for use as a tissue bulking agent, *J. Biomed. Mater. Res.*, 57:575–581.

McGlohorn, J.B., L.W. Grimes, S.S. Webster, and K.J.L. Burg. In press. Characterization of cellular carriers for use in injectable tissue engineering composites, *J. Biomed. Mater. Res.*

Mikos, A.G., Y. Bao, L.G. Cima, D.E. Ingber, J.P. Vacanti, and R. Langer. 1993. Preparation of poly(glycolic acid) bonded fiber structures for cell attachment and transplantation, *J. Biomed. Mater. Res.*, 27:183–189.

Mikos, A.G., A.J. Thorsen, L.A. Czerwonka, Y. Bao, R. Langer, D.N. Winslow, and J.P. Vacanti. 1994. Preparation and characterization of poly(L-lactic acid) foams, *Polymer*, 35:1068–1077.

Mooney, D.J., D.F. Baldwin, N.P. Suh, L.P. Vacanti, and R. Langer. 1996. Novel approach to fabricate porous sponges of poly(DL-lactic-co-glycolic acid) without the use of organic solvents, *Biomaterials*, 17:1417–1422.

Paige, K.T., L.G. Cima, M.J. Yaremchuk, B.L. Schloo, J.P. Vacanti, and C.A. Vacanti. 1996. De novo cartilage generation using calcium alginate-chondrocyte constructs, *Plast. Reconstr. Surg.*, 97:168–178.

Paige, K.T., L.G. Cima, M.J. Yaremchuk, J.P. Vacanti, and C.A. Vacanti. 1995. Injectable cartilage, *Plast. Reconstr. Surg.*, 96:1390–1398.

Park, A., B. Wu, and L.G.J. Griffith. 1998. Integration of surface modification and three-dimensional fabrication techniques to prepare patterned poly(L-lactide) substrates allowing regionally selective cell adhesion, *Biomater. Sci. Polym. Ed.*, 9:89–110.

Pitt, C.G. 1990. Poly-ε-caprolactone and its copolymers, in *Biodegradable Polymers as Drug Delivery Systems*, M. Chasin and R. Langer, Eds. New York: Dekker, pp. 71–120.

Roweton, S.L. 1994. A New Approach to the Formation of Tailored Microcellular Foams and Microtextured Surfaces of Absorbable and Non-Absorbable Thermoplastic Biomaterials, Master of Science thesis. Department of Bioengineering, Clemson University, Clemson, S.C.

Schugens, C., C. Grandfils, R. Jerome, P. Teyssie, P. Delree, D. Martin, B. Malgrange, and G. Moonen. 1995. Preparation of a macroporous biodegradable polylactide implant for neuronal transplantation, *J. Biomed. Mater. Res.*, 29:1349–1362.

Schuman, L., P. Buma, D. Versleyen, B. de Man, P.M. van der Kraan, W.B. van den Berg, and G.N. Homminga. 1995. Chondrocyte behavior within different types of collagen gel in-vitro, *Biomaterials*, 16:809–814.

Shalaby, S.W. and C.L. Linden, Jr. 1996. Radiochemical sterilization: a new approach to medical device processing, in *Irradiation of Polymers: Fundamentals and Technological Applications*, R.L. Clough and S.W. Shalaby, Eds. American Chemical Society: Washington, D.C., pp. 246–253.

Shalaby, S.W. and S.L. Roweton. 1997. Continuous Open-Cell Polymeric Foams Containing Living Cells, U.S. Patent 5,677,355.

Spargo, B.J., A.S. Rudolph, and F.M. Rollwagen. 1994. Recruitment of tissue resident cells to hydrogel composites: in-vivo response to implant materials, *Biomaterials*, 15:853–858.

Vainionpää, S., J. Kilpikari, J. Laiho, P. Helevirta, P. Rokkanen, and P. Tormala. 1987. Strength and strength retention in vitro, of absorbable, self-reinforced polyglycolide (PGA) rods for fracture fixation, *Biomaterials*, 8:46–48.

Van der Elst, M., C.P. Klein, J.M. de Blieck-Hogervorst, P. Patka, and H.J. Haarman. 1999. Bone tissue response to biodegradable polymers used for intra medullary fracture fixation: a long-term in vivo study in sheep femora, *Biomaterials*, 20:121–128.

Whang, K., T.K. Goldstick, and K.E. Healy. 2000. A biodegradable polymer scaffold for delivery of osteotropic factors, *Biomaterials*, 21:2545–2551.

Woodward, S.C. and T.N. Salthouse. 1986. The tissue response to implants and its evaluation by light microscopy, in *Handbook of Biomaterials Evaluation*, A.F. von Recum, Ed. New York: Macmillan Publishing Company, pp. 364–378.